

Occlusion of dentinal tubules by photoactive sintering of calcium phosphate minerals doped with erbium, aluminium and fluoride compounds

Esam B. Elmadani

Submitted in accordance with the requirements for the degree of
Doctor of Philosophy

The University of Leeds
Institute for Materials Research
School of Chemical and Process Engineering

May 2015

I confirm that the work submitted is my own and that appropriate credit has been given where reference has been made to the work of others.

This copy has been supplied on the understanding that it is copyright material and that no quotation from the thesis may be published without proper acknowledgement.

The right of Esam B. Elmadani to be identified as Author of this work has been asserted by him in accordance with the Copyright, Designs and Patents Act 1988.

© 2015 The University of Leeds and Esam B. Elmadani

Acknowledgements

I would like to express my appreciation to everyone who has directly and indirectly helped and participated in this research study. I would like to thank my supervisor Professor A. Jha and co – supervisor Professor M. Duggal for their support, encouragement, and guidance throughout this project.

I would like to thank the Paediatric Dentistry Department, School of Dentistry at the University of Leeds for their help and support on dental tissue preparation, the Photonic Materials and Devices Group at the University of Leeds and the Department of Physics and Astronomy at St. Andrews University for their collaboration in the laser irradiation trials, as well as the General Dental Council for their sponsorship of this project.

I would also like to thank the Energy and Resources Research Institute at the University of Leeds for their help on ICP/MS analysis, and the School of Electronic and Electric Engineering for their help on surface roughness analysis.

Finally, I would like to thank my parents and family for their support and encouragement, particularly throughout this project.

Abstract

Although the principles for the treatment of sensitive teeth are demonstrated successfully by many, the current treatments for tooth hypersensitivity are not effective in the long term or as a permanent solution.

The purpose of this research project was to investigate the occlusion of dentinal tubules by calcium phosphate minerals doped with erbium, aluminium, and fluoride compounds under laser irradiation. The investigation included the synthesis and characterisation of calcium phosphate (CaP) powders, preparation of hypersensitive dentine sections, and coating of dentine sections with CaP powders followed by laser irradiation.

CaP powders were synthesised by the chemical precipitation and hydrothermal methods. These powders were also chemically modified by the addition of different compounds (dopants) under various conditions to achieve substitutions for calcium, phosphate, and hydroxyl ions in the CaP structure. Dopants' compounds included erbium compounds (erbium oxide and erbium nitrate) to produce photoactive CaP minerals, aluminium compounds (aluminium phosphate and aluminium nitrate) and fluoride compounds (calcium fluoride and ammonium fluoride) to produce CaP minerals with high mechanical, chemical, and thermal stability. As well as chemically modifying the structure of CaP, the size and shape of CaP particles were investigated by varying pH and temperature of the synthesis method. The chemically modified CaP minerals were applied onto hypersensitive dentine sections by the dip coating method and laser irradiated by CW and pulsed lasers to achieve a complete occlusion of open

dentinal tubules. CaP powders in the form of pellets were also prepared for laser irradiation and acid erosion trials to determine their interaction with laser irradiation and solubility behaviour in an acid environment, respectively. CaP powders, CaP pellets, and laser irradiated – coated dentine sections were characterised using various analysis techniques, including SEM, SEM-EDX, static laser scattering, XRD, FTIR, DSC, ICP/MS, Micro – hardness, and Profile roughness.

Table of Contents

Acknowledgements	iii
Abstract	iv
Table of Contents	vi
List of Tables	x
List of Figures	xiv
List of Abbreviations	xxviii
Overview of the thesis contents	xxx
Chapter 1 Introduction	1
Teeth sensitivity (Dentine hypersensitivity)	1
Aims	2
Objectives	3
Chapter 2 Literature Review	5
2.1 Teeth sensitivity (Dentine hypersensitivity).....	5
2.2 Dental tissues (Teeth)	8
2.2.1 Enamel	9
2.2.2 Dentine	10
2.2.3 Cementum.....	12
2.2.4 Pulp and pulp cavity	13
2.3 Assessment and treatments of sensitive teeth	14
2.4 Sintering process.....	20
2.5 Laser background.....	25
2.5.1 Light/photon interaction with energy levels.....	30
2.5.1.1 Absorption, decay, and emission.....	31
2.5.1.2 Spontaneous and stimulated emission	33
2.5.2 Laser – tissue interaction	36
2.5.2.1 Laser – tissue interaction phenomena.....	38
2.5.2.1.1 Reflection and Refraction	38
2.5.2.1.2 Transmission	39
2.5.2.1.3 Absorption	39
2.5.2.1.4 Scattering	40
2.5.2.2 Laser – tissue interaction mechanisms	54
2.5.2.2.1 Photochemical interaction	54
2.5.2.2.2 Photothermal interaction.....	55

2.5.2.2.3 Photoablation	55
2.5.2.2.4 Plasma – induced ablation	56
2.5.2.2.5 Photodisruption	56
2.5.3. Dental lasers	57
2.6 Calcium phosphates (CaP)	62
2.6.1 Calcium orthophosphates.....	63
2.6.1.1 Monocalcium phosphate (MCP)	63
2.6.1.2 Dicalcium phosphate (DCP)	64
2.6.1.3 Octacalcium phosphate (OCP).....	65
2.6.1.4 Tricalcium phosphate (TCP).....	65
2.6.1.5 Tetracalcium phosphate (TTCP)	66
2.6.1.6 Amorphous calcium phosphate (ACP)	67
2.6.1.7 Apatites	68
2.6.1.7.1 Synthetic apatites	69
2.6.1.7.2 Biological apatites	76
2.6.2 Applications of calcium orthophosphates	79
2.6.2.1 Implant coating	79
2.6.2.2 Tissue engineering	79
2.6.2.3 Dental applications	80
2.6.2.4 Targeted drug delivery applications	81
2.6.2.5 Food industry applications.....	81
2.6.3 Calcium orthophosphate synthesis	82
2.6.3.1 Chemical precipitation method	84
2.6.3.2 Sol – gel method	91
2.6.3.3 Hydrothermal method.....	96
2.6.3.4 Synthesis methods used in this work	102
2.7 Doping of calcium orthophosphates	103
2.7.1 Rare earths (RE)	104
2.7.1.1 Internal $f-f$ electronic transitions.....	105
2.7.1.2 Transition cross sections.....	106
2.7.1.3 Lifetime (Decay time)	107
2.7.2 Aluminium compounds	114
2.7.3 Fluoride compounds.....	120
2.8 Properties of calcium orthophosphates and doping compounds.....	124
2.8.1 Properties of calcium orthophosphates	124

2.8.2 Properties of doping compounds.....	129
Chapter 3 Experimental Techniques	138
3.1 Calcium phosphate powder synthesis	139
3.1.1 Chemical precipitation of calcium phosphates.....	140
3.1.2 Hydrothermal synthesis of calcium phosphates	141
3.1.3 Doping of calcium phosphates	141
3.2 Calcium phosphate pellet preparation	143
3.3 Dentine section preparation.....	143
3.4 Dentine section coating and dentinal tubule occlusion	144
3.5 Laser irradiation sintering	145
3.6 Acid erosion of CaP pellets	148
3.7 Characterisation techniques.....	149
3.7.1 Particle size analysis	161
3.7.2 Scanning electron microscope (SEM)	164
3.7.3 X – ray diffraction (XRD)	168
3.7.4 Fourier transform infrared spectroscopy (FTIR)	170
3.7.5 Thermal analysis	176
3.7.6 Micro – hardness measurements	177
3.7.7 Inductively – coupled plasma/mass spectrometry (ICP/MS)	178
3.7.8 Profile roughness (Profilometry)	180
Chapter 4 Results and Discussions	183
Chapter 4.1 Synthesis and characterisation of calcium phosphates	184
4.1.1 CaP (pH 5.4 ± 0.2, RT).....	196
4.1.2 CaP (pH 10 ± 0.2, RT).....	207
4.1.3 CaP (pH 5.4 ± 0.2, 200°C hydrothermal).....	212
4.1.4 CaP (pH 10 ± 0.2, 200°C hydrothermal).....	217
4.1.5 Main findings	240
Chapter 4.2 Synthesis and characterisation of doped calcium phosphates	243
4.2.1 Doped CaP powders (batch A).....	245
4.2.1.1 Doped CaP batch A (pH 5.4 ± 0.2, RT)	245
4.2.1.2 Doped CaP batch A (pH 10 ± 0.2, RT)	255
4.2.1.3 Doped CaP batch A (pH 5.4 ± 0.2, 200°C hydrothermal)	261

4.2.1.4 Doped CaP batch A (pH 10 ± 0.2, 200°C hydrothermal).....	267
4.2.2 Doped CaP powders (batch B).....	288
4.2.2.1 Doped CaP batch B (pH 5.4 ± 0.2, RT).....	288
4.2.2.2 Doped CaP batch B (pH 10 ± 0.2, RT).....	295
4.2.2.3 Doped CaP batch B (pH 5.4 ± 0.2, 200°C hydrothermal).....	301
4.2.2.4 Doped CaP batch B (pH 10 ± 0.2, 200°C hydrothermal).....	306
4.2.3 Main findings	326
Chapter 4.3 Laser irradiation sintering investigation.....	329
4.3.1 Characterisation of prepared dentine sections	329
4.3.2 Characterisation of coatings.....	330
4.3.3 Laser irradiation sintering trials	332
4.3.3.1 Characterisation of laser – irradiated CaP pellets	333
4.3.3.2 Characterisation of laser – irradiated uncoated/coated dentine sections.....	337
4.3.3.2.1 First laser irradiation sintering trial	337
4.3.3.2.2 Second laser irradiation sintering trial	340
4.3.3.2.3 Third laser irradiation sintering trials.....	344
4.3.3.2.4 Characterisation of laser – irradiated CaP coatings.....	364
4.3.3.3 Temperature change during laser irradiation sintering ..	366
4.3.3.4 Micro – hardness of uncoated/coated dentine sections.....	367
4.3.3.5 Characterisation of acid eroded CaP pellets	369
4.3.3.5.1 pH variation measurements	371
4.3.3.5.2 Inductively – coupled plasma/mass spectroscopy.....	373
4.3.3.5.3 SEM-EDX measurements	379
4.3.3.5.4 Profile roughness measurements.....	380
4.3.4 Comparison between none and laser – irradiated coatings.....	383
4.3.5 Main findings	384
Chapter 5 Conclusions and Future Work.....	388
5.1 Conclusions.....	388
5.2 Suggestions for future work.....	392
List of References	394

List of Tables

Table 2.1 Tubules number and diameter ratios of hypersensitive dentine and non – sensitive dentine (3).....	10
Table 2.2 Summary of current possible treatments and materials for tooth hypersensitivity	19
Table 2.3 Wavelength ranges of different types of light spectrum (81, 82).....	26
Table 2.4 Summary of important commercially available lasers (83)	29
Table 2.5 Optical properties (Absorption coefficient $\mu_a \text{ cm}^{-1}$ and scattering coefficient $\mu_s \text{ cm}^{-1}$) for different light spectra and wavelengths in hard dental tissues (enamel and dentine) (86, 87, 89, 91-99).....	45
Table 2.6 Optical penetration depths for different light spectra and wavelengths in enamel and dentine (51, 56, 63, 86, 91, 94, 100-104).....	46
Table 2.7 Optical ablation/removal depths for pulsed and CW lasers in hard dental tissues enamel and dentine (117, 118).....	50
Table 2.8 Lasers and wavelengths used in dentistry (122, 123).....	61
Table 2.9 Properties and physical constants of calcium orthophosphates under standard conditions (pressure of 1 atm at RT ~ 25°C) (268-276).....	74
Table 2.10 Crystallographic data of calcium orthophosphates (146, 201, 202, 221, 277-283).....	75
Table 2.11 Unit cell parameters (average) of bone, dentine, enamel, and synthetic HAp	78
Table 2.12 Mechanical properties of biological and synthetic calcium phosphates (504)	128
Table 2.13 Physical constants of erbium oxide, aluminium phosphate, and calcium fluoride under standard conditions (pressure of 1 atm at RT ~ 25°C) (268, 505).....	130
Table 2.14 Physical constants of erbium nitrate pentahydrate, aluminium nitrate nonahydrate and ammonium fluoride under standard conditions (pressure of 1 atm at RT ~ 25°C) (268, 505).....	130
Table 3.1 Synthesis conditions for calcium phosphates	140
Table 3.2 List of various compounds investigated in the present study.....	141
Table 3.3 Solubility chart for CaP synthesis at room temperature under pressure of 1 atm	142
Table 3.4 Pulsed and CW laser parameters used in the laser irradiation sintering of coated dentine sections and CaP/doped CaP pellets	147

Table 3.5 List of analysis techniques and parameters used for characterisation.....	150
Table 3.6 Particle characteristics related to size, a particular measurable behaviour that varies as a function of particle size, and other variables that affect the size (531)	154
Table 3.7 Size measurement techniques, theoretical models and their assumptions (531).....	155
Table 3.8 Common functional groups and their absorption band frequencies (539, 540)	175
Table 3.9 Common inorganic ions (anionic groups) and their vibrational (stretching and bending) group frequencies (539, 540).....	175
Table 4.1.1 Synthesis conditions for CaP powders	184
Table 4.1.2 SEM-EDX measurements (element weight percentage) for CaP synthesised under room temperature and as – prepared pH 5.4 ± 0.2 conditions (first and second reactions)	199
Table 4.1.3 XRD 2 theta (2θ [°]), d – spacing (d [Å]), intensity (I [%]), and Miller indices (<i>hkl</i>) for monetite JCPDS file 01-070-1425 and CaP-undoped pH5 RT, 1 st reaction	202
Table 4.1.4 XRD 2 theta (2θ [°]), d – spacing (d [Å]), intensity (I [%]), and Miller indices (<i>hkl</i>) for brushite JCPDS file 01-072-0713 and CaP-undoped pH5 RT, 2 nd reaction	202
Table 4.1.5 Unit cell parameters for CaP-undoped pH5 RT (1st reaction) and CaP-undoped pH5 RT (2nd reaction), compared to those of monetite JCPDS file 01-070-1425 and brushite JCPDS file 01-072-0713	203
Table 4.1.6 SEM-EDX measurements (element weight percentage) for CaP synthesised under room temperature and pH 10 ± 0.2 conditions	209
Table 4.1.7 XRD 2 theta (2θ [°]), d – spacing (d [Å]), intensity (I [%]), and Miller indices (<i>hkl</i>) for HAp JCPDS file 009-0432, brushite JCPDS file 01-072-0713, and CaP pH 10 RT	211
Table 4.1.8 SEM-EDX measurements (element weight percentage) for CaP synthesised under as – prepared pH 5.4 ± 0.2 and 200°C hydrothermal conditions	214
Table 4.1.9 XRD 2 theta (2θ [°]), d – spacing (d [Å]), intensity (I [%]), and Miller indices (<i>hkl</i>) for HAp JCPDS file 009-0432 and CaP pH 5 200°C hydrothermal	216
Table 4.1.10 SEM-EDX measurements (element weight percentage) for CaP synthesised under pH 10 ± 0.2 and 200°C hydrothermal conditions	219
Table 4.1.11 XRD 2 theta (2θ [°]), d – spacing (d [Å]), intensity (I [%]), and Miller indices (<i>hkl</i>) for Monetite JCPDS file 01-070-1425 and CaP pH10 200°C hydrothermal.....	223

Table 4.1.12 XRD 2 theta (2θ [°]), d – spacing (d [Å]), intensity (I [%]), and Miller indices (<i>hkl</i>) for HAp JCPDS file 009-0432 and CaP pH10 200°C hydrothermal.....	223
Table 4.1.13 Particle size data for CaP powders.....	225
Table 4.1.14 Characteristic absorption bands of functional groups for HAp (552).....	227
Table 4.1.15 Characteristic absorption bands of functional groups for brushite (553).....	228
Table 4.1.16 Characteristic absorption bands of functional groups for monetite (553).....	229
Table 4.1.17 Characteristic IR Absorption Frequencies (cm^{-1}) of CaP powder functional groups, compared to reported data (552, 553) as a reference.....	236
Table 4.1.18 DSC peak centres of CaP powders (second reaction).....	239
Table 4.2.1 Synthesis conditions for doped calcium phosphate powders.....	243
Table 4.2.2 SEM-EDX measurements (element weight percentage) for doped CaP (batch A) synthesised under room temperature and as – prepared pH 5.4 ± 0.2 conditions.....	247
Table 4.2.3 Unit cell parameters for doped CaP powder (Batch A) synthesised under room temperature and as – prepared pH 5.4 ± 0.2 conditions, compared to those of brushite JCPDS file 01-072-0713.....	251
Table 4.2.4 SEM-EDX measurements (element weight percentage) for doped CaP (batch A) synthesised under room temperature and pH 10 ± 0.2 conditions.....	257
Table 4.2.5 SEM-EDX measurements (element weight percentage) for doped CaP (batch A) synthesised under as – prepared pH 5.4 ± 0.2 and 200°C hydrothermal conditions.....	263
Table 4.2.6 SEMEDX measurements (element weight percentage) for doped CaP (batch A) synthesised under pH 10 ± 0.2 and 200°C hydrothermal conditions.....	269
Table 4.2.7 TEM – EDX measurements (element weight percentage) for doped CaP synthesised under room temperature and as – prepared pH 5.4 ± 0.2 conditions.....	274
Table 4.2.8 Particle size data for doped CaP (batch A) powders.....	276
Table 4.2.9 Characteristic IR absorption frequencies (cm^{-1}) of functional groups for doped CaP powder (batch A), compared to those of reported data (552, 553, 564-566, 569).....	284
Table 4.2.10 DSC peak centres for doped CaP powders (batch A).....	286
Table 4.2.11 SEM-EDX measurements (element weight percentage) for doped CaP powder (batch B) synthesised under room temperature and as – prepared pH 5.4 ± 0.2 conditions.....	290

Table 4.2.12 Unit cell parameters for doped CaP powder (batch B) synthesised under room temperature and as – prepared pH 5.4 ± 0.2 conditions, compared to those of monetite JCPDS file 01-070-1425	293
Table 4.2.13 SEM-EDX measurements (element weight percentage) for doped CaP (batch B) synthesised under room temperature and pH 10 ± 0.2 conditions.....	298
Table 4.2.14 SEM-EDX measurements (element weight percentage) for doped CaP powder (batch B) synthesised under as – prepared pH 5.4 ± 0.2 and 200°C hydrothermal conditions.....	303
Table 4.2.15 SEM-EDX measurements (element weight percentage) for doped CaP powder (batch B) synthesised under pH 10 ± 0.2 and 200°C hydrothermal conditions	308
Table 4.2.16 Particle size data for doped CaP (batch B) powders	313
Table 4.2.17 Characteristic IR absorption frequencies (cm^{-1}) of functional groups for doped CaP powders (batch B), compared to those of reported data (495, 552, 553, 569).....	320
Table 4.2.18 DSC peak centres for CaP-doped (batch B) powders	322
Table 4.3.1 Temperature change measurements during 980 nm CW laser irradiation.....	366
Table 4.3.2 Micro – hardness measurements of laser – irradiated dentine sections	368
Table 4.3.3 pH values of 0.3% citric acid solution that contained the CaP and doped CaP pellets (unsintered, furnace sintered, and laser sintered) after 24 hour reaction	372
Table 4.3.4 Inductively – coupled plasma/mass spectrometry (ICP/MS) of the acid solutions that contained CaP pellets for 24 hours.....	375
Table 4.3.5 Inductively – coupled plasma/mass spectrometry (ICP/MS) of the acid solutions that contained doped CaP pellets for 24 hours	376
Table 4.3.6 ICP/MS comparison between the acid solutions that contained CaP pellets and those contained doped CaP pellets, as a function of solution calcium and phosphate concentrations	377
Table 4.3.7 SEM-EDX measurements (element weight percentage) of the citric acid solutions that contained doped CaP pellets after a 24 – hour reaction	379
Table 4.3.8 Profile roughness parameters (R_q and R_a) for CaP and doped CaP pellets (unsintered, furnace sintered. and laser sintered) before and after citric acid erosion	381
Table 4.3.9 Surface uniformity of CaP and doped CaP pellets (unsintered, furnace sintered and laser sintered) before and after citric acid erosion	382

List of Figures

Figure 2.1 Schematic of a tooth cross section indicating gum recession and exposed dentinal tubules.....	6
Figure 2.2 Schematic of a tooth cross section indicating main component parts of a natural tooth.....	9
Figure 2.4 Schematic of a dentine cross section indicating dentinal tubules, peritubular dentine and intertubular dentine.....	12
Figure 2.5 Schematic of a transverse electromagnetic wave (83).	26
Figure 2.6 Schematic indicating Bohr atom and its energy levels.	31
Figure 2.7 Schematic of atomic energy levels indicating different excitation states, to which an electron can be excited from the ground state E_1	33
Figure 2.8 Schematic indicating photon absorption.....	34
Figure 2.9 Schematic indicating spontaneous emission.....	34
Figure 2.10 Schematic indicating stimulated emission.	35
Figure 2.11 Schematic of energy levels showing photon absorption and photon's relaxation/decay routes to the ground level. (a) Thermalisation, through collision and vibrational relaxation, (b) fluorescence, through a short – lived photon emission, and (c) phosphorescence, through a long – lived photon emission (90).....	36
Figure 2.12 Schematic of the crystal structure of hydroxyapatite (HAp).....	70
Figure 2.13 Schematic of the crystal structure of fluorapatite (FAP).....	70
Figure 2.14 Flow chart for obtaining HAp by the chemical precipitation method.	85
Figure 2.15 Flow chart for obtaining HAp by the sol – gel method.	93
Figure 2.16 Flow chart for obtaining HAp by the hydrothermal method.....	98
Figure 2.17 Schematic showing the absorption bands of rare earth ions (in solutions) in the visible region (with no absorption for ytterbium) (398).....	108
Figure 3.1 TEM-EDX spectra of CaP and doped CaP powders, showing discounted element (Si, Cu, and C) from the analysis.	167
Figure 3.2 Schematic of Vickers diamond indenter.	177
Figure 3.3 Schematic of Knoop diamond indenter.....	178
Figure 3.4 Schematic of roughness profile parameters R_a and R_q	181
Figure 4.1.1 SEM of CaP particles prepared by the chemical precipitation method under room temperature and as – prepared pH 5.4 ± 0.2 conditions, showing platelet – like morphology of particles.....	185

Figure 4.1.2 XRD pattern of CaP powder prepared by the chemical precipitation method under room temperature and as – prepared pH 5.4 ± 0.2 conditions. Marked peaks (●) were assigned to monetite JCPDS file 01-070-1425.....	186
Figure 4.1.3 SEM of CaP particles synthesised under as – prepared pH 5.4 ± 0.2 and 80°C hydrothermal conditions for (a) 24 hours, (b) 48 hours, and (c) 72 hours.	187
Figure 4.1.4 SEM of CaP particles synthesised under as – prepared pH 5.4 ± 0.2 and 200°C hydrothermal conditions for (a) 24 hours and (b) 72 hours.....	188
Figure 4.1.5 SEM of CaP particles synthesised under as – prepared pH 5.4 ± 0.2 and 200°C hydrothermal conditions for 24 hours, after initial ageing of CaP mixture for (a) 2 weeks, (b) 4 weeks, and (c) 6 weeks.	189
Figure 4.1.6 XRD patterns of CaP powders prepared from solutions aged for 2, 4, and 6 weeks and treated hydrothermally at 200°C for 24 hours. Marked peaks (●) were assigned to monetite JCPDS file 01-070-1425.	190
Figure 4.1.7 SEM of CaP particles synthesised under 200°C hydrothermal conditions for 24 hours, with (a) pH 8 ± 0.2 , (b) pH 9 ± 0.2 , (c) pH 10 ± 0.2 , and (d) pH 11 ± 0.2	193
Figure 4.1.8 XRD patterns of CaP powders synthesised from mixtures with pH 8 ± 0.2 , 9 ± 0.2 , 10 ± 0.2 , and 11 ± 0.2 by the hydrothermal method at 200°C for 24 hours. Marked peaks (●) were assigned to HAp JCPDS file 009-0432, and (◆) were assigned to monetite JCPDS file 01-070-1425.....	194
Figure 4.1.9 SEM of CaP particles synthesised under pH 10 ± 0.2 and 140°C hydrothermal conditions for (a) 24 hours and (b) 72 hours.....	195
Figure 4.1.10 SEM of CaP particles synthesised under room temperature and pH 5.4 ± 0.2 conditions, by (a) the first reaction (fast addition for 15 minutes and stirring for 30 minutes) and (b) the second reaction (slow addition for 30 minutes and stirring for 60 minutes).....	198
Figure 4.1.11 Particle size distribution of CaP synthesised under room temperature and pH 5.4 ± 0.2 conditions, by the second reaction (slow addition for 30 minutes and stirring for 60 minutes).	198
Figure 4.1.12 Statistics graph of CaP synthesised under room temperature and pH 5.4 ± 0.2 conditions by the second reaction (addition for 30 minutes and stirring for 60 minutes), showing the mean with ± 1 standard deviation error bar.	199
Figure 4.1.13 XRD pattern of CaP synthesised under room temperature and as – prepared pH 5.4 ± 0.2 conditions by the first reaction (addition for 15 minutes and stirring for 30 minutes). Marked peaks (●) were assigned to monetite JCPDS file 01-070-1425.	201

Figure 4.1.14 XRD pattern of CaP synthesised under room temperature and as – prepared pH 5.4 ± 0.2 conditions by the second reaction (addition for 30 minutes and stirring for 60 minutes). Marked peaks (●) were assigned to brushite JCPDS file 01-072-0713, while one peak (◆) was assigned to monetite JCPDS file 01-070-1425.....	201
Figure 4.1.15 Hot stage XRD at 200°C of CaP synthesised under room temperature and as – prepared pH 5.4 ± 0.2 conditions by the second reaction, compared to monetite JCPDS file 01-070-1425. Marked peaks (●) were assigned to monetite.....	205
Figure 4.1.16 Hot stage XRD at 400°C of CaP synthesised under room temperature and as – prepared pH 5.4 ± 0.2 conditions by the second reaction, compared to calcium pyrophosphate JCPDS file 00-009-0346. Marked peaks (●) were assigned to calcium pyrophosphate (β -Ca ₂ P ₂ O ₇).....	205
Figure 4.1.17 Hot stage XRD at 600°C of CaP synthesised under room temperature and as – prepared pH 5.4 ± 0.2 conditions by the second reaction, compared to calcium pyrophosphate JCPDS file 00-009-0346. Marked peaks (●) were assigned to calcium pyrophosphate (β -Ca ₂ P ₂ O ₇).....	206
Figure 4.1.18 Hot stage XRD at 800°C of CaP synthesised under room temperature and as – prepared pH 5.4 ± 0.2 conditions by the second reaction, compared to calcium pyrophosphate JCPDS file 00-009-0346. Marked peaks (●) were assigned to calcium pyrophosphate (β -Ca ₂ P ₂ O ₇).....	206
Figure 4.1.19 SEM of CaP particles synthesised under room temperature and pH 10 ± 0.2 conditions, showing (a) micrometre agglomerated particles and (b) nanometre platelet – like CaP particles.....	208
Figure 4.1.20 Particle size distribution of CaP synthesised under room temperature and pH 10 ± 0.2 conditions.	208
Figure 4.1.21 Statistics graph of CaP synthesised under room temperature and pH 10 ± 0.2 conditions, showing the mean with ± 1 standard deviation error bar.	209
Figure 4.1.22 SEM of CaP synthesised under room temperature and pH 10 ± 0.2 conditions, showing the obtained EDX spectra.....	210
Figure 4.1.23 XRD pattern of CaP synthesised under room temperature and pH 10 ± 0.2 conditions. Marked peaks (●) were assigned to HAp JCPDS file 009-0432 and (◆) were assigned to brushite JCPDS file 01-072-0713.....	211
Figure 4.1.24 SEM of CaP synthesised under as – prepared pH 5.4 ± 0.2 and 200°C hydrothermal conditions, showing (a) micrometre agglomerates/clusters of CaP particles and (b) nanometre rod – like CaP particles.....	213
Figure 4.1.25 Particle size distribution of CaP synthesised under pH 5.4 ± 0.2 and 200°C hydrothermal conditions.	213

Figure 4.1.26 Statistics graph of CaP synthesised under pH 5.4 ± 0.2 and 200°C hydrothermal conditions, showing the mean with ± 1 standard deviation error bar.	214
Figure 4.1.27 SEM of CaP synthesised under as – prepared pH 5.4 ± 0.2 and 200°C hydrothermal conditions, showing the obtained EDX spectra.	215
Figure 4.1.28 XRD pattern of CaP synthesised under as – prepared pH 5.4 ± 0.2 and 200°C hydrothermal conditions, compared to HAp JCPDS file 009-0432. Marked peaks (●) were assigned to HAp.	216
Figure 4.1.29 SEM of CaP powder synthesised under pH 10 ± 0.2 and 200°C hydrothermal conditions, showing (a) micrometre agglomerates/clusters of CaP particles and (b) platelet – like and needle – like particles.	218
Figure 4.1.30 Particle size distribution of CaP synthesised under pH 10 ± 0.2 and 200°C hydrothermal conditions.	218
Figure 4.1.31 Statistics graph of CaP synthesised under pH 10 ± 0.2 and 200°C hydrothermal conditions, showing the mean with ± 1 standard deviation error bar.	219
Figure 4.1.32 SEM of CaP synthesised under pH 10 ± 0.2 and 200°C hydrothermal conditions, showing the obtained EDX spectra.	220
Figure 4.1.33 XRD pattern of CaP synthesised under pH 10 ± 0.2 and 200°C hydrothermal conditions, compared to the CaP synthesised under pH 8 ± 0.2 , pH 10 ± 0.2 and 200°C hydrothermal conditions from the initial investigation. Marked peaks (●) were assigned to HAp and (◆) were assigned to monetite.	222
Figure 4.1.34 XRD pattern of CaP synthesised under pH 10 ± 0.2 and 200°C hydrothermal conditions, compared to HAp JCPDS file 009-0432 and monetite JCPDS file 01-070-1425. Marked peaks (●) were assigned to HAp and (◆) were assigned to monetite.	222
Figure 4.1.35 FTIR spectra of CaP powders in the mid – infrared region and wavenumber range $1300 - 400 \text{ cm}^{-1}$	231
Figure 4.1.36 FTIR spectra of CaP powders in the mid – infrared region and wavenumber range $2500 - 1400 \text{ cm}^{-1}$	232
Figure 4.1.37 FTIR spectra of CaP powders in the mid – infrared region and wavenumber range $4000 - 3000 \text{ cm}^{-1}$	232
Figure 4.1.38 DSC of CaP powders (Endo up).	239
Figure 4.2.1 SEM of doped CaP powders (batch A) synthesised under room temperature and as – prepared pH 5.4 ± 0.2 conditions, showing (a) platelet – like particles and (b) nanoparticles fused to surface of platelet – like particles.	246
Figure 4.2.2 Particle size distribution of doped CaP (batch A) synthesised under room temperature and pH 5.4 ± 0.2 conditions. ...	246

Figure 4.2.3 Statistics graph of doped CaP (batch A) synthesised under room temperature and pH 5.4 ± 0.2 conditions, showing the mean with ± 1 standard deviation error bar.	247
Figure 4.2.4 SEM of doped CaP synthesised under room temperature and as – prepared pH 5.4 ± 0.2 conditions, showing the obtained EDX spectra.	248
Figure 4.2.5 XRD pattern of doped CaP powder (batch A) synthesised under room temperature and as – prepared pH 5.4 ± 0.2 conditions, compared to brushite, monetite, Er_2O_3 , AlPO_4 , and CaF_2 JCPDS files. Marked peaks (●) were assigned to brushite, (▼) were assigned to monetite, (◆) were assigned to Er_2O_3 , (▲) were assigned to AlPO_4 , and (■) were assigned to CaF_2	249
Figure 4.2.6 XRD pattern of doped CaP (batch A) synthesised under room temperature and as – prepared pH 5.4 ± 0.2 conditions, compared to that of CaP (CaP-undoped pH5 RT). Marked peaks (●) were assigned to brushite, (▼) were assigned to monetite, (◆) were assigned to Er_2O_3 , (▲) were assigned to AlPO_4 , and (■) were assigned to CaF_2	250
Figure 4.2.7 Hot stage XRD at 200°C of doped CaP (batch A) synthesised under room temperature and as – prepared pH 5.4 ± 0.2 conditions, compared to monetite JCPDS file 01-070-1425. Marked peaks (●) were assigned to monetite.	253
Figure 4.2.8 Hot stage XRD at 400°C of doped CaP (batch A) synthesised under room temperature and as – prepared pH 5.4 ± 0.2 conditions, compared to calcium pyrophosphate JCPDS file 00-009-0346. Marked peaks (●) were assigned to β – calcium pyrophosphate.	253
Figure 4.2.9 Hot stage XRD at 600°C of doped CaP (batch A) synthesised under room temperature and as – prepared pH 5.4 ± 0.2 conditions, compared to β – calcium pyrophosphate JCPDS file 00-009-0346. Marked peaks (●) were assigned to β – calcium pyrophosphate.	254
Figure 4.2.10 Hot stage XRD at 800°C of doped CaP (batch A) synthesised under room temperature and as – prepared pH 5.4 ± 0.2 conditions, compared to β – calcium pyrophosphate JCPDS file 00-009-0346. Marked peaks (●) were assigned to β – calcium pyrophosphate.	254
Figure 4.2.11 SEM of doped CaP (batch A) synthesised under room temperature and pH 10 ± 0.2 conditions, showing (a) continuous and uniform layer and (b) spherical particles that seem to be fused together.	256
Figure 4.2.12 Particle size distribution of doped CaP (batch A) synthesised under room temperature and pH 10 ± 0.2 conditions. ...	256
Figure 4.2.13 Statistics graph of doped CaP (batch A) synthesised under room temperature and pH 10 ± 0.2 conditions, showing the mean with ± 1 standard deviation error bar.	257

Figure 4.2.14 SEM of doped CaP synthesised under room temperature and pH 10 ± 0.2 conditions, showing the obtained EDX spectra.	258
Figure 4.2.15 XRD pattern of doped CaP (batch A) synthesised under room temperature and pH 10 ± 0.2 conditions, compared to HAp, Er_2O_3 , AlPO_4 , and CaF_2 JCPDS files. Marked peaks (●) were assigned to brushite, (◆) were assigned to Er_2O_3 , (▲) were assigned to AlPO_4 , and (■) were assigned to CaF_2	259
Figure 4.2.16 XRD pattern of doped CaP (batch A) synthesised under room temperature and pH 10 ± 0.2 conditions, compared to that of CaP (CaP-undoped pH 10 RT). Marked peaks (●) were assigned to brushite, (◆) were assigned to Er_2O_3 , (▲) were assigned to AlPO_4 , and (■) were assigned to CaF_2	260
Figure 4.2.17 SEM of doped CaP (batch A) synthesised under as – prepared pH 5.4 ± 0.2 and 200°C hydrothermal conditions, showing (a) non – uniform morphology of particles and (b) fusion and agglomeration of particles.	262
Figure 4.2.18 Particle size distribution of doped CaP (batch A) synthesised under pH 5.4 ± 0.2 and 200°C hydrothermal conditions.	262
Figure 4.2.19 Statistics graph of doped CaP (batch A) synthesised under pH 5.4 ± 0.2 and 200°C hydrothermal conditions, showing the mean with ± 1 standard deviation error bar.	263
Figure 4.2.20 SEM of doped CaP synthesised under as – prepared pH 5.4 ± 0.2 and 200°C hydrothermal conditions, showing the obtained EDX spectra.	264
Figure 4.2.21 XRD pattern of doped CaP (batch A) synthesised under as – prepared pH 5.4 ± 0.2 and 200°C hydrothermal conditions, compared to brushite, Er_2O_3 , AlPO_4 , and CaF_2 JCPDS files. Marked peaks (●) were assigned to brushite, (◆) were assigned to Er_2O_3 , (▲) were assigned to AlPO_4 , and (■) were assigned to CaF_2	265
Figure 4.2.22 XRD pattern of doped CaP (batch A) synthesised under as – prepared pH 5.4 ± 0.2 and 200°C hydrothermal conditions, compared to that of CaP (HAp) (CaP-undoped pH5 200°C hydrothermal). Marked peaks (●) were assigned to brushite, (◆) were assigned to Er_2O_3 , (▲) were assigned to AlPO_4 , and (■) were assigned to CaF_2	266
Figure 4.2.23 SEM of doped CaP (batch A) synthesised under pH 10 ± 0.2 and 200°C hydrothermal conditions, showing (a) spherical particles and (b) rod/needle – like particles.	268
Figure 4.2.24 Particle size distribution of doped CaP (batch A) synthesised under pH 10 ± 0.2 and 200°C hydrothermal conditions.	268
Figure 4.2.25 Statistics graph of doped CaP (batch A) synthesised under pH 10 ± 0.2 and 200°C hydrothermal conditions, showing the mean with ± 1 standard deviation error bar.	269

Figure 4.2.26 SEM of doped CaP synthesised under pH 10 ± 0.2 and 200°C hydrothermal conditions, showing the obtained EDX spectra.	270
Figure 4.2.27 XRD pattern of doped CaP (batch A) synthesised under pH 10 ± 0.2 and 200°C hydrothermal conditions, compared to HAp, Er_2O_3 , AlPO_4 , and CaF_2 JCPDS files. Marked peaks (●) were assigned to HAp, (◆) were assigned to Er_2O_3 , (▲) were assigned to AlPO_4 , and (■) were assigned to CaF_2	271
Figure 4.2.28 XRD pattern of doped CaP (batch A) synthesised under pH 10 ± 0.2 and 200°C hydrothermal conditions, compared to that of CaP (CaP-undoped pH10 200°C hydrothermal) synthesised under the same conditions. Marked peaks (●) were assigned to HAp, (◆) were assigned to Er_2O_3 , (▲) were assigned to AlPO_4 , and (■) were assigned to CaF_2	272
Figure 4.2.29 TEM of doped CaP synthesised under room temperature and as – prepared pH 5.4 ± 0.2 conditions, showing the obtained EDX spectra.	274
Figure 4.2.30 FTIR spectra of doped CaP powders (batch A) in the MIR region and wavenumber range $1300 - 400 \text{ cm}^{-1}$	282
Figure 4.2.31 FTIR spectra of doped CaP powders (batch A) in the MIR region and wavenumber range $2500 - 1400 \text{ cm}^{-1}$	282
Figure 4.2.32 FTIR spectra of doped CaP powders (batch A) in the NIR region and wavenumber range $4000 - 3000 \text{ cm}^{-1}$	283
Figure 4.2.33 DSC of doped CaP powders (batch A) (Endo up).	286
Figure 4.2.34 TGA of CaP-doped batch A pH5 RT ($\text{CaP-AlPO}_4.\text{Er}_2\text{O}_3.\text{CaF}_2$), compared to CaP-undoped pH5 RT (CaP-only), CaP-AlPO_4 , and $\text{CaP-AlPO}_4.\text{Er}_2\text{O}_3$	287
Figure 4.2.35 SEM of doped CaP powder (batch B) synthesised under room temperature and as – prepared pH 5.4 ± 0.2 conditions, showing (a) platelet – like and needle – like particles and (b) the formation of a platelet – like particle by the lateral aggregation of needle – like particles and bonding of particles by the diffusion of atoms to the interface of particles due to a driving energy.	289
Figure 4.2.36 Particle size distribution of doped CaP powder (batch B) synthesised under room temperature and as – prepared pH 5.4 ± 0.2 conditions.	289
Figure 4.2.37 Statistics graph of doped CaP powder (batch B) synthesised under room temperature and as – prepared pH 5.4 ± 0.2 conditions, showing the mean with ± 1 standard deviation error bar.	290
Figure 4.2.38 SEM of doped CaP powder (batch B) synthesised under room temperature and as – prepared pH 5.4 ± 0.2 conditions, showing the obtained EDX spectra.	291

Figure 4.2.39 XRD pattern of doped CaP powder (batch B) synthesised under room temperature and as – prepared pH 5.4 ± 0.2 conditions, compared to monetite JCPDS file 01-070-1425. Marked peaks (●) were assigned to doped monetite.	294
Figure 4.2.40 XRD pattern of doped CaP powder (batch B) synthesised under room temperature and as – prepared pH 5.4 ± 0.2 conditions (doped monetite), compared to that of CaP-undoped pH5 RT (brushite). Marked peaks (●) were assigned to doped monetite.	294
Figure 4.2.41 SEM of doped CaP powders (batch B) synthesised under room temperature and pH 10 ± 0.2 conditions, showing (a) agglomeration of rounded – like particles and (b) necking of nanoparticles.....	297
Figure 4.2.42 Particle size distribution of doped CaP powder (batch B) synthesised under room temperature and as – prepared pH 10 ± 0.2 conditions.	297
Figure 4.2.43 Statistics graph of doped CaP powder (batch B) synthesised under room temperature and pH 10 ± 0.2 conditions, showing the mean with ± 1 standard deviation error bar.	298
Figure 4.2.44 SEM of doped CaP powder (batch B) synthesised under room temperature and pH 10 ± 0.2 conditions, showing the obtained EDX spectra.	299
Figure 4.2.45 XRD pattern of doped CaP (batch B) synthesised under room temperature and pH 10 ± 0.2 conditions. Marked peaks (●) were assigned to doped HAp.	300
Figure 4.2.46 XRD pattern of doped CaP (batch B) synthesised under room temperature and pH 10 ± 0.2 conditions, compared to that of CaP (CaP-undoped pH10 RT). Marked peaks (●) were assigned to doped HAp.	300
Figure 4.2.47 SEM of doped CaP powder (batch B) synthesised under as – prepared pH 5.4 ± 0.2 and 200°C hydrothermal conditions, showing rounded – like particles at (a) lower magnification at $1 \mu\text{m}$ scale and (b) higher magnification at 200 nm scale.	302
Figure 4.2.48 Particle size distribution of doped CaP powder (batch B) synthesised under as – prepared pH 5.4 ± 0.2 and 200°C hydrothermal conditions.	302
Figure 4.2.49 Statistics graph of doped CaP powder (batch B) synthesised under as – prepared pH 5.4 ± 0.2 and 200°C hydrothermal conditions, showing the mean with ± 1 standard deviation error bar.	303
Figure 4.2.50 SEM of doped CaP powder (batch B) synthesised under as – prepared pH 5.4 ± 0.2 and 200°C hydrothermal conditions, showing the obtained EDX spectra.	304

Figure 4.2.51 XRD pattern of doped CaP powder (batch B) synthesised under as – prepared pH 5.4 ± 0.2 and 200°C hydrothermal conditions. Marked peaks (●) were assigned to doped HAp.	305
Figure 4.2.52 XRD pattern of doped CaP powder (batch B) synthesised under as – prepared pH 5.4 ± 0.2 and 200°C hydrothermal conditions, compared to that of CaP under the same conditions. Marked peaks (●) were assigned to doped HAp.	305
Figure 4.2.53 SEM of doped CaP powder (batch B) synthesised under pH 10 ± 0.2 and 200°C hydrothermal conditions, showing (a) agglomerations/clusters of particles and (b) rod – like nanoparticles.	307
Figure 4.2.54 Particle size distribution of doped CaP powder (batch B) synthesised under pH 10 ± 0.2 and 200°C hydrothermal conditions.	307
Figure 4.2.55 Statistics graph of doped CaP powder (batch B) synthesised under pH 10 ± 0.2 and 200°C hydrothermal conditions, showing the mean with ± 1 standard deviation error bar.	308
Figure 4.2.56 SEM of doped CaP powder (batch B) synthesised under pH 10 ± 0.2 and 200°C hydrothermal conditions, showing the obtained EDX spectra.	309
Figure 4.2.57 XRD pattern of doped CaP powder (batch B) synthesised under pH 10 ± 0.2 and 200°C hydrothermal conditions. Marked peaks (●) were assigned to doped HAp.	310
Figure 4.2.58 XRD pattern of doped CaP powder (batch B) synthesised under pH 10 ± 0.2 and 200°C hydrothermal conditions, compared to those of CaP (CaP-undoped pH10 200°C hydrothermal and CaP-undoped pH10 200°C hydrothermal (initial investigation)). Marked peaks (●) were assigned to doped HAp.	310
Figure 4.2.59 FTIR spectra of doped CaP powders (batch B) in the MIR region and wavenumber range $1300 - 400 \text{ cm}^{-1}$	315
Figure 4.2.60 FTIR spectra of doped CaP powders (batch B) in the MIR region and wavenumber range $2500 - 1400 \text{ cm}^{-1}$	315
Figure 4.2.61 FTIR spectra of doped CaP powders (batch B) in the NIR region and wavenumber range $4000 - 3000 \text{ cm}^{-1}$	316
Figure 4.2.62 DSC of doped CaP powders (batch B) (Endo up).	322
Figure 4.3.1 SEM of as – prepared dentine section of 1 – 2 mm in thickness, showing open dentinal tubules after acid etching treatments. (a) Low magnification at $2 \mu\text{m}$ and (b) high magnification at $1 \mu\text{m}$	329
Figure 4.3.2 SEM of a dentine section coated with CaP powder, showing open dentinal tubules and non – uniform occlusion with CaP particles.	331

Figure 4.3.3 SEM of a dentine section coated with doped CaP (batch A) powder, showing occluded dentinal tubules with doped CaP particles.....	331
Figure 4.3.4 SEM of CaP Pellet of 1 – 2 mm in thickness that was irradiated with 1520 nm pulsed laser, showing (a) the sintered area, and (b) change in surface morphology.....	335
Figure 4.3.5 SEM of thulium oxide – doped CaP pellet of 1 – 2 mm in thickness that was irradiated with 1520 nm pulsed laser, showing (a) the sintered area, and (b) change in surface morphology.....	335
Figure 4.3.6 SEM of erbium oxide, aluminium phosphate, and calcium fluoride – doped CaP pellet of 1 – 2 mm in thickness that was irradiated with 980 nm CW laser, showing (a) the sintered area, and (b) change in surface morphology.....	335
Figure 4.3.7 XRD patterns of CaP pellets irradiated with 1500 nm CW and 1520 nm pulsed lasers, compared to that of unsintered CaP pellet.....	336
Figure 4.3.8 XRD patterns of Tm ₂ O ₃ – doped CaP pellets irradiated with 1500 nm CW and 1520 nm pulsed lasers, compared to that of unsintered Tm ₂ O ₃ – doped CaP pellet.	336
Figure 4.3.9 SEM of a dentine section of 1 – 2 mm in thickness that was irradiated with 980 nm CW laser, showing the modification of dentine surface morphology without the occlusion/sealing of open dentinal tubules.....	338
Figure 4.3.10 SEM of dentine section coated with Er ₂ O ₃ .AlPO ₄ .CaF ₂ – doped CaP (batch A) that was irradiated with 980 nm CW laser, showing (a) unsintered and sintered areas and the change in surface morphology of doped CaP coating, and (b) the formation of rosette – like particles that are occluding large area of dentinal tubules.....	338
Figure 4.3.11 SEM of a dentine section coated with CaP that was irradiated with 980 nm CW laser, showing the change in surface morphology of CaP coating without occluding dentinal tubules, (a) sintered area, (b) heat accumulation and non – uniform absorption and distribution of energy, (c) difference between laser irradiated and non-irradiated areas, and (d) melted dentine surface and partially sealed dentinal tubules.	339
Figure 4.3.12 SEM of dentine sections coated with doped CaP that were irradiated with 1520 nm pulsed laser. (a-b) for 2 minutes, showing the crater surrounded by a wave – like effect with a minor distortion to the coating in the form of a crack – like, and (c-d) for 30 seconds, showing the crater surrounded by a wave – like effect without any distortion to the coating.	341
Figure 4.3.13 SEM of unaffected and effected areas by the 1520 nm pulsed laser irradiation, showing (a) open dentinal tubules away from the laser – irradiated area, and (b) completely occluded dentinal tubules around the laser – irradiated area.	342

Figure 4.3.14 SEM of doped CaP – coated dentine section that was irradiated using 1520 nm pulsed laser for 5 minutes.	342
Figure 4.3.15 SEM of doped CaP coated dentine section that was irradiated for 1 minute using 1520 nm pulsed laser with a beam diameter of 250 µm, showing (a-b) laser – irradiated area, compared to non – irradiated areas, and (c-d) in and around laser – irradiated area.	345
Figure 4.3.16 SEM of doped CaP coated dentine section that was irradiated for 2 minutes using 1520 nm pulsed laser with a beam diameter of 250 µm, showing (a-b) laser – irradiated area, compared to non – irradiated areas, and (c-d) in and around laser – irradiated area.	346
Figure 4.3.17 SEM of doped CaP coated dentine section that was irradiated using 1520 nm pulsed laser with a beam diameter of 250 µm, showing (a) the densification of laser – irradiated particles/coating, and (b) the area surrounding laser – irradiated area.	346
Figure 4.3.18 SEM of doped CaP coated dentine section that was irradiated for 1 and 2 minutes (bottom to top, respectively), using 1520 nm pulsed laser with a beam diameter of 125 µm.	347
Figure 4.3.19 SEM of doped CaP coated dentine section that was irradiated for 1 minute, using 1520 nm pulsed laser with a beam diameter of 125 µm, showing (a-b) the laser – irradiated area and densification of sintered area, and (c-d) the area surrounding and around the laser irradiation spot.	348
Figure 4.3.20 SEM of doped CaP coated dentine section that was irradiated with 1520 nm pulsed laser with a beam diameter of 125 µm, showing (a-b) the difference between exposure time of 1 and 2 minutes (left to right, respectively).	348
Figure 4.3.21 SEM of doped CaP coated dentine section that was irradiated for 1 and 2 minutes, using 1520 nm CW laser with a beam diameter of 250 µm.	349
Figure 4.3.22 SEM of doped CaP coated dentine section that was irradiated for 1 minute, using 1520 nm CW laser with a beam diameter of 250 µm, showing (a) laser – irradiated area, and (b) the densification of CaP coating with no open dentinal tubules.	349
Figure 4.3.23 SEM of doped CaP coated dentine section that was irradiated for 2 minutes, using 1520 nm CW laser with a beam diameter of 250 µm, showing (a) the laser – irradiated area, and (b) a deep crater and the densification of CaP coating around it with no open dentinal tubules.	349
Figure 4.3.24 SEM of doped CaP coated dentine section that was irradiated for 1 and 2 minutes (bottom to top, respectively) using 1520 nm CW laser with a beam diameter of 125 µm, showing (a-b) the laser – irradiated areas, and (c-d) the densified areas around the laser – irradiated areas.	351

Figure 4.3.25 SEM of CaP coated dentine section that was irradiated for 2 minutes using 1520 nm pulsed laser with a beam diameter of 250 μm , showing (a) the laser irradiation spot, and (b) melted dentine surface surrounding the laser irradiation spot and open dentinal tubules with few CaP particles surrounding melted dentine surface..... 352
352

Figure 4.3.26 SEM of CaP coated dentine section that was laser irradiated for 1 minute, using 1520 nm pulsed laser with a beam diameter of 250 μm , showing (a) the laser – irradiated area with a superficial effect, and (b-c) open dentinal tubules with few CaP particles in and around the laser – irradiated area. 352

Figure 4.3.27 SEM of CaP coated dentine section that was laser irradiated for (a) 1 minute and (b) 2 minutes, using 1520 nm pulsed laser with a beam diameter of 125 μm 353

Figure 4.3.28 SEM of CaP coated dentine section that was irradiated for 2 minutes, using 1520 nm pulsed laser with a beam diameter of 125 μm , showing (a) laser irradiation spot, (b) area surrounding the laser irradiation spot, (c) melted dentine surface and partially sealed dentinal tubules surrounding the laser irradiation spot, and (d) open dentinal tubules and CaP particles around the laser – irradiated area. 354

Figure 4.3.29 SEM of CaP coated dentine section that was irradiated for 1 minute, using 1520 nm pulsed laser with a beam diameter of 125 μm , showing (a) the laser – irradiated area with a melting effect, (b) open dentinal tubules with few CaP particles around the laser – irradiated area, and (c-d) melted dentine surface and partially sealed dentinal tubules within the laser – irradiated area. ... 355

Figure 4.3.30 SEM of CaP coated dentine section that was laser irradiated for (a) 1 and (b) 2 minutes, using 1520 nm CW laser with a beam diameter of 125 μm , showing (a-b) the laser – irradiated spots, and (c-d) modified dentine surface and partially sealed dentinal tubules..... 357

Figure 4.3.31 SEM of CaP coated dentine section that was laser irradiated for 2 minutes, using 1520 nm CW laser with a beam diameter of 250 μm , showing (a-b) the laser – irradiated area, and (b-c) melted dentine surface surrounding the laser – irradiated area and open dentinal tubules and CaP particles around the laser – irradiated area. 358

Figure 4.3.32 SEM of uncoated dentine section that was laser irradiated for 2 minutes, using 1520 nm pulsed laser with a beam diameter of 250 μm , showing (a) the laser – irradiated area (left hand side of image), and (b) higher magnification of the laser – irradiated area. 359

Figure 4.3.33 SEM of uncoated dentine section that was laser irradiated for 2 minutes, using 1520 nm pulsed laser with a beam diameter of 250 μm , showing (a) the laser irradiation spot, and (b) open dentinal tubules around the laser – irradiated area.	359
Figure 4.3.34 SEM of uncoated dentine section that was laser irradiated for 1 and 2 minutes, using 1520 nm pulsed laser with a beam diameter of 125 μm , showing no signs of laser irradiation effects.....	360
Figure 4.3.35 SEM of uncoated dentine section that was laser irradiated for 1 and 2 minutes, using 1520 nm CW laser with a beam diameter of 125 μm , showing (a) the laser irradiation spot, (b-c) higher magnification of laser irradiation spot with a very deep crater penetrating dentine surface, (d) area surrounding and around the laser irradiation spot, (e) area surrounding the laser irradiation spot with a modified dentine surface and partially sealed dentinal tubules, and (f) area around the laser irradiation spot with open dentinal tubules.	361
Figure 4.3.36 SEM of uncoated dentine section that was laser irradiated for 1 and 2 minutes, using 1520 nm CW laser with a beam diameter of 250 μm , showing no signs of any laser effects.	362
Figure 4.3.37 Cross – sectional SEM micrograph of 1520 nm pulsed laser – irradiated dentine section with a coating of CaP, showing open dentinal tubules as well as the presence of crack – like morphology in the dentine tissue.....	365
Figure 4.3.38 Cross – sectional SEM micrograph of 1520 nm pulsed laser – irradiated dentine section with a coating of doped CaP, showing the laser – irradiated coating with no open dentinal tubules.....	365
Figure 4.3.39 Temperature change (± 0.5) during 980 nm CW laser irradiation for 5 minutes on uncoated dentine section and CaP – and doped CaP (batch A) – coated dentine sections.	367
Figure 4.3.40 Micro – hardness indentation measurements (± 0.5) comparing the hardness number of uncoated dentine section and laser – irradiated – coated (CaP and doped CaP) dentine sections.	368
Figure 4.3.41 pH variation during immersion of CaP and doped CaP pellets (unsintered, furnace sintered, and laser sintered) in 0.3% citric acid solution with as – prepared pH 3.60 ± 0.02 for 24 hours. ..	373
Figure 4.3.42 Leached out component comparison between the acid solutions that contained unsintered, furnace sintered, and laser sintered CaP pellets with standard error bars.....	375
Figure 4.3.43 Leached out component comparison between the acid solutions that contained unsintered, furnace sintered, and laser sintered doped CaP pellets with standard error bars.....	376

Figure 4.3.44 Leached out calcium and phosphate comparison between of the acid solutions that contained unsintered, furnace sintered, and laser sintered CaP pellets with standard error bars.....	377
Figure 4.3.45 Leached out calcium and phosphate comparison between of the acid solutions that contained unsintered, furnace sintered, and laser sintered doped CaP pellets with standard error bars.	378
Figure 4.3.46 Leached out element (SEM-EDX element weight percentage) comparison between the citric acid solutions that contained unsintered, furnace sintered, and laser sintered doped CaP pellets with standard error bars.	380

List of Abbreviations

ACP	Amorphous calcium phosphate
CaP	Calcium phosphate
Ca:P	Calcium: phosphate
CDHAp	Calcium – deficient hydroxyapatite
ClAp	Chlorapatite
CW	Continuous wave
DCP	Dicalcium phosphate
DSC	Differential scanning calorimetry
DTA	Differential thermal analysis
EDJ	Enamel – dentine junction
EDX	Energy dispersive X – ray
Er:YAG	Erbium: yttrium – aluminum – garnet
Er:YSGG	Erbium: yttrium – scandium – gallium – garnet
Er,Cr:YSGG	Erbium, chromium: yttrium – scandium – gallium –
FELs	Free electron lasers
FAp	Fluorapatite
FTIR	Fourier transform infrared
HAp	Hydroxyapatite
Ho:YAG	Holmium: yttrium – aluminum – garnet
CHAp	Hydroxycarbonate apatite
ICP/MS	Inductively – coupled plasma/mass spectroscopy
JCPDS	Joint committee on powder diffraction standards
MCP	Monocalcium phosphate
min	Minute
M.W	Molecular weight
Nd	Neodymium
Nd:glass	Neodymium: glass
Nd:YAG	Neodymium: yttrium – aluminum – garnet
Nd:YLF	Neodymium: yttrium – lithium – fluoride
OCP	Octacalcium phosphate
pH	Potential Hydrogen
ppb	Parts per billion
ppm	Parts per million
Pt/Pd	Platinum/Palladium
RE	Rare earth
REE	Rare earth element
RT	Room temperature

s	Second
SEM	Scanning electron microscopy
Std.D	Standard deviation
TEM	Transmission electron microscopy
TGA	Thermogravimetric analysis
TTCP	Tetracalcium phosphate
TCP	Tricalcium phosphate
UV	Ultraviolet
Vis	Visible
wt%	Weight percentage
XRD	X – ray diffraction
YAG	Yttrium – aluminum – garnet

Overview of the thesis contents

There are five chapters in this thesis. Chapter 1 gives a brief introduction of present research study. Chapter 2 gives a more detailed overview of dentine hypersensitivity, hard dental tissues, particle sintering process, biological and synthetic calcium orthophosphates (CaP), and background of laser irradiation and doping compounds. A summary of the experimental techniques and conditions used in this work are covered in Chapter 3. Chapter 4 presents the results of the characterisation of CaP and doped CaP powders, including particle size, particle morphology, crystalline structure, composition, and thermal behaviour of the synthesised CaP particles, as well as the results of the characterisation of laser – irradiated CaP and doped CaP coatings for the occlusion of dentinal tubules. Finally, Chapter 5 presents the conclusions and future work for this research project.

Chapter 1 Introduction

Teeth sensitivity (Dentine hypersensitivity)

Teeth sensitivity or dentine hypersensitivity (*DH*) is still a challenging common condition amongst a large number of dental patients, commonly known as having 'sensitive teeth'. The condition is characterised by short and sharp pain in response to external stimuli in the oral environment due to dentine exposure. Dentine exposure normally occurs due to enamel loss or gum recession, which could be because of poor dental hygiene, vigorous brushing or acid erosion. Because dentine has micro – channels, known as dentinal tubules, containing a dentinal fluid, external stimuli, such as thermal, physical, electric, osmotic, and chemical stimuli can cause movement of the fluid within these tubules, whereby stimulating the nerves in the pulp and causing pain.

Dentine hypersensitivity treatments include the use of potassium nitrate as a nerve desensitiser, the use of calcium hydroxide particles for dentinal tubule occlusion, and the application of lasers to seal dentinal tubules. However, recurrence of sensitivity is common, as the current treatments are not ideal, and they are effective in the short term only. The most recent approach for hypersensitivity treatments involves the occlusion of dentinal tubules using toothpastes containing hydroxyapatite such as BioRepair plus toothpaste. Various fillers, such as potassium, strontium, stannous, and silica, are used in toothpastes. Commercially available toothpastes include Sensodyne containing strontium chloride or potassium nitrate, silica – based toothpaste containing strontium acetate and fluoride, bioactive glass Sensodyne

containing calcium sodium phosphosilicate, Crest sensitivity dentifrice, and Colgate toothpastes containing arginine, calcium carbonate, and fluoride. In addition, dental lasers are used to reduce tooth sensitivity, as well as other various dental procedures such as the removal of tooth decay, tooth preparation for a filling, and curing or hardening a filling.

The proposed technique for the treatment of sensitive teeth involves the occlusion of dentinal tubules using Er^{3+} , Al^{3+} , F^- – doped CaP under laser irradiation. In practice, the procedure would involve the application of Er^{3+} , Al^{3+} , F^- – doped CaP powder in the form of a paste or gel onto the hypersensitive tooth surface, which is then cured or hardened by the application of laser irradiation to fuse the doped CaP layer to the tooth surface and promote its bonding. Calcium phosphate mineral, hydroxyapatite (HAp), is chemically similar to the mineral component of bones and hard dental tissues, and therefore, it is the most suitable and potential biomaterial for the occlusion of dentinal tubules and the remineralisation of tooth tissues to prevent tooth sensitivity.

Aims

The project follows on from previous projects, investigating the synthesis of calcium orthophosphate (CaP) particles for the occlusion of pore channels in dentine and the potential treatment of sensitive teeth. In the proposed research study, it is intended to modify chemical composition of CaP to produce photoactive minerals, which interact with laser irradiation to induce photosensitivity and occlude dentinal tubules. The main aim is to demonstrate the effective use of CaP powders doped with erbium, aluminium, and fluoride compounds under laser irradiation in occluding open

dentinal tubules, so that the densification and growth of CaP onto dentine surfaces can be initiated by the energy absorbed and released when subjected to laser irradiation by a heat dissipation mechanism.

Objectives

- Synthesising calcium orthophosphate (CaP) minerals, undoped (CaP) and doped with erbium (Er_2O_3 and $\text{Er}(\text{NO}_3)_3 \cdot 5\text{H}_2\text{O}$), aluminium (AlPO_4 and $\text{Al}(\text{NO}_3)_3 \cdot 9\text{H}_2\text{O}$), and fluoride (CaF_2 and NH_4F) compounds, under various conditions, including temperature, pH, and reaction time, for bio – dental applications, particularly the occlusion of dentinal tubules.
- Characterising synthesised CaP minerals, and comparing the doped CaP powders to the control CaP powders. Characterisation techniques include scanning electron microscopy (SEM), laser scattering, energy dispersive X – ray (EDX), and X – ray diffraction (XRD) to characterise the morphology, particle size, elemental composition, and crystalline structure of synthesised CaP particles, as well as Fourier transform infrared spectroscopy (FTIR) and differential scanning calorimetry (DSC) to characterise the composition and thermal behaviour of CaP powders, respectively.
- In vitro preparation of human tooth sections, mimicking the conditions of tooth/dentine hypersensitivity.
- Coating of dentine sections with synthesised CaP/doped CaP powders for the occlusion of open dentinal tubules and post laser irradiation.
- Characterising CaP/doped CaP coatings and the occlusion of open dentinal tubules.

- Laser irradiation sintering of dentine sections coated with synthesised CaP/doped CaP powders as well as CaP pellets, using continuous wave (CW) and pulsed lasers, to promote densification of particles and fuse coatings to tooth surface and promote its bonding.
- Characterising laser – irradiated coatings and their effect on the occlusion of dentinal tubules using SEM and XRD.
- Characterising CaP/doped CaP coated dentine sections by measuring the temperature change during laser irradiation, and determining their hardness using a micro – hardness indentation technique.
- Characterising acid eroded CaP/doped CaP pellets, using inductively – coupled plasma/mass spectroscopy (ICP/MS), SEM-EDX, and Profile roughness measurements.

Chapter 2 Literature Review

2.1 Teeth sensitivity (Dentine hypersensitivity)

Teeth sensitivity or dentine hypersensitivity is affecting millions of people worldwide. The pain occurs during eating and drinking, and sometimes even during breathing. It is one of the most common complaints by dental patients, especially those suffering from gum recession, and those having suffered enamel loss due to abrasion or acid erosion (1, 2, 3).

Dentine hypersensitivity (*DH*) is still a challenging common condition amongst a large number of dental patients, commonly known as having 'sensitive teeth'. It is characterised by short and sharp pain in response to external stimuli in the oral environment due to dentine exposure (1, 2, 3). Dentine exposure normally occurs due to enamel loss or gum recession, which could be because of poor dental hygiene, vigorous brushing, or acid erosion. Because dentine has micro – channels, known as dentinal tubules, containing a dentinal fluid, external stimuli, such as thermal, physical, electric, osmotic, and chemical stimuli, can cause movement of the fluid within these tubules, whereby stimulating the nerves in the pulp and causing pain (1, 2, 3).

As shown in Figure 2.1, gum recession exposes cementum and dentine that are easily removed and modified, respectively, by abrasion and acid erosion. This in turn results in the opening of dentinal tubules in the exposed area (4). In addition, periodontal treatments involve the removal of dentine using dental scalers, leading to the exposure of dentinal tubules, which in turn

increases sensitivity. This is because sensitivity increases with increasing the number of dentinal tubules, which increases towards the inner tissue (pulp). Enamel loss due to abrasion and acid erosion is usually a result of aggressive tooth brushing and intake of acidic food, respectively (5).

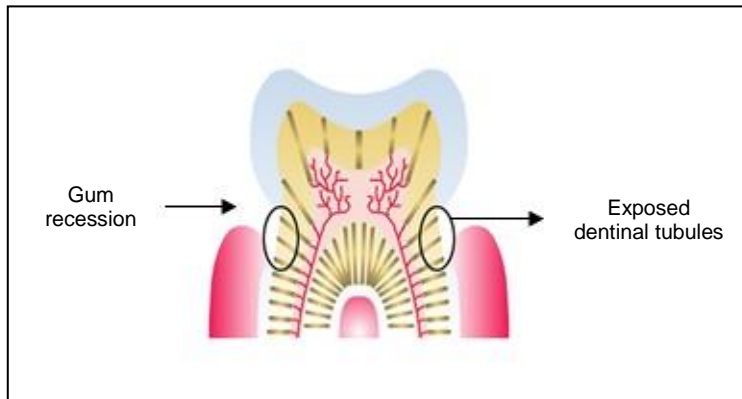


Figure 2.1 Schematic of a tooth cross section indicating gum recession and exposed dentinal tubules.

Several theories are proposed to explain the mechanism of teeth sensitivity. These include odontoblastic transduction, neural, and hydrodynamic theories. However, the most accepted theory to date is the hydrodynamic theory (2, 3, 6). The odontoblast theory suggests that odontoblastic processes are exposed on dentine surface and excited by chemical and mechanical stimuli, releasing neurotransmitters or impulses towards the nerve endings that cause pain. The neural theory suggests that the nerve endings are triggered by direct thermal and mechanical stimuli (6). On the other hand, the hydrodynamic theory suggests that the change in the flow of plasma – like biological fluid (dentinal fluid) inside the dentinal micro – channels triggers the nerve endings and causes pain (2, 3, 6).

Having sensitive teeth is a very common condition. It often occurs suddenly, and may range from a mild discomfort to severe pain when drinking cold, hot, or sweet drinks, chewing cold or hot food, and breathing cold air (7). Sensitivity is usually due to tooth damage, such as tooth decay, a cracked or fractured tooth, or enamel tissue loss, because of abrasion and/or acid erosion. Gum damage is another cause, which includes gum recession due to incorrect or hard tooth brushing, or gum diseases and other medical conditions (7). However, dentine exposure does not always lead to sensitive teeth. This is due to the formation of a natural smear layer and the continuous formation of secondary dentine as a protection mechanism throughout life (8).

The prevalence of dentine hypersensitivity varies due to the difference in populations and investigation techniques used. In addition, dentine hypersensitivity varies from one extreme to another, depending on various factors such as oral health condition, dietary intake, and individual oral hygiene habits (9). Abrasion and erosion are two types of tooth wear that can wear away tooth tissues and affect oral health. Tooth abrasion and erosion are believed to be the main causes of tooth wear (5).

Dental erosion is the dissolution of teeth by acids of non – bacterial origin. Tooth erosion is caused by chemicals due to dietary intake, which may result from foods or drinks containing acids such as citrus fruits, fruit juices, carbonated drinks, and wines, or due to the exposure of teeth to gastric (stomach) acids, which form in the stomach (5). Other chemicals, such those in swimming pools, can also cause erosion over time (5). Tooth abrasion is caused by many different activities. It is mainly caused by physical rubbing

against the teeth. Incorrect or aggressive brushing is a common cause of gum recession, which leads to the exposure of underlying soft tissues. Other causes include grinding teeth against each other or chewing on hard things (5, 10).

In order to understand the leading mechanism of the pain associated with sensitive teeth based on the hydrodynamic theory, and the potential of CaP particles for the treatment of hypersensitivity, knowledge of tooth tissues, structure, and morphology are of great importance. Dentine and pulp biology are the important tissues in understanding sensitivity and its treatments.

2.2 Dental tissues (Teeth)

A tooth consists of a crown and root portion. The crown is covered with enamel (the outer layer), whereas the root is covered with cementum, and they are joined at the cemento-enamel junction (CEJ). The crown is the visible part of the tooth exposed in the mouth, whereas the root is the hidden part of the tooth that is embedded in the jawbone (8). Only the cervical third of the crown, in healthy and young adults, is partly covered by gingiva (gum tissue), which is the most affected area by hypersensitivity in the case of enamel loss or gum recession by erosion and abrasion. These are usually found together due to chemical and mechanical stimuli, respectively (11).

A natural tooth is composed of four tissues – enamel, dentine, cementum, and pulp, which form the crown and root, as shown in Figure 2.2. Enamel, dentine, and cementum tissues are classified as hard tissues, whereas the pulp is a soft tissue (8).

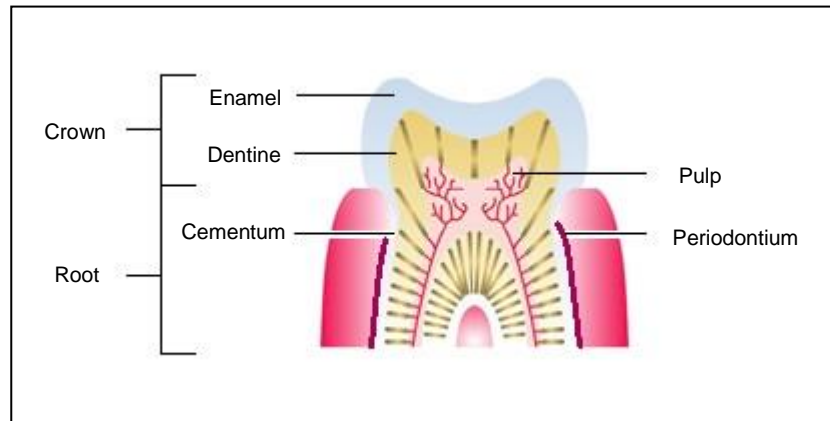


Figure 2.2 Schematic of a tooth cross section indicating main component parts of a natural tooth.

2.2.1 Enamel

Enamel is the outer surface of the anatomic crown. It is thickest over the tip of the crown, and becomes thinner until it ends at the cervical line. The colour of enamel varies with its thickness and mineralisation. Enamel is the most densely mineralised tissue in the human body, with a chemical composition of 96% inorganic material (hydroxyapatite crystals ($\text{Ca}_{10}(\text{PO}_4)_6\text{OH}_2$)), 4% organic material (proteins, 90% of low molecular weight amelogenins and 10% of high molecular weight non – amelogenins), and water (8, 12). The apatite mineral has some impurities/substitutions, including Na^+ , K^+ , and Mg^{2+} for Ca^{2+} ; CO_3^{2-} for PO_4^{3-} or HPO_4^{2-} , and F^- and CO_3^{2-} for OH^- . This densely mineralised tissue has the ability to resist wear that is subjected to a tooth. The mineral content varies within enamel. It is lowest at the enamel – dentine Junction (EDJ), and highest at the outer surface (12). Enamel has a porous structure. Pores are present between HAp crystals, which vary in size, form, orientation, and distribution. HAp

crystals have a hexagonal shape with a mean width of 60 – 70 nm and a mean thickness of 20 – 30 nm (12).

2.2.2 Dentine

Dentine forms the main body of a tooth; it forms the largest portion of the crown and root. Dentine is covered by enamel, which covers the crown, and covered by cementum, which covers the root. Dentine is a hard, dense, and calcified tissue. It is softer than enamel, and harder than cementum. It is yellow in colour and elastic in nature. The chemical composition comprises 70% inorganic material (hydroxyapatite crystals), 30% organic material (mainly of collagen fibrils, with a substance of mucopoly saccharides), and water (8, 12).

Dentine contains micro – sized tubules throughout its structure, known as dentinal tubules, which contain a dentinal fluid, as shown in Figure 2.3. The tubules vary in size from 1 μm to 3 μm in diameter, and density from 20,000 to 50,000 tubules per mm^2 (12). The tubules' number and diameter increase from the outer dentine towards the pulp, as shown in Table 2.1, which presents the number and diameter ratios of dentinal tubules on hypersensitive and non – sensitive dentine. The data show that the number of tubules on hypersensitive dentine is eight times that on non – sensitive dentine, and that the diameter of tubules on hypersensitive dentine is two times that on non – sensitive dentine (3).

Table 2.1 Tubules number and diameter ratios of hypersensitive dentine and non – sensitive dentine (3)

Tubules	Hypersensitive dentine	Non – sensitive dentine
Number – ratio	8	1
Diameter – ratio	0.83	0.4

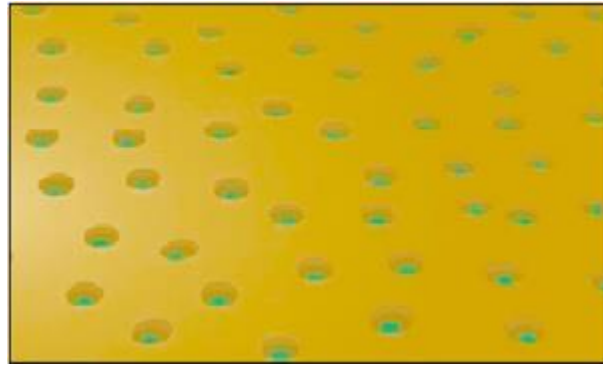


Figure 2.3 Schematic of dentine surface showing dentinal tubules containing a dentinal fluid.

The dentine area surrounding dentinal tubules is a highly crystallised area, known as peritubular dentine, whereas the rest of the dentinal material comprises microscopic structures, known as intertubular dentine (8, 13), as shown in Figure 2.4. The intertubular dentine consists mainly of type I collagen with carbonate apatite crystals, whereas the peritubular dentine consists mainly of carbonate apatite (13).

Unlike enamel, dentine is continually formed within the tooth, known as secondary dentine, which continues throughout tooth life. Increasing the formation of this type of dentine tends to reduce the overall permeability of dentine. This can be explained by open tubules on non – sensitive surfaces, being occluded deeper in dentine by secondary dentine. Dentine is also produced in the case of a trauma, which is known as reparative dentine (8).

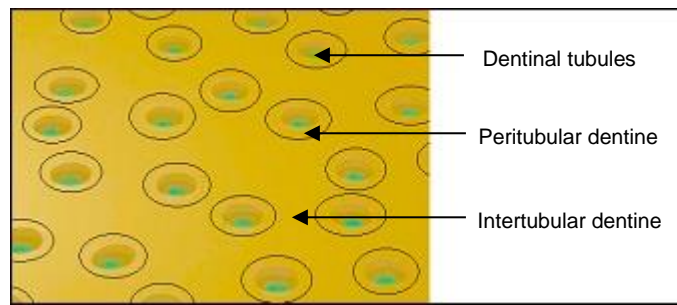


Figure 2.4 Schematic of a dentine cross section indicating dentinal tubules, peritubular dentine and intertubular dentine.

Another tooth process is the formation of a layer, known as the smear layer. When dentine is exposed, the layer forms and occludes dentinal tubules; however, it can be easily removed by acid erosion (14, 15) or in the case of reduced salivary flow quantity (16). The smear layer can be defined as a natural layer of debris consisting of particles of dentine or enamel, which are produced as a result of tooth preparation involving tooth cutting (12, 17-19). The layer may also contain bacteria and their by – products (12, 18, 19). It can also be produced naturally due to tooth fracture, eating/drinking, and tooth brushing (12), or by toothpaste, prophylaxis paste, and orangewood sticks (18). Smear layers, particularly thick layers, interfere with the adhesion capabilities of self – etching and total – etch systems, and the bonding between hard tooth tissues and restorative materials (17).

2.2.3 Cementum

Cementum is a bone – like substance that covers the root portion; it provides a medium for the attachment of tooth to alveolar bone through periodontal ligaments (periodontium) (20). Cementum is less durable than dentine and enamel, and it is chemically composed of 45% to 50% inorganic material (hydroxyapatite), and 50% to 55% organic material (collagen and protein

polysaccharides) (8). It is not as dense or as hard as enamel and dentine; however, it is more dense (mass/volume) than bone due to its more compact structure (8, 12).

Cementum is a porous structure that exposes small patches of dentine. It is quite thin at the cervical line, but it increases in thickness at the apex of the root and inter – radicular surfaces (21). The thickness variation could be explained by a continuous process throughout the life of a tooth. It involves the formation of more cementum in the upper portion and the apical region of the root, known as the secondary cementum, which occurs when a tooth is subjected to oral forces that transmit to the alveolar bone (20). Therefore, the cervical area is considered permeable, and its exposure makes dentine more easily exposed to the oral environment (12, 22).

2.2.4 Pulp and pulp cavity

Dental pulp is the nourishing, sensory, and dentine – reparative system of the tooth. It consists of pulp chamber and pulp canals. It is composed of blood vessels, lymphatic vessels, nerves, fibroblasts, collagen fibres, and connective tissues (8, 11). The pulp tissue is the centre of a tooth, which is covered by dentine. The pulp cavity walls are lined with odontoblast cells, which form the secondary dentine or reparative dentine, and are continuously activated and supported by the blood vessels. Blood vessels also supply the white blood cells to fight bacteria within the pulp, whereas the lymphatic tissue acts as a fluid filter. The nerve acts as a sensor, and responds to pain only (8, 11).

2.3 Assessment and treatments of sensitive teeth

Teeth hypersensitivity can be assessed by means of simulation methods, including thermal stimuli, mechanical (tactile) stimuli, chemical (osmotic) stimuli, cold air currents, cold water stimulation, thermoelectric systems, and electric stimulation (12, 23). Even though several factors can influence the measurement of hypersensitivity, the most common clinical methods are thermal and mechanical methods (24). Hypersensitivity is diagnosed after other possible conditions are eliminated (12). Diagnostic tests include a physical examination of gums and teeth for tenderness, which is done by tapping on teeth or with a tongue depressor (25). Radiology examination, using X – rays and blood tests (blood cell count), is another test to look for dental caries and dental infections, respectively (26).

Although the principles for treating teeth sensitivity are demonstrated successfully by many, the current treatments for teeth sensitivity are not effective in the long term or as a permanent solution (27).

Current treatments for sensitive teeth, as summarised in Table 2.2, result in partial pain relief, but recurrence of sensitivity is very common (28). Treatments can be divided into two strategies (2). The first strategy is the occlusion of exposed dentinal tubules using chemical agents such as strontium chloride, sodium fluoride (29), ferric oxalate (30), and calcium hydroxide (2, 31), or by using physical agents such as fluoride – releasing resin (32) (*e.g.* fluoride containing prophylaxy paste (33)). The second strategy involves the desensitisation of the nerve using potassium nitrate (2, 34). Other materials, such as bioglasses, result in excellent occlusion of dentinal tubules, and they significantly reduce dentine permeability when

incorporated into toothpastes (34, 35). Various toothpaste fillers, such as potassium, strontium, stannous, and silica, are reported (34, 36). Commercially available toothpastes include Sensodyne containing strontium chloride or potassium nitrate, (34) silica – based toothpaste containing strontium acetate and fluoride (34), bioactive glass Sensodyne containing calcium sodium phosphor – silicate (36), Crest sensitivity dentifrice, and Colgate containing arginine, calcium carbonate, and fluoride (34).

Various toothpastes containing different fillers, such as potassium, strontium, stannous, and silica, show various actions and results (34, 36). Sensodyne containing strontium acetate and bioactive glass Sensodyne containing calcium sodium phosphosilicate cause remineralisation and reduce sensitivity (34). On the other hand, toothpastes containing hydroxyapatite (37, 38), such as BioRepair plus (39), demonstrate a significant increase in oral fluoride and calcium, providing anticaries and anti – erosion benefits (37). The increase in oral fluoride is due to the release of fluoride by an anticaries agent (sodium monofluorophosphate), whereas the increase in calcium is due to the deposition of HAp particulate (37).

Toothpastes containing potassium salts, such as potassium nitrate, potassium chloride, and potassium citrate, as a desensitising agent, and Sensodyne containing 10% strontium chloride are less effective than silica – based toothpastes such as those containing 8% strontium acetate and/or fluoride (34). Colgate toothpastes containing arginine, calcium carbonate, and fluoride, known as Pro – Argin™ technology, claim clinically proven instant and lasting relief of dentin hypersensitivity (34). Silica – based agents containing NovaMin (34, 36), commercially known as Bioglass, are

significantly more effective in reducing sensitivity than the commercial desensitizing toothpaste containing strontium chloride (34).

Bioglass is a family of bioactive glasses that contain SiO_2 , Na_2O , CaO , and P_2O_5 in specific proportions. They have different compositions, which determine their properties and applications (40-42). Some bioglasses bond to bone and soft tissues, and others do not, depending on their compositions, particularly their $\text{CaO}:\text{P}_2\text{O}_5$ ratios. Bioglasses with lower $\text{CaO}:\text{P}_2\text{O}_5$ ratios do not bond to bone (40-42). In addition, there are those behaving as “nearly – inert” materials, and others, which are resorbable (40, 41). Common commercial bioactive glasses include 45S5 Bioglass (40-42), Perioglas, Biogran (43), and NovaMin (34, 36, 44). Perioglas and Biograns are Bioglass particulates that are used as bone fillers or graft extender (43). NovaMin was first developed as a bone regeneration material, but it is used for the treatment of dental hypersensitivity and remineralisation of enamel (34, 36, 44). It is highly reactive in water, because it consists of amorphous sodium – calcium phosphosilicate. The use of a toothpaste containing NovaMin Bioglass promotes the repair processes of damaged teeth. It deposits a protective layer of calcium phosphate, due to the exchange of sodium ions with hydrogen cations (H_3O) and the release of calcium and phosphate ions (34, 36, 44). Bioactive glasses exhibit class *A* bioactivity, *i.e.* being osteopductive materials, they bond to hard and soft tissues, and exhibit higher rate of bonding to hard tissues than bioactive ceramics (*e.g.* HAp), the latter which exhibit class *B* bioactivity, *i.e.* behaving as osteoconductive materials (42).

The use of nanotechnology is important in all science fields. The technology is used for the development of nanomaterials that “exhibit novel and significantly improved physical, chemical, and biological properties, phenomena and processes as a result of the limited size of their constituent particles or molecules” (45). Nano – structured materials, depending on the number of dimensions, which lie within the nanometre range, can be classified as those confined in one, two, and three dimensions (45). Those confined in three dimensions include nanopores (e.g. nanoporous silicon) and nanoparticles (e.g. colloidal particles). The latter can be a single crystal or polycrystalline (composed of a number of different crystalline regions or grains of differing crystallographic orientations). Those confined in two dimensions include nanowires, nanorods, nanofilaments, and nanotubes, which can be amorphous, single crystalline, or polycrystalline (with nanograins). Those confined in one dimension include discs, platelets, or ultrathin films, which can also be amorphous, single – crystalline, or nanocrystalline (45). Nanoparticles may also be present within a medium, such as nanoprecipitates in a matrix material, which may possess certain crystallographic orientation relationships with the atomic arrangement of the matrix. The coherence of the interface may lead to coherency strains in the particle and matrix (45).

The use of nanoparticles, particularly in dentistry, has gained a growing interest, due to its potential to improve the properties of dental restoratives. Inorganic nanoparticles include those based on metal oxides such as zinc oxide, iron oxide, and titanium dioxide (46, 47), and those based on metals such as gold, silver, iron, copper, and magnesium (46). The use of silicon dioxide, aluminium oxide, and alginate nanoparticles is also reported (46,

47). These nanoparticles can be used as antibacterial agents and growth inhibitors of various microorganisms due to their large surface area to volume ratios (46, 47). They have unique physical and chemical properties, biological properties and functionality due to their nanometre size. They also offer different morphologies, such as spheres, rods, and prisms, as well as improved biocompatibility (46). The concern of using nanoparticles in dental materials, is that they are highly reactive, and if released from dental materials, they could penetrate through biological matter (if inhaled or ingested) and cause adverse health effects to patients and dental staff (45).

Nanoparticles of HAp have been successfully demonstrated to occlude dentinal tubules in vitro for the potential remineralisation of hard tooth tissues (12, 48, 49). It is also reported that (in a short – term – in vitro assessment of desensitizing agents) agents containing 20% nano – hydroxycarbonate apatite (HCAp) are more effective in occluding dentinal tubules than those containing 10% strontium chloride (SrCl_2) (50). In addition, toothpastes containing hydroxyapatite (37, 38), such as BioRepair plus (39), demonstrate a significant increase in oral fluoride and calcium, providing anticaries and anti – erosion benefits (37). Toothpastes containing HAp are also found to be similarly effective in reducing dentine hypersensitivity to benchmark toothpastes for sensitive teeth (49). In addition, toothpastes containing monofluorophosphate (MFP) and dicalcium phosphate dehydrate (DCPD) are significantly more effective in sensitivity studies than those containing monofluorophosphate (MFP) and silica, particularly in preventing plaque pH drop and reducing solubility of enamel in rats' teeth, as well as providing extra supersaturation in saliva and plaque and enhancing anticaries efficacy in human teeth (49). Moreover, glass

ionomer cements containing HAp are light – cured cavity liners, which are commercially available such as Cavalite (Kerr Italia S.r.l.) (49). Therefore, the occlusion and growth of apatite (e.g. HAp) particles onto hard dental tissues, particularly under laser irradiation, could offer potential long – term treatment of dentine hypersensitivity and the repair of damaged teeth.

The use of laser irradiation to treat sensitive teeth is also one of the current treatment options (51-56). However, its effectiveness depends on the laser type and treatment conditions (2, 51, 56-59). The use of low – output power diode lasers such as helium – neon and gallium aluminium/arsenide (30, 51-56), and middle – output power lasers such as Nd:YAG and CO₂ (51-53, 56), with pulsed (52-54) and CW modes (52-56), are reported in conjunction with dentinal tubule occlusion for the treatment of sensitive teeth. Several studies indicate the potential of lasers for many dental treatments such as diagnosis of caries (60), cavity preparation/tissue ablation (61-63), periodontal therapy (64), oral surgery, implant dentistry (65), and the treatment of dentine hypersensitivity (54-56). However, their effectiveness is still not clear and requires further research (51-53, 56, 60-62, 65).

Table 2.2 Summary of current possible treatments and materials for tooth hypersensitivity

Treatment	Materials
Nerve desensitisation	Potassium nitrate
Chemical agents	Strontium chloride, Sodium fluoride, ferric oxalate and calcium hydroxide
Physical agents	Fluoride – releasing resin and fluoride containing prophylaxy paste
Restorative material	Composites, resins and bioglasses
Lasers	Helium – neon and gallium aluminium/arsenide, Nd:YAG, and CO ₂

2.4 Sintering process

Sintering can be defined as the process in which heat is applied to a material in order for its particles to adhere and chemically bond to each other, and thus, produce a dense material (66, 67). It can also be defined as the diffusion of atoms and grain growth under the application of heat (67). The sintering outcome of a material depends mainly on sintering temperature and particle size, particle size distribution, and composition of the material being sintered (66, 67).

Sintering can be divided into solid – state, liquid – phase, vitrification, and viscous sintering based on the material composition and the extent of the formation of secondary phases (67). Solid – state sintering involves atomic diffusion in the solid state, whereas liquid – phase sintering involves the formation of small volume of liquid of the original solid volume upon heating and solidification of the liquid phase at lower temperatures. Vitrification involves the formation of large volume of liquid of the original solid volume upon heating, whereas viscous sintering involves the densification of glass particles by a viscous flow under the influence of surface tension (67). Sintering can also be referred to as the process that introduces structural changes such as decomposition or phase transition. Changes in the microstructure can be divided into a primary and secondary process. The primary process involves nucleation and new generation grain growth, which exhibits continuous increase of average grain size during heat treatment without a change in grain size distribution. The secondary process involves nucleation and growth of some large grains (66).

Several mechanisms are responsible for the sintering of crystalline materials. These are vapour transport (evaporation/condensation), surface diffusion, lattice/volume diffusion, grain boundary diffusion, and dissolution motion (67). These mechanisms are responsible for the sintering stages, which involve an initial stage where necks are formed between particles, an intermediate stage where neck areas increase (neck growth), and a final stage where grain growth occurs (67). Therefore, sintering is a surface area driven process, which involves the elimination of a solid – vapour interface and the formation of solid – solid interface, resulting from the reduction in surface area and surface – free energy during sintering (66).

Particle size plays an important role during structural changes. Material transfer is rapidly achieved in smaller particles, due to the difference in vapour pressure between the particle surface and the junction between particles (neck). The lower the vapour pressure is, the faster the material transfer is; the smaller the particles is, the lower the vapour pressure difference is, as the contact surface between particles (neck area) increases and the surface of particles decreases. With larger particles, the vapour pressure difference is higher, as the contact surface between particles decreases and the surface of particles increases (66). As well as inducing changes in grain size and shape, changes in pore size and shape occur. Reduction of porosity results in a transformation from a porous structure to a more dense structure, and the material becomes densified (66, 67). Therefore, sintering process eliminates porosity and results in a dense material, and consequently, increases thermal conductivity of the material. In addition, as well as enhancing the thermal conductivity, the strength of the material can be enhanced by reducing its porosity (66).

Sintering is also applied to produce porous three – dimensional bioceramics of calcium orthophosphates. Such process involves more stages beyond the formation of a dense structure. This involves initial elimination of all moisture, carbonates, and all volatile chemicals such as nitrates and ammonia as gases, followed by the formation of a dense material. Further stages involve the concurrent increase in crystal size and the decrease in specific surface area, followed by chemical decomposition and transformation of acidic orthophosphates (PO_4^{3-}) into other phosphates ($2\text{HPO}_4^{2-} / \text{P}_2\text{O}_7^{4-} + \text{H}_2\text{O}$) (68, 69).

The type and structure of a material are very important in determining its thermal conductivity. For example, the thermal conductivity of porous materials is known to be poor due to the presence of pores within their structure, but it can be enhanced by reducing the amount of porosity and making it more dense, which can be achieved by sintering, whereby reducing pore shape and size, or even eliminating them to achieve optimum conductivity. In addition, the more complex the structure is, the more the thermal scattering of an atomic lattice wave is produced, and thus, the lower the thermal conductivity (66). Generally, thermal energy (heat) is transferred by either conduction, convection, or radiation; however, in solids, heat is transferred by conduction between atoms or molecules, and/or by electromagnetic irradiation interacting with the solid (70). Thermal conduction is defined as the process of transferring energy in the form of heat by atom interaction, which is measured in watts per Kelvin per meter (66). Generally, sintering techniques involve heating schedule and applied pressure, including conventional furnace sintering (e.g. rate – controlled sintering), plasma – assisted sintering, pressure – assisted sintering (e.g. hot

press) (67, 68), microwave sintering (67, 68, 71), and sintering under laser irradiation (66, 70, 71).

Sintering under laser irradiation is the absorption of heat from the incident irradiation, which transfers through atomic lattice vibrations (vibration waves) due to thermal motion of atoms, such as in most ceramics when movement of electrons is restricted within the structure (lattice vibration heat transfer systems) (66). Such vibration waves are scattered by atoms and/or defects in the structure, and result in thermal energy distribution (70). However, in such systems, heat transfer can be affected by the lattice vibration harmony. Harmonic vibration eases the heat flow, whereas anharmonic vibration creates heat flow resistance, and thus, limits heat transfer through the structure (66).

Moreover, in general, materials in powder form exhibit higher absorptance than those in dense/block forms (72). Measurements of absorption coefficients of single – and two – component powder materials, using Nd:YAG and CO₂ lasers, indicates that the powder absorptance is dependent on the wavelength of laser irradiation, and that the absorptance changes with time during laser processing. For example, the absorptance of metals and carbides decreases with increasing wavelength, while that of oxides and polymers increases with increasing wavelength (72).

Laser sintering of a single – component powder material indicates that “the particles either do not sinter at all for a given power density, or undergo a complete melting at a higher power density. The liquid surface – melt contracts to minimise its surface energy, resulting in resolidified droplets” (72). The process is described as being complicated due to the very narrow

processing window of sintering, particularly for materials with a high melting point. High – melting point powders are usually mixed with low – melting point powders as a binding material. Therefore, multi – component powder materials are considered more suitable for sintering than single – component powder materials (72).

Sintering is of great importance to produce bioceramics calcium orthophosphates such as HAp. Unsintered HAp is usually poorly crystalline and non – stoichiometric, such as calcium – deficient HAp (69, 73, 74) in the case of biological apatites (74), even though high crystalline HAp can be produced from aqueous solutions (75). Heat treatment of chemically precipitated HAp is usually carried out at 400 – 600°C in order to refine the crystal structure and improve crystallinity. However, fully crystallised HAp is obtained after sintering at ~ 1200°C (76). Sintering of HAp at $\leq 1000^\circ\text{C}$ introduces particle joining, little or no densification, and significant porosity reduction, whereas sintering at $\geq 1250^\circ\text{C}$ may lead to the decomposition of HAp due to its thermal instability at such elevated temperature. Therefore, HAp is preferably sintered up to the theoretical density between 1000°C and 1200°C (68). On the other hand, other studies report the decomposition of HAp at temperatures $> 600^\circ\text{C}$ and the transformation of HAp to β – TCP at temperature $\geq 700^\circ\text{C}$ (77). Sintering of other calcium orthophosphates, such as monetite and brushite, are carried out $< 400^\circ\text{C}$ (~ 300°C) and $< 100^\circ\text{C}$, respectively, above which the decomposition of these phases occurs (78, 164). Sintering of non – stoichiometric calcium orthophosphates, such as amorphous calcium phosphate (ACP) or calcium – deficient hydroxyapatite (CDHAp), at temperatures $> 700^\circ\text{C}$ results in the formation of biphasic calcium orthophosphates (BCP = HAp + TCP) (73, 74). Sintering of BCP

results in the transformation of α – TCP to β – TCP, and the sintering temperature increases with increasing HAp content in BCP (73, 74). Therefore, beside the sintering temperature and time, sintering of calcium orthophosphates depends on their type and composition (66, 67), particle characteristics such as particle size and particle size distribution (66, 67, 79, 80), and the synthesis rout (79, 80).

2.5 Laser background

The word 'laser' stands for light amplification by stimulated emission of radiation. It is defined as the mechanism for emitting coherent and intense beams of light (81-83). Table 2.3 shows the different types of light spectrum ranging from far – infrared to deep ultraviolet, with wavelengths in the range of 1 nm to 1000 μ m. Anything beyond the far – infrared range is considered radio waves, and anything beyond the ultraviolet range is considered X – rays and gamma rays.

Light is a transverse electromagnetic wave, as shown by the schematic wave in Figure 2.5. "It is a periodic undulation of something – maybe the surface of a pond, if it is a water wave – that moves with velocity, v , the wavelength, λ , is the length of one period. The frequency of the wave, f , is equal to the number of wavelengths that moves in one second past an observer" (83). The shorter the wavelength, or the faster the wave moves, the higher the frequency of the wavelength (83). The height of a wave represents its amplitude.

Equation 2.1 represents the relationship between the frequency (f) of a wave, its velocity (v) (c , the speed of light), and the wavelength (λ).

$$f = \frac{v}{\lambda} = \frac{c}{\lambda} \dots\dots (2.1)$$

Light waves are transverse, in contrast to sound waves, but similar to those of water due to the waving of the electric and magnetic fields in transverse direction to the direction of wave propagation (83).

Table 2.3 Wavelength ranges of different types of light spectrum (81, 82)

Light spectrum	Wavelength
Far – infrared	10 μm – 1000 μm
Near – infrared	700 nm – 10 μm
Visible light	400 nm – 700 nm
Ultraviolet	400 nm – 200 nm
Deep ultraviolet	200 nm – 1 nm

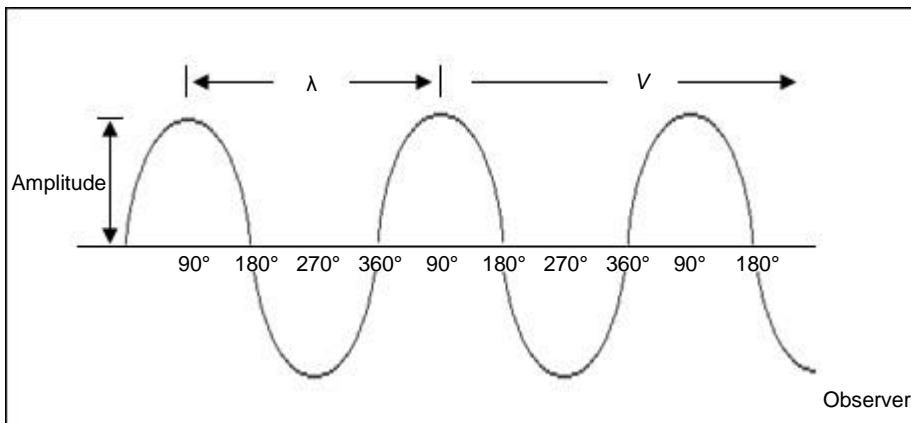


Figure 2.5 Schematic of a transverse electromagnetic wave (83).

Lasers are considered electromagnetic radiations through the process of stimulated emission, by which an electron (in energy state E_2 , and its decay path is to E_1) is disturbed by a passing photon (with energy $\sim E_2 - E_1$), resulting in a photon being emitted at exactly the same wavelength, direction, and phase as the passing photon (81-83). Electromagnetic waves range from radio waves of hundreds or thousands of meters long down to gamma rays in the order of 10^{-12} m (83).

Lasers can be classified according to their gain medium as solid – state (e.g. erbium laser), gaseous (e.g. CO₂ laser), and liquid (e.g. organic dye laser) lasers (83), or according to the laser operating mode as continuous wave and pulsed lasers (84). They can also be classified according to their spectrum region, wavelength range, or colour as infrared (700 nm – 1000 m), visible (400 nm – 700 nm), and ultraviolet (1 nm – 400 nm) lasers (81, 82, 85). In addition, they can be classified according to their effect on tissues as hard lasers (high – level devices) such as surgical and cutting lasers, and soft lasers (low – level devices) such as non – surgical lasers (86).

Medical lasers are required to satisfy three primary properties. These are monochromatic emission, collimation, and coherence (87). Monochromatic emission refers to the monochromatic light or a single wavelength, which is composed of one characteristic colour and associated with an energy gap (87). For example, argon laser beams are blue or blue – green, whereas He – Ne laser beams are red. Collimation or low – divergence of the laser beam is the minimal dispersion of the laser beam as it propagates a matter/tissue (87). “When the tissue's absorptive capacity is very high relative to its scattering ability, the laser beam remains strongly collimated in the tissue,

and the penetration depth is a function of the wavelength – dependent absorption coefficient" (87). Coherence refers to the laser light being in phase, which is useful for diagnostic applications in medicine (87).

Some important commercially available lasers, their best – known wavelengths or region of spectrum, and their average power range are listed in Table 2.4. The lasers can lase at different other wavelengths, and many lasers can produce more than a single, pure colour. CO₂ and Nd lasers are in the infrared region of the spectrum and cannot be seen by the human eye, whereas the red and blue lights from He – Ne and argon lasers, respectively, are visible, and they can be seen by the human eye (83).

The standard output of carbon dioxide (CO₂) lasers is at 10.6 μm , with an output power ranging from < 1 W to > 10 kW (81). Diode lasers are available at different wavelengths, ranging from 630 nm to $\geq 1.6 \mu\text{m}$, and different output powers, ranging from a few milliwatts to several watts (81). Nd:YAG lasers have a strong line at 1.06 μm , and they produce wavelengths in the visible and ultraviolet regions of the spectrum, whereas diode lasers produce wavelengths in the infrared and visible regions of the spectrum (83). Excimer lasers have short wavelengths, ranging from 100 to 300 nm (81). Blue argon – ion lasers at 488 nm wavelength have also been used for many years. Yttrium – aluminium – garnet (YAG), glass, fibre, and diode lasers are solid – state lasers, whereas CO₂, argon – ion, and excimer lasers are gas lasers. Lasers can be run in continuous wave and pulsed modes, except glass and excimer lasers, which run in a pulsed mode (83).

In addition, free electron lasers (FELs), as an infrared light source, are available and offer advantages over conventional lasers, particularly in the

biomedical fields (88, 89). FELs offer a wide wavelength tunability and ultrashort – pulse operation. They can be easily tuned in wavelength and continuously varied in a wavelength range. They have a pulse structure that consists of a chain of macropulses of about 15 μs in width, and each macropulse contains a chain of 300 – 400 ultrashort micropulses. The width of micropulses of 10 ps is measured in the accelerator operation condition for the mid – infrared range. They have a repetition rate of 10 Hz and a partition duration of 45 ns. The micropulses have a very high peak power of several megawatts and a duty factor as low as 3×10^{-8} , which results in a very low average power of 20 – 50 mW, and the influence of thermal effects is avoided in power transmission (89).

Table 2.4 Summary of important commercially available lasers (83)

Lasers	Wavelength	Average power
Carbon dioxide	10.6 μm	Milliwatts to tens of kilowatts
Nd:YAG	1.06 μm 532 nm	Milliwatts to hundreds of watts Milliwatts to watts
Nd:glass	1.05 μm	Watts
Diode	Visible and infrared	Milliwatts to kilowatts
Argon – ion	514.5 nm 488 nm	Milliwatts to tens of watts Milliwatts to watts
Fibre	Infrared	Watts to kilowatts
Excimer	Ultraviolet	Watts to hundreds of watts

2.5.1 Light/photon interaction with energy levels

Light is made up of particles, known as photons, which exhibit particle – like and wave – like properties (81). Each photon has an intrinsic energy, E , given by:

$$E = f \cdot h \dots\dots (2.2),$$

where (f) is the frequency of light, and (h) is Planck's constant. For a wave, the frequency of a wave (f) is given by:

$$f = \frac{c}{\lambda} \dots\dots (2.3),$$

where (c) is the speed of light in a vacuum, (f) is the frequency of light, and (λ) is the wavelength of light. Therefore, the energy of a photon (E) is given by:

$$E = \frac{hc}{\lambda} \dots\dots (2.4),$$

where the energy (E) is dependant of the wavelength of light (λ). The longer the wavelength, the lower the energy of a photon, and vice versa.

Since the interaction of light with matters occurs in detached packets of energy (photons), which are absorbed by atoms when the energy of a photon is equal to the energy differences between two energy states (e.g. E_1 and E_2), the energy of a photon is given by:

$$f \cdot h = E_2 - E_1 \dots\dots (2.5),$$

and consequently, the wavelength of a photon (λ) is given by:

$$\lambda = \frac{hc}{E_2 - E_1} \dots\dots (2.6),$$

where (h) is Planck's constant (6.626×10^{-34} Js), (f) is the optical frequency (c/λ , where (c) is the speed of light, and E_2 and E_1 are the upper and lower energy levels, respectively) (81, 82).

There are three main processes that occur during the interaction of photons with energy levels.

2.5.1.1 Absorption, decay, and emission

Electrons in atoms are distributed around the nucleus in groups, known as shells ($K, L, M, N...$) and sub – shells ($s, p, d, f, g, h, i...$), with a quantum number $n = 1, 2, 3, 4, \infty$ and $n - 1$, respectively. These shells and sub – shells represent the energy levels or states of electrons in an atom, which in turn make up energy bands of a solid (70). The atom's model, (19, 15) in which electrons orbit the nucleus of an atom, and the atom has limited of fixed orbits that are available to the electrons, is known as Boher atom or Boher's model, as shown in Figure 2.6 (81).

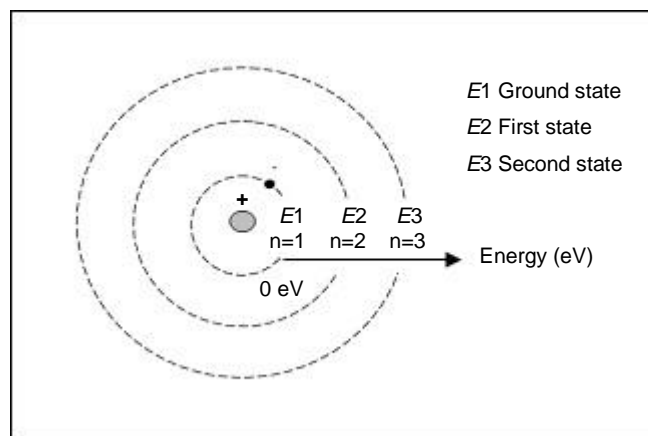


Figure 2.6 Schematic indicating Boher atom and its energy levels.

Atoms absorb energy, including photons, in many ways and move up to higher energy levels, as shown in Figure 2.7. Photons are absorbed when their energy is high enough to excite electrons from the ground state to a higher energy level. A photon is absorbed by an atom when its energy is equal to or greater than the gap energy between two energy levels (e.g. E_1 and E_2), and therefore, electrons are excited to a higher energy level (e.g. E_2), as shown in Figure 2.8. When the energy of a photon is less than the energy required to excite that atom, the photon is not absorbed, and the matter is said to be transparent (70, 81-83).

If the energy of a photon is equal to or greater than the energy level (e.g. E_2), electrons are excited to the energy level (E_2). However, if a valence electron absorbs energy and moves up to the ionisation level, it is released from the attraction forces of the nucleus. The electron is said to become a free electron and in the conduction band, which floats between the atoms and conducts electricity. Consequently, the atom becomes a positive ion (ionised) due to the loss of an electron. When an electron absorbs energy that exceeds the ionisation energy, the excess energy is referred to as the kinetic energy of the free electron outside the atom (70). Excited electrons at a higher energy level (e.g. E_2) are unstable and tend to return to their stable state (ground state, E_1). The decrease in energy is released or emitted as an electromagnetic radiation, and it is given by equation 2.7 (70, 81-83).

$$E_2 - E_1 = h \cdot f = \frac{hc}{\lambda} \dots (2.7),$$

where (f) is the frequency of the emitted radiation, (h) is Plank's constant, (c) is the speed of the electromagnetic waves, and (λ) is the wavelength of the radiation.

2.5.1.2 Spontaneous and stimulated emission

Most atoms are in their ground states, and therefore, incoming irradiation is more likely to be absorbed than to produce stimulated emission. However, if an atom is in an excited state, it may spontaneously (in the absence of photons) decay into a lower energy level after some time, releasing energy in the form of a photon, which is emitted in a random direction. Therefore, spontaneous emission occurs when an excited atom spontaneously relaxes (decay) to a lower energy in the absence of a photon, as shown in Figure 2.9 (70, 81-83). On the other hand, in the presence of photons, the emission can be stimulated by the incoming photons and emitted in the same direction as the incoming photons, which results in the amplification of the incoming irradiation (e.g. lasers). Therefore, stimulated emission occurs in the presence of a photon of the proper frequency, as shown in Figure 2.10 (70, 81-83).

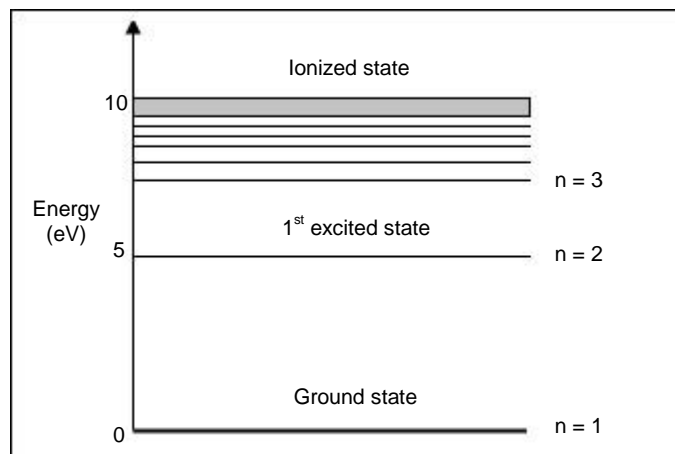


Figure 2.7 Schematic of atomic energy levels indicating different excitation states, to which an electron can be excited from the ground state E_1 .

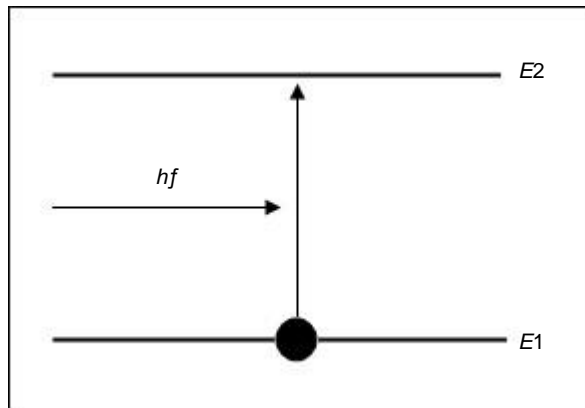


Figure 2.8 Schematic indicating photon absorption.

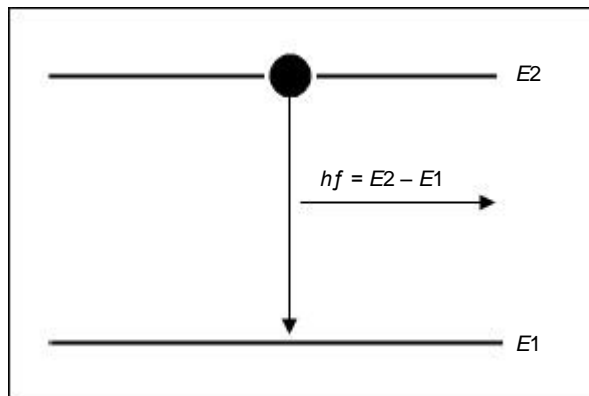


Figure 2.9 Schematic indicating spontaneous emission.

During photon absorption, the energy difference required ($hf = E_2 - E_1$) to excite an atom to a higher level is obtained from the incident electromagnetic wave. Spontaneous emission occurs when an atom is in a higher energy level (E_2) rather than the ground state (E_1); and because E_2 is greater than E_1 , the atom tends to relax (decay) to the ground state (E_1), resulting in energy difference, which is released by the atom in the form of an electromagnetic wave (radiative or non – radiative). Therefore, spontaneous emission can be characterised by the emission of a photon of energy ($E_2 - E_1$) (81-83).

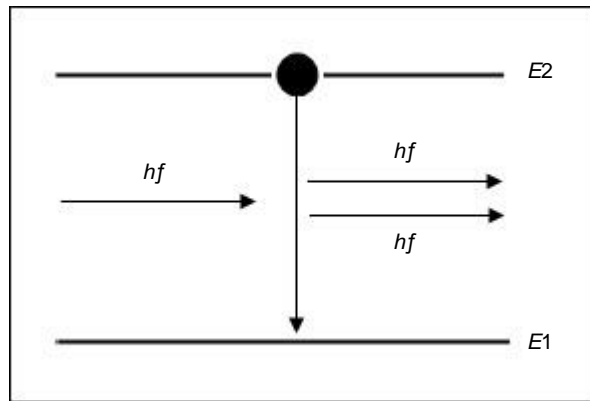


Figure 2.10 Schematic indicating stimulated emission.

On the other hand, in the case of stimulated emission, an excited atom, in the presence of an incident electromagnetic wave of frequency equal to that of a spontaneously emitted wave ($f = f_0$, respectively), is forced to decay, and the energy difference is released as an electromagnetic wave, which is added to the incident wave (81-83).

The process by which an atom gets from a higher energy level to a lower one is known as decay. The difference in energy is released in the form of radiative or non – radiative emission, and consequently, radiative and non – radiative decay. In radiative decay, the energy difference is released in the form of an electromagnetic wave, whereas in non – radiative decay, the energy difference is released in the form of kinetic or internal energy (heat) (81-83, 90). The photon's decay/relaxation to the ground state occurs in three main routes, as shown in Figure 2.11. Thermalisation or non – radiative emission occurs through the collision and vibrational relaxation, while radiative emission occurs through a short – lived photon emission, known as fluorescence, or through a long – lived photon emission, known as phosphorescence (90).

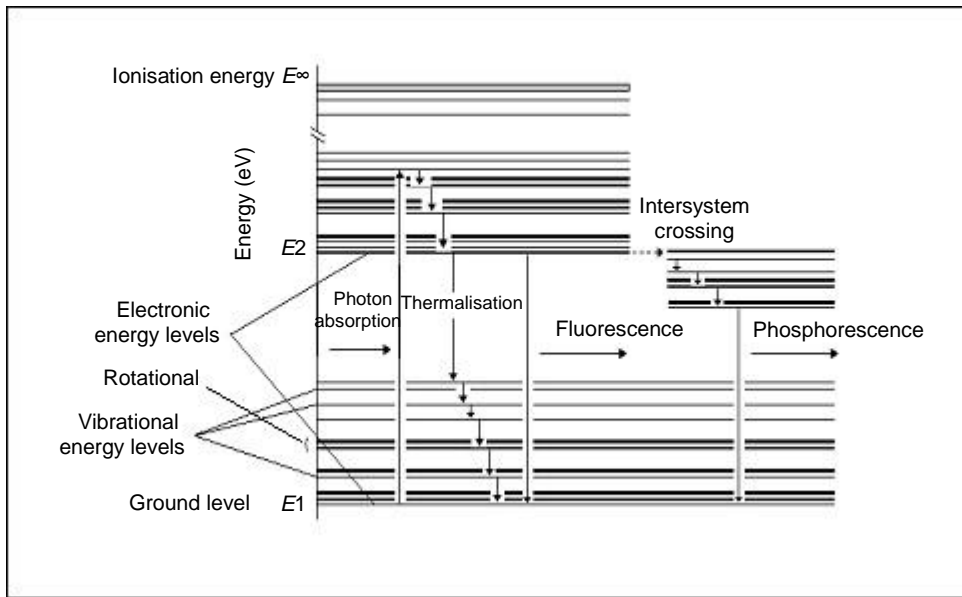


Figure 2.11 Schematic of energy levels showing photon absorption and photon's relaxation/decay routes to the ground level. (a) Thermalisation, through collision and vibrational relaxation, (b) fluorescence, through a short – lived photon emission, and (c) phosphorescence, through a long – lived photon emission (90).

2.5.2 Laser – tissue interaction

In principle, five basic phenomena occur when light interacts with matter/tissue. These are reflection, refraction, transmission, absorption, and scattering (84, 85). These interaction phenomena depend on the absorption properties of the tissue being laser irradiated (85). The effect of refraction in an opaque medium is difficult to measure due to absorption and scattering (84), whereas transmitted light can be detected behind the matter. The ratio of transmitted and incident intensities is known as transmittance. Reflection, absorption, and scattering of an incident beam depend primarily on the material type and the incident wavelength. The latter determines the index of refraction, absorption coefficient, and scattering coefficient. The index of refraction is important when using highly reflecting surfaces such as metallic dental implants (84).

Laser – tissue interaction results mostly in absorption and scattering inside the tissue, with small reflection of about 3%. The absorption of photons by a tissue results in a heat generation inside and around laser beam, whereas the absorbed scattered light might result in heat outside laser beam (87). The interaction of lasers with hard dental tissues involves the interaction of electromagnetic irradiation with tooth mineral, protein, and water, which can be determined by the level of absorption and scattering as well as the absorption depth (86), as follows:

- The level of light absorption in a tissue at a specific wavelength (absorption coefficient). The higher the absorption coefficient value, the higher the absorption of light (86).
- The level of light scattering in a tissue, which depends on the wavelength of light (scattering coefficients) (86). Scattered light is absorbed by a tissue and/or re – emerged from a tissue, and therefore, it generates heat outside laser beam (87).
- The absorption or penetration depth (absorbed energy), which is converted to heat, is released as a thermal radiation (86). It is defined as the depth, at which the collimated light is attenuated by a factor e^{-1} (37%). The penetration depth of a collimated light is the sum of absorption coefficient and the scattering coefficient of a tissue (87).

2.5.2.1 Laser – tissue interaction phenomena

2.5.2.1.1 Reflection and Refraction

The returning of laser irradiation by reflecting surfaces, upon which it is applied, is known as reflection. It occurs when the density of matter/tissue or angle of the incident beam is less than the refractive angle (85). Reflection requires that reflected beams lie within one plane, known as plane of incident, where the reflection angle is equal to the incident angle, however, other several beams do not lie within the plane of incident, and thus, no longer applies (84). There are two types of reflections, depending primarily on the surface irregularities and the wavelength of laser irradiation. When surface irregularities are smaller than the wavelength of laser irradiation, a speculum reflection occurs, but only in some cases such as wet tissue surfaces. On the other hand, diffuse reflection, which is the common phenomenon in all tissues, occurs when surface irregularities are comparable or larger than the wavelength of laser irradiation (84).

The measurement of the amount of reflected laser irradiation represents the surface reflectivity, which is the ratio of reflected and incident electric field amplitudes. Reflectance is the ratio of corresponding intensities or the square of reflectivity. Reflectivity and reflectance depend on the angle of incidence and polarisation of laser irradiation as well as the indices of refraction of surface. A refracted beam is the total conserved energy in incident and reflected beams. “In general, a reflecting surface is the physical boundary between two materials of different indices of refraction such as air and tissue”, which usually results in the phenomenon refraction (84). It is based on the change in the speed of light wave. Indices of refraction are difficult to measure because of absorption and scattering (84).

2.5.2.1.2 Transmission

During transmission process, laser irradiation passes through a matter/tissue, and thus, no interaction with matter/tissue occurs, and the laser propagates unchanged, or it is partially refracted (85). The interaction of dental hard tissues with laser irradiation is characterised by their large transparency to laser irradiation at the visible and near – infrared wavelengths, which results in a minimal reflection, while they reflect laser irradiation at the mid – infrared wavelengths (86).

2.5.2.1.3 Absorption

Absorption can be defined as the phenomenon, during which the intensity of an incident beam passing through a matter is attenuated. The absorbance of a matter is the ratio of absorbed and incident intensities. The measure of the level of absorption that occurs in hard dental tissues by a specific wavelength of laser irradiation is known as the absorption coefficient. Low – absorption coefficient values indicate little absorption, whereas high – absorption coefficient values indicate high absorption (86). Absorbed energy is converted to another form of energy, such as heat, depending on the amount of absorbed energy, for example, the absorption of low amount energy results in a biostimulation of the receptor tissue sites (85). During absorption, the energy of a beam is converted into heat wave or vibration of molecules of absorbing matter. Matters that permits light and do not absorb it are called transparent such as biological tissues, cornea, and lens. On the other hand, in opaque matters, incident laser irradiation is reduced to zero. Therefore, transparency and opacity depend on the wavelength of laser irradiation (84).

General absorption is the reduction in intensity of all wavelengths in the considered spectrum by a similar fraction, whereas selective absorption is the absorption of specific wavelengths. Absorption depends on the electronic constitution of atoms or molecules of absorbing matter, the wavelength of laser irradiation, and the thickness of absorbing matter, as well as internal factors such as temperature or concentration of absorbing agent. In biological tissues, absorption mainly occurs due to water molecules or proteins (84).

Laser irradiation absorption in enamel and dentine is very low at the visible and near – infrared wavelengths, while it is very high at the mid – infrared wavelengths. The absorption of mid – infrared wavelengths in enamel is much higher with CO₂ lasers than erbium lasers, particularly at wavelengths of 9.6 μm and 9.3 μm (86). Very low – absorption coefficient values result in ineffective tissue interaction, unless targeting pigmented carious lesions, which have higher absorption coefficient values at the visible and near – infrared wavelengths (86). Moreover, Er:YAG laser at 2.94 μm wavelength are absorbed by water in hard dental tissues, and thus, it is effective in tissue ablation. The absorption coefficient of water by Er:YAG lasers is 10⁴ cm⁻¹ and ~ 7 x 10² cm⁻¹ at wavelengths of 2.94 μm and 9 – 10 μm, respectively (89).

2.5.2.1.4 Scattering

Resonance and absorption occur if the frequency of laser irradiation is equal to the natural frequency of free vibrations of a particle, however, when the frequency of laser irradiation is not equal to the natural frequency of free vibrations of particles, scattering occurs. The forced vibration has the same frequency and direction of the electric force in incident laser irradiation, with

much smaller amplitude and different phase from incident laser irradiation. Some scattering may also occur if the interface of matter/tissue is rough or non – homogenous (85). There are mainly two types of scattering, elastic scattering such as Rayleigh scattering, and inelastic scattering such as Brillouin scattering. In elastic scattering, the energy of incident photons is the same as that of scattered photons. Most biological tissues scatter photons in the forward direction (84). During scattering, uncontrolled direction of laser radiation interacts to some extent with matter/tissue, such as back scattered irradiation, which is common with short wavelengths (e.g. diode and Nd:YAG lasers) (85). Although Nd:YAG lasers at wavelength of 1060 nm deeply penetrate tissues, 30 – 50% of laser irradiation re – emerges from tissues (87).

Laser irradiation scattering in enamel and dentine is negligible or not measurable at the mid – infrared wavelengths, while it is relatively higher at the visible and near – infrared wavelengths. Both CO₂ and erbium laser irradiation are not scattered in enamel and dentine. Laser irradiation scattering at the visible and near – infrared wavelengths is much higher in dentine than enamel, with dentine having similar scattering coefficient values, while scattering in enamel is relatively higher at the visible wavelengths than the near – infrared wavelengths (86).

The interaction of some lasers (of different light spectra and wavelengths) with hard dental tissues (enamel and dentine), determined by absorption coefficient and scattering coefficient, are presented in Table 2.5, which can be used to determine other optical properties such as penetration depth. Optical parameters in enamel and dentine are reported in the ultraviolet,

visible, and infrared spectral ranges and at wavelengths between 200 nm and 3000 nm (86, 87, 89, 91-99). Absorption in enamel is very weak in the visible range 400 – 700 nm, with an absorption coefficient of $< 1 \text{ cm}^{-1}$, which increases to $\mu_a > 10 \text{ cm}^{-1}$ in the ultraviolet range ($< 240 \text{ nm}$). Absorption in enamel is also very weak under YAG laser irradiation in the near – infrared range, at wavelengths of $\sim 1060 \text{ nm}$, with an absorption coefficient of $< 1 - \sim 1 \text{ cm}^{-1}$. However, absorption in enamel is very strong under CO_2 laser irradiation in the near – infrared range, at wavelengths of 930 – 1060 nm, with an absorption coefficient of 819 – 8000 cm^{-1} , and erbium laser irradiation in the mid – infrared range, at wavelengths of 2078 – 2094 nm, with an absorption coefficient of 480 – 1500 cm^{-1} . On the other hand, absorption in dentine is stronger than in enamel, with an absorption coefficient of 3 – 4 cm^{-1} under YAG laser irradiation in the visible range 400 – 700 nm and near – infrared range, at 1060 nm wavelength. Absorption in dentine is very strong under CO_2 laser irradiation in the near – infrared range, at 1060 nm wavelength, with an absorption coefficient of 813 cm^{-1} , and erbium laser irradiation in the mid – infrared range, at wavelengths of 2078 – 2094 nm, with an absorption coefficient of 660 – 2000 cm^{-1} .

Scattering in enamel is strong in the near ultraviolet range, at 1300 nm wavelength, with a scattering coefficient of 2 – 3 cm^{-1} , which decreases with increasing the wavelength (96). Scattering in enamel is much higher in the visible range than in the ultraviolet and infrared regions, with a scattering coefficient of 15 – 105 cm^{-1} . In contrast, scattering in dentin is strong throughout the near ultraviolet (96), visible, and near – infrared regions, with a scattering coefficient of 130 – 280 cm^{-1} . The scattering coefficient in

enamel and dentine in the mid – infrared range is approximately zero, because it is negligible or not measurable.

The data of absorption and scattering coefficients in Table 2.5 indicate that enamel and dentine greatly absorb light in the mid – infrared region of the spectrum, with scattering coefficient values of approximately zero, while in the near – infrared and visible regions, enamel and dentine transmit light due to their low absorption coefficient values, and thus, higher scattering coefficient. Never the less, dentine has an absorption coefficient value three to four times that of enamel, and the scattering coefficient values of dentine are much larger than that of enamel under the visible and near – infrared irradiation.

Moreover, optical penetration depths in enamel and dentine are reported in the ultraviolet, visible, and infrared spectral ranges and at wavelengths between 200 nm and 3000 nm (51, 56, 63, 86, 91, 94, 100-104), as presented in Table 2.6. The optical penetration depth in enamel is highest in the ultraviolet range 250 – 600 nm, with a penetration depth of 60 – 120 μm . The optical penetration depth in enamel varies in the visible and infrared regions, with penetration depths of $\sim 1.8 \mu\text{m}$ and 1 – 25 μm , respectively. Similarly, the optical penetration depth in dentine is highest in the ultraviolet range at wavelength of 248 nm, with a penetration depth of 83 μm , however, it is low in the visible and infrared regions, with penetration depths of 1.02 μm and 0.1 – 50 μm , respectively.

Successful application of lasers in dentistry requires basic knowledge of the optical properties of hard dental tissues such as absorption coefficient, scattering coefficient, and penetration depth (93), and similarly, the optical

properties of dental restorative materials. The degree of absorption and scattering of light in dental tissues depends on tissue structure (e.g. enamel and dentine) and composition (e.g. content of water and hydroxyapatite) (93), and similarly, the structure and composition of dental restorative materials such as synthetic apatite minerals. Absorption and scattering of light are much stronger in dentin than in enamel, and thus the scattering coefficient is much larger than the absorption coefficient (105, 106).

In general, absorption and transmission of laser irradiation in hard dental tissues depend on laser wavelength (107), and particularly, the absorption of laser energy by water and hydroxyapatite is wavelength dependent (91). Absolute values of absorption coefficient for tissues are in the range $10^2 - 10^4 \text{ cm}^{-1}$ (108). Absorption in water and HAp is low at wavelength of $2 \mu\text{m}$ and high at wavelengths of $3 \mu\text{m}$ and $10 \mu\text{m}$, and it is about 10,000 times lower at $1 \mu\text{m}$ wavelength than that at $3 \mu\text{m}$ (109-111). On the other hand, scattering coefficient is not related to the content of apatite mineral, and the mineral crystals are not the main cause of light scattering in dentine (95). Since scattering in dentine is low at the EDJ, which has a low density of dentinal tubules, and based on the scattering variation between low and high – density areas of dentinal tubules, dentinal tubules are responsible for scattering of light in dentine (95).

Table 2.5 Optical properties (Absorption coefficient $\mu_a \text{ cm}^{-1}$ and scattering coefficient $\mu_s \text{ cm}^{-1}$) for different light spectra and wavelengths in hard dental tissues (enamel and dentine) (86, 87, 89, 91-99)

Light irradiation type			Dental hard tissue				Ref
Light spectrum	Irradiation Type	Wavelength (nm)	Enamel		Dentine		No.
			$\mu_a \text{ cm}^{-1}$	$\mu_s \text{ cm}^{-1}$	$\mu_a \text{ cm}^{-1}$	$\mu_s \text{ cm}^{-1}$	
Ultraviolet	UV	< 240	> 10	-	-	-	98
		1300	-	2 – 3	-	-	
Visible	UV – Vis spectrometer	400 – 700	-	-	4 ^(0.1)	30 ^(0.5)	95
			-	-	8 ^(0.1)	80 ⁽¹⁾	
	Visible light	400 – 700	< 1	-	~ 4	-	98
			* 0.001	-	-	-	87
		543 (green)	-	105 ± 30	-	280 ± 84	94
			< 1	105	3 – 4	280	86, 93
			< 1	45	4	180	
		632 (red)	-	60 ± 18	-	280 ± 84	94
			< 1	60	3 – 4	280	86, 93
			< 1	25	4	130	
Infrared	Fibre coupled	1053	-	15 ± 5	-	260 ± 78	94
	Nd:YAG	1064	< 1	15	3 – 4	260	86, 93
	YAG	1060	~ 1	-	-	-	87
	Er:YAG	2940	1500	-	2000	-	91
			1000	-	-	-	89
			800	~ zero	-	~ zero	86, 97
			0.77 ^{Des}	-	0.77 ^{Des}	-	
			1 ^{Nat}	-	1 ^{Nat}	-	
	Er:YSGG	2790	480	~ Zero	-	~ Zero	86
	Er,Cr:YSGG	2780	500	-	660	-	91
			480	-	-	-	97
		2790	0.96 ^{Des}	-	0.55 ^{Des}	-	92
			0.96 ^{Nat}	-	0.68 ^{Nat}	-	
	CO ₂	930	5500	~ Zero	-	~ Zero	86, 99
			8000	~ Zero	-	~ Zero	
			1125	~ Zero	-	~ Zero	
			825	~ Zero	-	~ Zero	
1060			819	-	813	-	96

Des = desiccated, Nat = natural, “Des and Nat = absorption coefficients are normalised to the values for 2.94 μm in natural dentin and enamel”, and values in brackets ^() are the thickness of dentine sections in mm, and (*) is the absorption of water in enamel.

Table 2.6 Optical penetration depths for different light spectra and wavelengths in enamel and dentine (51, 56, 63, 86, 91, 94, 100-104)

Spectrum type	Irradiation type	Wavelength (nm)	Penetration depth (µm)		Ref	
			Enamel	Dentine		
					No.	
Ultraviolet	KrF excimer	248	-	83	102	
	UV – specific EPR	250 – 600	60 – 120	-	104	
Visible	Fibre coupled light	543	* 1.8 ± 0.1	* 1.02 ± 0.01	94	
		632				
		1053				
Infrared	Diode lasers	800		** 0.1	63	
	Nd:YAG	1060	-	** ~ 4	101	
			-	** < 4	56	
	Er lasers	-	-	** ~ 10	63	
	Er:YAG	2940	7	5	91, 100	
			12	-	86	
			+ 10 – 20	+ 30 – 50	91	
			+ 15	+ 30 – 40		
	Er,Cr:YSGG	2790	21	15	91, 100	
			25	-	86	
			-	10	103	
	CO ₂		930	2	-	86
			960	1	-	
			1030	9	-	
			1060	12	-	
-			-	** 2 – 8	51, 56	

(*) are the light penetration depth ratios, (**) are the sealing depths of dentinal tubules, and (+) are the crater's depths. EPR is the electron paramagnetic resonance.

Tissue components that demonstrate higher absorption coefficient for particular wavelength or spectrum of light energy are called chromophores (93). The absorption and scattering properties at each wavelength are important due to the variations in absorption associated with different chromophores in a tissue (87). The main biological tissue chromophores responsible for light absorption are melanin, haemoglobin, oxyhemoglobin, bilirubin, and water (94). Similarly, synthetic dental restorative materials have components that demonstrate higher absorption coefficient for particular wavelength or spectrum of light energy such as rare earth erbium in the present research study.

According to the light spectrum, ultraviolet light is well absorbed by water and HAp, whereas the mid – infrared light absorption by water and hydroxyapatite (HAp) varies depending on the wavelength of light (93). Light absorption in the near – infrared region with wavelengths longer than 1000 nm is dominated by water (94). In the visible and near – infrared regions, enamel and dentine show low values of absorption coefficient of $1 - 4 \text{ cm}^{-1}$, compared to their high values of scattering coefficient ($15 - 280 \text{ cm}^{-1}$). Despite such lower values of absorption coefficient, absorption of light by enamel and dentine is relatively high (10 – 20%), due to the high efficiency of travelling photons absorbed in a scattering medium and caused by the longer photon pathways within the scattering medium (108).

Er:YAG laser irradiation is strongly absorbed by water, while Er:YSGG irradiation is absorbed by water and OH group in apatite minerals (93). The wavelength of 2094 nm for Er:YAG laser corresponds to water, at which the vaporization of water occurs, while the wavelength of 2078 nm for

Er,Cr:YSGG laser corresponds to OH groups, at which the transfer of conductive heat from the mineral to water occurs (97). Pulsed Er:YSGG lasers at 2.79 μm wavelength have a very strong absorption by water, with an absorption coefficient of about 7000 cm^{-1} (92), which is much higher than the reported value of $\sim 480\text{ cm}^{-1}$ for CW Er:YSGG lasers in Table 2.5. Pulsed Er:YAG lasers, however, have an absorption coefficient of about 13000 cm^{-1} (92), which is within the reported values $800 - 1500\text{ cm}^{-1}$ in Table 2.5. Absorption by water in natural (an – hydrated) enamel and dentine is stronger at 2.94 μm wavelength than at 2.79 μm wavelength. However, absorption in dehydrated dentine decreases significantly, and both lasers (Er:YAG and Er:YSGG) have similar effects. The absorption in dehydrated enamel is higher at 2.79 μm wavelength than at 2.94 μm wavelength, which is caused by a strong absorption by hydroxyapatite (92). In addition, CO_2 laser wavelengths of 9.3 μm , 9.6 μm (86), and 10.6 μm (96) are strongly absorbed by hard dental tissues, particularly by the apatite mineral at wavelengths of 9.3 μm and 9.6 μm . The laser wavelength of 9.45 μm corresponds particularly to the infrared absorption of phosphate ions (89). Such strongly absorbed laser irradiation has the best effect at the lowest fluence (energy/surface area) (86).

The higher the absorption coefficient, the smaller the absorption depth (86). The latter is the depth, within which the majority of energy is absorbed during a laser pulse for pulsed lasers (86) or irradiation time for CW lasers (87). Absorption depth is the sum of tissue absorption and scattering coefficients (87). In enamel and dentine, CO_2 lasers at 10.6 μm wavelength have an absorption coefficient of $\sim 800\text{ cm}^{-1}$, which is smaller than that for Er:YAG lasers of $\sim 1000 - 2000\text{ cm}^{-1}$ at 2.94 μm wavelength. Therefore, the

wavelength of CO₂ lasers penetrates deeper than that of Er:YAG lasers (87). The range of wavelengths with deeper light penetration is referred to as the tissue optical window or therapeutic window, and it is used for various diagnostic and therapeutic treatments (93). Maximum light penetration into tissue occurs where water absorption is lowest, particularly, in the mid and near – infrared regions of the spectrum (90). Absorption by water is very low at wavelength range ~ 600 – 1300 nm, while it is strong at longer wavelengths > 1300 nm, which significantly reduces light penetration (93).

The right amount of laser energy is necessary to obtain desired effects. Energy exceeding a required amount results in energy absorption by the surrounding tissue and causes thermal stress or pulpal damage (86). Absorbed energy is converted to heat, and then heat flows as a thermal radiation into or out of tissue (86). Heat generation is determined by the local absorption of laser irradiation. Heat transfers to cooler regions by means of conduction, which depends on the thermal conductivity and diffusivity of tissues (87), and similarly, the thermal conductivity and diffusivity of dental restorative materials. Surface temperature of 400°C and above decomposes the apatite mineral in enamel and transforms it to a much less soluble apatite (112, 113), whereas temperatures of 800°C up to 1200°C melts the apatite mineral and transforms it when cooled (114, 115). Er,Cr:YSGG laser irradiation, even in the presence of a water spray, causes thermal damage to dentine in the form of brownish spots due to laser energy or repetition rate (91). This is due to a higher absorption of the Er,Cr:YSGG laser irradiation at 2.78 µm wavelength, compared to the Er:YAG laser irradiation at 2.94 µm wavelength (116), as well as the high content (~ 20%) of the organic material in dentine, which is mostly of collagen type I (91).

“The higher the penetration depth, the larger the volume of directly heated tissue that needs to be rapidly heated up, and the higher the laser pulse power that is required for efficient and cold ablation” (91). The ablation/removal depths for CW and pulsed lasers in enamel and dentine are compared in Table 2.7 (117, 118). The ablation/removal depths using ultrashort pulse fibre lasers are much larger in dentine than in enamel, with depths of 16 – 108 μm and 5 – 8.6 μm , respectively. They are also larger than the ablation/removal depths in dentine using CW CO_2 lasers (1 – 49 μm). Ablation of enamel and dentine requires the right laser wavelength, at which absorption is high enough to contain the energy deposition near the surface and avoid unnecessary scattering (86). In addition, the right energy is required to be above the ablation threshold, and the right pulse duration is required to deliver sufficient energy in an optimum period to achieve continuous ablation (86).

Table 2.7 Optical ablation/removal depths for pulsed and CW lasers in hard dental tissues enamel and dentine (117, 118)

Irradiation	Laser irradiation parameters				Ablation/removal depth (μm)		Ref
	Wavelength (nm)	Repetition rate (KHz)	Time-average power (W)	Pulse duration (ps)	Enamel	Dentine	
Ultrashort pulse fibre laser	1552	50	0.15	1.3	8.6	16	117
		62.5	0.18		5.3	28	
		100	0.29		6.1	33	
		250	0.73		5.0	65	
		500	1.31		5.7	108	
CW CO_2 laser	1060	Energy density J cm^{-2}	Power density W cm^{-2}	Irradiation time μs	Enamel	* Dentine	118
		5.3	15×10^3	350	-	3 – 8	
		8	13×10^5	6	-	1 – 4	
		13	95×10^3	140	-	2 – 7	
		13	33×10^4	39	-	2 – 5	
		50	13×10^5	38	-	11 – 16	
200	52×10^5	38	-	38 – 49			

Ps = picoseconds, (*) dentine sections parallel to DEJ – perpendicular to DEJ.

All erbium laser wavelengths operate in the spectrum region where high absorption by water occurs, and thus, they are the most suitable for tissue ablation. In contrast, CO₂ and Ho:YAG laser irradiation show significantly lower absorption in water, and thus, they are less suitable for tissue ablation (91). Er:YAG laser irradiation at wavelength of 2.94 μm (in the infrared region) is absorbed by water molecules in hard dental tissues and results in tissue ablation (89). Er:YSGG laser irradiation shows minor ablation effect, compared to Er:YAG laser irradiation, due to a lower absorption coefficient of hard dental tissues (92). Ablation at 9.4 μm wavelength in the area containing phosphate ions improves the crystalline structure of dentine, and subsequently, the surface structure of dentine (89). Therefore, erbium lasers are considered optimal dental lasers for effective, precise, and minimally – invasive ablation of hard dental tissues (116).

It can be concluded that more laser energy is needed to remove enamel tissue than dentine tissue, due to the high water content in dentine, which is almost twice that in enamel (8, 97). Differences in the ablation thresholds of enamel and dentine may also be due to variations in their structures and the presence of dentinal tubules (97). The ablation threshold depends on the parameters of hard dental tissue and laser irradiation used (97).

All infrared lasers (91), particularly Er:YAG and Er,Cr:YSGG lasers (100), exhibit the highest absorption by water and hydroxyapatite in hard dental tissues, and thus, they are suitable for optical drilling in hard dental tissues and dental composite materials (91, 100). The red and near – infrared light wavelengths enhance the transmission through sound (surrounding) tissue, and thus, they are suitable for caries detection. The latter involves the

delivery of low levels of power energy (energy over time) in the milliwatt region to a tissue as well as differentiating tissue (86). On the other hand, the mid – infrared wavelengths of 2.94 μm and 2.78 μm for Er:YAG and Er:YSGG lasers, respectively, are strongly absorbed by tissues, and thus, they are suitable for tissue ablation, the latter which requires the fluence to be above the ablation threshold (86). CO₂ lasers wavelengths of 9.3 – 10.6 μm are suitable for caries prevention, because they alter the apatite mineral and make it less soluble (86). In addition, strongly absorbed laser irradiation by water at wavelength of ~ 3 μm may also be useful in caries prevention (86). Moreover, Pulsed lasers with a repetition rate of 10 Hz and fluence as low as 2.5 J/cm² have a high inhibition of dental demineralization (86).

Therefore, the outcome of interaction of laser irradiation with hard dental tissues depends primarily on the laser irradiation parameters, including laser type, wavelength, power, and irradiation time, as well as the properties of tissue being irradiated such as absorption and scattering coefficients. Laser parameters include laser wavelength, laser mode (CW or pulsed) absorption properties, scattering, energy, fluence (energy/surface area), power density, repetition rate, and pulse duration. All these parameters contribute in the laser – tissue interaction, however, the extent of laser absorption by a tissue is primarily determined by the laser wavelength (84, 86).

Different wavelengths have different interaction outcomes. For example, infrared transmission in enamel is characterised by OH⁻ ion in HAp mineral, while absorption by water occurs at 3 μm and in the range 9 – 11 μm . The latter is also absorbed by phosphate (PO₄³⁻) and carbonate (CO₃²⁻) ions in the HAp mineral, whereas carbonate (CO₃²⁻) substitution for phosphate

(PO_4^{3-}) in the HAp mineral as well as absorption of amide groups in the protein occurs at 7 μm . (86). In addition, pulsed lasers are preferred to CW lasers, since the latter provide unnecessarily extra amount of energy, while pulsed lasers allow for the delivery of short and high intensity energy, with relaxation periods in order to avoid damaging the surrounding tissues such as pulp (86). Pulse durations also facilitate the dissipation of heat in a tissue during the relaxation periods (119, 120). Calculation and assessment of CW laser applications should include three variables: power, irradiation time, and spot size, whereas pulsed lasers are described in terms of the energy contained in each pulse – the integrated power of a pulse. “The average power pulse instead of being equal to the peak power divided by the pulse duration, is closer to one – half of that value” (87).

Therefore, the laser wavelength is the primary key in laser – tissue interaction, which ensures the right absorption of energy and avoid unnecessary scattering. Moreover, correct pulse durations are necessary for the delivery of the right energy. Longer pulse durations deposit some energy in the surface and the remainder in the subsurface, whereas “shorter pulse durations closer to the thermal relaxation time of tissues, are expected to use much lower fluencies to produce similar effects” (86). The fluence can vary depending on the desired effects, for example, the energy/surface area ratio should be below the ablation threshold to introduce surface effects, such as in caries preventive therapies, and it can exceed the ablation threshold to introduce subsurface effects (86).

2.5.2.2 Laser – tissue interaction mechanisms

There are various mechanisms for the interaction of laser irradiation and biological tissues, depending on tissue characteristics and laser parameters (84, 90). The optical tissue properties, reflection, absorption, and scattering coefficients, determine the total transmission of a tissue at a specific wavelength (84). Other important parameters include thermal properties of tissues such as heat conduction and heat capacity, and laser irradiation parameters such as wavelength, exposure time, applied energy, focal spot size, energy density, and power density (84, 90). There are three main light – tissue interaction mechanisms: photochemical, photothermal, and photoplasma (87). Other possible interaction mechanisms include photoablation and photodisruption (84, 90).

2.5.2.2.1 Photochemical interaction

The term photochemical indicates the ability of light (absorbed photons) to induce chemical effects and reactions within biological tissues (63, 84, 87, 90). Photochemical interaction takes place at a very low power density of 1 W/cm² (84, 87) and long exposure time (from 1 second to continuous wave) (84). Mostly, it involves the use of wavelengths in the visible range due to their efficiency and high penetration depths (84). During therapeutic applications (photodynamic therapy) (63, 84, 90), the use of a photosensitizer as a catalyst, such as organic dyes, is important to induce selective photochemical reactions for specific biological transformations (84, 90). Biostimulation is another special application of photochemical interaction with biological tissues, which occurs at very low laser powers (1 – 5 mW). Wound healing and tooth pain relief, using He – Ne and diode lasers, are some of biostimulation applications (84).

2.5.2.2.2 Photothermal interaction

The term photothermal indicates the ability of light (absorbed photons) to induce thermal effects within tissues, mainly, the increase in temperature (63, 84, 87, 90) due to the conversion of photon's energy into heat (63, 87, 90). Photothermal interaction can be induced by pulsed and CW lasers such as CO₂, Nd:YAG, Er:YAG, and diode lasers (84). It takes place at power densities and pulse durations ranging from 10 to 10⁶ W/cm² and 1 μs to 1 minute, respectively (84). Different thermal effects, such as coagulation, vaporization, melting (63, 84, 87), welding, and cutting (63, 90), depend on the laser duration and achieved temperature of biological tissues (63, 84). The interaction also involves heat transport to cooler regions by conduction, convection, or radiation (84, 87). The latter occurs if power densities of CW lasers are ≥ 10 W/cm², or if pulse duration of pulsed lasers is > 1 μs (84).

2.5.2.2.3 Photoablation

The term photoablation indicates the ability of light (absorbed photons) to induce ablation effects within tissues (63, 84, 87, 90). It was first identified as an ablative photodecomposition, due to the decomposition of materials when exposed to high intense laser irradiation (84). It can be defined as the removal of a tissue without any thermal damage, and the tissue is said to be "etched" (84). It works by direct breaking of molecular bonds by high – energy UV photons (84, 87, 90) such as ArF and KrF excimer lasers (84). It occurs at power densities and pulse durations ranging from 10⁷ to 10¹⁰ W/cm² and 10 to 100 ns, respectively (84). Its applications include refractive corneal surgery (84, 90).

2.5.2.2.4 Plasma – induced ablation

Plasma – induced ablation or plasma – mediated ablation can be defined as the removal of a tissue without any thermal or mechanical damage (84). It works by the formation of plasma (ionised molecules) (84, 90), using lasers such as Nd:YAG, Nd:YLF and Ti:Sapphire (84). The Plasma is formed at irradiance approximately $10^8 - 10^9 \text{ W/cm}^2$ (87). Plasma generation and shock – wave generation are physical effects associated with optical breakdown (84, 87). Plasma generation is generally referred to as dielectric breakdown (84, 87), however, the term optical breakdown indicates that plasma strongly absorbs ultraviolet, visible, and infrared light (84). The strength of local electric field is the most important factor, as it determines the breakdown, which occurs beyond a certain threshold value (84). It occurs if an applied electric field forces the ionization of molecules and atoms at power densities and pulse durations ranging from 10^{11} to 10^{13} W/cm^2 and 100 fs to 500 ps, respectively (84). Lens capsulotomy (84, 90) and dental caries (84) are some of its applications.

2.5.2.2.5 Photodisruption

Like plasma – induced ablation, photodisruption originates from optical breakdown (84). It can be defined as the mechanical effects associated with plasma formation (90), or the removal of a tissue by mechanical effects that occur under higher pulse/plasma energies (84). Mechanical effects include cavitation, jetting, and shockwaves (90). It occurs at power densities and pulse durations ranging from 10^{11} to 10^{16} W/cm^2 and 100 fs to 100 ns, respectively (84). Its applications include lens fragmentation (84) and lithotripsy (84, 90).

2.5.3. Dental lasers

Laser types include solid – state lasers, gas lasers (helium neon, helium cadmium, and carbon dioxide lasers), diode lasers, chemical lasers, optically pumped lasers, etc., all of which have many scientific applications (spectroscopy and analysis), industrial applications (cutting and welding), and clinical and medical applications (surgical procedures) (81, 82).

The occlusion of dentinal tubules by the proposed methodology in the present research study will require dental practices to buy a new laser suitable for the photoactivation of Er^{3+} , Al^{3+} , F^- – doped CaP material. In addition, Er^{3+} , Al^{3+} , F^- – doped CaP material will require a range of regulatory approval requirements and standards set out for healthcare products, which are fundamental to its success and to ensuring its suitability and safety.

In dentistry, there are two basic operation modes for dental lasers: continuous – wave mode such as carbon dioxide and diode lasers, and pulsed mode such as Nd:YAG, Er:YAG and Er,Cr:YSGG lasers (121). However, pulsed lasers are preferred to CW lasers, because they help minimizing some of the undesirable residual thermal damage associated with CW lasers (121).

There are significant differences in the penetration depth of lasers into dental tissues, as shown in Table 2.6. These include the penetration of a few millimetres by diode and Nd:YAG lasers, ~ 0.5 mm by CO_2 lasers, and just 5 μm (on tissue's surface) by erbium lasers (121). The amount of energy absorbed by dental tissues depends on characteristics of tissues, laser wavelength, and laser mode (63, 84). Hard tissues, such as teeth, are characterized by hydroxyapatite, water, and proteins, which interact with

laser irradiation (63, 84, 86). Long wavelengths between 2,000 and 10,600 nm interact more with water and hydroxyapatite (63). Pulsed lasers are absorbed more than CW lasers (63, 92), with the largest absorption peak for water is at the Er:YAG wavelength just below 3,000 nm (63, 89). Erbium lasers are also well absorbed by hydroxyapatite (63). The spot size of laser beam determines the concentration of laser energy and power density, which can be controlled by moving the beam towards and away from the irradiated area (63).

Available lasers that are used in dentistry are presented in Table.2.8, which shows laser name, wavelength, delivery system, and emission mode (122, 123). These lasers are in the visible, invisible, and non – ionizing region of the electromagnetic spectrum, with wavelengths of about 500 nm (0.5 μ) to 10,600 nm (10.6 μ), and they emit thermal irradiation (63).

Dental lasers used for the treatment of dentine hypersensitivity are classified as low – output power lasers (e.g. diode lasers) and middle – output power lasers (e.g. CO₂, Nd:YAG and Er:YAG lasers) (51, 52, 56). Lasers as a dentine hypersensitivity treatment for the occlusion of dentinal tubules (2, 51 – 56, 63) are also used in conjunction with other dental treatments such as desensitising agents and composites (51-53, 56, 62, 63). Different studies on the occlusion of dentinal tubules by laser irradiation (e.g. Nd:YAG, Er:YAG, CO₂, argon, and diode lasers) with and without desensitising agents (e.g. fluoride varnish/gel containing NaF₂/SnF₂, Bioglass, and carbonate apatite) show different speculations (51-54, 56, 62, 63, 124). However, the occlusion of dentinal tubules is more effective using

desensitising agents and laser irradiation together (51, 56, 124, 125, 126, 127, 128, 129).

The occlusion mechanism of desensitising agents is achieved mechanically by the precipitation of insoluble salts, such as calcium fluoride, in the case of fluoride gels (128). The occlusion mechanism of laser irradiation can be achieved by biostimulation/depolarisation or melting processes. The biostimulation/depolarisation process involves the use of low – level lasers, which prevents the diffusion of pain into the central nerve system (51, 52, 62, 128). On the other hand, the melting process involves the recrystallisation of the inorganic component of dentine (54, 58, 128, 130), the formation of a secondary/tertiary dentine (55, 131, 132), and the coagulation of the dentinal fluid (128, 133), using high – level lasers.

The mechanism of the occlusion of dentinal tubules using Nd:YAG laser irradiation alone is due to the narrowing of dentinal tubules (51, 134, 135), whereas the occlusion of dentinal tubules using Nd:YAG laser irradiation and fluoride desensitising agents is due to the burn out of agents into dentinal tubules (136). The mechanism of dentinal tubules occlusion by Er:YAG laser irradiation is due to a thermomechanical ablation (51, 52) and the deposition of insoluble salts (137). The mechanism of dentinal tubules occlusion using CO₂ laser irradiation is the same as Nd:YAG laser irradiation, which is by to the narrowing of dentinal tubules (51, 52, 138), while the combination of CO₂ laser irradiation and Bioglass 45S5 occludes dentinal tubules by the formation of calcium phosphate crystals (139). Also, the use of CO₂ laser irradiation with fluoride desensitising agents, such as NaF₂ (125) and SnF₂ (27, 140), is effective in occluding dentinal tubules (27, 125, 139, 141), due

to the formation of a highly resistance layer to external stimuli (142). Similarly, the use of Nd:YAG laser irradiation with NaF₂ is also a very effective treatment (141, 126). The use of diode laser irradiation along with fluoride agents, such as NaF₂ and SnF₂, is more effective than laser treatment alone (128, 129, 143).

In addition, free electron lasers (FELs) at 9.4 μm wavelength transform amorphous dentine surface to a crystallised structure (88). The structural and crystalline modification of dentine surface by CO₂ laser irradiation at 9.45 μm wavelength is similar to that produced by the 9.4 μm FELs. However, at high irradiance, free electron lasers (FELs) promote modification, while at high fluence, CO₂ lasers promote ablation (89).

Although the speculations about the occlusion of dentinal tubules using laser irradiation are widely reported, the mechanism of action of lasers is also controversial (144) and unclear (53, 54, 56, 145).

Table 2.8 Lasers and wavelengths used in dentistry (122, 123)

LASER	Argon	Diode	Nd:YAG	Ho:YAG	CO ₂	(Er,Cr:YSGG, Er:YAG)
Active medium	Argon gas	Solid semiconductor crystals/wafer composed of aluminium/indium, gallium and arsenic GaAlAs, InGaAs.	A solid garnet crystal combined with rare earth elements yttrium and aluminium doped with neodymium ions.	A solid crystal of YAG (yttrium aluminium garnet) sensitized with chromium (Cr) and doped with holmium and thulium ions.	A mixture of CO ₂ , helium (He) and nitrogen (N ₂) gases with a ratio of 8:7:1.	1. Er,Cr:YSGG (erbium chromium: yttrium scandium gallium garnet): A solid crystal of YSGG doped with Er and Cr. 2. Er:YAG (erbium : yttrium aluminium garnet): A solid crystal of YAG doped with Er.
Wavelength	(i) 488 nm (blue) (ii) 514 nm (blue – green) Two visible wavelengths	(i) 655 nm (a visible red diode) (ii) 800–830 nm (AlGaAs) (iii) 980 nm (InGaAs, GaAlAs) Wavelengths are placed at the near – infrared portion of the invisible non – ionizing spectrum.	1,064 nm Wavelength is placed in the invisible near – infrared portion of the electromagnetic spectrum.	2,100 nm Wavelength is placed in the near – infrared portion of the invisible non – ionizing irradiation spectrum.	9,300 nm 9,600 nm 10,600 nm Wavelengths are placed at the end of mid – infrared invisible non – ionizing portion of the spectrum.	(i) 2780 nm (Er,Cr:YSGG) (ii) 2,940 nm (Er:YAG) Wavelengths are placed at the beginning of the mid – infrared, invisible and non – ionizing portion of the spectrum.
Delivery system	Fibre-optic cable in: - Contact mode - Non – contact mode	Fibre-optic cable in: - Contact mode (for soft tissue surgery) and - Non – contact mode (for deeper coagulation)	Fibre-optic cable in: - Contact mode - Non – contact mode	Fibre-optic system Hollow waveguide with a hand piece in: - Contact mode - Non – contact mode	Fibre-optic cable for Er,Cr:YSGG	Hollow waveguide/ fibre-optic bundle for Er:YAG.
Emission mode	Continuous wave and gated pulsed mode	Continuous wave and gated pulsed mode	Free running pulsed mode	Free running pulsed mode	Continuous/ gated pulsed mode	Free running pulsed Mode

2.6 Calcium phosphates (CaP)

There is a large variety of calcium phosphate (CaP) minerals. The type of phosphate anion is used to distinguish between calcium phosphates and determine their types (69, 73, 74). Anions include orthophosphates (PO_4^{3-}), metaphosphates (PO_3^-), pyrophosphates ($\text{P}_2\text{O}_7^{4-}$), and polyphosphates ($(\text{PO}_3)_n^{n-}$). Orthophosphates and pyrophosphates are also distinguished by the number of hydrogen ions attached to phosphate anion (69, 73, 74) such as in monocalcium phosphates ($\text{Ca}(\text{H}_2\text{PO}_4)_2$), dicalcium phosphates (CaHPO_4), tricalcium phosphates ($\text{Ca}_3(\text{PO}_4)_2$), and tetracalcium phosphates ($\text{Ca}_2\text{P}_2\text{O}_7$) (49, 68, 69, 146).

Calcium orthophosphates are very important in many fields of science, including biology and medicine (49, 68, 69, 73, 74), due to their chemical similarity to the inorganic mineral of bones, teeth, and pathological calcified tissues (49, 69, 73, 74). Therefore, calcium orthophosphates are classified as biocompatible, bioactive (49, 68, 69, 73), and osteoconductive materials (49, 73, 74). Calcium orthophosphates are available in various forms, including powders, dense blocks, porous scaffolds, suspensions, pastes, and implant coatings. They are used as artificial bone grafts in the form of self – setting cements (49, 68, 69, 73), and as coatings (49, 68, 73) for hip joint prostheses and tooth substitutes (69, 73, 74). Porous calcium orthophosphates are used as scaffolds for tissue engineering applications (49, 69, 73). Compared to dense forms, porous forms provide better fixation of implants and bone grafts to tissues by a mechanical interlock mechanism, which allows tissues to grow into pores (68, 69). Although dense calcium orthophosphates have better mechanical properties than porous calcium orthophosphates, all calcium orthophosphates are used in low – load –

bearing applications due to their poor mechanical properties, compared to bones and teeth (68, 69).

The three major chemical elements of calcium orthophosphates are calcium (Ca^{2+}), phosphorus (P^{5+}), and oxygen (O^{2-}). Hydrogen is also present in many calcium phosphates as an acidic orthophosphate anion (e.g. HPO_4^{2-} / H_2PO_4^-) and/or water (H_2O) (69, 73, 74). The family/classification of calcium orthophosphates include monocalcium phosphate (MCP), dicalcium phosphate (DCP), octacalcium phosphate (OCP), tricalcium phosphate (TCP), tetracalcium phosphate (TTCP), amorphous calcium phosphate (ACP), hydroxyapatite (HAp), and fluorapatite (FAp) (49, 68, 69, 73, 74).

2.6.1 Calcium orthophosphates

2.6.1.1 Monocalcium phosphate (MCP)

Monocalcium phosphate monohydrate ($\text{Ca}(\text{H}_2\text{PO}_4)_2 \cdot \text{H}_2\text{O}$) and anhydrous ($\text{Ca}(\text{H}_2\text{PO}_4)_2$) are chemically known as calcium dihydrogen orthophosphate monohydrate (MCPM) and calcium dihydrogen orthophosphate anhydrous (MCPA), respectively. They are not found in biological calcified tissues due to their high acidity (69, 73, 74). The monohydrated type transforms into anhydrous type above 100°C (69, 73, 74). MCPM and MCPA have similar solubility in water of about 18 g/L and 17 g/L at room temperature ($\sim 25^\circ\text{C}$), respectively (49, 68, 69, 73, 74). Unlike anhydrous monocalcium phosphates, with limited applications due to their high hygroscopic properties (69, 73, 74), monohydrate monocalcium phosphates have many applications in medicine, as a component of many self – hardening cements (147-149) and an additive in tooth pastes (69, 73, 74, 150). Other applications of MCPM include food industry, as a nutrient and mineral

supplement (73, 74, 151, 152), which is marked as additive E341 under the European classification of food additives (69, 73, 74).

2.6.1.2 Dicalcium phosphate (DCP)

Dicalcium phosphate dihydrate ($\text{CaHPO}_4 \cdot 2\text{H}_2\text{O}$) and anhydrous (CaHPO_4) are chemically known as calcium hydrogen orthophosphate dihydrate (brushite) and calcium hydrogen orthophosphate anhydrous (monetite), respectively. They both can be crystallised from aqueous solutions at 100°C (69, 73, 74). The dehydrated type (brushite) transforms thermally into anhydrous type (monetite) (69, 73, 74, 153) above 80°C (69, 73, 74). Unlike monetite, brushite is found in pathological calcifications such as dental calculi (69, 154-156) and urinary stones (155-157). They both have many medical applications, such as in calcium phosphate cements (158-160), polishing agents (69, 151, 160) and anticaries in toothpastes (69, 151, 161, 162), as well as applications in the food industry, as nutrients and mineral supplements (marked as E341) (69, 73, 74, 151, 163). In medicine, brushite is also used as an intermediate for tooth remineralisation (73, 74, 164).

Brushite is a stable form of calcium orthophosphate (165). It is used as a precursor to form apatite phases such as hydroxyapatite (69, 73, 74, 166) and octacalcium phosphate (166). Brushite crystals consist of CaPO_4 parallel chains and water molecules in between (73, 74). Its crystal growth is in the form of platelet – like morphology, which reflects the (010) crystallographic plane (166-168). Its solubility in water is about 0.088 g/L at room temperature ($\sim 25^\circ\text{C}$) (49, 68, 69, 73, 74). On the other hand, Monetite is the anhydrous form of calcium hydrogen orthophosphate (69, 73, 74). It is less soluble in water than brushite, with a solubility of about 0.048 g/L at room temperature ($\sim 25^\circ\text{C}$) (49, 68, 69, 73, 74). Monetite may also be used

as a component in anticaries biocomposites, because it releases calcium and phosphate due to the decrease of its particle dimensions (169).

2.6.1.3 Octacalcium phosphate (OCP)

Octacalcium phosphate ($\text{Ca}_8(\text{HPO}_4)_2(\text{PO}_4)_4 \cdot 5\text{H}_2\text{O}$) forms as an unstable phase during aqueous precipitation of more stable phases of calcium orthophosphates such as calcium – deficient hydroxyapatite (69, 73, 74). Its structure composes of HAp – like apatite layers separated by H_2O layers (155, 156, 170). Its solubility in water is about 0.0081 g/L at room temperature ($\sim 25^\circ\text{C}$) (49, 68, 69, 73, 74). It is found as a stable component in dental and urinary calculi (171-173). OCP was first proposed to precipitate as an initial phase in enamel mineral and bone formation, and consequently, the hydrolysis of OCP (174-179). It is also proposed as a precursor for biological apatite in natural and synthetic heart valves (180-182). In dentistry, OCP might be used as a coating (183) and a component of biocomposites (184). In surgery, it is used as a bone repair implantation (185-187).

2.6.1.4 Tricalcium phosphate (TCP)

There are two types of tricalcium phosphates, β – tricalcium phosphate (β – $\text{Ca}_3(\text{PO}_4)_2$) and α – tricalcium phosphate (α – $\text{Ca}_3(\text{PO}_4)_2$), which are also known chemically as calcium orthophosphate tribasic beta and calcium orthophosphate tribasic alpha, respectively. Pure β – TCP and α – TCP are never found in biological calcifications (69, 73, 74), however, magnesium – substituted β – TCP is found in dental calculus, urinary calculus, and dental caries (154-156). β – TCP can be prepared by the thermal decomposition of calcium orthophosphates, such as CDHAp, above 800°C , whereas α – TCP can be prepared by the thermal treatment of β – TCP above 1125°C (69, 73,

74). They both have the same chemical composition but different crystal structure and solubility. β – TCP is less soluble in water than α – TCP, with a solubility of about 0.0005 g/L and 0.0025 g/L at room temperature (~ 25°C), respectively (49, 68, 69, 73, 74). β – TCP is more stable than α – TCP, the latter which is more reactive in aqueous systems (69, 73, 74). β – TCP and α – TCP are widely used in biomedicine and dentistry. TCP is the first calcium orthophosphate to be used in bone grafting trials (in rabbits) (188) and repairing periodontal defects (189). In biomedicine, they are used alone as calcium phosphate bone cements (158-160, 190-192), and in combination with HAp (a mixture of β – TCP/ α – TCP and HAp is known as a biphasic calcium phosphate) as bone substitution bioceramics/artificial bone grafts (190, 193-197). In dentistry, they are used as bone grafts (198), implant coatings (199), and a component of root canal sealers (200). In addition, β – TCP is also used as a polishing agent in toothpastes, and as a nutrient and mineral supplement (marked as E341) in food industry (69, 73, 74).

2.6.1.5 Tetracalcium phosphate (TTCP)

Tetracalcium phosphate ($\text{Ca}_4(\text{PO}_4)_2\text{O}$) is also known as the mineral hilgenstockite (69). It is considered the most basic calcium orthophosphate (69, 73, 74), with a solubility in water of about 0.0007 g/L at room temperature (~ 25°C) (49, 68, 69, 73, 74). It is not found in biological calcified tissues (69, 73, 74) due to its instability in aqueous solutions, which hydrolyses to hydroxyapatite and calcium hydroxide (146, 201, 202). TTCP can be prepared only by a solid – state reaction above 1300°C, for example, using DCPA and CaCO_3 in dry air/nitrogen (146, 201, 202). In biomedicine and dentistry, TTCP is used in combination with other calcium phosphates,

such as DCPD and DCPA (68, 203), due to its high solubility and acidity (68). It is used in biocomposites (203), self – setting calcium phosphate cements (203-206), and root canal sealers (207).

2.6.1.6 Amorphous calcium phosphate (ACP)

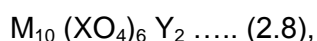
Amorphous calcium phosphate (ACP) is the amorphous form of other calcium orthophosphates (74). There are two types of ACP depending on the production temperature, low – temperature ACPs and high – temperature ACPs (74). Low – temperature ACPs are usually formed as a transient phase during the formation of calcium orthophosphates in aqueous solutions (69, 73, 74). The amorphous phase increases with increasing the concentration of calcium and orthophosphate and pH of solution at low temperatures (69, 73, 74). In addition, pyrophosphate, carbonate and/or magnesium promote the formation of ACP, whereas fluoride promotes the formation of a more crystalline calcium orthophosphate (146, 155, 201, 202). ACPs are proposed as an initial phase precipitating from a supersaturated solution of calcium and orthophosphate (146, 201, 202), due to their lower surface energy than other calcium orthophosphates such as OCP and HAp (208-210). However, at elevated temperatures, they transform into a better crystalline calcium orthophosphate such as calcium – deficient HAp (146, 155, 201, 202). High – temperature ACPs are formed at elevated temperatures by rapid quenching of melted calcium orthophosphates (74), for example, during plasma spraying of HAp (211), which results in anhydrous ACP (74).

Although ACPs have an amorphous structure, as observed by FTIR and XRD, SEM of ACPs shows nanospherical particles of 20 – 200 nm with no distinct morphology (69, 73, 74). Spherical clusters of ACPs with a chemical

composition $\text{Ca}_9(\text{PO}_4)_6$ (146, 201, 202) is also proposed as an initial phase during HAp crystallisation (212, 213, 214). Their solubility in water cannot be precisely measured, however, the solubility values of 0.0025, 0.0029, and 0.0032 g/L are reported at room temperature ($\sim 25^\circ\text{C}$) and pH values of pH 7.40, pH 6.00, and pH 5.28, respectively (49, 68, 69, 73, 74). ACPs are found in biological calcifications, particularly in soft – tissue pathological calcifications such as heart valves (154-156). In medicine, ACPs are used in calcium phosphate cements (68, 158-160) and bone grafts (215, 216). In dentistry, they are used as tooth filling materials (69, 73, 217), a component in toothpastes, and in calcium orthophosphate remineralisation systems (combined with casein phosphopeptides) (49). They could also be used in combination with polymers to form bioactive composites (218-220). In addition, ACPs might be used as mineral supplements in culture media, and they are used for syrup clearing in the food industry (69, 73, 74).

2.6.1.7 Apatites

Apatites are a structural type of calcium orthophosphates, which include hydroxyapatite (HAp), calcium – deficient hydroxyapatite (CDHAp), fluorapatite (FAp), hydroxycarbonate apatite (HCAp), and chlorapatite (ClAp) (49, 69, 73, 74, 221). Therefore, apatites are considered as different compounds of calcium orthophosphates with similar structures, but do not necessarily have similar compositions. They can be classified into biological and synthetic apatites, with a general chemical formula, as given by equation 2.8 (221, 222).



where (M) is usually a bivalent cation such as Ca^{2+} , or monovalent and trivalent cations such as K^+ and Al^{3+} , respectively, as well as rare earth

elements, (XO_4) is usually PO_4^{3-} , and it can also be SiO_4^{4-} or CO_3^{2-} , and (Y) is a monovalent anion such as OH^- , F^- , and Cl^- , or it can also be CO_3^{2-} (221, 223).

2.6.1.7.1 Synthetic apatites

HAp ($Ca_5(PO_4)_3 OH$) and FAp ($Ca_5(PO_4)_3 F$) are the most stable and least soluble calcium orthophosphates (49, 68, 69, 73, 74, 221). Their solubility in water is about 0.0003 g/L and 0.0002 g/L at room temperature ($\sim 25^\circ C$), respectively (49, 68, 69, 73, 74). The crystal unit cell of HAp and FAp, as shown in Figures 2.12 and 2.13, respectively, consists of two molecules, and therefore, their chemical formula are written as $Ca_{10}(PO_4)_6 (OH)_2$ and $Ca_{10}(PO_4)_6 F_2$, respectively. Pure apatites, including HAp, CDHAp and FAp, are not found in biological calcified tissues (69, 73, 74, 221), due to the fact that biological apatites are ion – substituted apatites (e.g. Na^+ , K^+ , Mg^{2+} , and Sr^{2+} for Ca^{2+} ; CO_3^{2-} for PO_4^{3-} or HPO_4^{2-} ; and F^- , Cl^- , and CO_3^{2-} for OH^-) (154-156).

Hydroxyapatite (HAp) is white in colour, and it is available in different forms such as powders, porous blocks, beads, and aqueous suspensions. Chemically, HAp is similar to the mineral component of bones and teeth, and therefore, it provides excellent biocompatibility and intergrowth with natural bone, and it induces bone formation (224). The crystal structure of HAp is in the monoclinic space group $P2_1/b$ (146, 221, 225, 226), which transforms into the most common hexagonal space group $P6_3/m$ (221) above $250^\circ C$ (146, 201, 202) or at ambient temperature in case of partial substitutions (e.g. OH^- by F^-) (69, 73, 74, 221).

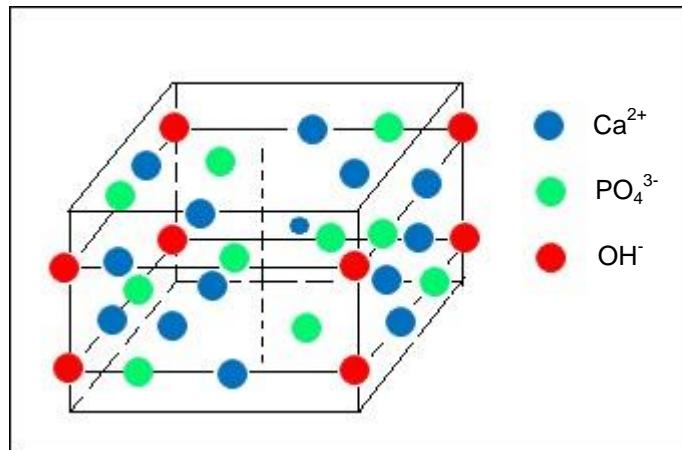


Figure 2.12 Schematic of the crystal structure of hydroxyapatite (HAp).

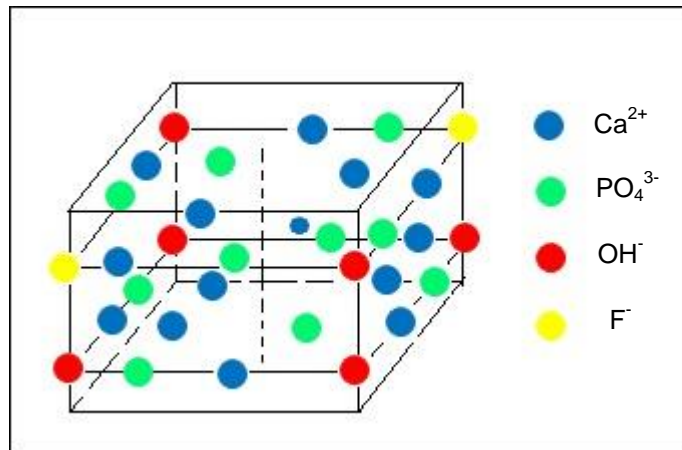


Figure 2.13 Schematic of the crystal structure of fluorapatite (FAP).

HAp was first reported as an aggregation of ACP ($\text{Ca}_9(\text{PO}_4)_6$) clusters, known as Posner's clusters (227-229). HAp can be synthesised in dense and porous forms, both of which have different biomedical and dental applications in supporting bone growth (49, 68, 69, 73, 74). Porous HAp, like other porous calcium orthophosphates, provides better fixation of implants and bone grafts to biological tissues than dense HAp, by allowing bone to grow into their pores (68, 69, 230). Therefore, porous HAp is a good example of a bioresorbable material, which dissolves completely and allows

bone to grow instead, whereas dense HAp is a good example of a bioactive material, which dissolves slightly and bonds to bone through a newly formed biological apatite (68, 73). However, both forms are used in low – load bearing areas due to their poor mechanical properties (68, 231, 232), particularly, their poor inelastic ability, which makes them brittle, and consequently, results in a fracture at the bone – HAp interface (231).

HAp and FAp are the most used calcium orthophosphates in dental applications (49). They are used in calcium phosphate cements (49, 68), toothpastes (49, 68, 69, 73), and as coatings for dental implants (49, 68, 233-235). They can also be used as a component of dental restorative materials such as glass ionomer cements (236), dental biocomposites (237), and self – setting formulations (238). In orthopaedic, HAp is used as a coating for the fixation of hip implants (68, 233-235) and as a bone replacement material (68, 231). In contrast, FAp is rarely used as a bone substitution material due to its toxicity of high amounts of fluorides as well as its lowest solubility (239-241). Although fluoride is found in biological systems, with the highest concentration is in bones and the lowest concentration is in teeth, the concentration of fluoride is not enough to form FAp (69, 73, 74).

HAp and FAp can be synthesised by various methods (FAp is prepared in the presence of an adequate amount of F^- ions using fluoride compounds such as NaF or NH_4F (69, 73, 74)), which can be divided into solid – state reaction and wet methods (69, 242, 243). The most common methods include chemical precipitation (69, 73, 74, 248-251), hydrothermal (69, 73,

74, 77, 79, 252, 253), hydrolysis of other calcium orthophosphates (69, 73, 74), and sol – gel (77, 251, 254, 255) methods.

Calcium – deficient HAp ($(Ca_{10-x} (PO_4)_6 x(OH)_2)$, where $0 < x < 1$) is considered as HAp with vacancies of Ca^{2+} and OH^- ions (256-258). It is found in biological tissues as a substituted CDHA only (154-156). Therefore, substituted CDHAp lacks stoichiometry due to the presence of other ions (e.g. Na^+ , K^+ , Mg^{2+} , and Sr^{2+} for Ca^{2+} ; CO_3^{2-} for PO_4^{3-} or HPO_4^{2-} ; F^- , Cl^- , and CO_3^{2-} for OH^-) filling the missing ions/vacancies (69, 259, 260), and consequently, different Ca:P ratios ranging from 1.5 to 1.67 due to such ion substitutions and surface adsorption (261-263). CDHAp is more soluble in water than FAp, HAp, OCP, TCP, and TTCP, with a solubility of about 0.0094 g/L at room temperature ($\sim 25^\circ C$) (49, 68, 69, 73, 74). Its structure and properties are similar to ACP precipitated in an alkaline solution ($pH > 8$), such as its poorly crystalline crystals (69, 73, 74). CDHAp can be prepared from aqueous solutions of calcium and orthophosphate at elevated temperatures, during which ACP, as an initial precipitated phase, transforms into CDHAp (69). Depending on its Ca:P ratio, CDHAp with Ca:P ratios of 1.5 and $1.5 < Ca:P < 1.67$ transforms into β – TCP (146, 155, 156, 190, 201, 202 264-266) and biphasic calcium phosphate (β – TCP and HAp), respectively, above $700^\circ C$ (190, 264-266).

As discussed above, calcium orthophosphate minerals vary in their chemical composition, physical form, Ca:P ratio, and solubility. Properties and physical constants (under standard conditions, pressure of 1 atm at room temperature $\sim 25^\circ C$) for calcium orthophosphate minerals are summarised in Table 2.9. Ca:P ratio is an important parameter, which is related to the

basicity/acidity, solubility, and stoichiometry of calcium orthophosphates. Ca:P ratio ranges from 0.5 for MCPM up to 2 for TTCP. The lower the Ca:P ratio, the more acidic and water – soluble the calcium orthophosphate (MCPM > DCP > TCP > HAp > FAp) (69, 155, 156, 201, 202). Also, stoichiometric Ca:P ratio of 1.67 for HAp is in contrast to non – stoichiometric Ca:P ratio within 1.5 – 1.67 for calcium – deficient HAp, the latter which is due to the presence of vacancies/missing ions (*e.g.* Ca^{2+} , PO_4^{3-} / HPO_4^{2-} , and OH^-), or due to their substitution with other ions (69, 259, 260). In addition, bending, compressive, and tensile strengths increase with increasing Ca:P ratio, and decrease with $\text{Ca:P} > 1.67$ (267).

Table 2.10 shows the crystallographic data of calcium orthophosphate minerals, including crystal system, space group (P, R, and C describing a Bravais lattice type, followed by point group symmetry), unit cell parameters (a , b , c , and α , β , γ), and formula units per unit cells. Some calcium orthophosphate, such as MCPM, MCPA, DCPA, and OCP, have the same crystal system (triclinic), but they have different unit cell parameters, formula units per unit cell, and chemical composition. Similarly, HAp and FAp have the same crystal system (hexagonal), but they have different chemical compositions. On the other hand, α – TCP and β – TCP have the same chemical composition, but they have different crystal structures, monoclinic and rhombohedral, respectively. These differences give calcium orthophosphates different properties, and thus, different applications.

Table 2.9 Properties and physical constants of calcium orthophosphates under standard conditions (pressure of 1 atm at RT ~ 25°C) (268-276)

CaP	Formula	Ca:P ratio	Mol. W	Physical form	Decomposition (°C)	Density (g cm ⁻³)	Solubility
MCPM	Ca(2HPO ₄) ₂ .H ₂ O	0.5	252.06	Coloured triclinic plates	≈ 100	2.22	Slightly soluble in H ₂ O and soluble in diluted acid
DCPD	CaHPO ₄ .2H ₂ O	1.0	172	Monoclinic crystalline	≈ 100	2.31	Insoluble in ethanol and soluble in diluted acid
DCPA	CaHPO ₄	1.0	136	White triclinic crystalline	~ 400 ^a	2.92	Insoluble in ethanol
TCP	Ca ₃ (PO ₄) ₂	1.5	310.17	White amorphous powder	1670	3.14	Insoluble in ethanol and soluble in diluted acid
HAp	Ca ₅ (PO ₄) ₃ .OH	1.67	502.3	Coloured hexagonal crystalline	> 900	3.15	Insoluble in ethanol and soluble in acid
FAP	Ca ₅ (PO ₄) ₃ .F	1.67	302	Coloured hexagonal crystalline	~ 1650	3.20	Insoluble in H ₂ O
TTCP	Ca ₄ (PO ₄) ₂ O	2	366	Monoclinic powder	< 660 ^b	3.05	Soluble in aqueous solutions ^b

(a) Adopted from reference (77) and (b) adopted from reference (270).

Table 2.10 Crystallographic data of calcium orthophosphates (146, 201, 202, 221, 277-283)

Compound	Crystal system and space group	Unit cell parameters	Units per unit cell
MCPM	Triclinic $P\bar{1}$	$a = 5.6261(5)$, $b = 11.889(2)$, $c = 6.4731(8)$ Å $\alpha = 98.633(6)^\circ$, $\beta = 118.262(6)^\circ$, $\gamma = 83.344(6)^\circ$	2
MCPA	Triclinic $P\bar{1}$	$a = 7.5577(5)$, $b = 8.2531(6)$, $c = 5.5504(3)$ Å $\alpha = 109.87(1)^\circ$, $\beta = 93.68(1)^\circ$, $\gamma = 109.15(1)^\circ$	2
DCPD	Monoclinic Ia	$a = 5.812(2)$, $b = 15.180(3)$, $c = 6.239(2)$ Å $\beta = 116.42(3)^\circ$	4
DCPA	Triclinic $P\bar{1}$	$a = 6.910(1)$, $b = 6.627(2)$, $c = 6.998(2)$ Å $\alpha = 96.34(2)^\circ$, $\beta = 103.82(2)^\circ$, $\gamma = 88.33(2)^\circ$	4
OCP	Triclinic $P\bar{1}$	$a = 19.692(4)$, $b = 9.523(2)$, $c = 6.835(2)$ Å $\alpha = 90.15(2)^\circ$, $\beta = 92.54(2)^\circ$, $\gamma = 108.65(1)^\circ$	1
α – TCP	Monoclinic $P2_1/a$	$a = 12.887(2)$, $b = 27.280(4)$, $c = 15.219(2)$ Å $\beta = 126.20(1)^\circ$	24
β – TCP	Rhombohedral $R\bar{3}Ch$	$a = b = 10.4183(5)$, $c = 37.3464(23)$ Å $\gamma = 120^\circ$	21*
HAp	Monoclinic $P2_1/b$	$a = 9.84214(8)$, $b = 2a$, $c = 6.8814(7)$ Å $\gamma = 120^\circ$	4
	hexagonal $P6_3/m$	$a = b = 9.4302(5)$, $c = 6.8911(2)$ Å $\gamma = 120^\circ$	2
FAP	Hexagonal $P6_3/m$	$a = b = 9.367$, $c = 6.884$ Å $\gamma = 120^\circ$	2
TTCP	Monoclinic $P2_1$	$a = 7.023(1)$, $b = 11.986(4)$, $c = 9.473(2)$ Å $\beta = 90.90(1)^\circ$	4

P, R, and C are describing a Bravais lattice type, followed by point group symmetry.

(*) Per hexagonal unit cell.

2.6.1.7.2 Biological apatites

Biological apatites are ion – substituted calcium orthophosphates with an apatitic structure (49, 69, 284-286), which can be considered as ion – substituted CDHAp (154-156, 221). They are the inorganic minerals of bones and teeth (154-156, 221), which form in vivo by biological mineralisation (74, 287, 288). Biological apatites of bone, enamel, and dentine are classified as carbonate apatites (221, 289, 290), and they consist of crystals that vary in shape from platelets (in bone and dentine) to rods (in enamel) (8, 12, 69, 73, 74). They are often poorly crystallised and non – stoichiometric due to the presence of impurities/substitutions, such those by carbonate, sodium, and magnesium (69, 73, 74, 221), which make them less stable and more reactive (69, 73, 74). However, the biological apatite of enamel contains fewer impurities (*e.g.* carbonate and magnesium) than that of dentine and bone, and thus, it has a lower solubility and higher crystallinity (69, 73, 74) due to its smaller lattice strains (284, 291-293).

Although the chemical composition and crystal structure of bone, dentine, and enamel are similar to that of synthetic apatites (unsubstituted), crystals of biological apatites are much smaller (*e.g.* HAp and CDHAp), which make them more soluble than synthetic apatites (69, 259,260). The chemical and structural similarity of biological apatites can be seen in XRD (42, 290, 294-296) and FTIR (42, 294-296) analysis of bone and teeth. However, their crystallinity varies from high crystallinity in enamel to low crystallinity in bone and dentine (42, 69, 73, 74), which is due to the different amount of substitutions, especially by carbonate (CO_3^{2-}) (69, 73, 74, 297, 298). The highest amount of carbonate is in bone, while the lowest amount is in enamel (69, 73, 74, 297). Bone, dentine, and enamel contain approximately

7.4, 5.6 and 3.5 wt% of carbonate, respectively (299). The amount of carbonate can determine the morphology of the apatite crystals, as demonstrated by Susan Liao et al. (298). The lower the amount, the more the crystals are platelet, and the higher the amount, the more the crystals are spherical (69, 73, 74, 298). There are two types of carbonate apatite, depending on the location of carbonate substitution in the apatite lattice; *A* – type and *B* – type substitutions (221, 300). The *A* – type involves the substitution of hydroxyl (OH^-), while *B* – type involves the substitution of phosphate (PO_4^{3-}) (221, 300).

According to FTIR spectroscopy, *A* – type carbonate apatite is characterized by a double band at around 1545 cm^{-1} and 1450 cm^{-1} that represents an asymmetrical stretch vibration (V_3), and a band at around 878 cm^{-1} that represents an out – of – plane bend vibration (V_2). On the other hand, *B* – type carbonate apatite is characterized by a double band at around 1410 cm^{-1} and 1455 cm^{-1} (V_3), and a band at around 873 cm^{-1} (V_2) (300). Biological apatites are reported to be *B* – type carbonate apatite, with a small amount of *A* – type (301), however, a recent study shows that the amount of *A* – type carbonate accounts for up to 50% of the total carbonate (300), with a ratio (*A*:*B*) in the range 0.7 – 0.9 (302). In addition, substitutions introduce changes in the lattice parameters, which depend on the type and size (ionic radius) of substituents (e.g. carbonate CO_3^{2-}) (221, 303), and consequently, modify the properties of apatite (69, 73, 74, 221, 284, 304). Cell volume usually increases or decreases due to an expansion in *a* – axis or a contraction in *c* – axis, respectively (303). For example, in the case of *A* – type carbonate apatite, expansion of the unit cell occurs, while a contraction of the unit cell occurs with *B* – type carbonate apatite. This is because the

CO₃ group is larger than the OH group and smaller than the PO₄ group (303), which could explain the difference in size and shape between biological apatites and synthetic HAp. The average lattice parameters of bone, dentine, enamel, and synthetic HAp are presented in Table 2.11.

Table 2.11 Unit cell parameters (average) of bone, dentine, enamel, and synthetic HAp

Cell parameters	Bone	Dentine	Enamel	Synthetic HAp
<i>a</i> – axis Å (±0.003)	9.41 ^a	9.42 ^a – 9.49 ^b	9.43 ^b – 9.44 ^a	9.41 ^b – 9.43 ^a
<i>c</i> – axis Å (±0.003)	6.89 ^a	6.88 ^a – 6.89 ^b	6.88 ^a – 6.89 ^b	6.88 ^b – 6.89 ^a

^(a) Values are adopted from references (155, 202, 305-308).

^(b) Values are adopted from reference (303).

Moreover, coupled substitutions may take place to maintain the charge neutrality (charge balance) and provide a geometric fit of the substituents within the crystal lattice (221, 309). Maintaining the charge balance means that every negative charge has to be balanced out by a positive charge, so the ionic compound has a net charge of zero. The charge balance is maintained either by a second substitution by an ion with a different charge, or by other vacancies in the crystal lattice (e.g. Ca²⁺ substituted by Na⁺ plus a vacancy in place of OH⁻) (221, 309). Therefore, unlike *A* – type substitution, *B* – type substitution requires to be coupled with other substitutions (e.g. Mg²⁺) to maintain the charge balance (221), which may suggest that biological apatites are principally *B* – type carbonate (301). However, due to the lack of complete structural analysis, the structure of biological apatites remains controversial (221).

Synthetic *A* – and *B* – type carbonate apatites (298, 304, 310, 311) and a mixture of *A* – and *B* – type carbonate apatite (300, 312) can be prepared in the laboratory. *A* – type carbonate apatite can only be prepared by a solid –

state reaction at around 1000°C (310, 311), whereas *B* – type carbonate apatite can be prepared by a precipitation reaction (298, 304) at temperature between 50°C and 100°C (310, 311).

2.6.2 Applications of calcium orthophosphates

Calcium orthophosphate minerals have many biomedical and dental applications as well as other applications. Their chemical compositions, structures, and properties are vital in determining their behaviour in relation to different applications. The size and shape of calcium orthophosphate particles are also the key to their applications. Calcium orthophosphates applications are summarised as follows.

2.6.2.1 Implant coating

All calcium orthophosphates are used in low – load – bearing applications due to their poor mechanical properties, compared to bones and teeth (68, 69). Therefore, coatings of calcium orthophosphates are commonly applied to metallic implants (49, 68, 69, 73, 74, 224) to alter their surface properties, and consequently, promote bone growth and improve their bioactivity and mechanical stability (313). Porous forms of calcium orthophosphates provide a good fixation of implants to tissues by a mechanical interlock mechanism, which allows bone to grow into their pores (68, 69). They are used as coatings (49, 68, 73) for hip joint prostheses (*e.g.* HAp coating (68, 233, 234, 235)) and tooth substitutes (69, 73, 74).

2.6.2.2 Tissue engineering

Dense and porous calcium orthophosphates have different applications for supporting bone growth in orthopaedic, dental, and maxillofacial applications (49, 68, 69, 73, 74, 231). Calcium orthophosphates are used as artificial bone grafts for bone repair in the form of self – setting cements (49, 68, 69,

73). Monohydrate monocalcium phosphates (147-149), monetite, brushite (158-160), ACP (68, 158-160), and TCP (158-160, 190-192) are used as a component in calcium phosphate cements, while OCP (185-187), biphasic calcium phosphate (190, 193-197), ACP (215, 216), and HAp (68, 231) are used as bone replacement materials or bone grafts. Porous calcium orthophosphates also provide a good fixation of bone grafts to tissues (68, 69), and therefore, they are widely used as scaffolds for tissue engineering applications (49, 69, 73). Porous calcium orthophosphates are used to fill bone defects and voids due to their ability to promote bone growth (314). In addition, OCP is proposed as a precursor for biological apatites in natural and synthetic heart valves (180-182).

2.6.2.3 Dental applications

HAp and FAp are the most used calcium orthophosphates in dental applications (49). They are used in calcium phosphate cements (49, 68) and as coatings for dental implants (49, 68, 233-235). They can also be used as a component of dental restorative materials such as glass ionomer cements (236), dental biocomposites (237), and self – setting formulations (238). They are also used in some toothpaste products (37, 49, 68, 69, 73), such as BioRepair toothpaste, which uses HAp microparticles (39) to achieve better tooth remineralisation and the build – up of enamel tissue.

Other calcium orthophosphates, including monohydrate monocalcium phosphates (69, 73, 74, 150), dicalcium phosphates (96, 151, 160-162), ACP (49), and β – TCP (69, 73, 74) are used as an additive in toothpaste products. Monetite and brushite are used in toothpastes as polishing agents (69, 151, 160) and anticaries (69, 151, 161, 162). Brushite (73, 74, 164) and

ACP (combined with casein phosphopeptides) (49) are used in calcium orthophosphate remineralisation systems.

In addition, OCP (183) and TCP (199) can be used as implant coatings, while OCP (184) TTCP (203) (in combination with DCPD and DCPA (68, 203)), and ACP (in combination with polymers) (218-220) are used as a component of biocomposites. TCP (200) and TTCP (207) are also used as a component of root canal sealers. Moreover, TCP (198) and TTCP (203-206) are used as maxillofacial bone grafts and self – setting calcium phosphate cements, respectively.

2.6.2.4 Targeted drug delivery applications

Calcium orthophosphates, such as HAp, have the potential to be used as a drug delivery system for pharmaceutical compounds to achieve therapeutic effects (68, 315-320). For example, porous HAp, as carriers for anticancer drugs and antibiotics, demonstrates sustained release profiles over 12 days (321) and 12 weeks (322), respectively. Calcium orthophosphates could also become effective carriers for growth factors, bioactive peptides, and various types of cells (e.g. bone cells) for tissue engineering purposes (68, 319, 323, 324). This is due to its capability of producing small crystal size with a large percentage of atoms on the surface of the crystals, which provide a large specific surface area for the sorption of ions, proteins, and drugs (325, 326).

2.6.2.5 Food industry applications

Some calcium orthophosphates are widely used in food industry, and they are marked as additive E341 under the European classification of food additives (69, 73, 74). These include MCPM (73, 74, 151, 152), dicalcium phosphates (69, 73, 74, 151, 163), and β – TCP (69, 73, 74), which are used as nutrients and mineral supplements.

2.6.3 Calcium orthophosphate synthesis

Calcium orthophosphates can be synthesised using various methods, which can be divided into solid – state reaction and wet methods (42, 69, 242, 243). The most common methods include chemical precipitation (42, 69, 73, 74, 248-251), hydrothermal (42, 69, 73, 74, 77, 252, 253, 327, 328), hydrolysis of other calcium orthophosphates (69, 73, 74), and sol – gel methods (42, 77, 251, 254, 255, 313). Other synthesis routes include mechanochemical (244-246) and electrochemical methods (247).

The solid – state method, also known as the ceramic method, is the oldest and most traditional method for the synthesis of inorganic solids (*e.g.* apatites) (42, 329). It involves a slow solid – solid reaction of starting reactants, such as oxides, carbonates, or salts, which are mixed in stoichiometric ratios and thermally treated at elevated temperatures for long periods to initiate the reaction (42, 329). The reaction starts at the contact points between solid reactants, and their chemical reactivity is usually determined by their crystalline structure and particle size, as well as the presence of defects (42). The smaller the particle size, the lower the number of complete unit cells forming the crystal, and thus, shorter diffusion route and higher level of reactivity (42). In addition, decomposition of reactants may decrease the particle size, which increases the surface area, and consequently, the chemical reactivity (329). Since solid – state methods involve elevated temperatures, they can produce very crystalline apatites, with particle size ranges between 25 nm and 50 nm (42), however, it is difficult for the reaction to proceed to completion, and it rarely results in a pure single – phase due to a continuous diffusion and reaction of constituents (42, 329). Synthetic crystalline HAp is an example of calcium

orthophosphate solids that can be prepared by the solid – state reaction of other calcium orthophosphates (*e.g.* MCPM, DCPA, DCPD, and OCP) with carbonate salts (*e.g.* CaO, Ca(OH)₂, or CaCO₃) (42, 69) at temperatures above 1200°C in an atmosphere of equal volumes of water and nitrogen (69, 74, 201). Similarly, β – TCP can be prepared by the solid – state reaction of DCPA and CaO (73, 74). In addition, TTCP can only be prepared by the solid – state reaction of DCPA and CaCO₃ above 1300°C in dry air or nitrogen (146, 201, 202).

On the other hand, the wet method is carried out using procurers in aqueous solutions, and it depends on the chemical reactivity of its constituents, mainly, the diffusion and concentrations of chemical species (42). Compared to the solid – state method, the wet method provides higher reactivity, lower reaction temperatures, and lower reaction time, as well as producing higher – quality, more homogeneous, and higher – density products with smaller particle size (particle size > 50 nm) (42). It is a suitable method for the synthesis of apatite biomaterials with small particle size and carbonate content similar to that of biological apatites (42). Wet methods can produce materials with desired crystallinity, morphology, surface area, and particle size for specific applications (330). The properties of final material depend on the conditions of synthesis (73, 74, 248, 250, 331).

The synthesis method as well as synthesis parameters (73, 74, 248, 250, 331), including solution concentration, pH, temperature, reaction time (12, 73, 74, 248), stirring technique (332), milling technique (333), and calcination/heat treatment (248, 334) are of great importance in determining the properties of calcium orthophosphates, which are discussed next.

2.6.3.1 Chemical precipitation method

Chemical precipitation is a very important method, because it can be considered as an initial reaction in both hydrothermal and sol – gel methods. Chemical precipitation from aqueous solutions is a widely used method for the synthesis of calcium orthophosphates due to its versatile and economic advantages (248), as well as its capability of producing large amounts of powder (331). The method involves obtaining a wet precipitate through several cycles, including ultrasonic bathing, filtration, and drying (42). It was first used by Jarcho and co-worker in 1976 to synthesis HAp (335). The precipitation method is conducted at low temperatures, usually room temperature, using inexpensive equipment (336-338), and yet can produce high percentages of pure materials (337, 338) such as stoichiometric HAp (Ca:P ratio of 1.67) (336). However, the precipitation method is not well – defined and lack reproducibility of orthophosphates (339, 340). This is due to the lack of precise control over the synthesis parameters, such as pH, temperature, and Ca:P ratio of reagents, which can result in different properties such as morphology, crystallinity, and stoichiometry (42). Therefore, the precipitation method can be carried out in a controlled system, known as the controlled crystallisation method, to control the synthesis parameters (42). The latter is of significant importance to control the properties of final product, including composition, impurities, morphology, and particle size (42, 73, 74, 248, 250, 331).

Several publications report the influence of synthesis parameters on final calcium orthophosphate product (42, 248-251, 341, 342). The chemical precipitation method usually involves the preparation of Ca^{2+} and HPO_4^{2-} aqueous solutions by dissolving reagents in deionised water. The solutions

are mixed by a drop – wise addition technique under vigorous stirring at room temperature. pH of the mixture can be varied and usually adjusted up to pH 12 using NaOH or NH_4OH (251, 252). The precipitation reaction is usually carried out at room temperature; however, the mixture can be thermally treated at low temperatures. Ageing of the mixture can be varied from hours to days. The wet precipitate is then washed, filtered, and dried at low temperatures $\sim 80^\circ\text{C}$ overnight. Heat treatment (calcination) of the obtained powder is usually carried out at high temperatures around 1000°C . A flow chart for obtaining HAp by the chemical precipitation method is shown in Figure 2.14.

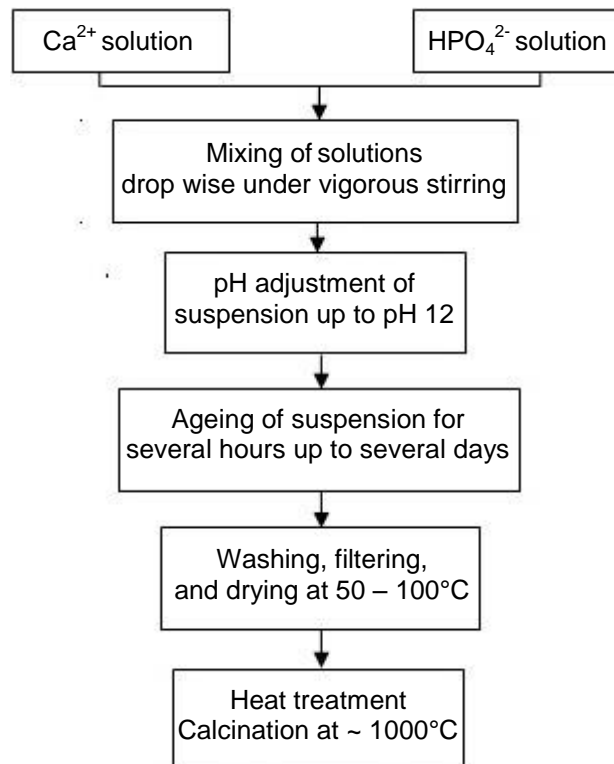
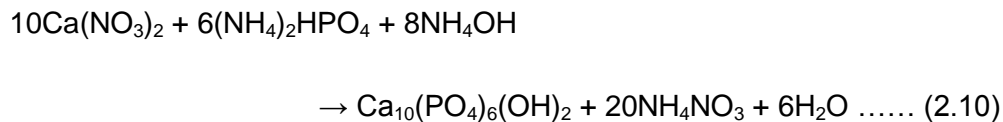


Figure 2.14 Flow chart for obtaining HAp by the chemical precipitation method.

The most common and used precipitation methods for the synthesis of calcium orthophosphates, particularly HAp, are Rathje's method (248, 341, 342, 251) and Hayek and Newesely's method (249-251, 341, 342). Rathje's method involves the reaction of calcium hydroxide (Ca(OH)_2) and phosphoric acid (H_3PO_4), as shown by equation 2.9, while Hayek and Newesely's method involves the reaction of calcium nitrate ($\text{Ca(NO}_3)_2 \cdot 4\text{H}_2\text{O}$) and ammonium hydrogen phosphate ($(\text{NH}_4)_2\text{HPO}_4$), as shown by equation 2.10.



Based on Rathje's method, the addition rate of reactants affects the stabilization and final pH value of suspension (341, 342). The addition rate also affects the size, shape, specific surface area, and purity of obtained HAp (341, 342). Monocrystalline and polycrystalline HAp are produced at temperatures $< 60^\circ\text{C}$ and $> 60^\circ\text{C}$, respectively (341, 342). In the presence of $\text{C}_3\text{H}_6\text{O}_3$, the precipitation reaction at room temperature, pH 10, ageing for 24 hours, and calcination at 1100°C for 1 hour produces nanoparticles and homogeneous HAp (343, 344). The precipitation reaction at 90°C for 1 hour, pH 11 – 12, stirring for another hour, ageing at room temperature for 72 hours, and drying at 110°C for 3 hours produces a single phase of non – stoichiometric HAp, with a Ca:P ratio < 1.67 (251). The latter is also obtained after calcination up to 850°C for 4 to 6 hours. A homogeneous size of HAp clusters is obtained with an average size of 400 nm (251).

Furthermore, following the precipitation reaction of $\text{Ca}(\text{OH})_2$ and H_3PO_4 with $\text{pH} > 10.5$, ageing time between 2 and 48 hours, drying at 1100°C , and calcination at 1200°C for 3 hours, HAp with a high degree of purity and crystallinity is obtained (248). The high addition rate of reactants affects the pH of suspension, which in turn affects the dissociation of phosphate reactant, and therefore, the unavailability of phosphate (PO_4^{3-}) leads to an incomplete precipitation of HAp (248). The latter can result in the formation of an apatite phase with other phases such as β – TCP. The high addition rate can also affect the stoichiometry of HAp, which may result in the formation of calcium deficient HAp (248). Therefore, a high addition rate and shorter ageing time lead to the formation of undesirable phases such as β – CP and CaO (248). In addition, increasing ageing time enhances the crystallinity of HAp and allows the crystal growth of HAp (248). However, crystallinity degree of about 90% can be obtained by calcination of powder at high temperatures around 1200°C (248).

In addition, the precipitation reaction at temperatures of 20°C and 70°C , pH 6, 7, 9 and 11, ageing for 20 hours, drying at 105°C , and calcination from 1000°C to 1300°C for 1 hour produces nanocrystalline agglomerates (grain size of 200 – 250 nm) with an apatitic structure (331). The temperature and pH parameters are found to significantly affect the crystal size and morphology. Increasing temperature increases the crystallinity and particle size. Low temperatures result in a smaller crystal size and needle – like morphology, while higher temperatures result in a larger crystal size and rounded morphology. A needle – like morphology with particle size of ~ 50 – 100 nm is obtained with pH 6 at 20°C , whereas a circular morphology with particle size of ~ 100 nm is obtained with pH 6 at 70°C . More rounded

crystal morphology can be obtained at higher temperatures. In addition, calcination of powders at 1000°C has a significant effect on phase composition and crystallinity. With pH 9 at 70°C, a single HAp phase is obtained, whereas with pH 6 at 70°C, a mixture of HAp and β – TCP (biphasic calcium orthophosphate) is obtained. High pH values of pH 9 and 11 result in the formation of a HAp phase, while a lower pH value of pH 6 increases the stability of β – TCP phase. Pure HAp is produced with pH 11 at 20°C and pH 9 at 70°C, while pure β – TCP is produced with pH 6 at 20°C. Calcination of powders at 1200°C also has a significant effect on phase composition and crystallinity. Increasing calcination temperature improves crystallinity and increases the content of biphasic phase, grain size, and density.

Other similar reactions involve the reaction of calcium hydroxide (Ca(OH)_2) with calcium hydrogen phosphate ($\text{Ca(H}_2\text{PO}_4)_2 \cdot \text{H}_2\text{O}$) and diammonium hydrogen phosphate ($(\text{NH}_4)_2 \cdot \text{HPO}_4$) (instead of H_3PO_4) (345). The precipitation reaction of Ca(OH)_2 and $\text{Ca(H}_2\text{PO}_4)_2 \cdot \text{H}_2\text{O}$ with unadjusted pH at room temperature results in the precipitation of HAp, whereas the precipitation reaction of Ca(OH)_2 and $(\text{NH}_4)_2 \cdot \text{HPO}_4$ with unadjusted pH at 40°C enhances the reaction kinetics of HAp formation and improves the dissolution of Ca(OH)_2 .

Based on Hayek and Newesely's method, the precipitation reaction of calcium nitrate ($\text{Ca(NO}_3)_2 \cdot 4\text{H}_2\text{O}$), ammonium hydrogen phosphate ($(\text{NH}_4)_2 \cdot \text{HPO}_4$), and NH_4OH at 95°C for 1 hour, ageing for 14 days, and drying at 250°C for 3 hours produces a single phase of non – stoichiometric HAp, with a Ca:P ratio < 1.67 (251). The latter is obtained even after

calcination up to 850°C. A homogeneous size of HAp clusters is obtained with an average size of 500 nm. The grain size of HAp can be controlled by varying the precipitation time and temperature (346, 347). Stirring at room temperature for 24 hours is also essential to obtain grain size of < 100 nm (341, 348). In addition, the same precipitation reaction (250) with pH 10, stirring for 3 hours at 40°C, ageing for 6 days, and calcination at 1050°C for 7 hours produces HAp with a high percentage of an amorphous phase. A well – crystallised HAp is obtained with a longer calcination period of 15 hours. The precipitation reaction with pH 10, stirring for 9 hours at 40°C, ageing for 3 days, and calcination at 1050°C for 7 hours produces a mixture of HAp and TCP phases. However, a single HAp phase is produced with pH 10, stirring for 3 hours, ageing for 5 days at room temperature, and calcination at 1050°C for 1 hour. On the other hand, the reaction with unadjusted pH 5 produces an amorphous calcium phosphate. In addition, the precipitation reaction with low (0.1:0.06 M) and high (1:0.6 M) solution concentrations (249), pH 11, at 100°C, and ageing for 24 hours produces powders with high and low densities, respectively. However, a mixture of HAp and tricalcium orthophosphate is obtained. Rod – like crystals with particle size < 100 nm are produced from both solution concentrations. However, a smaller average particle size is produced from high concentration solutions rather than low concentration solutions. Also, the amount of powder that is produced from low concentration solutions is less than that from high concentration solutions. Calcination of powders at 1200°C for 1 hour improves their crystallinity and grain size distribution, particularly, those that are produced from low concentration solutions, while

less improvement of crystallinity is associated with powders that are produced from high concentration solutions.

Moreover, in the presence of a synthetic human blood plasma at physiological pH and temperature (pH 7.4 and 37°C, respectively), the precipitation reaction of $(\text{Ca}(\text{NO}_3)_2 \cdot 4\text{H}_2\text{O})$ and $((\text{NH}_4)_2\text{HPO}_4)$ (349, 350) produces a bone – like nanosized hydroxycarbonate apatite. This type of synthesis is known as the biomimetic process (42). Under controlled conditions, at temperatures of 25 – 37°C and 90°C, apatites with a crystal size in the range of adult human bone and enamel, respectively, can be obtained (42). This could be due to uptake and incorporation of minor amounts of carbonate into the apatite structure during ageing of wet precipitate (42). In addition, Ca:P ratio of apatites can be increased by increasing the reaction time (42).

A different approach of precipitation using different starting reagents at different temperatures is also reported (351, 352). The precipitation reaction of $\text{Ca}(\text{EDTA})^{2-}$ (ethylene diamine tetra acetic) and HPO_4^{2-} in the presence of urea (351, 352) produces homogeneous monetite as an initial phase, which transforms to HAp between 125°C and 160°C (341, 342). The hydrolysis of the urea allows the incorporation of CO_3^{2-} into the HAp structure, and thus, the formation of carbonate HAp (341).

Calcium orthophosphate products with different properties can, therefore, be obtained by the chemical precipitation method, using different starting reagents and different synthesis conditions, including addition rate, stirring, pH, temperature, ageing time, and calcination, which are essential parameters in producing the desired product and properties.

2.6.3.2 Sol – gel method

The sol – gel chemical process is based on the hydrolysis and condensation or oxidation of precursors (42, 254). The term sol – gel is based on the increase in differential viscosity at a given instant, which indicates the gel formation (42). The sol – gel of apatites involves the preparation of aqueous solutions from calcium and phosphorus precursors (42, 341, 342). This method requires the study of synthesis parameters such as pH, concentration, and oxidation states (42). The sol – gel method involves several physical and chemical processes such as hydrolysis, gelation, drying, dehydration, and densification/calcination (42, 77, 254, 341, 342). These processes may or may not be adopted depending on the desired product (42, 255). The sol – gel method has many advantages, including the use of low temperatures, molecular level mixing of calcium and phosphorus, homogeneity and purity of products (42, 341, 342, 353, 354), and good control of size and morphology (42, 353, 354). In addition, it can be used easily to produce thin films and coatings on implants (42, 355, 356), which improve the stability of interface between an implant and bone tissues (357). On the other hand, the main disadvantage of the sol – gel method is the possible hydrolysis of phosphates as well as the high cost of raw materials, which is overcome by a simpler route using calcium nitrate tetrahydrate ($\text{Ca}(\text{NO}_3)_2 \cdot 4\text{H}_2\text{O}$) and phosphorous pentoxide (P_2O_5) to synthesise nano HAp (42).

The sol – gel reaction starts with mixing of precursors in solutions, during which hydrolysis of precursors takes place. The reaction rate can be increased in the presence of a catalyst such as an acid (42). The gelification stage involves continuous stirring of the mixture until the formation of a gel

containing water and alcohol. The latter are removed during the drying stage, which is usually carried out at temperatures $< 200^{\circ}\text{C}$ (42, 77). The removal of organic residues (e.g. CaO and CaO_3) and chemically bonded water usually takes place during the dehydration stage at temperatures between $400 - 800^{\circ}\text{C}$ (42, 77, 251, 254). The latter produces a material in a glass or microcrystalline form (42). The densification or calcination stage is carried out at high temperatures around 1000°C in order to produce a dense material (42) and improve its crystallinity (42, 254). A flow chart for obtaining HAp by the sol – gel method is shown in Figure 2.15.

The influence of synthesis parameters on the final calcium orthophosphate product is widely reported (77, 251, 254, 255, 341, 342). The most widely used sol – gel reactions for the synthesis of calcium orthophosphates, particularly HAp, are those involving the reaction of calcium nitrate tetrahydrate ($\text{Ca}(\text{NO}_3)_2 \cdot 4\text{H}_2\text{O}$) with triethyl phosphite ($\text{C}_2\text{H}_5\text{O}$)₃P) (77, 251, 358), diammonium hydrogen phosphate ($(\text{NH}_4)_2\text{HPO}_4$) (255), phosphorous pentoxide (P_2O_5) (254), phenyldichlorophosphite ($\text{C}_6\text{H}_5\text{PCl}_2$) (359, 360), or phosphonoacetic acid ($\text{HOOCCH}_2\text{PO}(\text{OH})_2$) (361, 362), as well as the reaction of calcium acetate with phosphoric acid (H_3PO_4), phosphorous pentoxide (P_2O_5) (363, 364), or triethyl phosphite (363-365). Other routes involve the reaction of calcium diethoxide ($\text{Ca}(\text{OEt})_2$) and triethyl phosphate ($\text{PO}(\text{OEt})_3$) (366, 367).

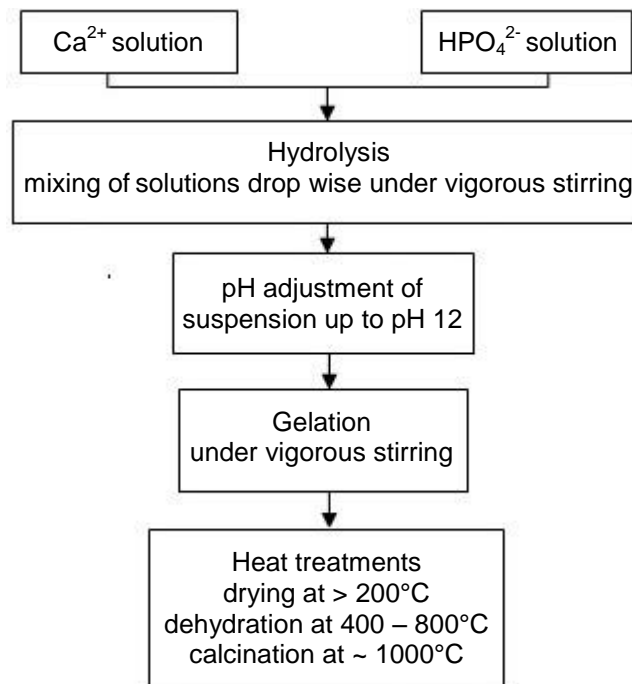


Figure 2.15 Flow chart for obtaining HAp by the sol – gel method.

The sol – gel reaction of calcium nitrate tetrahydrate ($\text{Ca}(\text{NO}_3)_2 \cdot 4\text{H}_2\text{O}$) and triethyl phosphite ($\text{C}_2\text{H}_5\text{O}$)₃P) (77) under vigorous stirring, ageing at room temperature for 16 – 24 hours, and powder calcination at 500°C and 700°C for 2 hours produces HAp with an equiaxed and rod – like morphology, with particle size mostly of 25 – 100 nm and a maximum of about 250 nm. Calcination at 700°C results in high values of size distribution, with an increased particle length of up to 250 nm. Decomposition of HAp also occurs at 700°C and results in the formation of β – TCP and CaO phases. The same reaction (251) in the presence of 2 – metoxiethanol ether, as an organic solvent, with pH 4, stirring and ageing for 4 days at 80°C , gelation at $90 - 100^\circ\text{C}$ for 16 hours, and drying at $180 - 200^\circ\text{C}$ for 4 hours produces HAp with CaO and CaCO_3 phases. Calcination at $600 - 800^\circ\text{C}$ for 12 hours also produces HAp with CaO and CaCO_3 phases. A chemical treatment is

required to eliminate such undesirable phases, and consequently, HAp clusters can be obtained with homogenous particle size of 300 nm (251). The formation of undesirable phases, such as CaCO_3 , could be due to the evaporation of unreacted triethyl phosphite in the sol or gel, whereas the formation of other phases, such as CaO and β – TCP, is due to the decomposition of HAp during calcination at 600 – 800°C (77). Recently developed sol – gel method (358), using calcium nitrate ($\text{Ca}(\text{NO}_3)_2 \cdot 4\text{H}_2\text{O}$) and triethyl phosphite ($(\text{C}_2\text{H}_5\text{O})_3\text{P}$), involves the hydrolysis of phosphite reagent by water for 24 hours, followed by the addition of calcium nitrate solution. At temperatures between 300°C and 400°C, a nanosized hydroxycarbonate apatite with low crystallinity and grain diameter of 20 – 50 nm is obtained (341).

On the other hand, the sol – gel reaction of calcium nitrate tetrahydrate ($\text{Ca}(\text{NO}_3)_2 \cdot 4\text{H}_2\text{O}$) and diammonium hydrogen phosphate ($(\text{NH}_4)_2\text{HPO}_4$) (255) at 75°C, pH 11, stirring for 12 hours, ageing for 24 hours, and drying at 85°C overnight produces a single phase of amorphous HAp with a platelet – like morphology and particle size of 35 – 65 nm. The sol – gel reaction of calcium nitrate tetrahydrate ($\text{Ca}(\text{NO}_3)_2 \cdot 4\text{H}_2\text{O}$) and phosphorous pentoxide (P_2O_5) (254) with a slow addition rate of reactants, stirring for 10 to 15 hours, gel drying and sintering at 400 – 750°C for 8 hours produces HAp and additional phases. However, a single – phase nano HAp is obtained with enhanced crystallinity after sintering at 750°C. Powders that are precipitated from calcium nitrate tetrahydrate ($\text{Ca}(\text{NO}_3)_2 \cdot 4\text{H}_2\text{O}$) and phenyldichlorophosphite ($\text{C}_6\text{H}_5\text{PCl}_2$) and calcined at 400°C produces poorly crystallised HAp with low purity, but can be transformed into a pure and well – crystallised HAp at 900°C (359, 360). The sol – gel reaction of calcium

nitrate tetrahydrate ($\text{Ca}(\text{NO}_3)_2 \cdot 4\text{H}_2\text{O}$) and phosphonoacetic acid ($\text{HOOCCH}_2\text{PO}(\text{OH})_2$) in aqueous solutions produces a pure HAp at 700°C , but its crystallinity can be enhanced at temperatures up to 1100°C (361, 362).

Therefore, increasing temperature and reaction time can result in the crystal growth of HAp (341), decomposition of HA, and formation of undesirable phases, which may greatly depend on the particle characteristics and synthesis route (79, 80). In addition, ageing time of > 24 hours during the precipitation reaction of calcium diethoxide ($\text{Ca}(\text{OEt})_2$) and triethyl phosphate ($\text{PO}(\text{OEt})_3$) at temperatures $> 600^\circ\text{C}$ is essential to stabilize the solution system, obtain a monophasic HAp (363, 364), and avoid the formation of undesirable phases such as CaO (365).

Moreover, HAp coatings can be produced by the sol – gel reaction of calcium acetate with different precursors, including phosphoric acid (H_3PO_4), phosphorous pentoxide (P_2O_5), or triethyl phosphite, at temperatures $> 600^\circ\text{C}$ (366, 367). The best result, such as wetting characteristic, is obtained using triethyl phosphite (366, 367). However, The reaction of calcium acetate ($\text{Ca}(\text{C}_2\text{H}_3\text{O}_2)_2$) and triethyl phosphate at 775°C requires further acid treatment to eliminate CaO and form a pure HA phase (368).

Therefore, different forms of HAp, such as dense forms and thin films, can be obtained by the sol – gel method using different starting reactants and different synthesis conditions, including pH, temperature, reaction time, aging time, and calcination temperature and time.

2.6.3.3 Hydrothermal method

The term hydrothermal was first introduced in the 19th century by the British geologist, Sir Rodrick Murchison, to describe the reaction of water at elevated temperature and pressure, which simulates the natural hydrothermal phenomena (327, 328). However, the method was popularized in the 20th century during 1940s by material scientists for the production of a wide variety of minerals such as single crystals of quartz and zeolites (327). It became commercially important in several branches of science and technology for the production of inorganic compounds such as ceramic powders (327, 328). Several hydrothermal – related techniques, such as hydrothermal synthesis, hydrothermal growth, hydrothermal treatment, hydrothermal sintering, and hydrothermal decomposition were developed in many interdisciplinary fields of science, including materials, engineering, chemistry, and biology (327). The success of the hydrothermal method is credited to the advanced development of hydrothermal apparatuses and the theories of hydrothermal chemistry and process modelling (327, 328).

Several definitions of the hydrothermal method are reported. It is usually defined as the process that refers to any single or heterogeneous reactions in the presence of aqueous solvents at elevated temperature ($> 25^{\circ}\text{C}$) and pressure ($> 100 \text{ KPa}$) that crystallise materials from solutions (327, 328, 370). Morey and Niggli define it as "...in the hydrothermal method the components are subjected to the action of water, at temperatures generally near though often considerably above the critical temperature of water ($\sim 370^{\circ}\text{C}$) in closed bombs, and therefore, under the corresponding high pressures developed by such solutions." (371). It is also defined by Rabenau as the heterogeneous reactions in aqueous media above 100°C and 1 bar

(372). Hydrothermal temperatures and pressures extend over 1000°C and 500 MPa, respectively (373), except those intended for research studies and commercial productions, where temperatures and pressures are usually < 350°C and < 50 MPa, respectively (12, 328). However, researchers also used the hydrothermal term to describe the growth from aqueous solutions at ambient conditions (328, 374).

Despite its different definitions, the hydrothermal method can be used for the synthesis of new phases, stabilize new complexes, crystal growth of many inorganic compounds, and preparation of micro – crystallites with well – defined size and morphology for specific applications (327). It offers many advantages over other methods, particularly those for the synthesis of ceramic materials such as HAp. It can produce different forms of ceramics, such as single crystals, powders, fibres, and coatings (328). Time and energy – consuming processing steps, such as calcination, are either not required or minimized (77, 328). In addition, it offers an improved control of size and morphology of crystallites and degree of agglomeration (327, 328).

The first attempt to synthesise hydroxyapatite (HAp) was carried out by Morey and Ingerson in 1937 (327). Hydrothermal synthesis of HAp offers a more controlled morphology, homogeneity in size, and high purity in composition, compared to other methods (253, 327, 328, 375). It can produce HAp particles with different particle size ranging from a couple of nanometres to tens of microns, with a high degree of crystallinity and a Ca:P ratio close to the stoichiometric value of 1.67 (12, 327, 328). However, obtaining a Ca:P ratio of 1.67 depends on the synthesis route and its parameters (77, 252, 376).

The hydrothermal method involves the preparation of aqueous solutions by dissolving reagents in deionised water, which are mixed by a drop – wise addition technique under vigorous stirring at room temperature. pH of the mixture can be adjusted up to 12 using NaOH or NH₄OH (251, 252). The mixture is then transferred to a reactor to be thermally treated at temperatures between 50°C and 350°C for a period of up to 72 hours. The precipitate is washed by deionised water through centrifugal and ultrasonic bath cycles, and it is dried at low temperatures ~ 80°C overnight. A flow chart for obtaining HAp by the hydrothermal method is shown in Figure 2.16.

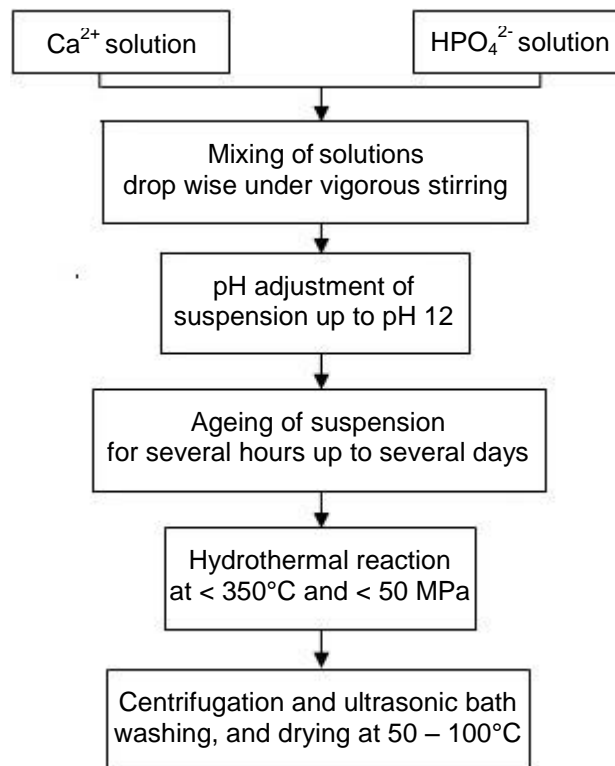


Figure 2.16 Flow chart for obtaining HAp by the hydrothermal method.

Several publications report the synthesis of HAp using different starting reactants and different synthesis parameters (12, 77, 341, 342, 252, 253, 369, 377, 378). The most widely used hydrothermal reactions for the synthesis of HAp involve the reaction of calcium nitrate tetrahydrate ($\text{Ca}(\text{NO}_3)_2 \cdot 4\text{H}_2\text{O}$) (12, 77, 341, 377, 379), calcium carbonate (CaCO_3) (369), or calcium hydroxide ($\text{Ca}(\text{OH})_2$) (253) with diammonium hydrogen phosphate ($(\text{NH}_4)_2\text{HPO}_4$). Other routes involve the hydrothermal treatment of calcium orthophosphates, such as $(\text{CaHPO}_4) \cdot \text{H}_2\text{O}$, with $\text{Ca}(\text{OH})_2$ and lactic acid ($\text{CH}_3\text{CH}(\text{OH})\text{COOH}$) (12), or cetyl trimethyl ammonium bromide (CTAB) (252, 380), or the hydrothermal treatment of calcium pyrophosphate ($\text{Ca}_2\text{P}_2\text{O}_7$) with calcium oxide (CaO) (381, 382).

The hydrothermal reaction of calcium nitrate tetrahydrate ($\text{Ca}(\text{NO}_3)_2 \cdot 4\text{H}_2\text{O}$) and ammonium hydrogen phosphate ($(\text{NH}_4)_2\text{HPO}_4$) with different pH values in the range pH 5 – 12, at $\sim 200^\circ\text{C}$ for 24 – 72 hours, and drying at $\sim 50^\circ\text{C}$ for 4 hours produces crystalline HAp with different particle size and morphology (12, 377). With pH 5 and 200°C for 24 hours, a single phase of HAp is produced, while longer reaction time of > 24 hours produces HAp and monetite phases. Rod – like particles with aspect ratios (length/diameter) in the range of 100 – 600 nm and 10 – 60 nm are produced with reaction times of 24 hours and 48 hours, respectively. On the other hand, higher pH values of pH 10 – 12 result in a smaller particle size with an equiaxed or spherical morphology. Another reaction with pH 11, at 200°C for 24 hours, and drying at $\sim 50^\circ\text{C}$ for 4 hours (77) produces rod – like crystalline HAp with lengths of ≤ 300 nm and aspect ratios (length/width) in the range 1.8 – 7.8. A similar reaction with pH 10 – 12 at temperature and pressure of 140°C and 0.3 MPa, respectively, for 2 hours (379) produces poorly crystallised apatite with

a rod – like morphology, crystal size of $23 \times 91 \text{ nm}^2$, and Ca:P ratio between 1.5 and 1.67. Calcination of powders at 1100°C results in a biphasic phase (HAp and β – TCP). Stoichiometric HAp (Ca:P ratio of 1.67) with similar dimensions and morphology (rod – like) can be obtained hydrothermally at temperature and pressure of 200°C and 2 MPa, respectively, for 10 hours (341).

The hydrothermal reaction of calcium carbonate (CaCO_3) (of marine algae) and diammonium hydrogen phosphate ($(\text{NH}_4)_2\text{HPO}_4$) (369) with pH 8.5 – 9, at 200°C for 48 hours, and drying at 80°C for 30 hours produces phases other than HAp, including OCP and TCP. However, in the presence of NH_4F aqueous solution under the same conditions, a single phase of non – stoichiometric CHAp can be obtained.

The hydrothermal reaction of calcium hydroxide ($\text{Ca}(\text{OH})_2$) and $(\text{CaHPO}_4 \cdot 2\text{H}_2\text{O})$ (253) with pH 6, 9 (using CH_3COOH), and 14 (using KOH), at 140°C for 24 hours, and drying at $60 - 100^\circ\text{C}$ for 2 hours produces pure HAp powders, except those produced with pH 6, which is accompanied by a secondary phase of monetite. However, powders that are obtained from solutions with pH 6 and 9 have better crystallinity than those with pH 14. A whisker morphology with aspect ratios (diameter:length) of $2 \mu\text{m}:20 \mu\text{m}$ and $100 \text{ nm}:2 \mu\text{m}$ is obtained with pH 6 and 9, respectively. On the other hand, a distinct morphology with an average particle size of 150 nm is obtained with pH 14. In addition, the same reaction with pH 9 at low temperatures of $< 120^\circ\text{C}$ results in the formation of HAp and monetite phases. However, a pure HAp phase with a needle – like morphology and a median diameter and

length of 40 nm and 600 nm, respectively, is obtained at $> 120^{\circ}\text{C}$ for 24 hours.

Moreover, the hydrothermal reaction of calcium orthophosphates, such as $(\text{CaHPO}_4)\cdot\text{H}_2\text{O}$, with NaOH and cetyl trimethyl ammonium bromide (CTAB) (252, 380) (CTAB, as a cationic surfactant (42)) at 150°C for 2 hours produces a single phase of HAp. The hydrothermally treatment of single crystals of DCPD in a beaker containing water, with pH 7.5 (using NH_4OH), at 220°C for 3 hours, and drying at room temperature (252) produces whisker particles with an average size of $4 \times 45 \mu\text{m}$. However, the same crystals in an empty glass beaker surrounded by water under the same conditions (252) produces hexagonal particles with an average size of $25 \mu\text{m}$. The physicochemical process involved can be explained by the reaction of DCPD ($\text{CaHPO}_4\cdot 2\text{H}_2\text{O}$) with OH^- ions produced by the evaporation of water (H^+ and OH^-), which leads to the formation of HAp. The reaction reactivity increases with increasing OH^- ions due to the increase in temperature (383). The incorporation of H_2O into HAp structure is not observed with HAp obtained from DCPD in the absence of water, which results in a higher crystallinity. Also, the addition of NH_4OH affects the growth rate of HAp crystals by increasing the reaction rate significantly (382). In addition, the hydrothermal reaction of calcium pyrophosphate $\text{Ca}_2\text{P}_2\text{O}_7$ with calcium oxide CaO produces a single phase of HAp, with a stoichiometric Ca:P ratio of 1.67 (381).

2.6.3.4 Synthesis methods used in this work

The wet method (chemical precipitation and hydrothermal methods) was used in the present investigation because it provides high reactivity, low reaction temperatures, and low reaction time, as well as it produces high – quality, homogeneous, and high – density products with small particle size (particle size > 50 nm) (42). It is a suitable method for the synthesis of apatite biomaterials with small particle size and carbonate content similar to that of biological apatites (42). Wet methods can produce materials with desired crystallinity, morphology, surface area, and particle size for specific applications (330).

In particular, the chemical precipitation method was used due to its versatile and economic advantages (248), as well as its capability of producing large amounts of powder (331). The precipitation method is conducted at low temperatures, usually room temperature, using inexpensive equipment (336-338), and yet can produce high percentages of pure materials (337, 338) such as stoichiometric HAp (Ca:P ratio of 1.67) (336). The properties of final product, including composition, impurities, morphology, and particle size (42, 73, 74, 248, 250, 331) can be controlled by controlling the synthesis parameters using a controlled system (controlled crystallisation method) (42).

On the other hand, the hydrothermal method was used because it offers a more controlled morphology, homogeneity in size, and high purity in composition, compared to other methods (253, 327, 328, 375). It can produce HAp particles with different particle size ranging from a couple of nanometres to tens of microns, with a high degree of crystallinity and a Ca:P ratio close to the stoichiometric value of 1.67 (12, 327, 328).

2.7 Doping of calcium orthophosphates

Doping of calcium orthophosphates with chemical elements, particularly through ion substitution, is an interesting and potential approach to produce materials with required and improved properties. Several metal ions, such as magnesium (Mg), strontium (Sr), manganese (Mn), iron (Fe), zinc (Zn), and silver (Ag) are incorporated successfully into the structure of calcium orthophosphates to improve their mechanical and biological properties (384).

Doping of calcium orthophosphates, particularly HAp, is widely investigated for many biomedical and dental applications. For example, FAp exhibits excellent properties, and therefore, it is the most used apatite in dental applications (49), including calcium phosphate cements (49, 68), toothpastes (49, 68, 69, 73), and coatings for dental implants (49, 68, 233-235). Aluminium doped calcium phosphate cements are also used in dentistry, as non – resorbable fillers (385). Rare earth doped HAp exhibits excellent luminescent properties, and thus, it can be used as a biological fluorescent probe (386). In addition, europium (Eu^{3+}) doped apatites are reported as potential orthopaedic medical materials and drug carriers (386). Therefore, the incorporation of RE (Er^{3+}), Al^{3+} , and F^- into the structure of calcium orthophosphates could offer optimum properties, particularly, for medical and dental applications.

2.7.1 Rare earths (RE)

Rare earths consist of 17 elements, fifteen of which are the lanthanides (from lanthanum (Ce) to lutetium (Lu)), and the other two are scandium (Sc) and yttrium (Y). Rare earths commonly share chemical properties due to the similarity in their outer electronic configurations ($(3d\ 4s)^3$ for Sc, $(4d\ 5s)^3$ for Y, and $(5d\ 6s)^3$ for La and trivalent lanthanides), which dominate their chemical interactions (387, 388). However, lanthanides (lanthanum (La) to lutetium (Lu)) are also characterised by the gradual filling of the 4f shell (from $N = 0$ (La) to $N = 14$ (Lu) in their electronic configurations $4f^N 5s^2 5p^6$) (387-389). Electrons in the 4f shell give the lanthanides their character (387, 388, 390) as well as additional properties, such as having magnetic structures, that scandium, yttrium, and lanthanum lack (387). Therefore, scandium, yttrium, and lanthanum are considered as a prototype of rare earths due to the absence of 4f electrons (387, 388). These 4f electrons are shielded and localized by the outer 5p, 5s shells (387-390), and therefore, they do not participate in the constant electric field conductivity. However, they participate in the optical conductivity alongside the 5d and 5s electrons (390).

Rare earths (RE) are classified into light RE (Sc, La, Ce, Pr, Nd, Pm, Sm, Eu, and Gd) and heavy RE (Y, Tb, Dy, Ho, Er, Tm, Yb, and Lu). Rare earths or lanthanides are commonly in the form of trivalent ions (Ln^{3+}), except for cerium, which exhibits a +4 – oxidation state in solutions (387). Rare earth ions (RE^{3+}) possess optical properties that have potential photonic applications in various fields of science and technology (387, 389, 391, 392). The incorporation of RE into the structure of calcium orthophosphates, particularly apatites, gives them luminescence properties that are of great

utility in laser industries (392). Optical properties of trivalent rare earth ions (RE^{3+}) depend primarily on their internal $f-f$ electronic transitions and other parameters such as transition cross sections and radiative lifetime.

2.7.1.1 Internal $f-f$ electronic transitions

Electronic transitions of rare earths usually occur within the 4f shell (389, 393). Therefore, their optical properties are generally due to the intra- f -shell absorptions and emissions by the optical active electrons in the 4f shell (389, 393). The character of the 4f electrons is the most interesting property of their electronic structure (387-390). Trivalent rare earth ions exhibit very narrow transition lines in the visible spectrum (389). They are characterised by the sharpness of many absorption and emission spectral lines (389, 390, 393), which are as narrow as the spectra of free atoms (388, 389). The atomic-like behaviour of their spectra is due to their electronic configurations (388, 389).

Most of absorption lines that are due to parity-forbidden $f-f$ electronic transitions (388, 393) result in small absorption cross-sections and inefficient direct optical excitation (393). However, indirect excitation can optimise their emission in the presence of organic (394) and inorganic (391) sensitizers.

The absorption of an atom or ion can be determined simply by measuring the decrease in optical intensity of incident beam as a function of wavelength (λ). In linear optics, according to Lambert-Beers law, the absorption coefficient (α) for a sample of thickness (L) is given by (395):

$$I_{(\lambda)} = I_{0(\lambda)} e^{-\alpha(\lambda)L} \dots\dots(2.11),$$

where (I) is the measured intensity in an optical path length (L), and (I_0) is the intensity of incident beam.

The absorption coefficient (α) is usually measured in cm^{-1} . The transmission and absorbance (optical density) ($A_{(\lambda)}$) of an atom or ion can be determined by the transmission coefficient ($T_{(\lambda)}$) (395):

$$T_{(\lambda)} = \frac{I_{(\lambda)}}{I_{0(\lambda)}} \dots\dots(2.12)$$

$$A_{(\lambda)} = -\log(T_{(\lambda)}) \text{ or } T_{(\lambda)} = 10^{-A_{(\lambda)}} \dots\dots(2.13)$$

2.7.1.2 Transition cross sections

Light absorption and emission can be quantified by cross sections of a transition between two states (e.g. 2 and 1) with energy $E_2 - E_1$. Cross sections describe the ability of an atom or ion to absorb or emit light. Absorption (σ_{12}) and emission (σ_{21}) cross sections are proportionality constants between absorbed (P_{abs})/emitted (P_{em}) power and incident light intensity (I) at a given frequency (396):

$$P_{\text{abs}} = I \sigma_{12} \quad \text{and} \quad P_{\text{em}} = I \sigma_{21} \dots\dots (2.14),$$

where (I) is the intensity of light incident upon the ion, (σ_{12}) and (σ_{21}) are the absorption and emission cross sections, respectively. Therefore, absorption and emission increase with decreasing the area, over which light is focused. The absorption bands of RE ions (in solutions) in the visible region are schematically shown in Figure 2.17. Absorption cross sections describe the ability of an atom or ion to absorb light, and it can be determined by equation 2.15 (395):

$$\sigma_{(\lambda)} = \frac{\alpha_{(\lambda)}}{N} \dots\dots (2.15),$$

where (N) is the density of absorbing centres (cm^{-3}).

The amount of power ($P_{(\lambda)}$) absorbed by an atom or ion at wavelength (λ) is given by (395):

$$P_{(\lambda)} = \frac{\sigma_{(\lambda)}}{I_{(\lambda)}} \dots (2.16),$$

where (I) is the intensity of incident beam in Watt cm^{-2} , while the dimension of (σ) is that of an area. The relation between absorption and emission cross sections is given by (396):

$$\sigma_{21}(\nu) = \sigma_{12}(\nu) e^{(q-h\nu)/kT} \dots (2.17),$$

where (q) is the mean transition energy between two manifolds, (k) is Boltzmann's constant, and ($h\nu$) is the energy of a photon at a given frequency (ν) and temperature (T).

2.7.1.3 Lifetime (Decay time)

Lifetime or decay time is the time, which an excited electron takes from an upper energy level to a lower one. Excited electrons can decay to lower energy levels either through radiative or non – radiative decay. Excited state lifetime is given by (396):

$$\frac{1}{T} = \left(\frac{1}{T_r}\right) + \left(\frac{1}{T_{nr}}\right) \dots (2.18),$$

where (T) is the total lifetime, (T_r) is the radiative lifetime, and (T_{nr}) is the non – radiative lifetime.

Radiative lifetimes in rare earths are usually long (on the microsecond or millisecond order) (397) due to the parity – forbidden $f - f$ electronic transitions (388, 393, 396). On the other hand, non – radiative transition probability is linked to the number of phonons required to bridge the energy gap as well being a temperature dependant.

Therefore, non – radiative lifetime can be given by equation 2.19 (396):

$$\left(\frac{1}{T_{nr}}\right)_{m,T} = \left(\frac{1}{T_{nr}}\right)_{m,0} [1 - e^{-(h\nu/KT)}]^{-m} \dots (2.19),$$

where $(1/T_{nr})_{m,0}$ is the transition rate at zero temperature, which decreases exponentially with the number of phonons required to bridge the energy gap.

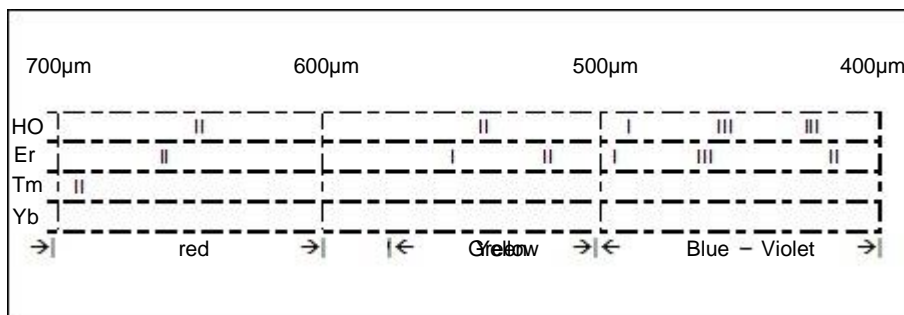


Figure 2.17 Schematic showing the absorption bands of rare earth ions (in solutions) in the visible region (with no absorption for ytterbium) (398).

Calcium phosphate minerals, particularly apatites, are the main host for RE elements in geological environments (399, 400) due to their high affinity to RE elements and many other metals (401).

The incorporation of rare earth elements into the structure of calcium orthophosphates results in materials with electrooptical (399), luminescence (392, 402, 403), and phosphorous (403) properties, which have potential technological, photonic, and medical applications (392, 400, 402-405). Rare earths are used in technological and photonic fields, as phosphors and magnetic materials, catalysts, and optical glasses (404, 406, 407). They can also be used in medical, physiological, and biochemical fields, as contrast mediums, for magnetic resonance imaging (404, 408), restriction enzymes, biocatalysts (404), and fuel cells (406, 407). The

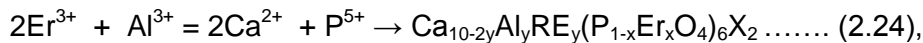
microstructure and optical properties of rare earth – substituted apatite can be controlled by varying heat treatment/annealing temperatures (403, 408). Heat treatments are also required for the diffusion of rare earths into the structure of apatites (408) and the formation of well – crystallised materials (403, 409, 410), however, heat treatments, particularly at high temperatures, result in the formation of large size apatite particles (408) or large size clusters (403) and may increase the concentration of rare earths (404).

Trivalent rare earth ions are commonly incorporated into the structure of apatites (e.g. HAp, FAp, ClAp) at the calcium structural sites (Ca1 and Ca2) (399-401, 404, 408, 411). The uptake of rare earths by apatites is not uniform throughout the 4f transition metal series (399-401, 411). The highest uptake is in the Nd – Gd range for natural apatite and near Nd for synthetic FAp (412, 413), and it is lowest for Lu (399, 411). The substitution behaviour results in a monotonic decrease in the ratio of RE – Ca2 to RE – Ca1 through the 4f transition metal series (399, 400, 411). Generally, light REs have a strong preference for Ca2 sites (399), whereas heavy REs are readily accommodated in Ca1 sites (400). This may be due to the incompatibility between trivalent heavy RE and the stereochemical environment of Ca2 sites rather than an increasing preference for Ca1 sites (400). On the other hand, there is some control by a substitution mechanism on the uptake and site preference of light RE (399). The substitution behaviour is probably controlled by charge compensation (equalization of Ca1 and Ca2 bond valences) and spatial accommodation of substituents (399, 400, 411). The apatite anion (OH, F, Cl) can also contribute in the selectivity of RE due to its influence on the stereochemical environment and effective size of Ca2 sites (399, 411). Therefore, the incorporation of RE into

the structure of apatites (HAp, FAp, and ClAp) can be primarily associated with charge compensation and spatial accommodation of substituents (399, 4011). The substitution of RE into HAp and FAp is charge compensated by (Si) and (Na and Si), respectively, with a strong and moderate preference of La for Ca₂ sites, respectively, and significant RE uptake. On the other hand, the substitution of RE into ClAp is charge compensated by (Na), with a weak preference of La for Ca₁ sites and weak RE uptake. Therefore, the incorporation of RE into the structure of apatites requires coupled substitutions to maintain the charge balance (399, 401, 411), which can be demonstrated by those dominate natural and synthetic apatites (412, 414, 415) as follows:



Similarly, the proposed substitution in synthetic apatites with Er³⁺, Al³⁺, and F⁻ may follow these coupled substitutions as follows:



where (X) is the anion (OH⁻) in HAp or (F⁻) in FAp.

The incorporation of fluoride (F⁻) along with RE into the HAp structure may be of great importance, because the uptake of RE by HAp is about 75% of that for FAp (400). The incorporation of RE into the structure of calcium phosphates is also reported to be coupled with CO₃²⁻ substitution for OH⁻

and PO_4^{3-} , which results in RE – carbonate apatite (e.g. RE – HCAp) (405, 416).

The incorporation of light rare earth ions (La^{3+} , Ce^{3+} , Pr^{3+} , Nd^{3+} , and Sm^{3+}) (405) and heavy rare earth ions (Y^{3+} , Gd^{3+} , Dy^{3+} , Er^{3+} , and Yb^{3+}) (416) into the apatite structure can be achieved by the precipitation method using rare earth nitrates ($\text{RE}(\text{NO}_3)_{3 \cdot n}\text{H}_2\text{O}$) (405, 416). Rare earth nitrate solutions are added to and in place of a portion of $\text{Ca}(\text{OH})_2$, to which H_3PO_4 solution is added. The reaction is carried out at pH 9.5 (using NH_4OH), stirring at room temperature for 1 hour, and ageing at 100°C for 48 hours. The precipitates are then washed, filtered, and dried at 70°C for 16 hours. The incorporation of RE results in the lengthening of short rod – like HAp particles and improve their crystallinity, which is also followed by the shortening of particle length and the reduction in crystallinity (405, 416). These RE – HAp powders are cation – deficient carbonate apatite to maintain the charge balance. They contain CO_3 groups instead of OH and PO_4 groups, which indicates A – and B – type RE – HCAp (405, 416).

Single crystals of RE – substituted apatites (HAp, FAp, and ClAp) can be grown by the hydrothermal method (399, 400, 411). The incorporation is coupled with Si substitution via SiO_2 . Single crystals of RE – substituted HAp are grown from volatile – rich melts in a reaction vessel. Calcium RE silicate ($\text{Ca}_4\text{RE}_6(\text{SiO}_4)_6\text{O}$) is prepared using CaCO_3 , RE_2O_3 , and SiO_2 , which are decarbonated in a platinum dish at 900°C and mixed with a commercial synthetic HAp. Also, single crystals of RE – substituted FAp (La, Nd, Gd, Dy – FAp; $\text{CaNaRE}(\text{PSiO}_4)\text{F}$) and double RE – substituted FAp (La.Gd – FAp, Ce.Dy – FAp, Pr.Er – FAp, and Eu.Lu – FAp) are grown from a

stoichiometric mixture of tribasic calcium phosphate and synthetic HAp, RE_2O_3 , CaF_2 , and amorphous SiO_2 under hydrothermal conditions at 900°C and 0.17 GPa (400). Similarly, single crystals of RE – substituted ClAp ($\text{Ca}_4\text{RE}_6(\text{SiO}_4)_6\text{Cl}_2$) are hydrothermally grown from a mixture of CaCO_3 , RE_2O_3 , SiO_2 , and CaCl_2 (411). In addition, the incorporation of RE (Eu^{3+} , Gd^{3+} , and Yb^{3+}) into the structure of HAp can be achieved by the reaction of commercial HAp in a RE – Cl_3 aqueous solution at 37°C for 72 hours (404). HAp is filtered from a RE – Cl_3 solution, dried, and sintered in air at 1100°C for 1 hour. The formation of Eu^{3+} doped HAp can also be obtained from solutions of ammonium dihydrogen phosphate ($(\text{NH}_4)_2\text{HPO}_4$), calcium nitrate ($\text{Ca}(\text{NO}_3)_2 \cdot 4\text{H}_2\text{O}$), and europium nitrate ($\text{Eu}(\text{NO}_3)_3 \cdot 6\text{H}_2\text{O}$) (386).

Rare earth elements can be incorporated into the structure of calcium orthophosphates via various rare earth compounds, including nitrates and oxides of rare earths. The incorporation of rare earths via nitrates can be achieved by the wet chemical methods (405, 416). On the other hand, rare earth oxides are insoluble in H_2O , but they are soluble in acid solutions (268) (e.g. HNO_3 , HCl and H_2SO_4) (oxides of Yb^{3+} and Ce^{3+} do not dissolve completely (405, 416)). Therefore, their incorporation into the structure of calcium orthophosphates can be achieved at elevated temperatures by the solid – state (42) and hydrothermal methods (399, 400, 411). At high temperatures, some oxides lose oxygen, with the creation of anion vacancies and associated reduction $2\text{O}^{2-} \rightarrow \text{O}_2 + 4\text{e}^-$, particularly in a reduced atmosphere. These free electrons form a mixed valence state with transition metal cations in the structure, which usually results in semiconducting or metallic materials (329).

Rare earth oxides have various applications, including electronic, optical, and glass applications, as well as medical applications (387, 417, 418). For example, Er_2O_3 and Yb_2O_3 are added as network modifiers to calcium aluminosilicate glasses, which replace Al_2O_3 and decrease their elastic modulus (417), whereas Y_2O_3 is used as a bio – inert substrate in orthopaedic implants (418).

Among rare earth elements of the lanthanide series that of interest to our research investigation is erbium and its compounds (erbium nitrate tetrahydrate ($\text{Er}(\text{NO}_3)_3 \cdot 4\text{H}_2\text{O}$) and erbium oxide (Er_2O_3)). Erbium is found in nature in many minerals. It is soft and malleable metal with a shiny silvery metallic colour. Its properties depend partially on the impurities present (419). It is stable in air, and it does not oxidize as rapidly as some other rare earth metals. The addition of erbium (e.g. to vanadium) lowers hardness and improves workability (419).

Erbium nitrate tetrahydrate ($\text{Er}(\text{NO}_3)_3 \cdot 4\text{H}_2\text{O}$) is very soluble in aqueous solutions, and therefore, it is a good source of erbium (Er^{3+}) ions. It provides adequate amount of Er^{3+} ions for the synthesis of erbium – doped apatites. On the other hand, erbium oxide Er_2O_3 is insoluble in water. It has excellent chemical and thermal stability, with a melting point of $\sim 2430^\circ\text{C}$ (420). It has a body – centred cubic (bcc) lattice, which transforms into a hexagonal polymorph at high temperatures of $\sim 2320^\circ\text{C}$ due to nucleation and growth (420). Sintering of Er_2O_3 at 1800°C modifies its microstructure and produces a $\sim 91\%$ dense material (421). Er_2O_3 is characterised by sharp absorption spectral bands in the visible, ultraviolet, and near – infrared due to its electronic structure, and it gives a pink colour. Erbium (Er^{3+}) ions under laser

irradiation with 1.54 μm wavelength show an intra – $4f$ shell transition from its first excited state ($4I_{13/2}$) to the ground state ($4I_{15/2}$) (422). Erbium oxide is used as a thermal and oxidation – resistant coating (421) and a network modifier in some glasses (417). It is used as a colorant in glasses and porcelain glazes (419). Erbium – doped materials also have potential optical and optoelectronic applications (423). Like most other rare earth oxides, erbium oxide is insoluble in water, but it is soluble in acid solutions such as HNO_3 , HCl , and H_2SO_4 (268, 405, 416). Therefore, the proposed incorporation of Er_2O_3 into the structure of calcium orthophosphates is expected to occur under hydrothermal conditions (399, 400, 411).

2.7.2 Aluminium compounds

Aluminium is found in nature in most rocks, as aluminosilicate minerals (424). Pure aluminium metal has a silvery – white colour, with many desirable characteristics. Aluminium and its compounds comprise about 8% of the Earth's surface (425). Aluminium is light, soft, and lacks strength, but it can be added to other materials to introduce various properties (419). It is non – toxic, non – magnetic, and non – sparking. It has a high thermal conductivity and excellent corrosion resistance, and it can be easily formed or cast (419). When evaporated in a vacuum, it forms a highly reflective coating for both visible light and radiant heat, which soon forms a thin layer of a protective oxide, and it does not deteriorate as do other coatings, particularly silver coatings (419). Aluminium is used in medical products, such as antacids and buffered aspirin, and it is considered safe at recommended doses (426). It is also used in coatings for decorative papers, packages, and toys (419).

Aluminium (Al^{3+}) ions are small and highly charged. They seek oxygen atoms of anions, such as hydroxide (OH^-) (427), and oxygen donor sites, such as phosphate (PO_4) (e.g. those in biological systems) (425), and they form covalent aluminium – oxygen bonds, which resist acid attacks (427).

Trivalent aluminium ionic compounds are more resistant to acid attacks than divalent ones (e.g. zinc ionic compounds) due to the formation of ionic crosslinks (427). Their solubility can be controlled by pH due to their high affinity to hydroxyl ions (425). Aluminium (Al^{3+}) – terminated surfaces react strongly with water (H_2O), whereas surface hydroxyl groups interact with metal ions (428).

Common compounds of aluminium include aluminium nitrate ($\text{Al}(\text{NO}_3)_3$), aluminium hydroxide ($\text{Al}(\text{OH})_3$), aluminium oxide (Al_2O_3), and aluminium phosphate (AlPO_4). Aluminium compounds are essential in materials engineering (429). Most of its compounds are solids with high melting points, and they are used as pharmaceutical, food additive, and cosmetic products (425). Aluminium compounds, such as $\text{Al}(\text{OH})_3$, Al_2O_3 , and AlPO_4 , exhibit adsorption properties due to the negative charges of OH^- , O^{2-} , and PO_4^{3-} , respectively, which can be improved by varying pH and temperature (425). Aluminium nitrate ($\text{Al}(\text{NO}_3)_3$) is a soluble compound (268) that forms $\text{Al}(\text{OH})_3$, which is one of the most common aluminium compounds for producing Al_2O_3 (430-433) under heat treatments (434). $\text{Al}(\text{OH})_3$ occurs in many crystallographic forms with different surface properties (425). It is used as an adsorbent, ion exchanger, and filtering medium, as well as in the production of glass, paper, and ceramics (435). It is also used in pharmaceutical and cosmetic products (425).

Aluminium oxide is a bio – inert bioceramic compound (436). It occurs in many crystallographic forms with different surface properties. The main forms include $\alpha - \text{Al}_2\text{O}_3$ and $\gamma - \text{Al}_2\text{O}_3$ (425). The stable $\alpha - \text{Al}_2\text{O}_3$ is very hard and resistant to hydration and acid attacks (437). It forms at high temperatures by heating $\text{Al}(\text{OH})_3$ at $\sim 1200^\circ\text{C}$ (425, 438), during which excess of $\text{Al}(\text{OH})_3$ can be provided at high pH values (439). On the other hand, $\gamma - \text{Al}_2\text{O}_3$ forms at lower temperatures around 500°C . It absorbs water and dissolves in acids (425). The structure of $\alpha - \text{Al}_2\text{O}_3$ depends on its hydration. It has oxygen anions (O^{2-}) at the surface, which are overlaid by water (H^+ and OH^-) on hydration (425). Al_2O_3 is used as an adsorbent, thermal resistant, food additive, and filtering medium, as well as in the production of glass, paper, and ceramics (425, 440, 441). It is also used in orthopaedics (442) and dental surgery (436), and it is used as an abrasive due to its hardness of up to 30 GPa (436). The addition of Al_2O_3 to hydroxyapatite (HAp) enhances its mechanical properties and improves its densification (436). The addition of Al_2O_3 to P_2O_5 results in a viscous and adhesive mixture, which forms a solid aluminium phosphate under heat treatment (443).

Aluminium phosphate (AlPO_4), also known as berlinite, is a pure chemical with 200 – mesh granularity (444). It can be synthesised from a solution of $\text{Al}(\text{OH})_3$ and phosphoric acid (H_3PO_4) (429), which upon heating at $500 - 800^\circ\text{C}$ produces aluminium metaphosphate (445). Single crystals of AlPO_4 can also be synthesised under hydrothermal conditions at $130 - 315^\circ\text{C}$ (446121). AlPO_4 is an inorganic compound that exhibits thermal and chemical stability, thermal shock, and oxidation resistance (447). It is chemically similar to $\alpha - \text{quartz}$ (silica) (448), with a high thermal stability and

a melting point over 1500°C (448). It has the ability to form a strong bond between organic and inorganic materials due to its great mechanical coupling factor, which is greater than that of α – quartz (449). Therefore, AlPO_4 shares various thermal, chemical, and physical properties with metals and ceramics. It has the excellence of metals, including strength, thermal and chemical stability, and corrosion resistance (327, 447, 448), as well as having similar structure and piezoelectric properties to that of silica (327, 448).

Aluminium phosphate has similar uses to $\text{Al}(\text{OH})_3$ and Al_2O_3 , including the production of paper, ceramics, dental cements, cosmetics, and pharmaceutical products (435, 441). AlPO_4 is used in composites and coatings (450-452), such as AlPO_4 – SiC composite, which is used as a heat – resistant coating (453). It is also used on graphite to improve its oxidation resistance (448, 454), by increasing onset oxidation temperature and lowering total mass loss rate (448). It can remain adsorbed to graphite materials at temperatures of up to 800°C (448). Its composites can also be used as wave – transparent materials, which interact with laser irradiation rather than scattering it (444).

In biomedical applications, AlPO_4 has the same role as phosphorus pentoxide (P_2O_5) in glass ceramics (455). Its addition improves their mechanical properties (447) and enhances the nucleation of silicate (456). It prompts their surface reaction and bioactivity through phosphate groups (455), as the bioactivity increases with decreasing calcium ions (455). The addition of AlPO_4 , particularly to fluorrichterite glass ceramics, promotes mica formation and bioactivity (457). In vivo, its bonding ability depends on

the formation of an apatite phase between bioactive materials (e.g. bioactive glass) and tissues (458-460). AlPO_4 also provides the necessary PO_4^{3-} for calcium phosphate formation, promotes the crystallisation of hydroxyapatite (455, 457), and increases the amount of hydroxyapatite powder (455).

Moreover, aluminium phosphate is also used as a binder (429, 445, 461). Its solid phases, $\text{Al}(\text{PO}_3)_3$ and AlPO_4 , form at high temperatures of 500 – 800°C (429, 445) and 1200°C (429), respectively, during the application of acid aluminium phosphate binders (liquid solution of phosphoric acid and an aluminium salt, such as $\text{Al}(\text{OH})_3$, with P:Al ratio > 3) (429). The addition of aluminium salts to acid phosphate binders enhances their bonding ability (462-464). Aluminium phosphate and acid aluminium phosphate binders are liquid solutions of phosphoric acid and aluminium salt, for example, $\text{Al}(\text{OH})_3$ with P:Al ratios of ≤ 3 and > 3 , respectively (429, 461). Acid aluminium phosphate is superior to commercial silica binders (429) for the binding of fibrous or particulate materials and coating of materials, particularly graphite as an oxidation resistant (429, 448, 454). AlPO_4 also improves the chemical and abrasion resistance (465), and it provides good strength, thermal stability (466), and moisture resistance (448) through its phosphate bonding (467).

Binding of materials in the absence of a binder can be achieved at high temperatures, and it is a non – cost effective process. However, the presence of a binder is an advantage, but it is more effective in a small quantity only (429). Post heat treatments in the presence of a binder is also required for the formation of solid phases (429, 445). Sintering of AlPO_4 results in a ceramic cementation (447) with a continuous network structure

(444). It results in crystalline and amorphous AlPO_4 phases, which depend on sintering temperature and reaction of binder with material being bounded or coated (429).

Among aluminium compounds that of interest to our research investigation are aluminium nitrate nonahydrate ($\text{Al}(\text{NO}_3)_3 \cdot 9\text{H}_2\text{O}$) and aluminium orthophosphate (AlPO_4). Aluminium nitrate nonahydrate ($\text{Al}(\text{NO}_3)_3 \cdot 9\text{H}_2\text{O}$) is very soluble in aqueous solutions, and therefore, it is a good source of Al^{3+} ions. It provides adequate amount of Al^{3+} ions for the synthesis of aluminium – doped apatites. On the other hand, AlPO_4 is insoluble in water. However, in a base solution, it may form $\text{Al}(\text{OH})_3$ precipitate (468). The effect of a heat treatment on AlPO_4 in a base solution is reported at various pH values (439). The precipitation reaction of aqueous solutions of AlPO_4 and sodium hydroxide results in an amorphous compound ($\text{AlPO}_4 \cdot x\text{Al}(\text{OH})_3 \cdot y\text{H}_2\text{O}$, where $x \leq 1$ and $y = 2 - 3$).

The thermal decomposition of the precipitate is proposed as follows (439):

- Amorphous $\text{AlPO}_4 \cdot x\text{Al}(\text{OH})_3 \cdot y\text{H}_2\text{O}$ at $\sim 110^\circ\text{C}$ produces amorphous $\text{AlPO}_4 \cdot \text{Al}(\text{OH})_3$.
- Amorphous $\text{AlPO}_4 \cdot \text{Al}(\text{OH})_3$ at $\sim 150^\circ\text{C}$ produces AlPO_4 and Al_2O_3 in the form of orthorhombic and/or tridymite.
- $\text{AlPO}_4 \cdot \text{Al}_2\text{O}_3$ at $\sim 700^\circ\text{C}$ produces AlPO_4 and $\gamma - \text{Al}_2\text{O}_3$.
- $\text{AlPO}_4 \cdot \gamma - \text{Al}_2\text{O}_3$ at $\sim 1200^\circ\text{C}$ produces AlPO_4 and $\alpha - \text{Al}_2\text{O}_3$.

The thermal decomposition of the precipitate is also affected by pH variation of solution (439). At pH 4, anhydrous amorphous AlPO_4 is formed at 400°C , crystalline orthorhombic and tridymite structures are formed at 500°C , and an orthorhombic form is formed at 1200°C . In contrast, At pH 10, anhydrous

amorphous AlPO_4 is formed at 700°C , crystalline orthorhombic and tridymite structures are formed at 900°C , and α – alumina with an orthorhombic structure is formed at 1200°C .

2.7.3 Fluoride compounds

Fluorine is a pale yellow and corrosive gas. It is the most electronegative and reactive element (469, 419), with desirable structural and optical properties (470). It reacts with all organic and inorganic substances (419). It occurs mainly in calcium fluoride (CaF_2) and sodium hexafluoroaluminate (Na_2AlF_6), as well as other minerals. Fluorine and fluoride ions (F^-) are highly toxic, and therefore, the recommended maximum allowable concentration is 1 ppm for a daily eight – hour time – weighted exposure (419). Fluorine, as a soluble fluoride, is added to water supplies for the prevention of tooth cavities (419, 471, 472). Fluoride is an important element for many living organisms, including humans. It is commonly added to drinking water (fluoridation), food, and dental products due to its action in preventing tooth decay and promoting good oral health (471, 472). It increases the resistance of the dental mineral to acid dissolution and decreases its solubility (472). However, it is only added in small quantities (the level of fluoride in public water supply in some parts of England is 1 mg per litre (471)), because large quantities can have adverse effects such as dental fluorosis (469, 471, 472). Fluoride has a low structural energy, and therefore, it is very stable in lattice sites (473). Fluoride ions (F^-) are similar to those of hydroxyl (OH^-) in terms of their charge and radius, and therefore, F^- commonly replaces OH^- in mineral structures, particularly hydroxyapatite (154-156, 474). They also promote the formation of more crystalline calcium orthophosphates (146, 155, 201, 202).

The incorporation of fluoride (F^-) into the structure of HAp significantly increases its chemical and thermal stability (475, 476) against dental caries (477, 478) without affecting its biocompatibility (479-482), and it improves its biological properties (473). It reduces its dissolution in acid environments (483) by stabilising its crystal structure (484). It does not only restrain its decomposition, but it also produces a dense material and increases its mechanical properties (485, 486), such as compressive strength, by decreasing its porosity (487). Fluoride addition reduces the crystal size and growth of the brushite mineral, and it decreases its Ca:P ratio from 1.21 to 1.06 – 1.08 (469). Besides the applications of Fluorapatite mentioned before, it is used in the treatment of osteoporosis (488), because it encourages the proliferation and differentiation of bone cells (489).

Fluoride exists only as compounds (469) such as KF, NaF, NH_4F , and CaF_2 . These compounds have different effects on the growth of calcium phosphate minerals. For example, KF suppresses the growth of brushite (DCPD) more than NaF (469). Among fluoride compounds that of interest to our research investigation are ammonium fluoride (NH_4F) and calcium fluoride (CaF_2). Ammonium fluoride (NH_4F) is very soluble in aqueous solutions, and therefore, it is a good source of fluoride ions (F^-). It provides adequate amount of F^- ions (69, 73, 74) for the synthesis of fluorapatite (FAp) by the solid – state reaction and wet methods (69, 242, 243). Its addition also promotes the formation of an apatite phase (369). The hydrothermal reaction of calcium carbonate ($CaCO_3$) (of marine algae) and diammonium hydrogen phosphate ($(NH_4)_2HPO_4$) with pH 8.5 – 9, at 200°C for 48 hours, and drying at 80°C for 30 hours produces phases other than HAp (e.g. OCP and TCP). However, in the presence of NH_4F under the same conditions, a single

phase of non – stoichiometric CHAp is obtained (369). In addition, the addition of 2.5 – 7.5 mol% of fluoride (F⁻) (via NH₄F) to calcium phosphates reduces grain size and increases fluoride content (473).

In contrast, calcium fluoride (CaF₂) has a negligible solubility in water. The addition of CaF₂ affects the mechanical properties of HAp composites (e.g. HAp – ZrO₂ composite), and it results in a cell morphology and proliferation rate in osteoblasts similar to that of HAp (485). CaF₂ also has an effect on the sintering of HAp – ZrO₂ composites (485), and it increases the densification of HAp significantly (473). Co – precipitated CaF₂ is an agglomeration of porous particles containing traces of water, the latter which can be liberated by a heat treatment without any structural changes (470). However, due to its large band gap and transparency, structural defects and colour centres can occur under laser irradiation (470).

The reaction of fluoride (via NaF) with HAp occurs through a double decomposition process, which results in CaF₂ at high fluoride concentrations (20F⁻ = > 2% NaF), as given by equation 2.25, or by an ion exchange process with the hydroxyl (OH⁻) group, which results in FAp at lower fluoride concentrations (2F⁻ = ≤ 2% NaF), as given by equation 2.26 (490).



At high fluoride concentrations (> 2% NaF), the Ca:P ratio increases with increasing calcium (Ca²⁺) ions and decreasing phosphate (PO₄³⁻), due to the formation of CaF₂ and the elimination of phosphate in the solution, respectively (490). On the other hand, at low fluoride concentrations (≤ 2%

NaF), the Ca:P ratio remains unchanged, since the only effect is the substitution of OH⁻ by F⁻ ions.

Low fluoride concentrations can also result in the formation of hydroxyl – fluorapatite, with no effect on the Ca:P ratio (490), according to the following reaction (491):



Fluoride (F⁻) can also be incorporated into the apatite structure as monofluorophosphate (PO₃F), which substitutes the orthophosphate group (492-494), but it is followed by the hydrolysis of orthophosphate and fluoride (493). The incorporation of (F⁻) into the structure of HAp occurs at two sites, corresponding to the normal halogen site and an oxygen site on the phosphate tetrahedron, which indicates the incorporation of two fluorides per unit cell of apatite (494). In contrast, the substitution of the orthophosphate group by monofluorophosphate (PO₃F) is coupled with sodium (Na⁺) substitution, and it results in the formation of monofluorophosphate apatite (Ca₆Na₄(PO₃F)₆O₂) (492).

Moreover, composites of fluorapatite (FAp) and ceramic oxides (e.g. Y₂O₃, ZrO₂, and Al₂O₃) have improved thermal and decomposition stability, and they show similar cell proliferation to that of HAp, with no cytotoxicity effects (482). FTIR investigation of heat treatments on Fluorapatite is reported (495). Spectra of FTIR reveals that calcination of FAp results in shifting and splitting of OH band, due to F⁻ – HO⁻ interactions. On the other hand, FTIR spectra of uncalcined FAp are similar to that of HAp, due to the lack of diffusion of fluoride ions at room temperature (495).

2.8 Properties of calcium orthophosphates and doping compounds

2.8.1 Properties of calcium orthophosphates

Calcium orthophosphates vary in their chemical formula, crystallographic structure, and Ca:P ratio, and therefore, they have different chemical, thermal, and mechanical properties. Properties of calcium orthophosphates, particularly mechanical properties (e.g. fracture toughness, bending strength, compressive strength, tensile strength, and Young's modulus), thermal decomposition, and solubility behaviour are of great importance for biomedical and dental applications.

Thermal decomposition and solubility behaviour of calcium orthophosphates depend primarily on their chemical composition and structure, taking into account thermal and solubility conditions. Monocalcium phosphate monohydrate (MCPM) (~ 18 g/L at $\sim 25^\circ\text{C}$) is slightly more soluble in water than monocalcium phosphate monohydrate anhydrous (MCPA) $\text{Ca}(\text{2HPO}_4)_2$ (~ 17 g/L at $\sim 25^\circ\text{C}$) (49, 68, 69, 73, 74), the former which (MCPM) transforms into the less soluble MCPA at temperatures above 100°C (69, 73, 74). Similarly, the solubility of brushite (DCPD) in water (~ 0.088 g/L at $\sim 25^\circ\text{C}$) is twice that of monetite (DCPA) (~ 0.048 g/L at $\sim 25^\circ\text{C}$) (49, 68, 69, 73, 74), the former which (DCPD) transforms into the less soluble DCPA (69, 73, 74, 153) at temperatures above 80°C (69, 73, 74). In contrast, α – TCP is more soluble in water (~ 0.0025 g/L at $\sim 25^\circ\text{C}$) and more reactive in aqueous systems (69, 73, 74) than β – TCP (~ 0.0005 g/L at $\sim 25^\circ\text{C}$) (49, 68, 69, 73, 74), however, the latter transforms into the more soluble α – TCP at temperatures above 1125°C (69, 73, 74). Tetracalcium orthophosphate (TTCP) solubility in water (~ 0.0007 g/L at $\sim 25^\circ\text{C}$) is similar to that of β –

TCP (49, 68, 69, 73, 74). However, the former is instable in aqueous solutions, and it hydrolyses to hydroxyapatite and calcium hydroxide (146, 201, 202).

On the other hand, hydroxyapatite (HAp) and Fluorapatite (FAp) are the most stable calcium orthophosphates (~ 0.0003 and 0.0002 g/L in H_2O at $\sim 25^\circ C$, respectively) (49, 68, 69, 73, 74). However, the monoclinic (space group $P2_1/b$) crystal structure of HAp (146, 221, 225, 226) transforms into hexagonal (space group $P6_3/m$) structure (221) at temperatures above $250^\circ C$ (146, 201, 202) or ambient temperatures through partial substitutions (e.g. OH^- by F^-) (69, 73, 74, 221), whereas the hexagonal crystal structure of FAp decomposes at $\sim 1650^\circ C$ (268-276). Calcium deficient hydroxyapatite (CDHAp) is more soluble in water (~ 0.0094 g/L in H_2O at $\sim 25^\circ C$) (49, 68, 69, 73, 74) than other calcium orthophosphates, including FAp, HAp, OCP, TCP, and TTCP, and its thermal decomposition depends on its Ca:P ratio. CDHAp with Ca:P ratios of 1.5 and $1.5 < Ca : P < 1.67$ transforms into β – TCP (146, 155, 156, 190, 201, 202 264-266) and biphasic calcium phosphate (β – TCP and HAp), respectively, at elevated temperatures above $700^\circ C$ (190, 264-266).

In addition, amorphous calcium orthophosphates (ACP) have lower surface energy than other calcium orthophosphates, such as OCP and HAp (208-210), with solubility in water of 0.0025, 0.0029, and 0.0032 g/L at $\sim 25^\circ C$ and pH values of pH 7.40, 6.00, and 5.28, respectively (49, 68, 69, 73, 74). However, at elevated temperatures, they transform into better crystalline and more soluble calcium – deficient HAp (~ 0.0094 g/L in H_2O at $\sim 25^\circ C$) (146, 155, 201, 202).

It is evident that the Ca:P ratio and chemical composition of calcium orthophosphates are related to their basicity/acidity, solubility, and thermal decomposition behaviour. The lower the Ca:P ratio, the more acidic and water – soluble the calcium orthophosphate (MCPM > DCP > TCP > HAp > FAp) (69, 155, 156, 201, 202). Similarly, the lower the Ca:P ratio, the lower the thermal decomposition temperature. MCPM and DCPD with Ca:P ratios of 0.5 and 1, respectively, decompose at relatively low temperatures around 100°C, whereas DCPA with a Ca:P ratio of 1.0 decomposes at ~ 400°C. On the other hand, TCP, HAp, and FAp with Ca:P ratios of 1.5, 1.67, and 1.67, respectively, decompose at higher temperatures of 1670°C, 900°C, and 1650°C, respectively. Properties, including thermal decomposition, solubility, and physical constants, and crystallographic data for calcium orthophosphates are presented in Table 2.9 and 2.10, respectively.

Moreover, Ca:P ratios can significantly influence the mechanical properties of calcium orthophosphates (496-499) as well as their biodegradability (497, 498, 500). For example, sintering of calcium – deficient HAp (Ca:P ratios of > 1.67) and calcium rich HAp (Ca:P ratio of < 1.67) results in the formation of CaO and TCP, respectively (496, 497), which decreases their mechanical strength (496-498) and increases their biodegradation rate, respectively (68, 497, 498, 500). However, depending on sintering temperature and parameters, the formation of these phases, particularly TCP, can be avoided (496, 499).

The mechanical properties of calcium orthophosphates are also influenced by the presence and absence of porosities (231). Porosities can be in the form of pores and voids of different shapes and sizes (231). Porosity is not a

measure of the size of pores or their distribution, but it is a physical property that determines the quality and utility of materials. Porous calcium orthophosphates are used as scaffolds for tissue engineering applications (49, 69, 73). They can provide a firmer fixation to hard tissues by a mechanical interlock mechanism, allowing tissues to grow into their pores, such as bone tissues growing into porous scaffolds, which increases the strength of an implant (68, 69). However, the fixation strength depends on the total porosity and pore size. Increasing porosity and pore interconnectivity increases bone ingrowth and fixation strength (378). On the other hand, the larger the pores, the weaker the fixation, and the smaller the pores, the stronger the fixation (501).

Porous HAp is preferred to dense HAp for the fixation of implants and bone grafts to biological tissues (68, 69, 230). It exhibits greater energy absorption and indentation creep ability (231). However, large pores of $\sim 100 \mu\text{m}$ can significantly decrease the mechanical strength of HAp (68), and subsequently, the strength of an implant. Therefore, porous calcium phosphates are used for low – load – bearing applications (68, 69). The mechanical strengths of porous HAp significantly decrease with increasing their porosity and vice versa (502, 503), and therefore, the strength of HAp can be controlled by controlling the geometry of pores (68). This can be achieved by varying the sintering temperature of HAp (231). Increasing the sintering temperature increases bulk density and decreases porosity (231). Small pore size (*e.g.* $< 10 \mu\text{m}$) can be produced by increasing the sintering temperature, however, dimensions of pores depend on material's composition, thermal cycle, and sintering time (68).

Some mechanical properties of dense and porous HAp, compared to those of dentine and enamel are presented in Table 2.12. Typical values of mechanical strengths for synthetic dense HAp include bending strength of 38 – 250 MPa, compressive strength of 120 – 900 MPa, and tensile strength of 38 – 300 MPa, which are much greater than those of synthetic porous HAp; bending strength of 2 – 11 MPa, compressive strength of 2 – 100 MPa, and tensile strength of 3 MPa. Fracture toughness of dense HAp is 0.8 – 1.2 MPa, while values of Young’s modulus include those in tension of 35 – 120 GPa and those in bending of 44 – 88 GPa.

Table 2.12 Mechanical properties of biological and synthetic calcium phosphates (504)

Mechanical property	Dentine	Enamel	Hydroxyapatite	
			Dense	Porous
Compressive Strength (MPa)	250 – 350	95 – 370	120 – 900	2 – 100
Young's modulus in compression (GPa)	11 – 17	9 – 84	-	-
Tensile strength (MPa)	21 – 53	10	38 – 300	3
Young's modulus in tension (GPa)	11 – 19	-	35 – 120	-
Flexural strength (MPa)	245 – 268	76	-	-
Young's modulus in bending (GPa)	12	131	44 – 88	-
Fracture toughness (MPa)	-	-	0.8 – 1.2	-
Bending strength (MPa)	-	-	38 – 250	2 – 11
Vickers hardness (GPa)	-	-	3.0 – 7.0	-

2.8.2 Properties of doping compounds

Properties and physical constants of doping compounds (Er_2O_3 , $\text{Er}(\text{NO}_3)_3 \cdot 4\text{H}_2\text{O}$, AlPO_4 , $\text{Al}(\text{NO}_3)_3 \cdot 9\text{H}_2\text{O}$, CaF_2 , and NH_4F), including physical form, density, melting point, and solubility under standard conditions (pressure of 1 atm at RT $\sim 25^\circ\text{C}$) are presented in Tables 2.13 and 2.14. The tables show simple descriptive formula, molecular weight (relative molar mass), descriptive physical forms (e.g. structure and colour), melting point /decomposition ($^\circ\text{C}$), density (g/cm^3), aqueous solubility (grams per 100g of solvent at room temperature) in water, and qualitative solubility in other solvents such as ethanol. These set of values of basic constants are recommended by the committee on data for science and technology (CODATA) (419, 505). Er_2O_3 is a red powder with a cubic structure, while AlPO_4 and CaF_2 are white powders with rhombohedral and cubic structures, respectively. These compounds (Er_2O_3 , AlPO_4 , and CaF_2) have a high melting point around 2344°C , $> 1460^\circ\text{C}$, and 1418°C , respectively (268, 505). $\text{Er}(\text{NO}_3)_3 \cdot 4\text{H}_2\text{O}$ is red crystals, while $\text{Al}(\text{NO}_3)_3 \cdot 9\text{H}_2\text{O}$ and NH_4F are white hygroscopic crystals with monoclinic and hexane structures, respectively. $\text{Er}(\text{NO}_3)_3 \cdot 4\text{H}_2\text{O}$ and $\text{Al}(\text{NO}_3)_3 \cdot 9\text{H}_2\text{O}$ decompose at relatively low temperatures of $\sim 130^\circ\text{C}$ and $\sim 135^\circ\text{C}$, respectively, while NH_4F has a melting point around 238°C (268, 505).

All ammonium salts and nitrates are soluble in water, except for oxides, according to the general rules of solubility, even though some compounds are more soluble under different conditions such as pH and temperature. It is well known that Er_2O_3 , AlPO_4 , and CaF_2 are insoluble (268, 419, 505), or they show negligible solubility in water, and therefore, they would form a composite with calcium orthophosphates/apatites. Therefore, the diffusion of

Er^{3+} , Al^{3+} , and F^- ions into the structure of calcium orthophosphate is unlikely to be achieved at ambient temperatures, but it is likely to be achieved at elevated temperatures (408, 495, 506) such those under solid – state (42) and hydrothermal conditions (399, 400, 411). On the other hand, $\text{Er}(\text{NO}_3)_3 \cdot 4\text{H}_2\text{O}$, $\text{Al}(\text{NO}_3)_3 \cdot 9\text{H}_2\text{O}$, and NH_4F show significant solubility in water (268, 419, 505). Therefore, the incorporation of Er^{3+} , Al^{3+} , and F^- ions is likely to be achieved at low temperatures by the wet methods (chemical precipitation and hydrothermal), which would result in the substitution of Ca^{2+} by trivalent ions Er^{3+} and Al^{3+} , as well as the substitution of OH^- by F^- ions.

Table 2.13 Physical constants of erbium oxide, aluminium phosphate, and calcium fluoride under standard conditions (pressure of 1 atm at RT ~ 25°C) (268, 505)

Compound	Formula	Mol. W	Physical form	Melting point (°C)	Density (g/cm ³)	Solubility in H ₂ O (g/100g)	Other solubility
Erbium oxide	Er_2O_3	382.5	Pink cubic powder	2344	8.64	Insoluble	Soluble in acid
Aluminium phosphate	AlPO_4	121.9	White rhombohedral plates	>1460	2.56	Insoluble	Slightly soluble in acid
Calcium fluoride	CaF_2	78.07	White cubic crystals or powder	1418	3.18	0.0016	Slightly soluble in acid

Table 2.14 Physical constants of erbium nitrate pentahydrate, aluminium nitrate nonahydrate and ammonium fluoride under standard conditions (pressure of 1 atm at RT ~ 25°C) (268, 505)

Compound	Formula	Mol. W	Physical form	Melting point (°C)	Density (g/cm ³)	Solubility in H ₂ O (g/100g)	qualitative solubility
Erbium nitrate pentahydrate	$\text{Er}(\text{NO}_3)_3 \cdot 5\text{H}_2\text{O}$	443.3	Red crystals	Decompose ~ 130	-	240.8	Soluble in ethanol and acetone
Aluminium nitrate nonahydrate	$\text{Al}(\text{NO}_3)_3 \cdot 9\text{H}_2\text{O}$	375.1	white monoclinic hygroscopic crystals	Decompose ~ 135	1.72	68.9	Very soluble in ethanol and insoluble in pyridine
Ammonium fluoride	NH_4F	37.03	white hexane hygroscopic crystals	238	1.015	83.5	Slightly soluble in ethanol

Various issues related to the occlusion of dentinal tubules/tooth surfaces for the treatment of tooth/dentine hypersensitivity, particularly using calcium orthophosphate/apatite materials and/or laser irradiation are reported. Several methodologies are reported for the treatment of dentine hypersensitivity, including the use of chemical agents such as strontium chloride, sodium fluoride (29), ferric oxalate (30), and calcium hydroxide (2, 31), physical agents such as fluoride – releasing resin (32) (e.g. fluoride containing prophylaxy paste (33)) and bioglasses (34, 35), and desensitisation of the nerve using potassium nitrate (2, 34). However, recurrence of sensitivity is common, as the current treatments are not ideal, and they are effective in the short term only (27, 28).

The most recent approach for the treatment of dentine hypersensitivity involves the occlusion of dentinal tubules with hydroxyapatite, such as toothpastes – containing hydroxyapatite (37-39), which demonstrate a significant increase in oral fluoride and calcium, and thus, provide anticaries and anti – erosion benefits (37). However, acid dissolution is still an issue and disadvantage of calcium orthophosphate/hydroxyapatite (4, 5), even though it is improved by the incorporation of fluoride to form fluorapatite. The latter, however, is still soluble in highly erosive environments below pH 4.5, which is the approximate critical pH for fluorapatite (507).

The other option for the treatment of dentine hypersensitivity is the application of laser irradiation to seal dentinal tubules (2, 51-56). Biologically, laser irradiation interacts mainly with apatite mineral, water, and proteins (63, 84, 86). However, long wavelengths between 2,000 and 10,600 nm interact more with hydroxyapatite mineral and water (63). In addition, pulsed

laser irradiation is absorbed more than CW (63, 92), with the largest absorption peak for water is at the Er:YAG wavelength just below 3,000 nm (63, 89). The occlusion mechanism of laser irradiation can be achieved by biostimulation/depolarisation using low – level lasers, which prevent the diffusion of pain to the central nerve system (51, 52, 62, 128), or by melting using high – level lasers, which recrystallise the dentine inorganic component (54, 58, 128, 130), form a secondary/tertiary dentine (55, 131, 132), and coagulate the dentinal fluid (128, 133). Surface temperatures of 400°C and above decompose the enamel mineral and transform it to a much less soluble apatite (112,113), while temperatures of 800°C up to 1200°C melt the enamel mineral and transform it when cooled (114,115). On the other hand, exceeding the required energy amount results in energy absorption by surrounding tissues, which causes undesirable outcomes such as thermal stresses or pulpal damage (86). Similarly, laser irradiation interacts with synthetic calcium orthophosphates/apatites, including their water and impurity contents, and alters their structure and surface, and subsequently, their properties (508-516). Alterations include decomposition, phase transformation, and surface melting and cracking, as well as alterations in surface area, grain size, and solubility.

High – energy laser irradiation (CO₂ laser at energy densities ranging from 21 to 500 J/cm²) causes crystalline transformations in apatites, which may lead to the formation of tricalcium phosphates (513). The transformation of HAp into TCP is reported at an energy density of > 4.0 J/mm² (509). Under CW CO₂ laser ($\lambda = 10.6 \mu\text{m}$ with a beam diameter of 300 μm) at temperatures 1200 – 1500°C (with an onset of 1350°C for the transformation of HAp to TCP), the transformation of HAp into TCP is accompanied by the

release of water (508). In addition, the phase transformation of HA to FA occurs in the presence of NaF under CO₂ laser, with a threshold energy density of 38 J/cm² (513). CO₂ Laser irradiation (20 – 50 W with a beam diameter of 14 mm for a total of 10 – 400 s) of HAP reduces its specific surface area (511). Selective laser sintering (a spot diameter of 1 mm and energy density of 2 – 5 J/mm²) of nano – hydroxyapatite powder increases its average grain size from ~ 0.211 µm to ~ 0.979 µm with increasing laser energy density from 2.0 to 5.0 J/mm², respectively (509).

ER, CR:YSGG laser irradiation with an energy density of 5.79 – 13.84 J/cm² also causes changes in the crystalline structure of HAP (514, 516). Above 600°C, the Ca:P ratio of HAp decreases to levels close to the theoretical ones, and the amount of carbonate decreases significantly without any phase transformation (514). The decrease in carbonate is also accompanied by a decrease in water and hydroxyl contents (516). The dominant phase in the centre of the laser crater is also reported to be a dehydrated apatite (515).

Such alterations by laser irradiation affect the solubility of HAp (511, 513, 516), which is also reported for dental enamel after laser irradiation (513). CO₂ laser irradiation (20 – 50 W with a beam diameter of 14 mm for a total of 10 – 400 s) of HAP reduces the dissolution rate in an acetate buffer (511). Like dental enamel, synthetic hydroxyapatite is affected/altered more with pulsed laser irradiation than CW laser irradiation. The latter has a much weaker effect on the atomic structure of synthetic HAp (515). Laser sintering of HAp results in a distortion more than shrinkage, particularly under direct laser sintering, which involves high temperatures (508). Er:YAG laser

irradiation (with an intensity of 100 mJ/pulse, 10 Hz) of HA – coated implants for 1 minute has no clear effects (510, 512). However, surface alterations, such as surface melting/flattening and cracks/micro – fractures are observed after laser irradiation for ≥ 1.5 minutes (510, 512). Surface alterations increase with increasing pulse energy and irradiation time (510). With intensities of 140 mJ/pulse and 180 mJ/pulse, surface melting and cracking are greatly increase with increasing irradiation time (512).

Melting, fusion, and transformation of inorganic compounds by laser irradiation are also dependent on the colour of surface being irradiated (517). For example, opaque porcelain, hydroxyapatite, and alumina are difficult to melt, particularly with 8000 Nd:YAG apparatus (0 – 60 W energy, 2.0 – 9.9 s exposure time, and 300 mm distance). This is due to the reflection of laser irradiation by white pigments (responsible for the whitish colour of opaque porcelain), which may affect the melting and fusing process. However, the addition of metal oxides, such as iron oxide, is effective in melting and fusing such dental porcelain (517).

The fusion of various calcium phosphates and doped calcium phosphates to dental enamel occurs under CO₂ and Nd:YAG laser irradiation (518-524). This include the fusing of hydroxyapatite – containing fluoride to dental enamel using CO₂ laser irradiation (519), and the fusing of α – tricalcium phosphate to dental enamel using Nd:YAG laser irradiation (520). In addition, other materials that fuse to enamel under laser irradiation include Bioglass (521, 522), calcium phosphate – glass, and low – melting porcelain (523).

Dental sealant materials preferably undergo melting and fusing under dental laser irradiation. A sealant material needs to melt at a low energy density to avoid damaging tooth surface, and it needs to have a Ca:P ratio lower than that of enamel or hydroxyapatite due to a possible rapid evaporation of phosphorus by laser irradiation (518). Such sealants, including MCPM and DCPD, melt at 971°C and 1348°C, respectively. Upon heating, MCPM transforms into γ – metacalcium phosphate, β – metacalcium phosphate, and δ – metacalcium phosphate, whereas DCPD transforms into DCPA, γ – calcium pyrophosphate, β – calcium pyrophosphate, and α – calcium pyrophosphate (518). Fusing of MCPM and DCPD under CO₂ laser irradiation with energy densities of 45.6 J/cm² (1.0 W for 0.1 s) and 365 J/cm² (8.0 W for 0.1 s), respectively, is characterised by a crater on the surface of MCPM and none on the surface of DCPD. The latter indicates that damage to enamel surface can be avoided with DCPD (518). In addition, solubility of laser – irradiated MCPM and DCPD in a 200 mM acetic acid buffer is found to be higher in MCPM than DCPD. Moreover, the fusion of a sealant, consisting of hydroxyapatite, to enamel without damaging enamel tissue requires an eutectic fluoride compound, such as CaF₂, to lower the sintering temperature of HA (524), which is about 1400 – 1500°C (525).

To collectively tackle and improve the mentioned issues related to calcium orthophosphate/apatite materials, particularly for the occlusion of dentinal tubules/tooth surfaces under laser irradiation, a novel approach is needed to improve the properties of these materials, particularly their photosensitivity and acid resistance. This is proposed by the addition of erbium, aluminium, and fluoride compounds to calcium orthophosphate/apatite. Based on the properties of erbium, aluminium, and fluoride compounds, their addition to

calcium orthophosphate/apatite offers great potential for the treatment of tooth sensitivity, particularly their fusion to tooth surface under laser irradiation, chemical stability, and solubility resistance in acid environments.

The proposed methodology offers a simple laboratory preparation of doped calcium orthophosphate/apatite powders, by 24 – hour reactions through the chemical precipitation and hydrothermal methods, without purification of reagents and calcination/heat treatment of powders. Sintering of calcium orthophosphate powders is designed to take place under CW and pulsed laser irradiation, after being coated onto dentine surfaces. The methodology is based on the incorporation of erbium (Er^{3+}) into the structure of apatite via a soluble compound such as $\text{Er}(\text{NO}_3)_3 \cdot 5\text{H}_2\text{O}$, or the formation of a composite with calcium orthophosphate/apatite by the addition of erbium oxide (Er_2O_3). Erbium (Er^{3+}) would act as an active medium (as in solid – state lasers) and facilitate the sintering of calcium orthophosphate/apatite layer onto dentine surface. The methodology also involves the incorporation of aluminium (Al^{3+}) and fluoride (F^-) into the structure of apatite via soluble compounds such as $\text{Al}(\text{NO}_3)_3 \cdot 9\text{H}_2\text{O}$ and NH_4F , or the formation of a composite with calcium orthophosphate/apatite by the addition of aluminium phosphate (AlPO_4) and calcium fluoride (CaF_2). Aluminium (Al^{3+}) and fluoride (F^-) would facilitate the incorporation of erbium (Er^{3+}) (for charge balance) and improve the acid resistance of calcium orthophosphate/apatite against non – bacterial acids (e.g. acidic drinks, which casus dental erosion) and bacterial acids (e.g. reaction of sugar with oral bacteria, which cause dental caries). In addition, the pink colour of erbium would be an advantage in facilitating the sintering of calcium orthophosphate/apatite, as well as matching the colour of gingiva (gum). The latter is important, particularly for the treatment of tooth

sensitivity due to a gum recession, where a restorative material is to be placed. In practice, the procedure would involve the application of doped calcium orthophosphate/apatite powder in the form of a paste or gel onto the hypersensitive tooth surface, and followed by the application of laser irradiation to cure and fuse the apatite layer onto tooth surface and promote its bonding.

Chapter 3

Experimental Techniques

In order to produce calcium orthophosphate/apatite powders with specific characteristics, as highlighted in the literature, synthesis parameters are required to be effectively adopted and investigated in the presence of the doping compounds. Therefore, to investigate and evaluate the effect of the doping compounds and different synthesis conditions on the properties of final calcium phosphate/apatite, various experimental techniques were used, which are covered in this chapter.

The present research study involved various experimental techniques, including powder synthesis, sample/tissue preparation, and characterisation, in order to meet its objectives. Most of these experimental techniques are well – known and common techniques in the field of materials engineering. These include the synthesis of calcium orthophosphates, undoped (CaP) and doped with erbium, aluminium, and fluoride compounds, under various conditions, including temperature, pH, and reaction time, in vitro preparation of dentine sections and their coating with CaP/doped CaP powders, laser irradiation of coated dentine sections, and characterisation of powders and dentine sections, using SEM, laser scattering, SEM-EDX, XRD, FTIR, and DSC. Other characterisation techniques include temperature change during laser irradiation, micro – hardness, ICP/MS, and Profilometry. A detailed summary of powder synthesis, sample/tissue preparation, and characterisation techniques used in this research study are described next.

3.1 Calcium phosphate powder synthesis

Powders that were synthesised include CaP minerals, as control samples, and CaP doped with erbium compounds (Er_2O_3 and $\text{Er}(\text{NO}_3)_3 \cdot 5\text{H}_2\text{O}$) (Fisher Scientific), aluminium compounds (AlPO_4 and $\text{Al}(\text{NO}_3)_3 \cdot 9\text{H}_2\text{O}$) (Fisher Scientific), and fluoride compounds (CaF_2 and NH_4F) (Fisher Scientific). These powders were synthesised by the chemical precipitation and hydrothermal methods. The chemical precipitation method was adopted to investigate the effects of chemical reaction of CaP and doped CaP solutions at room temperatures, and to produce CaP/doped CaP powders for the post – heat treatment by laser irradiation. The hydrothermal method was adopted to investigate the effects of hydrothermal reaction of CaP and doped CaP solutions at elevated temperatures, and because it has the ability to produce crystalline nano – CaP powders without the need for a post – heat treatment (77).

Synthesis of CaP powders, as control samples, was performed at room temperature, by preparing solutions (320 ml in volume) with 0.1 molar concentrations of calcium nitrate tetrahydrate ($\text{Ca}(\text{NO}_3)_2 \cdot 4\text{H}_2\text{O}$) (Fisher Scientific) and diammonium hydrogen phosphate ($(\text{NH}_4)_2\text{HPO}_4$) (Fisher Scientific) in distilled water. The two solutions were mixed under stirring, by the addition of a diammonium hydrogen phosphate solution drop by drop into a calcium nitrate tetrahydrate solution, to yield a suspension with a Ca:P molar ratio of 1.67, which is similar to that of HAp. Calcium phosphate powders were synthesised under different conditions, as shown in Table 3.1, in order to investigate their effects on CaP properties such as composition, crystal structure, particle size, and particle morphology.

Table 3.1 Synthesis conditions for calcium phosphates

Condition	Description
Synthesis method	Chemical precipitation and hydrothermal
pH	5.4 ± 0.2 and 10 ± 0.2
Temperature	RT ~ 25°C and hydrothermal 200°C
Solution dropping time	15 and 30 minutes
Solution stirring time	30 and 60 minutes

3.1.1 Chemical precipitation of calcium phosphates

The chemical precipitation synthesis was carried out at room temperatures. It involved the preparation of 150 ml of 0.1 M solution of calcium nitrate tetrahydrate ($\text{Ca}(\text{NO}_3)_2 \cdot 4\text{H}_2\text{O}$) (Fisher Scientific) and 90 ml of 0.1 M solution of diammonium hydrogen phosphate ($(\text{NH}_4)_2\text{HPO}_4$) (Fisher Scientific), which were mixed to yield a Ca:P molar ratio of 10:6. The solutions were mixed by the drop – wise technique for 15 – 30 minutes and stirred magnetically at ~ 400 rpm for 30 – 60 minutes to produce a milky mixture. The pH of as – prepared mixtures was recorded (pH 5.4 ± 0.2) as well as adjusted to pH 10 ± 0.2 using ammonium hydroxide (NH_4OH) (Fisher Scientific). The mixtures was left on standby in a fume cupboard at room temperature for 24 hours, for the precipitation to take place. The suspensions were then transferred to centrifugal tubes to be washed and decanted. This involved centrifugal sedimentation at 6000 rpm for 5 minutes and ultrasonic bathing for 5 minutes. Both cycles were repeated 6 times whilst monitoring the pH value of suspensions, until they reached pH 6.5 – 7. The final cycle was carried out using methanol to limit the agglomeration of CaP particles. The wet CaP sediment was collected and dried in an oven at 80°C for about 24 hours.

3.1.2 Hydrothermal synthesis of calcium phosphates

The hydrothermal synthesis involved the same initial preparations used in the chemical precipitation synthesis. After preparing a milky mixture, only 80 ml of the mixture was transferred to a Teflon – lined reactor with a capacity of 125 ml. The reactor was placed in a furnace over periods of 24 to 72 hours, at temperatures 80°C – 200°C, and at a heating rate of 5°C/minute. The reactor was then naturally cooled at room temperature. The suspension was treated the same way as in the chemical precipitation synthesis. Suspensions were transferred to centrifugal tubes to be washed and decanted. This involved centrifugal sedimentation at 6000 rpm for 5 minutes and ultrasonic bathing for 5 minutes. Both cycles were repeated 6 times whilst monitoring the pH value of suspension, until it reached pH 6.5 – 7. The final cycle was carried out using methanol to limit the agglomeration of CaP particles. The wet CaP sediment was collected and dried in an oven at 80°C for at about 24 hours.

3.1.3 Doping of calcium phosphates

Calcium phosphates were doped with different compounds under various conditions to investigate the formation of ion – substituted calcium phosphates and CaP composites. Chemical compounds that were investigated in the present study are presented in Table 3.2.

Table 3.2 List of various compounds investigated in the present study

Erbium compounds	Aluminium compounds	Fluoride compounds
Erbium oxide Er_2O_3 and erbium nitrate $\text{Er}(\text{NO}_3)_3 \cdot 5\text{H}_2\text{O}$	Aluminium phosphate AlPO_4 and aluminium nitrate $\text{Al}(\text{NO}_3)_3 \cdot 9\text{H}_2\text{O}$	Calcium fluoride CaF_2 and ammonium fluoride NH_4F

The first batch of powders (batch A) was prepared with erbium oxide (Er_2O_3) (Fisher Scientific), aluminium phosphate (AlPO_4) (Fisher Scientific), and calcium fluoride (CaF_2) (Fisher Scientific) to produce CaP composites due to the poor solubility of these compounds. The second batch (batch B) was prepared with erbium nitrate pentahydrate ($\text{Er}(\text{NO}_3)_3 \cdot 5\text{H}_2\text{O}$) (Fisher Scientific), aluminium nitrate nonahydrate ($\text{Al}(\text{NO}_3)_3 \cdot 9\text{H}_2\text{O}$) (Fisher Scientific), and ammonium fluoride (NH_4F) (Fisher Scientific) to produce doped CaP due to their excellent solubility and their ability to produce nanoscale and high – purity materials. A solubility chart for CaP synthesis under a pressure of 1 atm at room temperature is shown in Table 3.3.

Table 3.3 Solubility chart for CaP synthesis at room temperature under pressure of 1 atm

	CO_3^{2-}	F^-	OH^-	NO_3^-	O^{2-}	PO_4^{3-}
Ca^{2+}	I	S	sS	S	sS	I
Al^{3+}	-	S	I	S	I	I
Er^{3+}	-	S	I	S	I	I
NH_4^+	S	S	S	S	-	S

I = insoluble, sS = slightly soluble, S = soluble

Soluble ions result in an aqueous product, while slightly soluble and insoluble ions result in a solid product (precipitate). From the solubility chart (Table 3.3), it can be seen that eight possible products are expected. Calcium (Ca^{2+}) ions seem to precipitate as CaP and/or CaCO_3 , while Al^{3+} and Er^{3+} ions are expected to form hydroxide, oxide, and/or phosphate compounds. Therefore, batch (A) dopants, Er_2O_3 and AlPO_4 , are expected to precipitate together with CaP phase. On the other hand, batch (B) dopants, $\text{Er}(\text{NO}_3)_3 \cdot 5\text{H}_2\text{O}$ and $\text{Al}(\text{NO}_3)_3 \cdot 9\text{H}_2\text{O}$ are expected to produce a single – doped CaP phase.

Dopants of the first batch (A) (Er_2O_3 , AlPO_4 , and CaF_2) (Fisher scientific) and dopants of the second batch (B) ($\text{Er}(\text{NO}_3)_3 \cdot 5\text{H}_2\text{O}$, $\text{Al}(\text{NO}_3)_3 \cdot 9\text{H}_2\text{O}$, and NH_4F) (Fisher scientific) in solutions (distilled H_2O) were added to CaP solution. A 7.5 ml of 0.1 M solution of each dopant (7.5 ml x 3, 22.5 ml of batch A dopants and 22.5 ml of batch B dopants) was added to 240 ml of 0.1 M CaP solution. The mixture containing erbium, aluminium, and fluoride compounds was stirred for 1 hour at ~ 400 rpm. The mixture was covered to minimise the absorption of atmospheric CO_2 and left on standby at room temperature for 24 hours. Finally, the wet precipitate was collected and dried in an oven at 80°C for 24 hours.

3.2 Calcium phosphate pellet preparation

Calcium phosphate powders were also prepared in the form of pellets. 20 mg of each powder was pressed into a pellet of about 2 mm in thickness, using uniaxial press under a pressure of about 1 tonne for 30 minutes. These pellets were prepared for the laser irradiation sintering trials and the investigation of CaP/doped CaP erosion in an acid environment.

3.3 Dentine section preparation

Preparation of dentine sections aimed at mimicking naturally exposed dentine surface in extreme cases of sensitivity. Tooth cross – sections were prepared from clinically extracted human premolars/molars, which were collected from the tissue bank at the University of Leeds, School of Dentistry (Ethical approval No 270409/EE/22), after being sterilised by gamma irradiation. Sections of about 1 – 2 mm in thickness were cut from a region

beneath the enamel dentine junction, using a diamond – cutting machine (Well Precision Vertical Diamond Wire Saw, Model 3242).

After sectioning, tooth sections were polished by hand using 2500 grit silicon carbide (SiC) paper in the presence of water for 2 minutes per side, followed by a wash with distilled water for 20 seconds and an ultrasonic bath in distilled water for 1 minute. The sections were then etched with a 35% w/v phosphoric acid solution for 1 minute in a stirred bath to remove the natural smear layer and smear plugs, followed by a wash with distilled water in an ultrasonic bath for 1 minute. The sections were finally dehydrated using alcohol/water mixtures containing 50%, 70%, 90%, and 100% absolute ethanol for 30 minutes in each mixture, to minimise any tissue shrinkage by absolute alcohol. The sections were then left to dry in air, followed by reduced pressure in a vacuum desiccator containing calcium sulphate, as a desiccant, for 24 hours. “The resultant sections should mimic the surface of naturally exposed dentine common to extreme cases of dentine hypersensitivity, albeit with no fluid present within the tubules, as would be the case in vivo” (12).

3.4 Dentine section coating and dentinal tubule occlusion

Coating of dentine cross – sections with CaP and doped CaP powders involved the preparation of 5% w/v suspensions, by suspending CaP powders in methanol, as a liquid dispersion medium. These suspensions were then treated ultrasonically for ~ 10 minutes before being applied onto dentine sections. Dentine sections were coated by the dip coating technique manually and using a dipping machine. Manual dipping was carried out in the initial coating trials, under which the withdrawal of sections was kept at a

constant speed of ~ 1 cm per second. The sections were immersed in a beaker containing 20 ml CaP – methanol suspension (equal to ~ 3 cm in height). The withdrawal time of sections from the bottom of beaker and out of suspension was maintained at ~ 3 seconds. All other coating trials were then carried out using a mechanical manipulator, which allowed better control of the process of dipping and withdrawal. The withdrawal speed was set to 1 cm per second. The process was repeated for a maximum of 5 minutes. Moreover, the same suspension was applied drop – wise onto the dentine sections using a syringe (1 – 2 drops), in order to provide thicker and uniform coatings for laser irradiation trials. This was due to difficulties associated with the manual dipping. Finally, after the application of coatings, the coated dentine sections were left on standby to dry in air and then stored in a reduced pressure desiccator containing calcium sulphate.

3.5 Laser irradiation sintering

Laser irradiation experiments were carried out at the Institute for Materials Research, University of Leeds as well as the Department of Physics and Astronomy, University of St. Andrews. Initial laser irradiation trials were performed on CaP and doped CaP – coated dentine sections, using a CW laser at ~ 980 nm wavelength (output power of ~ 150 mW). Post – initial laser trials involved laser irradiation of CaP and doped CaP – coated dentine sections, using ~ 1520 nm CW (output power of ~ 150 mW) and ~ 1520 nm femto – second (fs) – pulsed lasers (beam power of ~ 130 mW, pulse duration of 100 fs, and repetition rate of 2.5 GHz). Although pulsed lasers have a higher energy, and they are expected to provide higher absorption and better distribution of energy than CW lasers, the latter were also

investigated despite their thermal accumulation, which was initially assumed to cause damage to calcium phosphate coatings and dentine tissue.

Laser irradiation trials were carried out using CW and pulsed lasers at two wavelength bands around 980 nm and 1500 nm. In these regions, erbium has strong absorption bands due to its electronic structure. The two wavelength bands at 980 nm and 1520 nm overlap with the corresponding ground state absorptions ($4 I_{15/2} \rightarrow 4 I_{11/2}$ and $4 I_{15/2} \rightarrow 4 I_{13/2}$) of Er^{3+} ions (526,527), which was chosen as the photoactive component in the doped calcium orthophosphate. The chosen laser sources were a 980 nm CW laser, a 1520 nm CW laser, and a 1520 nm pulsed laser (120 fs). The femto – second – pulsed source was with an output power of 130 mW and a repetition rate of 2.5 GHz, implying that the 2.5 billion pulses per second were incident at the focal spot. The output powers of the 980 nm and 1520 nm CW lasers were at 150 mW. Since the ground state absorption at 1520 nm wavelength (from overall ground state $4 I_{15/2} \rightarrow 4 I_{13/2}$ optical transition) is much smaller than at $4 I_{15/2} \rightarrow 4 I_{11/2}$ (527), the erbium – doped CaP absorbs much smaller fraction of CW laser energy at 1520 nm wavelength than that at 980 nm wavelength. This is because of a resonant condition at $4 I_{15/2} \rightarrow 4 I_{11/2}$.

Since the melting – induced – surface modification using 980 nm CW laser requires at least 5 minutes over $100 - 250 \mu\text{m}^2$ area, it was decided that for clinical application such an approach might prove too slow for ultimate treatment. Therefore, it was necessary also to compare the response of these minerals when irradiated with an ultra – fast laser (120 fs, 130 mW). Since a femto – second laser at 980 nm wavelength was unavailable; we

investigated the structural changes using a femto – second laser at 1520 nm wavelength only.

Laser irradiation sintering trials were also performed on CaP pellets for the investigation of laser – CaP interaction. The pellets were laser irradiated with CW lasers at 980 nm and 1500 nm wavelengths (output power of ~ 150 mW) and pulsed laser at 1520 nm wavelength. In addition, since erbium ions can also be excited at various optical frequencies, including 800 nm, CaP pellets were laser irradiated with 800 nm femto – second – pulsed laser (beam power of ~ 130 mW, pulse duration of 100 fs, and repetition rate of 250 – 1 KHz) for the investigation of CaP minerals in an acid environment. The laser parameters that were used in the laser irradiation trials are presented in Table 3.4. In addition, temperature change measurements were carried out during laser irradiation of uncoated and coated dentine sections (1 – 2 mm), using a CW laser at 980 nm wavelength. A chromel – alumel thermocouple was attached onto the back – side of dentine sections and pellets to record the increase or decrease in temperature.

Table 3.4 Pulsed and CW laser parameters used in the laser irradiation sintering of coated dentine sections and CaP/doped CaP pellets

Sample	Laser type	Wavelength	Exposure time	CaP powder
Pellets	CW laser	~ 980 nm	5 minutes	CaP–undoped and CaP–doped (batch A)
	CW laser	~ 1500 nm	1 minute	
	Pulsed laser (KHz)	~ 800 nm	5 minutes	
Dentine sections	CW laser	~ 980 nm	5 minutes	CaP–undoped and CaP–doped (batch A)
	Pulsed laser (GHz)	~ 1520 nm	30 seconds, 2 and 5 minutes	
	Pulsed laser (GHz)	~ 1520 nm	1 and 2 minutes	CaP–undoped and CaP–doped (batch B)
	CW laser	~ 1520 nm	1 and 2 minutes	

3.6 Acid erosion of CaP pellets

Acid erosion trials were carried out on CaP powders in the form of pellets. Pellets of CaP powders were prepared as described before. The investigated powders comprised CaP and Er_2O_3 . AlPO_4 . CaF_2 – doped CaP. The pellets were unsintered, furnace sintered at around 1000°C for 5 minutes, and laser irradiated with 800 nm pulsed laser for 5 minutes.

The pellets were mounted on a glass substrate, and they were then immersed in a 0.3% citric acid ($\text{C}_6\text{H}_8\text{O}_7$) solution with $\text{pH } 3.60 \pm 0.02$ at room temperature ($T = 23.3 \pm 0.02$). The solutions were then covered to minimise the absorption of atmospheric CO_2 , and they were left on standby for 24 hours under static conditions.

A citric acid erosive solution was prepared by mixing 15g of citric acid ($\text{C}_6\text{H}_8\text{O}_7$) powder with 5 litres of distilled water, which resulted in a citric acid solution with 0.3% concentration. The pH of acid solution was adjusted to pH 3.60 by the addition of 15 – 25% potassium hydroxide (KOH) solution, in order to mimic the acidity of many drinks such as fruit juices.

The 24 hour – reaction was initially investigated by monitoring the pH of citric acid solution containing CaP/doped CaP pellets. Surface roughness of CaP/doped CaP pellets was measured using a surface roughness profilometry, whereas leached out elements/components of CaP and doped CaP pellets in the citric acid solutions were measured using inductively – coupled plasma/mass spectrometry (ICP/MS) and SEM-EDX.

3.7 Characterisation techniques

Characterisation of synthesised powders, suspensions, pellets, and coated dentine sections involved the use of thermo – analytic, electron, and photo absorption spectroscopic techniques. The spectroscopy type, model, and analysis parameters are presented in Table 3.5. Powder characterisation involves the analysis of several properties such as particle size, particle morphology, crystal structure, and composition. Particle size can be measured by various methods such as sedimentation and microscopy. For statistical distribution of particle size, optical or electron microscopy can be used. Measurements are carried out by sedimentation on laser diffraction/scattering of a dilute suspension containing the powder sample. Phase/s and composition of sample material can be determined by various techniques, including XRD and FTIR spectroscopy.

CaP/doped CaP powders were characterised by their composition, crystal structure, particle size, particle size distribution, and particle morphology. The particle morphology and elemental composition of CaP powders were determined by SEM and SEM-EDX, while the crystal structure was determined by XRD. Particle size analysis was carried out by means of static laser scattering, using the Malvern Mastersizer 2000E. The composition and photo absorption properties of CaP/doped CaP powders were determined by FTIR, while their thermal behaviour was investigated by DCS. Laser – irradiated CaP/doped CaP – coated dentine sections and CaP/doped CaP pellets were characterised using SEM, SEM-EDX, and XRD. The hardness of coated dentine sections was determined by the micro – hardness test, using an computer – aided indenter machine.

Coatings of CaP/doped CaP were also characterised in terms of temperature change during laser irradiation. Moreover, CaP/doped CaP pellets were undergone acid erosion trials to determine their behaviour in an acid environment. Characterisation of eroded CaP/doped CaP pellets and solutions containing leached out elements/components included monitoring pH variation, inductively – coupled plasma/mass spectrometry (ICP/MS), SEM-EDX, and surface profile roughness.

Table 3.5 List of analysis techniques and parameters used for characterisation

Analysis technique	Type and model	Analysis parameters
Static laser scattering	Mastersizer 2000 E, Malvern Instruments	Size range 0.02 μm to 2000 μm , beam length 2.35 mm, water as the dispersant medium with a refractive index of 1.33. The refractive index and absorption index for CaP were 1.629 and 0.1, respectively.
SEM	LEO 1530 Gemini FEGSEM plus EDX	An accelerating voltage of 3 – 20 kV, an aperture of 30 μm , and working distance of 3 – 8 mm
XRD	PANalytical X'Pert MPD, Philips	0.154 nm CuK α , 2 theta range 5° – 90°, step size of 0.05, time per step of 99.6 s, and scan speed of 0.06 °/s
FTIR	VETEX 70, Bruker	Absorption at ambient conditions, using near – and mid - IR source in the wavelength range 4000 – 400 cm^{-1} with a spectral resolution of 0.4 cm^{-1}
DSC	Perkin Elmer DSC 8000	10 mg of sample, from room temperature up to 600°C at a heating rate of 10°C/min
ICP/MS	Perkin Elmer, Elan DRCe	Total quantitative mode for the determination of a large number of elements at ppb levels. Amount (ppm) in 1:5 diluted 0.3% citric acid – component solutions
Profile roughness	LOT – ORIEL Alpha Step IQ Surface Profiler	Diamond stylus with radius of 20 nm – 25 μm , vertical range of 10 nm – 1 mm and force range of 1 – 50 mg
Micro – hardness	Computer – aided Duramin Indenter Machine, Struers A/S, DK 26-10	Knoop diamond with a 25g load for an indentation time of 30 seconds

A particle is defined as “any relatively small subdivision of matter, ranging in diameter from a few angstroms to a few millimetres” (528). Particles (e.g. solid particles, liquid droplets, or gas bubbles) are three – dimensional objects with various shapes. Particle shapes include acicular (needle – like), angular (sharp edged or polyhedral – like), crystalline (a freely developed particle in a fluid medium of geometrical shape), dendritic (branched crystalline shape), fibrous (regular or irregular thread – like), flaky (plate – like), granular (equidimensional irregular shape), irregular (lacking any symmetry), nodular (rounded and irregular shape), and spherical (globular shape) (529).

The size and shape of particles cannot be fully described with a single dimension or figure, such as a radius or diameter, except in the case of perfect spherical objects that involves employing the concept of equivalent spheres (530). In the case of spherical particles, particle size can be defined by the diameter of an equivalent sphere, having the same property as the actual particle such as volume or mass. This concept is suitable for many types of particles with regular shapes. However, it may not always be appropriate for irregular shaped particles, such as needles or plates, where one dimension is significantly different from their other dimensions (530). In the case of rod shaped particles, a volume equivalent sphere would give a particle diameter that is not a very accurate description of its true dimensions. Therefore, the particle size of rod – like particles can be defined as a cylinder with the same volume, which has a length and width. This approach describes the particle size more accurately and in a meaningful way (530).

Techniques for the characterisation of particle shape are classified into physical and aerodynamic/hydrodynamic techniques (12). Aerodynamic or hydrodynamic techniques measure the equivalent spherical diameter based on Stoke's Law, whereas physical techniques, such as electron microscopy, measure the particle diameter based on characteristics such as length and width. The number of measurements depends on complexity of shape. Most shape factors work on ratios (12). These include aspect ratio (length to width), elongation/flatness (length, width and thickness of the particle), roundness (perimeter of a spherical particle with the same area as the particle, to the actual particle perimeter), and sphericity (surface area of a spherical particle with the same volume as the particle, to the actual particle surface area) (12).

There is no single comprehensive standard definition for particle size, which applies to any particle (531). For example, a definition based on geometry cannot apply to regular and irregular shapes and measurement techniques used. In the case of the geometry of a sphere and visual inspection, microscopy or image analysis is the simplest measurement technique. A sphere with its projected cross – sectional area, surface area, and volume can be described by the diameter of projected cross-section. The projected cross – sectional diameter is constant at all angles of view (geometrically isotropic).

Other regular and irregular shapes do not project the same cross – section at all angles of view, and therefore, surface area and volume cannot be determined from the cross – section (531). Irregular shaped particles can present different cross – sections, depending on their orientation. They have

different diameters, depending on where the chord is drawn. In this case, statistical geometric diameters can be employed by averaging over a large number of measurements (531). These include Martin's diameter (the length of the chord divides the cross – sectional shape into two equal areas), Feret's diameter (the distance between two parallel lines tangent to the projected cross – section), and area diameter (expresses particle size as the diameter of a circle that has the same projected area as the particle) (531). Another approach is to determine the perimeter of the projected cross – section and assign it to the diameter of a circle having the same perimeter (531). In addition, determining the volume of an irregular – shaped particle can define its diameter as the diameter of a sphere having the same volume (531).

Particle size can be determined indirectly from direct measurements of some parameters associated with a physical phenomenon involving the particles (531). These parameters are related to the particle geometry by a law (e.g. Ohm's law; equation 3.1, and Stoke's law; equation 3.2) and a theory or model (e.g. Mie theory) describing the physical phenomenon. These include particle's sedimentation velocity in a fluid and the pattern of scattered light by the particle. Table 3.6 presents the characteristics of particles related to size, a particular measurable behaviour that varies as a function of particle size, other variables that affect particle size, and measurement techniques utilizing the behaviour of attribute.

$$J = \sigma \cdot E \dots (3.1),$$

where (J) is the current density, (σ) is the conductivity of material, and (E) is the electric field.

$$V_t = \frac{gd^2(\rho_p - P_m)}{18\mu} \dots\dots (3.2),$$

where (V_t) is the terminal velocity, (g) is gravity, (d) is the particle diameter, (ρ_p) is the particle density, (P_m) is the medium density, and (μ) is the medium viscosity.

The concept of equivalent spherical size is employed in almost all particle size analysis, because the theory describing the behaviour of a particle or describing the interaction with a particle is solved for spherical particles only (531). In this case, particles behave as a spherical particle or have the same behaviour – controlling properties. For examples, particles pass through the same size aperture, settle at the same velocity, scatter light with the same intensity at the same angles, or displace the same volume of a liquid.

Table 3.6 Particle characteristics related to size, a particular measurable behaviour that varies as a function of particle size, and other variables that affect the size (531)

Characteristic	Behaviour/attribute related to size	Properties other than size that can affect the related behaviour or attribute	Measurement techniques utilizing the behaviour of attribute
Geometrical	Area or perimeter of cross section	Shape combined with Orientation	Microscopy, image recognition, and sieving
	Displacement volume	Porosity, wettability	Electrozone sensing
	Some linear dimension such as the diameter or statistical geometric diameter	Shape, orientation	Microscopy and image recognition
Hydrodynamic / Aerodynamic	Settling velocity Drag (resistance to motion)	Shape and density combined with properties of the surrounding fluid; Reynolds number; molecular homogeneity	Elutriation and sedimentation
Optical	Light scattering Characteristics	Refractive index, isotropy, shape, orientation and surface detail of particle. Refractive index of medium. Wavelength and polarity of incident light.	Static light scattering (Mie and Fraunhofer diffraction)

On the other hand, irregular shaped particles can produce different results (531). For example, particles that settle with the same velocity have the same Stoke's size, but they can scatter light differently, and thus, have different Mie's size. In addition, particles that have the same sieve size may have different volumetric size. Theoretically, in the case of spherical particles, all analysis techniques should give the same results, particularly when the instrument is applied correctly (531). However, there are other assumptions of the theoretical model of a particle other than being spherical that must be fulfilled, as shown in Table 3.7. Fulfilling these requirements and knowing or controlling the value of all other parameters required by the model, the results of spherical particles by different analysis techniques should be similar, particularly when the fundamental measurement data are of comparable quality (531).

Table 3.7 Size measurement techniques, theoretical models and their assumptions (531)

Measurement Technique	Model	Assumptions About the Particle System	Other Parameters of the Model
Image recognition	Plane geometry	Particles are spherical, cubical or of other regular solid geometry	Known relationship between particle size and image size
Electrozone sensing	Ohm's law expressed in terms of electrolyte resistivity, cross sectional area of aperture, and volume of displaced electrolyte (particle volume)	Spherical particles that are much less conductive than the electrolyte	Size of aperture through which particles pass
Sedimentation	Stoke's Law for the settling velocity of a spherical particle in a fluid medium	Spherical particle, laminar flow of fluid around settling particle, all particles in system of same density	Particle density, density and viscosity of medium at analysis temperature, gravity
Static light scattering	Mie theory of light scattering by a spherical particle (includes Fraunhofer theory)	Spherical particle, optically isotropic, no multiple scattering, monochromatic light, coherent light, plane wave	Refractive index of particle, refractive index of medium, wavelength of light, size and position of scattering pattern projected onto detector

In addition, the molecular structure (organic or inorganic molecules), homogeneity (homogeneous or inhomogeneous), state (solid or liquid), isotropy (isotropic or anisotropic), particle shape, and suspension medium may cause different size analysis techniques to respond differently to one particle (531).

Errors occur when measuring some attributes arising from a particle other than a spherical particle, and reducing data from those measurements using a spherical model (531). The extent of error depends on the analysis technique, data reduction method, and shape of particles. The mathematical complexities introduced by non – spherical geometry usually prevent models from being derived for other shapes, and prevent predicting how the error will affect the values (531). The effect can be negligible or severe, depending on the analysis technique and shape of particles. For example, particle sedimentation velocities are measured by employing Stoke's law, assuming that the particle density, liquid density, and liquid viscosity are accurately known (531). If the values of such parameters contain error (*e.g.* $\pm 5\%$), then the error will affect the calculation of particle size. In addition, light scattering measurements reduced by Mie theory produce yet more complex results of deviating from the assumptions of the model, which require the refractive index of the sample to be known. A refractive index with an uncertainty of $\pm 5\%$ in relation to the error exhibited in the reported size distribution is considerably more complex (531).

Light scattering measurements, including low angle laser light scattering and dynamic light scattering may not be always suitable (532). In the case of low angle laser light scattering, no homogeneous and/or non – spherical

particles can lead to incorrect results. In addition, strongly absorbing particles can present problems, because they may not produce usable scattering signals. On the other hand, dynamic light scattering has extremely low resolution, and particles must usually differ in size by 50% or more to detect two peaks reliably. The method does not really provide much size distribution data. In addition, small size particles can easily be hidden in large size particles (532).

Light may scatter elastically or inelastically. Elastic scattering involves no energy loss/transfer, but changes in direction of incident beam may occur. On the other hand, inelastic scattering involves energy loss/transfer of incident particle, as well as a possible change in direction of incident beam (533). In addition, light scattering can be coherent, such as small angle elastic scattering (e.g. diffraction from solids), or incoherent, such as inelastic scattering, as well as large angle elastic scattering that becomes rapidly incoherent (e.g. backscattering). In the case of coherent scattering, the scattered beam is in phase, whereas in incoherent scattering, the scattered beam is not in phase (533).

X – rays, electrons, and neutrons are radiations that can be described as wave – like ($v = f \cdot \lambda$, where v is the velocity, f is the frequency, and λ is the wavelength) and particle – like ($E = hv$, packets of energy such as photons of electromagnetic radiation) (533). X – rays are produced by X – ray tubes, and they are generated by electron bombardment of a metal target (anode) such as copper (Cu), aluminium (Al), and silver (Ag). The interaction of X – rays with matter involves inelastic collisions of incident electrons with inner shell electrons in the atoms of a sample (533). Energy transfers from

incident electrons and excites inner shell electrons to higher energy levels, creating a hole in the inner shell. De – excitation may occur by other electrons from higher energy levels to fill the hole, during which the excess energy is released as an X – ray photon. The difference in energy between energy levels involved in the de – excitation represents the energy of X – ray photon (533). A set of X – rays can be produced, including α and β X – rays, depending on the energy level electrons filling the hole. An X – ray beam is made parallel by collimators, and it may be restricted to one wavelength (monochromated) using filters or crystal monochromators. High intensity X – ray beams may also be produced by accelerating electrons around a storage ring of synchrotron as well as wiggling and undulating their trajectories (533).

X – rays that are elastically scattered by electrons in matter involve an interaction between negatively charged electrons and electromagnetic field of incident X – rays, which cause electrons to oscillate and emit an electromagnetic X – ray identical in wavelength and phase to that of incident X – ray (533). On the other hand, inelastically scattered X – rays involve a transfer of all energy of X – ray photons to individual electrons in atoms, and consequently, ionise or excite these electrons to higher energy levels, which are released as photoelectrons (e.g. X – ray photoelectron spectroscopy) (533). De – excitation of atoms in matter produces secondary electrons/signals (533). In addition, inelastically scattered X – rays can also transfer some of their energy to an electron in a high – energy collision (Compton scattering). Such scattering increases with increasing wavelength (533).

The interaction of neutrons with matter in materials analysis mainly involves an interaction of low energy (~ 0.1 eV) thermal neutrons with atomic nuclei through nuclear and magnetic forces (533). Elastic and inelastic scattering of such neutrons induce atomic vibrations, which are known as phonons.

Elastic scattering can be coherent at low angles ($1 - 10^\circ$), in which electrons interact with the electron cloud of atoms, or it can be incoherent at high angles ($10 - 180^\circ$), in which electrons interact with nuclei (533). On the other hand, inelastic scattering occurs at smaller angles than elastic scattering. It involves the excitation of atomic vibrations (phonons), oscillations of valence electron cloud in solid (plasmons), single electron excitation (ionisation), and emission of X – ray bremsstrahlung (braking radiation) (533). De – excitation of atoms in matter produces many secondary electrons/signals, which are used in analysis (533). The cross section for elastic and inelastic scattering varies as atomic number Z^2 and Z , respectively. In crystalline solids, atoms are arranged periodically in regular unit cells, and thus, a periodic distribution of electrons. Therefore, coherent elastic – scattered waves from different periodically arranged particles can undergo diffraction in specific directions (533).

The important parameter that describes the amplitude of elastically scattered waves at a particular angle by one scattering particle is the atomic scattering amplitude (factor) ($f(\theta)$) (533). It describes the diffraction degree of a particular set of atoms in matter. For incident X – rays and electrons, the atomic scattering factor depends on the atomic number Z and $Z-f_x$ (where f_x is the atomic scattering factor for X – rays), respectively, whereas neutrons have no dependence on the atomic number (533).

The volume, within which 95% of electrons are brought to rest by scattering, is known as the interaction volume (533). The electron interaction volume has a teardrop shape for low atomic number elements, and a spherical shape for large atomic number elements (534). The electron range is calculated from the point where beam electrons enter a sample and the point where they lose their energy and leave the sample as sample current (534). The electron interaction range can be calculated using Kanaya – Okayama formula (μm), as given by equation 3.3, taking into account the effects of elastic and inelastic scattering.

$$R = \frac{K \cdot E_0^n}{\rho} \dots (3.3),$$

where (R) is the depth penetration, (K) = $0.0276A / Z^{0.889}$ (A is the atomic weight (g/mole) and Z is the atomic number), (ρ) is the density (g/cm^3), (E_0) is the incident beam energy (keV), and (n) = 1.67.

The electron interaction volume decreases with increasing the atomic number, but it increases with increasing the energy of incident beam, the latter which decreases elastic scattering, and consequently, electrons penetrate deeper (533, 534). The X – ray range (μm) is smaller than the electron range, because characteristic X – rays are only produced when the energy of incident beam exceeds the excitation energy (E_c) (534). Therefore, with increasing the penetration depth, the electrons lose their energy and become unable to ionize the inner shells (534). The X – ray range can be calculated using Anderson and Hassler formula as follows:

$$R = \frac{K \cdot (E_0^n - E_c^n)}{\rho} \dots (3.4),$$

where (K) = 0.064 and (n) = 1.68.

3.7.1 Particle size analysis

Measuring the particle size of CaP and doped CaP powders was a challenging task due to the formation of agglomerates. CaP powders have the tendency to form agglomerates of irregular shape and dimensions, which caused problems during measurements. Similarly, the doped CaP, particularly batch A, has the tendency to bind because of the presence of AlPO_4 . Measurements of particle size (length and width) using SEM images were attempted, but were unsuccessful due to the agglomeration of particles in most powders. The agglomerates were formed even after the suspension of particles in methanol, which usually minimise agglomeration.

Despite the tendency of CaP in forming agglomerations and the presence of more than one phase, particularly in the case of doped CaP (batch A) powders, the particle size analysis was carried out by means of static laser scattering, using the Malvern Mastersizer 2000E. The Mastersizer is made up of an optical unit (detection system and light source), sample dispersion unit, and data management software. The detection system involves a red light (forward scattering, side scattering, and back scattering) and blue light (wide angle forward and back scattering), while the light source involves a red light (helium – neon laser) and blue light (solid – state light source) (530). Measurements involve dispersing particles in distilled water and passing them through a focused laser beam, which scatter light at an angle that is inversely proportional to their size (530). The angular intensity of the scattered light is measured by a series of photosensitive detectors. The particle size is calculated from a map of scattering intensity versus angle. The scattering of particles is predicted by the Mie scattering model, which is applied within the Malvern software (530). Successful measurements

depend on the optical performance as well as good performance of the sample dispersion unit (532).

Before measuring the samples, the background was measured for every sample, which was used to subtract the ambient light signals from the total scattering received from the sample. Each sample was then made into a paste using distilled water, before being placed into the dispersion unit to be analysed. The stirring rate was set at 2000 rpm, and each sample was measured 10 times. The measurements were then averaged to produce the particle size distribution. The particle size distribution was carried out in the size range 0.02 – 2000 μm , using a beam length of 2.35 mm and water as the dispersant medium with a refractive index of 1.33. The refractive index and absorption index for CaP used in these measurements were 1.629 and 0.1, respectively. The value of the refractive index for doped CaP was assumed as equal to CaP (1.629). This was because the refractive index is not known for most systems, particularly for new materials, as well as it is more complicated for multiphase systems such as doped CaP (batch A).

Results are based on a number of fundamental concepts, including the volume based particle size distribution and equivalent spheres based measurement (Mie theory) (530-532). Measurements are based on using the particle volume to measure its size. The particle volume is used to calculate the diameter of an imaginary particle that is equivalent in volume (Mie theory). The fundamental distribution is based on expressing the distribution in a set of size classes (532). It is used to calculate the distribution parameters and derived diameters, using the total contributions from each size band (532).

The distribution statistics are calculated from the derived diameters, using an international method of defining the mean and other values of particle size. The most common percentile measurements are $d(0.5)$, $d(0.1)$, and $d(0.9)$ (530). The percentile $d(0.5)$ is known as the median particle size by volume (mass median diameter), which gives a particle size at which 50% of the sample is smaller and 50% is larger than this size. The measure of the absolute deviation from median is known as the uniformity. The percentile $d(0.1)$ and $d(0.9)$ is the particle size for which 10% and 90% of the sample, respectively, is below this size. Therefore, $d(0.1)$, $d(0.5)$, and $d(0.9)$ values indicate that 10%, 50%, and 90% of particles, respectively, are less than or equal to the size stated. In addition, the volume weighted mean $d[4,3]$ represents the volume mean diameter (mean particle diameter), which is mathematically given by equation 3.5.

$$D_v = \frac{\sum D_i^4 N_i}{\sum D_i^3 N_i} \dots (3.5),$$

where (D_i) is the diameter of individual particles and (N_i) is the number of particles corresponding to the specific diameter.

The width of the distribution is known as the span, and it is calculated using equation 3.6. Smaller span values indicate narrower distribution, while larger span values indicate broad distribution.

$$\text{Span} = \frac{d(0.9) - d(0.1)}{d(0.5)} \dots (3.6)$$

3.7.2 Scanning electron microscope (SEM)

A scanning electron microscope is a very useful electron microscopy technique for the analysis of surfaces and subsurfaces of nanostructures. It has high resolution due to its accelerated electrons, which interact strongly with matter, and gives it imaging ability to scan surfaces and particles and determine their morphology and size (533). SEM uses a focused electron beam to scan samples in a raster way. The beam sweeps horizontally left to right and then blanks and moves back (one horizontal sweep per line and one vertical sweep per image) (533). The electron source of SEM is usually tungsten. Electrons are accelerated and then focused on a sample by condenser lenses. These electrons interact with the atoms in a sample, and a signal is produced as an image. These signals contain information about surface morphology and composition (533). They are commonly detected as secondary electrons, backscattered electrons, and energy dispersive X – ray. Secondary electrons are those electrons that emitted by atoms excited by primary electrons. They result from inelastic interaction with atoms, which involve energy loss (533). On the other hand, backscattered electrons involve the reflection of waves, particles, or signals back to the direction they came from. They result from elastic interaction with the nuclei of atoms, which involve no energy loss. Their intensity depends on the atomic number, and they reveal differences in composition (533).

SEM is commonly equipped with an analytical technique, known as energy dispersive X – ray (EDX) spectroscopy. EDX is used for elemental or chemical analysis to determine the composition and weight percentage ratio of substances in a sample (semi – quantitatively) (533). It involves the investigation of a sample through interactions between electromagnetic

radiation and matter, analysing X – rays emitted by matter in response to incident charged particles. EDX reveals the elemental composition of a sample, based on the unique atomic structure for each element. It involves the emission of a stimulated emission of X – ray beam by a sample. When a high – energy X – ray beam is focused on a sample, it excites an electron in the inner shell, which is ejected to create a hole, the latter which is filled by an electron from the outer shell. The difference in energy ($E_2 - E_1$) is released as X – rays and measured by an energy dispersive spectrometer. The elemental composition of a sample is measured based on the difference in energy between two energy levels and the atomic structure of the element. EDX composes of a beam source (a cathode and magnetic lenses to create and focus a beam of electrons), X – ray detector (convert X – ray energy into voltage signals), pulse processor (measures signals), and analyser (data display and analysis).

EDX measurements can be affect by many variants. EDX detector cannot detect elements with atomic number less than 5 (e.g. H, He, Li, or Be), due to the absorption of low – energy X – rays by the windows in front of silicon – lithium detector (535). Differing the over – voltage of EDX results in different peak sizes, while raising the over – voltage on SEM shifts the spectrum to the larger energies, making higher – energy peaks larger and lower – energy peaks smaller. Also, overlapping of peaks occurs for many elements. In addition, the nature of samples can affect the accuracy of EDX measurements. For example, X – rays emitted in all directions may not escape the sample. This depends on the X – ray energy and the amount and density of sample. Inhomogeneous and rough samples are examples of reduced accuracy of EDX.

Common complications related to EDX usually occur during data collection or analysis (536). Problems arising during data collection include poor sample preparation (particularly for thin films, which must be less than 10 nm in thickness), incorrect sample geometry (incorrectly tilted sample may result in blocking the path between the detector and sample, which reveals an inordinately low number of X – rays or absence of low energy X - rays), and contamination (collected X – rays can originate from areas other than that of interest such as sample holder). On the other hand, problems arising during data analysis include escaped peaks (some of X – rays generated in the sample and compacting the solid state detector may inadvertently knock out Si K – shell electrons in the detector, reducing the measured energy of X – rays), sum peaks (when two X – rays impact the detector instantaneously, the pulse created and measured is the sum of two X – ray energies), peak overlaps (poor separation of peaks), and excessive deadtime (during pulse pileup, the software cannot keep up with the X – rays impacting the detector, and therefore, adjust for the uncounted X – rays by calculating a deadtime correction; the larger the correction, the greater the margin of error).

SEM (LEO 1530 Gemini FEGSEM) was carried out with an accelerating voltage of 20 kV, an aperture of 30 μm , and working distance of ~ 8 mm. An accelerating voltage of 3 kV and working distance of ~ 3 mm were only adopted during the initial investigation of powders and coatings. In addition, the working distance was adjusted to ~ 25 mm during the analysis of coated dentine sections, in order to scan the entire dentine surface. Preparation of CaP/doped CaP samples for SEM and EDX analyses involved the suspension of powders in ~ 10 ml 100% absolute methanol, followed by an ultrasonic bath for ~ 10 minutes. A drop of the suspension was mounted on

an aluminium stub using a pipette, dried using a gentle hot air, and finally coated in a thin film of Pt/Pd (5 – 10 nm) using a high – resolution coater. Due to the doping of CaP powders with aluminium compounds, the aluminium mounting stubs were coated with carbon to minimise the interaction of X – rays with aluminium stub. EDX spectra (using TEM) showed elements that were discounted from the analysis, because they provided no information, particularly to CaP samples. These elements were silicon (Si), copper (Cu), and carbon (C), as shown by the spectra of CaP and doped CaP in Figure 3.1.

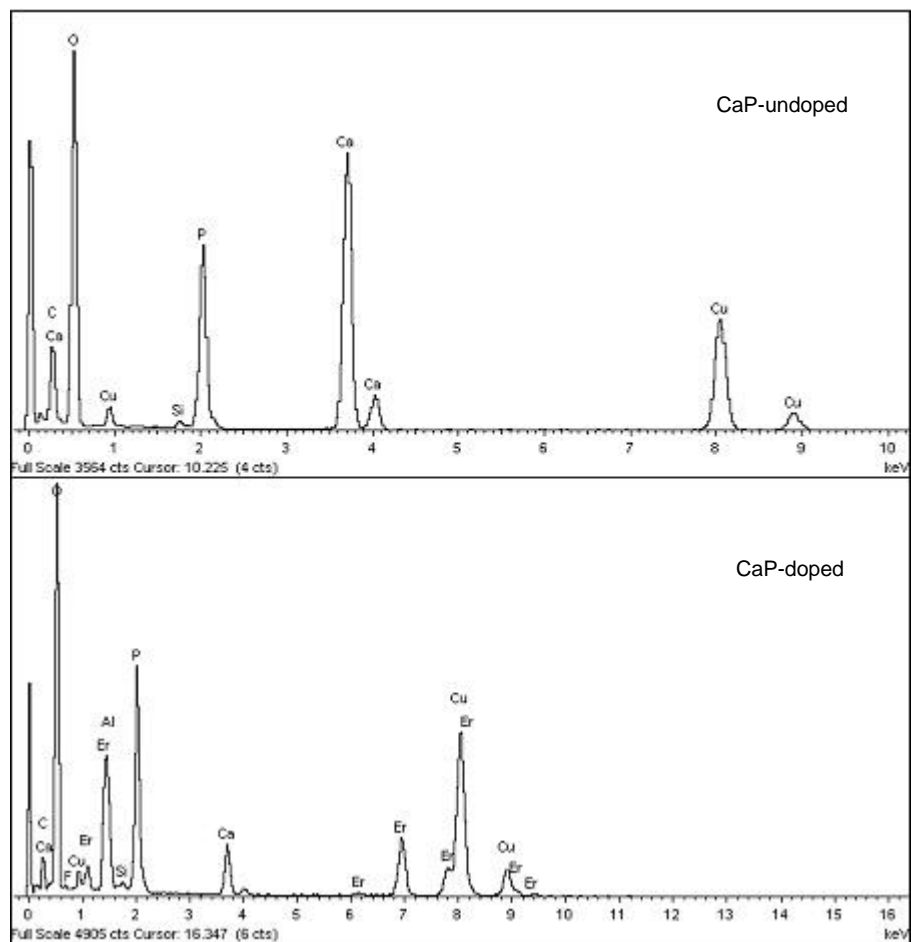


Figure 3.1 TEM-EDX spectra of CaP and doped CaP powders, showing discounted element (Si, Cu, and C) from the analysis.

3.7.3 X – ray diffraction (XRD)

X – ray diffraction is a powder diffraction technique that is useful in determining the crystallographic structure and crystallite size, as well as identifying substances based on the scattering of X – rays from powders. The intensity of peaks is due to the crystallographic structure and position of atoms as well as their thermal vibration, whereas the broadening and shape of peaks may be due to instrumental broadening, crystallite size broadening, and strain broadening (537).

XRD equipment consists of an X – ray tube as an electron source (*e.g.* copper), sample holder (moves with angle θ), and detector (moves with angle 2θ). Sample preparation involved packing powders in various sample holders, such as flat plate and spinner holders, which are designed for different XRD analysis. X – ray diffraction was carried out using XRD PANalytical X'Pert MPD, Philips, with CuK α ($\lambda = 1.54 \text{ \AA}$) radiation, in the 2θ range $5^\circ - 90^\circ$, a step size of 0.05, time per step of 99.6 second, and a scan speed of 0.06 $^\circ/\text{second}$. Hot stage XRD was carried out under atmospheric conditions from $\sim 25^\circ\text{C}$ up to 800°C , with CuK α ($\lambda = 1.54 \text{ \AA}$) radiation, in the 2θ range $5^\circ - 55^\circ$, a step size of 0.033, time per step of 99.6 second, and a scan speed of 0.04 $^\circ/\text{second}$.

XRD is used to determine the atomic and molecular structure of a crystal (537). It uses a beam of X – rays that diffracts by atoms or set of planes (in a sample) into specific directions. Since atoms in a crystal are arranged in a regular pattern, a constructive interface in phase waves results in very few directions. Diffracted beams are large number of scattered rays reinforcing one another. The difference in path length between set of planes (*e.g.* 1 to $\bar{1}$ and 2 to $\bar{2}$) is an integral number of wavelength. By measuring the angles

and intensities of diffracted beams, the density of electrons can be calculated, and consequently, the atom positions and bonds. X – ray – matter interaction involves elastic scattering, in which electrons oscillate at frequencies of incoming beam and become a source of radiation.

Using X – ray diffraction technique, the unit cell parameters, a – axis, b – axis, and c – axis, for a hexagonal structure can be calculated using equation 3.7.

$$\frac{1}{d^2} = \left(\frac{4}{3}\right) \left[\frac{h^2 + hk + k^2}{a^2} \right] + \left(\frac{l^2}{c^2}\right) \dots (3.7),$$

where (h, k, l) are the Miller indices of peaks, (a) and (c) are cell parameters ($a = b \neq c$), and (d) is the d – spacing, the latter which can be calculated using Bragg's law, as given by equation 3.8.

$$n\lambda = 2d \sin\theta \dots (3.8)$$

The unit cell volume (V) can be calculated using equation 3.9.

$$V = \frac{\sqrt{3}a^2c}{2} \dots (3.9)$$

The crystallite size (D) can be calculated using Scherrer equation 3.10.

$$D = \frac{K \cdot \lambda}{\beta \cos\theta} \dots (3.10),$$

where (k) is the shape factor ~ 0.9 , (λ) is the wavelength of X – ray (1.54 Å), and (β) is the line broadening (full width at half maximum (FWHM)) of intensity.

3.7.4 Fourier transform infrared spectroscopy (FTIR)

The technique is known as FTIR, because it is commonly used in the near, mid, and far – infrared spectrum regions. It is an absorption spectroscopy technique, which involves infrared, visible, and ultraviolet radiations with very high frequencies (> 600 GHz) (538). The technique uses a Fourier transform (FT) data processor that is used to process raw data into light output as a function of IR wavelength, and it is a complex mathematical function that converts an interferogram into a spectrum (539). FTIR has the ability to collect spectra, which can be used to identify compounds and their structures or investigate powder composition. An IR spectrum consists of characteristic absorption bands with known position and intensity, corresponding to functional groups of matter (538). An IR spectrum (transmittance or absorbance) is generated by passing a beam of IR light through a sample. The transmitted light reveals absorbed energy at each wavelength. Absorption characteristics contain details about the molecular structure of a sample. The incident beam passes through an interferometer and sample, and then onto a detector, the latter which detects a signal that results in an interferogram. Samples absorb specific frequencies of wavelengths that are subtracted from those in the interferogram. The variations in energy against time are detected by the detector and then converted by the FT into intensity against frequency (539).

FTIR analysis was carried out using FTIR VETEX 70 Bruker, in the near – and mid – IR spectrum regions, wavelength range $4000 - 400$ cm^{-1} , and a spectral resolution of 0.4 cm^{-1} . Sample preparation involved mixing powders with a mulling agent, known as Nujol, using a marble mortar and pestle. The paste/mix was applied onto and sandwiched between two plates of a high

purity salt of potassium bromide (KBr). The plates were then placed in a holder to be analysed.

Infrared spectra are formed due to the absorption of electromagnetic radiation at frequencies corresponding to the vibration of specific molecular bonds or functional groups in a molecule. Molecules rotate or vibrate at specific frequencies, corresponding to specific wavelengths of energy. Molecular motions (transitions) include electronic motions (changing energy levels of electrons or their directions of spin), translational motions (displacement of molecules to a new position in space), rotational motions (rotation of a molecule around its centre of mass, as a result of energy absorption in the microwave region), and vibrational motions (individual atoms within a molecule change position relative to one another without moving or rotating the molecule) (539, 540). The energy of infrared is weak on the electrons within an atom and does not affect them, and therefore, it corresponds to the energy required for translational, rotational, and vibrational motions (539). The latter are the strongest and most important in infrared spectroscopy. Vibrational energy is the result of energy absorption by a molecule, due to the vibration of component atoms around the mean centre of their chemical bonds (540). Molecular vibrations are commonly characterised by various modes, which contribute to the overall absorption spectrum (539, 540). These include stretching (increases or decreases the length of atom bonds), torsional (twisting of the backbone of a molecule), and bending (changes the bond angles of atoms relative to one another or to the rest of molecule). Vibration modes can also be symmetric or asymmetric.

Since atoms in a molecule are constrained by molecular bonds and move together in specific directions (degrees of freedom/number of normal modes), molecular transitions of a known molecular structure can be predicted (539, 540). A minimum set of fundamental motions, based on a threefold set of coordinate axes (x, y, z) are used to describe models (540). All molecules have three translational degrees of freedom, since the centre of mass of a molecule can move in x, y, and z directions. A non – linear molecule also has three rotational degrees of freedom, since it can spin around x, y, and z axes, whereas a linear molecule has only two rotational degrees of freedom, since two rotation directions are the same (539). The number of normal modes/degrees of freedom of vibration, for a given molecule with N (number) atoms, is $3N - 6$ and $3N - 5$ for non – linear and linear molecules, respectively (539, 540).

The number of normal modes (degrees of freedom) specifies the maximum number of fundamental/first order vibrations (change from the molecular ground state to the first energy level) for a molecule (539). Absorption of energy must be infrared active to be seen as an absorption band in the infrared spectrum. Active infrared absorptions primarily require a net change in dipole moment during the vibration of a molecule or functional group (539, 540). Asymmetrical vibrations (in a heteronuclear molecule) change the dipole moment by changing the distance between the two nuclei, which creates a dipolar electric field that absorbs a specific energy corresponding to that transition. On the other hand, symmetrical vibrations (in a heteronuclear molecule) and vibrations in a homonuclear diatomic molecule cannot be seen in the infrared spectrum, because they do not change their dipole moment (539). Therefore, the number of modes observed in an

infrared spectrum is far less corresponding to asymmetric and symmetric stretching and bending modes (540). Observed absorption bands can be affected by the occurrence of two vibrational modes at identical frequencies (degeneracy), overlapping or weak absorptions, or vibrational modes outside the instrument range (abundant) (539, 540). Absorption bands may also be affected by the detection of weak/forbidden absorptions, known as overtones (transitions beyond the first order), and/or combination of absorption bands (539, 540).

All functional groups have characteristic vibrational frequencies, which are used to identify materials and determine their structure in a compound. The position (frequency/wavenumber) of an absorption band depends on the mass of atoms in the absorbing group as well as the strength of molecular bonds (539, 540).

Absorption and transmission are the main interactions in FTIR analysis. Energy absorbed by a molecule does not reach the detector, the latter which reproduces missing absorptions as absorption bands. On the other hand, photons transmitted by a sample reach the detector intact. The two interactions are inversely related, as given by equation 3.11 (539).

$$A = \frac{\log 1}{T} \dots (3.11),$$

where (A) is absorbance and (T) is transmittance (% T/100).

Most of analytical applications are found in the mid – infrared region (~ 4000 – 400 cm⁻¹). The near – infrared region (~ 14000 – 4000 cm⁻¹) is useful for quantitative work, including in situ monitoring of reactions, due to the fact that qualitative band assignments are quite impossible because of many

overlapping bands of all organic species in this region. On the other hand, the far – infrared region ($\sim 400 - 10 \text{ cm}^{-1}$) is useful for detecting molecular vibrations that are sensitive to changes in the overall structure of a molecule and difficult to detect in the mid – infrared region (539).

In the mid – infrared region, the region between 4000 and 1300 cm^{-1} is known as the group frequency region, while the region between 1300 and 500 cm^{-1} is known as the fingerprint region (539). The main absorption bands in the group frequency region are assigned to vibrational modes and correspond to individual functional groups, including NH – OH ($4000 - 3000 \text{ cm}^{-1}$), C – H stretch region ($3000 - 2800 \text{ cm}^{-1}$), window material region ($2800 - 1800 \text{ cm}^{-1}$), and carbonyl region ($1800 - 1500 \text{ cm}^{-1}$). On the other hand, in the fingerprint region, absorption bands are due to single – bond and skeletal vibrations of polyatomic systems. Assignment of individual bands is difficult, however, the overall pattern is useful for material identification when matched to a reference spectrum (539). Some functional groups and their absorption band frequencies, as well as common inorganic ions (anionic groups) and their vibrational (stretching and bending) frequencies are presented in Tables 3.8 and 3.9, respectively.

Absorption bands produced by molecular vibrations within an anion functional group, known as internal vibrations, are very useful for characterising inorganics. Complex anion – attached cations (e.g. Ca^{2+} or Mg^{2+}) have a slight effect on the position of absorption bands, while heavier cations usually shift bands to a lower frequency (539).

Table 3.8 Common functional groups and their absorption band frequencies (539, 540)

Functional group	Formula	Absorption band frequencies
Hydroxyl	- OH	A broad-envelope-type band centred at 3400 cm^{-1} ($3570 - 3200\text{ cm}^{-1}$) Hydrogen bonding can change position and shape.
Unsaturated CH	- H - ϕ C, - H - C = C -	CH stretches from aromatic hydrocarbons at $3100 - 3000\text{ cm}^{-1}$. CH stretches from a carbon double bond at $\sim 3030\text{ cm}^{-1}$.
Aliphatic CH-methylene	- CH ₂ -	CH stretches at $\sim 2925\text{ cm}^{-1}$ ($2935 - 2915\text{ cm}^{-1}$) (asymmetric) and 2850 cm^{-1} ($2865 - 2845\text{ cm}^{-1}$) (symmetric). Vibrations for bending at $\sim 1465\text{ cm}^{-1}$ ($1485 - 1445\text{ cm}^{-1}$) and rocking at $\sim 730\text{ cm}^{-1}$ ($750 - 720\text{ cm}^{-1}$) (only for CH ₂ sequences greater than 4).
Aliphatic CH-methyl	- CH ₃	CH stretches at $\sim 2962\text{ cm}^{-1}$ ($2970 - 2950\text{ cm}^{-1}$) (asymmetric) and ~ 2872 ($2880 - 2860\text{ cm}^{-1}$) (symmetric) cm^{-1} . Vibrations for CH bending at $\sim 1450\text{ cm}^{-1}$ ($1470 - 1430\text{ cm}^{-1}$) (asymmetric) and 1380 cm^{-1} ($1380 - 1870\text{ cm}^{-1}$) (symmetric).
Carbon – carbon multiple bonds	- C = C -, - C \equiv C -	A carbon double bond stretch at $\sim 1640\text{ cm}^{-1}$ ($1680 - 1620\text{ cm}^{-1}$) and a carbon triple bond at $\sim 2120\text{ cm}^{-1}$ ($2140 - 2100\text{ cm}^{-1}$). Aromatic carbon stretching vibrations at $\sim 1600\text{ cm}^{-1}$ ($1615 - 1580\text{ cm}^{-1}$) and 1500 cm^{-1} ($1510 - 1450\text{ cm}^{-1}$). Out-of-plane bending mode vibrations may produce strong sharp bands at $1000\text{-}650\text{ cm}^{-1}$, depending on the pattern of substitution.
Carbon – nitrogen	- C \equiv N, - N = C = O, - S - C \equiv N	A nitrile stretch at $\sim 2240\text{ cm}^{-1}$ an isocyanate stretch at $\sim 2265\text{ cm}^{-1}$ ($2276 - 2240\text{ cm}^{-1}$) and a thiocyanate at $\sim 2160\text{ cm}^{-1}$ ($2175 - 2140\text{ cm}^{-1}$).
Carbonyl	- C = O	The highly polar carbonyl bond produces a strong absorption at $1850\text{-}1650\text{ cm}^{-1}$. Carbonyl type ester at 1740 and ketone at 1710 cm^{-1} .
Amide	- CONH -	N-H stretch at $\sim 3350\text{ cm}^{-1}$. Primary amide I at $\sim 1650\text{ cm}^{-1}$, secondary amide at $\sim 1550\text{ cm}^{-1}$, and tertiary amide at $\sim 1450\text{ cm}^{-1}$ "in stair-step-type intensities".
Acid salts	- CO ₂ ⁻	Asymmetric stretch for the carbon-oxygen bonds at $\sim 1650\text{-}1540\text{ cm}^{-1}$, depending on structure.
Carbonate	- CO ₃ ⁻	Broad stretching band at $\sim 1450\text{ cm}^{-1}$ ($1490 - 1410\text{ cm}^{-1}$) with sharp bands at $900\text{-}700\text{ cm}^{-1}$, depending on cation.
Carbon – oxygen	- C – O -	C-O stretch at $1200\text{-}1000\text{ cm}^{-1}$. Varies with hydrogen bonding and molecular structure.

Table 3.9 Common inorganic ions (anionic groups) and their vibrational (stretching and bending) group frequencies (539, 540)

Anion	Stretching cm^{-1}	Bending cm^{-1}
Water of hydration (H ₂ O)	3800 – 3200	1700 – 1600
Carbonate (CO ₃ ²⁻)	1550 – 1350	900 – 650
Nitrate (NO ₃ ⁻)	1500 – 1250	850 – 700
Sulphate (SO ₄ ²⁻)	1200 – 1050	680 – 600
Phosphate (PO ₄ ³⁻)	1300 – 900	600 – 550
Silicate (SiO ₃ ⁴⁻)	1200 – 800	800 – 400

3.7.5 Thermal analysis

Thermal analysis can be defined as the measurement of physical properties of a material as a function of temperature as it is subjected to a controlled temperature programme, such as heating and cooling at a constant rate and/or isothermal holds. Measurements can be absolute, differential, or derivative measurements, with an output in the form of a curve representing thermal events (changes in a material such as phase transitions, decomposition, oxidation, and sintering) in the form of reaction peaks or discontinuities (541). Common thermal analysis techniques include differential thermal analysis (DTA), differential scanning calorimetry (DSC), and thermogravimetric analysis (TGA).

DSC was the main thermal analysis technique used for Cap/doped CaP powders. It involves controlled heating of a sample and inert reference to determine any temperature difference between them in the form of heat absorption or development (541). It measures the difference in heat flow. Samples may undergo phase transition (endothermic reaction) or crystallisation (exothermic reaction), the latter which involves less heat flow (541). CaP/doped CaP powders were characterised using DCS Perkin Elmer 8000 fitted with TS0801RO automated sample robot. The analyses were carried out in the temperature range ~ 25 – 600°C and at a heating rate of 10°C/min. The working temperature is controlled by a water bath. It provides an inlet for nitrogen gas to purge the system whilst operated. It also has an automatic carousel sample loading system for automatic analyses. Sample preparation involved loading a weighted 10 mg of powder into an aluminium crucible pan (40 microlitre) to be heated.

3.7.6 Micro – hardness measurements

Micro – hardness measurements involve micro – indentation using a diamond indenter, Vickers or Knoop, as shown in Figure 3.2 and Figure 3.3, respectively. Measurements of hardness (hardness number) of materials are carried out under known applied forces of ≤ 1 kgf (ASTM standards) usually for ~ 15 seconds (542). A hardness number can be calculated from the surface area of an indent divided by the applied force (kgf/mm^2 , which is then converted to N/m^2), but expressed without units in the form of a hardness number (HV/force value). Vickers (HV) and Knoop (HK) hardness numbers are calculated using equations 3.12 and 3.13, respectively (542).

$$\text{HV} = \frac{1854 \cdot F}{d^2} \dots\dots (3.12),$$

where (F) is the force and (d) is the mean of the two diagonals of the indent.

$$\text{HK} = \frac{P}{C_p L^2} \dots\dots (3.13),$$

where (P) is the load, (C_p) is the correction factor (0.0702), and (L) is the length of indentation along its long axis.

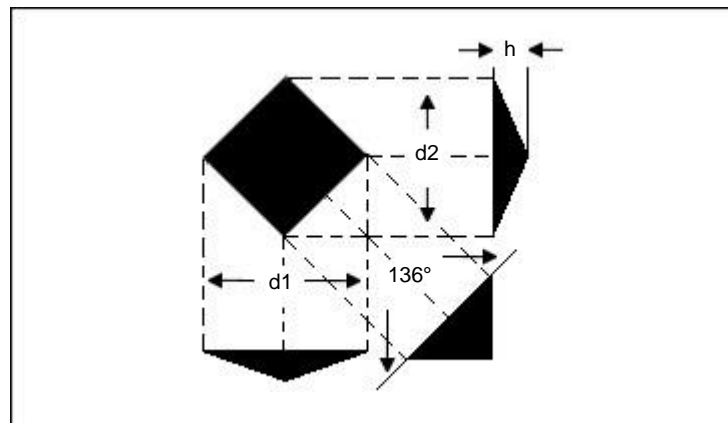


Figure 3.2 Schematic of Vickers diamond indenter.

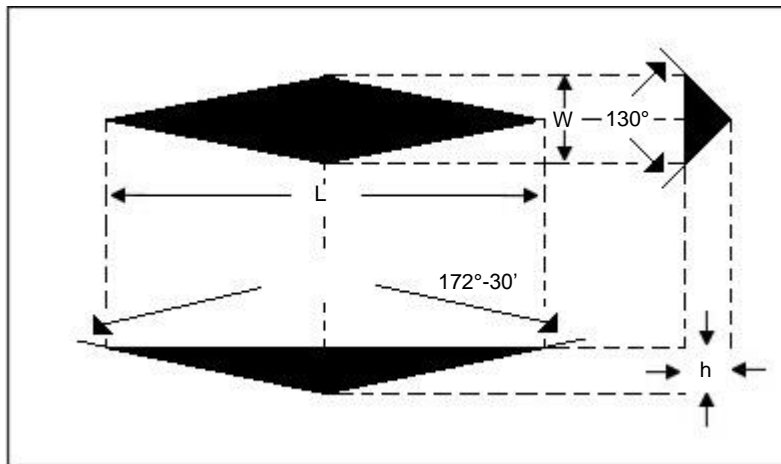


Figure 3.3 Schematic of Knoop diamond indenter.

Micro – hardness measurements were carried out at the University of Leeds, Paediatric Dentistry Department, School of dentistry, using a computer – aided Duramin indenter machine (Knoop diamond indenter), to determine the effect of laser irradiation sintering on coated dentine sections, in terms of their resistance to permanent deformation. Measurements were taken after two indentations per section, under a 25g load for 30 seconds, and the indents were measured in microns by an image analysis software.

3.7.7 Inductively – coupled plasma/mass spectrometry (ICP/MS)

ICP/MS is an elemental analysis technique that is used to determine the level of traces of elements in a solution. A Perkin Elmer Elan DRCE ICP/MS (543) allows the determination of major and trace metals and other elements at ppb levels. It can also be used to determine the presence of metals in organic liquids. The instrument is capable of precisely determining a small or large number of elements in a solution. It is an important method for chemistry – based compositional analyses of various materials. It relies on separating materials into different compositional groups, and it can provide

compositional data for over 130 isotopes, including rare earth, as well as measuring individual/specific isotopes of an element (543). Most ICP/MS analysis are quantitative, but an excellent semi quantitative analysis can also be performed, providing it is within $\pm 30\%$ of the quantitative values (543). In addition, ICP/MS can provide isotope dilution and isotope ratio analysis (543).

ICP/MS consists of a sample introduction system (a nebulizer and spray chamber), ICP torch and RF coil (generates an argon plasma, as an ion source), vacuum system (high vacuum for ion optics, quadrupole, and detector), interface (links the ICP ion source to the vacuum mass spectrometer), collision cell (removes interferences that can degrade the detection limits achieved), ion optics (direct the desired ions into the quadrupole), mass spectrometer (a mass filter, which separates ions by their mass – to – charge ratio), detector (counts individual ions leaving the quadrupole), and data handling and system controller (produces final concentration results) (543).

Samples are introduced as aerosol droplets (particle or liquid droplets in air/gas) into the argon plasma. The latter dries the aerosol, separates the molecules, and removes electrons to form ions (single charge) (543). The ions are then directed into the mass spectrometer, which separate the ions based on their mass – to – charge ratio. At any given time, one mass – to – charge ratio passes through the mass spectrometer (543). The ions then reach the detector (dynode or electron multiplier) and release electrons, which are amplified to produce a measurable pulse (543). ICP/MS measurements were carried out at the University of Leeds, energy and

resources research institute, using Perkin Elmer Elan DRCe ICP/MS in total quantitative mode for the determination of elements at ppb levels.

3.7.8 Profile roughness (Profilometry)

Profile roughness, also known as profilometry, is a surface profile technique. It uses an optical or contact profilometer. The optical profilometer uses a beam of light to measure the surface roughness by comparing the optical path difference between a sample surface and reference surface. On the other hand, the contact profilometer uses a diamond stylus with radius of 20 nm to 25 μm (544). The stylus moves vertically (height range from 10 nm to 1 mm) and then horizontally (horizontal resolution is controlled by the scan speed and data signal sampling rate) across the sample for a specified distance under a specified contact force (tracking force from < 1 to 50 mg) (544). Small surface variations in vertical stylus displacement are measured as a function of position. An analogue signal is produced from the height position of the stylus and converted into a digital signal (544).

The surface roughness measurements were carried out at the University of Leeds, School of Electronic and Electric Engineering, using LOT – ORIEL Alpha Step IQ Surface Profiler. The latter is a surface roughness profiler that provides 2D high accurate measurements, by scanning a sharp diamond tipped stylus (5 μm in radius) across a substrate surface. It can determine topography information such as thin step heights and surface micro roughness. It can measure heights of 400 μm with an accuracy of 5 nm and maximum scan length of 10 mm. The surface roughness measurements were carried out on CaP/doped CaP pellets before and after immersion in a citric acid solution. Surface roughness is determined by measuring roughness profile parameters, roughness average (R_a) and root mean

square roughness (R_q). Roughness profile parameters (R_a and R_q) are the functions of the profile deviations from a mean line (545), as shown in Figure 3.4. The mean line is given by equation 4.3.14 (546).

$$\bar{Z} = \frac{1}{L} \sum_{x=0}^{L-1} Z_x \quad \dots (3.14)$$

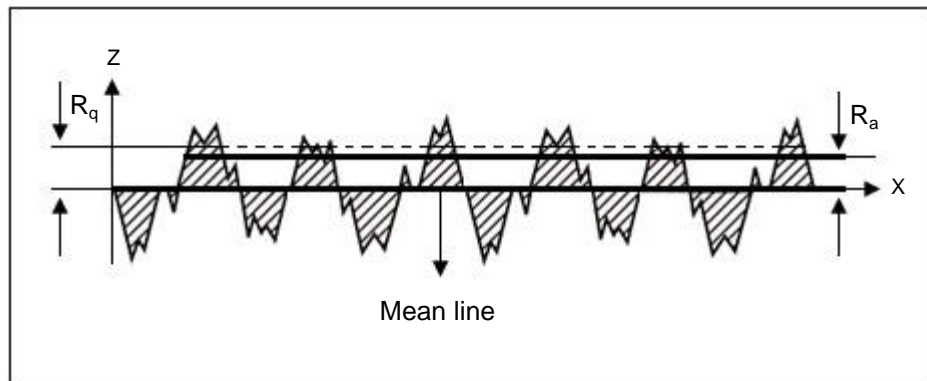


Figure 3.4 Schematic of roughness profile parameters R_a and R_q .

Roughness average (R_a) is the arithmetic average of the absolute values of the roughness profile ordinates, as given by equation 4.3.15 (546).

$$R_a = \frac{1}{L} \sum_{x=0}^{L-1} (|Z_x - \bar{Z}|) \quad \dots (3.15)$$

Root mean square roughness (R_q) is the root mean square average of the roughness profile ordinates, as given by equation 4.3.16 (546).

$$R_q = \sqrt{\frac{1}{L} \sum_{x=0}^{L-1} (Z_x - \bar{Z})^2} \quad \dots (3.16),$$

where (Z) is the surface profile height, (L) is the the sampling length, (x) is a reference mean line, over which the topographical heights are measured, and (Z_x) is the height amplitude at each iteration over the entire measurement length from $X = 0$ to $L - 1$ (546).

Roughness average (R_a) values indicate whether a friction coefficient is high or low, and thus, the weariness of a surface. A surface with a large roughness average (R_a) value has a high friction coefficient, and thus, wear quickly. On the other hand, a surface with a small roughness average (R_a) value has a low friction coefficient, and thus, wear slowly. Statistically, the relation between roughness parameters (R_a) and (R_q) is given by $R_q \geq R_a$, which depends on the sample surface profile. The difference between (R_a) and (R_q) values is an indication of the uniformity of a surface.

Chapter 4

Results and Discussions

Chapter 4 is divided into three sub chapters. Each chapter has a summary at the end, detailing the principle findings. The first chapter (4.1) is on the synthesis of calcium orthophosphates, via the chemical precipitation and hydrothermal methods under various synthesis conditions. The second chapter (4.2) is on the synthesis of doped calcium orthophosphates, via the chemical precipitation and hydrothermal methods under various synthesis conditions. The second chapter is divided into two parts. The first part is on the synthesis of doped calcium phosphates, via Er_2O_3 , AlPO_4 , and CaF_2 compounds (batch A), while the second part is on the synthesis of doped calcium phosphates, via $\text{Er}(\text{NO}_3)_3 \cdot 5\text{H}_2\text{O}$, $\text{Al}(\text{NO}_3)_3 \cdot 9\text{H}_2\text{O}$, and NH_4F compounds (batch B). The third chapter (4.3) is on the laser irradiation sintering investigation, which includes the characterisation of as prepared dentine, CaP/doped CaP – coated – dentine, and laser irradiation sintering of CaP/doped CaP pellets and CaP/doped CaP – coated – dentine sections. The third chapter also includes temperature change measurements during laser irradiation of CaP/doped CaP pellets and CaP/doped CaP – coated – dentine sections, acid erosion of CaP and doped CaP pellets, and micro – hardness measurements of as prepared dentine sections and CaP/doped CaP – coated – dentine sections.

Chapter 4.1 Synthesis and characterisation of calcium phosphates

Calcium orthophosphate (CaP) powders were synthesised as control samples, and they were prepared by the chemical precipitation and hydrothermal methods under different conditions, as shown in Table 4.1.1. CaP powders were investigated in terms of their particle size, morphology, composition, phase purity, and thermal behaviour, using SEM, SEM-EDX, static laser scattering, XRD, FTIR, and DSC analysis techniques.

Table 4.1.1 Synthesis conditions for CaP powders

Powder	Synthesis method	As – prepared pH	Adjusted pH	Temperature	Reaction time
CaP	Chemical precipitation	5.4 ± 0.2	10 ± 0.2	RT	24 hours
	Hydrothermal	5.4 ± 0.2	10 ± 0.2	200°C	

The synthesis conditions in Table 4.1.1, including the synthesis method, pH, temperature, and reaction time were adopted based on an initial investigation, involving the synthesis of CaP powders via the chemical precipitation and hydrothermal methods under different synthesis conditions. These conditions included temperature, pH, reaction time, and ageing time. The initial investigation involved the characterisation of CaP Powders by SEM and XRD analysis techniques, to investigate the effect of such conditions on the morphology of particles and CaP phase, which are presented and discussed next.

Figure 4.1.1 shows SEM of CaP particles that were prepared by the chemical precipitation method. The particles were allowed to precipitate for 24 hours, under room temperature and as – prepared pH 5.4 ± 0.2 conditions. The CaP particles were in the micrometre scale, with a platelet – like morphology. The particles appeared to be poorly crystallised, which was probably due to the slow rate of nucleation at room temperature. Figure 4.1.2 shows the XRD pattern of CaP synthesised by the chemical precipitation method under room temperature and as – prepared pH 5.4 ± 0.2 conditions. The XRD pattern indicated the formation of a monetite phase, as compared to monetite JCPDS file 01-070-1425. The formation of the monetite phase was credited to the room temperature and as – prepared pH 5.4 ± 0.2 conditions. The formation of the monetite phase was also supported by the formation of platelet – like particles, which is usually linked to monetite.

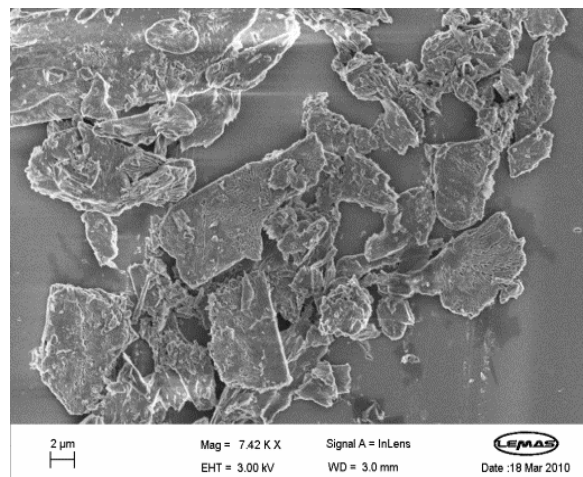


Figure 4.1.1 SEM of CaP particles prepared by the chemical precipitation method under room temperature and as – prepared pH 5.4 ± 0.2 conditions, showing platelet – like morphology of particles.

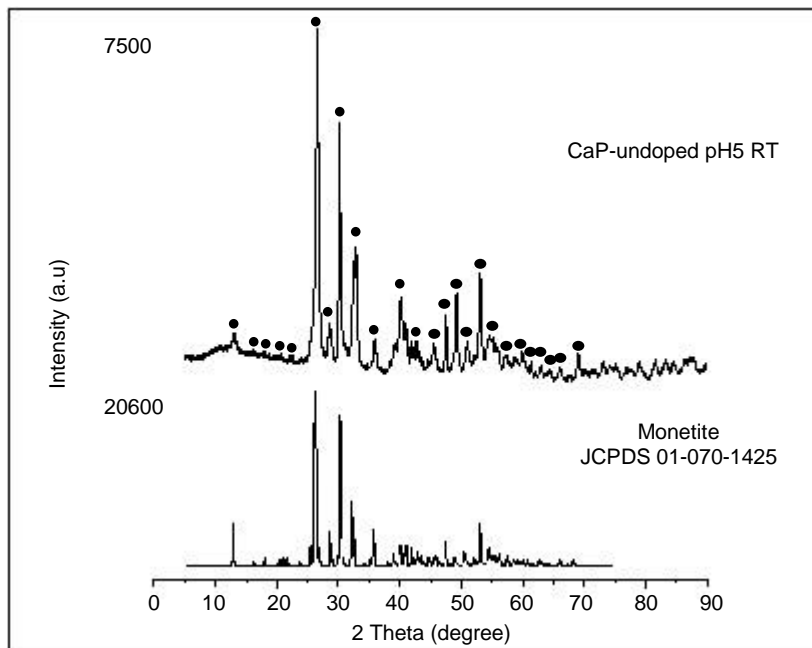


Figure 4.1.2 XRD pattern of CaP powder prepared by the chemical precipitation method under room temperature and as – prepared pH 5.4 ± 0.2 conditions. Marked peaks (●) were assigned to monetite JCPDS file 01-070-1425.

Figure 4.1.3 shows SEM of CaP particles that were synthesised under as – prepared pH 5.4 ± 0.2 and 80°C hydrothermal conditions. The particles were synthesised for 24, 48, and 72 hours, as shown in Figure 4.1.3 (a), (b), and (c), respectively. The hydrothermal synthesis at 80°C resulted in the formation of elongated particles, which indicated particle growth at the *c* – axis. The particles appeared to be well crystallised, which was probably due to the increase in the rate of nucleation. This indicated that the micrometre platelet – like particles that were produced at room temperature with the same pH 5.4 ± 0.2 were not favoured under 80°C hydrothermal conditions, and instead, elongated particles with reduced particle size and enhanced crystallinity were formed. The particles also varied in size and shape, depending on the reaction time. Figure 4.1.3 (a) shows a mixture of elongated platelet – like and needle – like particles that were synthesised

hydrothermally at 80°C for 24 hours. Increasing the reaction time to 48 hours resulted in the formation of needle – like particles with relatively decreased particle size, as shown in Figure 4.1.3 (b). on the other hand, increasing the reaction time to 72 hours resulted in the formation of elongated rod – like particles with increased particle dimension, compared to those synthesised for 48 hours. This suggested that prolonging the reaction time to 48 hours reduced the mean width of CaP particles significantly, while prolonging the reaction time to 72 hours increased the mean length of CaP particles significantly.

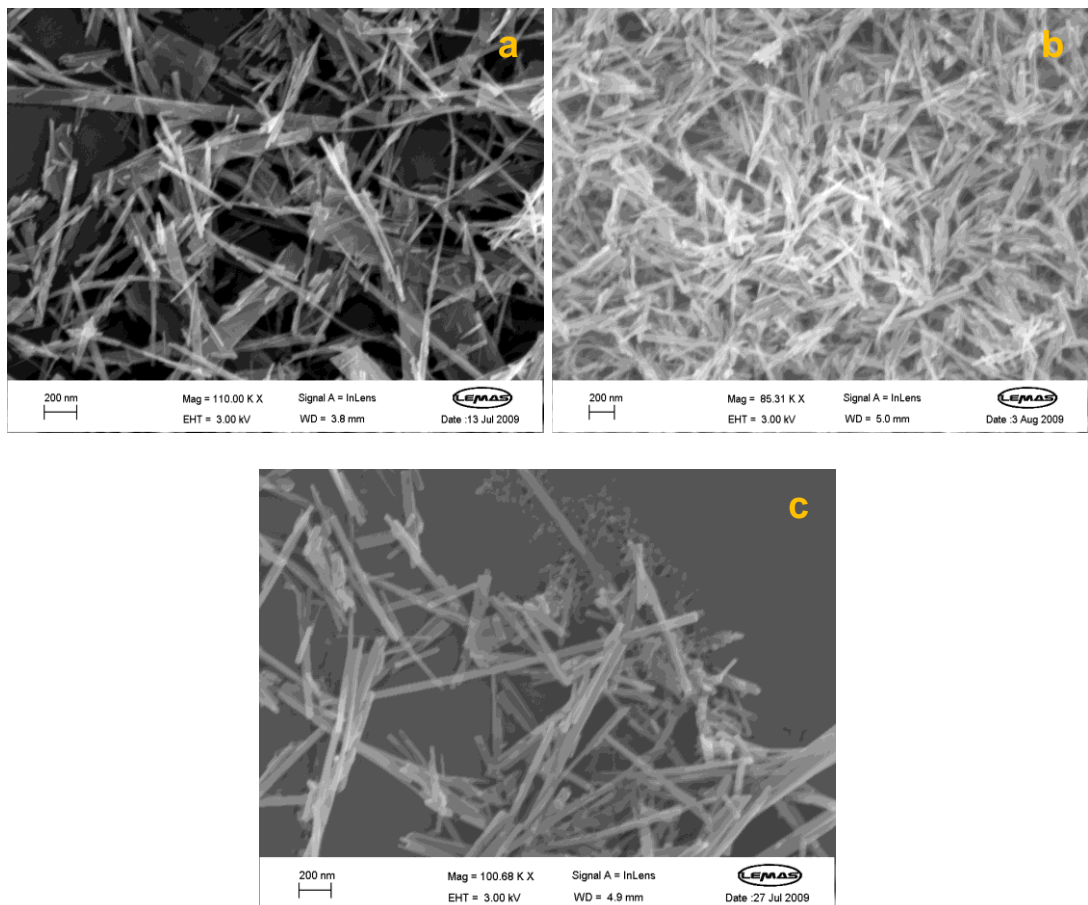


Figure 4.1.3 SEM of CaP particles synthesised under as – prepared pH 5.4 ± 0.2 and 80°C hydrothermal conditions for (a) 24 hours, (b) 48 hours, and (c) 72 hours.

CaP powders were also synthesised under as – prepared pH 5.4 ± 0.2 and 200°C hydrothermal conditions for 24 and 72 hours. The hydrothermal reaction for 24 hours resulted in the formation of a mixture of elongated platelet – like and needle – like particles, as shown by SEM in Figure 4.1.4 (a). On the other hand, the hydrothermal reaction for 72 hours resulted in needle – like particles with relatively reduced particle size (aspect ratio; length:width), as shown by SEM in Figure 4.1.4 (b). This suggested that prolonging the reaction time to 72 hours reduced the aspect ratio (length:width) of CaP particles significantly without affecting the morphology.

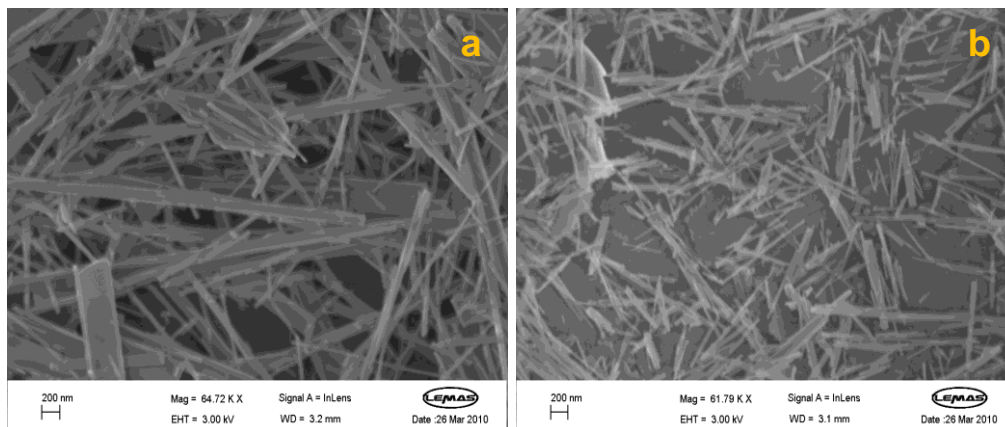


Figure 4.1.4 SEM of CaP particles synthesised under as – prepared pH 5.4 ± 0.2 and 200°C hydrothermal conditions for (a) 24 hours and (b) 72 hours.

CaP powders were also synthesised under as – prepared pH 5.4 ± 0.2 and 200°C hydrothermal conditions for 24 hours, after initial ageing of the starting CaP mixture under static conditions for 2, 4, and 6 weeks, as shown by SEM in Figure 4.1.5 (a), (b), and (c), respectively. Ageing of the starting CaP mixture had a slight effect on the particle size and morphology. Particles with elongated platelet – like and needle – like morphology were produced after ageing of the starting CaP mixture for 2, 4, and 6 weeks. The

CaP particles appeared to be slightly altered in size and morphology after ageing for 4 and 6 weeks, compared to ageing for 2 weeks. After ageing for 4 and 6 weeks, the shape of particles appeared to favour the needle – like morphology, with a slight reduction in their aspect ratio (length:width).

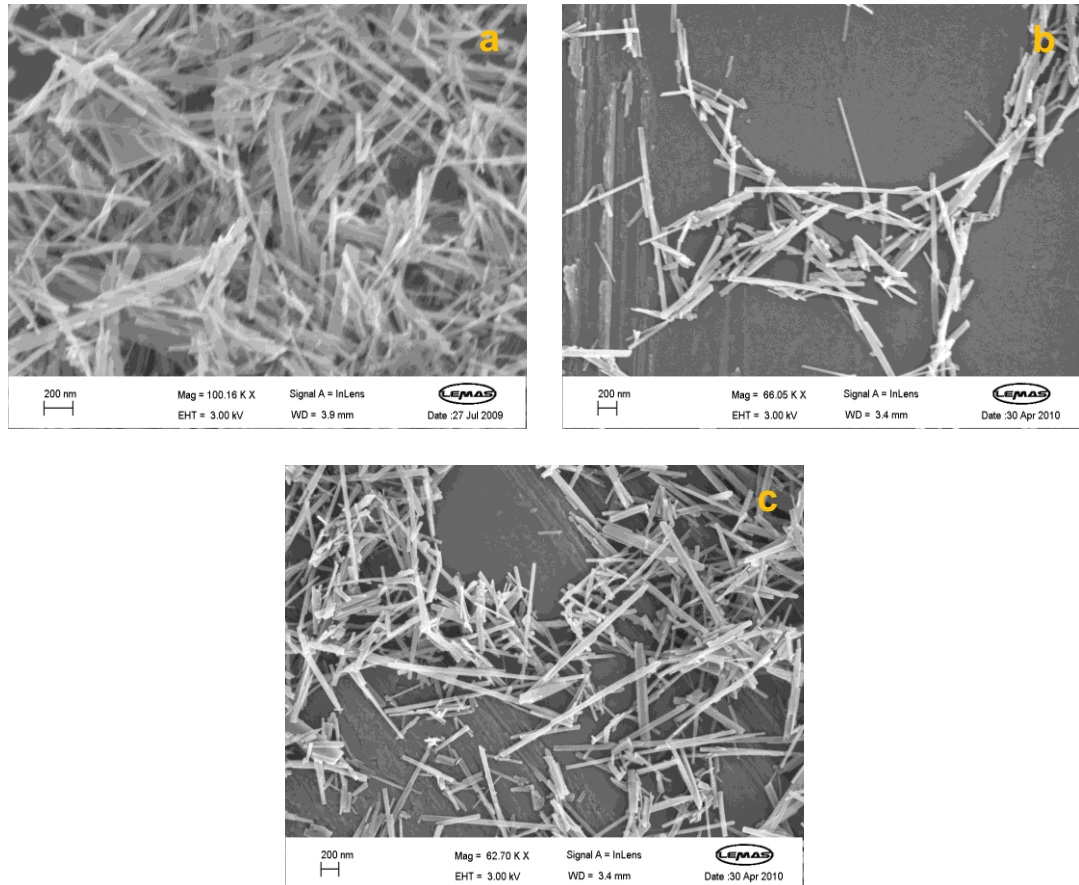


Figure 4.1.5 SEM of CaP particles synthesised under as – prepared pH 5.4 ± 0.2 and 200°C hydrothermal conditions for 24 hours, after initial ageing of CaP mixture for (a) 2 weeks, (b) 4 weeks, and (c) 6 weeks.

The XRD patterns of these particles (CaP aged 2wks 200°C , CaP aged 4wks 200°C , and CaP aged 6wks 200°C) indicated the formation of a monetite phase, as compared to monetite JCPDS file 01-070-1425, after ageing of the starting CaP mixture for 2, 4, and 6 weeks, as shown in Figure 4.1.6. However, the XRD peaks at 2 theta 32.39° , 32.82° and 35.85° , in

particular, were significantly reduced, whereas peaks at 2 theta 13°, 26.5°, and 40° were in good agreement with those of monetite JCPDS file 01-070-1425. The main slight difference between CaP XRD patterns was the reduction of peak intensities after ageing of the starting CaP mixture for 4 and 6 weeks, compared to that for 2 weeks. This was probably because ageing of the starting CaP mixture was carried out under static conditions, and therefore, the ageing stage hardly affected the CaP particles. The results under hydrothermal conditions indicated that CaP particles grew at the *c* – axis, which was accompanied by a decrease in growth at the other directions. This was in good agreement with the increase of *c* – axis with increasing hydrothermal temperatures (547).

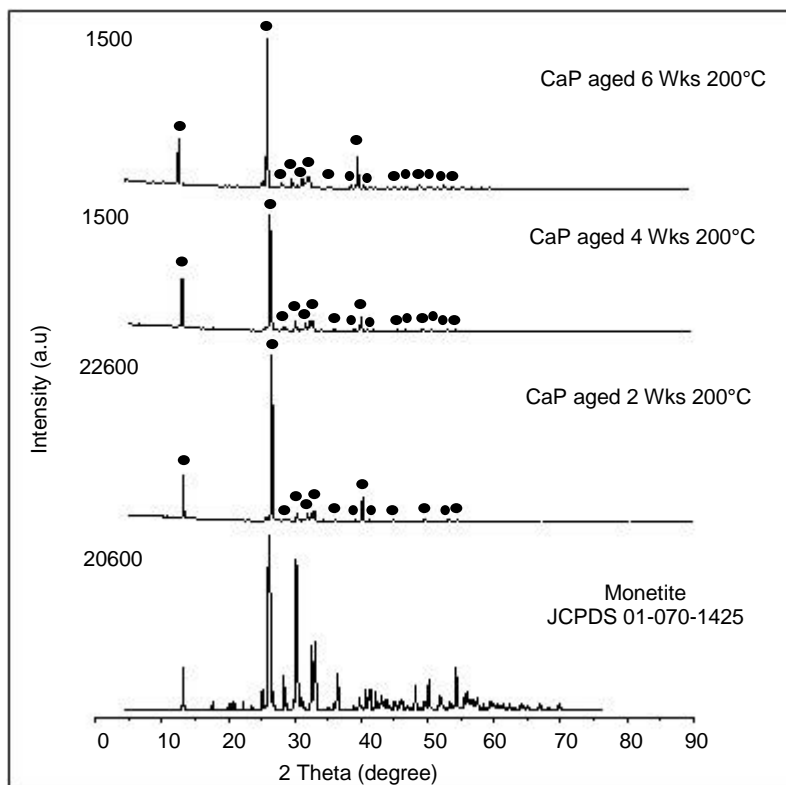


Figure 4.1.6 XRD patterns of CaP powders prepared from solutions aged for 2, 4, and 6 weeks and treated hydrothermally at 200°C for 24 hours. Marked peaks (●) were assigned to monetite JCPDS file 01-070-1425.

Moreover, CaP particles were also synthesised under hydrothermal conditions, after adjustment of pH of the starting CaP mixture. This resulted in significant alteration of particle size and morphology. CaP particles that were synthesised under 200°C hydrothermal conditions for 24 hours, with different pH values of pH 8 ± 0.2 , 9 ± 0.2 , 10 ± 0.2 , and 11 ± 0.2 , are shown by SEM in Figure 4.1.7 (a), (b), (c), and (d), respectively. Figure 4.1.7 (a) and (b) shows SEM of needle – like particles that were synthesised with pH 8 ± 0.2 and pH 9 ± 0.2 , respectively, with reduced particle size, compared to those synthesised with pH 5.4 ± 0.2 . Figure 4.1.7 (c) and (d) shows SEM of rod – like particles that were synthesised with pH 10 ± 0.2 and pH 11 ± 0.2 , respectively, with further reduction in particle size, compared to those synthesised with pH 8 ± 0.2 and pH 9 ± 0.2 . All particles had aspect ratios in the nanoscale. This indicated that increasing the pH of CaP starting mixture reduced the mean aspect ratio (length:width) of CaP particles significantly.

The change in size and shape as a function of pH is due to the provision of OH⁻ ions. High concentration of OH⁻ ions tends to reduce the diameter of CaP particles, particularly the mean length of particles, and drive the particles' shape close to rod – like or spherical morphology (547). The preferential adsorption of OH⁻ ions, from the starting mixture at pH ≥ 9 , onto nuclei appeared to guide the crystal growth along preferential plane (547). This suggested that there was no an oriented crystal growth in alkaline conditions (547). This was because CaP nuclei have a high tendency to grow at the *c* – axis in moderate acidic conditions (547). Under room temperature and low pH (~ 5.4) conditions, the particles grew at the *c* – axis along (001) direction, which led to the formation of platelet – like particles. The platelet – like particles also exhibited [110] orientation, growing along

the (211) direction (548). Under high temperature ($> RT$) and low pH conditions, the particles grew at the c – axis in unidirectional growth, which resulted in elongated platelet – like and needle – like particles. Under high pH conditions (> 5.4), the growth of particles in the c – axis appeared to be inhibited, which led to the formation of short rod – like particles. Elongated rod – like particles exhibited $[\bar{2}21]$ orientation and grew along the (102) direction (550).

The dependence of particle morphology on the pH of starting mixture can be explained by the supersaturation of solution and particles' surface charge (549). The increase of supersaturation tends to decrease the nucleation activation energy, and consequently, increases the nucleation rate (549). Therefore, the increase of supersaturation with increasing pH levels may increase the nucleation rate, and consequently, reduces the particle size. Under high pH conditions, the adsorption of more negatively charged OH^- ions tends to increase the particle shell negative charge, causing particle repulsion and preventing particle agglomeration, which may help maintaining the nanosize of particles (549).

XRD patterns of CaP powders that were hydrothermally synthesised at $200^\circ C$ for 24 hours with different pH values are shown in Figure 4.1.8. Under $pH\ 8 \pm 0.2$ conditions, the XRD pattern ($pH8\ 200^\circ C\ 24h$) indicated the formation of two phases of HAp and monetite, as compared to HAp JCPDS file 009-0432 and monetite JCPDS file 01-070-1425, respectively. Under $pH \geq 9$ conditions, the XRD patterns ($pH9\ 200^\circ C\ 24h$, $CaP\ pH10\ 200^\circ C\ 24h$, and $CaP\ pH11\ 200^\circ C\ 24h$) indicated the formation of a single HAp phase, as compared to HAp JCPDS file 009-0432.

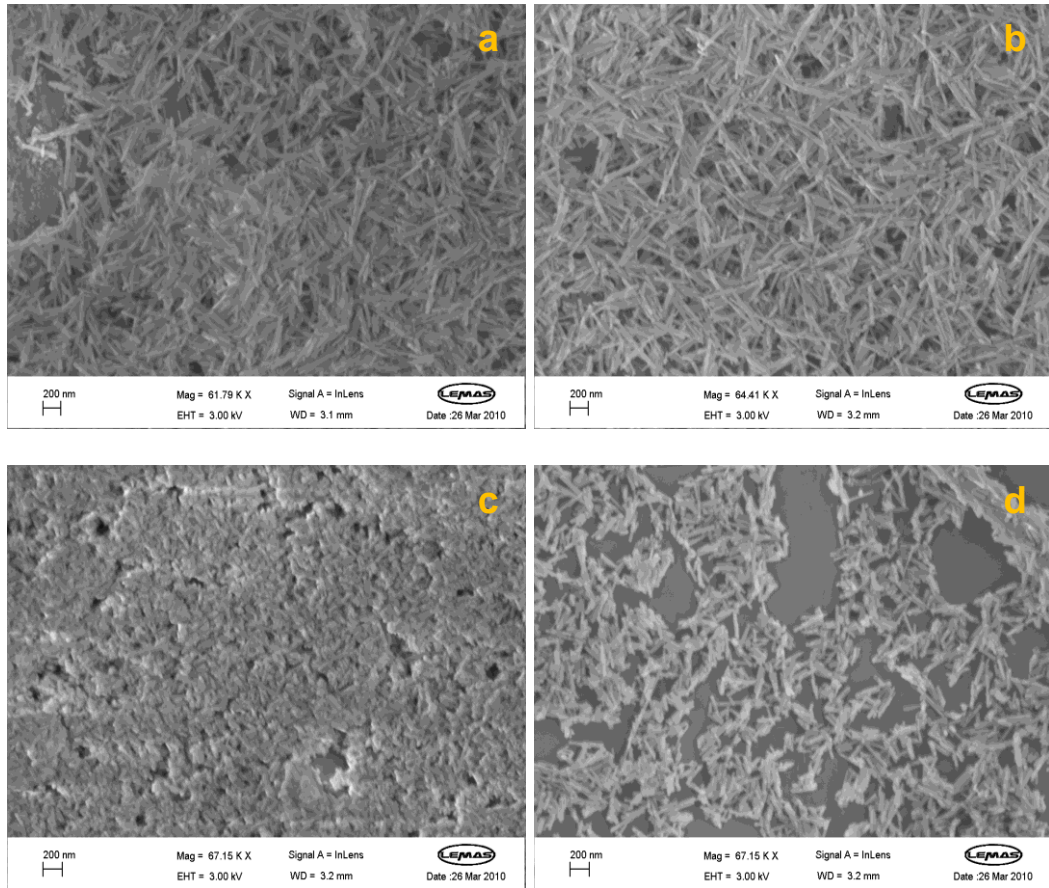


Figure 4.1.7 SEM of CaP particles synthesised under 200°C hydrothermal conditions for 24 hours, with (a) pH 8 ± 0.2 , (b) pH 9 ± 0.2 , (c) pH 10 ± 0.2 , and (d) pH 11 ± 0.2 .

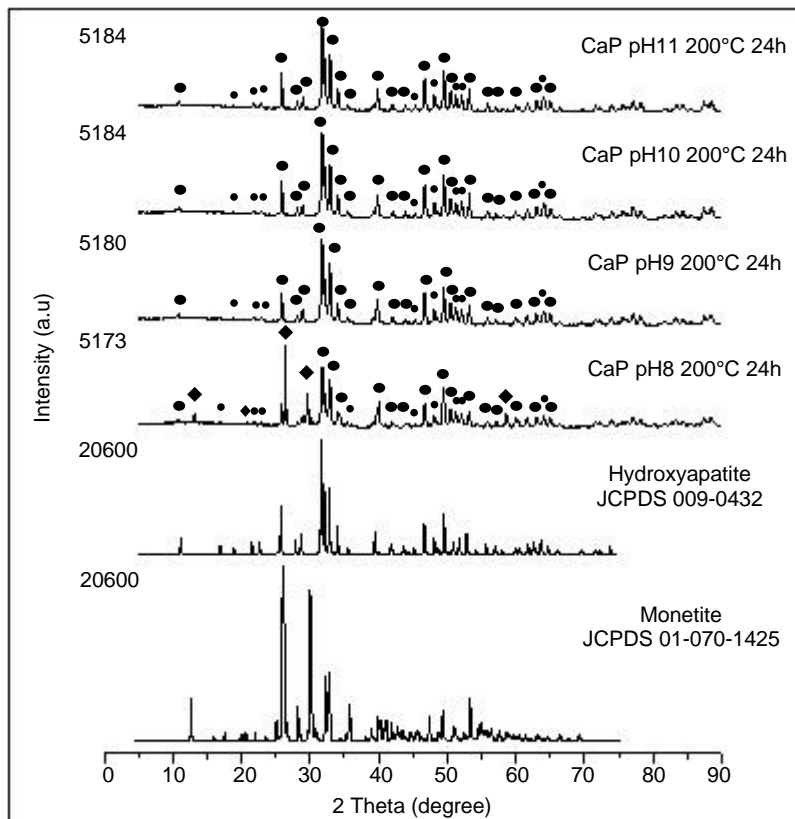


Figure 4.1.8 XRD patterns of CaP powders synthesised from mixtures with pH 8 ± 0.2 , 9 ± 0.2 , 10 ± 0.2 , and 11 ± 0.2 by the hydrothermal method at 200°C for 24 hours. Marked peaks (●) were assigned to HAp JCPDS file 009-0432, and (◆) were assigned to monetite JCPDS file 01-070-1425.

Since a single HAp phase, with nanosized and rod – like particles, was formed under pH ≥ 9 and 200°C hydrothermal conditions, the starting CaP mixture with pH 10 ± 0.2 was investigated at a lower hydrothermal temperature of 140°C for 24 and 72 hours, as shown by SEM in Figure 4.1.9 (a) and (b), respectively. The hydrothermal synthesis at 140°C for 24 hours produced rod – like CaP particles in the nanoscale, which were relatively reduced in size after 72 hours. Although rod – like nanoparticles were obtained at 140°C after 24 and 72 hours, the hydrothermal synthesis at 200°C for 24 hours produced much smaller nanoparticles, as shown in Figure 4.1.7 (c).

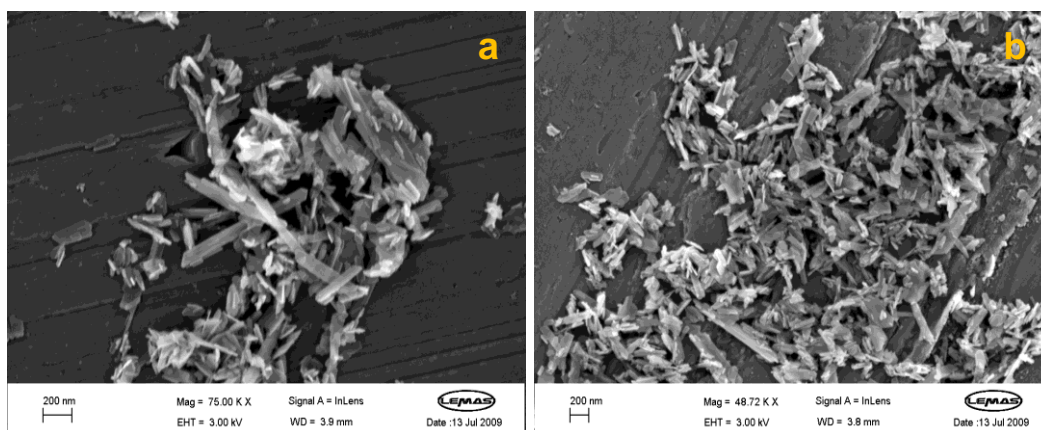


Figure 4.1.9 SEM of CaP particles synthesised under pH 10 ± 0.2 and 140°C hydrothermal conditions for (a) 24 hours and (b) 72 hours.

The initial investigation can be summarised as follows. Temperature and reaction time affected the particles' size and shape, producing poorly crystallised and platelet – like particles at room temperature, and well – crystallised and elongated – shaped particles, with reduced particle size, at hydrothermal temperature. The reaction time of 24 hours was concluded most adequate, as the reaction time over 24 hours insignificantly affected the particles' size and shape. Ageing of the starting CaP mixture and post hydrothermal treatment (200°C) barely affected the particles' size and morphology, and it had no effect on the obtained CaP phase. In contrast, adjusting the pH of starting CaP mixture ($\text{pH} \geq 9$) and post hydrothermal treatment (200°C) significantly affected the particles' size and shape, producing nanosized and rod – like particles of a single HAp phase. The results indicated the importance of temperature, pH, and reaction time in modifying the size and shape of CaP particles (12), and therefore, they were adopted to investigate the synthesis of CaP and doped CaP powders under room temperature, 200°C hydrothermal temperature, as – prepared pH 5.4 ± 0.2 , adjusted pH 10 ± 0.2 , and a reaction time of 24 hours.

4.1.1 CaP (pH 5.4 ± 0.2, RT)

CaP with as – prepared pH 5.4 ± 0.2 was synthesised at room temperature by two different reactions to investigate the effect of addition and stirring time on CaP particles, as follows:

- First reaction: A solution of diammonium hydrogen phosphate ((NH₄)₂HPO₄) was added to a solution of calcium nitrate tetrahydrate (Ca(NO₃)₂·4H₂O) by a fast dropping/addition technique for 15 minutes whilst being magnetically stirred at ~ 400 rpm for 30 minutes.
- Second reaction: A solution of diammonium hydrogen phosphate ((NH₄)₂HPO₄) was added to a solution of calcium nitrate tetrahydrate (Ca(NO₃)₂·4H₂O) by a slow dropping/addition technique for 30 minutes whilst being magnetically stirred at ~ 400 rpm for 60 minutes.

The mixtures were then treated as described before, covered to minimise the absorption of atmospheric CO₂, left on standby at room temperature for 24 hours, and finally, the wet precipitate was collected and dried in an oven at 80°C for 24 hours.

Representative SEM of CaP particles that were synthesised under room temperature and as – prepared pH 5.4 ± 0.2 conditions by the first and second reactions is shown in Figure 4.1.10 (a) and (b), respectively. SEM showed the formation of platelet – like particles under both reactions. Figure 4.1.10 (a) shows SEM of CaP particles that were synthesised under room temperature and as – prepared pH 5.4 ± 0.2 conditions by the fast addition of ((NH₄)₂HPO₄) solution to (Ca(NO₃)₂·4H₂O) solution. The fast addition of phosphate solution took 15 minutes whilst being magnetically stirred at ~ 400 rpm for 30 minutes. On the other hand, Figure 4.1.10 (b) shows SEM of

CaP particles that were synthesised under room temperature and as – prepared pH 5.4 ± 0.2 conditions by the slow addition of $((\text{NH}_4)_2\text{HPO}_4)$ solution to $(\text{Ca}(\text{NO}_3)_2 \cdot 4\text{H}_2\text{O})$ solution. The slow addition of phosphate solution took 30 minutes whilst being magnetically stirred at ~ 400 rpm for 60 minutes.

The platelet – like particles that were synthesised by the slow dropping technique appeared to be well crystallised, compared to those synthesised by the fast dropping technique. The latter appeared to be poorly crystallised due to the presence of grooves, indicating incomplete crystallinity of particles, which was probably due to the short addition and stirring time of reactants. This suggested that the crystallinity was influenced by the addition time of solution – containing PO_4^{3-} to solution – containing Ca^{2+} , while the stirring time influenced the particles' size and shape (12). This was supported by the unchanged morphology of needle – like particles (Figure 4.1.5) that were aged under static conditions (non – stirred) for 2, 4, and 6 weeks. Figure 4.1.11 shows the volume – based distribution of CaP particles (second reaction), as measured by the Malvern Mastersizer 2000E, with standard percentile values $d(0.1)$, $d(0.5)$, $d(0.9)$, and volume weighted mean $D[4,3]$. The particles had a volume weighted mean $D[4,3]$ of $51.2 \mu\text{m}$ with ± 1 standard deviation error bar, as shown in Figure 4.1.12.

SEM-EDX measurements (element weight percentage) of CaP powders that were synthesised under room temperature and as – prepared pH 5.4 ± 0.2 conditions by the first (fast addition for 15 minutes and stirring for 30 minutes) and second (slow addition for 30 minutes and stirring for 60 minutes) reactions are shown in Table 4.1.2. The SEM-EDX measurements

indicated a Ca:P ratio of 1.0 for CaP powders that were precipitated from the first and second reactions.

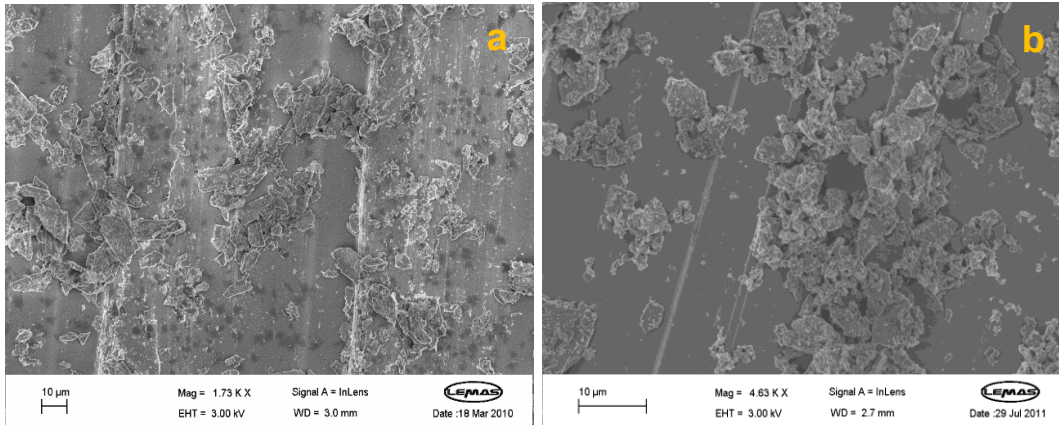


Figure 4.1.10 SEM of CaP particles synthesised under room temperature and pH 5.4 ± 0.2 conditions, by (a) the first reaction (fast addition for 15 minutes and stirring for 30 minutes) and (b) the second reaction (slow addition for 30 minutes and stirring for 60 minutes).

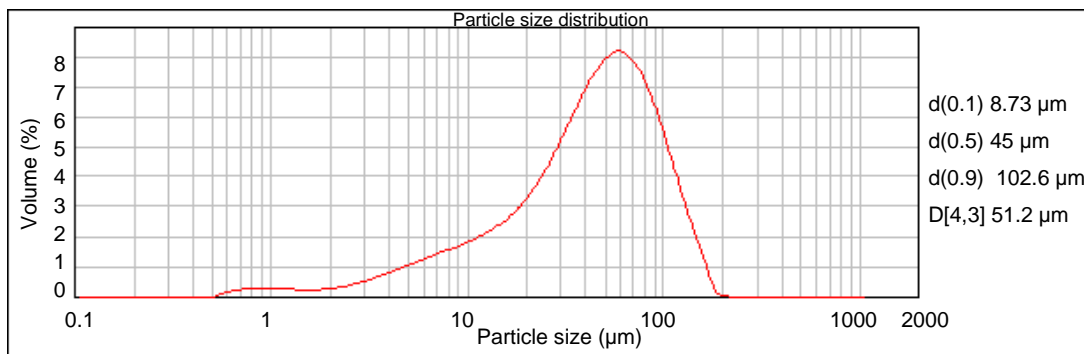


Figure 4.1.11 Particle size distribution of CaP synthesised under room temperature and pH 5.4 ± 0.2 conditions, by the second reaction (slow addition for 30 minutes and stirring for 60 minutes).

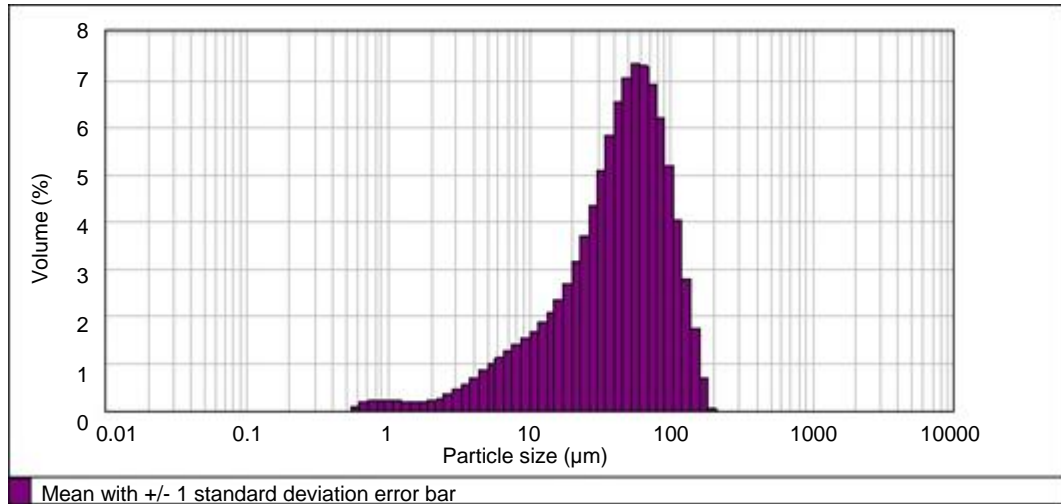


Figure 4.1.12 Statistics graph of CaP synthesised under room temperature and pH 5.4 ± 0.2 conditions by the second reaction (addition for 30 minutes and stirring for 60 minutes), showing the mean with ± 1 standard deviation error bar.

Table 4.1.2 SEM-EDX measurements (element weight percentage) for CaP synthesised under room temperature and as – prepared pH 5.4 ± 0.2 conditions (first and second reactions)

Element	CaP-undoped pH5 RT first reaction	CaP-undoped pH5 RT second reaction
	Weight %	
O K	50.09	46.82
P K	20.48	18.90
Ca K	21.71	20.37
Ca:P ratio	1.06	1.07

XRD patterns of CaP powders that were synthesised under room temperature and as – prepared pH 5.4 ± 0.2 conditions by the first (CaP-undoped pH5 RT 1st reaction) and second (CaP-undoped pH5 RT 2nd reaction) reactions are shown in Figures 4.1.13 and 4.1.14, respectively. The XRD patterns indicated the formation of a monetite phase in the case of CaP powder that was synthesised by the first reaction, and the formation of a brushite phase in the case of CaP powder that was synthesised by the second reaction. The XRD patterns are in good agreement with monetite and brushite JCPDS files 01-070-1425 and 01-072-0713, respectively. The XRD pattern of CaP powder that was synthesised by the second reaction (CaP-undoped pH 5 RT 2nd reaction) showed a negligible monetite peak at 2 theta 26.3° , compared to the major peaks of brushite. The main Miller indices (*hkl*) in Table 4.1.3 and Table 4.1.4 correspond to monetite JCPDS file 01-070-1425 and brushite JCPDS file 01-072-0713, respectively, which confirmed the crystallographic data of the synthesised monetite and brushite phases, respectively.

The Miller indices (*hkl*) and 2 theta of CaP that was synthesised under room temperature and as – prepared pH 5.4 ± 0.2 conditions (CaP-undoped pH5 RT) by the first and second reactions (monetite and brushite, respectively) were refined in the triclinic and monoclinic systems, respectively, using UnitCell program (Tim Holland's software), to determine the crystallographic parameters. The latter were calculated using 1.54 \AA wavelength and minimising the sum of squares of residuals in 2 theta.

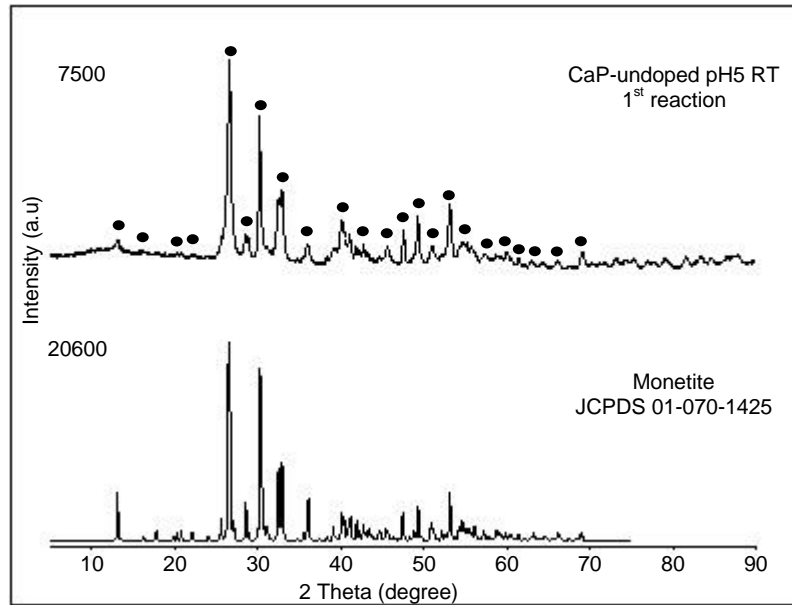


Figure 4.1.13 XRD pattern of CaP synthesised under room temperature and as – prepared pH 5.4 ± 0.2 conditions by the first reaction (addition for 15 minutes and stirring for 30 minutes). Marked peaks (●) were assigned to monetite JCPDS file 01-070-1425.

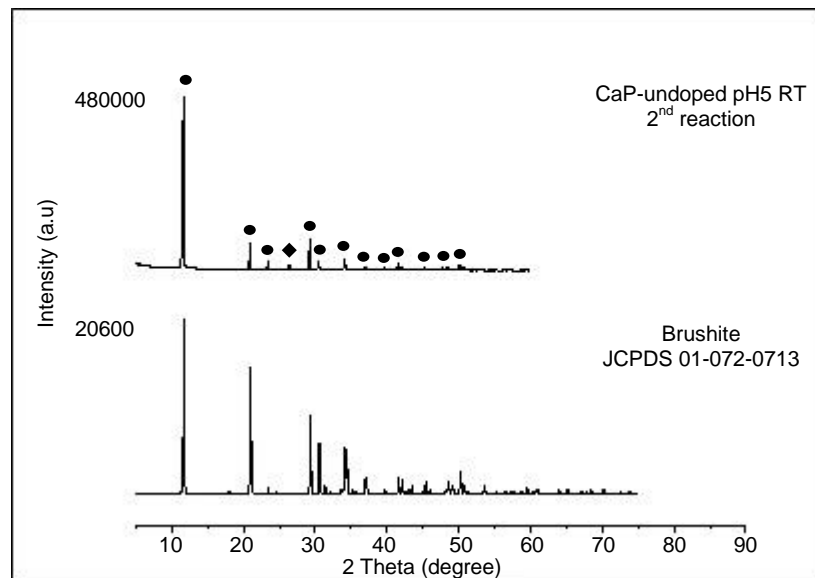


Figure 4.1.14 XRD pattern of CaP synthesised under room temperature and as – prepared pH 5.4 ± 0.2 conditions by the second reaction (addition for 30 minutes and stirring for 60 minutes). Marked peaks (●) were assigned to brushite JCPDS file 01-072-0713, while one peak (◆) was assigned to monetite JCPDS file 01-070-1425.

Table 4.1.3 XRD 2 theta (2θ [°]), d – spacing (d [Å]), intensity (I [%]), and Miller indices (*hkl*) for monetite JCPDS file 01-070-1425 and CaP-undoped pH5 RT (1st reaction)

Miller indices			Monetite JCPDS file 01-070-1425			CaP-undoped pH5 RT (1 st reaction)		
<i>h</i>	<i>k</i>	<i>l</i>	2θ [°]	d [Å]	I [%]	2θ [°]	d [Å]	I [%]
0	0	1	13.09	6.75	23.1	13.19	6.70	12.1
1	1	1	25.60	3.47	14.5	-	-	-
0	0	2	26.36	3.37	93.2	25.93	3.43	10.95
-1	0	2	26.59	3.34	100	26.47	3.36	100
-1	-1	2	28.5	3.12	28.5	28.60	3.12	5.54
1	2	0	30.18	2.95	86.9	30.22	2.95	12.04
-1	-2	1	30.39	2.93	45.5	30.46	2.93	5.37
1	0	2	32.39	2.76	19	31.80	2.81	45.1
2	0	1	32.53	2.74	36.4	32.23	2.77	21.22
-2	0	2	32.82	2.72	59.3	32.93	2.71	39.34
0	-2	2	35.85	2.50	20.4	35.48	2.52	3
2	1	1	35.94	2.49	14.9	36.05	2.49	4.31
0	0	3	40.01	2.25	18.6	39.83	2.26	14.57
-1	2	2	40.25	2.23	14.6	40.13	2.24	27.45
2	-2	1	41.68	2.16	16.2	41.97	2.15	4.7
-3	2	0	49.11	1.85	24.6	49.48	1.84	16.83

Table 4.1.4 XRD 2 theta (2θ [°]), d – spacing (d [Å]), intensity (I [%]), and Miller indices (*hkl*) for brushite JCPDS file 01-072-0713 and CaP-undoped pH5 RT (2nd reaction)

Miller indices			Brushite JCPDS file 01-072-0713			CaP-undoped pH5 RT (2 nd reaction)		
<i>h</i>	<i>k</i>	<i>l</i>	2θ [°]	d [Å]	I [%]	2θ [°]	d [Å]	I [%]
0	2	0	11.65	7.59	100.0	11.6	7.62	100
1	2	-1	20.94	4.23	79.5	20.88	4.25	15.02
0	4	0	23.42	3.79	4.6	23.36	3.80	5.4
-	-	-	-	-	-	26.33	3.38	1.98
1	4	-1	29.29	3.04	53.7	29.22	3.05	17.36
1	2	1	30.54	2.92	34.9	30.44	2.93	4.87
1	5	0	34.17	2.62	32.4	34.07	2.63	5.73
2	0	0	34.43	2.60	19.9	34.34	2.61	2.21
1	4	1	36.92	2.43	10.2	36.80	2.44	1.86
1	5	-2	41.58	2.17	12.4	41.48	2.17	3.3
2	4	0	42.06	2.14	10.9	41.95	2.15	1.85

Unit cell parameters of CaP that were synthesised by the first (CaP-undoped pH5 RT, 1st reaction) and second (CaP-undoped pH5 RT, 2nd reaction) reactions are shown in Table 4.1.5. The results indicated that the crystal structure of CaP (CaP-undoped pH 5 RT, 1st reaction) was in a triclinic system with space group P-1, whereas the crystal structure of CaP (CaP-undoped pH 5 RT, 2nd reaction) was in a monoclinic system with space group Ia. Unit cell parameters of CaP-undoped pH 5 RT, 1st reaction are in good agreement with those of monetite JCPDS file 01-070-1425, whereas those of CaP-undoped pH 5 RT, 2nd reaction are in good agreement with those of brushite JCPDS file 01-072-0713, except that *a* – axes (6.35 Å) and *c* – axes (5.83 Å) are opposite to those of brushite JCPDS file 01-072-0713, 5.81 Å and 6.23 Å, respectively. This indicated particle growth in *a* – axes rather than reported growth in *c* – axes (548). The results also indicated that the synthesis of CaP by the second reaction (CaP-undoped pH 5 RT, 2nd reaction) led to the formation of brushite with smaller cell volume by 184.8 Å³.

Table 4.1.5 Unit cell parameters for CaP-undoped pH5 RT (1st reaction) and CaP-undoped pH5 RT (2nd reaction), compared to those of monetite JCPDS file 01-070-1425 and brushite JCPDS file 01-072-0713

Cell parameter	CaP-undoped pH5 RT (1st reaction)	Std.D	Monetite JCPDS file 01-070-1425	CaP-undoped pH5 RT (2nd reaction)	Std.D	Brushite JCPDS file 01-072-0713
a (Å)	6.91	0.001	6.91	6.35	0.0006	5.81
b (Å)	6.63	0.001	6.62	15.18	0.001	15.18
c (Å)	6.99	0.002	6.99	5.83	0.0005	6.23
Alpha (°)	95.99	0.02	96.34	90	-	90
Beta (°)	103.82	0.01	103.82	118.6	0.007	116.43
Gamma (°)	88.21	0.01	88.33	90	-	90
Cell volume (Å ³)	310.06	0.06	309.28	494.86	0.05	492.91

Std.D = Standard deviation

CaP powders that were synthesised under room temperature and as – prepared pH 5.4 ± 0.2 conditions by the second reaction were investigated by hot stage XRD from $\sim 25^\circ\text{C}$ up to 800°C . The hot stage XRD patterns are shown and compared to JCPDS file references in Figures 4.1.15 – 4.1.18. The XRD pattern in Figure 4.1.15 indicated that the brushite phase was transformed into monetite phase upon heating at 200°C due to the dehydration of brushite, which is in good agreement with monetite JCPDS file 01-070-1425. The XRD pattern in Figure 4.1.16 indicated the formation of calcium pyrophosphate phase ($\beta\text{-Ca}_2\text{P}_2\text{O}_7$) at 400°C , which is in good agreement with calcium pyrophosphate JCPDS file 00-009-0346. The XRD patterns in Figures 4.1.17 and 4.1.18 indicated that calcium pyrophosphate phase ($\beta\text{-Ca}_2\text{P}_2\text{O}_7$) remained unchanged at 600°C and 800°C , respectively. The phase transformations from brushite to monetite at around 200°C and from monetite to calcium pyrophosphate ($\beta\text{-Ca}_2\text{P}_2\text{O}_7$) at around 400°C are also in good agreement with the reported phase transformations between 200°C and 800°C (550, 551).

Since CaP powder that was synthesised by the second reaction had relatively better crystallinity, the second reaction parameters (addition for 30 minutes and stirring at ~ 400 rpm for 60 minutes) were adopted to synthesis all CaP powders. The slow addition for 30 minutes and longer stirring time for 60 minute appeared to allow sufficient time for the reaction of reactants to take place, and consequently, the formation of a particular CaP phase with improved crystallinity. These parameters were adopted alongside other synthesis parameters, as stated before, including pH 5.4 ± 0.2 , pH 10 ± 0.2 , room temperature, 200°C hydrothermal conditions, and reaction time for 24 hours.

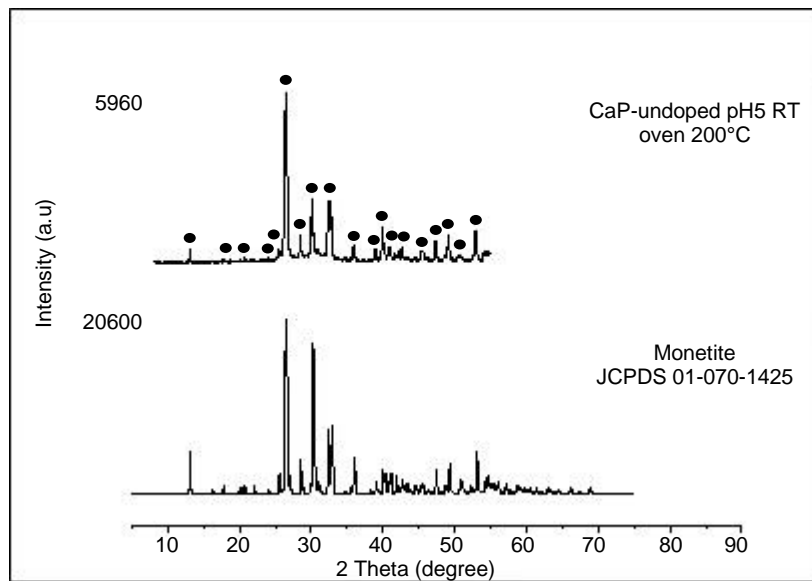


Figure 4.1.15 Hot stage XRD at 200°C of CaP synthesised under room temperature and as – prepared pH 5.4 ± 0.2 conditions by the second reaction, compared to monetite JCPDS file 01-070-1425. Marked peaks (●) were assigned to monetite.

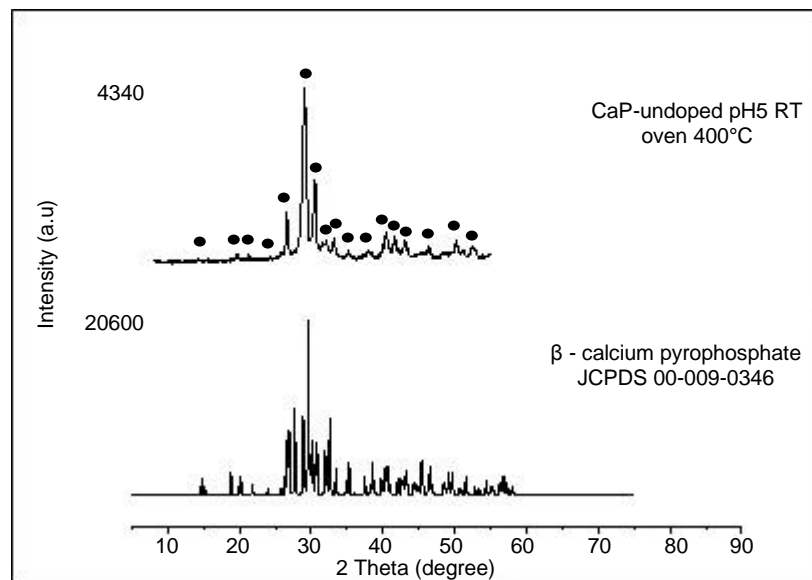


Figure 4.1.16 Hot stage XRD at 400°C of CaP synthesised under room temperature and as – prepared pH 5.4 ± 0.2 conditions by the second reaction, compared to calcium pyrophosphate JCPDS file 00-009-0346. Marked peaks (●) were assigned to calcium pyrophosphate (β-Ca₂P₂O₇).

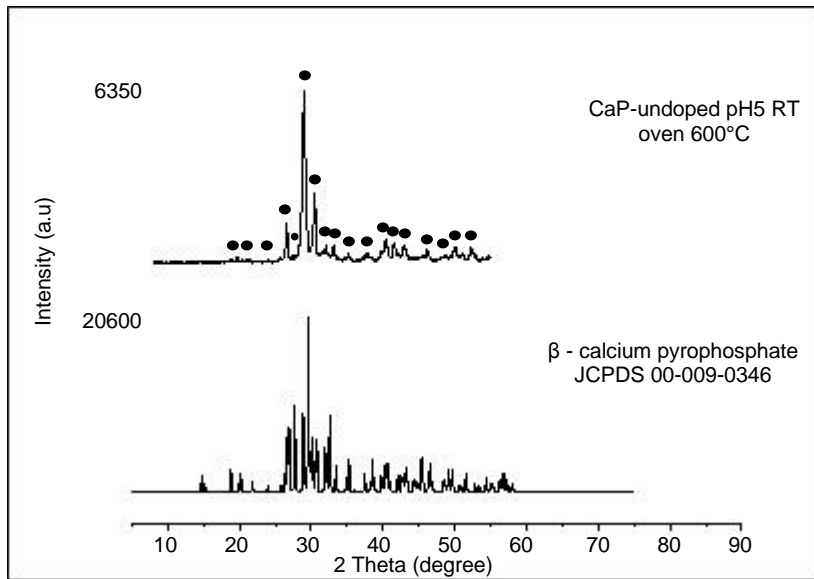


Figure 4.1.17 Hot stage XRD at 600°C of CaP synthesised under room temperature and as – prepared pH 5.4 ± 0.2 conditions by the second reaction, compared to calcium pyrophosphate JCPDS file 00-009-0346. Marked peaks (●) were assigned to calcium pyrophosphate (β - $\text{Ca}_2\text{P}_2\text{O}_7$).

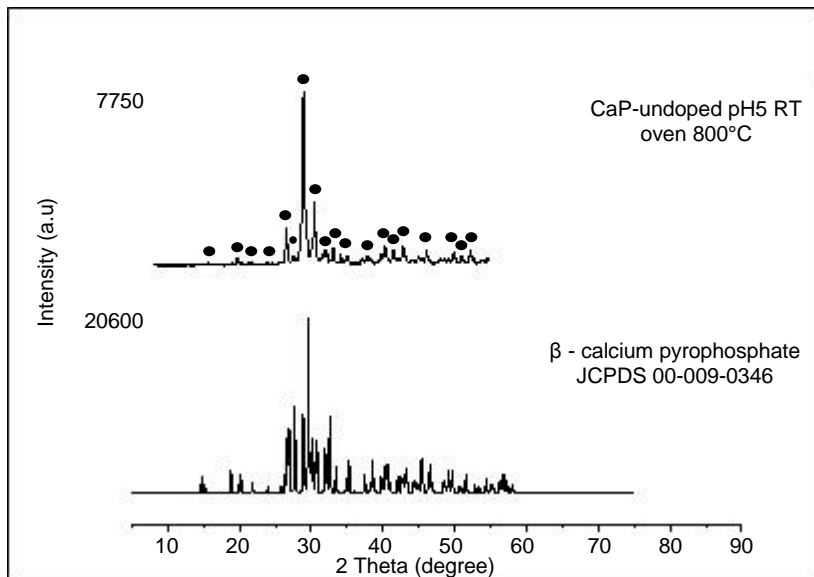


Figure 4.1.18 Hot stage XRD at 800°C of CaP synthesised under room temperature and as – prepared pH 5.4 ± 0.2 conditions by the second reaction, compared to calcium pyrophosphate JCPDS file 00-009-0346. Marked peaks (●) were assigned to calcium pyrophosphate (β - $\text{Ca}_2\text{P}_2\text{O}_7$).

4.1.2 CaP (pH 10 ± 0.2, RT)

Representative SEM of CaP powder that was synthesised under room temperature and pH 10 ± 0.2 conditions is shown in Figure 4.1.19. Figure 4.1.19 (a) shows micrometre agglomerates with platelet – like morphology. The agglomerates (clusters) appeared to show platelet – like particles in the nanoscale, as shown in Figure 4.1.19 (b). The micrometre particles appeared to have an amorphous – like morphology, which was probably due to the agglomeration of fine platelet – like particles, as shown in Figure 4.1.19 (b).

The particles varied in size from micrometre agglomerates to nanometre platelet – like particles. Figure 4.1.20 shows the volume – based distribution of CaP particles, as measured by the Mastersizer 2000E, with standard percentile values $d(0.1)$, $d(0.5)$, $d(0.9)$, and volume weighted mean $D[4,3]$. The particles had a volume weighted mean $D[4,3]$ of 81.4 μm with a ± 1 standard deviation error bar, as shown in Figure 4.1.21. The values seem to be in good agreement with the agglomerates shown by SEM.

SEM-EDX measurements (element weight percentage) of CaP that was synthesised under room temperature and pH 10 ± 0.2 conditions are shown in Table 4.1.6. The SEM-EDX measurements of five spectra, as shown by SEM in Figure 4.1.22, indicated a mean Ca:P ratio of 1.29 (~ 1.3).

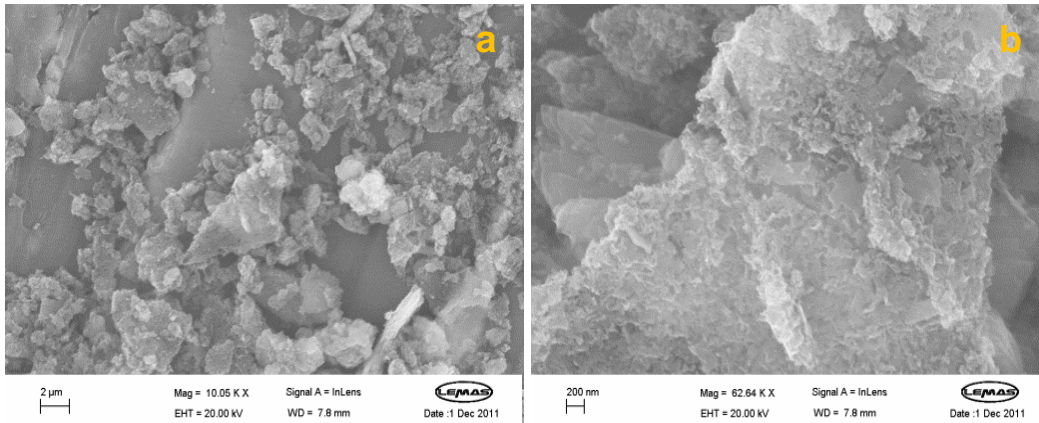


Figure 4.1.19 SEM of CaP particles synthesised under room temperature and pH 10 ± 0.2 conditions, showing (a) micrometre agglomerated particles and (b) nanometre platelet – like CaP particles.

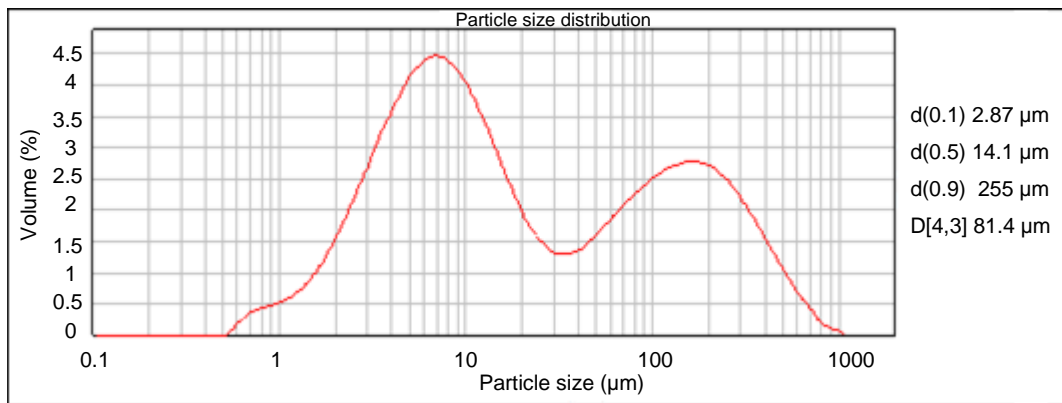


Figure 4.1.20 Particle size distribution of CaP synthesised under room temperature and pH 10 ± 0.2 conditions.

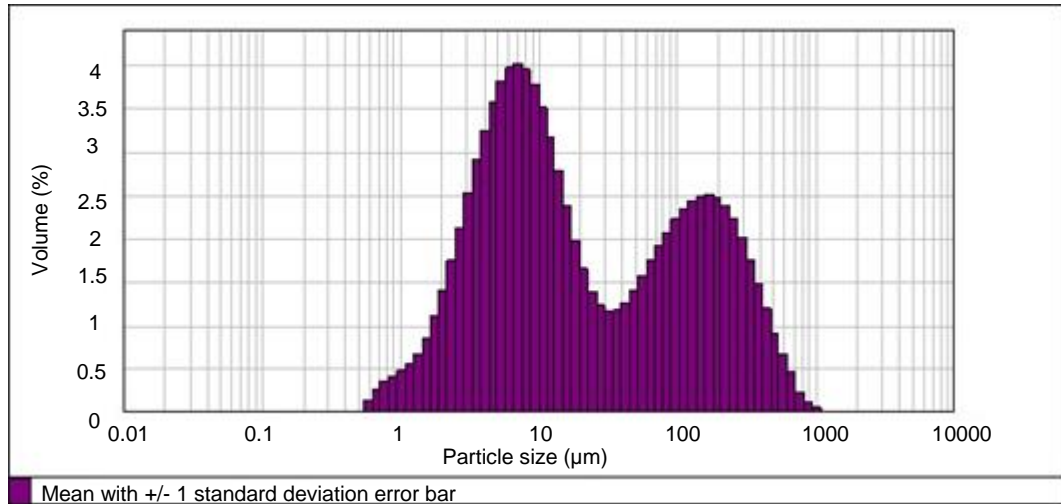


Figure 4.1.21 Statistics graph of CaP synthesised under room temperature and pH 10 ± 0.2 conditions, showing the mean with ± 1 standard deviation error bar.

Table 4.1.6 SEM-EDX measurements (element weight percentage) for CaP synthesised under room temperature and pH 10 ± 0.2 conditions

Spectrum	O	P	Ca	Ca:P ratio
Spectrum 1	50.22	15.71	21.06	1.34
Spectrum 2	62.2	11.59	14.35	1.23
Spectrum 3	61.33	11.79	14.31	1.21
Spectrum 4	58.67	11.19	15.53	1.38
Spectrum 5	62.33	10.31	13.48	1.30
Mean	58.95	12.12	15.75	1.29
Std. Deviation	5.1	2.09	3.06	0.07

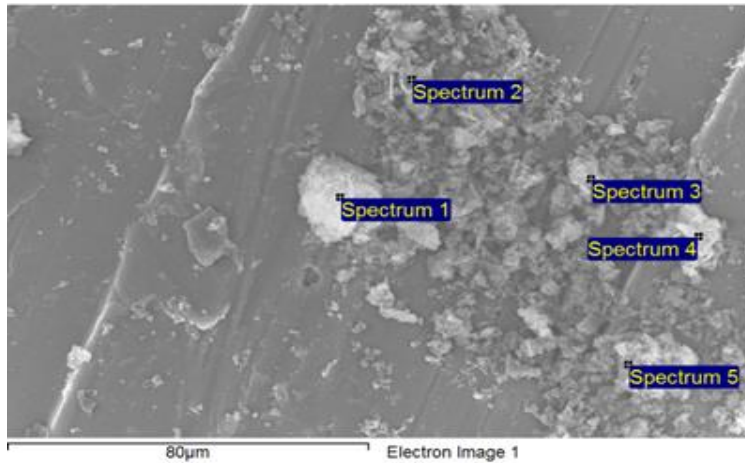


Figure 4.1.22 SEM of CaP synthesised under room temperature and pH 10 ± 0.2 conditions, showing the obtained EDX spectra.

XRD pattern of CaP synthesised under room temperature and pH 10 ± 0.2 conditions (CaP-undoped pH 10 RT) is shown in Figure 4.1.23. The XRD pattern indicated the formation of HAp and brushite phases, which are in good agreement with HAp JCPDS file 009-0432 and brushite JCPDS file 01-072-0713. Reduced peak intensities were observed, particularly at 2θ 13° , which could be due to inhibition of particle growth in the c – axis under high pH levels (550). The main Miller indices (hkl) in Table 4.1.7 correspond to HAp JCPDS file 009-0432 and brushite JCPDS file 01-072-0713, which confirmed the crystallographic data of the synthesised HAp and brushite phases. The broadening of HAp peaks reflected the nanosize of platelet – like particles, shown by SEM in Figure 4.1.19 (b). The XRD indicated that increasing the pH of CaP starting mixture to pH 10 ± 0.2 promoted the formation of HAp phase, but together with a brushite phase, the latter which was formed under as – prepared pH 5.4 ± 0.2 conditions.

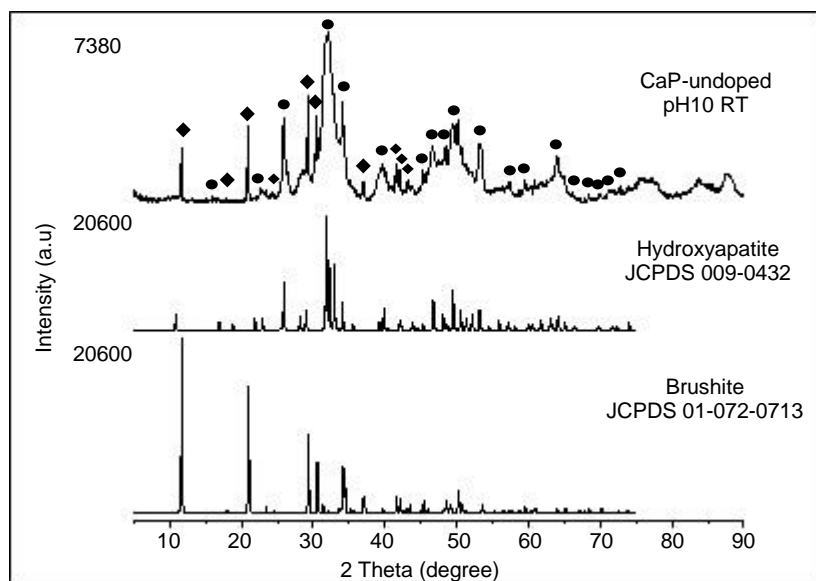


Figure 4.1.23 XRD pattern of CaP synthesised under room temperature and pH 10 ± 0.2 conditions. Marked peaks (●) were assigned to HAp JCPDS file 009-0432 and (◆) were assigned to brushite JCPDS file 01-072-0713.

Table 4.1.7 XRD 2 theta (2θ [°]), d – spacing (d [Å]), intensity (I [%]), and Miller indices (hkl) for HAp JCPDS file 009-0432, brushite JCPDS file 01-072-0713, and CaP pH 10 RT

Miller indices			HAp JCPDS file 009-0432			CaP pH10 RT		
h	k	l	2θ [°]	d [Å]	I [%]	2θ [°]	d [Å]	I [%]
1	1	1	22.90	3.88	10	22.70	3.91	4.92
0	0	2	25.87	3.44	40	25.87	3.44	48.93
2	1	1	31.77	2.81	100	31.65	2.82	93.58
1	1	2	32.19	2.77	60	32.13	2.78	100
2	0	2	34.04	2.63	25	34.11	2.62	58.7
3	1	0	39.81	2.26	20	39.70	2.27	19.54
2	2	2	46.71	1.94	30	46.53	1.95	23.84
3	1	2	48.10	1.89	16	48.42	1.87	24.29
2	1	3	49.46	1.84	40	49.33	1.84	38.98
0	0	4	53.14	1.72	20	53.16	1.72	28.39
3	0	4	64.08	1.45	13	63.96	1.45	23.89
Miller indices			Brushite JCPDS file 01-072-0713			CaP pH10 RT		
h	k	l	2θ [°]	d [Å]	I [%]	2θ [°]	d [Å]	I [%]
0	2	0	11.65	7.59	100.0	11.60	7.62	32.47
1	2	-1	20.94	4.23	79.5	20.90	4.24	48.12
1	4	-1	29.29	3.04	53.7	29.2	3.05	60.23
1	2	1	30.54	2.92	34.9	30.47	2.93	46.03
1	4	1	36.92	2.43	10.2	36.84	2.43	10.09
1	5	-2	41.58	2.17	12.4	41.54	2.17	19.11
2	4	0	42.06	2.14	10.9	42.01	2.15	14.89

4.1.3 CaP (pH 5.4 ± 0.2, 200°C hydrothermal)

Representative SEM of CaP powder that was synthesised under as – prepared pH 5.4 ± 0.2 and 200°C hydrothermal conditions is shown in Figure 4.1.24. Figure 4.1.24 (a) shows micrometre agglomerates of CaP particles, while Figure 4.1.24 (b) shows rod – like particles in the nanometre scale. The CaP agglomerates (Figure 4.1.24 b) appeared to have an amorphous – like morphology, which was probably due to the agglomeration of nanosized particles. The particle size varied from micrometre agglomerates to nanometre rod – like particles. Figure 4.1.25 shows the volume – based distribution of CaP particles, as measured by the Malvern Mastersizer 2000E, with standard percentile values $d(0.1)$, $d(0.5)$, $d(0.9)$, and volume weighted mean $D[4,3]$. The particles had a volume weighted mean $D[4,3]$ of 101 μm with a ± 1 standard deviation error bar, as shown in Figure 4.1.26. The values seem to be in good agreement with the agglomerates shown by SEM.

SEM-EDX measurements (element weight percentage) of CaP powder that was synthesised under as – prepared pH 5.4 ± 0.2 and 200°C hydrothermal conditions are shown in Table 4.1.8. The SEM-EDX measurements of five spectra, as shown by SEM in Figure 4.1.27, indicated a mean Ca:P ratio of 1.73. Although the spectra were taken from CaP particles at the time of the measurement, spectrum number three was way out, compared to the other spectra, which could be because it was not centred onto the CaP particle, and thus, it was influenced by the carbon – based SEM stub.

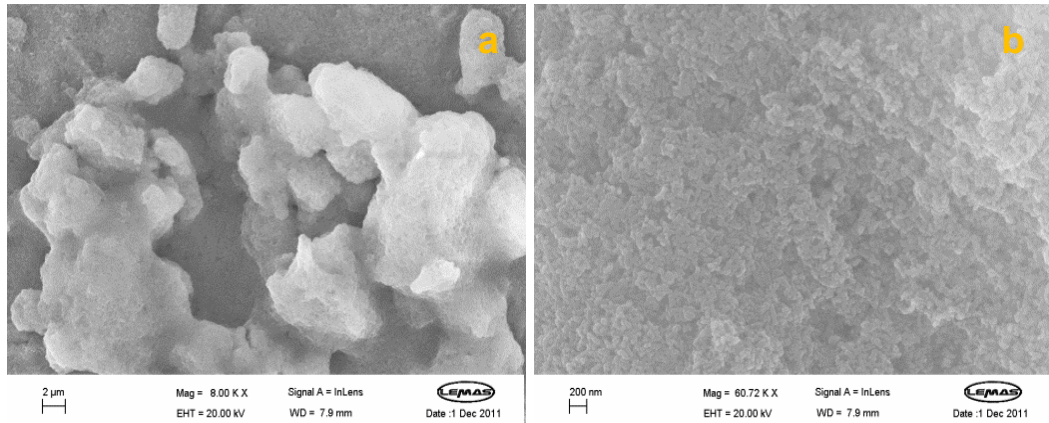


Figure 4.1.24 SEM of CaP synthesised under as – prepared pH 5.4 ± 0.2 and 200°C hydrothermal conditions, showing (a) micrometre agglomerates/clusters of CaP particles and (b) nanometre rod – like CaP particles.

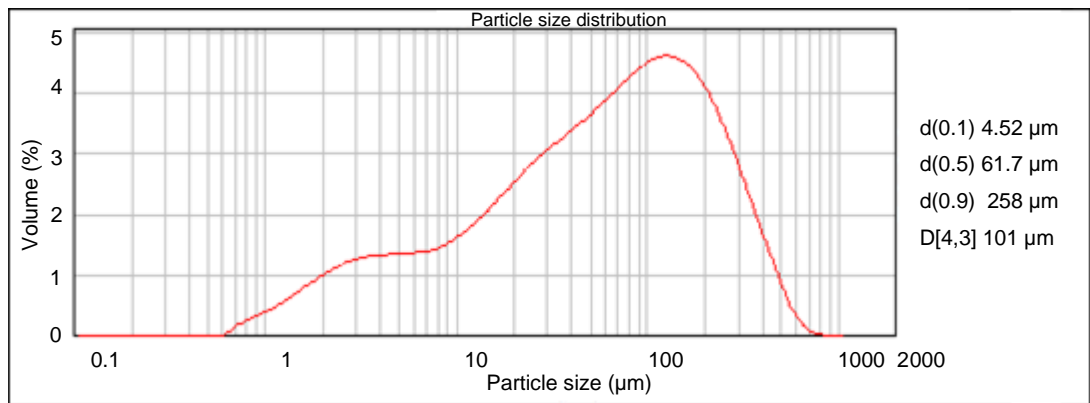


Figure 4.1.25 Particle size distribution of CaP synthesised under pH 5.4 ± 0.2 and 200°C hydrothermal conditions.

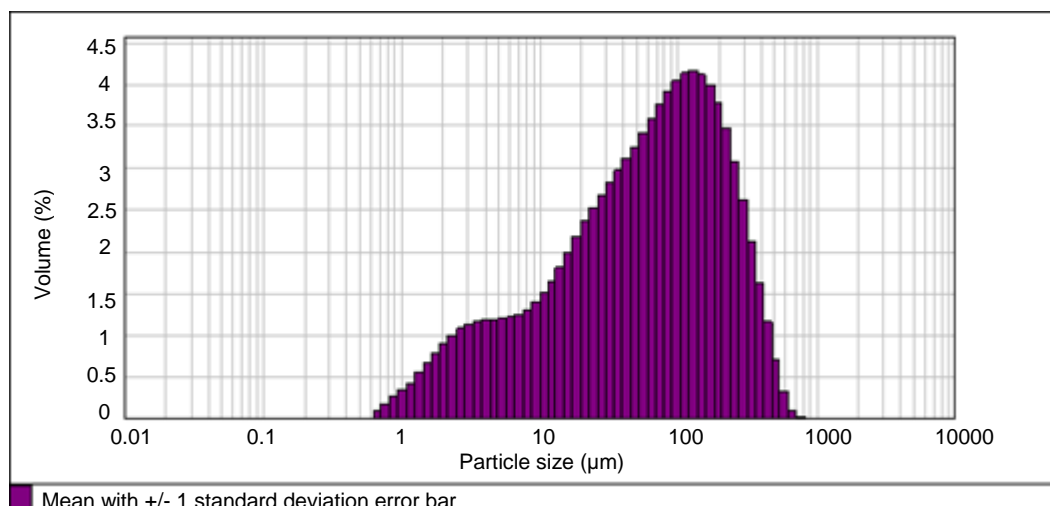


Figure 4.1.26 Statistics graph of CaP synthesised under pH 5.4 ± 0.2 and 200°C hydrothermal conditions, showing the mean with ± 1 standard deviation error bar.

Table 4.1.8 SEM-EDX measurements (element weight percentage) for CaP synthesised under as – prepared pH 5.4 ± 0.2 and 200°C hydrothermal conditions

Spectrum	O	P	Ca	Ca:P ratio
Spectrum 1	46.07	15.03	27.62	1.83
Spectrum 2	48.34	14.33	26.34	1.83
Spectrum 3	60.49	3.72	5.78	1.55
Spectrum 4	67.42	6.27	10.2	1.62
Spectrum 5	52	12.46	22.95	1.84
Mean	54.87	10.36	18.58	1.73
Std. Deviation	8.91	5.07	9.94	0.1

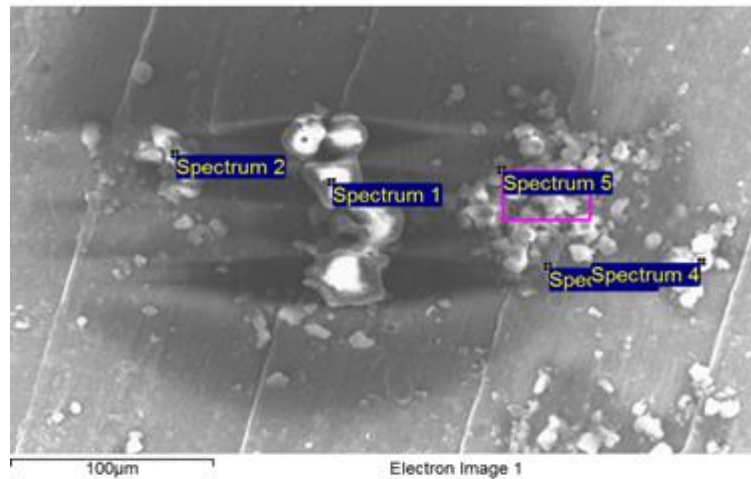


Figure 4.1.27 SEM of CaP synthesised under as – prepared pH 5.4 ± 0.2 and 200°C hydrothermal conditions, showing the obtained EDX spectra.

XRD pattern of CaP (CaP-undoped pH5 200°C hydrothermal) that was synthesised under as – prepared pH 5.4 ± 0.2 and 200°C hydrothermal conditions is shown in Figure 4.1.28. The XRD pattern indicated the formation of a HAp phase, which is in good agreement with HAp JCPDS file 009-0432. The formation of HAp is also in good agreement with Ca:P ratio of 1.73.

The main Miller indices (hkl) in Table 4.1.9 correspond to HAp JCPDS file 009-0432, which confirmed the crystallographic data of the synthesised HAp phase. The peaks of XRD pattern appeared to be broad enough to reflect the nanosize of HAp particles shown by SEM in Figure 4.1.24 (b), even though the particle size analysis indicated the particle size in the micrometre scale.

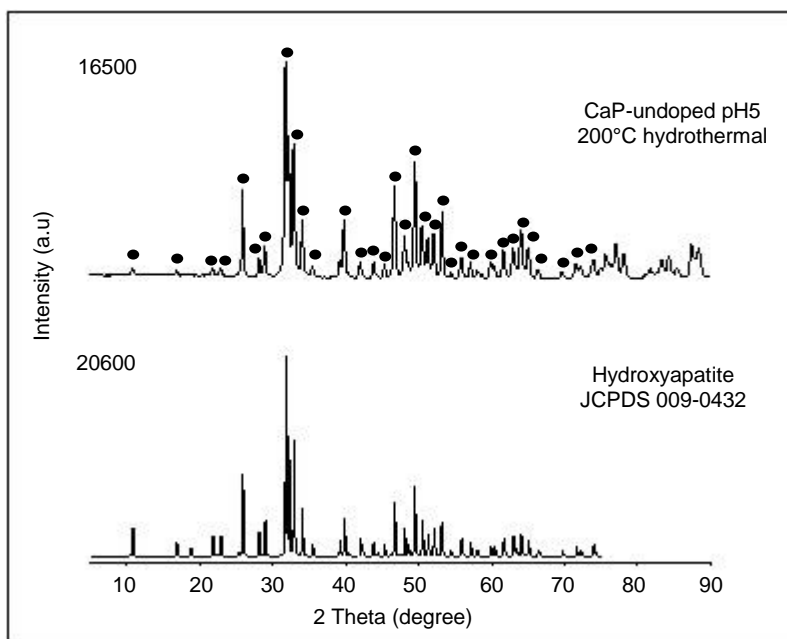


Figure 4.1.28 XRD pattern of CaP synthesised under as – prepared pH 5.4 ± 0.2 and 200°C hydrothermal conditions, compared to HAp JCPDS file 009-0432. Marked peaks (●) were assigned to HAp.

Table 4.1.9 XRD 2 theta (2θ [°]), d – spacing (d [Å]), intensity (I [%]), and Miller indices (*hkl*) for HAp JCPDS file 009-0432 and CaP pH5 200°C hydrothermal

Miller indices			HAp JCPDS file 009-0432			CaP pH5 200°C hydrothermal		
<i>h</i>	<i>k</i>	<i>l</i>	2θ [°]	d [Å]	I [%]	2θ [°]	d [Å]	I [%]
1	0	0	10.82	8.17	12	10.74	8.23	3.1
2	0	0	21.82	4.07	10	21.71	4.09	3.17
1	1	1	22.90	3.88	10	22.83	3.89	3.93
0	0	2	25.87	3.44	40	25.85	3.44	42.24
1	0	2	28.12	3.17	12	28.10	3.17	9.16
2	1	0	28.96	3.08	18	28.88	3.09	13.86
2	1	1	31.77	2.81	100	31.72	2.82	100
1	1	2	32.19	2.77	60	32.17	2.78	64.37
3	0	0	32.90	2.72	60	32.86	2.72	61.61
2	0	2	34.04	2.63	25	34.03	2.63	25.46
3	1	0	39.81	2.26	20	39.74	2.26	27.04
2	2	2	46.71	1.94	30	46.66	1.94	42.11
3	1	2	48.10	1.89	16	48.03	1.89	17.78
2	1	3	49.46	1.84	40	49.45	1.84	52.6
3	2	1	50.49	1.80	20	50.43	1.80	22.42
4	1	0	51.28	1.78	12	51.21	1.78	16.37
4	0	2	52.10	1.75	16	52.03	1.75	18.83
0	0	4	53.14	1.72	20	53.17	1.72	29.62
3	0	4	64.08	1.45	13	63.96	1.45	20.76

4.1.4 CaP (pH 10 ± 0.2, 200°C hydrothermal)

Representative SEM of CaP that was synthesised under pH 10 ± 0.2 and 200°C hydrothermal conditions is shown in Figure 4.1.29. Figure 4.1.29 (a) shows micrometre agglomerates of CaP particles, whereas Figure 4.1.29 (b) shows platelet – like and needle – like particles. The platelet – like particles appeared to be trapped in a mesh of needle – like particles, as shown in Figure 4.1.29 (b). The particle size varied from micrometre platelet – like particles to nanometre needle – like particles. Figure 4.1.30 shows the volume – based distribution of CaP particles, as measured by the Malvern Mastersizer 2000E, with standard percentile values $d(0.1)$, $d(0.5)$, $d(0.9)$, and volume weighted mean $D[4,3]$. The particles had a volume weighted mean $D[4,3]$ of 58.2 μm with a ± 1 standard deviation error bar, as shown in Figure 4.1.31. The values seem to be in good agreement with the agglomerates shown by SEM.

SEM-EDX measurements (element weight percentage) of CaP powder that was synthesised under pH 10 ± 0.2 and 200°C hydrothermal conditions are shown in Table 4.1.10. The SEM-EDX measurements of four spectra, as shown by SEM in Figure 4.1.32, indicated a mean Ca:P ratio of 1.66.

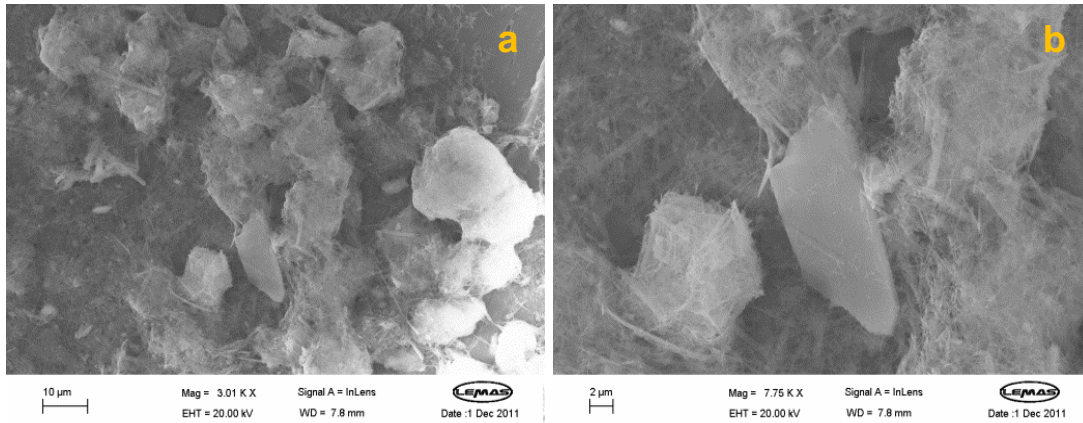


Figure 4.1.29 SEM of CaP powder synthesised under pH 10 ± 0.2 and 200°C hydrothermal conditions, showing (a) micrometre agglomerates/clusters of CaP particles and (b) platelet – like and needle – like particles.

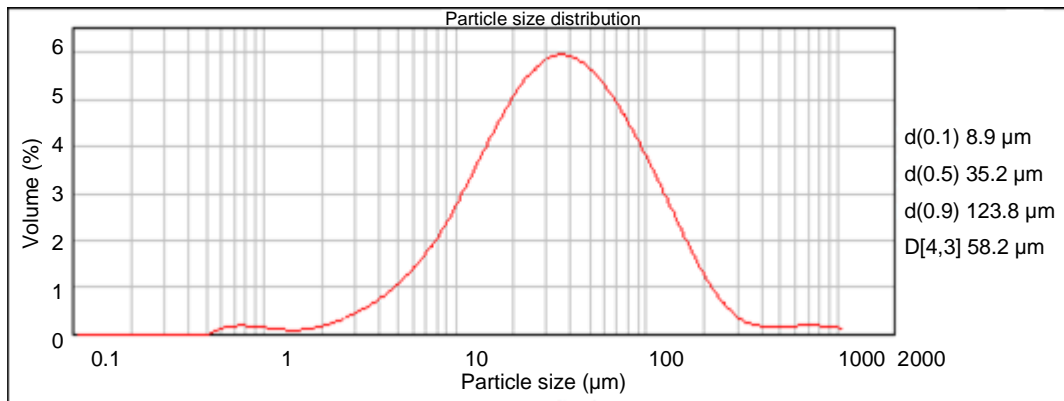


Figure 4.1.30 Particle size distribution of CaP synthesised under pH 10 ± 0.2 and 200°C hydrothermal conditions.

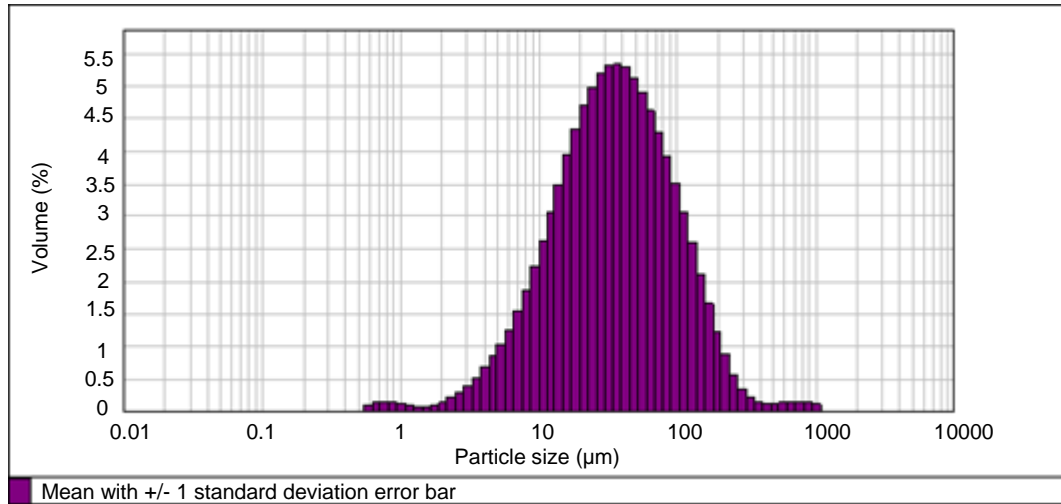


Figure 4.1.31 Statistics graph of CaP synthesised under pH 10 ± 0.2 and 200°C hydrothermal conditions, showing the mean with ± 1 standard deviation error bar.

Table 4.1.10 SEM-EDX measurements (element weight percentage) for CaP synthesised under pH 10 ± 0.2 and 200°C hydrothermal conditions

Spectrum	O	P	Ca	Ca:P ratio
Spectrum 1	55.05	10.76	18.01	1.67
Spectrum 2	58.26	9.57	15.53	1.62
Spectrum 3	52.38	11.48	20.07	1.74
Spectrum 4	55.6	10.45	17.2	1.64
Mean	55.32	10.57	17.7	1.66
Std. Deviation	2.41	0.79	1.89	0.05

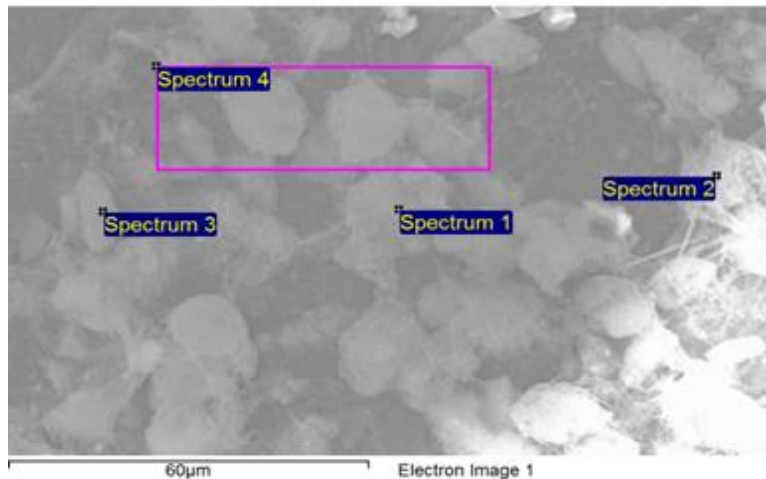


Figure 4.1.32 SEM of CaP synthesised under pH 10 ± 0.2 and 200°C hydrothermal conditions, showing the obtained EDX spectra.

The reasons for the formation of platelet – like particles together with needle – like particles under pH 10 ± 0.2 and 200°C hydrothermal conditions are unclear; however, this was most likely due to an incorrect pH reading of the CaP starting mixture. This conclusion was based on the comparison of XRD pattern (CaP-undoped pH10 200°C hydrothermal) with those obtained during the initial investigation (CaP-undoped pH10 200°C hydrothermal (initial investigation) and CaP-undoped pH8 200°C hydrothermal (initial investigation)), as shown in Figure 4.1.33. The XRD pattern (CaP-undoped pH10 200°C hydrothermal) is in good agreement with that (CaP-undoped pH8 200°C hydrothermal (initial investigation)) from the initial investigation. Although the XRD patterns (CaP-undoped pH10 200°C hydrothermal) and (CaP-undoped pH8 200°C hydrothermal (initial investigation)) are in good agreement, the SEM for (CaP-undoped pH8 200°C hydrothermal (initial investigation)) showed needle – like particles only (Figure 4.1.7 a). Repetition of the synthesis of this CaP batch (CaP-undoped pH10 200°C

hydrothermal) was not carried out, because the effect of pH 10 and 200°C hydrothermal conditions was already demonstrated during the initial investigation, which resulted in a single HAp phase with nanometre rod – like particles.

XRD pattern of CaP powder (CaP-undoped pH10 200°C hydrothermal) that was synthesised under pH 10 ± 0.2 and 200°C hydrothermal conditions is shown and compared to HAp JCPDS file 009-0432 and monetite JCPDS file 01-070-1425 in Figure 4.1.34. The XRD pattern indicated the formation of two phases of HAp and monetite, which are in good agreement with HAp JCPDS file 009-0432 and monetite JCPDS file 01-070-1425, respectively. The main Miller indices (*hkl*) in Tables 4.1.11 and 4.1.12 correspond to monetite JCPDS file 01-070-1425 and HAp JCPDS file 009-0432, respectively, which confirmed the crystallographic data of the synthesised monetite and HAp phases. This is also in good agreement with the formation of monetite platelet – like particles and HAp needle – like particles shown by SEM in Figure 4.1.29.

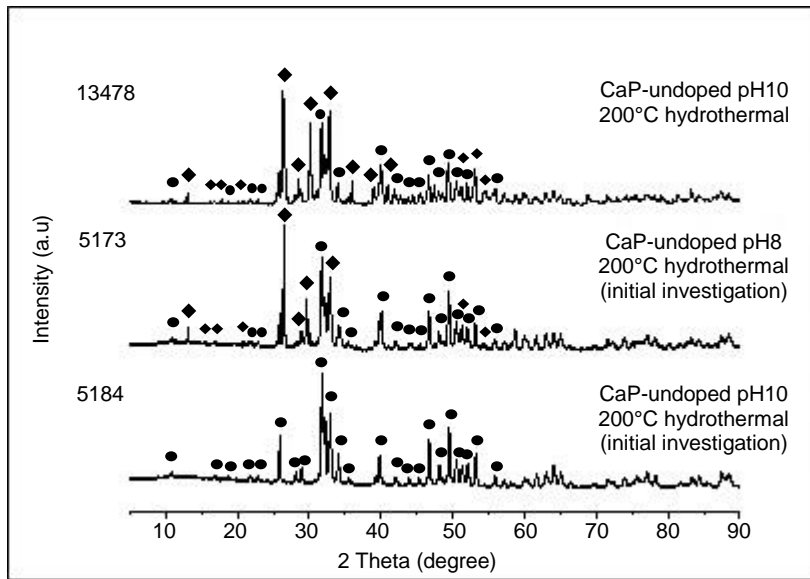


Figure 4.1.33 XRD pattern of CaP synthesised under pH 10 ± 0.2 and 200°C hydrothermal conditions, compared to the CaP synthesised under pH 8 ± 0.2 , pH 10 ± 0.2 and 200°C hydrothermal conditions from the initial investigation. Marked peaks (●) were assigned to HAp and (◆) were assigned to monetite.

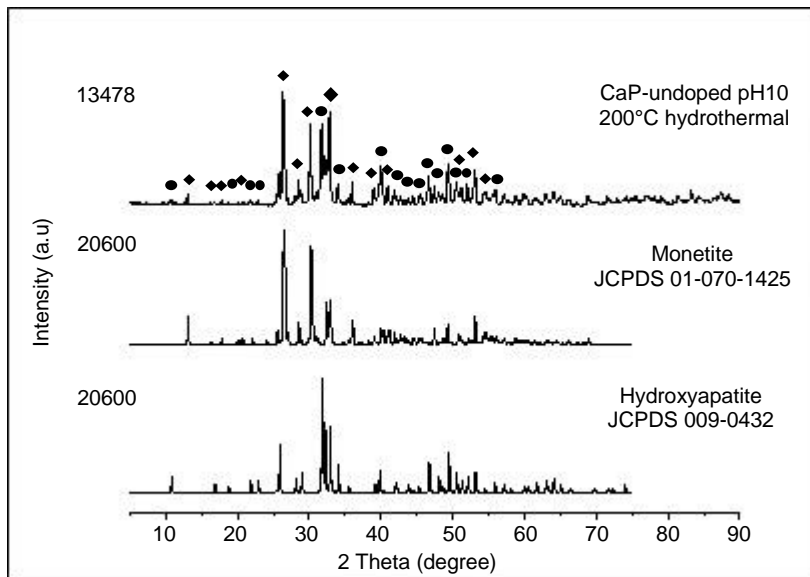


Figure 4.1.34 XRD pattern of CaP synthesised under pH 10 ± 0.2 and 200°C hydrothermal conditions, compared to HAp JCPDS file 009-0432 and monetite JCPDS file 01-070-1425. Marked peaks (●) were assigned to HAp and (◆) were assigned to monetite.

Table 4.1.11 XRD 2 theta (2θ [°]), d – spacing (d [Å]), intensity (I [%]), and Miller indices (hkl) for Monetite JCPDS file 01-070-1425 and CaP pH10 200°C hydrothermal

Miller indices			Monetite JCPDS file 01-070-1425			CaP pH10 200°C hydrothermal		
<i>h</i>	<i>k</i>	<i>l</i>	2θ	d [Å]	I [%]	2θ	d [Å]	I [%]
0	0	1	13.09	6.75	23.1	13.04	6.78	9.77
0	0	2	26.36	3.37	94.4	26.32	3.38	100
-1	0	2	26.59	3.34	100	26.59	3.35	56.83
-1	-1	2	28.5	3.12	28.5	28.47	3.13	19.98
1	2	0	30.18	2.95	86.9	30.10	2.96	70.76
1	0	2	32.39	2.76	19	32.43	2.76	37.13
-2	0	2	32.82	2.72	59.3	32.79	2.73	80.47
2	1	1	35.94	2.49	14.9	35.96	2.49	19.84
0	0	3	40.01	2.25	18.6	40.01	2.25	34.73
-1	2	2	40.25	2.23	14.6	40.96	2.20	17.75
2	-2	1	41.68	2.16	16.2	41.78	2.16	12.18
-3	2	0	49.11	1.85	24.6	49.40	1.84	31.06

Table 4.1.12 XRD 2 theta (2θ [°]), d – spacing (d [Å]), intensity (I [%]), and Miller indices (hkl) for HAp JCPDS file 009-0432 and CaP pH10 200°C hydrothermal

Miller indices			HAp JCPDS file 009-0432			CaP pH10 200°C hydrothermal		
<i>h</i>	<i>k</i>	<i>l</i>	2θ	d [Å]	I [%]	2θ	d [Å]	I [%]
1	0	0	10.82	8.17	12	10.73	8.23	3.03
2	0	0	21.82	4.07	10	21.77	4.08	2.31
1	1	1	22.90	3.88	10	22.79	3.90	3.66
0	0	2	25.87	3.44	40	25.81	3.45	28.87
1	0	2	28.12	3.17	12	28.05	3.18	5.58
2	1	0	28.96	3.08	18	28.83	3.09	11.92
2	1	1	31.77	2.81	100	31.68	2.82	69.54
1	1	2	32.19	2.77	60	32.11	2.78	40.3
3	0	0	32.90	2.72	60	32.79	2.73	80.47
2	0	2	34.04	2.63	25	33.99	2.63	16.62
3	1	0	39.81	2.26	20	40.01	2.25	34.73
2	2	2	46.71	1.94	30	46.62	1.94	22.96
3	1	2	48.10	1.89	16	48.01	1.89	7.91
2	1	3	49.46	1.84	40	49.40	1.84	31.06

CaP powders that were synthesised at different temperatures (room temperature and 200°C hydrothermal conditions) and different pH values (as – prepared pH 5.4 ± 0.2 and adjusted pH 10 ± 0.2) are compared in terms of their particle size distribution in Table 4.1.13. The refractive index and absorption index for CaP used in these calculations are 1.629 and 0.1, respectively. The measured median particle diameter $d(0.5)$, absolute deviation from median (uniformity), span, and the 10% and 90% size distribution by volume percentage (v%) for CaP particles are presented in Table 4.1.13.

The results indicated that the mean diameter $D[4,3]$ was lowest (51.2 μm) in the case of CaP-undoped pH5 RT and highest (101 μm) in the case of CaP-undoped pH5 200°C hydrothermal. In the case of CaP-undoped pH10 RT and CaP-undoped pH10 200°C hydrothermal, the mean diameter $D[4,3]$ was 81.4 μm and 58.2 μm , respectively. These values seem to be in good agreement with SEM of CaP agglomerates. Since the CaP powders (CaP-undoped pH10 RT and CaP-undoped pH10 200°C hydrothermal) are agglomerates of nanoparticles, the accuracy of particle size measurements depend on the quality of the powder dispersion.

The small span values in the case of CaP-undoped pH5 RT, CaP-undoped pH5 200°C hydrothermal, and CaP-undoped pH10 200°C hydrothermal indicated a narrow distribution, while the large span value in the case of CaP-undoped pH10 RT indicated a broad distribution. This indicated that the particles of CaP-undoped pH5 RT, CaP-undoped pH5 200°C hydrothermal, and CaP-undoped pH10 200°C hydrothermal are more uniform in size than CaP-undoped pH10 RT.

Table 4.1.13 Particle size data for CaP powders

Sample	d(0.1) μm	d(0.5) μm	d(0.9) μm	Uniformity	Span	D[4,3] μm
CaP-undoped pH5 RT	8.73	45	102.63	0.64	2.08	51.28
CaP-undoped pH10 RT	2.87	14.14	255	5.33	17.83	81.41
CaP-undoped pH5 200°C hydrothermal	4.52	61.72	258.83	1.29	4.12	101.72
CaP-undoped pH10 200°C hydrothermal	8.9	35.2	123.82	1.15	3.26	58.2

The SEM and XRD results indicated that temperature and pH of starting mixture are of great importance in producing a particular CaP phase with desired particle size and shape. The effect of pH of starting mixture on the CaP particle morphology was explained by the solution supersaturation and particles' surface charge (549). The increase of supersaturation with increasing pH levels may increase the nucleation rate, and consequently, reduces the particle size. Under high pH conditions, an increase in the particle shell negative charge causes particle repulsion, which may help maintaining the nanosize of particles. In addition, post heat treatments are also important in introducing phase transformations, which were demonstrated by the hot stage XRD investigation between $\sim 25^{\circ}\text{C}$ and 800°C .

XRD and FTIR are two important techniques that complement each other in determining the structure of the synthesised CaP, phase composition, and functional groups. XRD patterns provide data about the crystal structure and its phase composition. On the other hand, FTIR is effective in detecting functional groups and characterizing covalent bonding data. It provides data about chemical bonds in a molecule by producing IR spectra. The latter produce a distinctive molecular fingerprint, which is used to analyse samples

for many different components. FTIR spectra provide data about sample composition and degree of atoms' order in the unit cell, based on location of absorption band and bandwidth, respectively.

Characteristic absorption bands of functional groups for HAp, brushite, and monetite phases are widely reported (552, 553), as shown in Tables 4.1.14, 4.1.15, and 4.1.16, respectively. Vibrational modes can be symmetrical stretching (ν_1), asymmetrical stretching (ν_2), bending in and out of plane (ν_3), and bending in plane (ν_4). Absorption bands of functional groups that indicate the formation of a typical HAp structure are widely reported (554-558). Absorption bands at 3570 cm^{-1} and 631 cm^{-1} are assigned to the stretching and liberation modes of structural OH group (O–H). An absorption band at 472 cm^{-1} is assigned to the O–P–O bending variation of PO_4 (ν_2) group, which is characteristic to HAp tetrahedral structure. A double band at 570 cm^{-1} and 602 cm^{-1} is assigned to the O–PO asymmetric and symmetric deformation modes of PO_4 group (ν_4). An absorption band at 963 cm^{-1} is assigned to the symmetric stretching mode of PO_4 group. Strong absorption bands at 1090 cm^{-1} and 1040 cm^{-1} are assigned to the P–O asymmetrical stretching mode of PO_4 group (ν_3). An absorption band with a weak intensity in the range $2100 - 1950\text{ cm}^{-1}$ is assigned to both PO_4 (ν_3) and PO_4 (ν_1) modes.

Absorption bands at 2365 cm^{-1} and 2344 cm^{-1} are due to the absorption of atmospheric CO_2 . Absorption bands in the range $1600 - 1400\text{ cm}^{-1}$ and at 875 cm^{-1} are assigned to CO_3 group. Absorption bands with a weak intensity at 1418 cm^{-1} and 1458 cm^{-1} are assigned to the C–O symmetrical and asymmetrical stretching modes of CO_3 group (ν_3). An absorption band at \sim

875 cm^{-1} is assigned to the stretching mode of CO_3 group (ν_2) or HPO_4 group (555, 557). The CO_3 group (ν_2) may be difficult to observe, particularly when it is covered by the absorption band of HPO_4 group. The absorption band of CO_3 group (ν_2) determines the absorption of atmospheric CO_2 in alkaline solutions (552).

The presence of absorption bands of CO_3 group (ν_3) around 1460 cm^{-1} and 875 cm^{-1} indicates *B* – type substitution of PO_4 group with CO_3 group, whereas the presence of absorption band of CO_3 group (ν_3) around 1460 cm^{-1} indicates *A* – type CO_3 substitution for OH group (555, 559). An absorption band of CO_3 group at 875 cm^{-1} indicates *AB* – type substitution of PO_4 and OH groups with CO_3 group. A weak absorption band at 3571 cm^{-1} can also indicate *AB* – type substitution (559). A wide absorption band in the range 3600 – 3100 cm^{-1} is assigned to the stretching modes of H_2O molecules (ν_3) and (ν_1), while an absorption band at 1629 cm^{-1} is assigned to the deformation mode of H_2O molecules (ν_2) (555), indicating the presence of adsorbed water (552).

Table 4.1.14 Characteristic absorption bands of functional groups for HAp (552)

Chemical groups	Absorption bands (cm^{-1})
PO_4	472, 570, 602, 963, and 1140 – 1000
H_2O adsorbed	3600 – 3100
OH	631 and 3570
HPO_4	875
CO_3	875, 1418, 1458, 1632, 1650, and 1994

Absorption bands of functional groups that indicate the formation of a brushite structure are reported (553). An absorption band at 3492 cm^{-1} is assigned to the O–H stretching mode of H_2O molecules, while a shoulder at 2964 cm^{-1} is assigned to the stretching mode of OH group. In addition, an absorption band at 1651 cm^{-1} is assigned to the bending mode of H_2O molecules, and an absorption band at 1218 cm^{-1} is assigned to the in – plane – bending mode of OH group, while an absorption band at 795 cm^{-1} is assigned to the liberation mode of H_2O molecules. Absorption bands at 1066 cm^{-1} , 875 cm^{-1} , and 530 cm^{-1} are characteristics of PO_4 group. Absorption bands at 1066 cm^{-1} and 875 cm^{-1} are assigned to the stretching modes of PO_4 (P–O) and PO_4 (P–O(H)), respectively, while an absorption band at 530 cm^{-1} is assigned to the P–O bending mode of PO_4 group.

Table 4.1.15 Characteristic absorption bands of functional groups for brushite (553)

Absorption bands (cm^{-1})	Functional groups and mode
3492	OH, O–H Stretching of water
2964	OH, O–H Stretching (shoulder)
1651	H_2O Bending
1218	OH, O–H in-plane bending
1066	PO_4 , PO Stretching
875	PO_4 , P–O(H) Stretching
795	H_2O Liberation
530	PO_4 , PO Bending

Absorption bands of functional groups that indicate the formation of a monetite structure are reported (553). Absorption bands at 3415 cm^{-1} , 1404 cm^{-1} , and 866 cm^{-1} are characteristics of OH group. An absorption band at 3415 cm^{-1} is assigned to the stretching mode of OH group, while absorption

bands at 1404 cm^{-1} and 866 cm^{-1} are assigned to the in – plane and out – of – plane bending modes of OH group, respectively. Absorption bands at 2369 cm^{-1} and 893 cm^{-1} are assigned to the stretching modes of P–O(H) and P–O(H) (v3), respectively. Absorption bands in the range $1176 – 996\text{ cm}^{-1}$ and $584 – 430\text{ cm}^{-1}$ are assigned to the stretching and bending modes of PO_4 group, respectively. Absorption bands at 1132 cm^{-1} and 1070 cm^{-1} as well as a shoulder at 1176 cm^{-1} are assigned to the P–O stretching mode of PO_4 group (v3), whereas an absorption band at 996 cm^{-1} is assigned to the P–O stretching mode of PO_4 group (v1). Absorption bands at 584 cm^{-1} and 531 cm^{-1} are assigned to the O–P–O bending mode of PO_4 group (v4), whereas those at 430 cm^{-1} and 405 cm^{-1} are assigned to the O–P–O bending mode of PO_4 group (v2).

Table 4.1.16 Characteristic absorption bands of functional groups for monetite (553)

Absorption bands (cm^{-1})	Functional groups and mode
3415	OH, O–H Stretching
2369	PO–H Stretching
1404	OH, O–H in plane bending
1176	PO_4 , PO Stretching (v3) (shoulder)
1132	PO_4 , PO Stretching (v3)
1070	PO_4 , PO Stretching (v3)
996	PO_4 , PO Stretching (v1)
893	P–O(H) Stretching (v3)
866	OH, O–H out-of-plane bending
584	PO_4 , PO Bending (v4)
531	PO_4 , PO Bending (v4)
430	PO_4 , PO Bending (v2)
405	PO_4 , PO Bending (v2)

Moreover, absorption bands can also be donated to impurities that are absorbed by KBr pellets. These are usually OH group and H₂O molecules at 3500 cm⁻¹ and 1630 cm⁻¹, NO₂ at 1390 cm⁻¹, and SO₄ at 1160 – 1140 cm⁻¹. Wide water absorption bands in the spectrum are donated to the absorbed water molecules by KBr pellets from the environment (552).

FTIR spectra of CaP powders were obtained in the wavenumber range 1300 – 400 cm⁻¹, 2500 – 1400 cm⁻¹, and 4000 – 3000 cm⁻¹, as shown in Figures 4.1.35, 4.1.36, and 4.1.37, respectively. FTIR absorption bands and their assigned references are in good agreement, and they are presented in Table 4.1.17. The FTIR spectra in the entire wavenumber range 4000 – 400 cm⁻¹ showed characteristic absorption bands for CaP powders. These include PO₄ group (v1) (P–O) at 960 cm⁻¹, PO₄ group (v2) (O–P–O) at 500 – 450 cm⁻¹, PO₄ group (v4) (O–P–O) at 650 – 450 cm⁻¹, PO₄ group (v3) (P–O) at 1200 – 960 cm⁻¹, HPO₄ group at 875 cm⁻¹, CO₃ group (v3) (C–O) at 1550 cm⁻¹, absorbed CO₃ at 2400 – 2100 cm⁻¹, absorbed H₂O molecules at 1650 – 1600 cm⁻¹, and structural OH group (O–H) at 3540 cm⁻¹.

The PO₄ group (v2) (O–P–O) was observed with a very weak intensity in all powders, except that synthesised under as – prepared pH 5.4 ± 0.2 and 200°C hydrothermal conditions. The absorption band at 720 cm⁻¹ was assigned to the Nujol agent, and it was observed in all samples. The absorption band of PO₄ group (v1) (P–O) at 960 cm⁻¹ was only observed with CaP powder that was synthesised under room temperature and as – prepared pH 5.4 ± 0.2 conditions. The absorption band of CO₃ group (v3) at 1550 cm⁻¹ was donated to the substitution of CO₃ group for OH group (A – type).

The absorption bands at $1650 - 1600 \text{ cm}^{-1}$ and $3450 - 3400 \text{ cm}^{-1}$ were assigned to the absorbed water (H_2O) molecules, while the absorption band at 3470 cm^{-1} was assigned to the structural OH group. The water absorption bands gradually changed as the synthesis conditions changed, particularly as temperature increased. The absorption bands of absorbed H_2O at $1650 - 1600 \text{ cm}^{-1}$ and 3540 cm^{-1} were absent in powders that were synthesised under 200°C hydrothermal conditions, which indicated the liberation of absorbed water. The latter powders showed the characteristic stretching of structural OH group for HAp at 3570 cm^{-1} .

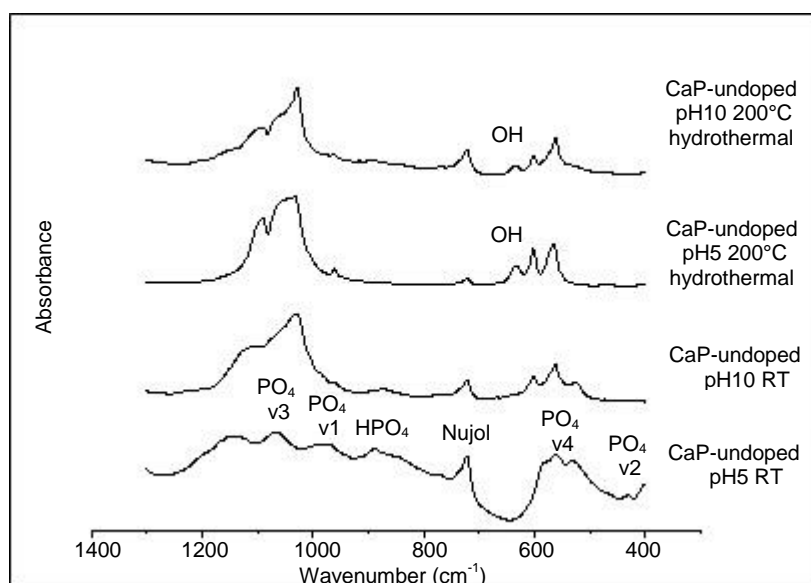


Figure 4.1.35 FTIR spectra of CaP powders in the mid – infrared region and wavenumber range $1300 - 400 \text{ cm}^{-1}$.

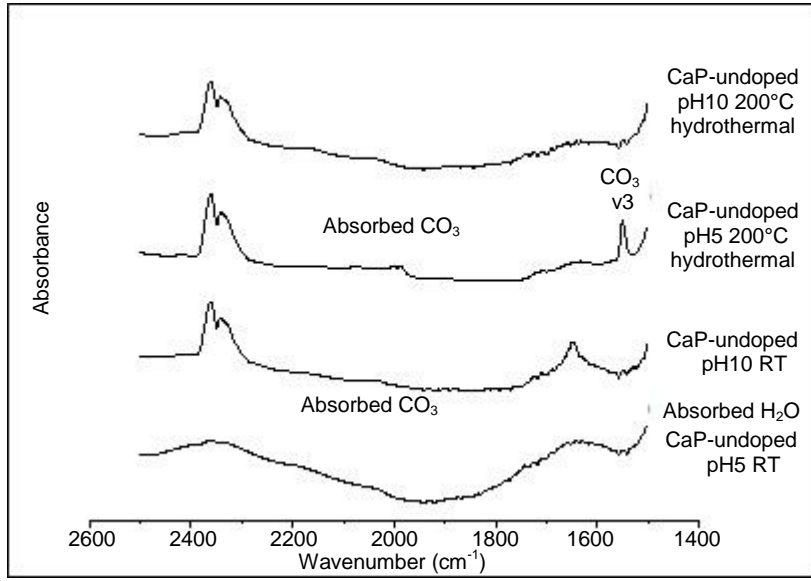


Figure 4.1.36 FTIR spectra of CaP powders in the mid – infrared region and wavenumber range 2500 – 1400 cm^{-1} .

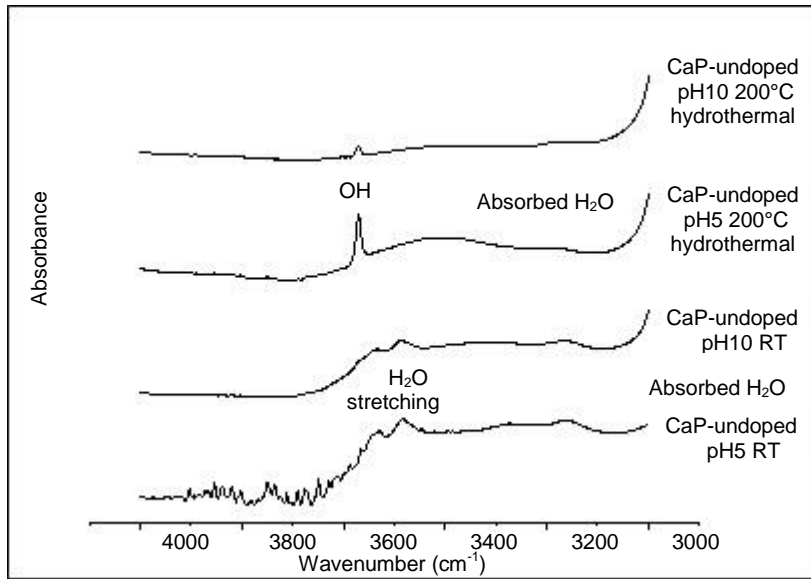


Figure 4.1.37 FTIR spectra of CaP powders in the mid – infrared region and wavenumber range 4000 – 3000 cm^{-1} .

Under room temperature and as – prepared pH 5.4 ± 0.2 conditions, the synthesised brushite ($\text{CaHPO}_4 \cdot 2\text{H}_2\text{O}$) showed broad absorption bands of PO_4 group (ν_2) (O–P–O) and PO_4 group (ν_1) (P–O) at $500 - 450 \text{ cm}^{-1}$ and 960 cm^{-1} , respectively, as well as PO_4 group (ν_4) (O–P–O) and PO_4 group (ν_3) (P–O) at $650 - 550 \text{ cm}^{-1}$ and $1200 - 1100 \text{ cm}^{-1}$, respectively. The absorption band of HPO_4 group at 870 cm^{-1} was the characteristic absorption band for brushite. A weak absorption band of CO_3 group was observed around $1480 - 1420 \text{ cm}^{-1}$, which indicated A – type substitution, whereas the absorption bands of CO_3 group at $2400 - 2100 \text{ cm}^{-1}$ are due to the absorption of atmospheric CO_2 . The absorption band at 1650 cm^{-1} was assigned to the bending mode of absorbed H_2O . The double band at 3482 cm^{-1} and 3565 cm^{-1} was attributed to the two H_2O molecules in the brushite unit cell (553).

Under room temperature and pH 10 ± 0.2 conditions, the PO_4 group (ν_1) (P–O) was absent, and the PO_4 group (ν_4) (O–P–O) and PO_4 group (ν_3) (P–O) started taking shape and merged as one band with shoulders. The absorption band at around $660 - 630 \text{ cm}^{-1}$ was assigned to the liberation modes of structural OH group. The characteristic absorption band of HPO_4 group was observed at 875 cm^{-1} , which indicated the presence of brushite alongside HAp, as revealed by XRD. The absorption band of absorbed H_2O molecules at 1650 cm^{-1} was small and sharp. A weak absorption band of CO_3 group was observed around $1480 - 1420 \text{ cm}^{-1}$, which indicated A – type substitution, while the absorption bands of CO_3 group at $2400 - 2100 \text{ cm}^{-1}$ are due to the absorption of atmospheric CO_2 .

Under as – prepared pH 5.4 ± 0.2 and 200°C hydrothermal conditions, the absorption bands of PO_4 group (ν_2) (O–P–O) and PO_4 group (ν_1) (P–O) were absent, while the characteristic absorption bands of PO_4 group (ν_4) (O–P–O) and PO_4 group (ν_3) (P–O) were well defined and sharp. The absorption band at $660 - 630 \text{ cm}^{-1}$ was assigned to the structural OH group. The strong absorption band of CO_3 group was observed at 1550 cm^{-1} , which indicated the substitution of OH group with CO_3 group (A – type), while the absorption bands of CO_3 group at $2400 - 2100 \text{ cm}^{-1}$ were due to the absorption of atmospheric CO_2 . The absorption band of adsorbed H_2O molecules at 1634 cm^{-1} was absent, and the absorption band for OH group at 3470 cm^{-1} was defined and sharp.

Under pH 10 ± 0.2 and 200°C hydrothermal conditions, the PO_4 group (ν_2) (O–P–O) and PO_4 group (ν_1) (P–O) were absent, while the characteristic absorption bands of PO_4 group (ν_4) (O–P–O) and PO_4 group (ν_3) (P–O) were well defined and sharp. The small absorption band of HPO_4 group at 870 cm^{-1} was assigned to the presence of a monetite phase alongside HAp, as revealed by XRD. The absorption band at $660 - 630 \text{ cm}^{-1}$ was assigned to the structural OH group. A weak absorption band of CO_3 group was observed at $1480 - 1420 \text{ cm}^{-1}$, which indicated A – type substitution, while the absorption bands of CO_3 group at $2400 - 2100 \text{ cm}^{-1}$ were due to the absorption of atmospheric CO_2 . The absorption band of adsorbed H_2O molecules at 1634 cm^{-1} was absent, and the absorption band of OH group at 3470 cm^{-1} was small and sharp.

The absorption band of CO_3 group at $1480 - 1420 \text{ cm}^{-1}$ was observed with all powders, which indicated A – type CO_3 substitution for OH group.

However, a strong absorption band was observed only under as – prepared pH 5.4 ± 0.2 and 200°C hydrothermal conditions. The absorption band of absorbed H_2O molecules at 3450 cm^{-1} and stretching of OH group at 3471 cm^{-1} were observed with CaP powders that were synthesised under 200°C hydrothermal conditions. The absorption band of absorbed H_2O molecules was reduced under 200°C hydrothermal conditions, while the stretching of OH group (O–H) increased under 200°C hydrothermal conditions.

Table 4.1.17 Characteristic IR Absorption Frequencies (cm^{-1}) of CaP powder functional groups, compared to reported data (552, 553) as a reference

Functional group and Absorption cm^{-1} (References)	CaP-undoped pH5 RT		CaP-undoped pH10 RT		CaP-undoped pH5 200°C Hydrothermal		CaP-undoped pH10 200°C Hydrothermal	
	cm^{-1}	Intensity	cm^{-1}	Intensity	cm^{-1}	Intensity	cm^{-1}	Intensity
500–450 cm^{-1} PO ₄ v2	431	v. weak	474	v. weak	472	v. weak	474	v. weak
650–550 cm^{-1} PO ₄ v4	532	Small	526	Small	-	-	-	-
	561	Small	563	Medium	565	Strong	561	Small
	-	-	601	Small	603	Strong	601	Medium
634 cm^{-1} Structural OH	-	-	-	-	632	Medium	634	Small
720 cm^{-1} Nujol	723	Small	721	Small	721	Small	721	Small
875 cm^{-1} HPO ₄	875	Weak	873	Weak	-	-	-	-
960 cm^{-1} PO ₄ v1	973	Small	962	weak-sh	962	Small	962	weak, small
	991	weak-sh	-	-	-	-	-	-
1200–1000 cm^{-1} PO ₄ v3	1066	Small	1029	medium	1033	Strong	1029	Medium
	1128	weak-sh	1106	Sh	1091	Small	1091	Small
	1149	Small	-	-	-	-	-	-
1650–1400 cm^{-1} CO ₃ v3	1548	v. weak	1547	medium-sharp	1550	v. weak	1548	v. weak
1650–1600 cm^{-1} H ₂ O absorbed	1641	medium-broad	1648	medium-sharp	1641	small-broad	1641	Weak
2400–2100 cm^{-1} CO ₂ absorbed	2339	medium, broad	2341	strong, sharp	2341	strong, sharp	2341	strong, sharp
	2358	medium, broad	2360	strong, sharp	2360	strong, sharp	2360	strong, sharp
3600–3100 cm^{-1} H ₂ O absorbed	3160	Small	3164	Small	-	-	-	-
	3482	small-sharp	3484	small-sharp	3405	weak-broad	3375	weak-broad
3600 – 3400 cm^{-1} H ₂ O stretching	3565	v. small – sharp	3565	Medium – sharp	-	-	-	-
3571 cm^{-1} OH stretching	-	-	-	-	3569	strong-sharp	3571	small-sharp

v = very, sh = shoulder, vibrational modes (v1 = symmetrical stretching, v2 = asymmetrical stretching, v3 = bending in and out of plane, and v4 = bending in plane)

Thermal behaviour of CaP powders was investigated using differential scanning calorimetry (DSC). The latter was used to measure the difference in heat flow rate ($\text{mW} = \text{mJ/sec}$) between CaP sample and inert reference, as a function of time and temperature. Any temperature difference that would result from a thermal event in CaP sample is compensated for (541). For example, during an exothermic process, more heat is supplied to the reference (equivalent to withdrawing energy from CaP sample), whereas during an endothermic process, additional amount of energy is supplied to the CaP sample heater. The difference in heat supplied to CaP sample and reference is recorded as a function of temperature. This signal is proportional to the CaP sample specific heat, which determines the amount of heat that is necessary to change the temperature of CaP sample by a given amount (541).

DSC of CaP powders are compared in Figure 4.1.38, and DSC peak centres are presented in Table 4.1.18. Heat flow of DSC measurements was set to Endo up, which indicates that endothermic changes are peaked up, while exothermic changes are peaked down. CaP powder (CaP-undoped pH5 RT) that was synthesised under room temperature and as – prepared pH 5.4 ± 0.2 conditions showed an endothermic peak at 493.4°C , which was assigned to the explosion of lattice water (560), whereas CaP powder (CaP-undoped pH10 RT) that was synthesised under room temperature and pH 10 ± 0.2 conditions showed a small endothermic peak at 190.9°C and an even smaller exothermic peak at 301.7°C , which were assigned to the liberation of water and elimination of CO_3 , respectively (560).

Under 200°C hydrothermal conditions, CaP powder (CaP-undoped pH5 200°C hydrothermal) that was synthesised with as – prepared pH 5.4 ± 0.2 showed a negligible broad endothermic peak around 185.3°C, which was assigned to the liberation of water. The broad peak indicated gradual and continuous liberation or elimination of absorbed water and explosion of lattice water (560). CaP powder (CaP-undoped pH10 200°C hydrothermal) that was synthesised with pH 10 ± 0.2 showed a small endothermic peak at 501.5°C, which was assigned to the explosion of lattice water (560).

The explosion of lattice water in CaP powders (CaP-undoped pH5 RT) and (CaP-undoped pH10 200°C hydrothermal) and the liberation of water in CaP powders (CaP-undoped pH10 RT) and (CaP-undoped pH5 200°C hydrothermal) were due to the chemical reaction of OH radicals, which were liberated from the CaP structure during heating. These results indicated that CaP powders were hydrated, and that the endothermic peaks were due to dehydration of powders. In addition, the results may support hot stage XRD phase transformations upon heating from room temperature up to 800°C. The endothermic reactions at 493°C and 501°C in CaP powders (CaP-undoped pH5 RT) and (CaP-undoped pH10 200°C hydrothermal), respectively, are in good agreement with hot stage XRD phase transformation from monetite to calcium pyrophosphate (β -Ca₂P₂O₇) between 400°C and 800°C. In addition, the endothermic reaction at 190°C in CaP powders (CaP-undoped pH10 RT) is in good agreement with hot stage XRD phase transformation from brushite to monetite at 200°C.

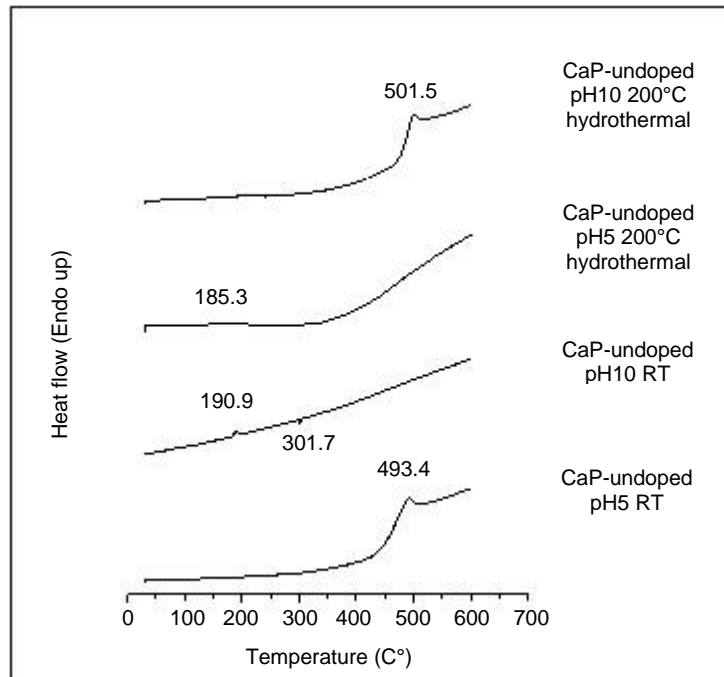


Figure 4.1.38 DSC of CaP powders (Endo up).

Table 4.1.18 DSC peak centres of CaP powders (second reaction)

CaP-undoped pH5 RT	CaP-undoped pH10 RT	CaP-undoped pH5 200°C hydrothermal	CaP-undoped pH10 200°C hydrothermal
493.4°C	190.9°C	185.3°C	501.5°C
-	301.7°C	-	-

4.1.5 Main findings

Based on the initial investigation of synthesis conditions (temperature, pH, reaction time, and ageing time), temperature, pH, and reaction time were the most effective parameters in modifying the size and shape of CaP particles. In particular, the temperature, pH, and reaction time of 200°C, pH \geq 9, and 24 hours, respectively, were the most effective parameters in producing CaP particles in the nanometre size and forming a single HAp phase. Adjusting the pH of starting CaP mixture and followed by a hydrothermal treatment at 200°C was the most effective route in modifying the size and shape of CaP particles, which produced nanosized and rod – like particles. Therefore, temperature and pH are of great importance, particularly in obtaining the desired phase, size, and shape of CaP particles. In addition, it was important to allow sufficient time for the reaction of reactants to take place. This was demonstrated by the improved crystallinity of brushite particles that were synthesised under room temperature and as – prepared pH 5.4 ± 0.2 conditions by the slow addition technique, compared to the poorly crystallised monetite particles that were synthesised by the fast addition technique.

A brushite phase with micrometre platelet – like morphology was obtained under room temperature and as – prepared pH 5.4 ± 0.2 conditions, as revealed by SEM, XRD pattern and FTIR characteristic bands. The latter were those of HPO₄ group at 870 cm⁻¹ and two H₂O molecules at 3482 cm⁻¹ and 3565 cm⁻¹. Adjusting the pH of CaP starting mixture to pH 10 ± 0.2 resulted in the formation of fine platelet – like particles (in clusters) in the nanometre size, which indicated the effectiveness of high pH levels (pH 10) in reducing the particle size. However, the pH 10 ± 0.2 resulted in the

formation of HAp and brushite phases, which were revealed by XRD pattern. The brushite phase was confirmed by FTIR characteristic absorption band of HPO_4 group at 875 cm^{-1} . The hydrothermal treatment at 200°C of CaP starting mixture with as – prepared pH 5.4 ± 0.2 resulted in the formation of rod – like particles in the nanometre size and the formation of a single HAp phase, which indicated the effectiveness of hydrothermal treatments in reducing the particle size and the formation of a single HAp phase. The latter was revealed by XRD pattern and confirmed by FTIR characteristic absorption bands of structural OH group at 634 cm^{-1} and 3470 cm^{-1} . Adjusting the pH of CaP starting mixture to pH 10 ± 0.2 and followed by a hydrothermal treatment at 200°C resulted in the formation of monetite platelet – like particles together with HAp needle – like particles, which was donated to an incorrect pH reading of CaP starting mixture. This was in contrast to CaP (CaP-undoped pH10 200°C hydrothermal (initial investigation)) that was obtained during the initial investigation, which resulted in the formation of a single HAp phase and rod – like particles. Although SEM revealed the formation of agglomerates of CaP nanoparticles in the case of CaP-undoped pH10 RT and CaP-undoped pH5 200°C hydrothermal powders, the particle size analysis revealed the particle size in the micrometre scale, which is in good agreement with micrometre agglomerates. This is because the measurement of nanoparticles depends on the deagglomeration of CaP particles. However, agglomerates of CaP particles were observed after dispersion of CaP powders in methanol and distilled water under ultrasonic bath conditions for ~ 10 minutes. This might indicate the formation of hard agglomerates of CaP particles or that a longer deagglomeration treatment was required.

The absorption band of CO_3 group around $1480 - 1420 \text{ cm}^{-1}$ was observed with all powders, which indicated that all CaP powders are A – type carbonate CaP. Under 200°C hydrothermal conditions, the absorption band of absorbed H_2O molecules was reduced, while the stretching of structural OH group increased, which indicated the formation of less hydrated powders and the formation of HAp.

The Hot stage XRD results (CaP-undoped pH5 RT) indicated that a phase transformation from brushite to monetite occurred at 200°C , while a phase transformation from monetite to calcium pyrophosphate ($\beta\text{-Ca}_2\text{P}_2\text{O}_7$) occurred at 400°C up to 800°C . Similarly, DSC results indicated that phase transformations may have taken place upon heating from room temperature up to 600°C , and that CaP powders were hydrated, due to the endothermic reactions corresponding to dehydration of powders.

Chapter 4.2

Synthesis and characterisation of doped calcium phosphates

Doped calcium phosphates were synthesised by the chemical precipitation and hydrothermal methods under different conditions, as shown in Table 4.2.1. Doped CaP powders were investigated in terms of their particle size, morphology, composition, phase purity, and thermal behaviour, using SEM, SEM-EDX, static laser scattering, XRD, FTIR, and DSC.

Table 4.2.1 Synthesis conditions for doped calcium phosphate powders

Powder	Synthesis method	As – prepared pH	Adjusted pH	Temperature	Reaction time
Doped CaP	Chemical precipitation	5.4 ± 0.2	10 ± 0.2	RT	24 hours
	Hydrothermal	5.4 ± 0.2	10 ± 0.2	200°C	

Doping of calcium phosphate was carried out with different compounds, which was divided into two batches (A and B). Batch A powders were doped with Er_2O_3 , AlPO_4 , and CaF_2 , which are considered insoluble compounds, while batch B powders were doped with $\text{Er}(\text{NO}_3)_3 \cdot 5\text{H}_2\text{O}$, $\text{Al}(\text{NO}_3)_3 \cdot 9\text{H}_2\text{O}$, and NH_4F , which are highly soluble compounds.

It is well known that Er_2O_3 , AlPO_4 and CaF_2 are insoluble (268, 419, 505) or can show negligible solubility in water, and therefore, they would form a composite with calcium orthophosphates/apatites. Consequently, the diffusion of Er^{3+} , Al^{3+} , and F^- ions into calcium orthophosphate structure is unlikely to be achieved at room temperature, but it is likely to be achieved at

elevated temperatures (495, 506) such those under solid – state (42) and hydrothermal conditions (399, 400, 411).

On the other hand, $\text{Er}(\text{NO}_3)_3 \cdot 4\text{H}_2\text{O}$, $\text{Al}(\text{NO}_3)_3 \cdot 9\text{H}_2\text{O}$, and NH_4F show significant solubility in water (268, 419, 505), and therefore, the incorporation of Er^{3+} , Al^{3+} , and F^- ions is likely to be achieved at low temperatures by the wet methods (chemical precipitation and hydrothermal), which would result in the substitution of Ca^{2+} by trivalent ions Er^{3+} and Al^{3+} as well as the substitution of OH^- by F^- ions.

Doped CaP powders were synthesised the same way as CaP powders. A solution of $((\text{NH}_4)_2\text{HPO}_4)$ was added to a solution of $(\text{Ca}(\text{NO}_3)_2 \cdot 4\text{H}_2\text{O})$ by the slow dropping/addition technique for 30 minutes whilst being magnetically stirred at ~ 400 rpm for 60 minutes. 7.5 ml of 0.1 M solution of each dopant (22.5 ml in total) was then added to 240 ml of CaP mixture under stirring, covered to minimise the absorption of atmospheric CO_2 , and left on standby at room temperature for 24 hours, or hydrothermally treated at 200°C for 24 hours. Finally, the wet precipitate was collected and dried in an oven at 80°C for 24 hours.

4.2.1 Doped CaP powders (batch A)

4.2.1.1 Doped CaP batch A (pH 5.4 ± 0.2, RT)

Representative SEM of doped CaP powder (batch A) that was synthesised under room temperature and as – prepared pH 5.4 ± 0.2 conditions is shown in Figure 4.2.1. SEM showed well – crystallised particles with platelet – like morphology. The platelet – like particles appeared to have spherical particles incorporated and fused to their surfaces. These morphological changes were due to the addition of dopants (Er_2O_3 , AlPO_4 , and CaF_2), which increase the particles' surface area for greater sintering. The particle size varied from micrometre platelet – like particles to nanospherical particles. Figure 4.2.2 shows the volume – based distribution of CaP particles, as measured by the Malvern Mastersizer 2000E, with the standard percentile values $d(0.1)$, $d(0.5)$, $d(0.9)$, and volume weighted mean $D[4,3]$. The particles had a volume weighted mean $D[4,3]$ of 30.5 μm with a ± 1 standard deviation error bar, as shown in Figure 4.2.3. The values appears to be in good agreement with the platelet – like particles shown by SEM.

SEM-EDX measurements (element weight percentage) of doped CaP powder (batch A) that was synthesised under room temperature and as – prepared pH 5.4 ± 0.2 conditions are shown in Table 4.2.2. The SEM-EDX measurements of four spectra, as shown by SEM in Figure 4.2.4, indicated a mean Ca:P ratio of 1.06. Spectra number three and four were way out, compared to spectra number one and two, which was probably due to the area where the spectra were obtained from, as shown by SEM in Figure 4.2.4. Spectrum number three does not appear to be centred onto CaP particle, and spectra number four appears to include a large area of carbon – based SEM stub. Therefore, the Ca:P ratios were possibly influenced by

SEM carbon – coated SEM stub. However, obtaining a range of Ca:P ratios can also indicate a nonhomogeneous distribution of elements (Ca, P, and dopants) in the powder.

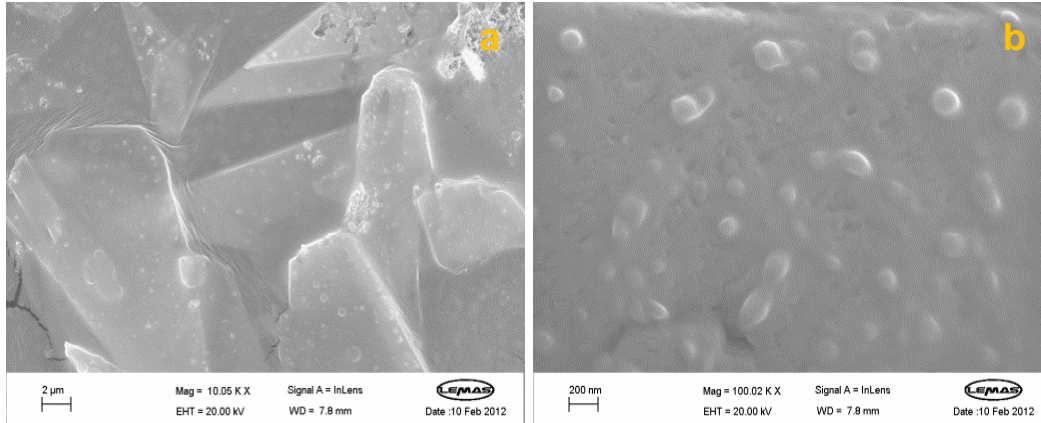


Figure 4.2.1 SEM of doped CaP powders (batch A) synthesised under room temperature and as – prepared pH 5.4 ± 0.2 conditions, showing (a) platelet – like particles and (b) nanoparticles fused to surface of platelet – like particles.

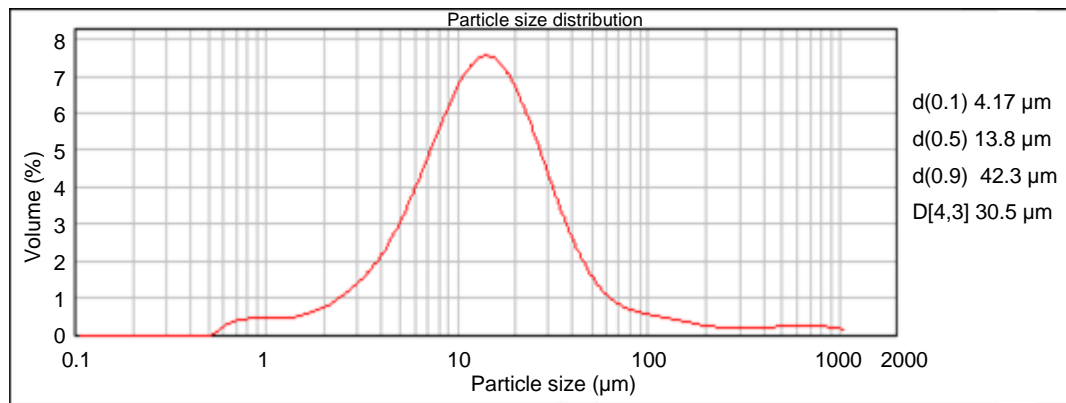


Figure 4.2.2 Particle size distribution of doped CaP (batch A) synthesised under room temperature and pH 5.4 ± 0.2 conditions.

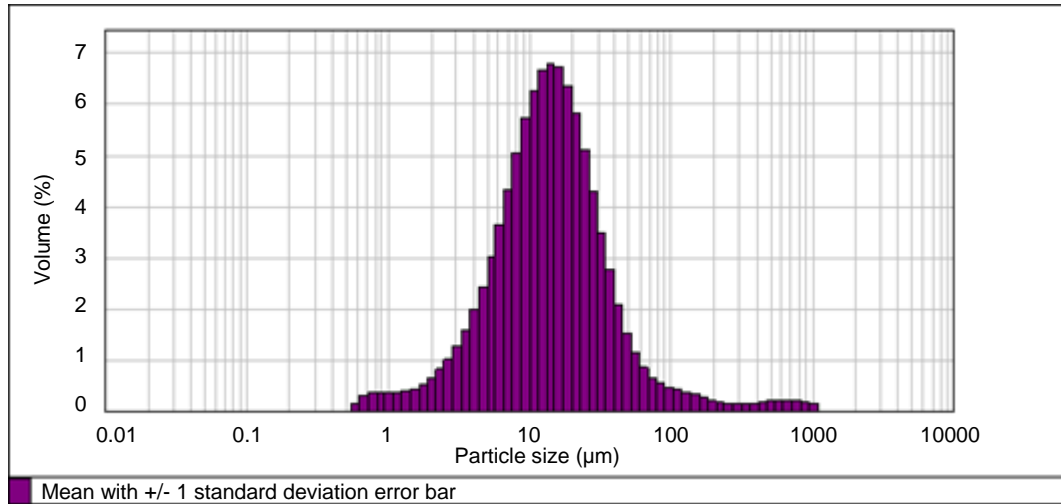


Figure 4.2.3 Statistics graph of doped CaP (batch A) synthesised under room temperature and pH 5.4 ± 0.2 conditions, showing the mean with ± 1 standard deviation error bar.

Table 4.2.2 SEM-EDX measurements (element weight percentage) for doped CaP (batch A) synthesised under room temperature and as – prepared pH 5.4 ± 0.2 conditions

Spectrum	O	F	Al	P	Ca	Er	Ca:P ratio
Spectrum 1	54.3	0.2	0.1	7.41	7.91	0.05	1.06
Spectrum 2	51.3	0.1	0.2	11.2	13.0	0.07	1.15
Spectrum 3	25.7	0.6	0.7	1.8	1.13	37.1	0.61
Spectrum 4	35.9	0.3	0.4	3.51	3.47	-	0.98
Mean	41.8	0.3	0.4	6.01	6.39	9.31	1.06
Std. Deviation	13.4	0.1	0.2	4.2	5.2	18.5	0.2

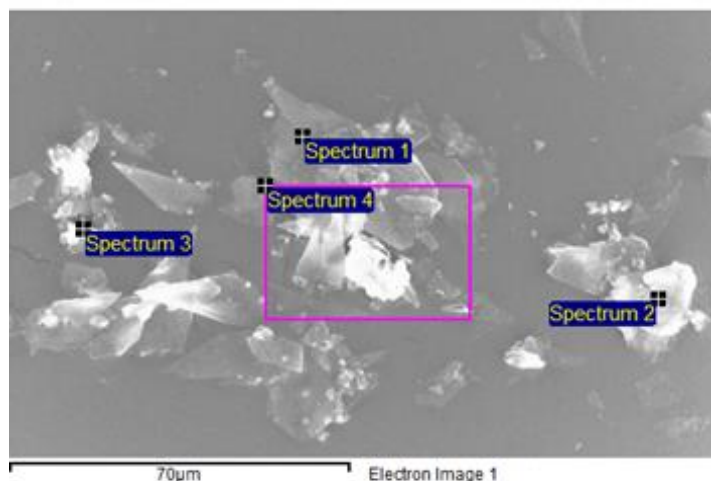


Figure 4.2.4 SEM of doped CaP synthesised under room temperature and as – prepared pH 5.4 ± 0.2 conditions, showing the obtained EDX spectra.

XRD pattern of doped CaP powder (CaP-doped batch A pH5 RT) that was synthesised under room temperature and as – prepared pH 5.4 ± 0.2 conditions is shown in Figure 4.2.5 and compared to that of CaP powder (Cap-undoped pH5 RT) under the same conditions in Figure 4.2.6. The XRD pattern of doped CaP (Cap-doped batch A pH5 RT) in Figures 4.2.5 and 4.2.6 indicated the formation of multiple phases of brushite and monetite, and that brushite was the dominant phase, which is in good agreement with brushite JCPDS file 01-072-0713 and monetite JCPDS file 01-070-1425. The XRD pattern also indicated the presence of dopants' phases. The dopants' peaks appeared to overlapped with some brushite and monetite peaks, as shown in Figure 4.2.5. This is in good agreement with the major peaks at 2 theta 29.9° and 34.7° for Er_2O_3 JCPDS file 00-026-0604, 2 theta 20.7° and 26.4° for AlPO_4 JCPDS file 01-072-1064, and 2 theta 28.2° and 46.9° for CaF_2 JCPDS file 03-065-0535. It was noted that peaks at higher 2

theta angles were undetected or present with reduced intensities, which could be due to the preferred orientation of particles.

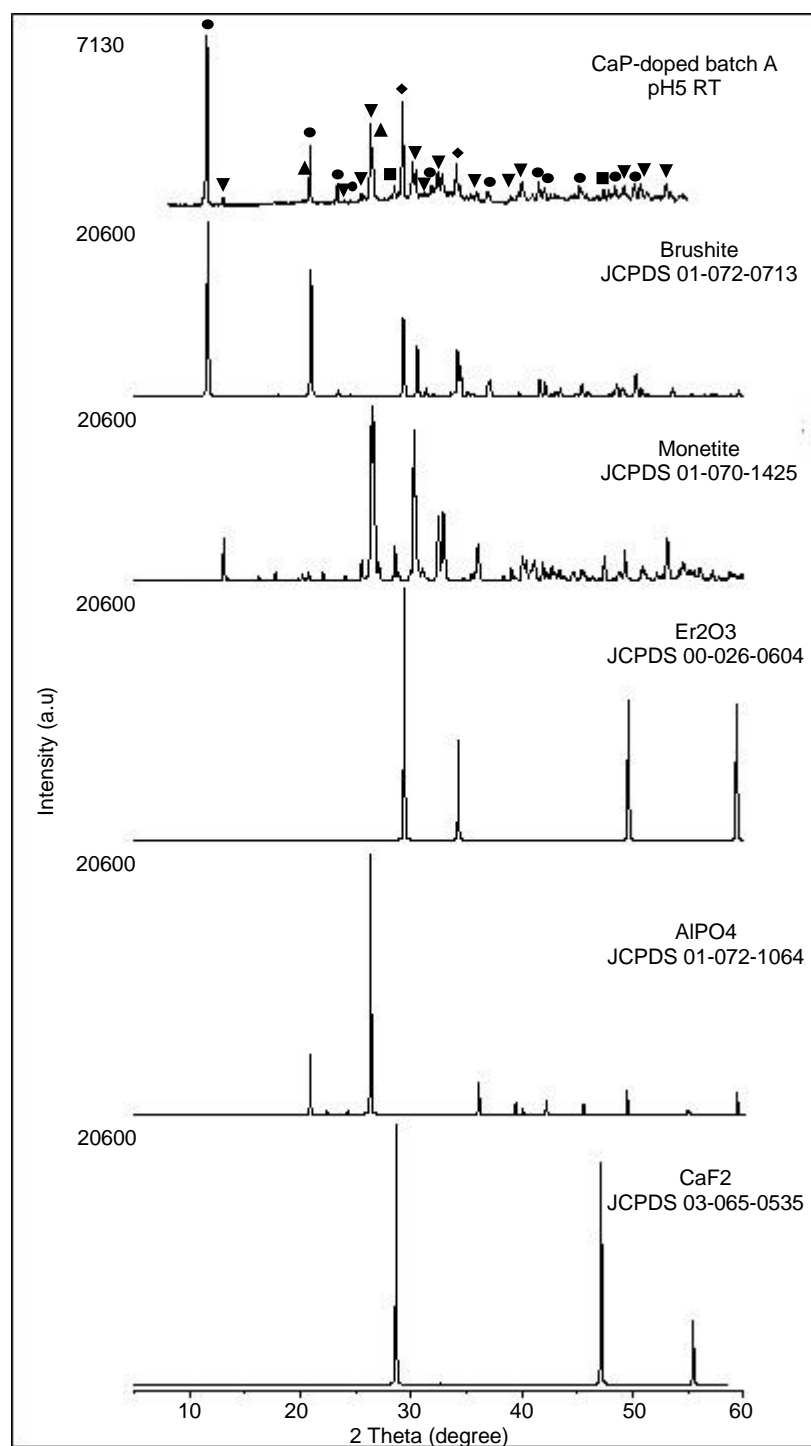


Figure 4.2.5 XRD pattern of doped CaP powder (batch A) synthesised under room temperature and as – prepared pH 5.4 ± 0.2 conditions, compared to brushite, monetite, Er_2O_3 , AlPO_4 , and CaF_2 JCPDS files. Marked peaks (●) were assigned to brushite, (▼) were assigned to monetite, (◆) were assigned to Er_2O_3 , (▲) were assigned to AlPO_4 , and (■) were assigned to CaF_2 .

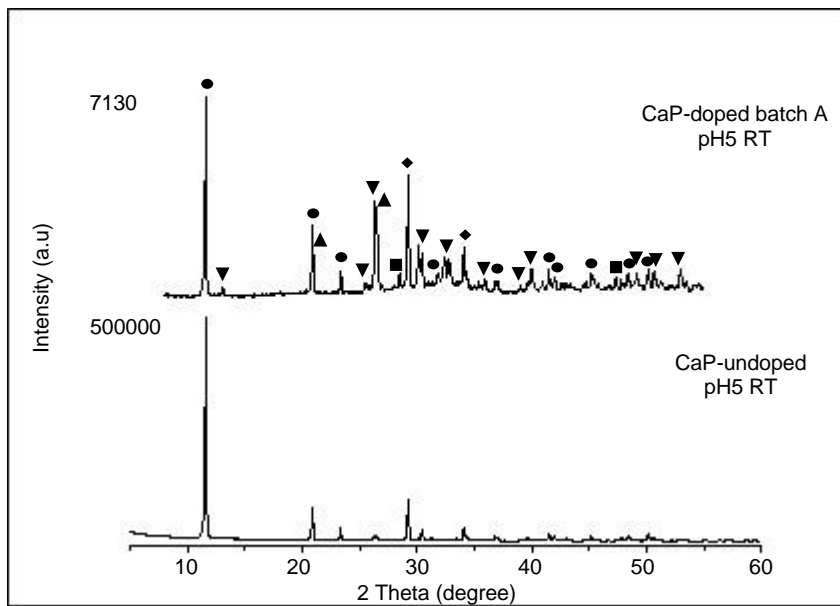


Figure 4.2.6 XRD pattern of doped CaP (batch A) synthesised under room temperature and as – prepared pH 5.4 ± 0.2 conditions, compared to that of CaP (CaP-undoped pH5 RT). Marked peaks (●) were assigned to brushite, (▼) were assigned to monetite, (◆) were assigned to Er_2O_3 , (▲) were assigned to AlPO_4 , and (■) were assigned to CaF_2 .

It must be noted that the formation of multiple phases and the overlapping of peaks made it very difficult to assign the peaks. The formation of the brushite phase together with the dopants' phases may indicate that the doping resulted in a composite of Er_2O_3 , AlPO_4 , CaF_2 , monetite and brushite, which is in good agreement with spherical particles fused to platelet – like particles shown by SEM.

The Miller indices (hkl) and 2θ of doped CaP powder (batch A) that was synthesised under room temperature and as – prepared pH 5.4 ± 0.2 conditions were refined in the monoclinic system by UnitCell (Tim Holland's software), using 1.54 \AA wavelength and minimising the sum of squares of residuals in 2θ , to determine the crystallographic parameters. Unit cell parameters for doped CaP powder are shown in Table 4.2.3.

The results indicated that the crystal structure of doped CaP (batch A) was in the monoclinic system with space group Ia. Unit cell parameters of CaP-doped pH 5 RT are similar to those of CaP-undoped pH 5 RT, 2nd reaction (Table 4.1.5), with *a* – axes (6.36 Å) and *c* – axes (5.81 Å) opposite to those of brushite JCPDS file 01-072-0713, 5.81 Å and 6.23 Å, respectively, which also indicated particle growth in the *a* – axes rather than *c* – axes. However, compared to unit cell parameters of CaP-undoped pH 5 RT, 2nd reaction (brushite), there was a shrinkage of the cell volume of 0.54 Å³. In addition, the unit cell parameters, *a* – axes, *b* – axes, and *c* – axes, of doped CaP (CaP-doped batch A pH5 RT) were modified slightly, with an increase of 0.01 Å in *a* – axes and 0.02 Å in *b* – axes, and decrease of 0.02 Å in *c* – axes.

Table 4.2.3 Unit cell parameters for doped CaP powder (Batch A) synthesised under room temperature and as – prepared pH 5.4 ± 0.2 conditions, compared to those of brushite JCPDS file 01-072-0713

Cell parameter	CaP-doped pH5 RT (batch A)	Std.D	Brushite JCPDS file 01-072-0713
<i>a</i> (Å)	6.36	0.0007	5.81
<i>b</i> (Å)	15.20	0.001	15.18
<i>c</i> (Å)	5.81	0.0005	6.23
Alpha (°)	90	-	90
Beta (°)	118.56	0.007	116.43
Gamma (°)	90	-	90
Cell volume (Å ³)	494.32	0.05	492.91

Std.D = Standard deviation

Doped CaP powder (CaP-doped batch A pH5 RT) was also investigated by hot stage XRD from ~ 25°C up to 800°C. The hot stage XRD patterns at 200°C, 400°C, 600°C, and 800°C are compared to and in good agreement with JCPDS files, as shown in Figures 4.2.7 – 4.2.10.

The XRD pattern in Figure 4.2.7 indicated that the brushite phase was transformed into a monetite phase upon heating at 200°C, due to the dehydration of brushite, which is in good agreement with monetite JCPDS file 01-070-1425. The XRD patterns in Figures 4.2.8, 4.2.9, and 4.2.10 indicated the formation of calcium pyrophosphate (β -Ca₂P₂O₇) at 400°C, 600°C, and 800°C, which is in good agreement with calcium pyrophosphate (β -Ca₂P₂O₇) JCPDS file 00-009-0346. On the other hand, peaks of dopants' phases were not detected under hot stage XRD between 200°C and 800°C. The disappearance of peaks of dopants' phases is unclear, however, it was most probably due to the diffusion of dopants' ions (Er³⁺, Al³⁺, and F⁻) into CaP structure at elevated temperatures (408, 495, 506), which resulted in the substitution of Er³⁺ and Al³⁺ for Ca²⁺ and F⁻ for OH⁻.

The phase transformations from brushite to monetite at 200°C and from monetite to calcium pyrophosphate (β -Ca₂P₂O₇) from 400°C to 800°C are also in good agreement with CaP phase transformations between 200°C and 800°C (550, 551). Doped CaP powder (batch A) behaved in the same manner as CaP powder.

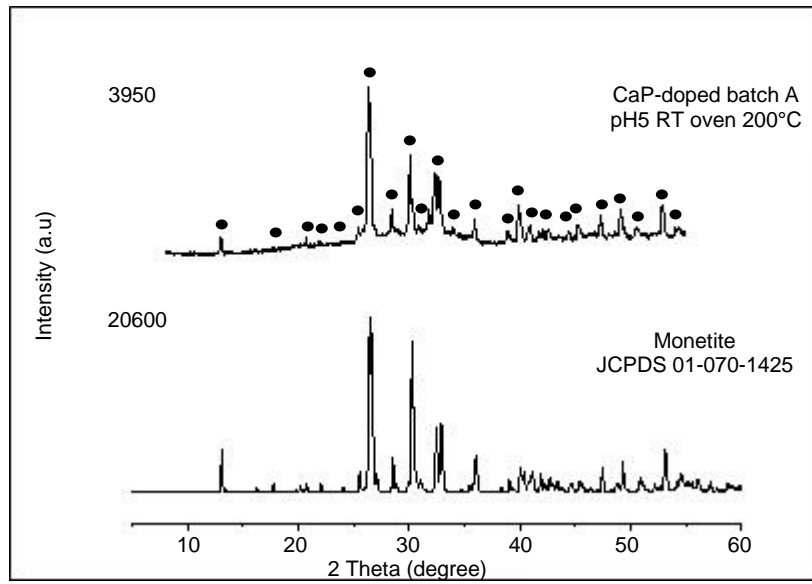


Figure 4.2.7 Hot stage XRD at 200°C of doped CaP (batch A) synthesised under room temperature and as – prepared pH 5.4 ± 0.2 conditions, compared to monetite JCPDS file 01-070-1425. Marked peaks (●) were assigned to monetite.

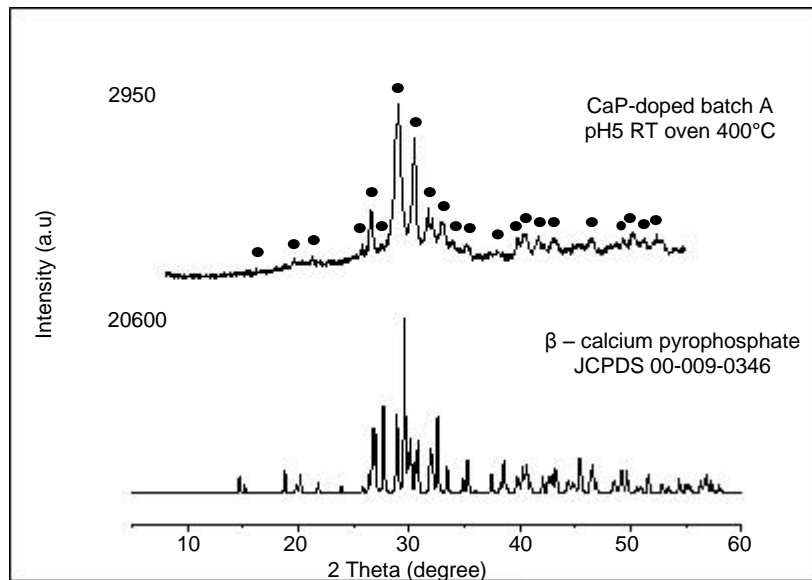


Figure 4.2.8 Hot stage XRD at 400°C of doped CaP (batch A) synthesised under room temperature and as – prepared pH 5.4 ± 0.2 conditions, compared to calcium pyrophosphate JCPDS file 00-009-0346. Marked peaks (●) were assigned to β – calcium pyrophosphate.

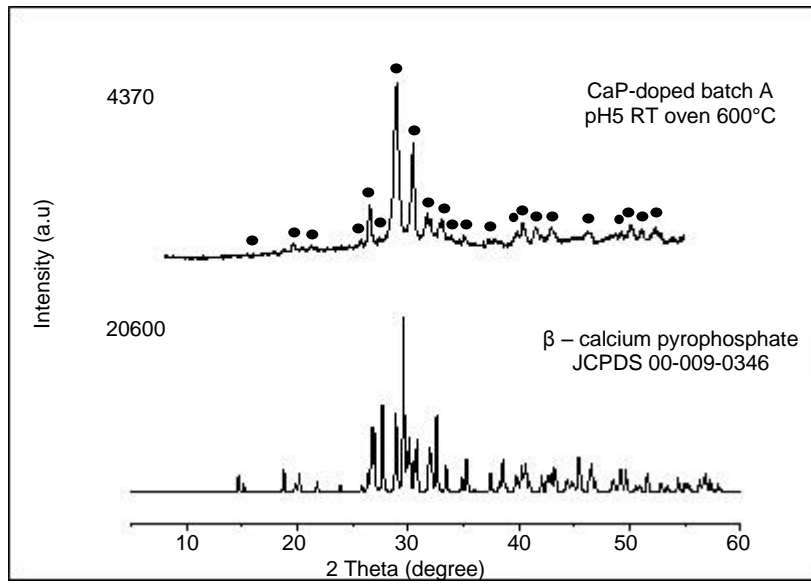


Figure 4.2.9 Hot stage XRD at 600°C of doped CaP (batch A) synthesised under room temperature and as – prepared pH 5.4 ± 0.2 conditions, compared to β – calcium pyrophosphate JCPDS file 00-009-0346. Marked peaks (●) were assigned to β – calcium pyrophosphate.

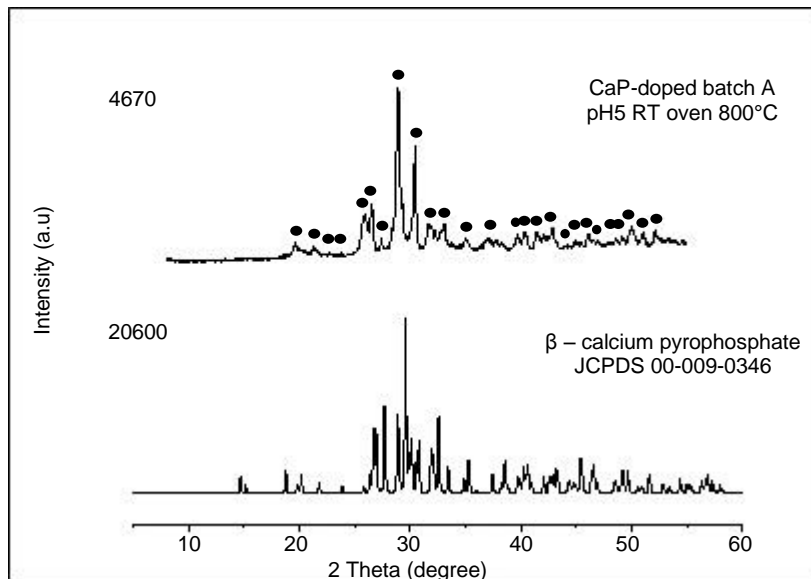


Figure 4.2.10 Hot stage XRD at 800°C of doped CaP (batch A) synthesised under room temperature and as – prepared pH 5.4 ± 0.2 conditions, compared to β – calcium pyrophosphate JCPDS file 00-009-0346. Marked peaks (●) were assigned to β – calcium pyrophosphate.

4.2.1.2 Doped CaP batch A (pH 10 ± 0.2, RT)

Representative SEM of doped CaP powder (batch A) that was synthesised under room temperature and pH 10 ± 0.2 conditions is shown in Figure 4.2.11. SEM showed well – crystallised spherical particles, which appeared to be fused together (Figure 4.2.11 b), forming a continuous and uniform layer (Figure 4.2.11 a). The particles appeared to be in the nanometre size, which would be ideal for the occlusion of dentinal tubules, because they would provide a uniform coating with a large surface area for optimum laser irradiation sintering. Figure 4.2.12 shows the volume – based distribution of doped CaP particles, as measured by the Malvern Mastersizer 2000E, with the standard percentile values d(0.1), d(0.5), d(0.9), and volume weighted mean D[4,3]. The particles had a volume weighted mean D[4,3] of 122.3 µm with a ± 1 standard deviation error bar, as shown in Figure 4.2.13. Although the values are not in good agreement with the nanoscale of particles (Figure 4.2.11), they seem to be in good agreement with doped CaP agglomerates, as shown by SEM in Figure 4.2.14.

SEM-EDX measurements (element weight percentage) of doped CaP powder (batch A) that was synthesised under room temperature and pH 10 ± 0.2 conditions are shown in Table 4.2.4. The SEM-EDX measurements of four spectra, as shown by SEM in Figure 4.2.14, indicated a mean Ca:P ratio of 1.68. The four spectra were in agreement, which indicated that the doped CaP powder consists of more homogeneous phases than previous one.

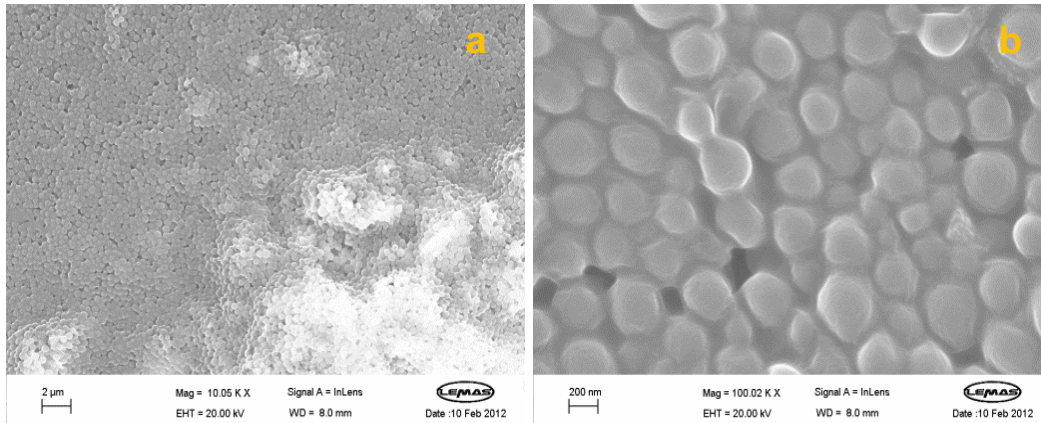


Figure 4.2.11 SEM of doped CaP (batch A) synthesised under room temperature and $\text{pH } 10 \pm 0.2$ conditions, showing (a) continuous and uniform layer and (b) spherical particles that seem to be fused together.

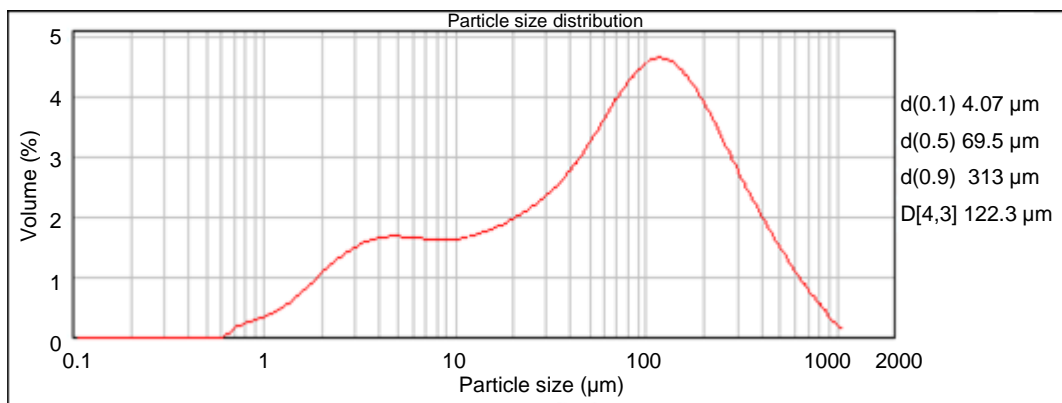


Figure 4.2.12 Particle size distribution of doped CaP (batch A) synthesised under room temperature and $\text{pH } 10 \pm 0.2$ conditions.

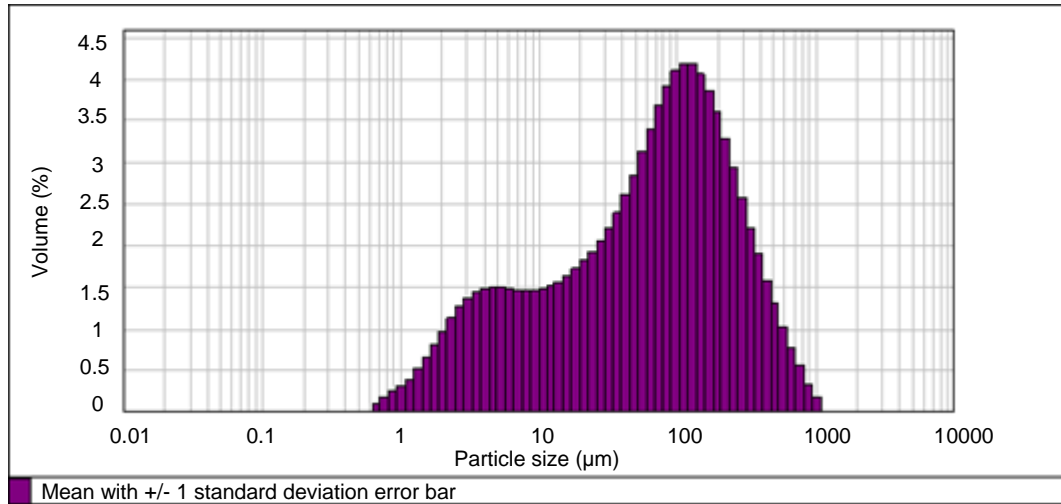


Figure 4.2.13 Statistics graph of doped CaP (batch A) synthesised under room temperature and pH 10 ± 0.2 conditions, showing the mean with ± 1 standard deviation error bar.

Table 4.2.4 SEM-EDX measurements (element weight percentage) for doped CaP (batch A) synthesised under room temperature and pH 10 ± 0.2 conditions

Spectrum	O	F	Al	P	Ca	Er	Ca:P ratio
Spectrum 1	16.4	0.3	0.03	0.3	0.6	0.04	1.82
Spectrum 2	20.6	0.9	0.2	3.8	6.2	-	1.64
Spectrum 3	18.5	0.05	0.2	4.2	6.7	-	1.57
Spectrum 4	16.6	0.1	0.1	1.6	2.7	-	1.69
Mean	18.0	0.3	0.1	2.5	4.0	-	1.68
Std. Deviation	1.9	0.4	0.1	1.8	2.9	0.04	0.1

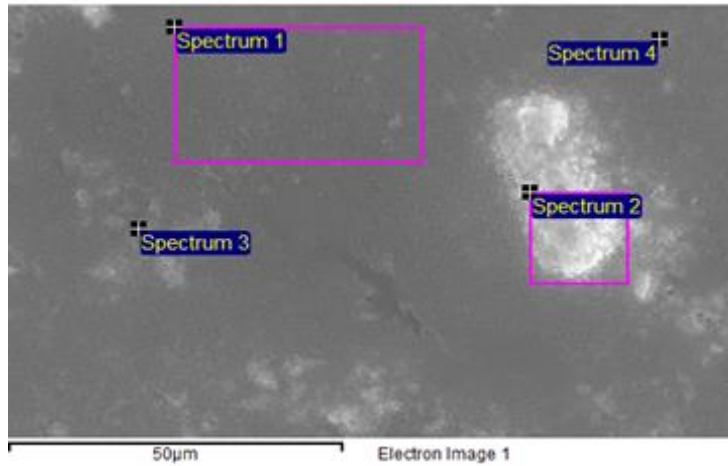


Figure 4.2.14 SEM of doped CaP synthesised under room temperature and pH 10 ± 0.2 conditions, showing the obtained EDX spectra.

XRD pattern of doped CaP powder (CaP-doped batch A pH10 RT) that was synthesised under room temperature and pH 10 ± 0.2 conditions is shown in Figure 4.2.15 and compared to that of CaP (CaP-undoped pH10 RT) under the same conditions in Figure 4.2.16. The XRD pattern in Figure 4.2.15 indicated the formation of an apatite phase together with Er_2O_3 , AlPO_4 , and CaF_2 phases, which is in good agreement with HAp JCPDS file 009-0432, Er_2O_3 JCPDS file 00-026-0604, AlPO_4 JCPDS file 01-072-1064, and CaF_2 JCPDS file 03-065-0535, respectively, but with a slight shift of Er_2O_3 peaks at higher 2 theta angle (49.9° , 59.2° , and 62.3°) to lower 2 theta angle. The presence of AlPO_4 might explain the fusing of spherical particles, as shown by SEM in Figure 4.2.11 (b), because of its binding role (429, 445, 461).

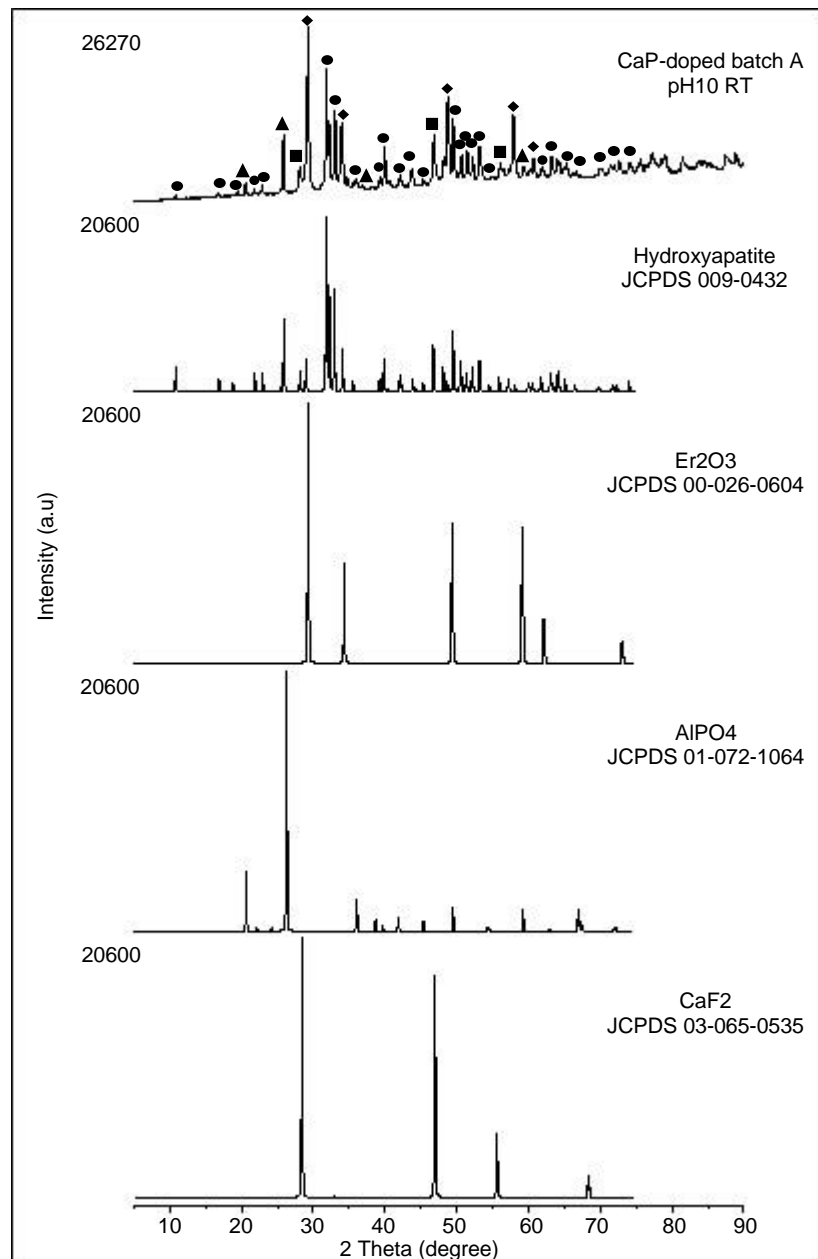


Figure 4.2.15 XRD pattern of doped CaP (batch A) synthesised under room temperature and pH 10 ± 0.2 conditions, compared to HAp, Er₂O₃, AlPO₄, and CaF₂ JCPDS files. Marked peaks (●) were assigned to brushite, (◆) were assigned to Er₂O₃, (▲) were assigned to AlPO₄, and (■) were assigned to CaF₂.

Figure 4.2.16 compares the XRD pattern of doped CaP (CaP-doped batch A pH10 RT) to that of CaP (CaP-undoped pH10 RT). The XRD patterns indicated that the XRD peaks of doped CaP (CaP-doped batch A pH10 RT) were well – defined and modified due to the addition of dopants. The brushite phase (together with HAp) that was formed with CaP (CaP-undoped pH10 RT) was not formed in the case of doped CaP (CaP-doped batch A pH10 RT), which indicated the effect of dopants' addition on the phase formation of CaP. The dopants' effect was also observed with SEM in Figure 4.2.11, which indicated the significant transformation, particularly in terms of phases' homogeneity and morphology of particles.

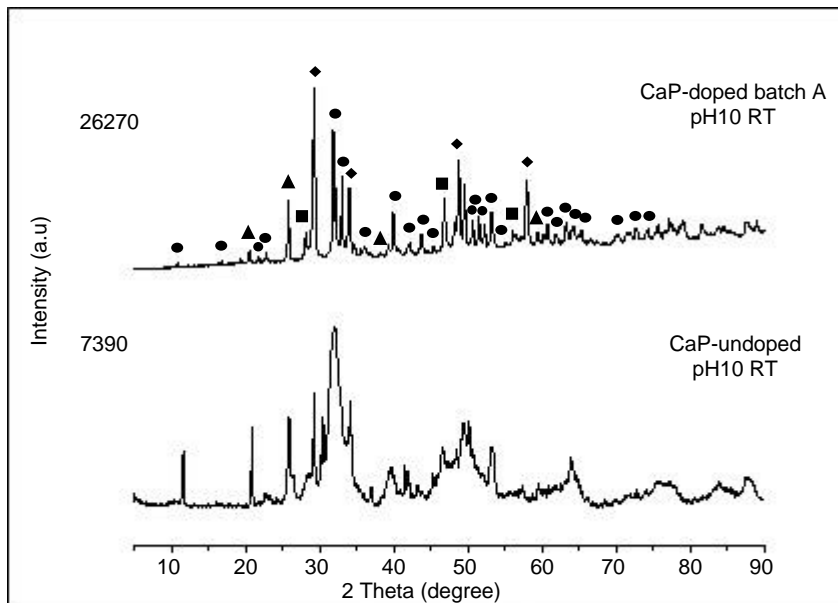


Figure 4.2.16 XRD pattern of doped CaP (batch A) synthesised under room temperature and pH 10 ± 0.2 conditions, compared to that of CaP (CaP-undoped pH 10 RT). Marked peaks (●) were assigned to brushite, (◆) were assigned to Er_2O_3 , (▲) were assigned to AlPO_4 , and (■) were assigned to CaF_2 .

4.2.1.3 Doped CaP batch A (pH 5.4 ± 0.2 , 200°C hydrothermal)

Representative SEM of doped CaP (batch A) that was synthesised under as – prepared pH 5.4 ± 0.2 and 200°C hydrothermal conditions is shown in Figure 4.2.17. SEM indicated the formation of particles with various morphologies, mainly rod – like, rounded – like, and platelet – like particles, as shown in Figure 4.2.17 (a). The particles appeared to be fused together in agglomerates, as shown in Figure 4.2.17 (b), and their particle size varied from nanometre to micrometre. Figure 4.2.18 shows the volume – based distribution of doped CaP particles, as measured by the Malvern Mastersizer 2000E, with the standard percentile values $d(0.1)$, $d(0.5)$, $d(0.9)$, and volume weighted mean $D[4,3]$. The particles had a volume weighted mean $D[4,3]$ of $54.3 \mu\text{m}$ with a ± 1 standard deviation error bar, as shown in Figure 4.2.19. The values seem to be in good agreement with the agglomerates shown by SEM.

SEM-EDX measurements (element weight percentage) of doped CaP (batch A) that was synthesised under as – prepared pH 5.4 ± 0.2 and 200°C hydrothermal conditions are shown in Table 4.2.5. The SEM-EDX measurements of five spectra, as shown in Figure 4.2.20, indicated a mean Ca:P ratio of 1.29. However, since spectrum number two, three, and four were way out, compared to spectrum number one and five, the measurements were not reliable, but they indicated that the phases were not homogenous, as established by SEM. As stated before, obtaining a range of Ca:P ratios indicates a nonhomogeneous distribution of elements (Ca, P, and dopants) in the powder.

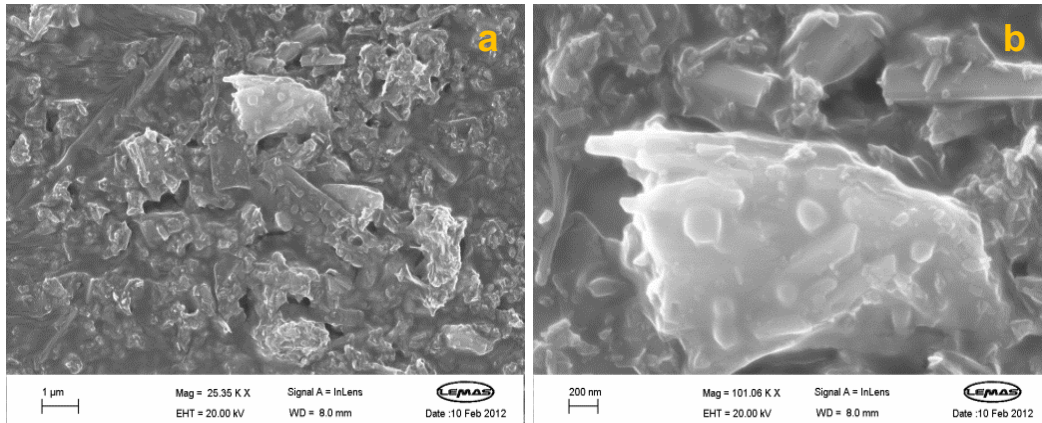


Figure 4.2.17 SEM of doped CaP (batch A) synthesised under as – prepared pH 5.4 ± 0.2 and 200°C hydrothermal conditions, showing (a) non – uniform morphology of particles and (b) fusion and agglomeration of particles.

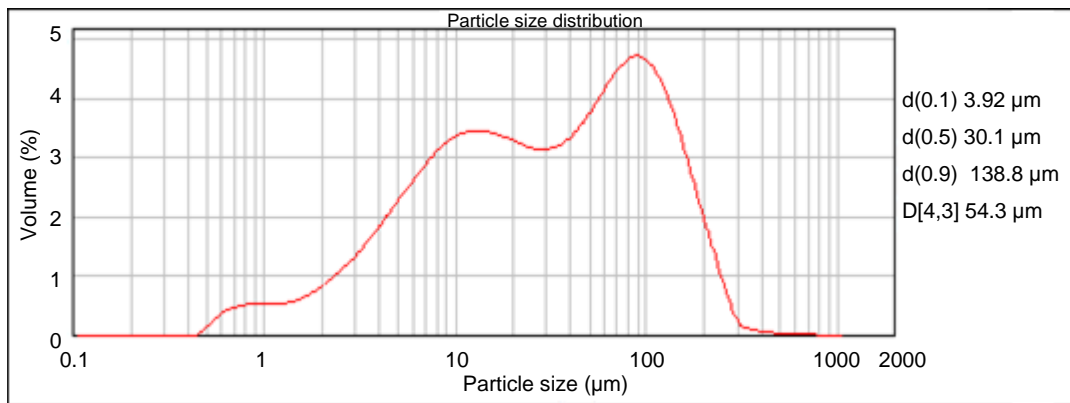


Figure 4.2.18 Particle size distribution of doped CaP (batch A) synthesised under pH 5.4 ± 0.2 and 200°C hydrothermal conditions.

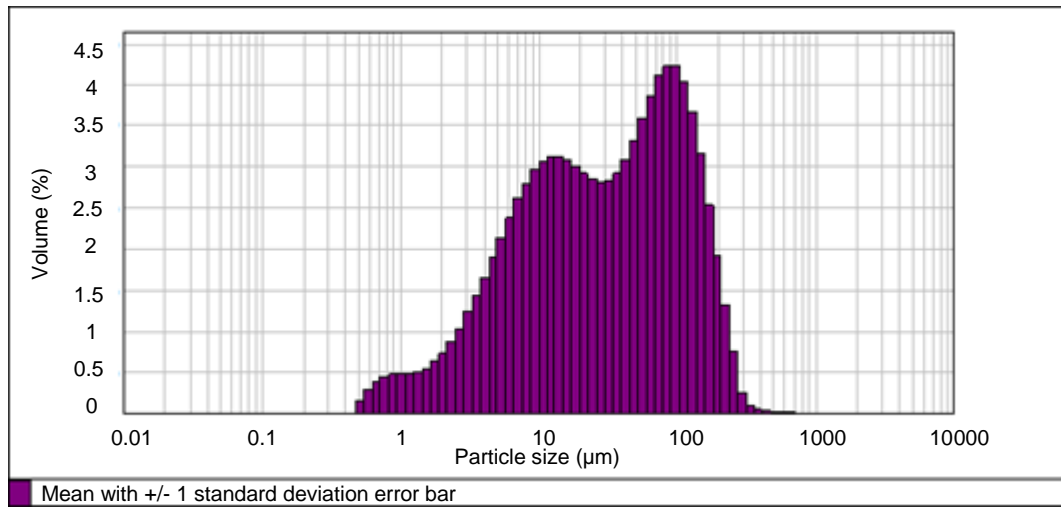


Figure 4.2.19 Statistics graph of doped CaP (batch A) synthesised under pH 5.4 ± 0.2 and 200°C hydrothermal conditions, showing the mean with ± 1 standard deviation error bar.

Table 4.2.5 SEM-EDX measurements (element weight percentage) for doped CaP (batch A) synthesised under as – prepared pH 5.4 ± 0.2 and 200°C hydrothermal conditions

Spectrum	O	F	Al	P	Ca	Er	Ca:P ratio
Spectrum 1	24.6	2	0.1	11.3	20.6	-	1.81
Spectrum 2	12.2	0.5	0.5	3.53	1.8	47.5	0.52
Spectrum 3	39	0.4	3.5	5.47	1.6	0.1	0.30
Spectrum 4	10.4	0.3	0.3	2.53	0.8	66.4	0.34
Spectrum 5	27.2	1.6	0.07	4.91	8.6	0.86	1.76
Mean	22.7	1	0.9	5.55	6.7	22.9	1.29
Std. Deviation	11.7	0.7	1.4	3.4	8.3	31.7	0.7

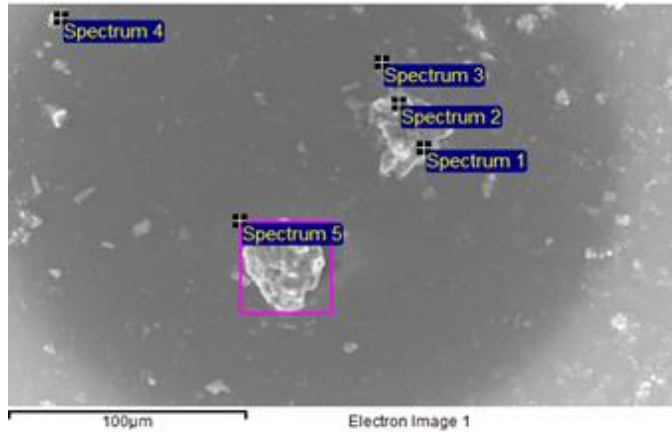


Figure 4.2.20 SEM of doped CaP synthesised under as – prepared pH 5.4 ± 0.2 and 200°C hydrothermal conditions, showing the obtained EDX spectra.

XRD pattern of doped CaP (CaP-doped batch A pH5 200°C hydrothermal) that was synthesised under as – prepared pH 5.4 ± 0.2 and 200°C hydrothermal conditions is shown in Figure 4.2.21. The XRD pattern of doped CaP (Cap-doped batch A pH5 200°C hydrothermal) indicated the formation of a brushite phase together with dopants' phases (Er_2O_3 , AlPO_4 , and CaF_2), which is in good agreement with brushite JCPDS file 01-072-0713, Er_2O_3 JCPDS file 00-026-0604, AlPO_4 JCPDS file 01-072-1064, and CaF_2 JCPDS file 03-065-0535, respectively, but with a slight shift of Er_2O_3 peaks at higher 2 theta angle (59.2° , and 62.3°) to lower 2 theta angle.

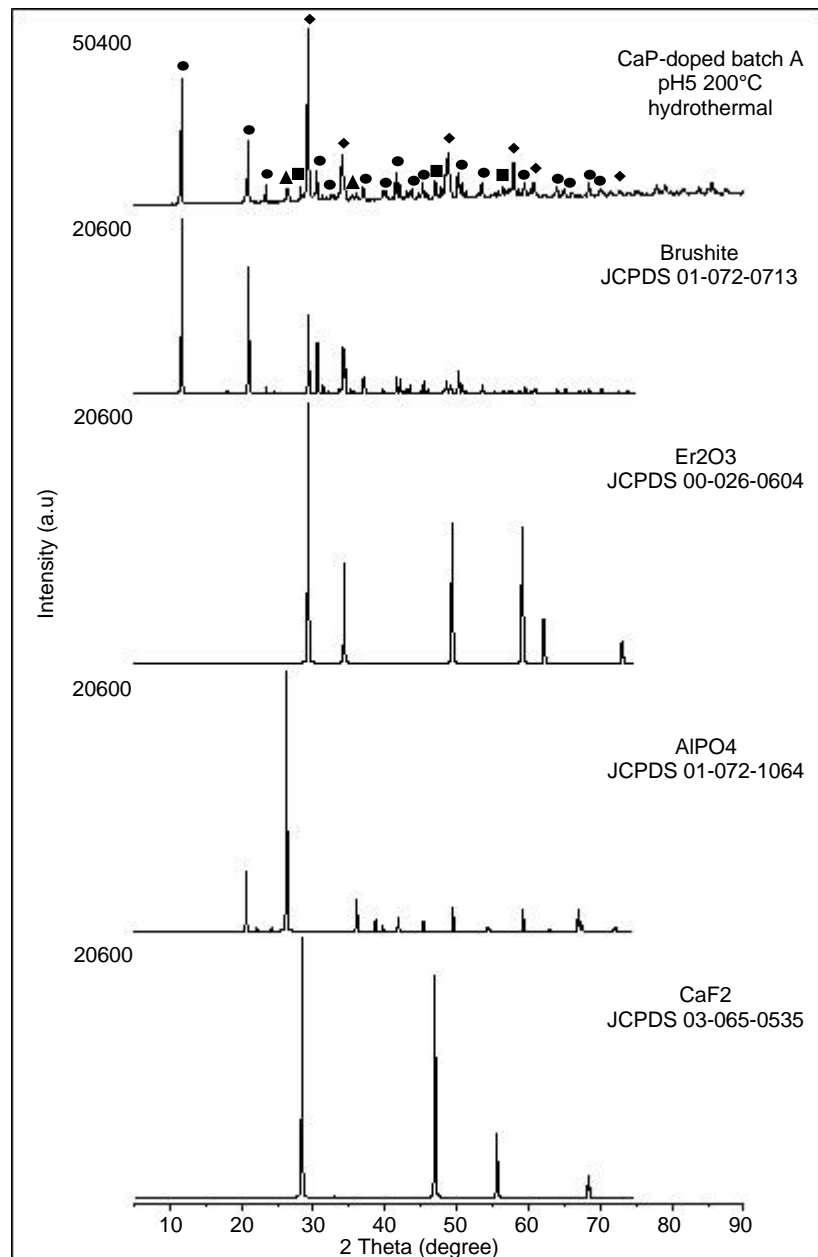


Figure 4.2.21 XRD pattern of doped CaP (batch A) synthesised under as – prepared pH 5.4 \pm 0.2 and 200°C hydrothermal conditions, compared to brushite, Er₂O₃, AlPO₄, and CaF₂ JCPDS files. Marked peaks (●) were assigned to brushite, (◆) were assigned to Er₂O₃, (▲) were assigned to AlPO₄, and (■) were assigned to CaF₂.

The XRD pattern of doped CaP (batch A) (CaP-doped batch A pH5 200°C hydrothermal) is compared to that of CaP (CaP-undoped pH5 200°C hydrothermal) under the same conditions in Figure 4.2.22. The as – prepared pH 5.4 ± 0.2 and 200°C hydrothermal conditions (Cap-undoped pH5 200°C hydrothermal) resulted in the formation of a HAp phase, which was not the case in the presence of dopants, and instead, a brushite phase was formed together with dopants' phases. This indicated that the presence of dopants prohibited the formation of HAp under as – prepared pH 5.4 ± 0.2 and 200°C hydrothermal conditions. In other words, the 200°C hydrothermal conditions were unable to produce HAp phase in the presence of dopants. This was unclear, however, it was probably because the hydrothermal energy was absorbed by dopants, particularly Er_2O_3 and AlPO_4 .

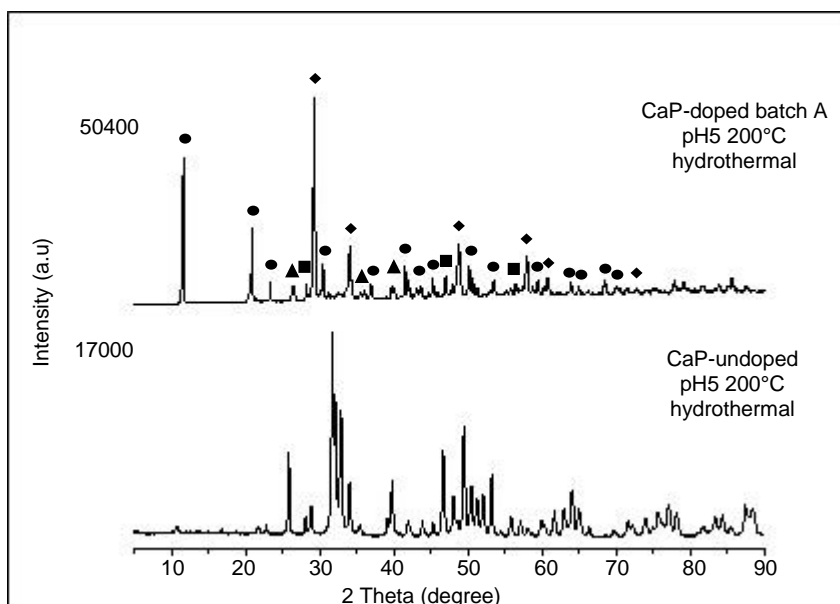


Figure 4.2.22 XRD pattern of doped CaP (batch A) synthesised under as – prepared pH 5.4 ± 0.2 and 200°C hydrothermal conditions, compared to that of CaP (HAp) (CaP-undoped pH5 200°C hydrothermal). Marked peaks (●) were assigned to brushite, (◆) were assigned to Er_2O_3 , (▲) were assigned to AlPO_4 , and (■) were assigned to CaF_2 .

4.2.1.4 Doped CaP batch A (pH 10 ± 0.2 , 200°C hydrothermal)

Representative SEM of doped CaP (batch A) that was synthesised under pH 10 ± 0.2 and 200°C hydrothermal conditions is shown in Figure 4.2.23. SEM showed agglomerations (clusters) of spherical particles, as shown in Figure 4.2.17 (a), as well as the presence of rod – and/or needle – like particles, as shown in Figure 4.2.20 (b). The spherical particles appeared to be in the nanometre scale, while the rod/needle – like particles appeared to be in the micrometre scale. Figure 4.2.24 shows the volume – based distribution of doped CaP particles, as measured by the Malvern Mastersizer 2000E, with the standard percentile values $d(0.1)$, $d(0.5)$, $d(0.9)$, and volume weighted mean $D[4,3]$. The particles had a volume weighted mean $D[4,3]$ of $85.9 \mu\text{m}$ with a ± 1 standard deviation error bar, as shown in Figure 4.2.25. The values seem to be in good agreement with the agglomerates shown by SEM in Figure 4.2.26.

SEM-EDX measurements (element weight percentage) of doped CaP (batch A) that was synthesised under pH 10 ± 0.2 and 200°C hydrothermal conditions are shown in Table 4.2.6. The SEM-EDX measurements of six spectra, as shown in Figure 4.2.26, indicated a mean Ca:P ratio of 1.73. Spectrum number four was not taking into account, because it was way out, compared to the other spectra.

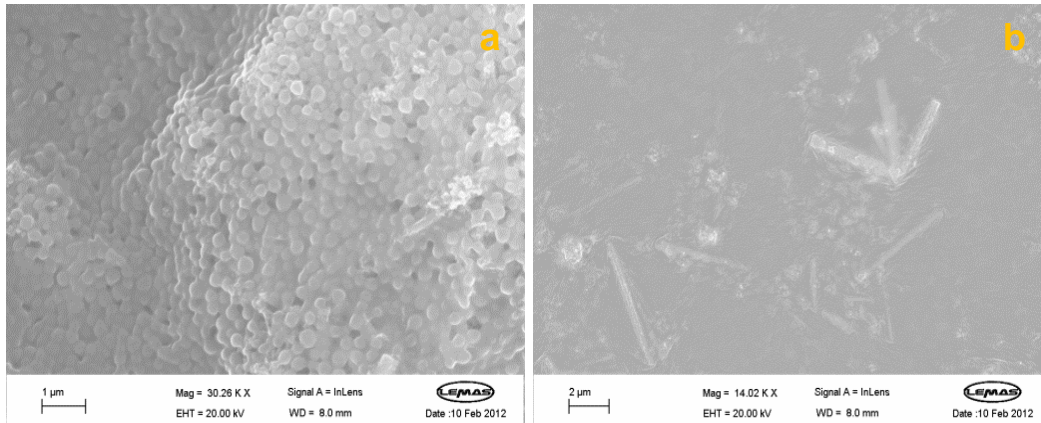


Figure 4.2.23 SEM of doped CaP (batch A) synthesised under $\text{pH } 10 \pm 0.2$ and 200°C hydrothermal conditions, showing (a) spherical particles and (b) rod/needle – like particles.

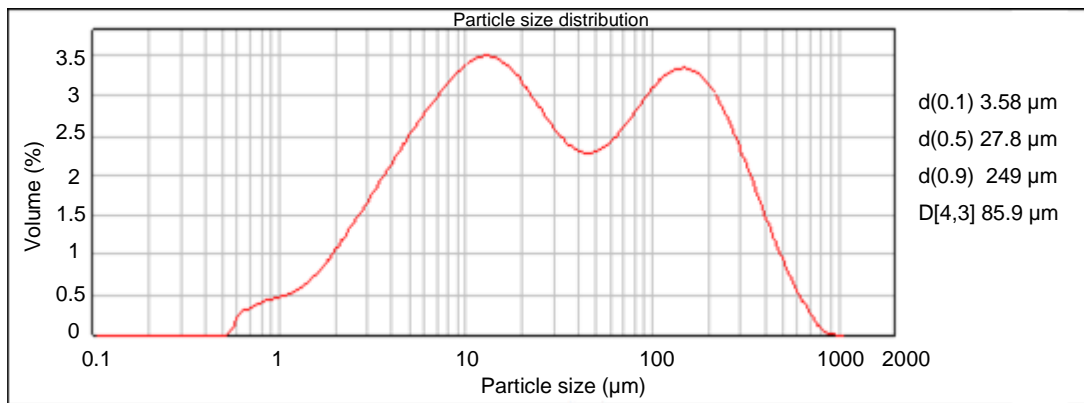


Figure 4.2.24 Particle size distribution of doped CaP (batch A) synthesised under $\text{pH } 10 \pm 0.2$ and 200°C hydrothermal conditions.

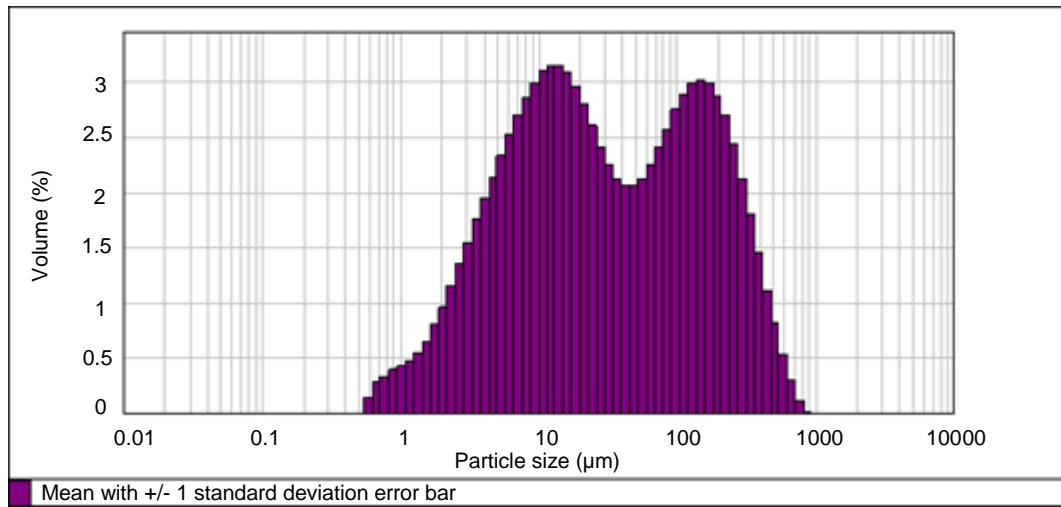


Figure 4.2.25 Statistics graph of doped CaP (batch A) synthesised under pH 10 ± 0.2 and 200°C hydrothermal conditions, showing the mean with ± 1 standard deviation error bar.

Table 4.2.6 SEMEDX measurements (element weight percentage) for doped CaP (batch A) synthesised under pH 10 ± 0.2 and 200°C hydrothermal conditions

Spectrum	O	F	Al	P	Ca	Er	Ca:P ratio
Spectrum 1	28.5	1.2	0.05	4.1	7.3	0.1	1.77
Spectrum 2	26.5	0.7	0.1	5	9	-	1.80
Spectrum 3	21.8	1.1	0.4	7.5	13.3	-	1.75
Spectrum 5	28	1.4	0.3	6	10.1	0.1	1.68
Spectrum 6	22.5	1.1	0.1	3.5	5.8	-	1.66
Mean	22.5	1	0.2	4.5	7.7	8.8	1.73
Std. deviation	7.8	0.3	0.1	2.2	4.2	21.6	0.05

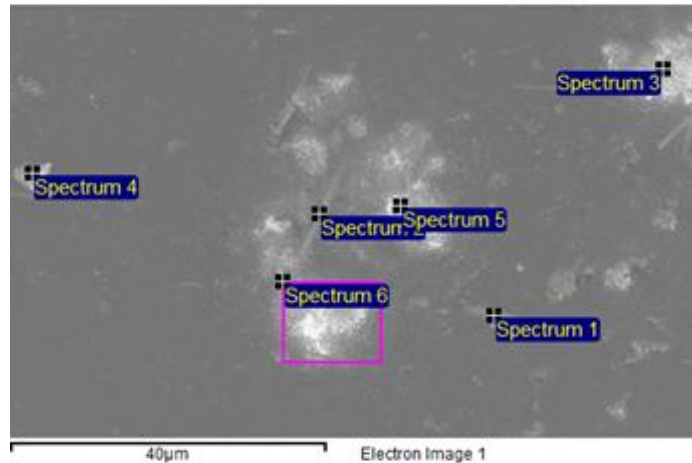


Figure 4.2.26 SEM of doped CaP synthesised under pH 10 ± 0.2 and 200°C hydrothermal conditions, showing the obtained EDX spectra.

XRD pattern of doped CaP (CaP-doped batch A pH10 200°C hydrothermal) that was synthesised under pH 10 ± 0.2 and 200°C hydrothermal conditions is shown in Figure 4.2.27 and compared to that of CaP (CaP-undoped pH10 200°C hydrothermal) under the same conditions in Figure 4.2.28. The XRD pattern in Figure 4.2.27 indicated the formation of an apatite phase together with dopants' phases, which is in good agreement with HAp JCPDS file 009-0432, Er_2O_3 JCPDS file 00-026-0604, AlPO_4 JCPDS file 01-072-1064, and CaF_2 JCPDS file 03-065-0535, respectively, but with a slight shift of Er_2O_3 peaks at higher 2 theta angle (49.9° , 59.2° , and 62.3°) to lower 2 theta angle. The formation of HAp phase was also in good agreement with the XRD pattern of CaP (HAp) synthesised during the initial investigation (CaP-undoped pH10 200°C hydrothermal (initial investigation)) under the same conditions (Figure 4.2.28). The latter XRD pattern comparison also confirmed the presence of dopants' phases in the doped CaP (CaP-doped batch A pH10 200°C hydrothermal).

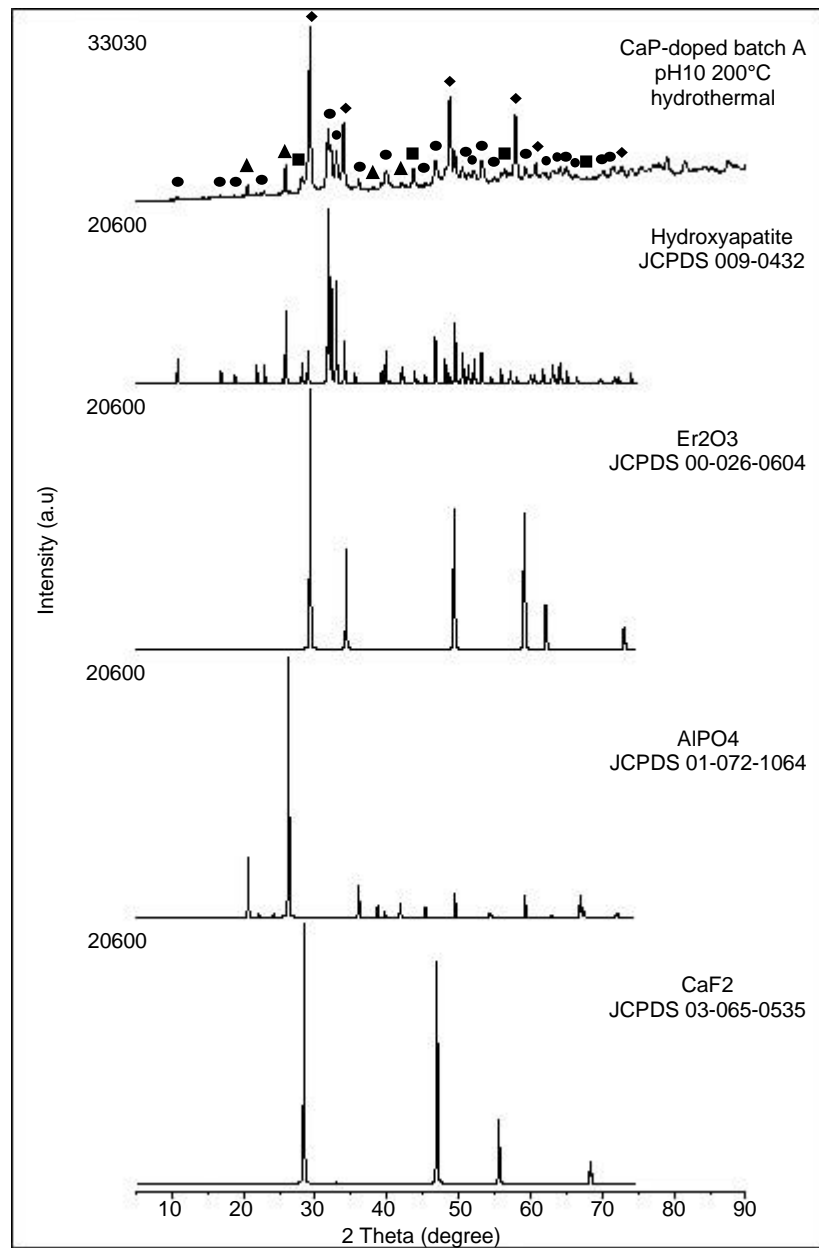


Figure 4.2.27 XRD pattern of doped CaP (batch A) synthesised under pH 10 ± 0.2 and 200°C hydrothermal conditions, compared to HAp, Er_2O_3 , AlPO_4 , and CaF_2 JCPDS files. Marked peaks (●) were assigned to HAp, (◆) were assigned to Er_2O_3 , (▲) were assigned to AlPO_4 , and (■) were assigned to CaF_2 .

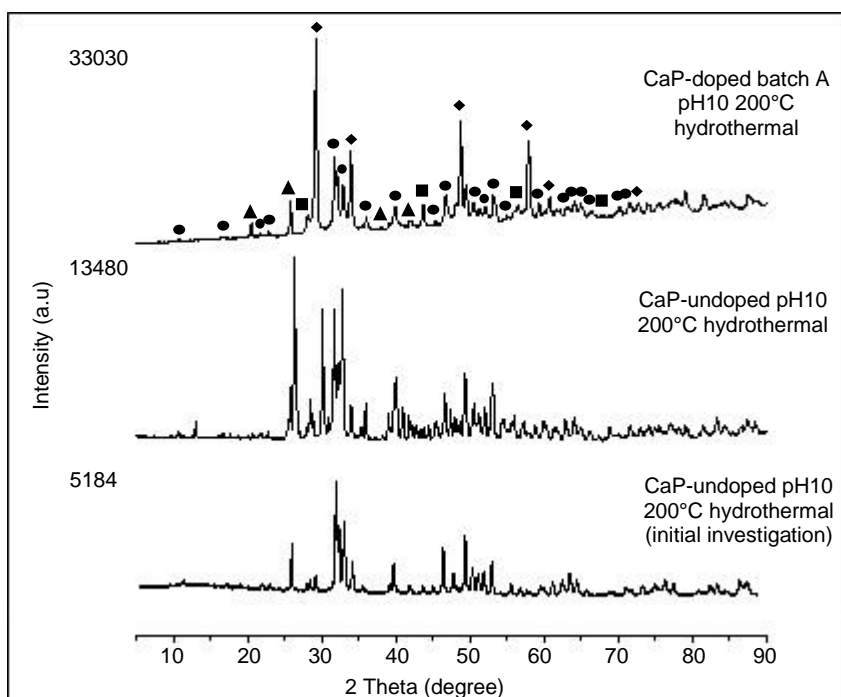


Figure 4.2.28 XRD pattern of doped CaP (batch A) synthesised under pH 10 ± 0.2 and 200°C hydrothermal conditions, compared to that of CaP (CaP-undoped pH10 200°C hydrothermal) synthesised under the same conditions. Marked peaks (●) were assigned to HAp, (◆) were assigned to Er_2O_3 , (▲) were assigned to AlPO_4 , and (■) were assigned to CaF_2 .

SEM and XRD of doped CaP (batch A) indicated the formation of different CaP phases and different particle morphologies under different conditions. The crystallised platelet – like particles with nanospherical particles of doped CaP (batch A) that were synthesised under room temperature and as – prepared pH 5.4 ± 0.2 conditions (Figure 4.2.1) seem to be in good agreement with the XRD pattern of brushite, monetite, and dopants' phases (Er_2O_3 , AlPO_4 , and CaF_2). The XRD pattern (Figure 4.2.5) indicated multiple phases, and that the doping may have resulted in a composite of Er_2O_3 , AlPO_4 , CaF_2 , monetite, and brushite. The presence of secondary phases was supported by transmission electron microscopy (TEM) and TEM – EDX measurements, as shown in Figure 4.2.29 and Table 4.2.7, respectively.

Under room temperature and pH 10 ± 0.2 conditions, the formation of well – crystallised spherical particles (Figure 4.2.11), fused together and forming a continuous and uniform layer, indicated homogenous phases. The XRD pattern (Figure 4.2.15) indicated the formation of HAp together with dopants' phases. The presence of AlPO_4 phase, as a binder, explained the fusing of the spherical particles. Under as – prepared pH 5.4 ± 0.2 and 200°C hydrothermal conditions, the formation of particles with various morphology, mainly rod – like, rounded – like, and platelet – like particles (Figure 4.2.17) is in good agreement with XRD pattern (Figure 4.2.21), which indicated the formation of a brushite phase together with dopants' phases. Under pH 10 ± 0.2 and 200°C hydrothermal conditions, the formation of spherical particles as well as the presence of rod – and/or needle – like particles (Figure 4.2.23) are in good agreement with their XRD pattern (Figure 4.2.27), the latter which indicated the formation of HAp together with dopants' phases.

The results indicated that the effective addition of dopants was observed under high pH levels (pH 10 ± 0.2), which resulted in homogenous phases and affected the size and shape of particles. As stated before, the reduction of particle size was probably due to the increase of the nucleation rate with increasing pH levels (549).

Table 4.2.8 compares the volume – based distribution of doped CaP (batch A) powders. The refractive index and absorption index for doped CaP (batch A) used in these calculations were the same as those for CaP (1.629 and 0.1, respectively). The measured median particle diameter $d(0.5)$, absolute deviation from median (uniformity), span, and 10% and 90% size distribution

by volume percentage (v%) for doped CaP particles (batch A) are presented in Table 4.2.8.

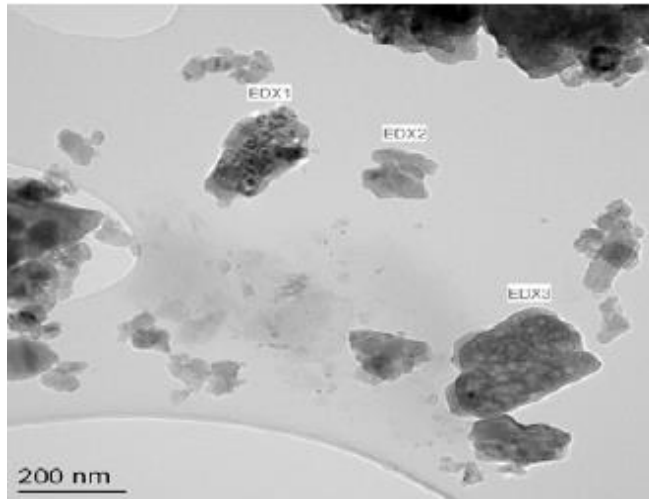


Figure 4.2.29 TEM of doped CaP synthesised under room temperature and as – prepared pH 5.4 ± 0.2 conditions, showing the obtained EDX spectra.

Table 4.2.7 TEM – EDX measurements (element weight percentage) for doped CaP synthesised under room temperature and as – prepared pH 5.4 ± 0.2 conditions

Element	CaP-doped batch A pH5 RT (Weight %)			Mean	Std. Deviation
	Spectrum 1	Spectrum 2	Spectrum 3		
O K	10.67	19.14	40.52	23.44	15.38
F K	30.42	20.22	0.20	16.94	15.37
Al K	2.25	6.25	0.37	2.95	3
P K	3.08	6.07	17.91	9.02	7.84
Ca K	36.42	21.62	24.25	27.43	7.89
Er L	2.17	-0.82	-0.66	0.23	1.68

The results indicated that the mean diameter $D[4,3]$ was lowest (30.5 μm) in the case of CaP-doped batch A pH5 RT and highest (122.3 μm) in the case of CaP-doped batch A pH10 RT. In the case of CaP-doped batch A pH5 200°C hydrothermal and CaP-doped batch A pH10 200°C hydrothermal, the mean diameter $D[4,3]$ was 54.3 μm and 85.9 μm , respectively. These values are in good agreement with doped CaP (batch A) particles that were synthesised under room temperature and pH 5.4 ± 0.2 conditions and doped CaP agglomerates in the rest of doped CaP (batch A) powders. Although the particles that were synthesised under 200°C hydrothermal and/or pH 10 ± 0.2 conditions were shown to be in the nanoscale by SEM, the mean diameter was affected by the formation of agglomerations. As stated before, this is because the accuracy of these measurements depends on the quality of the powder dispersion.

Moreover, the small span value (2.76) in the case of CaP-doped batch A pH5 RT indicated a narrow distribution, while the large span values (4.44, 4.47, and 8.8) in the case of CaP-doped batch A pH10 RT, CaP-doped batch A pH5 200°C hydrothermal, and CaP-doped batch A pH10 200°C hydrothermal indicated a broader distribution. This indicated that the particles of CaP-doped batch A pH5 RT were more uniform in size than those of the rest of powders (CaP-doped batch A pH5 200°C hydrothermal, and CaP-doped batch A pH10 200°C hydrothermal and CaP-doped batch A pH10 RT).

Table 4.2.8 Particle size data for doped CaP (batch A) powders

Sample	d(0.1) μm	d(0.5) μm	d(0.9) μm	Uniformity	Span	D[4,3] μm
CaP-doped batch A pH5 RT	4.17	13.8	42.3	1.66	2.76	30.55
CaP-doped batch A pH10 RT	4.07	69.5	313	1.42	4.44	122.32
CaP-doped batch A pH5 200°C hydrothermal	3.92	30.16	138.8	1.43	4.47	54.34
CaP-doped batch A pH10 200°C hydrothermal	3.58	27.8	249	2.72	8.8	85.94

Doped CaP powders (batch A) were also characterised by FTIR in order to detect their functional groups and bonds. FTIR spectra of doped CaP powders (batch A) in the wavenumber range of 4000 – 400 cm^{-1} are compared and shown in Figures 4.2.30, 4.2.31, and 4.2.32. FTIR absorption bands and their assigned references are presented in Table 4.2.9.

Erbium oxide (Er_2O_3) has a fingerprint region that shows characteristic absorption bands at 563 cm^{-1} and 471 cm^{-1} , which correspond to Er–O–Er and Er–O, respectively, while absorption bands in the range 1200 – 4000 cm^{-1} correspond to the surface activity of Er_2O_3 (564). Aluminium phosphate (AlPO_4) has two types of tetrahedral structures AlO_4 and PO_4 , which correspond to stronger P–O and weaker Al–O bonds (565). However, FTIR spectrum of AlPO_4 shows tetrahedral basic structural elements of AlPO_4 with P–O symmetric stretching mode at 1100 cm^{-1} , asymmetric stretching mode at 1250 cm^{-1} , symmetric bending mode at 480 cm^{-1} , and asymmetric bending mode at 695 cm^{-1} (565). Absorption bands in the region 1270 – 1200 cm^{-1} correspond to asymmetric stretching of bridging of PO^{-2} ($\text{O}=\text{P}-\text{O}-$), while absorption bands around 900 cm^{-1} correspond to asymmetric stretching of P–O–P (566). Absorption bands in the region 1120 – 1080 cm^{-1} correspond to asymmetric stretching of PO_3 group, while absorption bands in the region

1030 – 1000 cm^{-1} correspond to symmetric stretching of PO_3 group (566). In addition, AlPO_4 has a strong and narrow absorption peak at 690 cm^{-1} as well as a broad absorption peak in the region 520 – 400 cm^{-1} (567). FTIR spectrum of CaF_2 shows an absorption band at 443 cm^{-1} , which corresponds to stretching mode of Ca–F (568). In the case of fluoride – doped CaP/HAp, absorption bands at 647 – 630 cm^{-1} , 680 – 673 cm^{-1} , and 720 – 713 cm^{-1} are due to the substitution of fluoride ion for OH group (495). In the presence of CaF_2 , absorption bands at 744 cm^{-1} , 716 cm^{-1} , 713 cm^{-1} , 674 cm^{-1} , and 666 cm^{-1} are associated with the formation of OH–F–OH bonds, while an absorption band at 3538 cm^{-1} is associated with the formation of OH–F bonds (569).

FTIR spectra of doped CaP powders (batch A) showed CaP absorption bands of PO_4 group at 600 – 550 cm^{-1} , 1100 – 960 cm^{-1} , and 2100 cm^{-1} ; HPO_4 group at 875 cm^{-1} , CO_3 group at 2400 – 2300 cm^{-1} , absorbed H_2O molecules at 1650 – 1600 cm^{-1} , and OH group at 3570 and 634 cm^{-1} (552, 553). The PO_4 group around 2100 cm^{-1} and OH group at 634 cm^{-1} are the characteristic absorption bands for hydroxyapatite, as observed with control CaP powders. The effect of dopants was associated with absorption bands at 1250 cm^{-1} , 780 cm^{-1} , 660 cm^{-1} , and 522 cm^{-1} , which were only observed with doped CaP powder (CaP-doped batch A pH5 RT), as compared to CaP powder (CaP-undoped pH5 RT). The absorption band at 3540 cm^{-1} was observed with (CaP-doped batch A pH5 RT) and (CaP-doped batch A pH10 200°C hydrothermal), which was assigned to the formation of OH–F bonds (569). FTIR spectra of (CaP-doped batch A pH10 RT), (CaP-doped batch A pH5 200°C hydrothermal), and (CaP-doped batch A pH10 200°C hydrothermal) were similar to those of CaP powders under the same

conditions. The absorption bands around 2400 cm^{-1} and 1545 cm^{-1} that were assigned to CO_3 group in the case of CaP powders were significantly decreased with all doped CaP powders (batch A). This may indicate that the doped CaP powders (batch A) are less carbonated than undoped CaP powders.

Under room temperature and as – prepared pH 5.4 ± 0.2 conditions, the doped CaP (CaP-doped batch A pH5 RT) showed absorption bands of PO_4 group (v1) (P–O) at 985 cm^{-1} , PO_4 group (v4) (O–P–O) at 574 and 601 cm^{-1} , and PO_4 group (v3) (P–O) at $1054 - 1035\text{ cm}^{-1}$. These bands were sharper, defined, and more developed than those of CaP (CaP-undoped pH5 RT). The PO_4 group (v2) (O–P–O) at 425 cm^{-1} that was observed with CaP powder (CaP-undoped pH5 RT) was absent in doped CaP powder (CaP-doped batch A pH5 RT). The characteristic absorption band of HPO_4 group at 871 cm^{-1} confirmed the presence of DCP brushite/monetite, as revealed by XRD. The absorption bands at 1230 cm^{-1} and 1132 cm^{-1} were assigned to P–O asymmetric stretching and symmetric stretching of AlPO_4 , respectively, while the absorption band at 522 cm^{-1} was assigned to Er–O–Er of Er_2O_3 . In addition, the absorption bands around 784 cm^{-1} and 665 cm^{-1} were assigned to the formation of OH–F–OH bond. The absorption band of absorbed H_2O at 1650 cm^{-1} was sharp, and it was assigned to the bending mode of absorbed H_2O . The absorption band of CO_3 group at 2300 cm^{-1} was smaller than that of CaP (CaP-undoped pH5 RT). In the region $4000 - 3000\text{ cm}^{-1}$, the absorption bands of stretched and absorbed H_2O were observed at 3490 cm^{-1} and 3160 cm^{-1} , respectively, while the absorption band at 3538 cm^{-1} was assigned to the formation of F–OH bond.

Under room temperature and pH 10 ± 0.2 conditions, the absorption band of PO_4 group (ν_3) (P–O) at $1150 - 950 \text{ cm}^{-1}$ was shaped and merged as one band with shoulders, as occurred with CaP powder (CaP-undoped pH10 RT). The absorption bands of PO_4 group (ν_4) (O–P–O) at $600 - 550 \text{ cm}^{-1}$ were shaped into two absorption bands, instead of three absorption bands that were observed with CaP powder (CaP-undoped pH10 RT). The absorption band at 634 cm^{-1} was assigned to the structural OH group, which was absent in the CaP powder (CaP-undoped pH10 RT). On the other hand, the absorption band of HPO_4 group at 875 cm^{-1} that was observed with the CaP powder (CaP-undoped pH10 RT) was absent. The absorption band of absorbed H_2O at 1650 cm^{-1} was broader and more intense, and the absorption band of CO_3 group at 2350 cm^{-1} was significantly reduced, compared to the CaP powder (CaP-undoped pH10 RT). The absorption bands in the region $4000 - 3000 \text{ cm}^{-1}$, corresponding to the stretched and absorbed H_2O molecules at 3490 cm^{-1} and 3160 cm^{-1} , respectively, were very weak and broad. The absorption band of structural OH group and F–OH were observed at 3570 cm^{-1} and 3538 cm^{-1} , respectively, with very weak intensities.

Under as – prepared pH 5.4 ± 0.2 and 200°C hydrothermal conditions, the absorption band of PO_4 group (ν_1) was absent, while the characteristic absorption bands of PO_4 group (ν_3) (P–O) at $1150 - 950 \text{ cm}^{-1}$ and PO_4 group (ν_4) (O–P–O) at $600 - 550 \text{ cm}^{-1}$ were broader than those of CaP powder (CaP-undoped pH5 200°C hydrothermal). The absorption band of structural OH group at 634 cm^{-1} was absent, which was observed with the CaP powder (CaP-undoped pH5 200°C hydrothermal). The absorption band of HPO_4 group at 875 cm^{-1} was observed with weak intensity, which

confirmed the presence of brushite, as revealed by XRD. The absorption band of absorbed H₂O molecules at 1650 cm⁻¹ was similar to that of CaP powder (CaP-undoped pH5 200°C hydrothermal). On the other hand, the absorption band of CO₃ group at 2350 cm⁻¹ was significantly reduced, and the absorption band of CO₃ group (v3) at 1550 cm⁻¹ was absent, compared to the CaP powder (CaP-undoped pH5 200°C hydrothermal). The absorption bands in the region 4000 – 3000 cm⁻¹, corresponding to the stretched and absorbed of H₂O molecules at 3490 cm⁻¹ and 3160 cm⁻¹, respectively, as well as the absorption bands of structural OH group and F–OH bond were observed at 3570 cm⁻¹ and 3538 cm⁻¹, respectively, with weak intensities.

Under pH 10 ± 0.2 and 200°C hydrothermal conditions, the absorption band of PO₄ group (v1) was absent, and the characteristic absorption bands of PO₄ group (v3) (P–O) at 1150 – 950 cm⁻¹ and PO₄ group (v4) (O–P–O) at 600 – 550 cm⁻¹ were broader than those of CaP powder (CaP-undoped pH10 200°C hydrothermal). The absorption band of structural OH group was observed at 634 cm⁻¹, as with the CaP powder (CaP-undoped pH10 200°C hydrothermal). The absorption band of HPO₄ group at 875 cm⁻¹ was absent. The absorption band of absorbed H₂O molecules at 1650 cm⁻¹ was more intense and broader than that of CaP powder (CaP-undoped pH10 200°C hydrothermal). On the other hand, the absorption band of CO₃ group at 2350 cm⁻¹ was significantly reduced, compared to CaP powder (CaP-undoped pH10 200°C hydrothermal). In the region 4000 – 3000 cm⁻¹, the stretching of H₂O molecules was observed at 3490 cm⁻¹ with a broad absorption band, whereas the absorbed H₂O molecules at 3160 cm⁻¹ was absent. In addition, the absorption bands of structural OH group and the formation of F–OH bond were observed at 3570 cm⁻¹ and 3538 cm⁻¹, respectively.

The P–O bond at 1230 – 1132 cm^{-1} and Er–O–Er bond at 522 cm^{-1} confirmed the presence of Er_2O_3 and AlPO_4 , respectively, in the doped CaP powder (CaP-doped batch A pH5 RT), whereas the OH–F–OH and F–OH bonds at 784 – 665 cm^{-1} and 3438 cm^{-1} , respectively, indicated the possible incorporation of F^- into the structure of CaP. On the other hand, in the rest of doped CaP powders (batch A), the broadening of absorption bands of PO_4 group (v3) (P–O) at 1150 – 950 cm^{-1} and PO_4 group (v4) (O–P–O) at 600 – 550 cm^{-1} could be due to the presence of dopants, or it might indicate the possibility of some degree of incorporation of Er^{3+} and Al^{3+} . The formation F–OH bond at 3438 cm^{-1} in the case of doped CaP powders that were synthesised under pH 10 ± 0.2 conditions (RT and 200°C hydrothermal conditions) indicated the possible incorporation of F^- into the structure of HAp, and thus, the formation of fluorohydroxyapatite. Although FTIR of doped CaP (batch A) indicated the possible incorporation of F^- into the CaP structure, the formation of F – doped phases, such as fluorohydroxyapatite, was not observed in the XRD patterns. The latter indicated the formation of CaP phase/s together with dopants' phases (Er_2O_3 , AlPO_4 , and CaF_2).

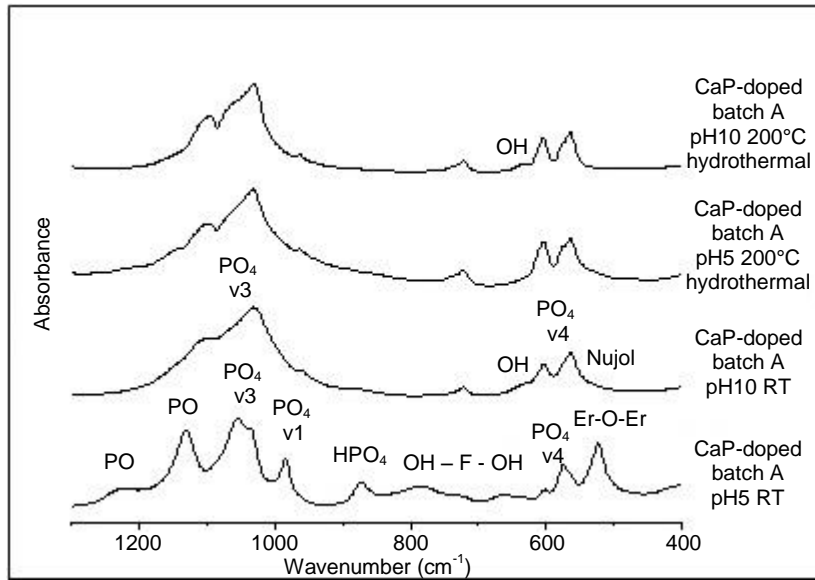


Figure 4.2.30 FTIR spectra of doped CaP powders (batch A) in the MIR region and wavenumber range 1300 – 400 cm⁻¹.

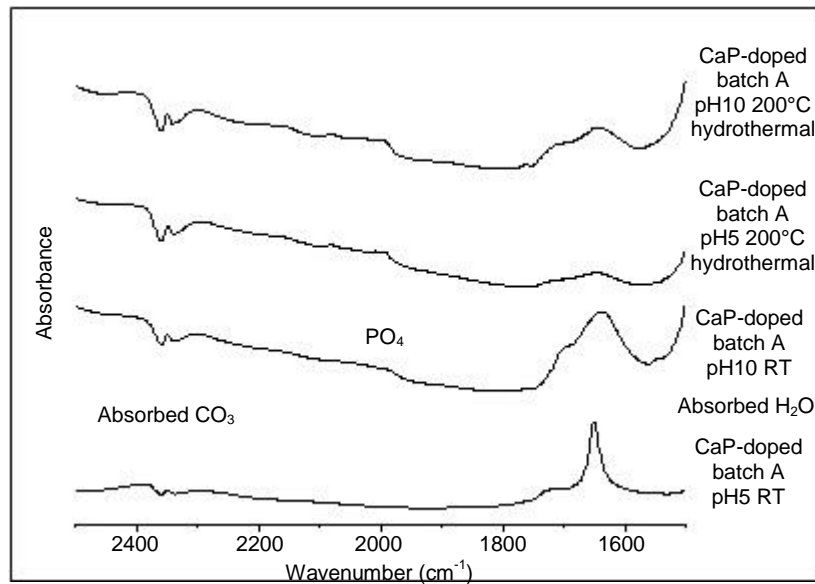


Figure 4.2.31 FTIR spectra of doped CaP powders (batch A) in the MIR region and wavenumber range 2500 – 1400 cm⁻¹.

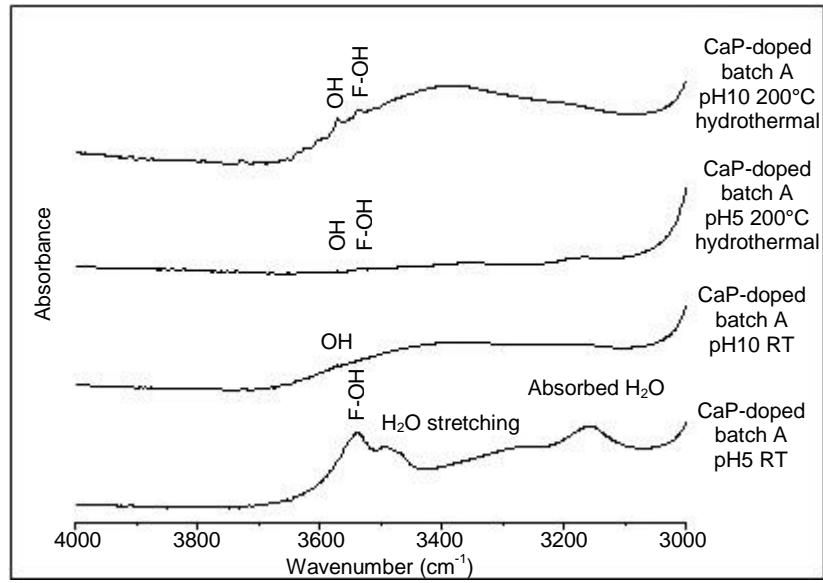


Figure 4.2.32 FTIR spectra of doped CaP powders (batch A) in the NIR region and wavenumber range 4000 – 3000 cm^{-1} .

Table 4.2.9 Characteristic IR absorption frequencies (cm^{-1}) of functional groups for doped CaP powder (batch A), compared to those of reported data (552, 553, 564-566, 569)

Functional group and Absorption cm^{-1} (Reference)	Doped CaP A pH5 RT		Doped CaP A pH10 RT		Doped CaP A pH5 200°C hydrothermal		Doped CaP A pH10 200°C hydrothermal	
	cm^{-1}	Intensity	cm^{-1}	Intensity	cm^{-1}	Intensity	cm^{-1}	Intensity
Er-O-Er	522	Medium-strong	-	-	-	-	-	-
550–650 cm^{-1} PO ₄ v4	574	Small-medium	563	Small-medium	565	Small-medium	565	Medium
	601	Weak-small	603	Small	603	Small-medium	603	Medium
634 cm^{-1} Structural OH	-	-	634	weak-sh	-	-	634	weak-small
666 cm^{-1} OH-F-OH	663	Weak-small	-	-	-	-	-	-
720 cm^{-1} Nujol	721	weak	721	Small	723	Small	721	Small
780 cm^{-1} OH-F-OH	780	weak	-	-	-	-	-	-
875 cm^{-1} HPO ₄	873	Small	-	-	-	-	-	-
960 cm^{-1} PO ₄ v1	985	Small-medium	962	small-like sh	964	small-like sh	964	small-like sh
	1035	Sh	1031	Strong	1031	Strong	1031	Strong
1000–1200 cm^{-1} PO ₄ v3	1054	Strong	1095	small-like sh	1097	small-like sh	1095	small-like sh
1100 cm^{-1} PO (AIPO ₄)	1132	Strong	-	-	-	-	-	-
1250 cm^{-1} PO (AIPO ₄)	1224	small	-	-	-	-	-	-
1600–1650 cm^{-1} H ₂ O absorbed	1650	Strong-sharp	1641	Strong broad	1648	Small broad	1645	Medium broad
2000–2100 cm^{-1} PO ₄	-	-	-	-	2053	v. weak	2050	v. weak
	-	-	2080	weak	2080	Weak-small	2080	Small
2100–2400 cm^{-1} CO ₂ absorbed	2348	small	2348	small	2348	Small	2348	Small
3100–3600 cm^{-1} H ₂ O absorbed	3158	Small-medium	-	-	3166	v. weak	-	-
3580–3600 cm^{-1} H ₂ O stretching	3492	Weak-small	3374	Weak broad	3349	v. weak	3374	Weak broad
3535 cm^{-1} F-OH	3538	Small	-	-	-	-	3538	Small
3571 cm^{-1} Structural OH	-	-	3570	weak	3570	v. weak	3570	Small

v = very, sh = shoulder, vibrational modes (v1 = symmetrical stretching, v2 = asymmetrical stretching, v3 = bending in and out of plane, and v4 = bending in plane)

Thermal behaviour of doped CaP powders was investigated using differential scanning calorimetry (DSC). As with CaP powders, the heat flow of DSC measurements was set to Endo up, which indicates that endothermic changes are peaked up, while exothermic changes are peaked down. DSC of doped CaP powders (batch A) are compared in Figure 4.2.33, and DSC peak centres are presented in Table 4.2.10. CaP powder (CaP-doped batch A pH5 RT) that was synthesised under room temperature and as – prepared pH 5.4 ± 0.2 conditions showed a sharp and intense endothermic peak at 168.2°C and a very weak endothermic peak at 434.5°C , which were assigned to the liberation of water and explosion of lattice water, respectively (560).

Although no endothermic peaks around 168.2°C were observed with CaP powder (CaP-undoped pH5 RT), the endothermic peaks at 168.2°C and 434.5°C in the doped CaP powder (CaP-doped batch A pH5 RT) are in good agreement with the reported phase transformations from brushite to monetite at $\sim 200^{\circ}\text{C}$ and from monetite to calcium pyrophosphate ($\beta\text{-Ca}_2\text{P}_2\text{O}_7$) at $\sim 400^{\circ}\text{C}$ (550, 551). As with CaP powders, the explosion of lattice water and the liberation of water were probably due to the chemical reaction of OH radicals, which were liberated from doped CaP structure during heating. This indicated that the doped CaP powder was hydrated, and that the endothermic peaks were due to dehydration of powder, as established with CaP powders.

The rest of doped CaP powders (CaP-doped batch A pH10 RT), (CaP-doped batch A pH5 200°C hydrothermal), and (CaP-doped batch A pH10 200°C hydrothermal) showed no reactions. This was in contrast to the CaP

powders under the same conditions, which showed weak endothermic peaks that corresponded to the liberation of water and the explosion of lattice water. This indicated that these doped CaP powders were an – hydrated and thermally stable, and that no phase transformation took place upon heating from room temperature up to 600°C.

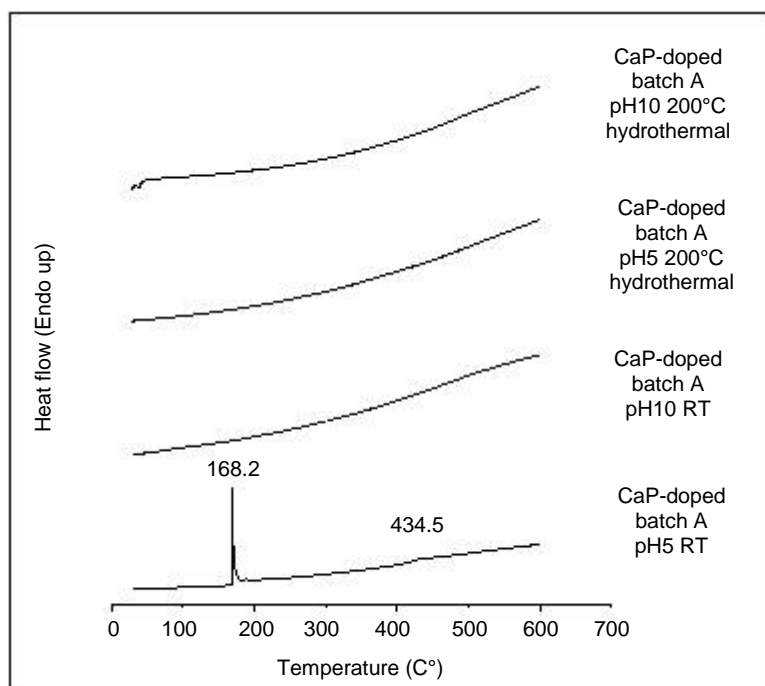


Figure 4.2.33 DSC of doped CaP powders (batch A) (Endo up).

Table 4.2.10 DSC peak centres for doped CaP (batch A) powders

CaP-doped batch A pH5 RT	CaP-doped batch A pH10 RT	CaP-doped batch A pH5 200°C hydrothermal	CaP-doped batch A pH10 200°C hydrothermal
168.2°C	-	-	-
434.5°C	-	-	-

Thermogravimetric analysis (TGA) of doped CaP powder CaP-doped batch A pH5 RT ($\text{CaP-AIPO}_4\text{.Er}_2\text{O}_3\text{.CaF}_2$) is compared to that of CaP powder CaP-undoped pH5 RT (CaP-only) and doped CaP powders (CaP- AlPO_4 and CaP- $\text{AlPO}_4\text{.Er}_2\text{O}_3$), as shown in Figure 4.2.34. TGA measurements were performed using a laboratory – built TGA instrument, to determine changes in weight in relation to the change in temperature. Powders were heated up from room temperature to 1100°C (in air) at 5°C/min heating rate. Figure 4.2.34 shows weight losses of 22.7%, 16.8%, 7.3%, and 7.2% that correspond to (CaP-only / CaP-undoped pH5 RT), (CaP- AlPO_4 and CaP- $\text{AlPO}_4\text{.Er}_2\text{O}_3$), and (CaP- $\text{AlPO}_4\text{.Er}_2\text{O}_3\text{.CaF}_2$ / CaP-doped batch A pH5 RT), respectively. Doped CaP (CaP- $\text{AlPO}_4\text{.Er}_2\text{O}_3\text{.CaF}_2$ / CaP-doped batch A pH5 RT) showed the lowest weight loss percentage by about 15% less than CaP powder (CaP-only / CaP-undoped pH5 RT). This indicated that the addition of dopants (AlPO_4 , Er_2O_3 , and CaF_2) improved the thermal stability of CaP powder significantly.

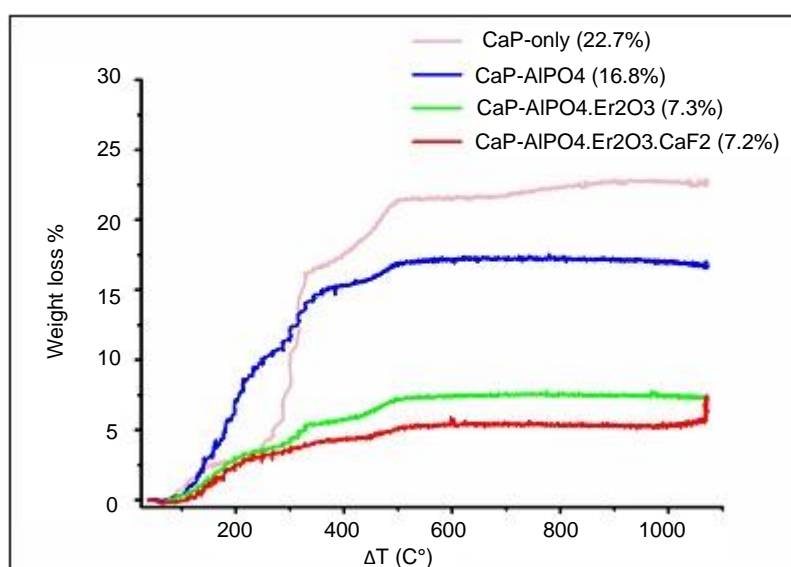


Figure 4.2.34 TGA of CaP-doped batch A pH5 RT ($\text{CaP-AIPO}_4\text{.Er}_2\text{O}_3\text{.CaF}_2$), compared to CaP-undoped pH5 RT (CaP-only), CaP- AlPO_4 , and CaP- $\text{AlPO}_4\text{.Er}_2\text{O}_3$.

4.2.2 Doped CaP powders (batch B)

4.2.2.1 Doped CaP batch B (pH 5.4 ± 0.2 , RT)

Representative SEM of doped CaP powder (batch B) that was synthesised under room temperature and as – prepared pH 5.4 ± 0.2 conditions is shown in Figure 4.2.35. SEM showed the formation of micrometre platelet – like particles, as shown in Figure 4.2.35 (a), as well as presence of needle – like particles that may be associated with the formation of platelet – like particles. This was based on a platelet – like particle that appeared to be formed by the lateral aggregation of needle – like particles, as shown in Figure 4.2.35 (b). Bonding of particles may occur by the diffusion of atoms to the interface of particles due to a driving energy. The formation of doped CaP platelet – like particles is in good agreement with the formation of CaP platelet – like particles under the same conditions. The platelet – like morphology could be beneficial, not only in the occlusion of dentinal tubules, but also in enhancing heat transfer during laser irradiation, as well as reducing the risk of tissue damage. Figure 4.2.36 shows the volume – based distribution of doped CaP particles, as measured by the Malvern Mastersizer 2000E, with the standard percentile values $d(0.1)$, $d(0.5)$, $d(0.9)$, and volume weighted mean $D[4,3]$. The particles had a volume weighted mean $D[4,3]$ of $54.1 \mu\text{m}$ with a ± 1 standard deviation error bar, as shown in Figure 4.2.37. The values seem to be in good agreement with doped CaP platelet – like particles shown by SEM.

SEM-EDX measurements (element weight percentage) of doped CaP powder (batch B) that was synthesised under room temperature and as – prepared pH 5.4 ± 0.2 conditions are shown in Table 4.2.11. The SEM-EDX

measurements of five spectra, as shown in Figure 4.2.38, indicated a mean Ca:P ratio of 0.94 (~ 1.0).

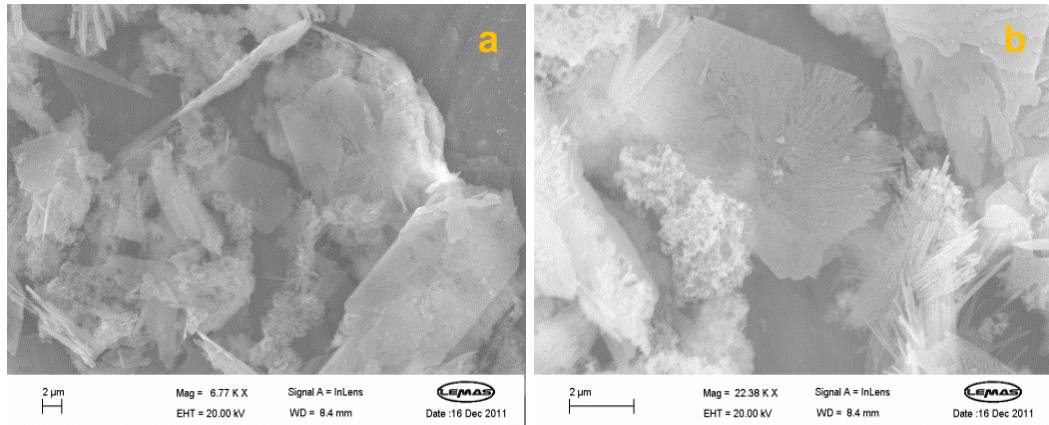


Figure 4.2.35 SEM of doped CaP powder (batch B) synthesised under room temperature and as – prepared pH 5.4 ± 0.2 conditions, showing (a) platelet – like and needle – like particles and (b) the formation of a platelet – like particle by the lateral aggregation of needle – like particles and bonding of particles by the diffusion of atoms to the interface of particles due to a driving energy.

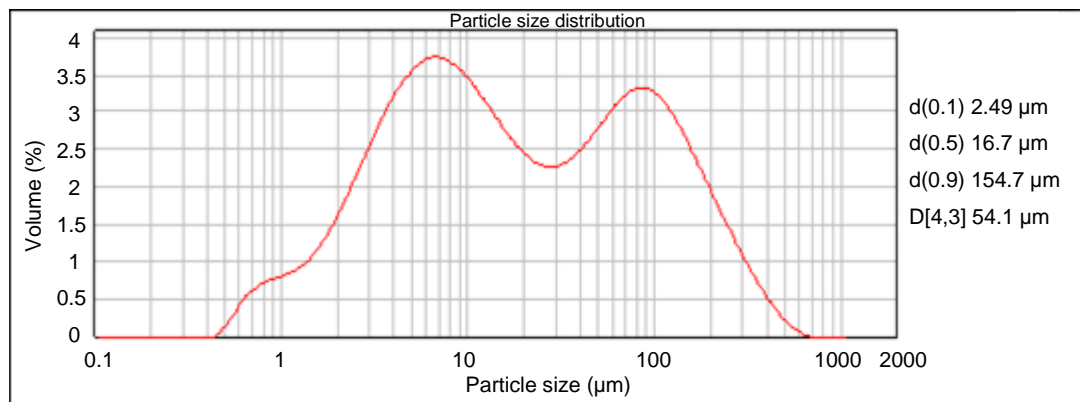


Figure 4.2.36 Particle size distribution of doped CaP powder (batch B) synthesised under room temperature and as – prepared pH 5.4 ± 0.2 conditions.

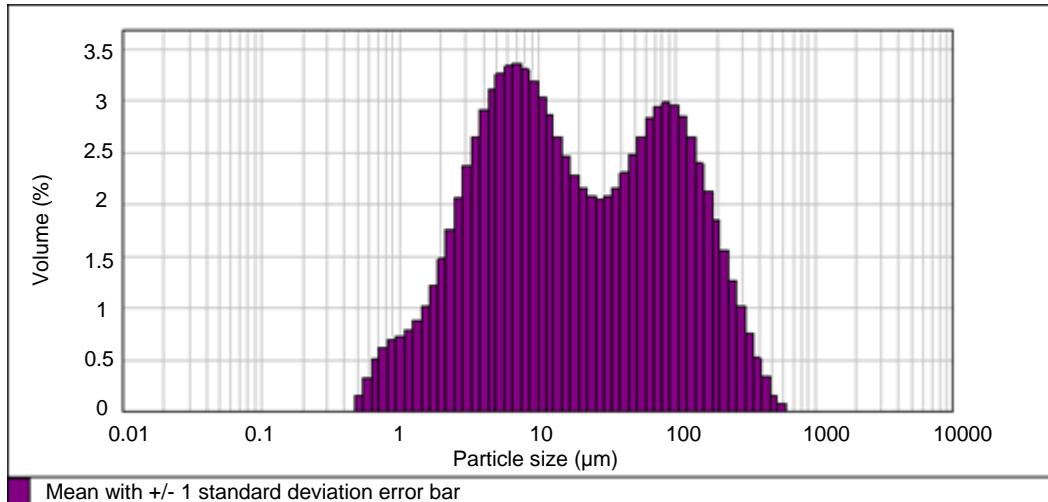


Figure 4.2.37 Statistics graph of doped CaP powder (batch B) synthesised under room temperature and as – prepared pH 5.4 ± 0.2 conditions, showing the mean with ± 1 standard deviation error bar.

Table 4.2.11 SEM-EDX measurements (element weight percentage) for doped CaP powder (batch B) synthesised under room temperature and as – prepared pH 5.4 ± 0.2 conditions

Spectrum	O	F	Al	P	Ca	Er	Ca:P ratio
Spectrum 1	39.1	0.5	0.5	10.8	9.4	3.6	0.86
Spectrum 2	43.6	0.5	0.3	11.3	10.8	1.5	0.95
Spectrum 3	38.3	0.8	0.5	10.4	9.5	2.9	0.91
Spectrum 4	43.3	0.9	0.2	8.1	8.4	1.2	1.03
Spectrum 5	35.4	1.3	0.5	7.1	6.8	3.1	0.96
Mean	40	0.8	0.4	9.5	9	2.4	0.94
Std. Deviation	3.4	0.3	0.1	1.8	1.4	1.0	0.06

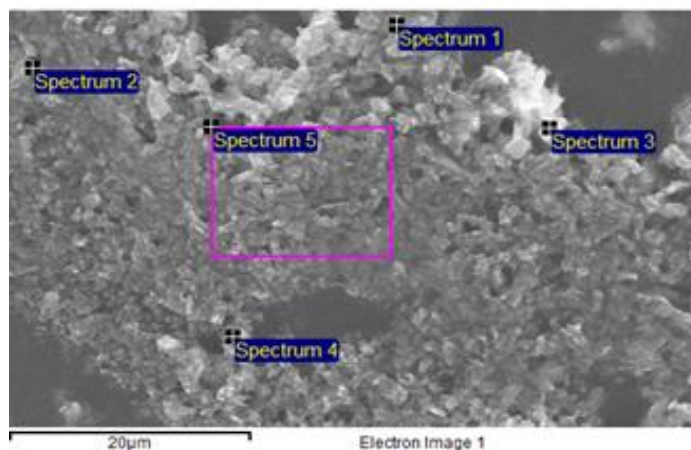


Figure 4.2.38 SEM of doped CaP powder (batch B) synthesised under room temperature and as – prepared pH 5.4 ± 0.2 conditions, showing the obtained EDX spectra.

XRD pattern of doped CaP powder (CaP-doped batch B pH5 RT) that was synthesised under room temperature and as – prepared pH 5.4 ± 0.2 conditions is shown in Figure 4.2.39 and compared to that of CaP (CaP-undoped pH5 RT) in Figure 4.2.40. The XRD pattern indicated the formation of a single monetite phase, which is in good agreement with monetite JCPDS file 01-070-1425. The peaks at 2 theta 26.5° , 30.3° , 32.5° , 40° , 47.5° , 49° , 53° , and 59° appeared to be in good agreement with major peaks of dopants and monetite, with a slight shift of dopants' peaks, which indicated that Er^{3+} , Al^{3+} , and F^- were incorporated into the structure of monetite. The slight shift in peak positions and change in peak intensities are usually associated with the incorporation of a dopant into CaP structure (570). This indicated that Er^{3+} and Al^{3+} substituted a certain amount of Ca^{2+} in the monetite structure, as well as the incorporation of F^- by the possible formation of F–OH bond, as observed in the FTIR spectrum of doped CaP powder (batch A), which will be verified by FTIR. Figure 4.2.40 compares the XRD pattern of doped CaP powder (batch B) (CaP-doped batch B pH5 RT)

to that of CaP (CaP-undoped pH5 RT), which indicated the formation of doped monetite and brushite phases, respectively. On the other hand, in the case of doped CaP powder batch A (CaP-doped batch A pH5 RT), a brushite phase was formed together with dopants' phases (multiple phases). Therefore, the formation of a single doped monetite phase indicated the effective addition of batch B dopants, and that batch B dopants were more successful in doping CaP than batch A dopants under room temperature and pH 5.4 ± 0.2 conditions.

The Miller indices (hkl) and 2θ of doped CaP powder (batch B) that was synthesised under room temperature and as – prepared pH 5.4 ± 0.2 conditions were refined in the monoclinic system by UnitCell program (Tim Holland's software), using 1.54 \AA wavelength and minimising the sum of squares of residuals in 2θ , to determine the crystallographic parameters. Unit cell parameters for doped CaP powder pH5 RT (batch B) are shown in Table 4.2.12. The results indicated that the crystal structure of doped CaP (batch B) was in the triclinic system with space group P-1. Unit cell parameters of CaP-undoped batch B pH 5 RT are in good agreement with those of monetite JCPDS file 01-070-1425, however, compared to unit cell parameters of CaP-undoped pH 5 RT, 1st reaction (monetite), there was a shrinkage of the cell volume of 1.06 \AA^3 . The unit cell parameters, a – axes, b – axes, and c – axes, of doped CaP (CaP-doped batch B pH5 RT) were modified, with an increase of 0.02 \AA in b – axes, and decrease of 0.04 \AA in a – axes, whereas 6.99 \AA in c – axes was the same as that of CaP (CaP-undoped pH5 RT). In addition, compared to doped CaP (CaP-doped batch A pH5 RT), the cell volume of doped CaP (CaP-doped batch B pH5 RT) is smaller by 185.32 \AA^3 .

Table 4.2.12 Unit cell parameters for doped CaP powder (batch B) synthesised under room temperature and as – prepared pH 5.4 ± 0.2 conditions, compared to those of monetite JCPDS file 01-070-1425

Cell parameter	CaP-doped pH5 RT (batch B)	Std.D	Monetite JCPDS file 01-070-1425
a (Å)	6.87	0.001	6.91
b (Å)	6.65	0.001	6.62
c (Å)	6.99	0.0005	6.99
Alpha (°)	97.12	0.017	96.34
Beta (°)	103.57	0.009	103.82
Gamma (°)	88.34	0.012	88.33
Cell volume (Å ³)	309	0.043	309.28

Std.D = Standard deviation

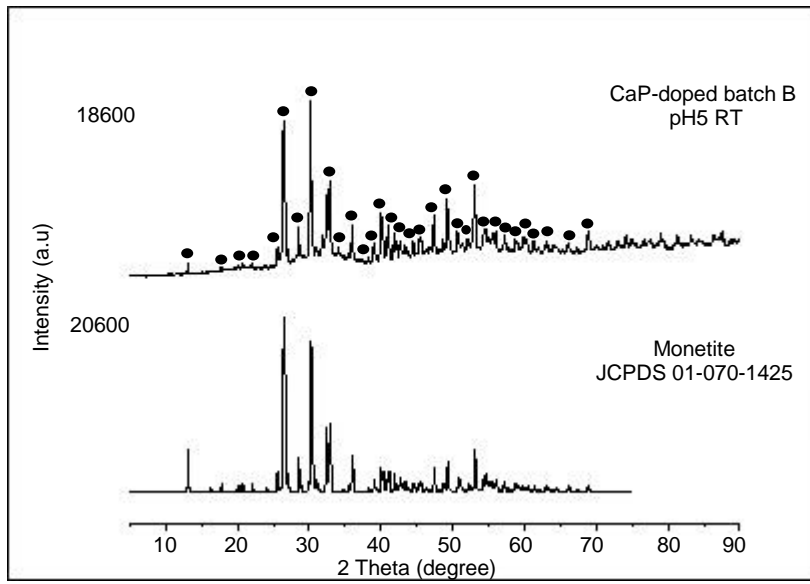


Figure 4.2.39 XRD pattern of doped CaP powder (batch B) synthesised under room temperature and as – prepared pH 5.4 ± 0.2 conditions, compared to monetite JCPDS file 01-070-1425. Marked peaks (●) were assigned to doped monetite.

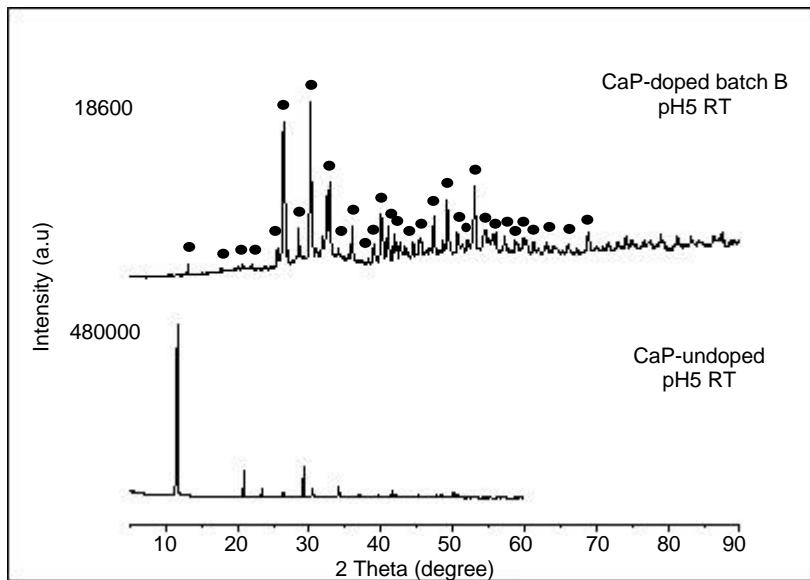


Figure 4.2.40 XRD pattern of doped CaP powder (batch B) synthesised under room temperature and as – prepared pH 5.4 ± 0.2 conditions (doped monetite), compared to that of CaP-undoped pH5 RT (brushite). Marked peaks (●) were assigned to doped monetite.

4.2.2.2 Doped CaP batch B (pH 10 ± 0.2, RT)

Representative SEM of doped CaP powder (batch B) that was synthesised under room temperature and pH 10 ± 0.2 conditions is shown in Figure 4.2.41. SEM shows the formation of agglomerations (clusters) of rounded – like particles, as shown in Figure 4.2.41 (a and b). The rounded – like particles appeared to be in the nanometre scale. Figure 4.2.42 shows the volume – based distribution of doped CaP particles, as measured by the Malvern Mastersizer 2000E, with the standard percentile values $d(0.1)$, $d(0.5)$, $d(0.9)$, and volume weighted mean $D[4,3]$. The particles had a volume weighted mean $D[4,3]$ of 97.2 μm with a ± 1 standard deviation error bar, as shown in Figure 4.2.43. The values are not in good agreement with the nanoscale of particles, but they seem to be in good agreement with the agglomerations of rounded – like particles shown by SEM.

The particles are very similar to those synthesised by Ramesh et al. (571), which are described as loosely packed particles, and they are reported to attain a final density of ~ 98% when sintered above 1050°C. The agglomerates were also observed with CaP powder that was synthesised under the same conditions. Agglomerates of particles are undispersed clusters of aggregates necking/held together by weak (van der Waals) forces or binders (572). Necking of particle refers to the bonding of particles by the diffusion of atoms to the interface of particles due to a driving force such as heat. Powders produced commercially by aerosol reactors are usually agglomerates of particles held together by necks due to sintering (572).

Necking of particles and neck growth by surface diffusion and grain boundary usually occur at the initial stage of sintering (573). The latter involves surface transport by surface diffusion and evaporation –

condensation mechanism, which leads to neck formation and neck growth without densification (574). Sufficiently small sized – particles in contact may lead to higher sintering activity, which in turn allows sintering at relatively lower temperatures. The neck formation and growth may also lead to shortening the initial stage of sintering (575). Therefore, under laser irradiation sintering, much of the thermal energy can be employed for grain growth rather than necking of particles.

The rounded – like nanoparticles would be ideal for the occlusion of dentinal tubules, because they would provide excellent infiltration and occlusion of dentinal tubules, with a uniform coating and large surface area for optimum sintering. As indicated above, they would also be beneficial under laser irradiation, as they would sinter at a relatively low temperature, and consequently, shorten the initial stage of sintering.

SEM-EDX measurements (element weight percentage) of doped CaP powder (batch B) that was synthesised under room temperature and pH 10 ± 0.2 conditions are shown in Table 4.2.13. The SEM-EDX measurements of five spectra, as shown in Figure 4.2.44, indicated a mean Ca:P ratio of 1.5.

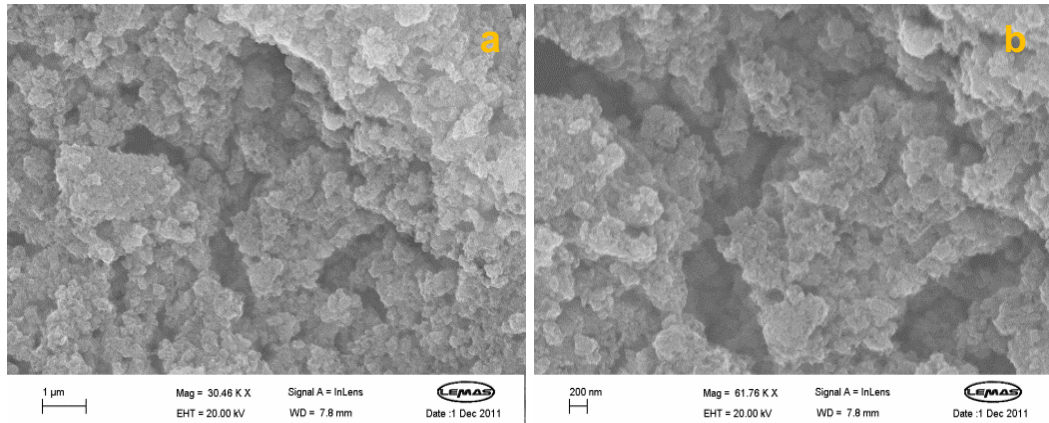


Figure 4.2.41 SEM of doped CaP powders (batch B) synthesised under room temperature and pH 10 ± 0.2 conditions, showing (a) agglomeration of rounded – like particles and (b) necking of nanoparticles.

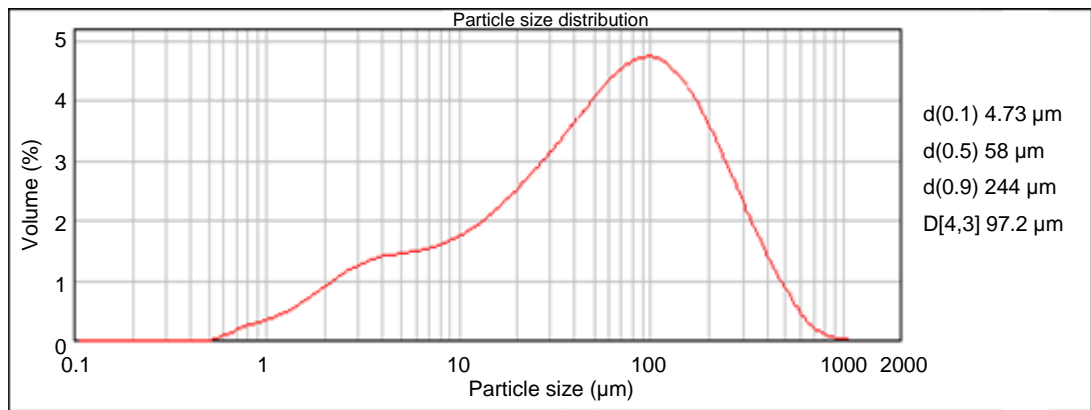


Figure 4.2.42 Particle size distribution of doped CaP powder (batch B) synthesised under room temperature and as – prepared pH 10 ± 0.2 conditions.

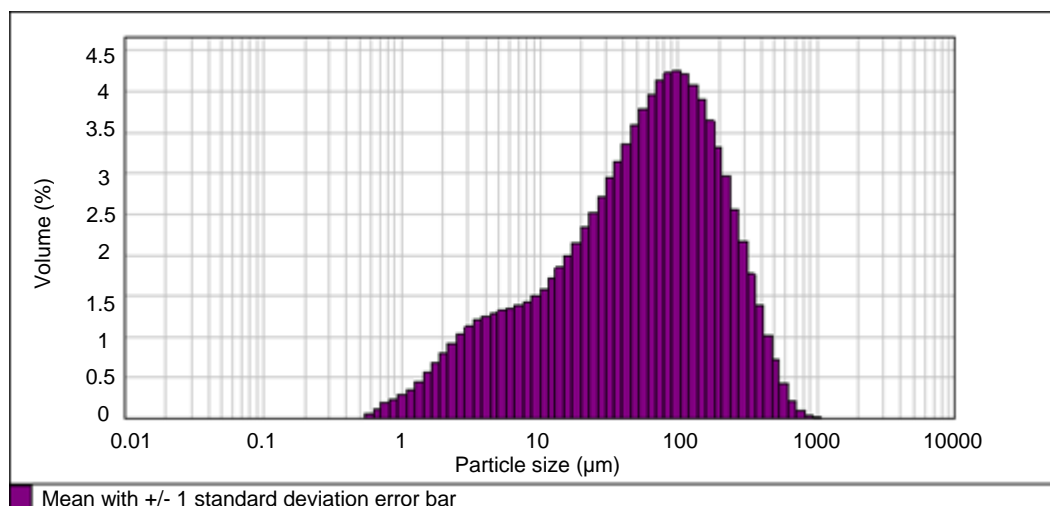


Figure 4.2.43 Statistics graph of doped CaP powder (batch B) synthesised under room temperature and pH 10 ± 0.2 conditions, showing the mean with ± 1 standard deviation error bar.

Table 4.2.13 SEM-EDX measurements (element weight percentage) for doped CaP (batch B) synthesised under room temperature and pH 10 ± 0.2 conditions

Spectrum	O	F	Al	P	Ca	Er	Ca:P ratio
Spectrum 1	24.2	0.7	0.3	6.75	10.2	3.30	1.52
Spectrum 2	30.5	1	0.4	7.7	11.7	2.44	1.51
Spectrum 3	42.0	1.5	0.5	7.9	11.2	3.58	1.41
Spectrum 4	36.7	1.1	0.5	10.1	15.7	4.65	1.55
Spectrum 5	35.6	1	0.5	9.6	14.5	3.55	1.51
Mean	33.8	1.1	0.5	8.4	12.7	3.50	1.5
Std. Deviation	6.7	0.3	0.08	1.4	2.3	0.7	0.05

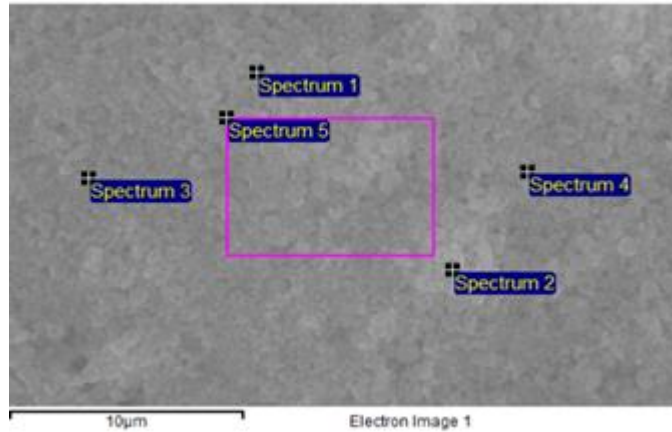


Figure 4.2.44 SEM of doped CaP powder (batch B) synthesised under room temperature and pH 10 ± 0.2 conditions, showing the obtained EDX spectra.

XRD pattern of doped CaP (CaP-doped batch B pH10 RT) that was synthesised under room temperature and pH 10 ± 0.2 conditions is shown in Figure 4.2.45 and compared to that of CaP (CaP-undoped pH10 RT) under the same conditions in Figure 4.2.46. The XRD pattern indicated the formation of a hydroxyapatite phase, which is in good agreement with HAp JCPDS file 009-0432. There was also a change in peak intensities, which indicated that Er^{3+} and Al^{3+} substituted a certain amount of Ca^{2+} in the HAp structure, as well as the incorporation of F^- by the possible formation of F–OH bond, which will be verified by FTIR. The XRD peaks were broad and reflected the nanometre size of particles, which is in good agreement with the nanometre rounded – like particles shown by SEM.

Figure 4.2.46 compares the XRD pattern of doped CaP powder (batch B) (CaP-doped batch B pH10 RT) to that of CaP (CaP-undoped pH10 RT), the latter which was identified as multiple phases of HAp and brushite. The formation of a single doped HAp (CaP-doped batch B pH10 RT) indicated the effect of dopants' addition on the phase formation of CaP.

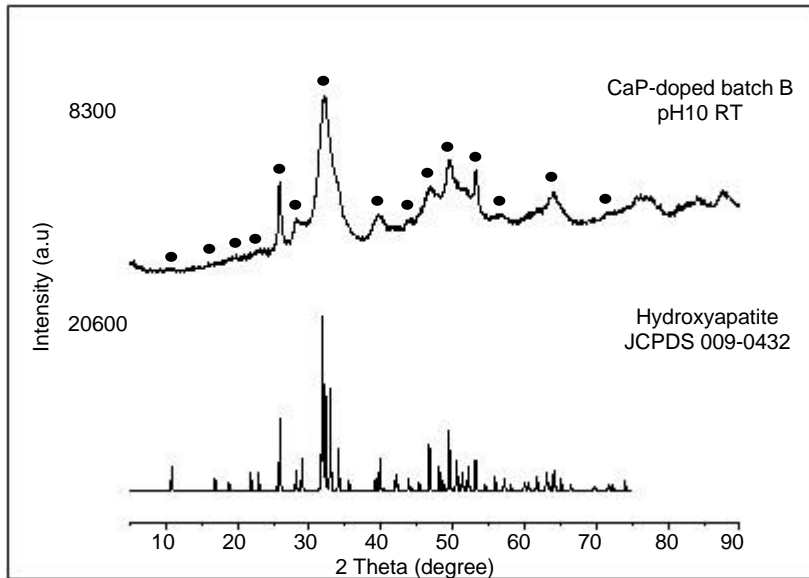


Figure 4.2.45 XRD pattern of doped CaP (batch B) synthesised under room temperature and pH 10 ± 0.2 conditions. Marked peaks (●) were assigned to doped HAP.

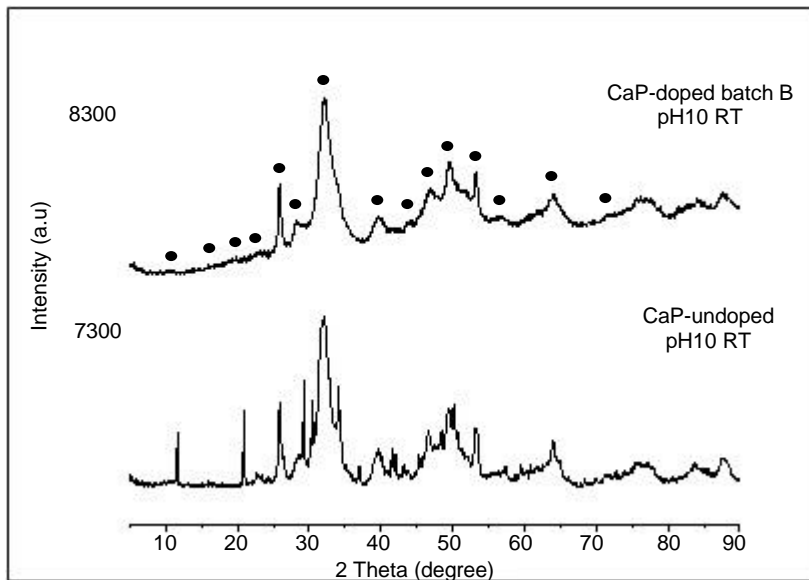


Figure 4.2.46 XRD pattern of doped CaP (batch B) synthesised under room temperature and pH 10 ± 0.2 conditions, compared to that of CaP (CaP-undoped pH10 RT). Marked peaks (●) were assigned to doped HAP.

4.2.2.3 Doped CaP batch B (pH 5.4 ± 0.2, 200°C hydrothermal)

Representative SEM of doped CaP powder (batch B) that was synthesised under as – prepared pH 5.4 ± 0.2 and 200°C hydrothermal conditions is shown in Figure 4.2.47. SEM showed the formation of rounded – like particles, as shown in Figure 4.2.47 (a and b). The particles were different to those of CaP that were synthesised under the same conditions, which had fine platelet – like particles. Irregular particle morphology was also observed, which appeared to be due to the agglomeration and necking of few particles. The particles appeared to be in the nanometre scale. Figure 4.2.48 shows the volume – based distribution of doped CaP particles, as measured by the Malvern Mastersizer 2000E, with the standard percentile values $d(0.1)$, $d(0.5)$, $d(0.9)$, and volume weighted mean $D[4,3]$. The particles had a volume weighted mean $D[4,3]$ of 38.5 μm with a ± 1 standard deviation error bar, as shown in Figure 4.2.49. The values are not in good agreement with the nanoscale of particles, but they are in good agreement with the agglomerates shown by SEM in Figure 4.2.50. Similar to doped CaP (CaP-doped batch B pH10 RT), these nanoparticles would be ideal for the occlusion of dentinal tubules, because they would provide excellent infiltration and occlusion of dentinal tubules, with a uniform coating and large surface area for optimum sintering.

SEM-EDX measurements (element weight percentage) of doped CaP powder (batch B) that was synthesised under as – prepared pH 5.4 ± 0.2 and 200°C hydrothermal conditions are shown in Table 4.2.14. The SEM-EDX measurements of five spectra, as shown in Figure 4.2.50, indicated a mean Ca:P ratio of 0.93 (~ 1.0).

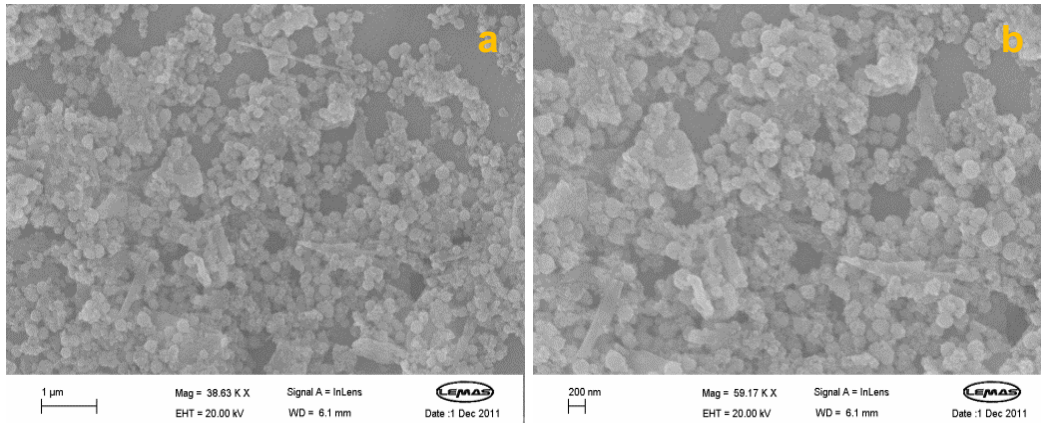


Figure 4.2.47 SEM of doped CaP powder (batch B) synthesised under as – prepared pH 5.4 ± 0.2 and 200°C hydrothermal conditions, showing rounded – like particles at (a) lower magnification at $1 \mu\text{m}$ scale and (b) higher magnification at 200 nm scale.

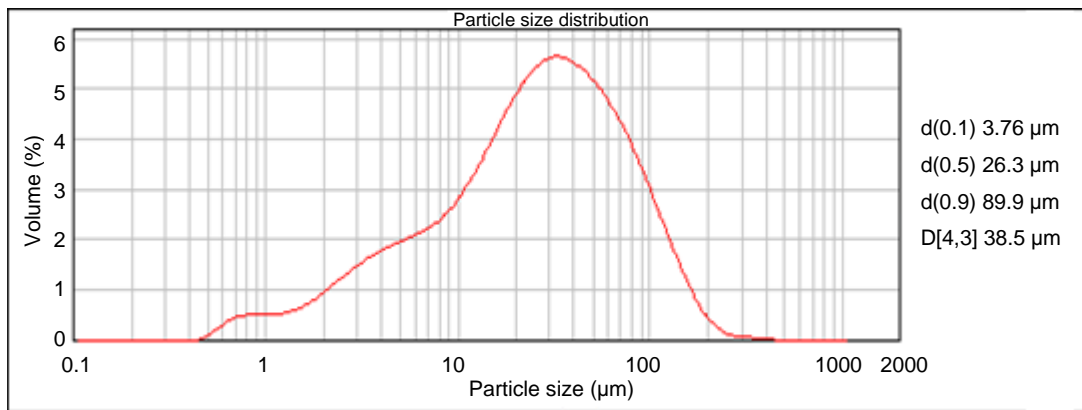


Figure 4.2.48 Particle size distribution of doped CaP powder (batch B) synthesised under as – prepared pH 5.4 ± 0.2 and 200°C hydrothermal conditions.

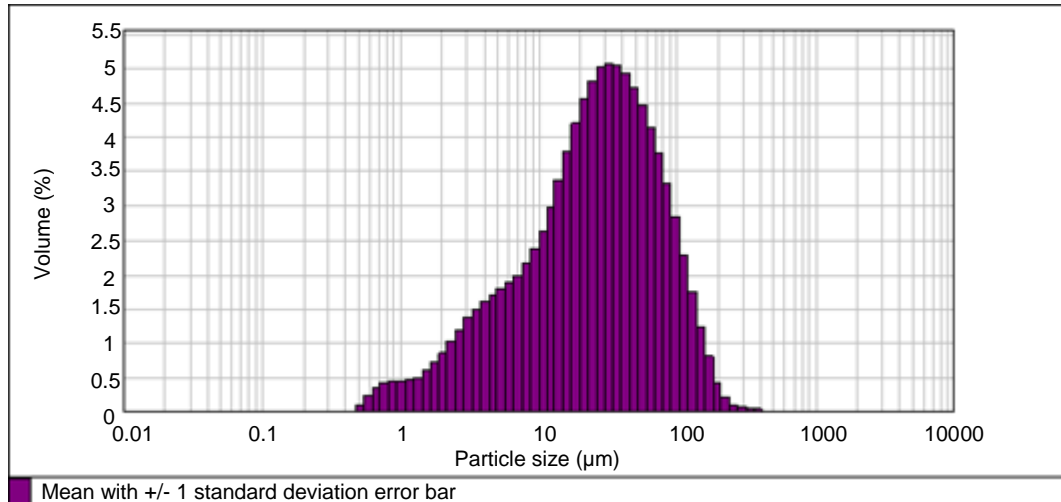


Figure 4.2.49 Statistics graph of doped CaP powder (batch B) synthesised under as – prepared pH 5.4 ± 0.2 and 200°C hydrothermal conditions, showing the mean with ± 1 standard deviation error bar.

Table 4.2.14 SEM-EDX measurements (element weight percentage) for doped CaP powder (batch B) synthesised under as – prepared pH 5.4 ± 0.2 and 200°C hydrothermal conditions

Spectrum	O	F	Al	P	Ca	Er	Ca:P ratio
Spectrum 1	34.4	2.2	0.3	5.5	5.3	7.2	0.96
Spectrum 2	36.1	2.2	0.4	6.2	6.7	7.9	1.07
Spectrum 3	28.2	0.9	0.3	4.1	3.8	9.1	0.92
Spectrum 4	36.3	1.7	0.2	3.6	3.4	5.9	0.94
Spectrum 5	32.9	1	0.3	3.9	3.1	8.3	0.78
Mean	33.6	1.6	0.3	4.7	4.5	7.7	0.93
Std. Deviation	3.3	0.6	0.06	1.1	1.5	1.2	0.1

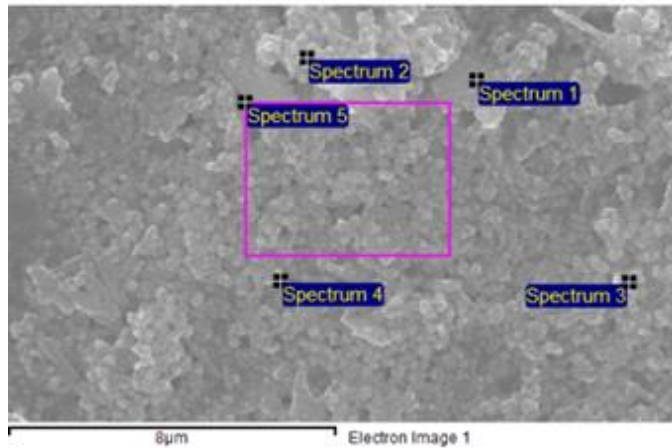


Figure 4.2.50 SEM of doped CaP powder (batch B) synthesised under as – prepared pH 5.4 ± 0.2 and 200°C hydrothermal conditions, showing the obtained EDX spectra.

XRD pattern of doped CaP (CaP-doped batch B pH5 200°C hydrothermal) that was synthesised under as – prepared pH 5.4 ± 0.2 and 200°C hydrothermal conditions is shown in Figure 4.2.51 and compared to that of CaP (CaP-undoped pH5 200°C hydrothermal) under the same conditions in Figure 4.2.52. The XRD pattern indicated the formation of a hydroxyapatite phase, which is in good agreement with HAp JCPDS file 009-0432. The XRD peaks were broad and reflected the nanometre size of particles, which is in good agreement with the nanometre scale of rounded – like particles shown by SEM.

The XRD pattern of doped CaP (CaP-doped batch B pH5 200°C hydrothermal) is also in good agreement with that of CaP (CaP-undoped pH5 200°C hydrothermal), as shown in Figure 4.2.52. However, a slight shift in peak positions and change in peak intensities were observed, which indicated that Er^{3+} and Al^{3+} , and F^{-} substituted a certain amount of Ca^{2+} and OH^{-} , respectively, in the HAp structure.

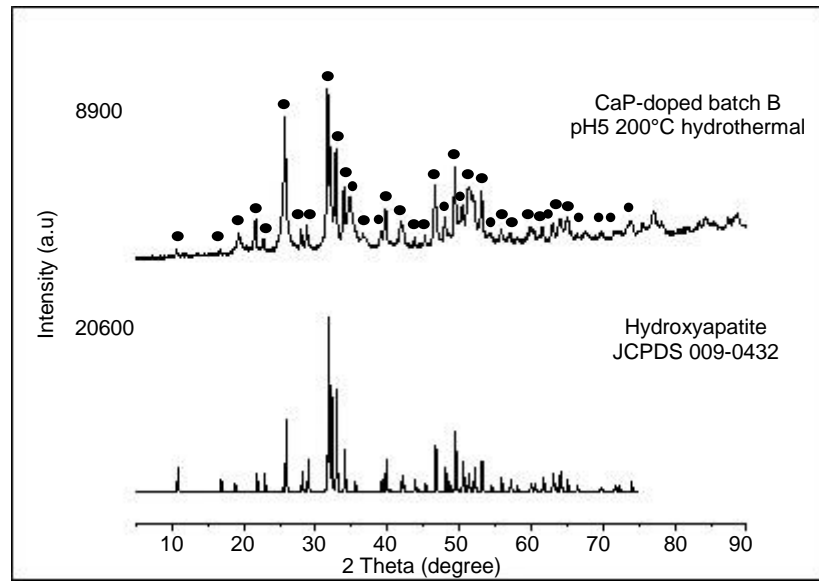


Figure 4.2.51 XRD pattern of doped CaP powder (batch B) synthesised under as – prepared pH 5.4 ± 0.2 and 200°C hydrothermal conditions. Marked peaks (●) were assigned to doped HAp.

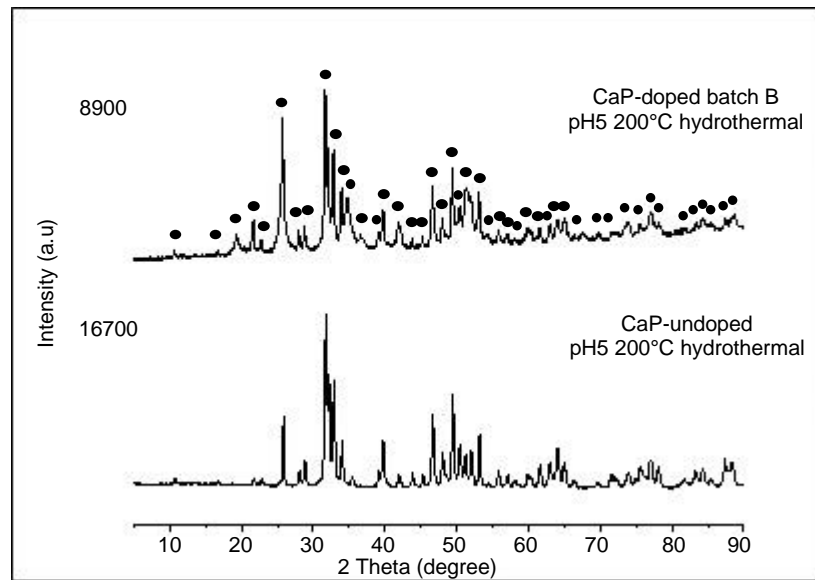


Figure 4.2.52 XRD pattern of doped CaP powder (batch B) synthesised under as – prepared pH 5.4 ± 0.2 and 200°C hydrothermal conditions, compared to that of CaP under the same conditions. Marked peaks (●) were assigned to doped HAp.

4.2.2.4 Doped CaP batch B (pH 10 ± 0.2, 200°C hydrothermal)

Representative SEM of doped CaP powder (batch B) that was synthesised under pH 10 ± 0.2 and 200°C hydrothermal conditions is shown in Figure 4.2.53. SEM showed agglomeration (clusters) of doped CaP particles in the micrometre scale, as shown in Figure 4.2.53 (a). However, the particles in clusters appeared to have a rod – like morphology in the nanometre scale, as shown in Figure 4.2.53 (b). Figure 4.2.54 shows the volume – based distribution of doped CaP particles, as measured by the Malvern Mastersizer 2000E, with the standard percentile values d(0.1), d(0.5), d(0.9), and volume weighted mean D[4,3]. The particles had a volume weighted mean D[4,3] of 62 µm with a ± 1 standard deviation error bar, as shown in Figure 4.2.55. The values are not in good agreement with the nanoscale of particles, but they are in good agreement with the agglomerates shown by SEM, particularly in Figure 4.2.56.

SEM-EDX measurements (element weight percentage) of doped CaP powder (batch B) that was synthesised under pH 10 ± 0.2 and 200°C hydrothermal conditions are shown in Table 4.2.15. The SEM-EDX measurements of five spectra, as shown in Figure 4.2.56, indicated a mean Ca:P ratio of 1.58.

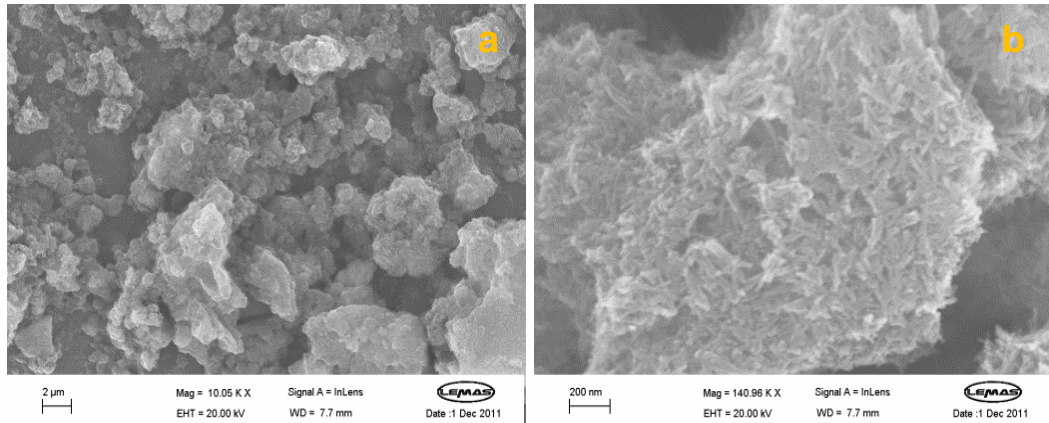


Figure 4.2.53 SEM of doped CaP powder (batch B) synthesised under pH 10 ± 0.2 and 200°C hydrothermal conditions, showing (a) agglomerations/clusters of particles and (b) rod – like nanoparticles.

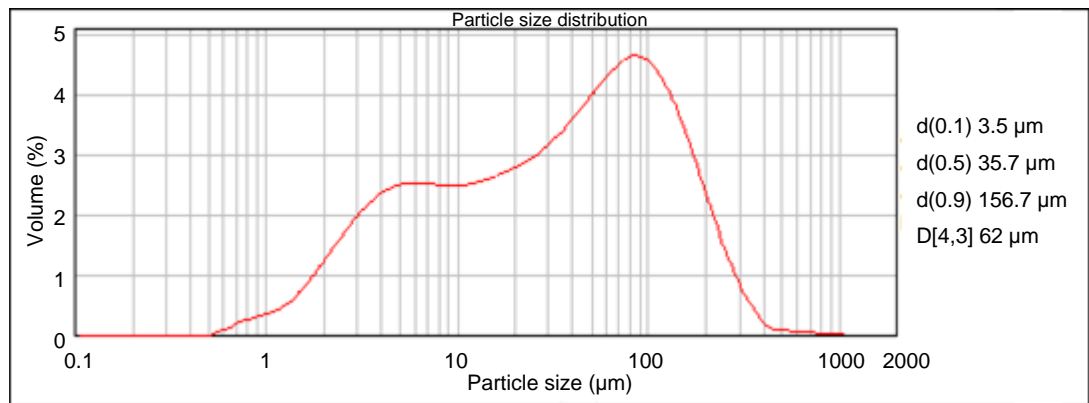


Figure 4.2.54 Particle size distribution of doped CaP powder (batch B) synthesised under pH 10 ± 0.2 and 200°C hydrothermal conditions.

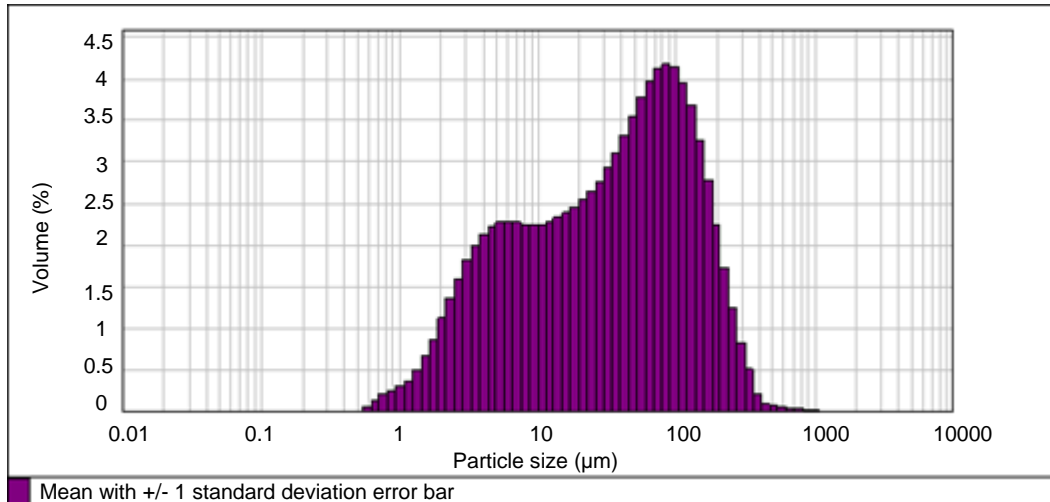


Figure 4.2.55 Statistics graph of doped CaP powder (batch B) synthesised under pH 10 ± 0.2 and 200°C hydrothermal conditions, showing the mean with ± 1 standard deviation error bar.

Table 4.2.15 SEM-EDX measurements (element weight percentage) for doped CaP powder (batch B) synthesised under pH 10 ± 0.2 and 200°C hydrothermal conditions

Spectrum	O	F	Al	P	Ca	Er	Ca:P ratio
Spectrum 1	34.6	1	0.6	11	18.1	4.3	1.63
Spectrum 2	39.8	1.5	0.5	9.7	14.7	3.2	1.51
Spectrum 3	32.3	0.8	0.7	9.8	15.8	2.8	1.6
Spectrum 4	33.7	1	0.6	8.4	13.5	2.7	1.6
Spectrum 5	25.5	0.3	0.09	1.3	2.1	0.4	1.57
Mean	33.2	0.9	0.5	8	12.8	2.7	1.58
Std. Deviation	5.1	0.4	0.2	3.8	6.2	1.4	0.04

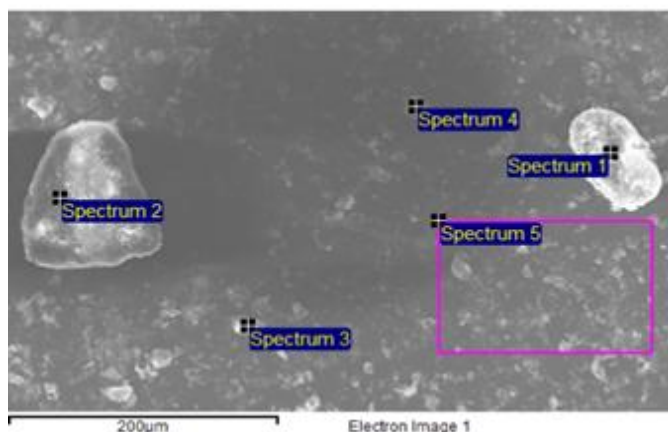


Figure 4.2.56 SEM of doped CaP powder (batch B) synthesised under pH 10 ± 0.2 and 200°C hydrothermal conditions, showing the obtained EDX spectra.

XRD pattern of doped CaP (CaP-doped batch B pH10 200°C hydrothermal) that was synthesised under pH 10 ± 0.2 and 200°C hydrothermal conditions is shown in Figure 4.2.57 and compared to those of CaP (CaP-undoped pH10 200°C hydrothermal and CaP-undoped pH10 200°C hydrothermal (initial investigation)) under the same conditions in Figure 4.2.58. The XRD pattern indicated the formation of a hydroxyapatite phase, which is in good agreement with HAp JCPDS file 009-0432. The XRD peaks were broad and reflected the nanometre size of particles, which is in good agreement with the nanometre scale of rod – like particles shown by SEM (Figure 4.2.53 b).

The XRD pattern of doped CaP powder (CaP-doped batch B pH10 200°C hydrothermal) is also in good agreement with that of CaP synthesised in the initial investigation under the same conditions (CaP-undoped pH10 200°C hydrothermal (initial investigation)), as shown in Figure 4.2.58. However, as stated before, shift in peak positions and change in peak intensities were observed, which indicated that Er^{3+} and Al^{3+} , and F^{-} substituted a certain amount of Ca^{2+} and OH^{-} , respectively, in the HAp structure.

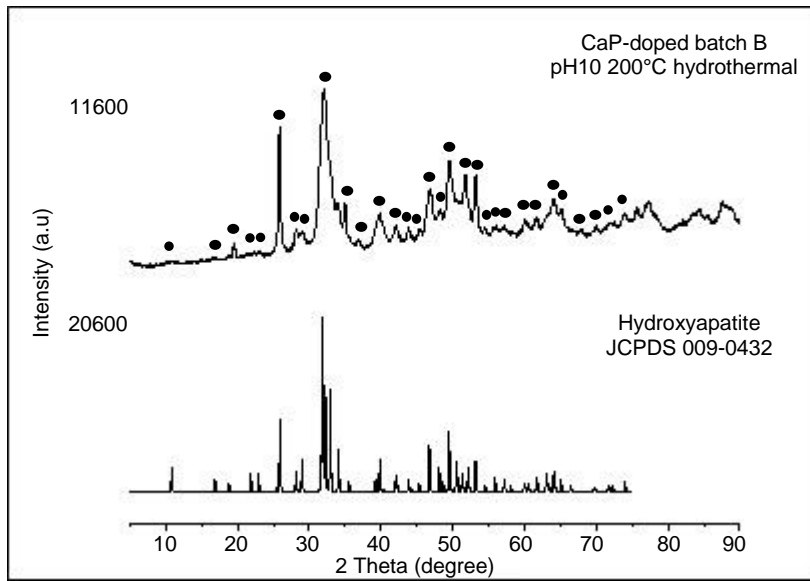


Figure 4.2.57 XRD pattern of doped CaP powder (batch B) synthesised under pH 10 ± 0.2 and 200°C hydrothermal conditions. Marked peaks (●) were assigned to doped HAp.

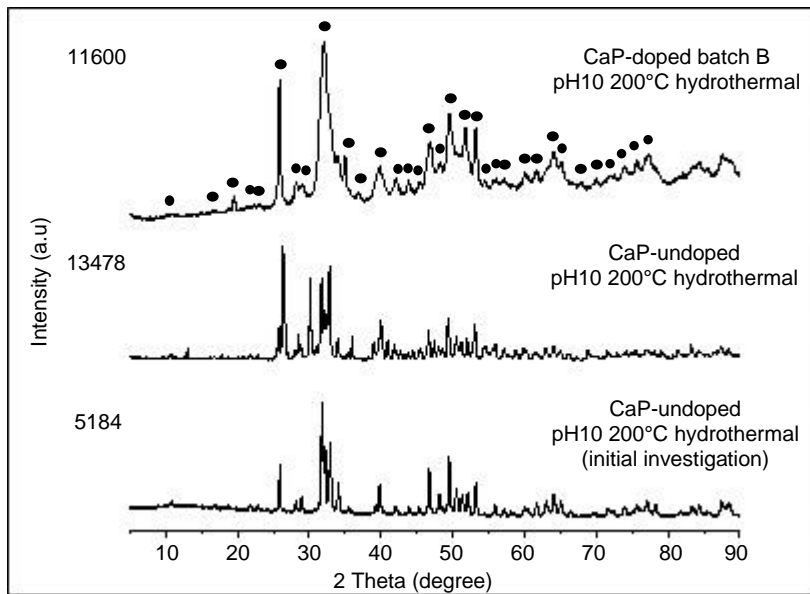


Figure 4.2.58 XRD pattern of doped CaP powder (batch B) synthesised under pH 10 ± 0.2 and 200°C hydrothermal conditions, compared to those of CaP (CaP-undoped pH10 200°C hydrothermal and CaP-undoped pH10 200°C hydrothermal (initial investigation)). Marked peaks (●) were assigned to doped HAp.

XRD patterns of doped CaP powders (batch B) indicated the formation of single CaP phases under all conditions, which were the doped monetite phase in the case of doped CaP powder (CaP-doped batch B pH5 RT) and doped HAp phase in the rest of doped CaP powders (CaP-doped batch B pH10 RT), (CaP-doped batch B pH5 200°C hydrothermal), and (CaP-doped batch B pH10 200°C hydrothermal). This was supported by the SEM of doped CaP powders (batch B), which showed homogenous particle size and morphology. The crystallised platelet – like particles of doped CaP powder that was synthesised under room temperature and as – prepared pH 5.4 ± 0.2 conditions (Figure 4.2.35) were in good agreement with the XRD pattern of doped monetite phase (Figure 4.2.39). Under pH 10 ± 0.2 conditions, the particles had rounded – like morphology of a single doped HAp phase, as revealed by SEM (Figure 4.2.41) and XRD (Figure 4.2.45), respectively. Under as – prepared pH 5.4 ± 0.2 and 200°C hydrothermal conditions, rounded – like nanoparticles were formed (Figure 4.2.47), and the formation of a doped HAp phase was confirm by XRD (Figure 4.2.51), particularly when compared to that of CaP under the same conditions (Figure 4.2.52). Similarly, under pH 10 ± 0.2 and 200°C hydrothermal conditions, rod – like nanoparticles were formed (Figure 4.2.53), and the formation of a doped HAp phase was confirm by XRD (Figure 4.2.57), particularly when compared to that of CaP synthesised in the initial investigation under the same conditions (Figure 4.2.58).

As established with CaP powders, SEM and XRD patterns of doped CaP (batch B) indicated the effectiveness of elevated pH and/or hydrothermal conditions in reducing the particle size and modifying the particle morphology. In addition to the reduction of particle size due to the increase

of the nucleation rate with increasing pH levels (549), the ionic radius of Ca^{2+} (1.14 Å) is smaller than that of Er^{3+} (1.03 Å) and Al^{3+} (0.53 Å) (561), and therefore, any substitution of Er^{3+} and Al^{3+} for Ca^{2+} would cause a decrease in lattice parameters, and thus, the unit cell volume. For example, substitutions of Ca^{2+} by smaller cations, such as Mg^{2+} , Zn^{2+} , and Y^{3+} , cause a shrinkage of the HAp crystal, whereas larger cations, such as La^{3+} , cause an expansion of the HAp crystal (562). Similarly, fluoride ion (F^-) is smaller than hydroxyl ion (OH^-), and thus, the substitution of F^- for OH^- would cause a shrinkage of the HAp crystal (563).

Table 4.2.16 compares the volume – based distribution of doped CaP (batch B) powders. The refractive index and absorption index for doped CaP (batch B) used in these calculations were the same as for CaP (1.629 and 0.1, respectively). The measured median particle diameter $d(0.5)$, absolute deviation from median (uniformity), span, and 10% and 90% size distribution by volume percentage (v%) for doped CaP particles (batch B) are presented in Table 4.2.16.

The results indicated that the mean diameter $D[4,3]$ was lowest (38.5 μm) in the case of CaP-doped batch B pH5 200°C hydrothermal and highest (97.2 μm) in the case of CaP-doped batch B pH10 RT. In the case of CaP-doped batch B pH5 RT and CaP-doped batch B pH10 200°C hydrothermal, the mean diameter $D[4,3]$ was 54.1 μm and 62 μm , respectively. These values are in good agreement with doped CaP (batch B) particles that were synthesised under room temperature and pH 5.4 ± 0.2 conditions and doped CaP (batch B) agglomerates under the rest conditions. Although the particles that were synthesised under 200°C hydrothermal and/or pH $10 \pm$

0.2 conditions were shown to be in the nanoscale by SEM, the mean diameter was affected by the formation of agglomerations. As stated before, this is because the accuracy of these measurements depends on the quality of the powder dispersion.

The small span values (4.12, 3.26, and 4.28) in the case of CaP-doped batch B pH5 200°C hydrothermal, CaP-doped batch B pH10 RT, and CaP-doped batch B pH10 200°C hydrothermal indicated a narrow distribution, while the large span value (9.08) in the case of CaP-doped batch B pH5 RT indicated a broader distribution. This indicated that the particles of CaP-doped batch B pH5 RT were less uniform in size than those of the rest of doped CaP (CaP-doped batch B pH10 RT, CaP-doped batch B pH5 200°C hydrothermal, and CaP-doped batch B pH10 200°C hydrothermal).

Table 4.2.16 Particle size data for doped CaP (batch B) powders

Sample	d(0.1) μm	d(0.5) μm	d(0.9) μm	Uniformity	Span	D[4,3] μm
CaP-doped batch B pH5 RT	2.49	16.75	154.76	2.85	9.08	54.133
CaP-doped batch B pH10 RT	4.73	58	244	1.3	4.12	97.29
CaP-doped batch B pH5 200°C hydrothermal	3.76	26.38	89.96	1.02	3.26	38.51
CaP-doped batch B pH10 200°C hydrothermal	3.5	35.76	156.7	1.39	4.28	62

Doped CaP powders (batch B) were also characterised by FTIR in order to detect their functional groups and bonds. FTIR spectra of doped CaP powders (batch B) in the wavenumber range 4000 – 400 cm^{-1} are compared and shown in Figures 4.2.59, 4.2.60, and 4.2.61. FTIR absorption bands and their assigned references are presented in Table 4.2.17.

FTIR spectra of doped CaP powders (batch B) showed CaP absorption bands of PO_4 group at 2100 cm^{-1} , $1200 - 960\text{ cm}^{-1}$, and $600 - 500\text{ cm}^{-1}$, CO_3 group at $2400 - 2300\text{ cm}^{-1}$ and 1546 cm^{-1} , HPO_4 group at 870 cm^{-1} , absorbed H_2O molecules at $3600 - 3100\text{ cm}^{-1}$ and $1650 - 1600\text{ cm}^{-1}$, and OH group at 3570 cm^{-1} (552, 553). The absorption band of PO_4 group was observed around 2100 cm^{-1} , which is the characteristic absorption band for hydroxyapatite, as observed with control CaP powders. The characteristic absorption band of OH group at 634 cm^{-1} for HAp was absent, and instead, an absorption band around 644 cm^{-1} was observed with all powders, however, the absorption band was more defined in the case of doped CaP powder (CaP-doped batch B pH5 200°C hydrothermal). The absorption band at 644 cm^{-1} was assigned to F, and it is in good agreement with the substitution of F^- for OH^- in the HAp structure (495). In the case of doped CaP powder (CaP-doped batch B pH5 RT), the absorption band at 644 cm^{-1} indicated the incorporation of fluoride ion (F^-) into the monetite structure through the formation of OH-F-OH bond (569). In addition, weak absorption bands at 3540 cm^{-1} were observed with all powders, which also indicated the incorporation of fluoride ions into CaP structure (569). FTIR spectra of (CaP-doped batch B pH10 RT), (CaP-doped batch B pH5 200°C hydrothermal), and (CaP-doped batch B pH10 200°C hydrothermal) were similar to those of CaP and doped CaP (batch A) powders, but with modifications due to dopants' substitution.

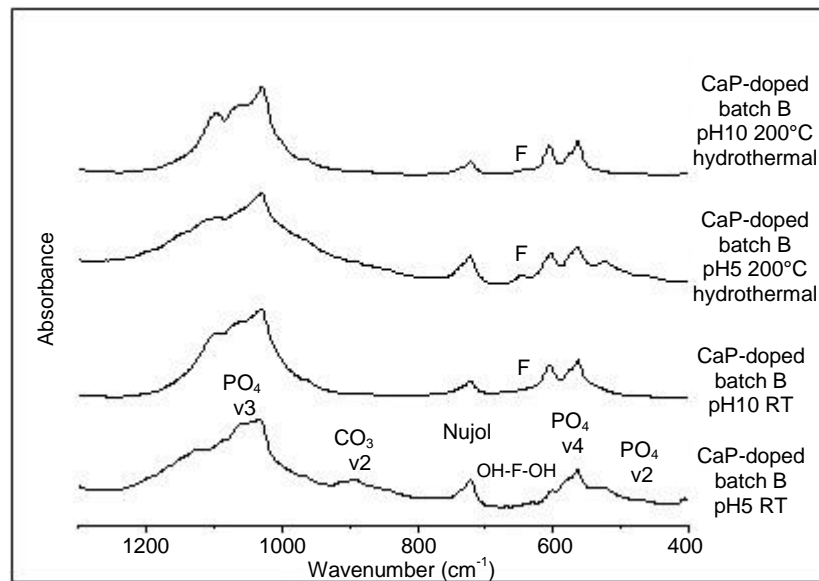


Figure 4.2.59 FTIR spectra of doped CaP powders (batch B) in the MIR region and wavenumber range 1300 – 400 cm⁻¹.

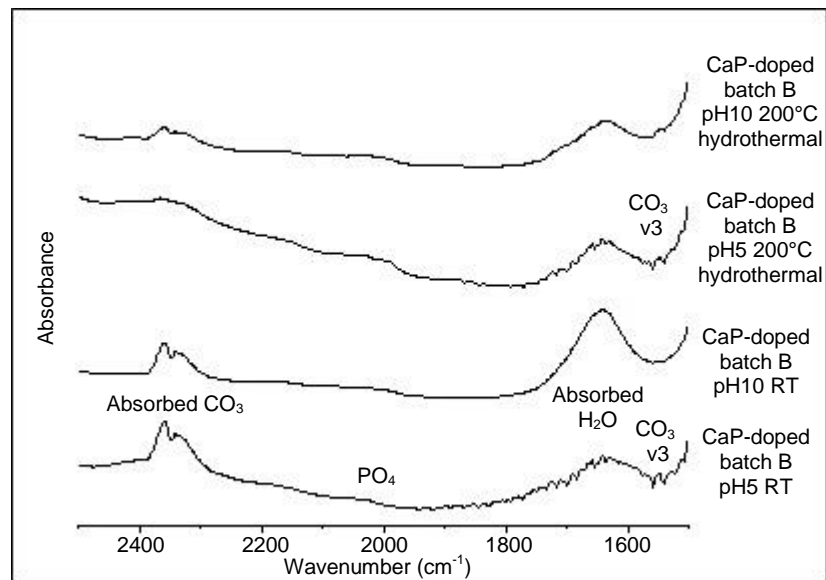


Figure 4.2.60 FTIR spectra of doped CaP powders (batch B) in the MIR region and wavenumber range 2500 – 1400 cm⁻¹.

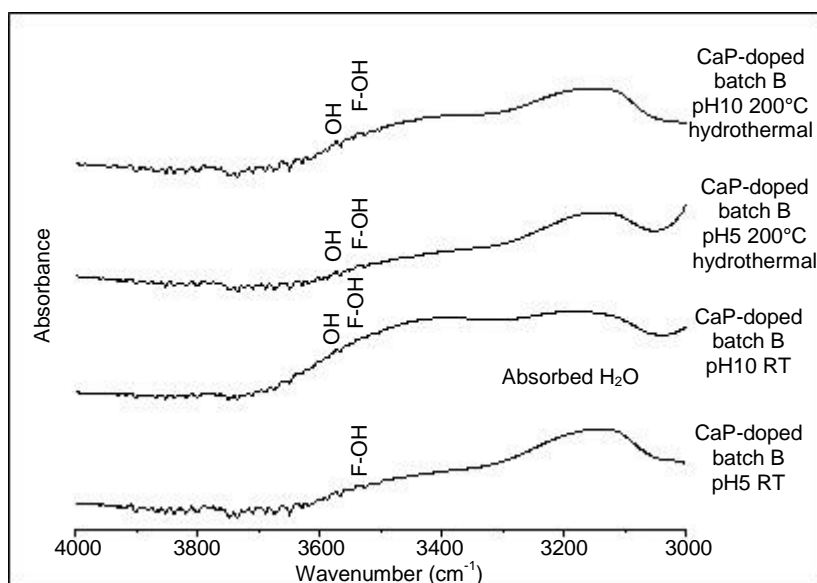


Figure 4.2.61 FTIR spectra of doped CaP powders (batch B) in the NIR region and wavenumber range 4000 – 3000 cm^{-1} .

Under room temperature and as – prepared pH 5.4 ± 0.2 conditions, doped CaP powder (CaP-doped batch B pH5 RT) showed the characteristic absorption band of HPO_4 group at 878 cm^{-1} , which is in good agreement with the formation of a monetite phase (CaHPO_4), as revealed by XRD. The absorption band of PO_4 group (ν_3) (P–O) at $1200 - 1100 \text{ cm}^{-1}$ appeared as one band with shoulders, and similarly, the absorption band of PO_4 group (ν_4) (O–P–O) at $600 - 550 \text{ cm}^{-1}$, which were in contrast to those of CaP powder (CaP-undoped pH5 RT) and doped CaP powder (CaP-doped batch A pH5 RT). This was most likely due to the incorporation of Er^{3+} and Al^{3+} into the monetite structure, as revealed by XRD. The absorption band of PO_4 group (ν_1) (P–O) was observed as a shoulder at 960 cm^{-1} , while the absorption band of PO_4 group (ν_2) (O–P–O) was observed at 425 cm^{-1} with a very weak intensity. Weak absorption bands around $666 - 644 \text{ cm}^{-1}$ were observed, and they were assigned to the incorporation of fluoride ions

through the formation of OH–F–OH bond. The absorption band of absorbed H₂O was observed at 1650 cm⁻¹, and it was similar to that of CaP (CaP-undoped pH5 RT). The absorption band of CO₃ group at 2300 cm⁻¹ was increased, compared to that of CaP (CaP-undoped pH5 RT) and doped CaP (CaP-doped batch A pH5 RT). In the region 4000 – 3000 cm⁻¹, the absorption band of absorbed H₂O molecules was observed at 3160 cm⁻¹, while the absorption band of F–OH bond at 3538 cm⁻¹ was weak.

Under room temperature and pH 10 ± 0.2 conditions, the absorption band of PO₄ group (ν₃) (P–O) at 1200 – 960 cm⁻¹ was merged as one band with shoulders, as occurred with CaP (CaP-undoped pH10 RT) and doped CaP (CaP-doped batch A pH10 RT). The absorption band of PO₄ group (ν₁) (P–O) was observed as a shoulder at 960 cm⁻¹. The absorption bands of PO₄ group (ν₄) (O–P–O) at 600 – 500 cm⁻¹ were shaped into two bands, instead of three bands that were observed with CaP powder (CaP-undoped pH10 RT). The absorption bands of PO₄ group (ν₄) (O – P – O) at 600 – 500 cm⁻¹ were similar to those of doped CaP (CaP-doped batch A pH10 RT). The absorption band of structural OH group at 634 cm⁻¹ was absent, however, a weak absorption band at 644 cm⁻¹ was observed, and it was assigned to the incorporation of fluoride ions and the substitution of F⁻ for OH⁻. The absorption band of absorbed H₂O at 1650 cm⁻¹ was broader and stronger, and the absorption band of CO₃ group at 2350 cm⁻¹ was smaller, compared to that of CaP (CaP-undoped pH10 RT). The absorption bands in the region 4000 – 3000 cm⁻¹, corresponding to the stretched and absorbed H₂O molecules at 3490 cm⁻¹ and 3160 cm⁻¹, respectively, were weak and broad. These absorption bands were similar to those of doped CaP (CaP-doped batch A pH10 RT). The absorption band of structural OH group and F–OH

bond at 3570 cm^{-1} and 3540 cm^{-1} , respectively, were observed with weak intensities.

Under as – prepared pH 5.4 ± 0.2 and 200°C hydrothermal conditions, the characteristic absorption band of PO_4 group (ν_3) (P–O) at $1200 - 960\text{ cm}^{-1}$ was broader than that of doped CaP (CaP-doped batch A pH5 200°C hydrothermal), with the development of a third shoulder – like. These were most likely due to the incorporation of Er^{3+} and Al^{3+} into the HAp structure, as indicated by XRD. The absorption band of PO_4 group (ν_1) (P–O) was observed as a shoulder at 960 cm^{-1} . A new absorption band at 525 cm^{-1} was developed near the absorption bands of PO_4 group (ν_4) (O–P–O) at $600 - 500\text{ cm}^{-1}$, which was not observed with CaP (CaP-undoped pH5 200°C hydrothermal) and doped CaP (CaP-doped batch A pH5 200°C hydrothermal). The absorption band at 525 cm^{-1} is in good agreement with the reported Er–O–Er bond (564), however, it was probably due to the incorporation of Er^{3+} into the HAp structure through the formation of ErPO_4 (416). The absorption band of structural OH group at 634 cm^{-1} was absent, but a small absorption band was observed at 644 cm^{-1} , which was assigned to the incorporation of fluoride ions and the substitution of F^- for OH^- . The absorption band of absorbed H_2O molecules at 1650 cm^{-1} was stronger than that of CaP (CaP-undoped pH5 200°C hydrothermal) and doped CaP (CaP-doped batch A pH5 200°C hydrothermal). On the other hand, the absorption bands of CO_3 group at 2350 cm^{-1} and CO_3 group (ν_3) at 1546 cm^{-1} were significantly reduced, compared to those of CaP (CaP-undoped pH5 200°C hydrothermal). The absorbed H_2O molecules were observed with a small and broad absorption band at 3160 cm^{-1} , while weak absorption bands of

structural OH group and F–OH bond were observed at 3570 cm^{-1} and 3538 cm^{-1} , respectively.

Under $\text{pH } 10 \pm 0.2$ and 200°C hydrothermal conditions, the characteristic absorption bands of PO_4 group (ν_3) (P–O) at $1200 - 960\text{ cm}^{-1}$ and PO_4 group (ν_4) (O–P–O) at $600 - 550\text{ cm}^{-1}$ were similar to those of doped CaP (CaP-doped batch A pH10 200°C hydrothermal). However, a third shoulder – like was developed at the absorption band of PO_4 group (ν_3) (P–O) at $1200 - 960\text{ cm}^{-1}$, with the broadening of absorption bands of PO_4 group (ν_3) (P – O) at $1200 - 1100\text{ cm}^{-1}$ and PO_4 group (ν_4) (O–P–O) at $600 - 550\text{ cm}^{-1}$. These changes indicated the incorporation of Er^{3+} and Al^{3+} into the HAp structure, as indicated by XRD. The absorption band of structural OH group at 634 cm^{-1} was absent, but a weak absorption band was observed at 644 cm^{-1} , which was assigned to the incorporation of fluoride ions (F^-) and the substitution of F^- for OH^- . The absorption band of absorbed H_2O molecules at 1650 cm^{-1} was stronger than that of CaP (CaP-undoped pH10 200°C hydrothermal), but similar to that of doped CaP (CaP-doped batch A pH10 200°C hydrothermal). Like doped CaP (CaP-doped batch A pH10 200°C hydrothermal), the absorption bands of CO_3 group at 2350 cm^{-1} and CO_3 group (ν_3) at 1546 cm^{-1} were significantly reduced, compared to those of CaP (CaP-undoped pH5 200°C hydrothermal), which indicated that they were less carbonated. The absorbed H_2O molecules were observed with a small and broad absorption band at 3160 cm^{-1} , while weak bands of structural OH group and F–OH bond were observed at 3570 cm^{-1} and 3538 cm^{-1} , respectively.

Table 4.2.17 Characteristic IR absorption frequencies (cm^{-1}) of functional groups for doped CaP powders (batch B), compared to those of reported data (495, 552, 553, 569)

Functional group and absorption cm^{-1} (References)	CaP-doped B pH5 RT		CaP-doped B pH10 RT		CaP-doped B pH5 200°C hydrothermal		CaP-doped B pH10 200°C hydrothermal	
	cm^{-1}	Intensity	cm^{-1}	Intensity	cm^{-1}	Intensity	cm^{-1}	Intensity
450-500 cm^{-1} PO ₄ v2	468	Weak	470	Weak	470	weak	472	weak
500-600 cm^{-1} PO ₄ v4	528	small-like sh	528	v. weak sh	524	small	526	v. weak-like sh
	565	small-medium	563	Small-medium	565	small-medium	563	small-medium
	601	weak-sh	605	Small-medium	601	Small-medium	605	small-medium
647-630 cm^{-1} F incorporation	640	v. Weak	644	v. weak	644	Small	644	v. weak
720 cm^{-1} Nujol	721	Small	721	Small	723	Small	721	Small
875 cm^{-1} HPO ₄	878	Weak-small	-	-	-	-	-	-
960 cm^{-1} PO ₄ v1	964	weak-sh	964	weak-sh	964	weak-sh	964	weak-like sh
1000-1200 cm^{-1} PO ₄ v3	1033	Strong	1031	Strong	1031	Strong	1029	Strong
	-	-	-	-	-	-	1062	Sh
	1124	small-sh	1097	small-sh	1093	small-sh	1097	small-like sh
1400-1650 cm^{-1} CO ₃ v3	1548	Weak	1546	Weak	1548	Weak	1546	Weak
1600-1650 cm^{-1} H ₂ O absorbed	1641	Small-medium	1641	medium	1641	Small-medium	1641	small-medium
2000-2100 cm^{-1} PO ₄	2038	weak-small	2038	weak-small	2050	weak-small	2034	Small
2100-2400 cm^{-1} absorbed CO ₃	2341	Small-medium	2341	Small	2343	v. weak	2343	v. weak
	2360	Small-medium	2360	Small	2366	weak-small	2360	Weak-small
3100-3600 cm^{-1} absorbed H ₂ O	3137	medium-broad	3182	small-broad	3139	medium-broad	3151	medium-broad
3580-3600 cm^{-1} H ₂ O stretching	-	-	3400	smaller-broad	-	-	3400	Weak-broad
3535 cm^{-1} F-OH	3540	v. weak	3540	v. weak	3540	v. weak	3540	v. weak
3571 cm^{-1} structural OH	3570	v. weak	3570	v. weak	3570	Weak	3570	Weak

v = very, sh = shoulder, vibrational modes (v1 = symmetrical stretching, v2 = Asymmetrical stretching, v3 = bending in and out of plane and v4 = bending in plane)

Thermal behaviour of doped CaP powders (batch B) was investigated using differential scanning calorimetry (DSC). As with CaP and doped CaP (batch A) powders, the heat flow of DSC measurements was set to Endo up, which indicates that endothermic changes are peaked up, while exothermic changes are peaked down. DSC of doped CaP powders (batch B) is compared in Figure 4.2.62, and DSC peak centres are shown in Table 4.2.18. Doped CaP powders (CaP-doped batch B pH5 RT) and (CaP-doped batch B pH10 RT) showed negligible broad endothermic peaks at 439°C and 111°C, respectively, which were assigned to the explosion of lattice water and liberation of water, respectively (560). The endothermic peak at 439°C is in good agreement with the reported phase transformation from monetite to calcium pyrophosphate (β -Ca₂P₂O₇) around 400°C (551). As stated before, the explosion of lattice water was due to the chemical reaction of OH radicals, which were liberated from the CaP structure during heating. This indicated that the powders were hydrated, and that the endothermic peaks were due to dehydration of powders, as established with CaP and doped CaP (batch A) powders.

The other two doped CaP powders (CaP-doped batch B pH5 200°C hydrothermal and CaP-doped batch B pH10 200°C hydrothermal) showed no reactions. This was in contrast to CaP powders, but similar to doped CaP (batch A) powders under the same conditions. This indicated that these doped CaP powders were anhydrous and thermally stable, and that no phase transformations took place upon heating from room temperature up to 600°C.

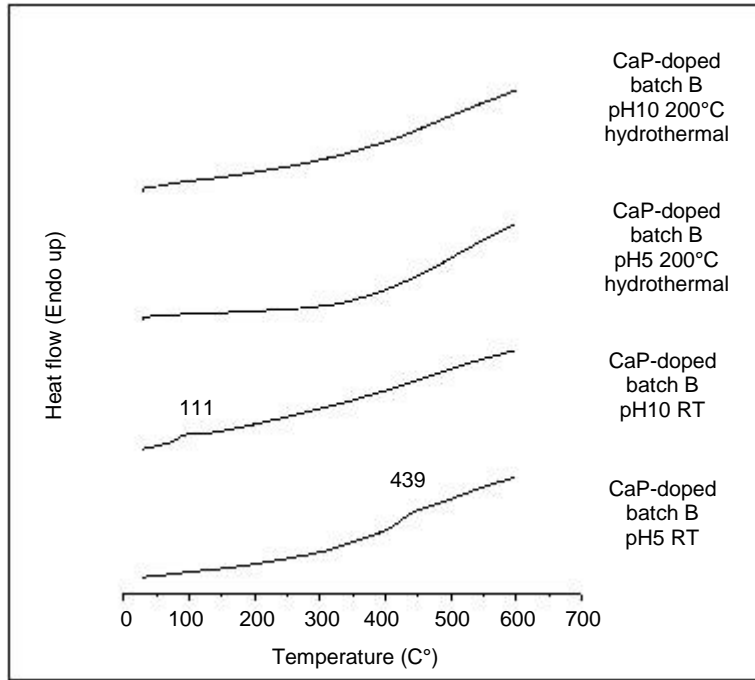


Figure 4.2.62 DSC of doped CaP powders (batch B) (Endo up).

Table 4.2.18 DSC peak centres for doped CaP (batch B) powders

CaP-doped batch B pH5 RT	CaP-doped batch B pH10 RT	CaP-doped batch B pH5 200°C hydrothermal	CaP-doped batch B pH10 200°C hydrothermal
439°C	111°C	-	-

Doping of CaP via batch A and B dopants can be summarised as follows. Under room temperature and as – prepared pH 5.4 ± 0.2 conditions, SEM of doped CaP (batch A) powder showed nanospherical particles fused to the surface of platelet – like particles, corresponding to CaP (brushite and monetite) and dopants' phases (Er_2O_3 , AlPO_4 , and CaF_2), as indicated by XRD, whereas SEM of doped CaP (batch B) powder showed platelet – like particles, corresponding to a homogeneous doped monetite, as indicated by XRD. Under room temperature and pH 10 ± 0.2 conditions, SEM of doped CaP (batch A) powder showed well – crystallised spherical particles fused together, forming a continuous and uniform layer, corresponding to the formation of homogenous HAp and dopants' phases, the latter which (phases) were revealed by XRD. On the other hand, SEM of doped CaP (batch B) powder showed rounded – like particles (necking together), corresponding to the formation of Er^{+3} , Al^{3+} , and F^- – doped HAp, as indicated by XRD. Under as – prepared pH 5.4 ± 0.2 and 200°C hydrothermal conditions, SEM of doped CaP (batch A) powder showed platelet – like, rod – like, and rounded – like particles, corresponding to the formation of brushite and dopants' phases, as indicated by XRD, whereas SEM of doped CaP (batch B) powder showed rounded – like particles, corresponding to the formation of Er^{+3} , Al^{3+} , and F^- – doped HAp, as indicated by XRD. Under pH 10 ± 0.2 and 200°C hydrothermal conditions, SEM of doped CaP (batch A) powder showed spherical particles and rod/needle – like particles, corresponding to the formation of HAp and dopants' phases, as indicated by XRD. On the other hand, SEM of doped CaP (batch B) powder showed rod – like particles, corresponding to the formation of Er^{+3} , Al^{3+} , and F^- – doped HAp, as indicated by XRD.

In the case of doped CaP (batch A) (CaP-doped batch A pH5 RT), the P–O bond at 1230 – 1132 cm^{-1} and Er–O–Er bond at 522 cm^{-1} confirmed the presence of Er_2O_3 and AlPO_4 phases, respectively. The OH–F–OH and F–OH bonds at 784 – 665 cm^{-1} and 3438 cm^{-1} , respectively, indicated the possible incorporation of F^- into the CaP structure. In the case of the rest of doped CaP (batch A) powders, the F–OH bond at 3438 cm^{-1} indicated the incorporation of F^- into CaP structure, while the broadening of absorption bands of PO_4 group (ν_3) (P–O) at 1150 – 950 cm^{-1} and PO_4 group (ν_4) (O–P–O) at 600 – 550 cm^{-1} was donated to the presence of dopants' phases (Er_2O_3 and AlPO_4) or that some degree of substitution by Er^{3+} and Al^{3+} for Ca^{2+} may have taken place. On the other hand, in the case of doped CaP powder (batch B) (CaP-doped batch B pH5 RT), the absorption bands around 666 – 644 cm^{-1} and 3538 cm^{-1} indicated the incorporation of fluoride ion into the monetite structure through the formation of OH–F–OH and F–OH bonds, respectively. In the case of the rest of doped CaP (batch B) powders, the absence of characteristic OH group at 634 cm^{-1} for HAp and the presence of absorption bands at 644 cm^{-1} and 3538 cm^{-1} indicated the substitution of F^- for OH^- in the HAp structure and the formation of F–OH bond, respectively. FTIR spectra of (CaP-doped batch B pH10 RT), (CaP-doped batch B pH5 200°C hydrothermal), and (CaP-doped batch B pH10 200°C hydrothermal) were similar to those of doped CaP (batch A) powders. However, the former powders showed broader absorption bands of PO_4 group (ν_3) (P–O) at 1150 – 950 cm^{-1} and PO_4 group (ν_4) (O–P–O) at 600 – 550 cm^{-1} , and the development of new absorption bands, which indicated clearer incorporation of Er^{3+} , Al^{3+} , and F^- into the HAp structure.

DSC results of doped CaP (batch A) powders indicated that CaP-doped batch A pH5 RT was hydrated, and supported phase transformations from brushite to monetite and from monetite to calcium pyrophosphate (β -Ca₂P₂O₇) at 168.2°C and 434.5°C, respectively, that were revealed by hot stage XRD at 200°C and 400°C. The rest of doped CaP (batch A) powders (CaP-doped batch A pH10 RT), (CaP-doped batch A pH5 200°C hydrothermal), and (CaP-doped batch A pH10 200°C hydrothermal) showed no reactions, which indicated that these doped CaP powders were anhydrous, and that no phase transformations took place upon heating from room temperature up to 600°C. On the other hand, DSC results of doped CaP (batch B) powders indicated that CaP-doped batch B pH5 RT and CaP-doped batch B pH10 RT were hydrated, and supported a phase transformation from monetite to calcium pyrophosphate (β -Ca₂P₂O₇) at 439°C (CaP-doped batch B pH5 RT) that was revealed by hot stage XRD at 400°C. The other two doped CaP (batch B) powders (CaP-doped batch A pH5 200°C hydrothermal and CaP-doped batch A pH10 200°C hydrothermal) showed no reactions, which indicated that these doped CaP powders were anhydrous, and that no phase transformations took place upon heating from room temperature up to 600°C.

The results indicated that doped CaP (batch B) powders are more promising than doped CaP (batch A) powders. This is because the doping of CaP with soluble compounds (Er(NO₃)₃.5H₂O, Al(NO₃)₃.9H₂O, and NH₄F) was more effective and evident than with insoluble compounds (Er₂O₃, AlPO₄, and CaF₂). Doping of CaP powders (batch B) resulted in the formation of homogeneous single phase and particle morphology, while doping of CaP powders (batch A) resulted in the formation of inhomogeneous phases and

particle morphology, except that synthesised under room temperature and pH 10 ± 0.2 conditions (CaP-doped batch A pH10 RT), which resulted in the formation of homogeneous phases and particle morphology. The latter would be effective in occluding dentinal tubules, and most importantly, they would sinter homogeneously under laser irradiation than the rest of doped CaP (batch A) powders. Similarly, doped CaP (batch B) powders, particularly those synthesised under pH 10 ± 0.2 and/or 200°C hydrothermal conditions, would be effective in occluding and infiltrating dentinal tubules, with or without the application of laser irradiation, but they would probably sinter homogeneously, and they would be more effective in occluding dentinal tubules under laser irradiation.

4.2.3 Main findings

The results indicated the formation of inhomogeneous phases in the case of doped CaP (batch A) powders, except that synthesised under room temperature and pH 10 ± 0.2 conditions (CaP-doped batch A pH10 RT), which resulted in the formation of homogeneous phases. On the other hand, a single homogenous phase was formed in the case of doped CaP (batch B) powders. The results indicated the formation of a single CaP phase under all conditions with no secondary phases, which was the doped monetite phase in the case of doped CaP powder (CaP-doped batch B pH5 RT) and doped HAp phase in the rest of doped CaP (batch B) powders.

The results also indicated that the incorporation of dopants (batch A) was most effective under room temperature and high pH conditions (CaP-doped batch A pH10 RT), which resulted in the formation of homogenous phases and significantly affected the size and shape of particles, compared to CaP

powder (CaP-undoped pH10 RT). On the other hand, the results indicated that the incorporation of dopants (batch B) was effective under all conditions, which resulted in the formation of a single doped CaP phase.

Although SEM revealed the formation of nanoparticles (in agglomerates), particularly in the case of CaP and doped CaP (batch B) powders, the particle size analyses revealed the particle size in the micrometre scale, which was in good agreement with the micrometre agglomerates. As established with CaP powders, this is because the measurement of nanoparticles depends on the deagglomeration of doped CaP particles. These agglomerates were formed in methanol and distilled water under ultrasonic bath conditions for ~ 10 minutes, which might indicate the formation of hard agglomerates of particles or that a further deagglomeration treatment was required.

The FTIR results of powders that were synthesised under room temperature and as – prepared pH 5.4 ± 0.2 conditions indicated the incorporation of fluoride ions into CaP structure through the formation of OH–F–OH and F–OH bonds in the case of doped CaP powders (batch A) and (batch B). The P–O bond at $1230 - 1132 \text{ cm}^{-1}$ and Er–O–Er bond at 522 cm^{-1} , corresponding to the presence of Er_2O_3 and AlPO_4 phases, were observed with doped CaP (CaP-doped batch A pH5 RT), while the incorporation of Er^{3+} and Al^{3+} was observed with doped CaP (batch B) powders (monetite). In the case of the rest of doped CaP powders (batch A and B), other than those synthesised under room temperature and as – prepared pH 5.4 ± 0.2 conditions, FTIR results indicated that the incorporation of Er^{3+} , Al^{3+} , and F^-

into the CaP structure was clearer and more evident in the case of doped CaP (batch B) powders than doped CaP (batch A) powders.

The DSC results indicated that doped CaP powders (batch A and B) that were synthesised under 200°C hydrothermal conditions were anhydrous, and they had better thermal stability than those synthesised under room temperature conditions. This was in contrast to the hydrated CaP powders that were synthesised under 200°C hydrothermal conditions. This indicated the effectiveness of 200°C hydrothermal conditions and the addition of dopants in driving off water molecules and improving the thermal stability of CaP powders.

Chapter 4.3 Laser irradiation sintering investigation

4.3.1 Characterisation of prepared dentine sections

Preparation of dentine sections was aimed at mimicking the naturally exposed dentine surface to extreme cases of sensitivity, as shown in Figure 4.3.1. These dentine cross – sections (~ 1 – 2 mm in thickness) were prepared from clinically extracted human teeth (University of Leeds, School of Dentistry, tissue bank No: 270409/EE/22), after they were sterilised by gamma irradiation.

Figure 4.3.1 (a and b) shows the prepared dentine surfaces, which were used for the coating and laser irradiation sintering trials. SEM showed open dentinal tubules, after the dentine sections were subjected to acid etching treatments to mimic the condition of hypersensitivity associated with teeth.

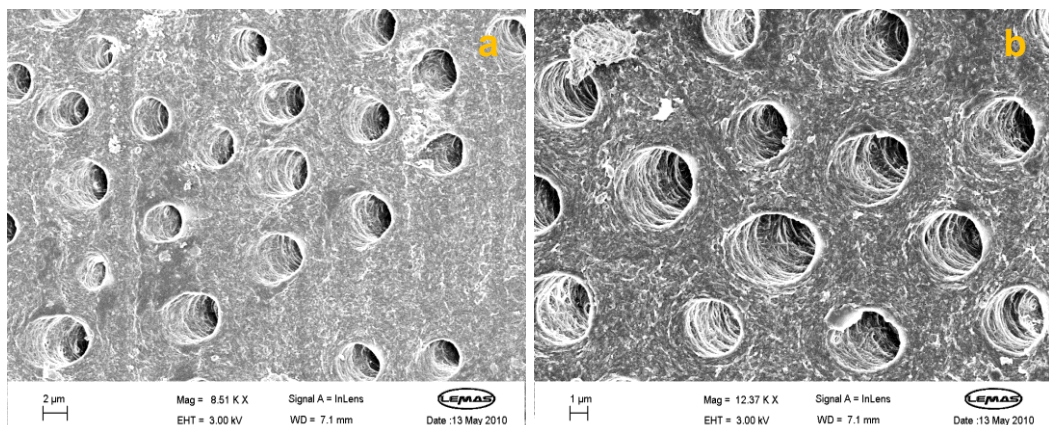


Figure 4.3.1 SEM of as – prepared dentine section of 1 – 2 mm in thickness, showing open dentinal tubules after acid etching treatments. (a) Low magnification at 2 μm and (b) high magnification at 1 μm.

4.3.2 Characterisation of coatings

Dentine sections were coated with 5% w/v CaP and doped CaP powder suspensions (in methanol) by the dip coating technique, manually and using a dipping machine. The manual dipping was carried out in the initial coating trials, under which the withdrawal of all sections was kept at a constant speed of ~ 1 cm per second. Although the manual dipping technique was manageable, the withdrawal speed of dentine sections was difficult and time consuming. All other coating trials were then carried out using a dipping machine. The withdrawal speed of dentine sections was set to 1 cm per second. The dipping of dentine sections was carried out for a maximum of 5 minutes. The coatings were further improved by the application of the same suspension, drop wise onto dentine sections using a syringe, which provided thicker coatings for laser irradiation sintering trials. The coated dentine sections were stored in a reduced pressure desiccator, until they were laser irradiated and characterised.

Quality check of the coatings was carried out by the naked eye to examine their physical appearance, and by scanning electron microscopy to assess their morphology. The colour contrast between the coatings (white powders in the case of CaP and pink powders in the case of doped CaP) and dentine sections made it possible to examine the coatings by the naked eye, particularly after they were dried in a reduced pressure desiccator.

The coating/occlusion of dentinal tubules was characterised by SEM. Figure 4.3.2 and Figure 4.3.3 show platelet – like particles of CaP and doped CaP powders, respectively, occluding open dentinal tubules, after initial trials with a single dip coating. Although a better and uniform coating was achievable

using a dipping machine, the initial coating with both powders provided a satisfactory CaP/doped CaP coating to interact with post laser irradiation.

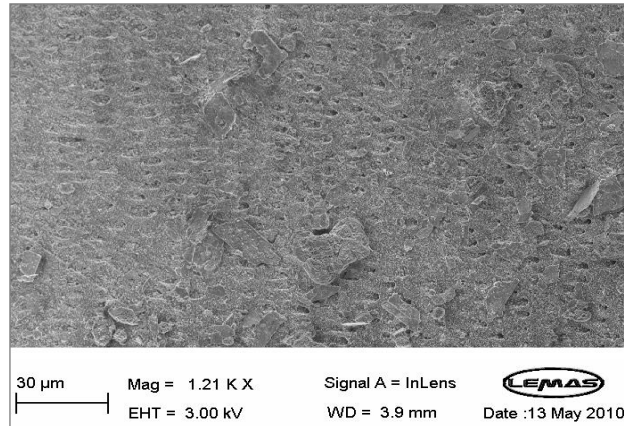


Figure 4.3.2 SEM of a dentine section coated with CaP powder, showing open dentinal tubules and non – uniform occlusion with CaP particles.

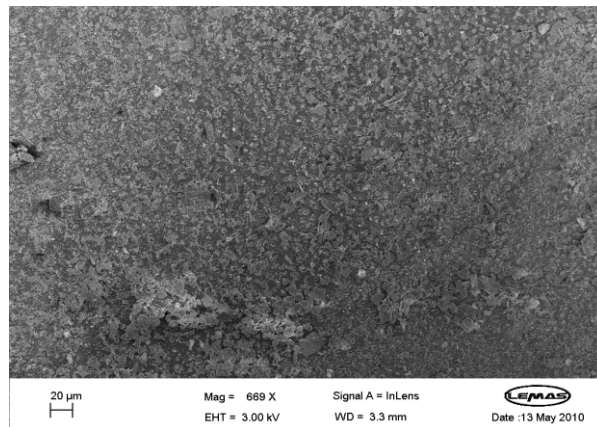


Figure 4.3.3 SEM of a dentine section coated with doped CaP (batch A) powder, showing occluded dentinal tubules with doped CaP particles.

4.3.3 Laser irradiation sintering trials

Laser irradiation sintering experiments were carried out at the University of Leeds, Institute for Materials Research as well as the University of St. Andrews, Department of Physics and Astronomy. Initial laser irradiation trials were performed on CaP – and doped CaP – coated dentine sections, using a continuous wave (CW) laser at 980 nm wavelength (output power of ~ 150 mW). Both doped CaP powders (batch A and B) were investigated under laser irradiation. Post – initial laser irradiation trials involved laser irradiation sintering of CaP – and doped CaP – coated dentine sections with ~ 1520 nm CW laser (output power of ~ 150 mW) and ~ 1520 nm femto – second (fs) – pulsed laser (beam power of ~ 130 mW, pulse duration of 100 fs, and repetition rate of 2.5 GHz).

Laser irradiation sintering trials were also performed on CaP/doped CaP pellets for the investigation of laser – CaP interaction. The pellets were laser irradiated with CW lasers at 980 nm and 1500 nm wavelengths and pulsed laser at 1520 nm wavelength. In addition, CaP/doped CaP pellets were laser irradiated with 800 nm femto – second – pulsed laser (beam power of ~ 130 mW, pulse duration of 100 fs, and repetition rate of 250 – 1 KHz) for the investigation of CaP/doped CaP pellets in an acidic environment.

Laser type, CaP/doped CaP sample (coatings and pellets), and exposure time were reported in Table 3.4 (chapter 3). The effects of CW and pulsed laser irradiation on CaP/doped CaP particles in the form of pellets and on coated and uncoated dentine sections were characterised mainly by SEM. Other characterisation techniques, such as XRD, micro – hardness, profilometry, and ICP/MS were also used in some trials.

4.3.3.1 Characterisation of laser – irradiated CaP pellets

The use of CaP/doped CaP powders in the form of pellets was aimed at investigating the interaction between CaP particles and laser irradiation. Although the pressed pellets would sinter different to coatings onto dentine sections, sintering of pellets would allow comparing the behaviour of CaP and doped CaP particles under laser irradiation. The effect of 1520 nm pulsed laser irradiation and 980 nm CW laser irradiation for 1 minute and 5 minutes, respectively, on CaP/doped CaP particles were demonstrated on pressed pellets of ~ 1 – 2 mm in thickness. The laser – irradiated areas were examined by SEM for morphological changes.

During the early stages of this research study, rare earth oxide (Tm_2O_3) was involved in the initial investigation only. The single dopant of rare earth (Tm_2O_3) was used to assess the effect and interaction of rare earth – doped CaP powder with laser irradiation. Therefore, the interaction of Tm_2O_3 – doped CaP pellet under laser irradiation, particularly 1520 nm pulsed laser, was included in this section to demonstrate the effectiveness of rare earths in improving the laser irradiation sintering of CaP. In the case of CaP powder, the pellet showed poor interaction with the 1520 nm pulsed laser irradiation for 1 minute, as shown by the poorly sintered area and insignificant change in surface morphology in Figure 4.3.4 (a) and (b), respectively. On the other hand, in the case of rare earth doped CaP powder, the Tm_2O_3 – doped CaP pellet showed a significant interaction with the 1520 nm pulsed laser irradiation for 1 minute, as shown by the well – sintered area and significant change in surface morphology in Figure 4.3.5 (a) and (b), respectively. This indicated the strong absorption of thulium (Tm^{3+}) at 1520 nm wavelength, which resulted in a densified surface with

increased thickness, as shown in Figure 4.3.5 (b). On the other hand, in the case of $\text{Er}_2\text{O}_3\cdot\text{AlPO}_4\cdot\text{CaF}_2$ – doped CaP powder, the doped CaP pellet showed some degree of interaction with the 980 nm CW laser irradiation for 5 minutes, as shown by the sintered area and change in surface morphology in Figure 4.3.6 (a) and (b), respectively. However, the change in surface morphology was not significant, compared to that with Tm_2O_3 – doped CaP pellet under 1520 nm pulsed laser irradiation, which was probably due to the weak absorption of erbium (Er^{3+}) at 980 nm as well as the CW laser mode.

In addition, XRD was carried out on CaP and Tm_2O_3 – doped CaP pellets, which were irradiated with 1500 nm CW and 1520 nm pulsed lasers, as shown in Figures 4.3.7 and 4.3.8. The XRD patterns indicated reduced peak intensities of CaP and doped CaP pellets under CW and pulsed laser irradiation, compared to those of unsintered CaP pellets. The reduction in peak intensities was relatively higher under CW laser irradiation than pulsed laser irradiation, which might explain the heat accumulation during CW laser irradiation. In addition, the XRD patterns indicated that no phase transformation took place under CW and pulsed laser irradiation.

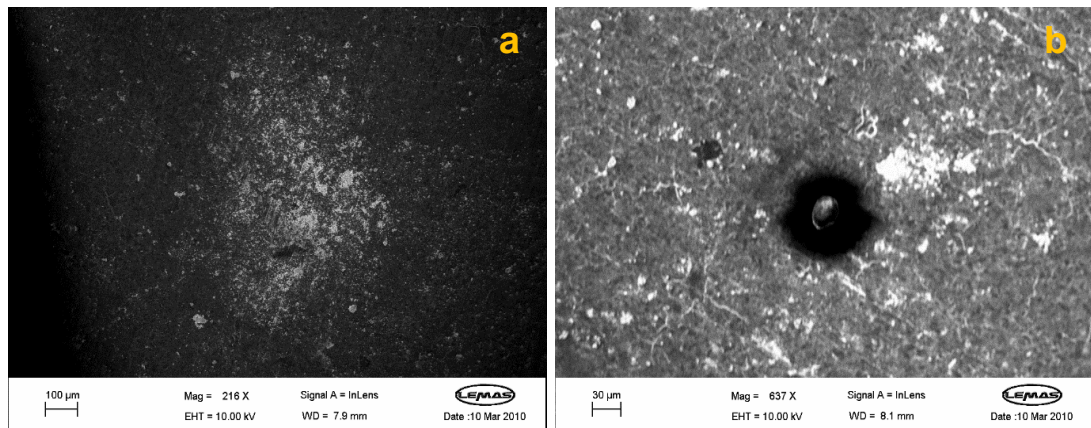


Figure 4.3.4 SEM of CaP Pellet of 1 – 2 mm in thickness that was irradiated with 1520 nm pulsed laser, showing (a) the sintered area, and (b) change in surface morphology.

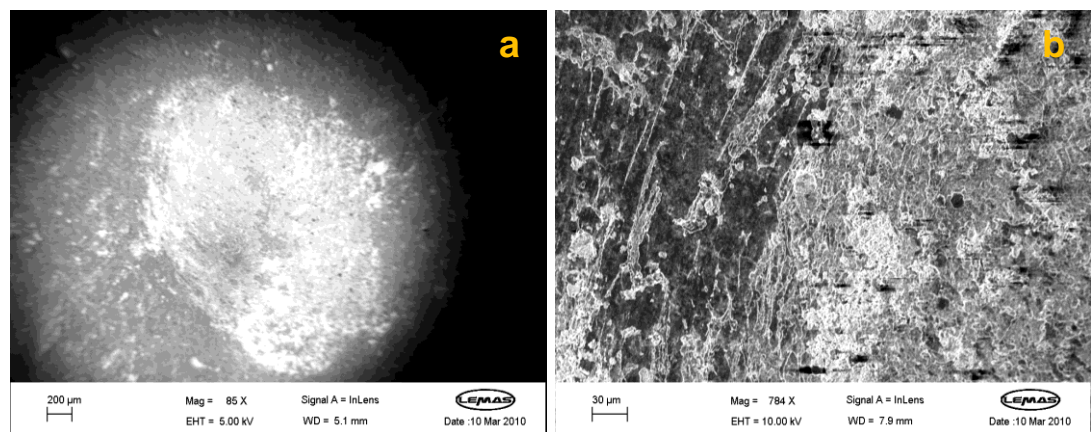


Figure 4.3.5 SEM of thulium oxide – doped CaP pellet of 1 – 2 mm in thickness that was irradiated with 1520 nm pulsed laser, showing (a) the sintered area, and (b) change in surface morphology.

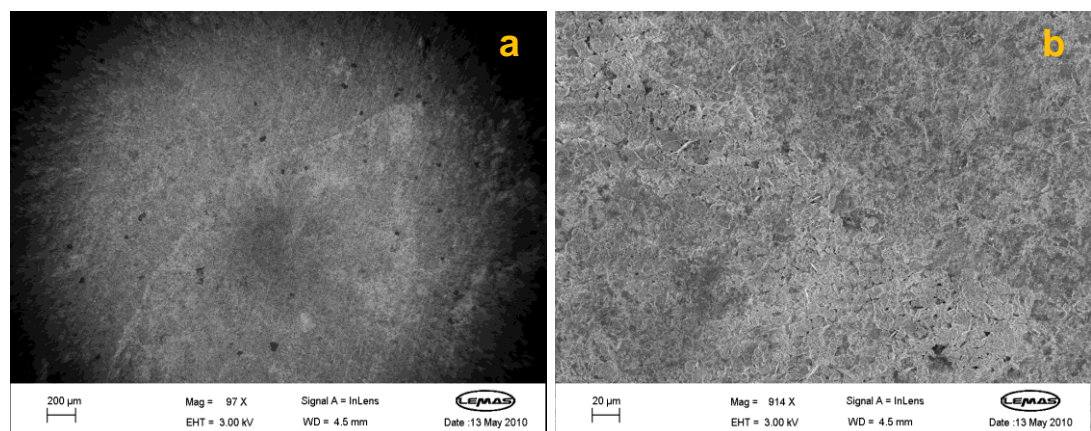


Figure 4.3.6 SEM of erbium oxide, aluminium phosphate, and calcium fluoride – doped CaP pellet of 1 – 2 mm in thickness that was irradiated with 980 nm CW laser, showing (a) the sintered area, and (b) change in surface morphology.

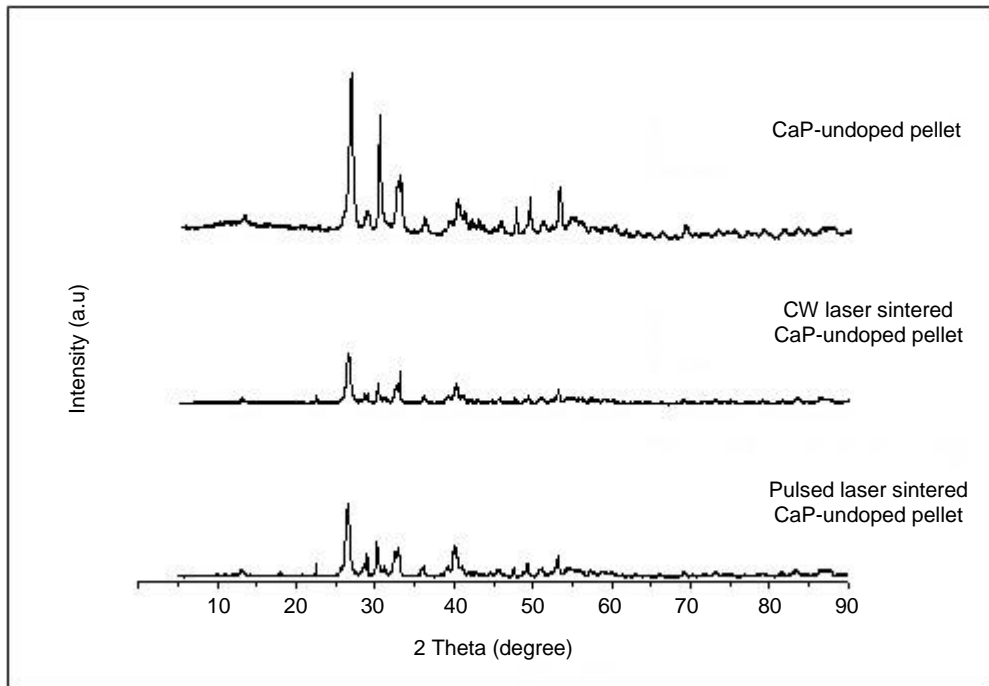


Figure 4.3.7 XRD patterns of CaP pellets irradiated with 1500 nm CW and 1520 nm pulsed lasers, compared to that of unsintered CaP pellet.

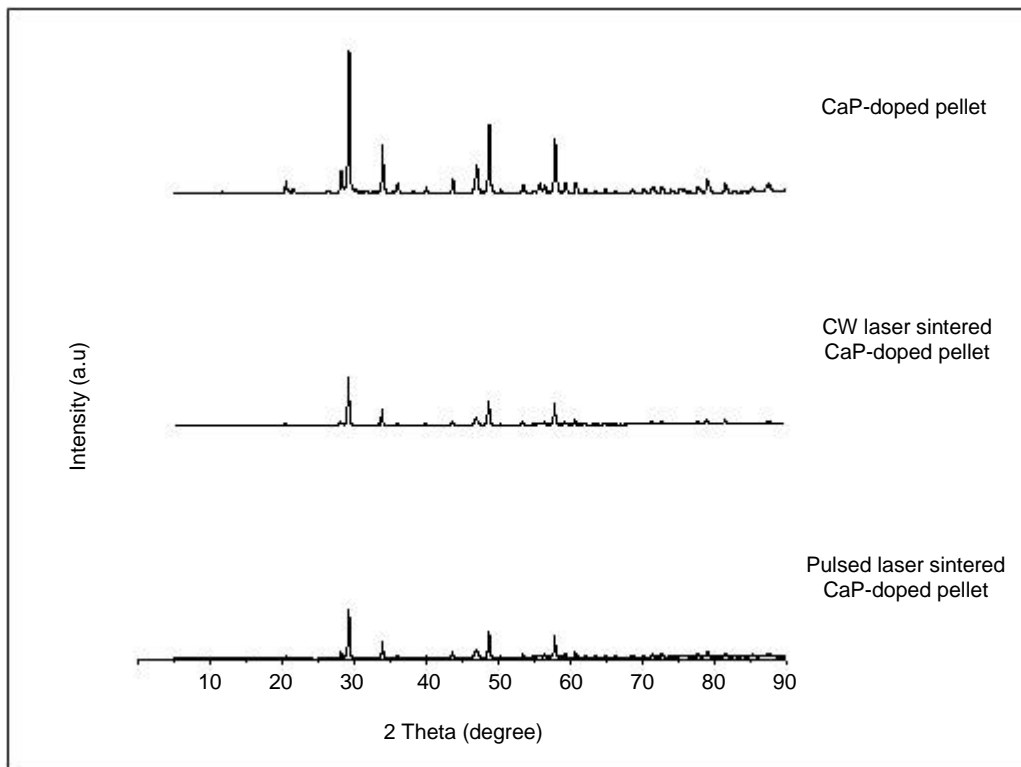


Figure 4.3.8 XRD patterns of Tm₂O₃ – doped CaP pellets irradiated with 1500 nm CW and 1520 nm pulsed lasers, compared to that of unsintered Tm₂O₃ – doped CaP pellet.

4.3.3.2 Characterisation of laser – irradiated uncoated/coated dentine sections

4.3.3.2.1 First laser irradiation sintering trial

The first laser irradiation sintering trial was carried out to investigate the effectiveness of CW and pulsed laser irradiation, in terms of their interaction with CaP/doped CaP coatings. The first laser irradiation trial was carried out on uncoated and CaP (CaP and doped CaP batch A) – coated dentine sections, as shown in Figures 4.3.9 – 4.3.11.

The uncoated dentine section that was irradiated with 980 nm CW laser for 5 minutes showed no evidence of occlusion/sealing of dentinal tubules, as shown in Figure 4.3.9. On the other hand, the dentine sections coated with CaP and $\text{Er}_2\text{O}_3\cdot\text{AlPO}_4\cdot\text{CaF}_2$ – doped CaP (batch A) powders that were irradiated with 980 nm CW laser for 5 minutes showed some level of interaction, as shown in Figure 4.3.11 (a-d) and Figure 4.3.10 (a-b), respectively.

The post solidification structure of CaP and $\text{Er}_2\text{O}_3\cdot\text{AlPO}_4\cdot\text{CaF}_2$ – doped CaP showed poorly densified area and rosette – like structure, respectively, as shown in Figure 4.3.11 (b) and Figure 4.3.10 (b), respectively. This clear evidence of poor absorption and non – uniform densification by both powders was most probably because the energy was not evenly distributed and due to the weak absorption at 980 nm wavelength, particularly by erbium (Er^{3+}).

Moreover, CaP – coated dentine section that was irradiated with 980 nm CW laser for 5 minutes exhibited heat accumulation, which caused distortion to CaP layer, as shown in Figure 4.3.11 (b), which was because the energy was not evenly absorbed and distributed to induce a uniform densification.

The laser irradiation interacted with CaP coating and poorly densified it, but it also melted the dentine surface, as shown in Figure 4.3.11 (c-d). On the other hand, in the case of $\text{Er}_2\text{O}_3\cdot\text{AlPO}_4\cdot\text{CaF}_2$ – doped CaP – coated dentine section, the interaction of laser irradiation with doped CaP particles caused them to grow like rosettes, which occluded large areas of dentinal tubules, as shown in Figure 4.3.10 (b). The difference between 980 nm CW laser – irradiated and non – irradiated areas of CaP and doped CaP coatings is shown in Figure 4.3.11 (c) and Figure 4.3.10 (a), respectively.

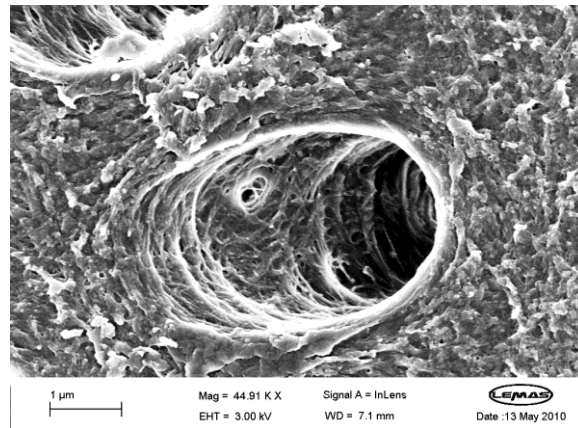


Figure 4.3.9 SEM of a dentine section of 1 – 2 mm in thickness that was irradiated with 980 nm CW laser, showing the modification of dentine surface morphology without the occlusion/sealing of open dentinal tubules.

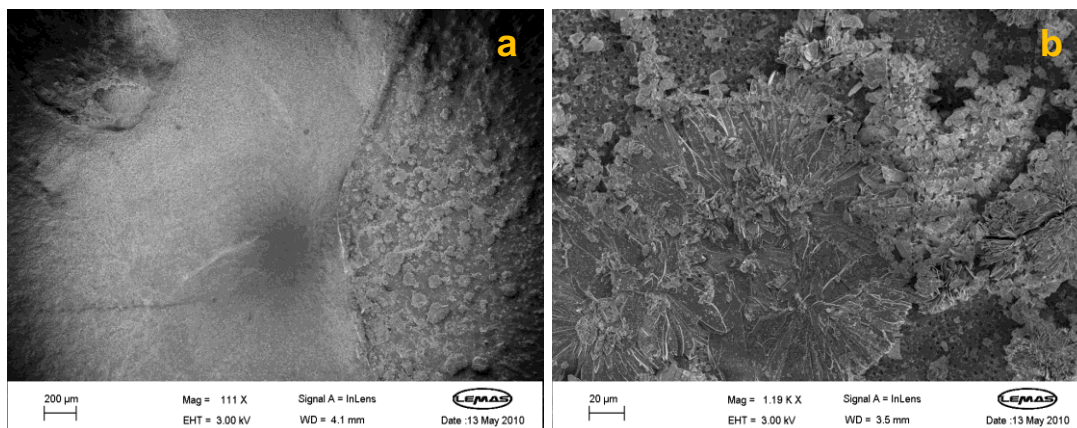


Figure 4.3.10 SEM of dentine section coated with $\text{Er}_2\text{O}_3\cdot\text{AlPO}_4\cdot\text{CaF}_2$ – doped CaP (batch A) that was irradiated with 980 nm CW laser, showing (a) unsintered and sintered areas and the change in surface morphology of doped CaP coating, and (b) the formation of rosette – like particles that are occluding large area of dentinal tubules.

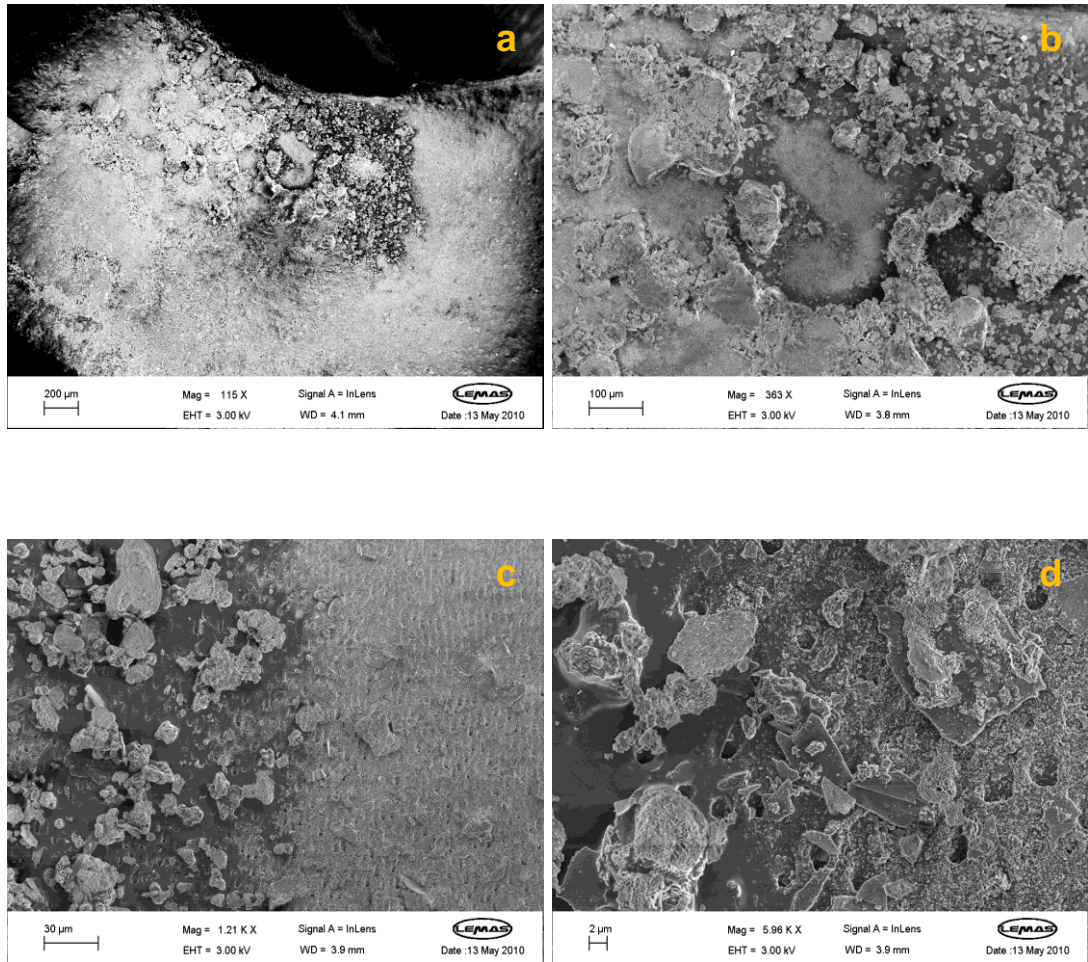


Figure 4.3.11 SEM of a dentine section coated with CaP that was irradiated with 980 nm CW laser, showing the change in surface morphology of CaP coating without occluding dentinal tubules, (a) sintered area, (b) heat accumulation and non – uniform absorption and distribution of energy, (c) difference between laser irradiated and non-irradiated areas, and (d) melted dentine surface and partially sealed dentinal tubules.

4.3.3.2.2 Second laser irradiation sintering trial

The second laser irradiation sintering trial involved laser irradiation of CaP – and doped CaP (batch A) (Er_2O_3 , AlPO_4 , and CaF_2) – coated dentine sections, using 1500 nm CW laser and 1520 nm pulsed laser for an exposure time from 30 seconds up to 5 minutes, as shown in Figures 4.3.12 – 4.3.15. The results of 1500 nm CW laser irradiation were not included due to a lack of clear evidence of effects. One of the characteristics of laser irradiation sintering is the formation of a crater, due to a plastic deformation and projection of coating and/or dentine surface. A crater is usually filled back due to the fall back of projected coating, crater lip, and crater wall. Therefore, the crater should ideally be as shallow and spread wide as possible, with optimum sintering effects on the surrounding areas.

Doped CaP – coated dentine sections that were irradiated with 1520 nm pulsed laser for 30 seconds and 2 minutes are shown in Figure 4.3.12 (a-d). In contrast to 980 nm CW and 1500 nm CW (not included) laser irradiation, 1520 nm pulsed laser irradiation of doped CaP – coated dentine sections for 30 seconds and 2 minutes exhibited better interaction. The laser irradiation resulted in a more uniform densification and the occlusion of dentinal tubules in and around the laser – irradiated area, which probably was due to the wave – like energy distribution shown in Figure 4.3.12.

The laser irradiation sintering for 2 minutes resulted in a less – uniform densification of CaP coating, and it caused a minor distortion in the form of a crack – like, as shown in Figure 4.3.12 (a and b), which probably was due to the long exposure time of 2 minutes. On the other hand, the laser irradiation sintering for 30 seconds resulted in a uniform and excellent densification of CaP coating without distortion, which in turn resulted in a complete occlusion

of dentinal tubules, as shown in Figure 4.3.12 (c and d). The difference between the 1520 nm pulsed laser – irradiated and non – irradiated areas of doped CaP – coated dentine sections is shown in Figure 4.3.13 (b) and (a), respectively. Open dentinal tubules were observed in the unsintered areas away from the laser – irradiated area, as shown in Figure 4.3.13 (a), whereas a complete occlusion of dentinal tubules was observed in and around the laser – irradiated area, as shown in Figure 4.3.13 (b).

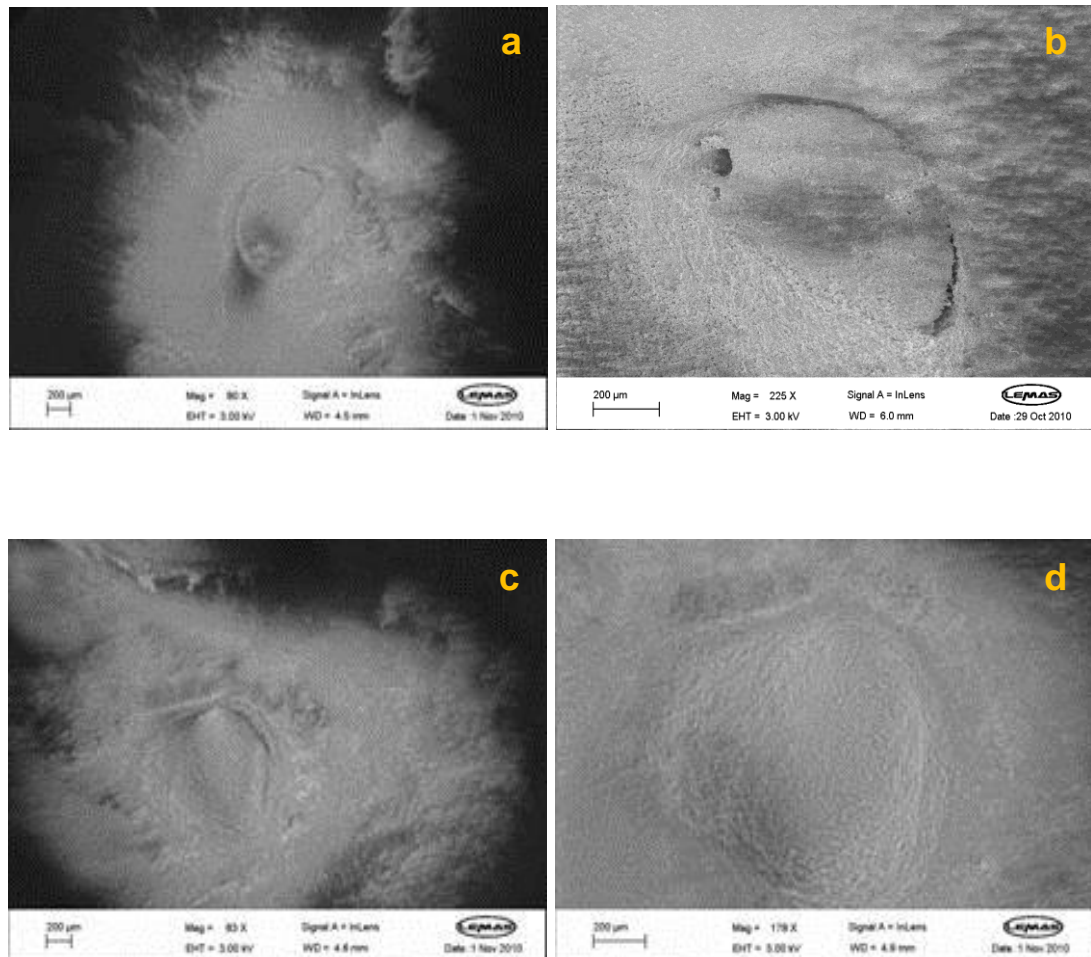


Figure 4.3.12 SEM of dentine sections coated with doped CaP that were irradiated with 1520 nm pulsed laser. (a-b) for 2 minutes, showing the crater surrounded by a wave – like effect with a minor distortion to the coating in the form of a crack – like, and (c-d) for 30 seconds, showing the crater surrounded by a wave – like effect without any distortion to the coating.

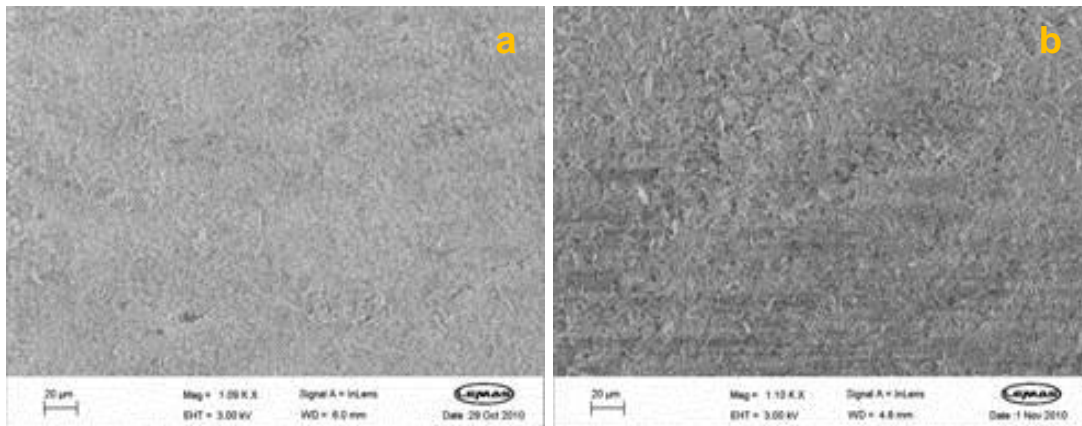


Figure 4.3.13 SEM of unaffected and effected areas by the 1520 nm pulsed laser irradiation, showing (a) open dentinal tubules away from the laser – irradiated area, and (b) completely occluded dentinal tubules around the laser – irradiated area.

Moreover, doped CaP – coated dentine section that was irradiated with 1520 nm pulsed laser for 5 minutes is shown in Figures 4.3.14. The laser irradiation sintering resulted in the formation of a deep crater without a wave – like effect, which indicated the possible penetration of dentine surface. Since the crater was deep and did not spread wide, the laser irradiation sintering for 5 minutes was concluded ineffective.

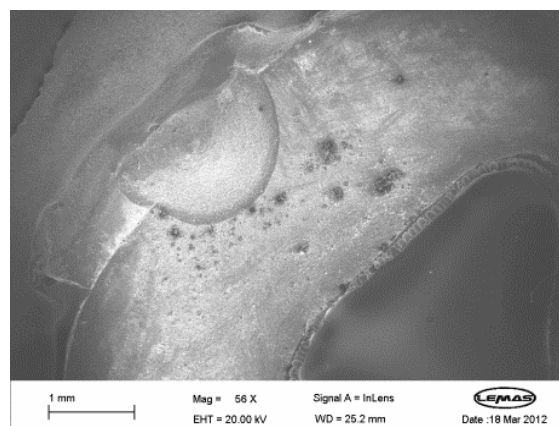


Figure 4.3.14 SEM of doped CaP – coated dentine section that was irradiated using 1520 nm pulsed laser for 5 minutes.

The first and second laser irradiation trials can be summarised as follows. CaP pellet interacted poorly with the 1520 nm pulsed laser irradiation for 1 minute, which resulted in insignificant changes in surface morphology. In contrast, Tm_2O_3 – doped CaP pellet interacted very well with the 1520 nm pulsed laser irradiation for 1 minute, which resulted in significant changes in surface morphology with a densified surface and increased thickness. Similarly, $\text{Er}_2\text{O}_3.\text{AlPO}_4.\text{CaF}_2$ – doped CaP pellet showed some degree of interaction with the 980 nm CW laser irradiation for 5 minutes, however, the change in surface morphology was not significant, compared to that with Tm_2O_3 – doped CaP pellet under 1520 nm pulsed laser irradiation. In addition, CaP and $\text{Er}_2\text{O}_3.\text{AlPO}_4.\text{CaF}_2$ – doped CaP coatings under 980 nm CW laser irradiation for 5 minutes showed poor absorption and non – uniform densification, which was due to poorly distributed energy and weak absorption at 980 nm wavelength. In contrast, the 1520 nm pulsed laser irradiation for 30 seconds was more effective than that for 2 and 5 minutes, as it resulted in a uniform and excellent densification of coating without any distortion, and thus, it resulted in a complete occlusion of dentinal tubules.

Therefore, pulsed lasers were preferred to CW lasers due to the heat accumulation associated with CW lasers. Despite the laser type (CW and pulsed), doped CaP coatings were superior to CaP coating. The doped CaP coating interacted more effectively with CW laser irradiation and was densified uniformly under pulsed laser irradiation without any distortion, which indicated the protection of the underlying dentine surface. The pulsed laser irradiation for 30 seconds was the most effective irradiation time, due to the formation of a shallow and spread crater without causing any damage to the CaP coating.

4.3.3.2.3 Third laser irradiation sintering trials

The third and final laser irradiation sintering trial was carried out on dentine sections uncoated and coated with CaP and doped CaP powders (batch B) ($\text{Er}(\text{NO}_3)_3$, $\text{Al}(\text{NO}_3)_3$, and NH_4F). Laser irradiation sintering was carried out using CW and pulsed lasers at ~ 1500 nm wavelength, exposure time of 1 and 2 minutes, and beam diameters of 125 μm and 250 μm . The final laser irradiation sintering trial was carried out to investigate the interaction of CaP and doped CaP powder (batch B), as well as to investigate the different effects of laser irradiation with beam diameters of 125 μm and 250 μm for 1 and 2 minute exposure time.

Under 1520 nm pulsed laser irradiation with a beam diameter of 250 μm for exposure time of 1 and 2 minutes, no morphological signs of laser craters were observed, as shown in Figure 4.3.15 and Figure 4.3.16. However, the highly charged areas are in good agreement with the laser irradiation spots, which showed the growth and densification of doped CaP particles/coatings. Although the effect of laser irradiation was superficial, the doped CaP particles were packed together with no sign of open dentinal tubules in and around the laser – irradiated area, as shown in Figure 4.3.17 (a and b).

Under 1520 nm pulsed laser irradiation with a beam diameter of 125 μm , clear morphological signs of laser craters were observed after exposure time of 1 and 2 minutes, as shown in Figures 4.3.18 – 4.3.20. Laser irradiation for exposure time of 1 minute formed a crater that appeared to spread in all directions with a superficial effect. The particles were packed together with no open dentinal tubules in and around the laser – irradiated area, as shown in Figure 4.3.19 (c and d).

Figure 4.3.20 (a and b) shows the difference between laser irradiation exposure time of 1 and 2 minutes. The exposure time of 2 minutes resulted in a deep penetration of doped CaP coating, which indicated the possible damage to the underlying dentine tissue. In contrast, the exposure time of 1 minute resulted in a laser crater with no signs of damage or open dentinal tubules. The exposure time of 1 minute also resulted in a crater with a smaller diameter than that under the exposure time of 2 minutes.

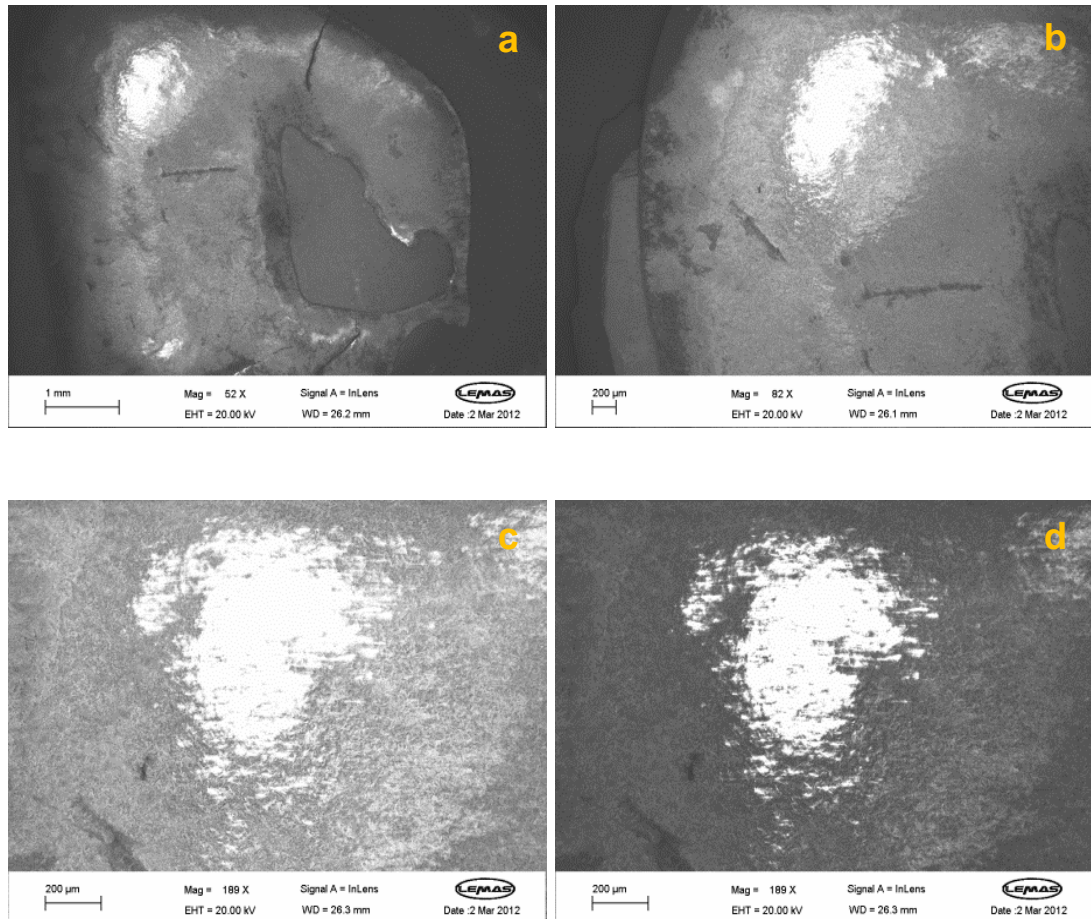


Figure 4.3.15 SEM of doped CaP coated dentine section that was irradiated for 1 minute using 1520 nm pulsed laser with a beam diameter of 250 μm, showing (a-b) laser – irradiated area, compared to non – irradiated areas, and (c-d) in and around laser – irradiated area.

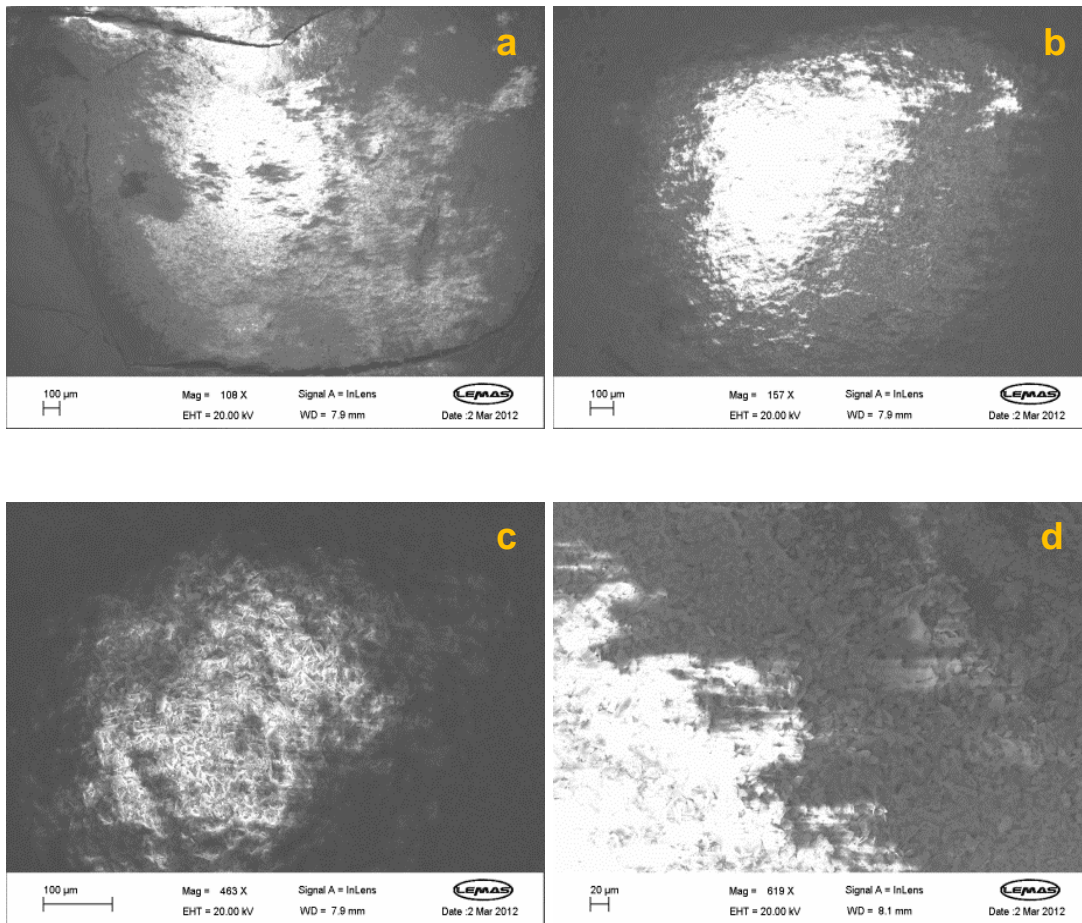


Figure 4.3.16 SEM of doped CaP coated dentine section that was irradiated for 2 minutes using 1520 nm pulsed laser with a beam diameter of 250 μm , showing (a-b) laser – irradiated area, compared to non – irradiated areas, and (c-d) in and around laser – irradiated area.

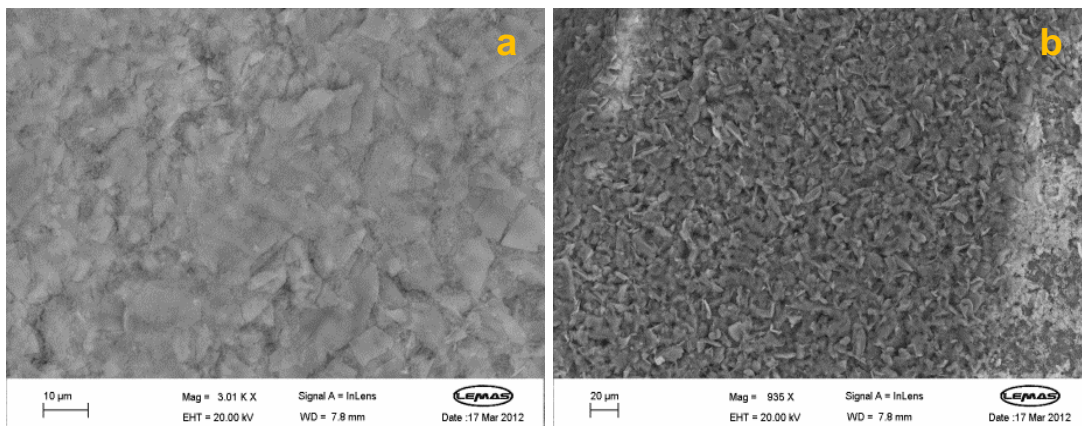


Figure 4.3.17 SEM of doped CaP coated dentine section that was irradiated using 1520 nm pulsed laser with a beam diameter of 250 μm , showing (a) the densification of laser – irradiated particles/coating, and (b) the area surrounding laser – irradiated area.

The laser – irradiated areas of doped CaP – coated dentine sections for exposure time of 1 and 2 minutes, using 1520 nm CW laser with a beam diameter of 250 μm , are shown in Figure 4.3.21. Under 1520 nm CW laser irradiation with a beam diameter of 250 μm for 1 minute, no clear signs of laser craters were observed, however, the highly charged areas are in good agreement with the laser – irradiated areas, as shown in Figure 4.3.22 (a). The particles were densified and packed together with no sign of open dentinal tubules in and around the laser – irradiated area, as shown in Figure 4.3.22 (b). Under CW laser irradiation with a beam diameter of 250 μm for 2 minutes, a deep crater was observed, as shown in Figure 4.3.23 (a and b). The deep crater indicated the penetration of coating and possible damage to the underlying dentine surface. However, the area around the laser irradiation spot indicated the densification and packing of particles with no sign of open dentinal tubules, as shown in Figure 4.3.23 (b).

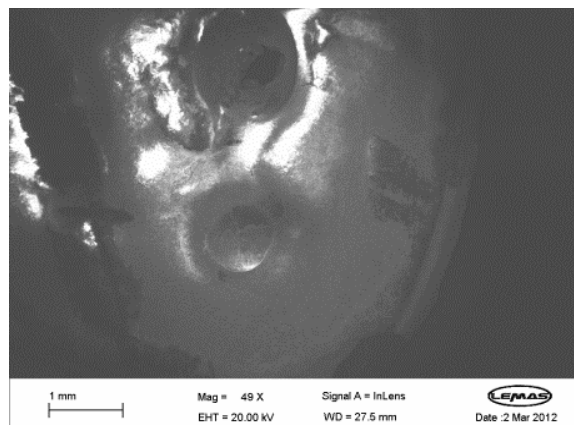


Figure 4.3.18 SEM of doped CaP coated dentine section that was irradiated for 1 and 2 minutes (bottom to top, respectively), using 1520 nm pulsed laser with a beam diameter of 125 μm .

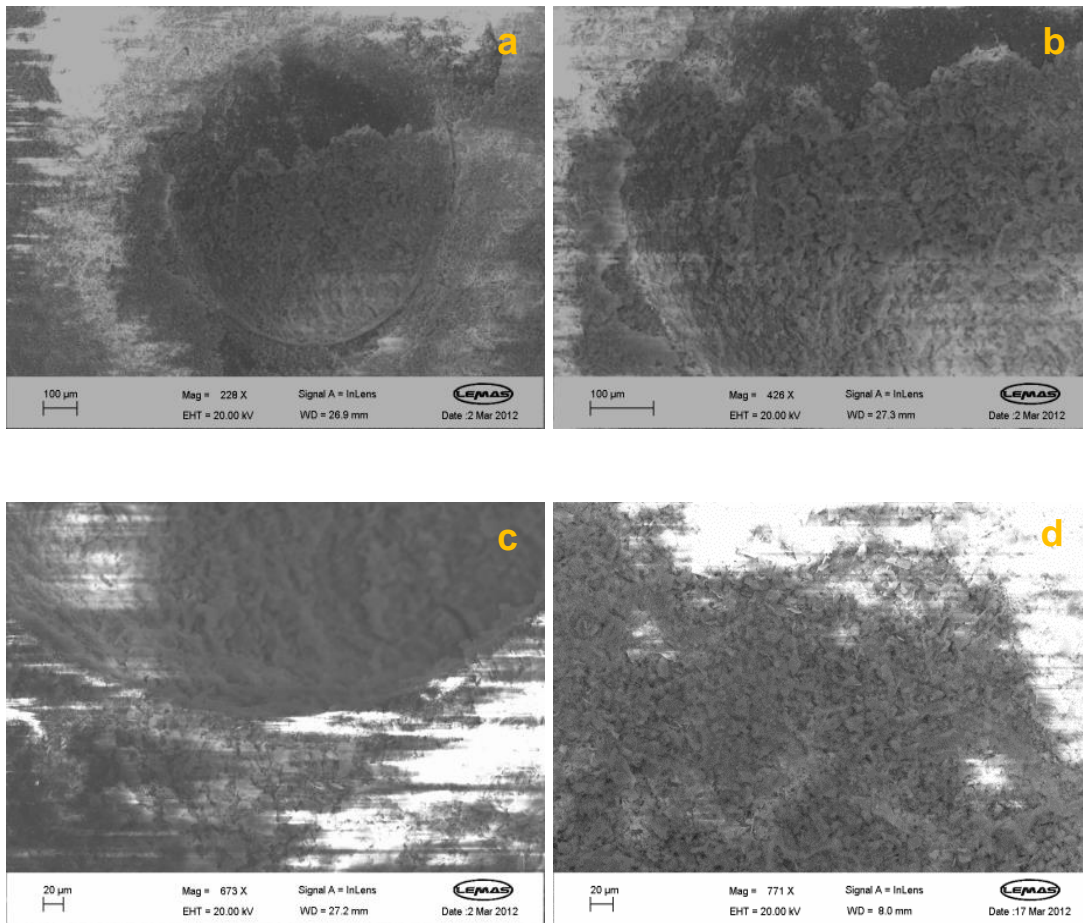


Figure 4.3.19 SEM of doped CaP coated dentine section that was irradiated for 1 minute, using 1520 nm pulsed laser with a beam diameter of 125 μm, showing (a-b) the laser – irradiated area and densification of sintered area, and (c-d) the area surrounding and around the laser irradiation spot.

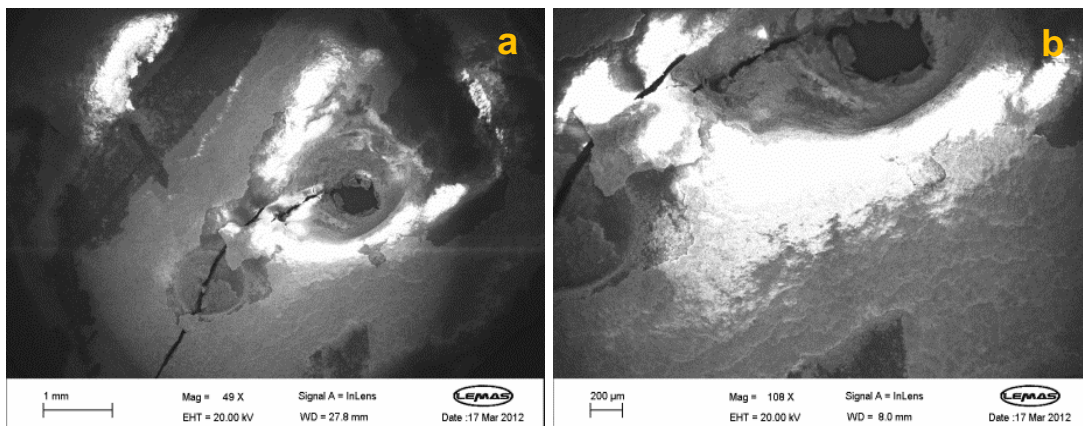


Figure 4.3.20 SEM of doped CaP coated dentine section that was irradiated with 1520 nm pulsed laser with a beam diameter of 125 μm, showing (a-b) the difference between exposure time of 1 and 2 minutes (left to right, respectively).

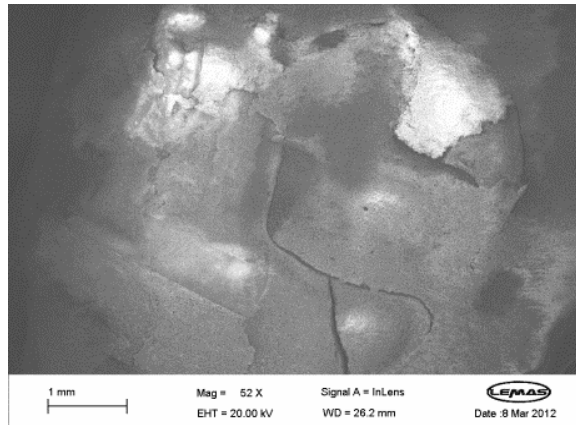


Figure 4.3.21 SEM of doped CaP coated dentine section that was irradiated for 1 and 2 minutes, using 1520 nm CW laser with a beam diameter of 250 μ m.

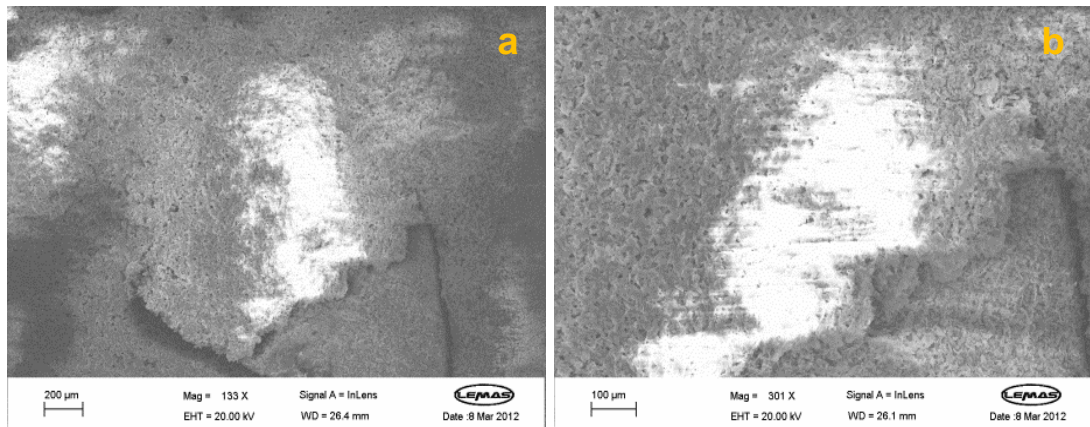


Figure 4.3.22 SEM of doped CaP coated dentine section that was irradiated for 1 minute, using 1520 nm CW laser with a beam diameter of 250 μ m, showing (a) laser-irradiated area, and (b) the densification of CaP coating with no open dentinal tubules.

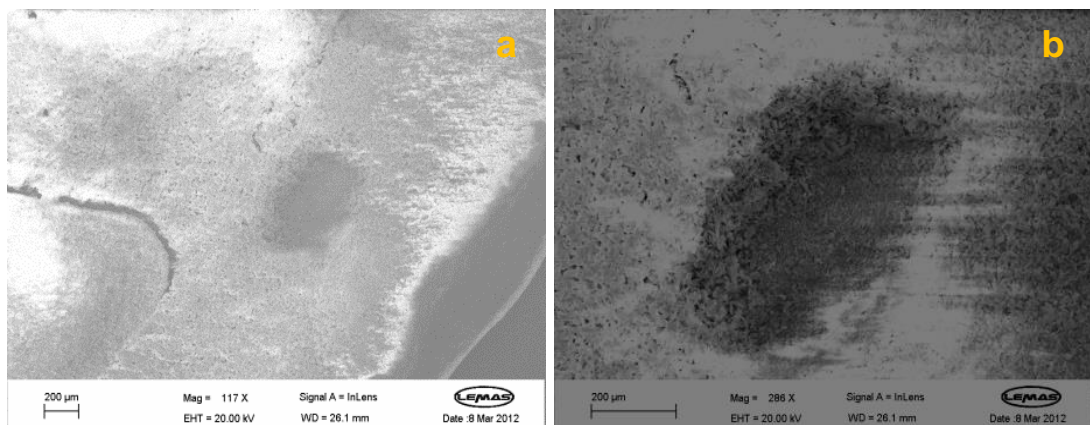


Figure 4.3.23 SEM of doped CaP coated dentine section that was irradiated for 2 minutes, using 1520 nm CW laser with a beam diameter of 250 μ m, showing (a) the laser-irradiated area, and (b) a deep crater and the densification of CaP coating around it with no open dentinal tubules.

Under 1520 nm CW laser irradiation with a beam diameter of 125 μm for exposure time of 1 and 2 minutes, clear morphological signs of laser craters were observed, as shown in Figure 4.3.24 (a and b). The highly charged areas are in good agreement with the area around the laser irradiation spots. Although the craters appeared deep, the particles around the laser irradiation spots were densified and packed together with no sign of open dentinal tubules, as shown in Figure 4.3.24 (c and d).

Under 1520 nm pulsed laser irradiation with a beam diameter of 250 μm for an exposure time of 2 minutes, morphological signs of a laser crater were observed, as shown in Figure 4.3.25 (a). Although a shallow crater was formed, melted dentine surface surrounding the laser irradiation spot and open dentinal tubules with few CaP particles surrounding the melted dentine surface were observed, as shown in Figure 4.3.25 (b). This indicated the poor interaction of CaP coating with laser irradiation as well as the possible damage to dentine surface under the exposure time of 2 minutes.

Under 1520 nm pulsed laser irradiation with a beam diameter of 250 μm for an exposure time of 1 minute, a laser – irradiated area with a superficial irradiation effect and without the formation of a crater was observed, as shown in Figure 4.3.26 (a). The CaP coating in and around the laser – irradiated area was not affected, with the presence of open dentinal tubules and few CaP particles in and around the laser – irradiated area, as shown in Figure 4.3.26 (b and c).

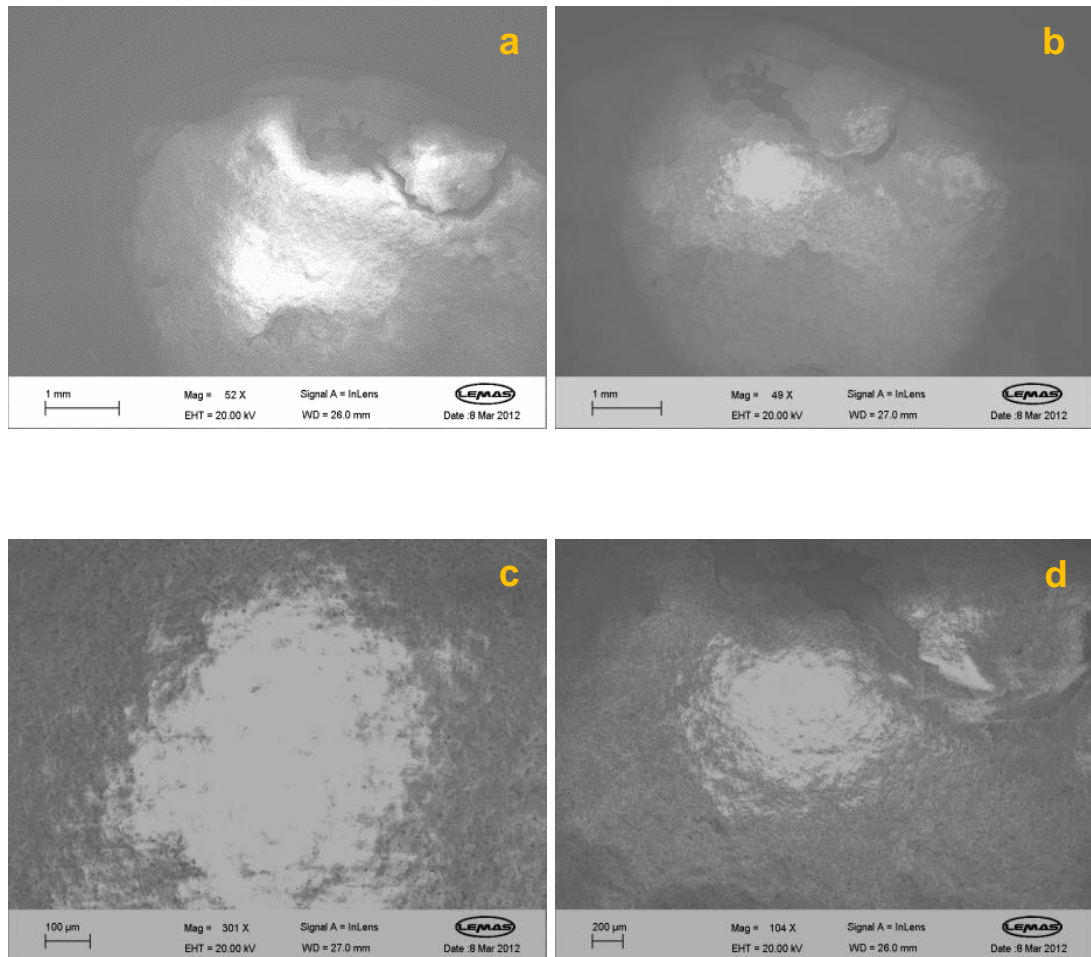


Figure 4.3.24 SEM of doped CaP coated dentine section that was irradiated for 1 and 2 minutes (bottom to top, respectively) using 1520 nm CW laser with a beam diameter of 125 μm , showing (a-b) the laser – irradiated areas, and (c-d) the densified areas around the laser – irradiated areas.

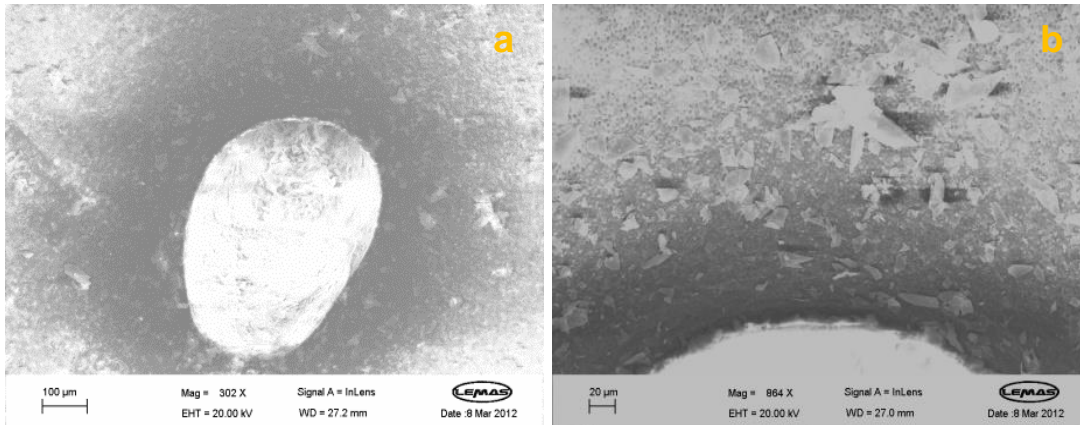


Figure 4.3.25 SEM of CaP coated dentine section that was irradiated for 2 minutes using 1520 nm pulsed laser with a beam diameter of 250 μm, showing (a) the laser irradiation spot, and (b) melted dentine surface surrounding the laser irradiation spot and open dentinal tubules with few CaP particles surrounding melted dentine surface.

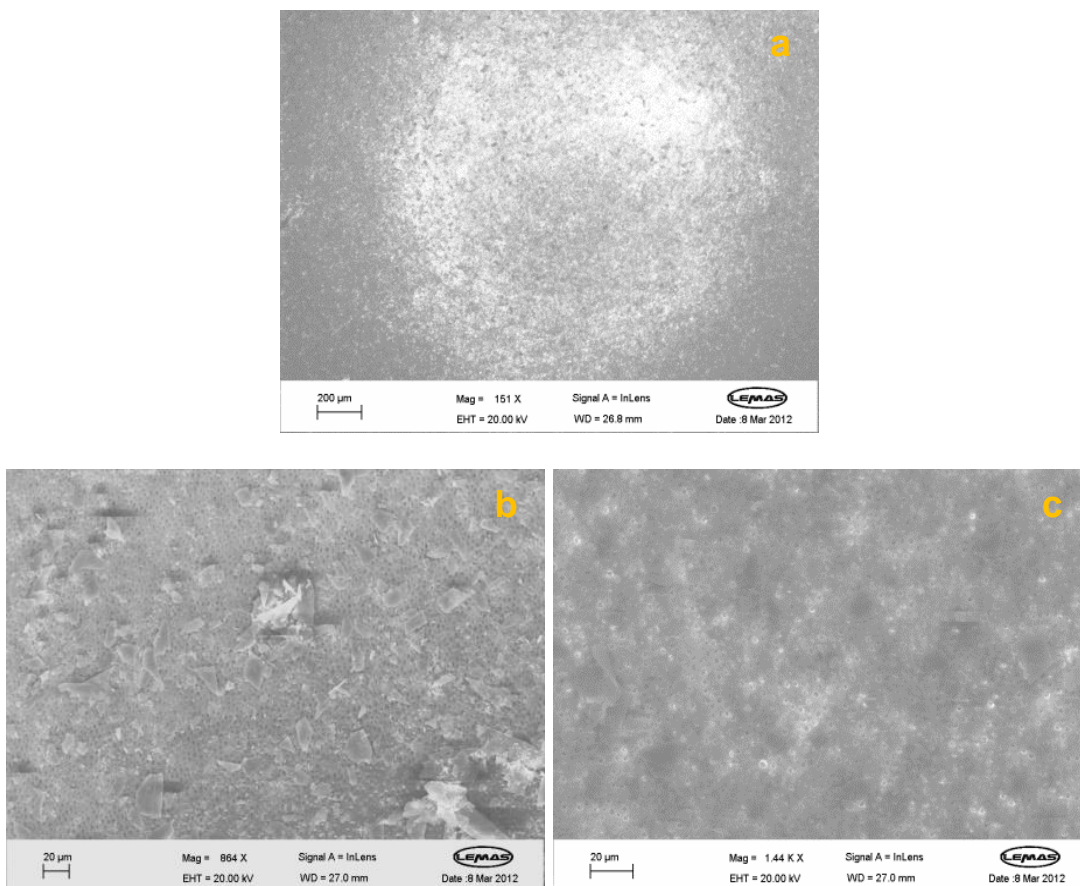


Figure 4.3.26 SEM of CaP coated dentine section that was laser irradiated for 1 minute, using 1520 nm pulsed laser with a beam diameter of 250 μm, showing (a) the laser – irradiated area with a superficial effect, and (b-c) open dentinal tubules with few CaP particles in and around the laser – irradiated area.

CaP – coated dentine section that was irradiated for exposure time of 1 and 2 minutes, using 1520 nm pulsed laser with a beam diameter of 125 μm , are shown in Figure 4.3.27 (a and b). A laser crater was observed with exposure time of 2 minutes, as shown in Figure 4.3.28 (a), while no laser crater was observed with exposure time of 1 minute, as shown in Figure 4.3.29 (a). As with the previous CaP – coated dentine sections, the pulsed laser irradiation formed a crater without affecting CaP coatings, as shown in Figure 4.3.28 (b-d). Melted dentine surface and partially sealed dentinal tubules were observed surrounding the laser – irradiated spot, as shown in Figure 4.3.28 (c), while open dentinal tubules with CaP platelet – like particles were observed around the laser – irradiated spot, as shown in Figure 4.3.28 (d). On the other hand, under exposure time of 1 minute, no laser crater was observed, however, a laser – irradiated area with a melting effect was observed, as shown in Figure 4.3.29 (a), with the presence of partially sealed dentinal tubules within the laser – irradiated area, as shown in Figure 4.3.29 (c and d). Open dentinal tubules with few CaP particles were observed around the laser – irradiated area, as shown in Figure 4.3.29 (b).

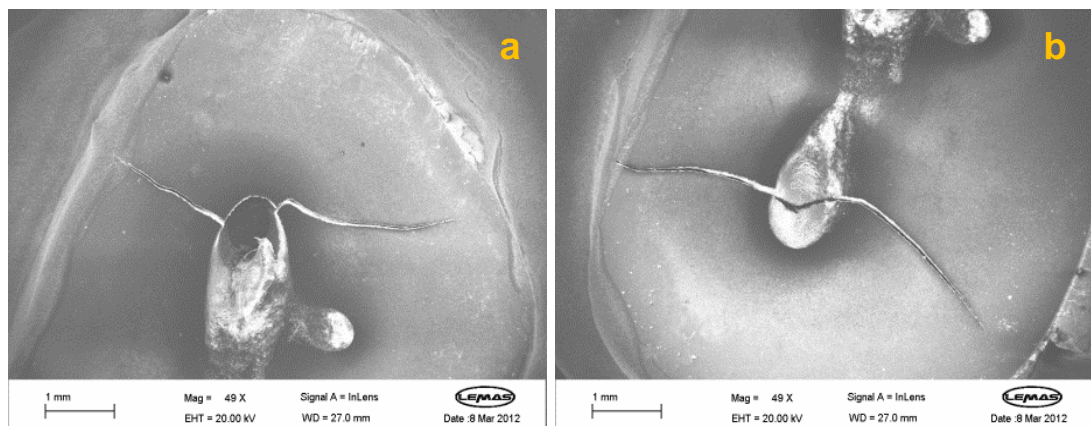


Figure 4.3.27 SEM of CaP coated dentine section that was laser irradiated for (a) 1 minute and (b) 2 minutes, using 1520 nm pulsed laser with a beam diameter of 125 μm .

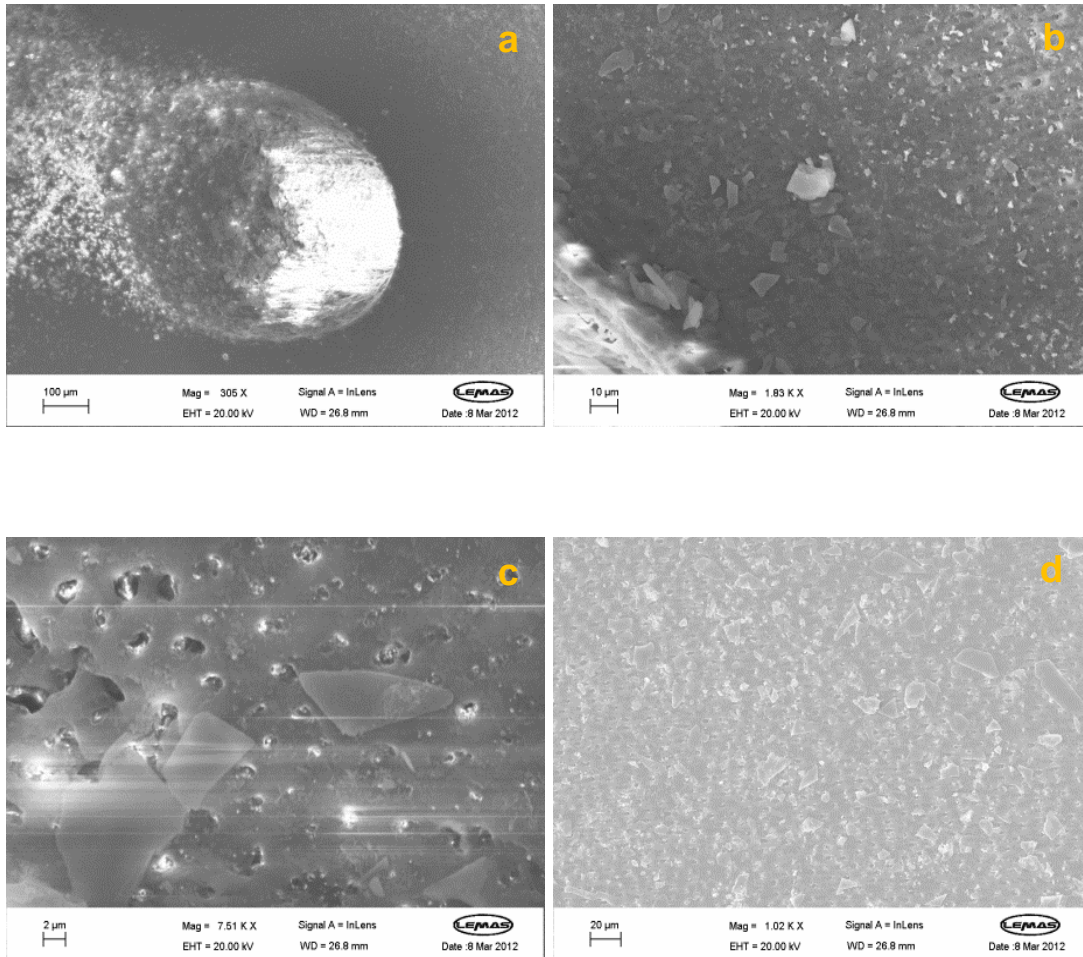


Figure 4.3.28 SEM of CaP coated dentine section that was irradiated for 2 minutes, using 1520 nm pulsed laser with a beam diameter of 125 μm , showing (a) laser irradiation spot, (b) area surrounding the laser irradiation spot, (c) melted dentine surface and partially sealed dentinal tubules surrounding the laser irradiation spot, and (d) open dentinal tubules and CaP particles around the laser – irradiated area.

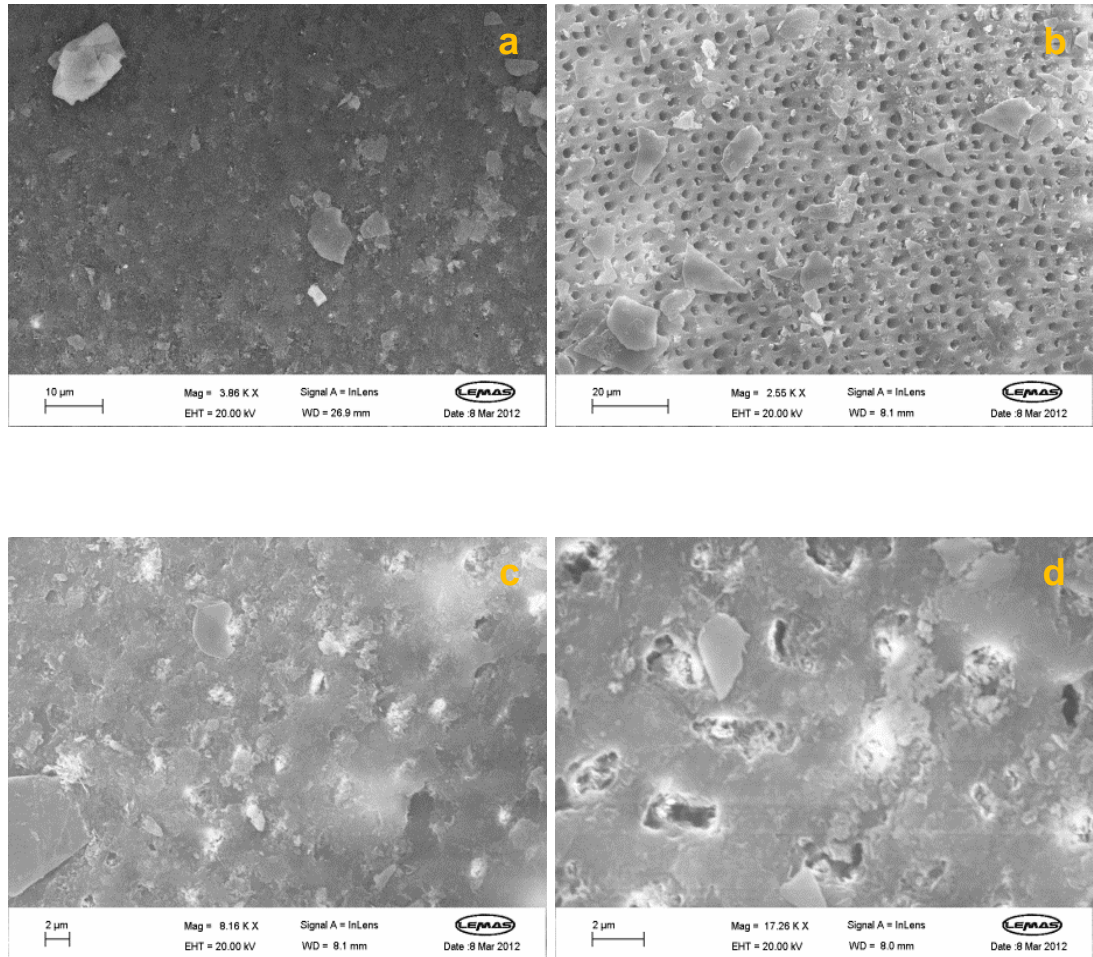


Figure 4.3.29 SEM of CaP coated dentine section that was irradiated for 1 minute, using 1520 nm pulsed laser with a beam diameter of 125 μm , showing (a) the laser – irradiated area with a melting effect, (b) open dentinal tubules with few CaP particles around the laser – irradiated area, and (c-d) melted dentine surface and partially sealed dentinal tubules within the laser – irradiated area.

Under 1520 nm CW laser irradiation with a beam diameter of 125 μm for exposure time of 1 and 2 minutes, laser craters were observed, as shown in Figure 4.3.30 (a and b). However, the craters resulted in a modified and melted dentine surface and partially sealed dentinal tubules, with the presence of few CaP platelet – like particles, as shown in Figure 4.3.30 (c and d). Under 1520 CW laser irradiation with a beam diameter of 250 μm for exposure time of 2 minutes, a laser crater was observed, as shown in Figure 4.3.31 (a and b). However, the CaP coating area around the crater was unaffected, and the laser irradiation resulted in a melted dentine surface surrounding the laser – irradiated spot and open dentinal tubules and CaP platelet – like particles around the laser – irradiated spot, as shown in Figure 4.3.31 (c and d). Under 1520 nm CW laser irradiation with a beam diameter of 250 μm for an exposure time of 1 minute, no signs of laser effects were observed (not included).

Finally, in the case of uncoated dentine sections, under 1520 nm pulsed laser irradiation with a beam diameter of 250 μm , a clear morphological sign of laser crater was observed after an exposure time of 2 minutes, as shown in Figure 4.3.32 (a and b). Although the pulsed laser irradiation modified the structure of dentine surface, as shown in Figure 4.3.33 (a), open dentinal tubules inside and outside the laser irradiation spot were observed, as shown in Figure 4.3.33 (b).

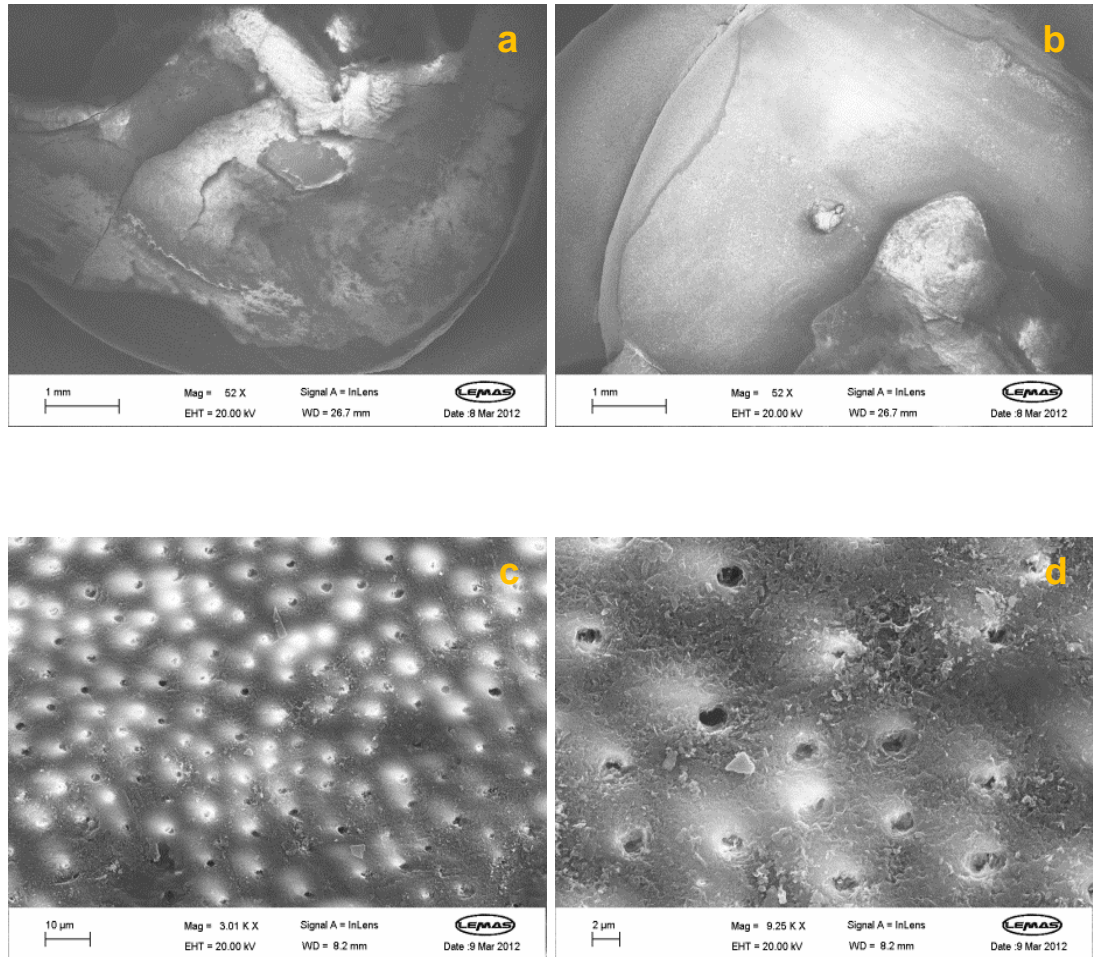


Figure 4.3.30 SEM of CaP coated dentine section that was laser irradiated for (a) 1 and (b) 2 minutes, using 1520 nm CW laser with a beam diameter of 125 μ m, showing (a-b) the laser – irradiated spots, and (c-d) modified dentine surface and partially sealed dentinal tubules.

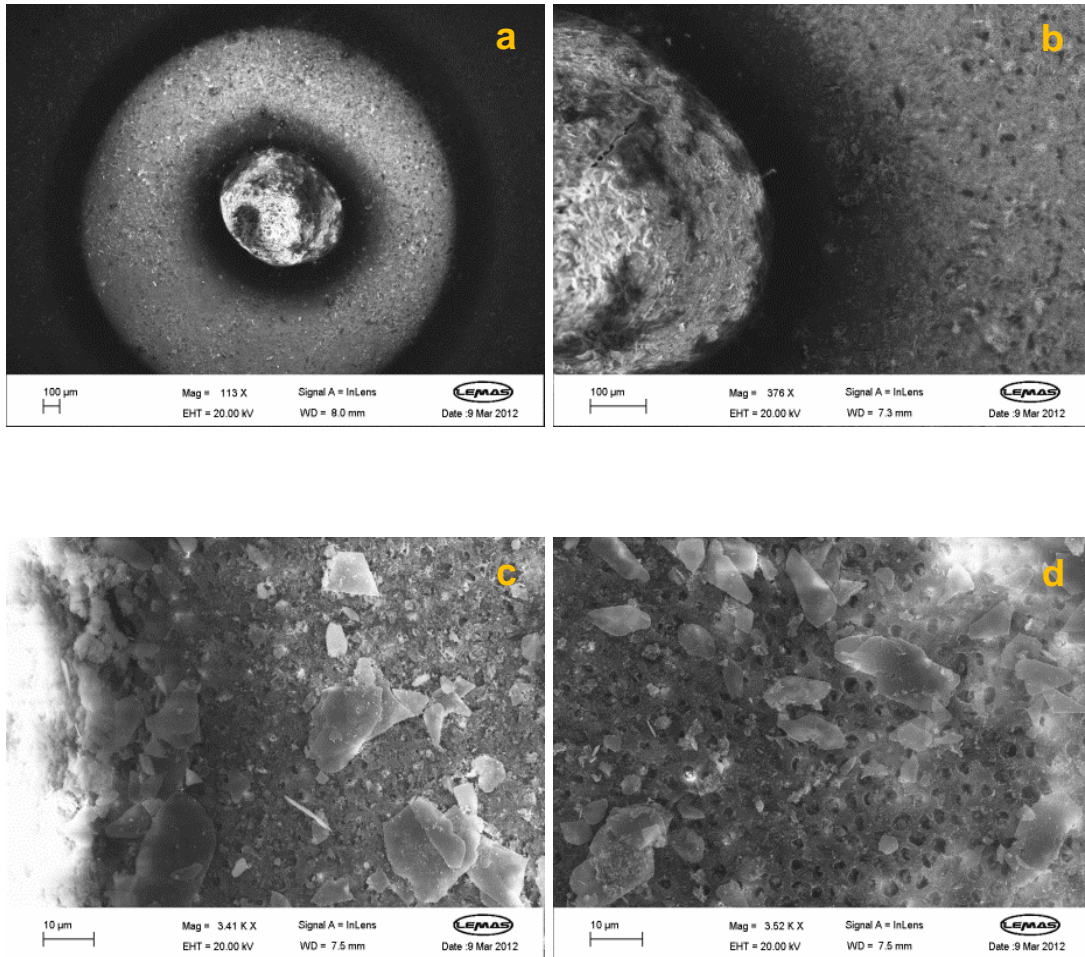


Figure 4.3.31 SEM of CaP coated dentine section that was laser irradiated for 2 minutes, using 1520 nm CW laser with a beam diameter of 250 μm, showing (a-b) the laser – irradiated area, and (b-c) melted dentine surface surrounding the laser – irradiated area and open dentinal tubules and CaP particles around the laser – irradiated area.

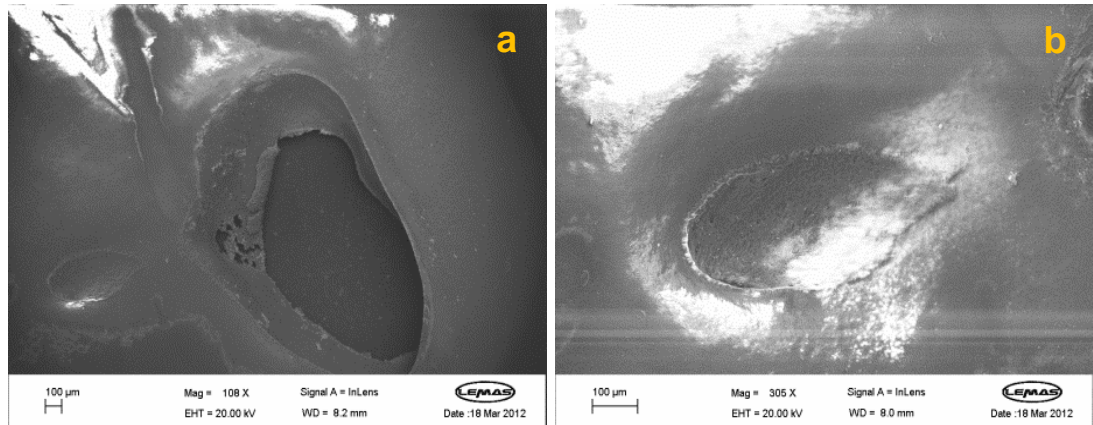


Figure 4.3.32 SEM of uncoated dentine section that was laser irradiated for 2 minutes, using 1520 nm pulsed laser with a beam diameter of 250 µm, showing (a) the laser – irradiated area (left hand side of image), and (b) higher magnification of the laser – irradiated area.

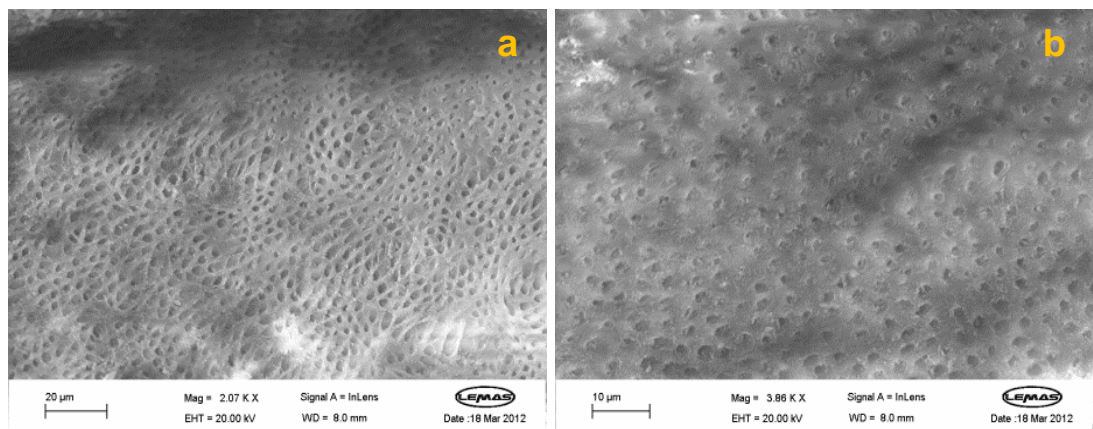


Figure 4.3.33 SEM of uncoated dentine section that was laser irradiated for 2 minutes, using 1520 nm pulsed laser with a beam diameter of 250 µm, showing (a) the laser irradiation spot, and (b) open dentinal tubules around the laser – irradiated area.

Under 1520 nm pulsed laser irradiation with a beam diameter of 125 μm for exposure time of 1 and 2 minutes, no morphological signs of laser craters or minor effects were observed, as shown in Figure 4.3.34. On the other hand, under 1520 nm CW laser irradiation with a beam diameter of 125 μm for exposure time of 1 and 2 minutes, clear morphological signs of laser craters were observed, as shown in Figure 4.3.35 (a). The laser irradiation resulted in a very deep crater, which penetrated the dentine surface, particularly under 2 minute exposure time, as shown in Figure 4.3.35 (b and c). The areas surrounding and around the laser irradiation spot were partially affected, as shown in Figure 4.3.35 (d). Modification of dentine surface and partially sealed dentinal tubules were observed surrounding the laser irradiation spot, as shown in Figure 4.3.35 (e), while open dentinal tubules were observed around the laser irradiation spot, as shown in Figure 4.3.35 (f). Finally, under 1520 CW laser irradiation with a beam diameter of 250 μm for exposure time of 1 and 2 minutes, no morphological signs of laser craters or minor effects were observed, as shown in Figure 4.3.36.

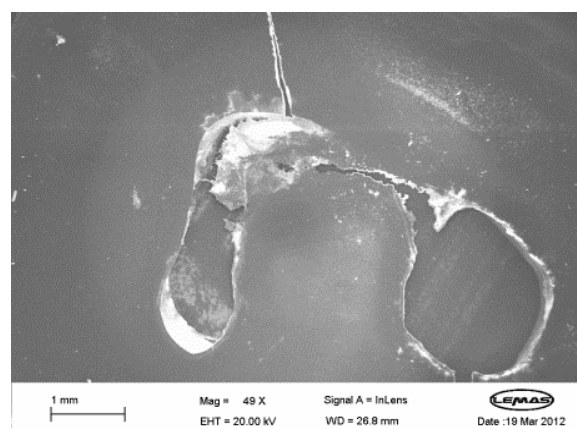


Figure 4.3.34 SEM of uncoated dentine section that was laser irradiated for 1 and 2 minutes, using 1520 nm pulsed laser with a beam diameter of 125 μm , showing no signs of laser irradiation effects.

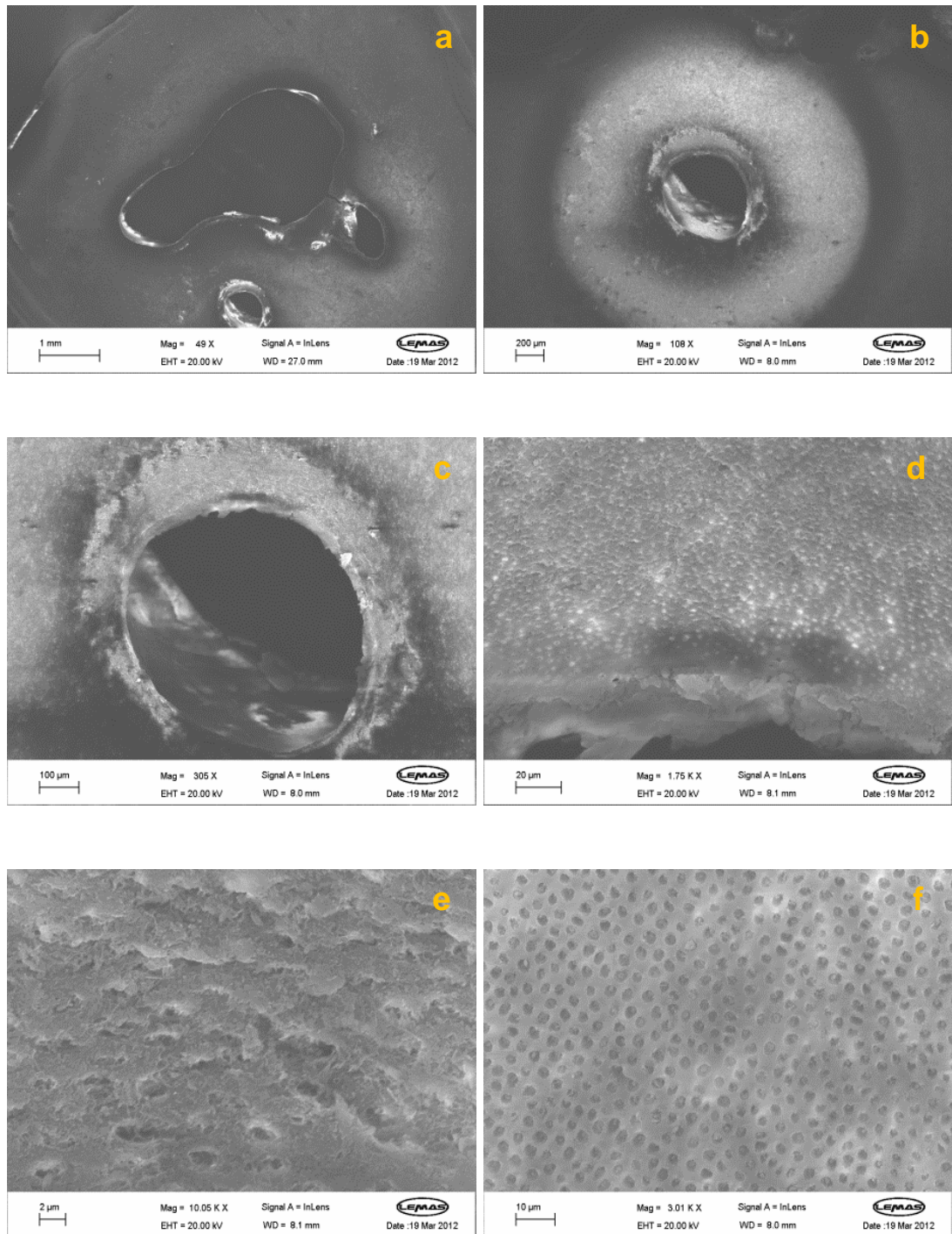


Figure 4.3.35 SEM of uncoated dentine section that was laser irradiated for 1 and 2 minutes, using 1520 nm CW laser with a beam diameter of 125 μ m, showing (a) the laser irradiation spot, (b-c) higher magnification of laser irradiation spot with a very deep crater penetrating dentine surface, (d) area surrounding and around the laser irradiation spot, (e) area surrounding the laser irradiation spot with a modified dentine surface and partially sealed dentinal tubules, and (f) area around the laser irradiation spot with open dentinal tubules.

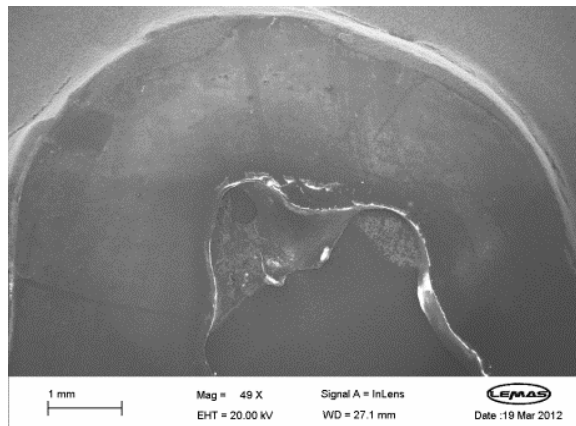


Figure 4.3.36 SEM of uncoated dentine section that was laser irradiated for 1 and 2 minutes, using 1520 nm CW laser with a beam diameter of 250 μm , showing no signs of any laser effects.

The laser irradiation sintering trials can be summarised as follows. The 980 nm CW laser irradiation for 5 minutes resulted in poor absorption and non – uniform densification of CaP and doped CaP coatings, which was due to the poor distribution of energy and weak absorption at 980 nm wavelength. The 980 nm CW laser irradiation introduced heat accumulation, which caused distortion to CaP coating and melting of dentine surface.

The 1520 nm pulsed laser irradiation for 5 minutes resulted in the formation of a deep crater in the doped CaP coating without a wave – like effect, which indicated the possible penetration of dentine surface. The 1520 nm pulsed laser irradiation for 2 minutes resulted in a less uniform densification of doped CaP coating than that for 1 minute exposure time, and it caused a minor distortion to CaP coating in the form of a crack – like, which was probably due to the long exposure time. In the case of CaP coatings, the 1520 nm pulsed laser irradiation with both beam diameters (125 μm and 250 μm) for 1 and 2 minute – exposure time resulted in poor absorption and

densification of CaP coating, melted dentine surface surrounding the laser irradiation spot, and open dentinal tubules with few CaP particles surrounding the melted dentine surface. The 1520 nm CW laser irradiation with beam diameters of 125 μm and 250 μm for 1 and 2 minute – exposure times resulted in a modified and melted dentine surface and partially sealed dentinal tubules with the presence of few CaP platelet – like particles.

The 1520 nm pulsed laser irradiation of doped CaP coating with exposure time of 30 seconds was concluded the most effective laser treatment, due to the formation of a shallow and spread crater, without causing any damage to the CaP coating. The laser irradiation resulted in a uniform and excellent densification of CaP coating without any distortion, which in turn resulted in a complete occlusion of dentinal tubules in and around the laser irradiation spot.

In addition, in terms of the laser beam diameter, the beam diameter of 250 μm was more effective than 125 μm , because the latter exhibited higher power density and resulted in deep craters, with the possible penetration of dentine surface in most coatings. By contrast, the beam diameter of 250 μm resulted in a deep crater under 2 minute – exposure time only. Therefore, the 1520 nm pulsed laser irradiation of doped CaP coating with a beam diameter of 250 μm and an exposure time of 1 minute was also concluded the most effective treatment.

4.3.3.2.4 Characterisation of laser – irradiated CaP coatings

Following the microstructural investigations, more analysis was carried out on the coated and occluded regions of dentinal tubules to determine the effectiveness of the pulsed laser irradiation sintering. The microstructure of interface between the dentine surface and laser – irradiated CaP and doped CaP coatings are shown in Figure 4.3.37 and Figure 4.3.38, respectively.

The 1520 nm pulsed laser irradiation of CaP – coated dentine section resulted in open dentinal tubules and crack – like morphology in the dentine tissue, as shown by the cross – sectional SEM micrograph in Figure 4.3.37. On the other hand, the 1520 nm pulsed laser irradiation of doped CaP – coated dentine section resulted in a sintered coating and the occlusion of dentinal tubules, as shown by the cross – sectional SEM micrograph in Figure 4.3.38.

It appeared that the densification of CaP and doped CaP coatings, using 1520 nm pulsed laser, did not follow a melting and solidification process. In the case of doped CaP coating, there was a clear evidence of the formation of a two – layer structure, one of which was the occluded region with 10 μm across and above the dentinal tubules, as shown in Figure 4.3.38. The layer appeared to be much denser and continuous without any defects in the doped CaP coating (Figure 4.3.38) than that in the CaP coating (Figure 4.3.37). The second layer was a partially dense over layer, which appeared to extend across the micrograph with brighter undissolved Er_2O_3 particles (Figure 4.3.38). The over layer appeared less sintered than the underlying layer, however, the occlusion of dentinal tubules appeared quite uniform in the doped CaP coating than in the CaP coating.

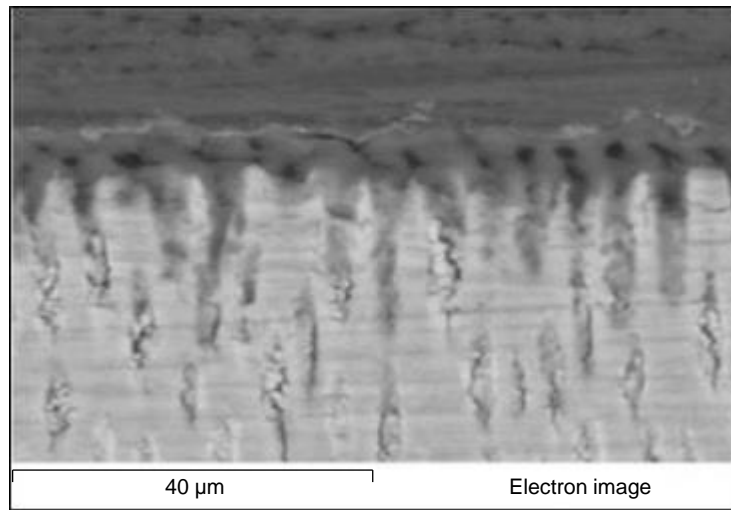


Figure 4.3.37 Cross – sectional SEM micrograph of 1520 nm pulsed laser – irradiated dentine section with a coating of CaP, showing open dentinal tubules as well as the presence of crack – like morphology in the dentine tissue.

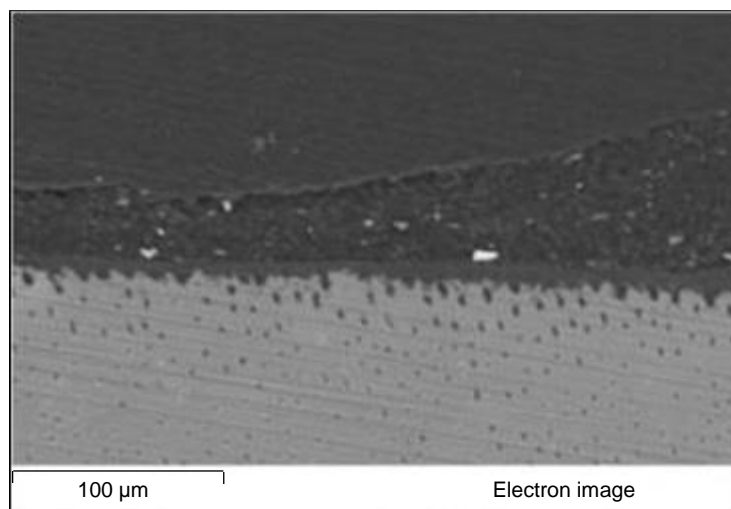


Figure 4.3.38 Cross – sectional SEM micrograph of 1520 nm pulsed laser – irradiated dentine section with a coating of doped CaP, showing the laser – irradiated coating with no open dentinal tubules.

4.3.3.3 Temperature change during laser irradiation sintering

Although pulsed lasers provide more energy than CW lasers, the latter were used to irradiate uncoated and CaP (CaP and $\text{Er}_2\text{O}_3\cdot\text{AlPO}_4\cdot\text{CaF}_2$ – doped CaP batch A) – coated dentine sections to measure the temperature change as the laser irradiation being applied. Since the residual absorption at 1520 nm wavelength is much less than that at 980 nm wavelength, the temperature change was recorded using 980 nm CW laser only. The change in temperature for an exposure time of 5 minutes was recorded by a temperature reader in the presence of a thermocouple in contact with the backside of dentine sections. The temperature change measurements are shown in Table 4.3.1 and Figure 4.3.39.

The temperature change measurements during 980 nm CW laser irradiation indicated that CaP – coated dentine sections absorbed more energy than uncoated dentine section, and that $\text{Er}_2\text{O}_3\cdot\text{AlPO}_4\cdot\text{CaF}_2$ – doped CaP coating absorbed 3 times the energy absorbed by CaP coating, as shown in Figure 4.3.39. This could be beneficial for the densification of CaP coating over dentine surface and the protection of dentine surface from any damage by the laser irradiation.

Table 4.3.1 Temperature change measurements during 980 nm CW laser irradiation

Dentine section	Initial temperature (T1)	Final temperature (T2)	ΔT (T2 – T1) error $\pm 0.5^\circ\text{C}$
Uncoated dentine section	22.8°C	26°C	3.2°C
Undoped CaP – coated dentine section	22.8°C	24.9°C	2.1°C
Doped CaP – coated dentine section	22.8°C	23.2°C	0.4°C

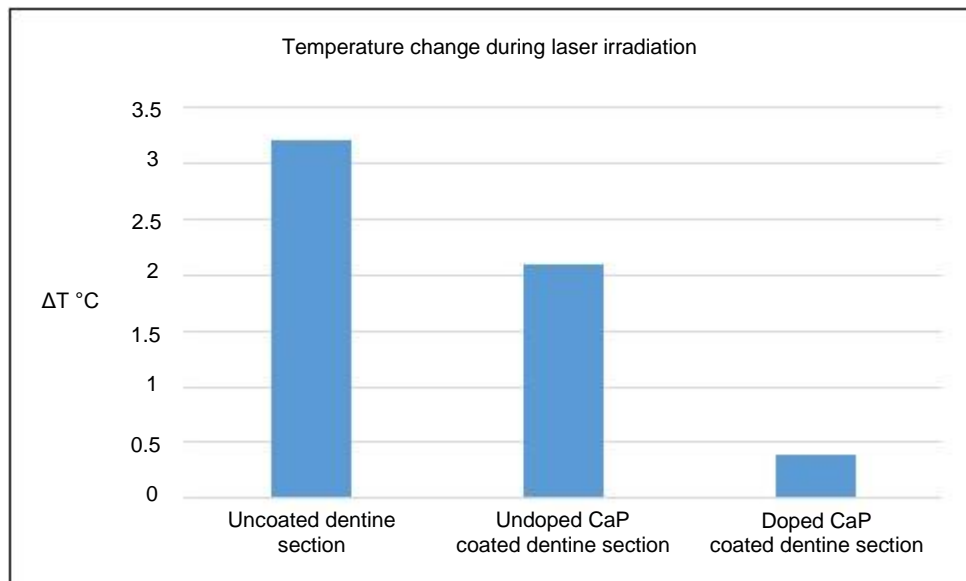


Figure 4.3.39 Temperature change (± 0.5) during 980 nm CW laser irradiation for 5 minutes on uncoated dentine section and CaP – and doped CaP (batch A) – coated dentine sections.

4.3.3.4 Micro – hardness of uncoated/coated dentine sections

Micro – hardness measurements were carried out on laser – irradiated uncoated and CaP (undoped and $\text{Er}_2\text{O}_3 \cdot \text{AlPO}_4 \cdot \text{CaF}_2$ – doped CaP batch A) – coated dentine sections, as shown in Table 4.3.2. All sections were laser irradiated using 980 nm CW laser for an exposure time of 5 minutes. Micro – hardness measurements were performed using a computer –controlled Duramin Indenter Machine (Struers A/S, DK 26- 10, Ballerup, Denmark). The micro – hardness measurements presented in Table 4.3.2 were taken after two indentations per section with a Knoop diamond under a 25g load for 30 seconds, and the indents were measured in microns by an image analysis software. The measurements indicated that the laser – irradiated dentine section coated with doped CaP (batch A) had the highest hardness number of 1104.71 MPa, which was almost twice that of laser – irradiated dentine section coated with CaP (681.56 MPa), and four times that of

uncoated dentine surface (240.75 MPa), as shown in Figure 4.3.40. The micro – hardness results indicated that the laser – irradiated doped CaP coating significantly enhanced the resistance of the dentine section to permanent deformation. The enhanced resistance of doped CaP coating to permanent deformation can be credited to the addition of dopants (Er_2O_3 , AlPO_4 , CaF_2) and the application of laser irradiation.

Table 4.3.2 Micro – hardness measurements of laser – irradiated dentine sections

Dentine section	Indent Size (μm)	KH error ± 0.5	Average	MPa
Uncoated dentine section	126.4	22.3	24.55	240.75
	115.3	26.8		
Undoped CaP coated dentine section	71	70.5	69.5	681.56
	76	68.5		
Doped CaP coated dentine section	56.6	110.9	112.65	1104.71
	55.8	114.4		

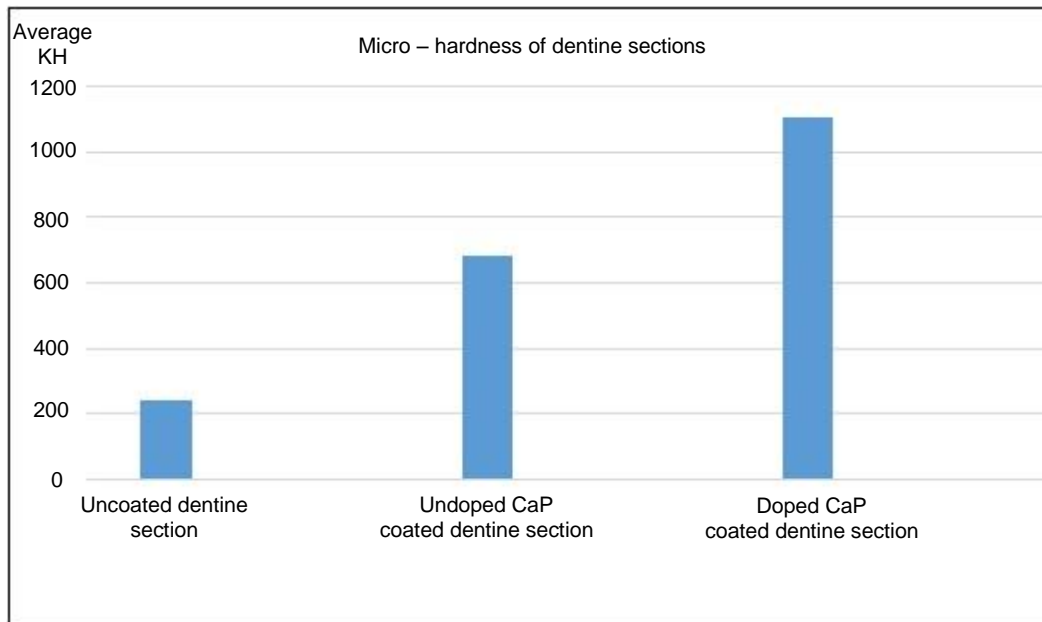
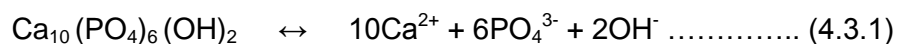


Figure 4.3.40 Micro – hardness indentation measurements (± 0.5) comparing the hardness number of uncoated dentine section and laser – irradiated – coated (CaP and doped CaP) dentine sections.

4.3.3.5 Characterisation of acid eroded CaP pellets

The dissolution of CaP and doped CaP powders in an acidic environment was carried out in citric acid solutions, using pellets only. The dissolution of CaP – and doped CaP – coated dentine sections was not carried due to the quantity limitation of tooth samples from the tissue bank. The teeth samples were used for coating and laser irradiation trials. In addition, the coated and laser – irradiated dentine sections could not be reused, because they were primarily characterised by SEM. The latter also required the application of a Pt/Pd coating, which would have influenced the dissolution behaviour of coatings. Three pellets of CaP and three of doped CaP were investigated, which were unsintered, furnace sintered, and laser sintered. CaP and doped CaP pellets were furnace sintered between 850°C and 1000°C for 5 minutes and laser sintered with 800 nm pulsed laser for 5 minutes. A moving stage was used during the 800 nm pulsed laser sintering to achieve a uniform sintering of the entire surface of CaP and doped CaP pellets.

The dissolution of CaP and doped CaP pellets in citric acid (C₆H₈O₇) solutions was investigated mainly as a function of solution calcium and phosphate concentrations. Many citric drinks and food have a pH value below the critical pH 5.5 (576), at which the hydroxyapatite mineral of enamel dissolves. However, the critical pH varies depending on the concentrations of calcium and phosphate in a solution (577). The dissolution of HAp mineral in water and acidic solutions are described by equation 4.3.1 (577) and equation 4.3.2, respectively (578).



The dissolution of HAp mineral depends primarily on pH and saturation of solutions with respect to the HAp mineral (577). When pH of solution is above the critical pH, the solution is supersaturated with respect to the HAp mineral, the latter which tends to precipitate out. On the other hand, when pH of solution is below the critical pH, the solution is unsaturated with respect to the HAp mineral, the latter which tends to dissolve until the saturation of solution (577).

The solubility of HAp mineral increases with decreasing pH of solution and vice versa. The solubility of HAp in water is due to the removal of OH^- ions by H^+ ions to form H_2O . The removal of OH^- ions increases in acidic solutions due to the increase in H^+ ions (577, 578). Similarly, the concentration of PO_4^{3-} decreases with decreasing pH of solution (577, 578). On the other hand, concentration of Ca^{2+} ions is unaffected (577), but a complexation between Ca^{2+} ions and the buffer anion may occur (578, 579). Citric acid ($\text{C}_6\text{H}_8\text{O}_7$) has a complex interaction with HAp mineral. Citric acid solution exists as H^+ ions, acid anions (citrate), and undetached acid molecules, and their amounts are determined by the acid dissociation constant (pKa) and pH of solution (579). Besides the activity of H^+ ions in removing OH^- and PO_4^{3-} from the crystal surface (577-579), the citrate anion may also remove Ca^{2+} from the crystal surface and/or saliva and form a calcium – citrate complex (579). Mineral loss by acid attack takes place in a repeated cycle of lowering pH at the enamel surface and dissolving calcium and phosphate components, which results in softening of the enamel surface (579). In the absence of a remineralisation component, such as fluoride, the cycle is repeated and the mineral continues to dissolve (579).

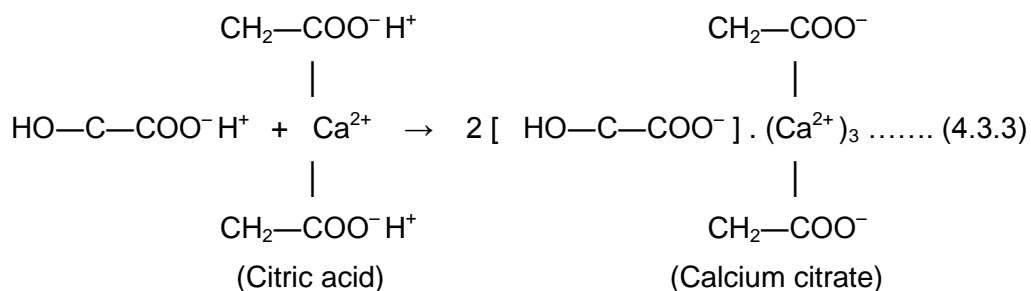
The surface loss of CaP and doped CaP pellets was investigated and characterised based on pH variation during acid – CaP pellets interaction, surface roughness of CaP and doped CaP pellets, and amount of leached out components in the citric acid solution. The pH values were recorded every 30 minutes for 24 hours without agitation (static conditions). The surface roughness was measured using a surface profilometry, while the leached out components/elements were measured using inductively – coupled plasma/Mass spectrometry (ICP/MS) and SEM-EDX spectroscopy.

4.3.3.5.1 pH variation measurements

The pH variation of citric acid solutions that contained the pellets (three pellets of CaP and three of doped CaP, unsintered, furnace sintered, and laser sintered) was monitored and recorded during a 24 hour reaction (static conditions), starting with as – prepared pH 3.60 ± 0.02 . The final pH readings after 24 hours are shown in Table 4.3.3 and Figure 4.3.41. It must be noted that CaP and doped CaP pellets exhibited no phase transformations under laser irradiation, as established by XRD (Figure 4.3.7 and Figure 4.3.8).

The activity or transfer of hydrogen (H^+) ions between chemical species determines pH of a solution, which can be determined by measuring their concentration in the solution. The increased pH readings from pH 3.6 to pH 4 in the case of CaP pellets indicated that the acidity of the citric acid solution was decreased, which was probably due to the activity of H^+ ions and the removal of OH^- to form H_2O , as well as the removal of PO_4^{3-} (577-579). The increased pH values could also be due to the removal of impurities, such as carbonates, which make HAp mineral more soluble in acidic environments (577, 579). In addition, the activity of pH variation was

probably due to the uptake of Ca^{2+} ions from CaP pellets by the carboxyl groups (-COOH) of the citric acid, which resulted in the precipitation of a Ca – complexed carboxylate compound and/or metal complexed carboxylate groups ($\text{metal}^+ \text{ } ^-\text{OOC}-$), such as calcium citrate ($\text{Ca}_3(\text{C}_6\text{H}_8\text{O}_7)_2$) (579), as given by equation 4.3.3.



On the other hand, the pH readings of solutions that contained doped CaP pellets were reduced slightly, which indicated a slight hydrogen activity. The pH values were reduced to pH 3.54 in the case of unsintered and laser – sintered pellets, and pH 3.45 in the case of furnace – sintered pellet. The slight reduction in the pH values indicated a slight increase in H^+ concentration in the solutions, which was probably due to a further dissociation of H^+ from the citric acid. Based on the pH variation readings, it can be concluded that the doped CaP pellets were more stable in the citric acid environment than the CaP pellets.

Table 4.3.3 pH values of 0.3% citric acid solution that contained the CaP and doped CaP pellets (unsintered, furnace sintered, and laser sintered) after 24 hour reaction

Sample	Unsintered	Furnace sintered 850-1000°C for 5 minutes	800 nm pulsed laser sintered for 5 minutes
Undoped CaP			
pH ± 0.02	4.01	4.07	4.12
Doped CaP (batch A)			
pH ± 0.02	3.54	3.45	3.54

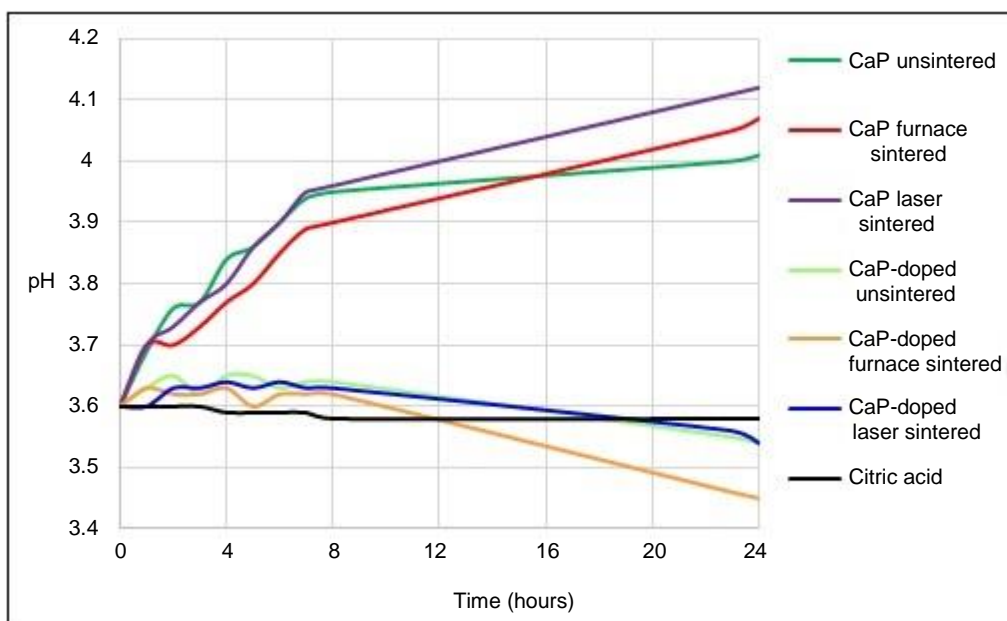


Figure 4.3.41 pH variation during immersion of CaP and doped CaP pellets (unsintered, furnace sintered, and laser sintered) in 0.3% citric acid solution with as – prepared pH 3.60 ± 0.02 for 24 hours.

Furthermore, to investigate the behaviour of CaP and doped CaP pellets in the citric acid solutions after 24 hours, the solutions were analysed for any leached out components, using inductively – coupled plasma/mass spectrometry (ICP/MS) and SEM-EDX (element weight percentage).

4.3.3.5.2 Inductively – coupled plasma/mass spectroscopy

The Amount of components (ppm in 1:5 diluted solutions) that leached out from the pellets (three pellets of CaP and three of doped CaP, which were unsintered, furnace sintered, and laser sintered) to the citric acid solutions after a 24 hour reaction without agitation (static conditions) were analysed by ICP/MS. The measurements of CaP and doped CaP pellets are presented in Tables 4.3.4 and 4.3.5, and Figures 4.3.42 and 4.3.43, respectively. The measurements indicated that a large amount of cations and anions were leached from all CaP pellets, compared to the doped CaP pellets. The

doped CaP pellets, as a group, showed an improved solubility resistance, compared to the CaP pellets, however, the furnace – sintered doped CaP pellet showed the least amount of leached out components, whereas the laser – sintered doped CaP pellet showed an improved solubility resistance, compared to the unsintered doped CaP pellet.

As a function of solution calcium and phosphate concentrations, the doped CaP pellets showed less leached out components, compared to CaP pellets, as shown in Table 4.3.6 and Figures 4.3.44 – 4.3.45. The furnace – sintered pellets, as a group, were found to leach out the least amount of calcium and phosphate in both samples (CaP and doped CaP). On the other hand, the laser – sintered pellets were found to leach out fewer components in the case of doped CaP pellets and slightly more in the case of CaP pellets. In addition, the unsintered doped CaP pellet showed much less leached out components than the unsintered CaP pellet. The results indicated that the doping of CaP improved the solubility resistance of CaP (unsintered pellet group), and that the laser irradiation sintering improved the solubility resistance of doped CaP pellets more than CaP pellets.

Table 4.3.4 Inductively – coupled plasma/mass spectrometry (ICP/MS) of the acid solutions that contained CaP pellets for 24 hours

Sample	Undoped CaP pellets		
Component leached out	Unsintered	Furnace sintered 850-1000°C for 5 minutes	800 nm pulsed laser sintered for 5 minutes
Amount (ppm) in 1:5 diluted 0.3% citric acid – component solutions			
Cations			
Calcium	55.47	45.86	65.61
Sodium	0.33	0.25	0.37
Potassium	100.01	103.85	101.17
Magnesium	0.41	-	0.3
Anions			
Phosphate	311.21	114.65	314.53
Chloride	2.74	2.03	1.92

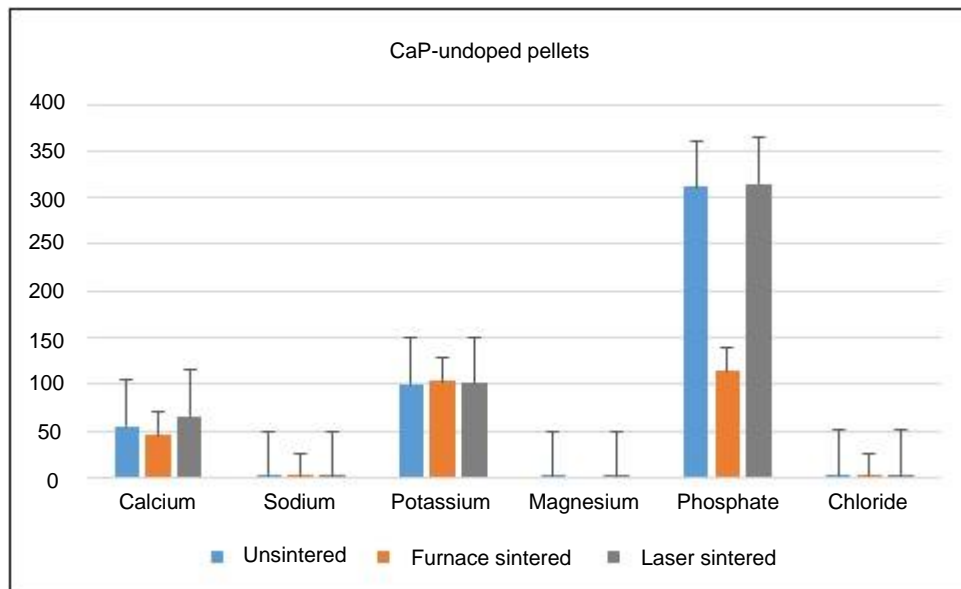


Figure 4.3.42 Leached out component comparison between the acid solutions that contained unsintered, furnace sintered, and laser sintered CaP pellets with standard error bars.

Table 4.3.5 Inductively – coupled plasma/mass spectrometry (ICP/MS) of the acid solutions that contained doped CaP pellets for 24 hours

Sample	Er ₂ O ₃ -AlPO ₄ -CaF ₂ – CaP pellets		
Component leached out	Unsintered	Furnace sintered 850-1000°C for 5 minutes	800 nm pulsed laser sintered for 5 minutes
	Amount (ppm) in 1:5 diluted 0.3% citric acid – component solution		
Cations			
Calcium	22.63	4.77	21.44
Sodium	0.39	0.37	0.37
Potassium	95.48	98.27	96.64
Ammonium	6.15	-	4.08
Anions			
Phosphate	201.76	66.83	191.52
Fluoride	2.2	1.5	1.95
Chloride	2.04	2.06	1.75

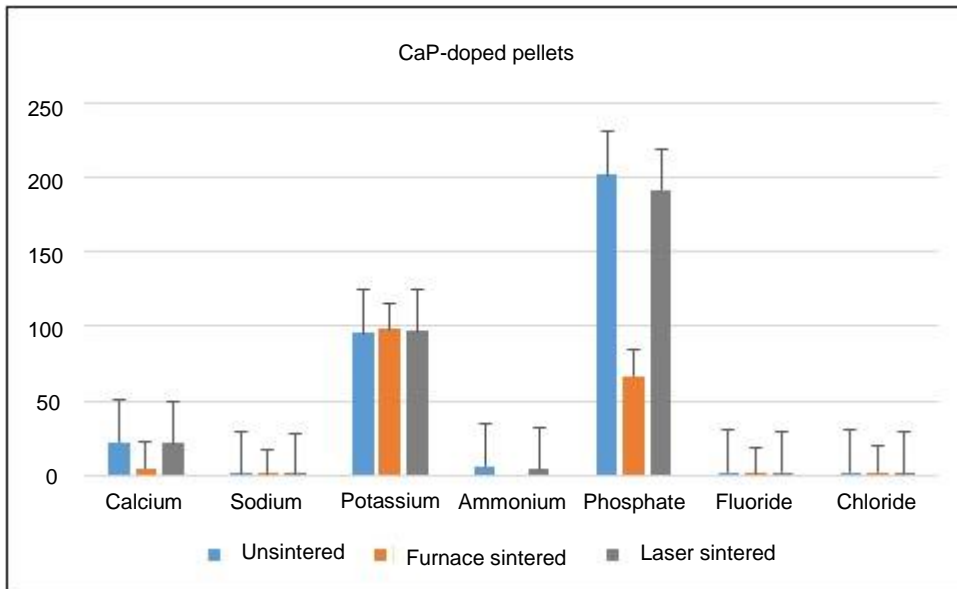


Figure 4.3.43 Leached out component comparison between the acid solutions that contained unsintered, furnace sintered, and laser sintered doped CaP pellets with standard error bars.

Table 4.3.6 ICP/MS comparison between the acid solutions that contained CaP pellets and those contained doped CaP pellets, as a function of solution calcium and phosphate concentrations

Component leached out	Unsintered	Furnace sintered 850-1000°C for 5 minutes	800 nm pulsed laser sintered for 5 minutes
Undoped CaP pellets			
Calcium	55.47	45.86	65.61
Phosphate	311.21	114.65	314.53
Er₂O₃.AlPO₄.CaF₂ – CaP pellets			
Calcium	22.63	4.77	21.44
Phosphate	201.76	66.83	191.52

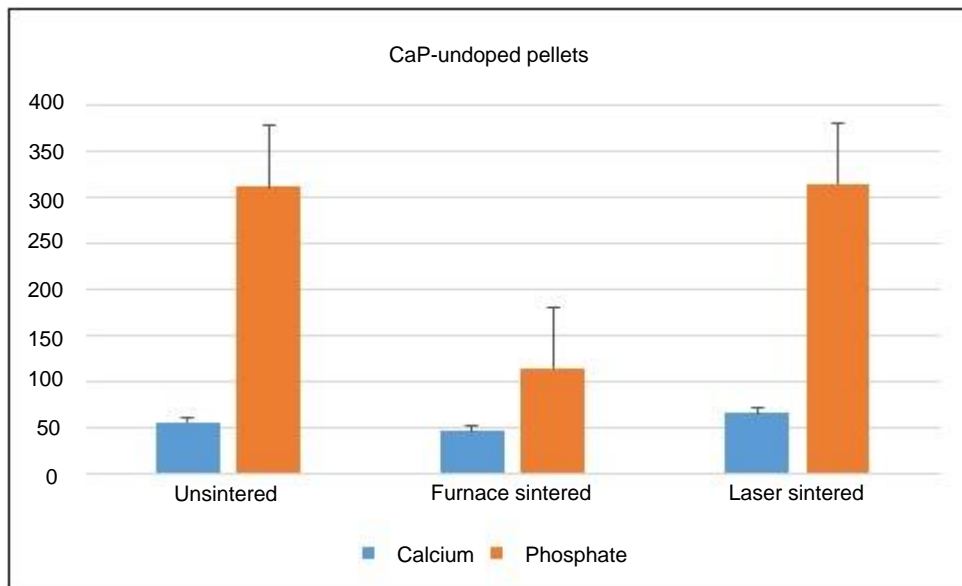


Figure 4.3.44 Leached out calcium and phosphate comparison between of the acid solutions that contained unsintered, furnace sintered, and laser sintered CaP pellets with standard error bars.

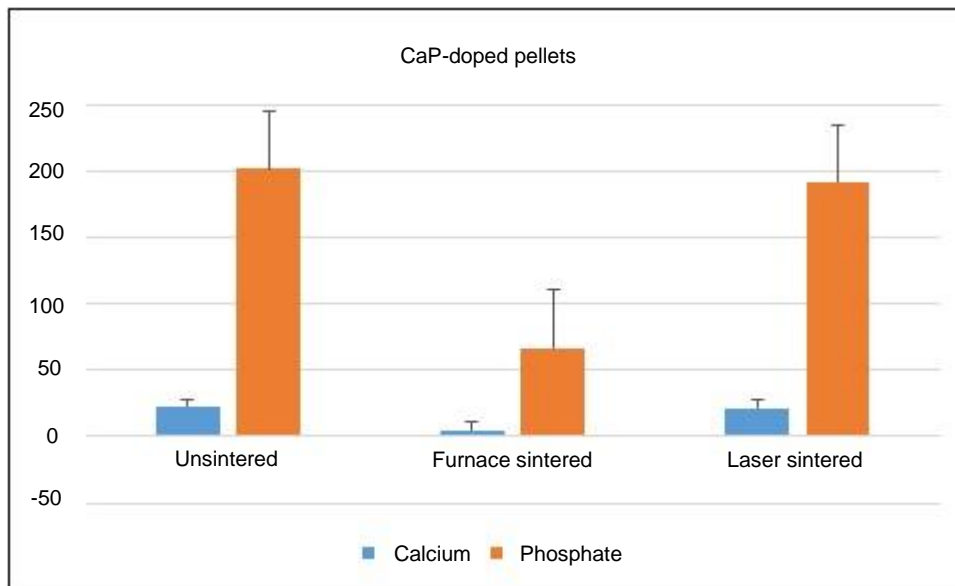


Figure 4.3.45 Leached out calcium and phosphate comparison between of the acid solutions that contained unsintered, furnace sintered, and laser sintered doped CaP pellets with standard error bars.

Inductively – coupled plasma/mass spectrometry (ICP/MS) of the acid solutions that contained CaP pellets and those contained doped CaP pellets revealed the leaching out of components, mainly calcium (Ca^{2+}), phosphate (PO_4^{3-}), sodium (Na^+), potassium (K^+), and chloride (Cl^-), as well as fluoride (F^-) from the doped CaP pellets, but it did not reveal the leaching out of erbium (Er^{3+}) and aluminium (Al^{3+}) cations from the doped CaP pellets. Therefore, due to the limitation of ICP/MS in detecting the leached out Er^{3+} and Al^{3+} cations in the case of doped CaP pellets, samples of the acid solutions that contained doped CaP pellets were further analysed by energy dispersive X – ray spectroscopy (SEM-EDX).

4.3.3.5.3 SEM-EDX measurements

SEM-EDX measurements (element weight percentage) of the acid solutions that contained the doped CaP pellets (unsintered, furnace sintered, and laser sintered) are shown in Table 4.3.7 and compared in Figure 4.3.46. Although the SEM-EDX measurements indicated that the furnace – sintered – doped CaP pellet leached out the least amount of elements, compared to the unsintered doped CaP pellet and laser – sintered – doped CaP pellet, the latter showed less amount of leached out elements than unsintered doped CaP pellet. This indicated that laser – sintered – doped CaP pellet showed an improved solubility resistance in the citric acid environment, compared to unsintered doped CaP pellet. These findings are in good agreement with the results obtained by pH variation and ICP/MS measurements. Although the furnace – sintered pellets were the most stable in the citric acid environment, it can be concluded that the dissolution of CaP (pellets) was significantly reduced in the case of doped CaP pellets (unsintered and laser sintered), due to the presence of dopants and the application of laser irradiation.

Table 4.3.7 SEM-EDX measurements (element weight percentage) of the citric acid solutions that contained doped CaP pellets after a 24 – hour reaction

Element	citric acid-doped CaP unsintered pellet solution	citric acid-doped CaP furnace sintered pellet solution	citric acid-doped CaP laser sintered pellet solution
	Weight %		
O	59.18	1.13	29.78
F	11.49	0.06	4.17
Al	1.92	1.46	0.35
P	4.06	0	1.14
K	5.73	0	1.03
Ca	6.45	0	3.24
Er	11.17	0.01	3.82

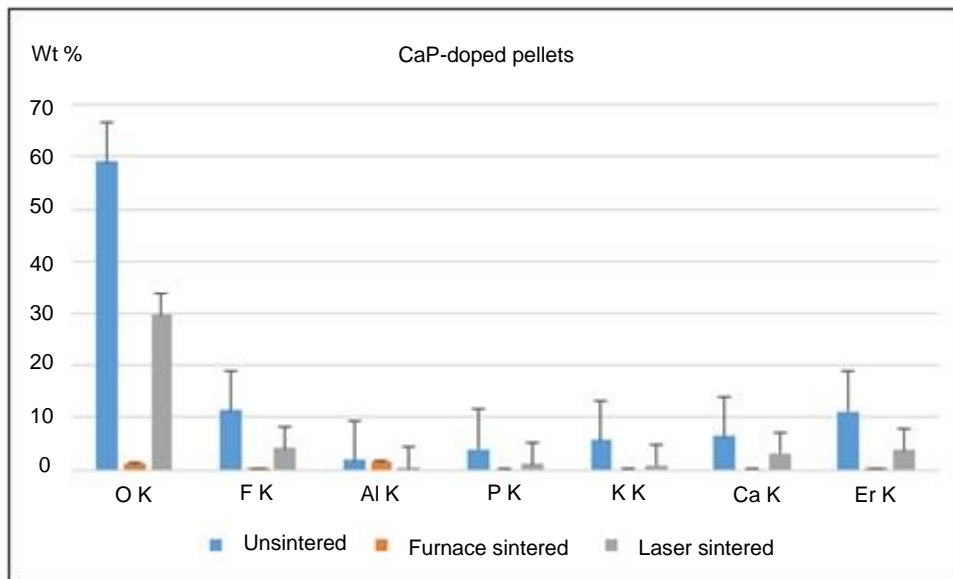


Figure 4.3.46 Leached out element (SEM-EDX element weight percentage) comparison between the citric acid solutions that contained unsintered, furnace sintered, and laser sintered doped CaP pellets with standard error bars.

4.3.3.5.4 Profile roughness measurements

Roughness, also known as surface roughness, is a measure of the texture of a surface, which is determined by vertical variations of a real surface from its ideal form. Large variations indicate that a surface is rough, whereas small variations indicate that a surface is less rough or smooth. A surface with a large roughness average (R_a) value has a high friction coefficient, and thus, wears quickly and vice versa. Roughness as in surface irregularities may act as nucleation sites for cracks or corrosion, and therefore, the surface wears quickly; however, a rough surface may also promote adhesion, providing mechanical interlocking when interacting with its environment (580).

Profile roughness parameters, root mean square roughness (R_q) and roughness average (R_a), of CaP and doped CaP pellets (unsintered, furnace sintered, and laser sintered), before and after the acid erosion trials, were measured using simple two dimension profilometry (LOT – ORIEL Alpha

Step IQ Surface Profiler). Roughness parameters (R_q) and (R_a) before and after immersion of CaP and doped CaP pellets in the citric acid solution are presented in Table 4.3.8.

Table 4.3.8 Profile roughness parameters (R_q and R_a) for CaP and doped CaP pellets (unsintered, furnace sintered. and laser sintered) before and after citric acid erosion

Sample	Roughness	Undoped CaP pellet		Doped CaP pellet	
		Before erosion (nm)	After erosion (nm)	Before erosion (nm)	After erosion (nm)
Unsintered	R_q	1040	1412	1744	1174
	R_a	831	1075	1309	913
Furnace sintered	R_q	1511	216	1349	279.9
	R_a	1127	172	1035	224
Laser sintered	R_q	1435	440	1026	429
	R_a	1099	361	848	336

R_q is the root mean square roughness and R_a is the roughness average.

Roughness average (R_a) values indicated that the roughness of unsintered CaP pellet increased after acid erosion and decreased in the case of furnace – and laser – sintered CaP pellets. On the other hand, the roughness of all doped CaP pellets (unsintered, furnace sintered, and laser sintered) decreased after citric acid erosion.

Before citric acid erosion, the unsintered CaP pellet had a smaller R_a value than that of unsintered – doped CaP pellet. However, in the case of the furnace – sintered and laser – sintered pellets, the doped CaP pellets showed less R_a values than the CaP pellets. This indicated that the sintering was more effective with doped CaP pellets than CaP pellets.

After citric acid erosion, the unsintered CaP pellet had a larger R_a value than that of unsintered – doped CaP pellet, and similarly, in the case of laser sintered pellets. However, this unexpectedly was not the case with the furnace – sintered pellets, as the furnace – sintered CaP pellets had a smaller R_a value than that of doped CaP pellets. Although the highest R_a value was assigned to the unsintered – doped CaP pellet, the doped CaP pellet showed smaller R_a values than the CaP pellet under laser irradiation sintering, which is in good agreement with the effective use of laser irradiation in the presence of dopants. The difference between R_a and R_q values is an indication of the uniformity of a surface, since the R_q is more weighted by large values of peak height and valley depth (581). All R_q values were higher than the R_a values, which indicated that the surface was not entirely uniform. However, the most uniform surface before acid erosion was that of laser – irradiated doped CaP pellet. After acid erosion, the surfaces were more uniform in the case of furnace and laser sintered pellets, as a group.

Table 4.3.9 Surface uniformity of CaP and doped CaP pellets (unsintered, furnace sintered and laser sintered) before and after citric acid erosion

Sample	Surface uniformity	Undoped CaP pellet		Doped CaP pellet	
		Before erosion	After erosion	Before erosion	After erosion
Unsintered	$R_q - R_a$	209	337	435	261
Furnace sintered	$R_q - R_a$	384	44	314	55.9
Laser irradiated	$R_q - R_a$	336	79	178	93

4.3.4 Comparison between none and laser – irradiated coatings

The non – laser – irradiated coatings (Figure 4.3.2 and Figure 4.3.3) indicated that the doped CaP particles exhibited better and more uniform occlusion of dentinal tubules than the CaP particles. However, both coatings were quite ineffective in occluding the dentinal tubules completely, because the particles were not packed together. Although the coatings were improved using the dipping machine and the application of additional drops of CaP suspensions, the lack of particles' packing still revealed open dentinal tubules away from laser – irradiated area (Figure 4.3.13 a).

In contrast, the laser – irradiated coatings showed improved packing and densification of particles and the occlusion of dentinal tubules, particularly with the doped CaP coatings under 1520 nm pulsed laser irradiation. The CaP and doped CaP coatings that were irradiated with 980 nm CW laser were densified non – uniformly and resulted in open dentinal tubules (Figure 4.3.11 and Figure 4.3.10, respectively), with the melting of dentine surface in the case of CaP coating (Figure 4.3.11 d). Similarly, the CaP coatings that were irradiated with 1520 nm CW and pulsed lasers (Figures 4.3.25 – 4.3.31) were poorly densified, without the occlusion of dentinal tubules in and around the laser – irradiated areas. On the other hand, the doped CaP coating that was irradiated with 1520 nm pulsed laser for 30 seconds (Figure 4.3.13 b) was well densified, with a complete occlusion of dentinal tubules in and around the laser – irradiated area. Similarly, the doped CaP coating that was irradiated with 1520 nm pulsed laser with a beam diameter of 250 μm for 1 minute (Figure 4.3.17) was well densified, with a complete occlusion of dentinal tubules in and around the laser – irradiated area.

4.3.5 Main findings

The CW and pulsed laser irradiation sintering at wavelengths of 980 nm and 1520 nm, respectively, for an exposure time of 5 minutes were concluded ineffective. The CaP and doped CaP coatings under 980 nm CW laser irradiation showed poor absorption and non – uniform densification. The 980 nm CW laser irradiation introduced heat accumulation, which caused distortion to the CaP coating and melting of dentine surface. Similarly, the 1520 nm pulsed laser irradiation sintering for 5 minutes was concluded ineffective, because it resulted in the formation of a deep crater in the doped CaP coating, with the possible damage of underlying dentine tissue.

On the other hand, the 1520 nm pulsed laser irradiation for 30 seconds and 2 minutes exhibited much better interaction with the doped Cap coatings than 980 nm CW and 1520 nm pulsed laser irradiation for 5 minutes. It resulted in a uniform densification and the occlusion of dentinal tubules in and around the laser – irradiated area, which was due to the wave – like energy distribution. However, the 1520 nm pulsed laser irradiation of doped CaP coating for 30 seconds – exposure time was concluded the most effective treatment, due to the formation of a shallow and spread crater, without causing any damage to the doped CaP coating. The laser irradiation sintering resulted in a uniform and excellent densification of CaP coating without distortion, which in turn resulted in a complete occlusion of dentinal tubules in and around the laser irradiation spot.

The CaP and doped CaP coatings under 1520 nm CW laser irradiation with beam diameters of 125 μm and 250 μm for exposure time of 1 and 2 minutes exhibited deep craters and the penetration of coatings, with the

possible damage of underlying dentine tissue. This was most likely due to the heat accumulation by CW laser mode. In particular, the CaP coatings exhibited poor absorption and densification, which led to the melting of dentine surface and open dentinal tubules surrounding and around the laser irradiation spot.

On the other hand, the doped CaP coatings under 1520 nm pulsed laser irradiation with beam diameters of 125 μm and 250 μm for exposure time of 1 and 2 minutes exhibited better densification and sintering than under 1520 nm CW laser irradiation. However, the exposure time of 1 minute resulted in more uniform densification of the doped CaP coating than the exposure time of 2 minutes, the latter which caused a minor distortion to the coating.

Moreover, the beam diameter of 250 μm was concluded more effective than the beam diameter of 125 μm , the latter which exhibited higher power density and resulted in deep craters, with the possible damage of underlying dentine tissue in most coatings. By contrast, the beam diameter of 250 μm resulted in a deep crater under the exposure time of 2 minutes only. Therefore, the beam diameter of 250 μm for an exposure time of 1 minute was also concluded the most effective treatment. This indicated that the effectiveness of laser irradiation sintering increased with increasing the beam diameter (around 200 μm) and decreasing the exposure time (between 30 seconds and 1 minute).

The microstructure of interface between the dentine surface and the 1520 nm pulsed laser – irradiated coatings revealed that the occlusion of dentinal tubules under laser irradiation was much more effective with doped CaP coating than CaP coating. The latter exhibited open dentinal tubules with

crack – like morphology in underlying dentine tissue, while the doped CaP coating exhibited a sintered and densified coating and the occlusion of dentinal tubules.

The temperature change measurements indicated that the doped CaP coating absorbed 3 times the energy absorbed by the CaP coating during 980 nm CW laser irradiation sintering, which could be beneficial in the densification of coatings and the protection of dentine surface from any damage by laser irradiation. In addition, the micro – hardness measurements indicated that the laser – irradiated – doped CaP coating had a hardness number (1104.71 MPa) almost twice that of laser – irradiated CaP coating (681.56 MPa) and four times that of dentine surface (240.75 MPa). This indicated that the laser – irradiated – doped CaP coating significantly enhanced the resistance of dentine section to permanent deformation, and similarly, the addition of dopants (Er_2O_3 , AlPO_4 , and CaF_2) enhanced the resistance of CaP coating to permanent deformation.

Moreover, following the acid erosion trial, the pH variations indicated that doped CaP pellets were more stable in the citric acid environment than CaP pellets. The laser – irradiated – doped CaP pellets were also found to leach out fewer components than the laser – irradiated CaP pellets, which indicated that the laser irradiation sintering was more effective with doped CaP pellets than CaP pellets. Similarly, the unsintered doped CaP pellets were found to leach out fewer components than the unsintered CaP pellets, which indicated that doped CaP pellets were more stable in the citric acid solution than CaP pellets. This was revealed by ICP/MS and SEM-EDX measurements, which indicated an improved solubility resistance of the

unsintered – and laser irradiated – doped CaP pellets in the citric acid environment, compared to the unsintered – and laser irradiated – CaP pellets. Moreover, the roughness profile measurements indicated that the laser – irradiated doped CaP pellets had smaller R_a values than the laser – irradiated CaP pellets, which indicated the effectiveness of laser irradiation sintering in the presence of dopants.

Chapter 5

Conclusions and Future Work

5.1 Conclusions

The present research study reported the results of a research methodology for the treatment of tooth sensitivity. The main aim of research study was to demonstrate the effective use of calcium orthophosphates doped with erbium, aluminium, and fluoride compounds and laser irradiation for the occlusion of dentinal tubules. The research study involved various experimental techniques, which provided reliable information about the composition, particle size and morphology, crystal structure, and thermal behaviour of powders and coatings. However, SEM-EDX provided semi quantitative analyses, which were not reliable in some cases. In addition, hot stage XRD and DSC analyses offered limited temperature ranges, from room temperature up to 800°C and 600°C, respectively, which limited the investigation of phase transformations beyond these temperatures.

Following the synthesis of control CaP powders, temperature, pH, and reaction time played an important role, particularly in obtaining the desired phase, size, and shape of CaP particles. The temperature, pH, and reaction time of 200°C, pH \geq 9, and 24 hours, respectively, were the most effective parameters in the modification of particle morphology and the production of CaP particles in the nanometre size, as well as the formation of a single phase of HAp. In addition, allowing sufficient time for the reaction of reactants to take place was very important to produce the desired phase and improve the crystallinity of CaP.

In the case of doped CaP powders, doping of CaP with $\text{Er}(\text{NO}_3)_3 \cdot 5\text{H}_2\text{O}$, $\text{Al}(\text{NO}_3)_3 \cdot 9\text{H}_2\text{O}$, and NH_4F compounds was more effective and promising than with Er_2O_3 , AlPO_4 , and CaF_2 compounds. Doping of CaP with Er_2O_3 , AlPO_4 , and CaF_2 compounds resulted in the formation of inhomogeneous phases, except that synthesised under room temperature and high pH conditions (pH 10), which resulted in the formation of homogeneous phases and significantly affected the size and shape of particles. On the other hand, doping of CaP with $\text{Er}(\text{NO}_3)_3 \cdot 5\text{H}_2\text{O}$, $\text{Al}(\text{NO}_3)_3 \cdot 9\text{H}_2\text{O}$, and NH_4F compounds resulted in a homogenous single phase under all conditions. In addition, the incorporation of Er^{3+} , Al^{3+} and F^- ions into the CaP structure was evidently observed with doped CaP powders (batch B).

The doped CaP powders (batch A and B) that were synthesised under hydrothermal conditions were anhydrous and had better thermal stability (up to 600°C) than those synthesised under room temperature conditions. This indicated the effectiveness of the hydrothermal treatment at 200°C and the addition of dopants in driving off water molecules and improving the thermal stability of CaP powders. In addition, the phase transformation of doped CaP (batch A) during hot stage XRD indicated that Er_2O_3 , AlPO_4 , and CaF_2 can be diffused into CaP structure at $\geq 200^\circ\text{C}$.

The micrometre platelet – like particles that were obtained under room temperature and as – prepared pH 5.4 ± 0.2 conditions were beneficial in the occlusion of dentinal tubules and heat transfer during laser irradiation sintering, particularly with the doped CaP coatings. However, the nanometre spherical particles in the case of doped CaP (batch A) and the nanometre rounded – like and rod – like particles in the case of doped CaP (batch B)

are more promising in the infiltration and occlusion of dentinal tubules, and most importantly, the provision of larger surface area for laser irradiation sintering. Although SEM revealed the formation of nanoparticles in agglomerations (clusters), the particle size analysis revealed the particle size in the micrometre scale, which was in good agreement with the micrometre agglomerates. Agglomerations of particles were observed after the dispersion of CaP and doped CaP powders in methanol and distilled water under ultrasonic bath conditions for ~ 10 minutes, which might indicate the formation of hard agglomerates, or that a further deagglomeration treatment was required.

Following the characterisation of coated dentine sections, the doped CaP powders exhibited better coating than the CaP powders, despite the fact that manual dipping technique was not an ideal coating technique to obtain a uniform coating. However, both coatings were quite ineffective in occluding the dentinal tubules completely. In contrast, laser irradiation improved the packing of particles, densification, and occlusion of dentinal tubules, particularly in the case of doped CaP coatings under 1520 nm pulsed laser irradiation. In addition, the laser – irradiated doped CaP coating exhibited more energy absorption than CaP coating during 980 nm CW laser irradiation, which is important in facilitating the densification of coatings and the protection of underlying dentine tissue. This was demonstrated by the microstructure of interface between dentine surface and 1520 nm pulsed laser – irradiated coatings, which revealed that the sintering of coating and occlusion of dentinal tubules were much more effective, without damaging dentine tissue, with doped CaP coating than CaP coating. In addition, the laser – irradiated doped CaP coating significantly enhanced the resistance of

dentine section to permanent deformation. Also, following the citric acid erosion of pellets, the doping of CaP and laser irradiation sintering of doped CaP were effective in improving the solubility resistance of CaP powders.

Following laser irradiation of coatings, the 980 nm CW laser irradiation for 5 minutes was concluded ineffective treatment, due to the poor densification of coatings and occlusion of dentinal tubules. Also, the pulsed 1520 nm and CW 1520 nm (beam diameters of 125 μm and 250 μm) laser irradiation for 5 minutes and 1 – 2 minutes, respectively, were concluded ineffective treatments, due to the formation of deep craters and possible damage of underlying dentine tissue.

In contrast, the 1520 nm pulsed laser irradiation of doped CaP coatings for 30 seconds and 2 minutes exhibited excellent interaction. However, the 1520 nm pulsed laser irradiation for 30 seconds was the most effective sintering treatment, due to the formation of a shallow crater, and uniform and excellent densification of coating without distortion, which resulted in a complete occlusion of dentinal tubules in and around laser irradiation spot.

Moreover, the pulsed 1520 nm beam diameter of 250 μm was more effective than the beam diameter of 125 μm , particularly for 1 minute. This indicates that the effectiveness of laser irradiation sintering increases with increasing beam diameter ($\sim 200 \mu\text{m}$) and decreasing exposure time (30 seconds – 1 minute). Therefore, 1520 nm pulsed laser irradiation of doped CaP coating, with exposure time of 30 seconds – 1 minute and beam diameter of 250 μm , was concluded the most effective treatment in achieving a uniform densification and completely occlusion of dentinal tubules, without inducing distortion to coating and underlying tissue.

Adequate laser irradiation trials were successfully carried out, however, it was difficult to laser irradiate the samples using a static stage, and more difficult to analyse the laser – irradiated areas and determine microstructural changes. A laser moving stage would have been ideal to achieve a uniform laser irradiation of entire coated dentine section, and most importantly, to investigate microstructural changes more clearly on a larger scale.

Although calcium orthophosphate minerals, such as HAp, are suitable candidate for promoting bone growth and remineralisation of hard dental tissues, erbium, aluminium, and fluoride – doped CaP minerals offer greater mechanical and thermal behaviour as well as improved solubility resistance in citric acid environments, particularly under laser irradiation, for the occlusion of dentinal tubules. Although the mechanism of laser irradiation sintering with high repetition rate pulsed laser is much different from the CW, and this aspect is a subject of ongoing research investigation, ultra – pulsed lasers and doped CaP minerals offer a good opportunity for bringing a new application for the occlusion of dentinal tubules and the treatment of dentine hypersensitivity.

5.2 Suggestions for future work

Future experiments of laser irradiation sintering of doped calcium orthophosphates are required, which must have a firm idea about the "dosage" of radiation required to expose a spot (or an area) adequately, to avoid overexposure and inadequately exposing samples, which might damage dental tissues. The following variables are ought to be investigated in details in future work.

- The use of doped calcium phosphate minerals synthesised under elevated temperature and pH conditions rather than those synthesised under room temperature and as – prepared pH conditions.
- Laser irradiation power and spot size to establish the exact threshold, below which no damage occurs to coatings and hard dental tissues.
- Dwell time on each spot to be exposed (e.g. 3x10 seconds and 1x30 seconds) to investigate whether it has a cumulative effect or not.
- Comparison between continuously moving and static scans (dwelling on spots).
- Investigating phase transformations induced by laser irradiation, by analysing changes in laser – irradiated samples, using XRD for any modified XRD peaks, FTIR, e.g., for the disappearance of absorption band of HPO_4 group after laser irradiation, and DTA/GTA for any loss of water and organic materials.
- Investigating acid erosion of laser – irradiated – doped CaP – coated dentine sections to determine their effectiveness in improving solubility resistance.

List of References

- [1] Bender, I. B. Pulpal pain diagnosis – A review. *Journal of Endodontics*. 2000, 26(3), pp.175-179.
- [2] Walters, P. A. Dentinal hypersensitivity: A review. *Journal of Contemporary Dental Practice*. 2005, 6(2), pp.107-117.
- [3] Addy, M. Dentine hypersensitivity: New perspectives on an old problem. *International Dental Journal*. 2002, 52(S5P2), pp.367-375.
- [4] Dababneh, R. H., Khouri, A. T. and Addy, M. Dentine hypersensitivity an enigma: A review of terminology, epidemiology, mechanisms, aetiology and management. *British dental journal*. 1999, 187(11), pp.606-611.
- [5] Lussi, A. (ed). *Dental erosion: From diagnosis to therapy*. Basel: Karger, 2006.
- [6] Bartold, P. M. Dentinal hypersensitivity: A review. *Australian Dental Journal*. 2006, 51(3), pp.212-218.
- [7] American Dental Association. Sensitive teeth: Causes and treatment. *Journal of the American Dental Association*. 2003, 134(6), pp.666-787.
- [8] Brand, R. W., Isselhard, D. E. and Satin, E. *Anatomy of orofacial structures*. Seventh edition. St. Louis: Mosby, 2003.
- [9] Chu, C. H. Management of dentine hypersensitivity. *The Hong Kong medical diary*. 2010, 15(3), pp.21-23.
- [10] Carini, F., Scardina, G. A., Leone, A., Messina, P. and Valenza, V. Effects of ferric oxlate dentine desensitizer. *Research Journal of Biological Sciences*. 2007, 2(2), pp.147-149.

- [11] Prietsch, J. R., De Souza, M. A. L. and De Souza, G. A. Unusual dental erosion caused by a cola drink. *Journal of Clinical Orthodontics*. 2004, 36(10), pp.549-552.
- [12] Earl, J. S. *In vitro Study of dentine tubule infiltration by hydroxyapatite and silica nanoparticles*. Ph.D. thesis, University of Leeds, 2007.
- [13] Marshall, G. W. Dentine microstructure and characterisation. *Quintessence International*. 1993, 24(9), pp.606-617.
- [14] Rees, J. S., Loyn, T., Rowe, W., Kunst, Q. and McAndrew, R. The ability of fruit teas to remove the smear layer: An in vitro study of tubule patency. *Journal of Dentistry*. 2006, 34(1), pp.67-76.
- [15] Strassler, H. E., Drisko, C. L. and Alexander, D. C. Dentin Hypersensitivity: Its inter – relationship to gingival recession and acid erosion. *AEGIS Communications*. 2008, 29(5), pp.1-9.
- [16] Haywood, V. B. Dentine hypersensitivity: Bleaching and restorative consideration for successful management. *International Dental Journal*. 2002, 52(S5P2), pp.376-384.
- [17] Oliveira, S. S. A., Pugach, M. K., Hilton, J. F., Watanabe, L. G., Marshall, S. J. and Marshall Jr, G. W. The influence of the dentin smear layer on adhesion: A self – etching primer vs. a total – etch system. *Dental Materials*. 2003, 19(8), pp.758-767.
- [18] Eldarrat, A. H., High, A. S. and Kale, G. M. In vitro analysis of 'smear layer' on human dentine using ac – impedance spectroscopy, Ac – impedance spectroscopy of smear layer. *Journal of Dentistry*. 2004, 32(7), pp.547-554.

- [19] Violich, D. R. and Chandler, N. P. The smear layer in endodontics – A review. *International Endodontic Journal*. 2010, 43(1), pp.2-15.
- [20] Bernier, J. L. The histology of bone and cementum with special reference to movement of teeth. *American Journal of Orthodontics and Oral Surgery*. 1942, 28(10), pp.B599-B604.
- [21] Stamfelj, I., Vidmar, G., Cvetko, E. and Gaspersic, D. Cementum thickness in multirooted human molars: A histometric study by light microscopy. *Annals of Anatomy*. 2008, 190(2), pp.129-139.
- [22] Neuvald, L. and Consolaro, A. Cementoenamel junction: Microscopic analysis and external cervical resorption. *Journal of Endodontics*. 2000, 26(9), pp.503-508.
- [23] Ricarte, J. M., Matoses, V. F., Llacer, V. J. F., Fernandez, A. J. F. and Moreno, B. M. Dentinal sensitivity: Concept and methodology for its objective evaluation. *Medicina Oral, Patologia Oral y Cirugia Bucal*. 2008, 13(3), pp.E201-E206.
- [24] Akca, A. E., Gokce, S., Kurkcu, M., and Ozdemir, A. Clinical assessment of bond and fluoride in dentine hypersensitivity. *Arastirma*. 2006, 30(4), pp.92-100.
- [25] Mansour, M. H. and Cox, S. C. Patients presenting to the general practitioner with pain of dental origin. *Medical Journal of Australia*. 2006, 185(2), pp.64-67.
- [26] Oikarinen, K., Zubaid, M., Thalib, L., Soikkonen, K., Rashed, W. and Lie, T. Infectious dental diseases in patients with coronary artery disease: An

orthopantomographic case – control study. *Journal of the Canadian Dental Association*. 2009, 75(1), pp.1-35.

[27] Moritz, A., Schoop, U., Goharkhay, K., Aoid, M., Reichenbach, P., Lothaller, M. A., Wernisch, J. and Sperr, W. Long – term effects of CO2 laser irradiation on treatment of hypersensitive dental necks: Results of an in vivo study. *Journal of Clinical Laser Medicine & Surgery*. 1998, 16(4), pp.211-215.

[28] Aranha, A. C., Pimenta, L. A. and Marchi, G. M. Clinical evaluation of desensitizing treatments for cervical dentine hypersensitivity. *Brazilian Oral Research*. 2009, 23(3), pp.333-339.

[29] Kishore, A., Mehrotra, K. K. and Saimbi, C. S. Effectiveness of desensitizing agents. *Journal of Endodontics*. 2002, 28(1), pp.34-35.

[30] Carini, F., Scardina, G. A., Leone, A., Messina, P. and Valenza, V. Effects of ferric oxlate dentine desensitizer. *Research Journal of Biological Sciences*. 2007, 2(2), pp.147-149.

[31] Pashley, D.H., Kalathoor, S. and Burnham, D. The effects of calcium hydroxide on dentine permeability. *Journal of Dental Research*. 1986, 65(3), pp.417-420.

[32] Kasten, F. H., Pineda, L. F., Schneider, P. E., Rawls, H. R. and Foster, T. A. Biocompatibility testing of an experimental fluoride releasing resin using human gingival epithelial cells in vitro. *In Vitro Cellular & Developmental Biology*. 1989, 25(1), pp.57-62.

- [33] Duran, I., Sengun, A., Hadimli, H. H. and Ulker, M. Evaluation of antibacterial effectiveness of desensitizers against oral bacteria. *European Journal of Dentistry*. 2008, 2(1), pp.43-47.
- [34] Godoy, F. G. Pro – Argin™ Technology: New research on superior dentin hypersensitivity relief with stain removal. *American Journal of Dentistry*. 2010, Special Issue A.23, pp.1A-40A.
- [35] Wang, Z., Sa, Y., Sauro, S., Chen, H., Xing, W., Ma, X., Jiang, T. and Wang, Y. Effect of desensitising toothpastes on dentinal tubule occlusion: A dentine permeability measurement and SEM in vitro study. *Journal of Dentistry*. 2010, 38(5), pp.400-410.
- [36] Burwell, A. K., Litkowski, L. J. and Greenspan, D. C. Calcium sodium phosphosilicate (NovaMin®): Remineralization potential. *Advances in Dental Research*. 2009, 21(1), pp.35-39.
- [37] Schafer, F., Beasley, T. and Abraham, P. In vivo delivery of fluoride and calcium from toothpaste containing 2% hydroxyapatite. *International Dental Journal*. 2009, 59(6), pp.321-324.
- [38] Tschoppe, P., Zandim, D. L., Martus, P. and Kielbassa, A. M. Enamel and dentine remineralization by nano hydroxyapatite toothpastes. *Journal of Dentistry*. 2011, 39(6), pp.430-437.
- [39] Roveri, N. *BioRepair plus: The enamel repairer*. University of Bologna, 2009.
- [40] Shi, D. (ed). *Biomaterials and tissue engineering*. Berlin: Springer, 2004.

- [41] Ratner, B. D., Hoffman, A. S., Schoen, F. J. and Lemons, J. E. (eds). *Biomaterials sciences: An introduction to materials in medicine*. Third edition. California: Academic Press, 2013.
- [42] Regi, M. V. and Arcos, D. *Biomimetic nanoceramics in clinical use: From materials to applications*. Cambridge: Royal Society of Chemistry, 2008.
- [43] Shapoff, C. A. and Katta, S. A. Evaluation of bioactive glass as a bone graft extender in sinus elevation surgeries. *International Journal of Oral Implantology & Clinical Research*. 2010, 1(3), pp.155-162.
- [44] Gjorgievska, E. and Nicholson, J. W. Prevention of enamel demineralization after tooth bleaching by bioactive glass incorporated into toothpaste. *Australian Dental Journal*. 2011, 56(2), pp.193-200.
- [45] Kelsall, R. W., Hamley, I. W. and Geoghegan, M. (eds). *Nanoscale science and technology*. Chichester: John Wiley & Sons, Inc., 2005.
- [46] Hamouda, I. M. Current perspectives of nanoparticles in medical and dental biomaterials. *Journal of Biomedical Research*. 2012, 26(3), pp.143-151.
- [47] Saunders, S. A. Current practicality of nanotechnology in dentistry. Part 1: Focus on nanocomposite restoratives and biomimetics. *Clinical, Cosmetic and Investigational Dentistry*. 2009, 2009(1), pp.47-61.
- [48] Ohta, K., Kawamata, H., Ishizaki, T. and Hayman, R. Occlusion of dentinal tubules by nano hydroxyapatite. *Journal of Dental Research*. 2007, 86(Special Issue A), p.1.

- [49] Dorozhkin, S. V. Calcium orthophosphates in dentistry. *Journal of Materials Science: Materials in Medicine*. 2013, 24(6), pp.1335-1363.
- [50] Lee, S. Y., Kwon, H. K. and Kim, B. I. Effect of dentinal tubule occlusion by dentifrice containing nano – carbonate apatite. *Journal of Oral Rehabilitation*. 2008, 35(11), pp.847–853.
- [51] Mao, T. and Toby, J. Lasers as a treatment modality for dentinal hypersensitivity. *IOSR Journal of dental and medical sciences*. 2013, 9(2), pp.29-32.
- [52] Asnaashari, M. and Moeini, M. Effectiveness of lasers in the treatment of dentin hypersensitivity. *Journal of Lasers in Medical Sciences*. 2013, 4(1), pp.1-7.
- [53] He, S., Wang, Y., Li, X. and Hu, D. Effectiveness of laser therapy and topical desensitising agents in treating dentine hypersensitivity: A systematic review. *Journal of Oral Rehabilitation*. 2011, 38(5), pp.348-358.
- [54] Akca, A. E., Gokce, S., Kurkcu, M. and Ozdemir, A. A clinical investigation of low level laser irradiation on hypersensitive dentine. *Arastirma*. 2006, 30(2), pp.94-99.
- [55] Ladalardo, T. C., Pinheiro, A., Campos, R. A., Brugnera Jr, A., Zanin, F., Albernaz, P. L. and Weckx, L. L. Laser therapy in the treatment of dentine hypersensitivity. *Brazilian Dental Journal*. 2004, 15(2), pp.144-150.
- [56] Kimura, Y., Wilder-Smith, P., Yonaga, K. and Matsumoto, K. Treatment of dentine hypersensitivity by lasers: A review. *Journal of Clinical Periodontology*. 2000, 27(10), pp.715-721.

- [57] Kimura, Y., Wilder-Smith, P., Yonaga, K. and Matsumoto, K. Treatment of dentine hypersensitivity by lasers: A review. *Journal of Clinical Periodontology*. 2000, 27(10), pp.715-721. In: Orchardson, R. and Gillam, D. G. Managing dentine hypersensitivity. *Journal of the American Dental Association*. 2006, 137(7), pp.990-998.
- [58] Aranha, A. C. and Eduardo Cde, P. Effects of Er:YAG and Er,Cr:YSGG lasers on dentine hypersensitivity. Short – term clinical evaluation. *Lasers in Medical Science*. 2012, 27(4), pp.813-818. In: Asnaashari, M. and Moeini, M. Effectiveness of lasers in the treatment of dentin hypersensitivity. *Journal of Lasers in Medical Sciences*. 2013, 4(1), pp.1-7.
- [59] Kimura, Y., Smith, P. W., Yonaga, K. and Matsumoto, K. Treatment of dentine hypersensitivity by lasers: A review. *Journal of Clinical Periodontology*. 2000, 27(10), pp.715-721. In: He, S., Wang, Y., Li, X. and Hu, D. Effectiveness of laser therapy and topical desensitising agents in treating dentine hypersensitivity: A systematic review. *Journal of Oral Rehabilitation*. 2011, 38(5), pp.348-358.
- [60] Longbottom, C. and Pitts, N. B. CO₂ laser and the diagnosis of occlusal caries: In vitro study. *Journal of Dentistry*. 1993, 21(4), pp.234-239.
- [61] Husein, A. Applications of lasers in dentistry: A review. *Archives of Orofacial Sciences*. 2006, 1, pp.1-4.
- [62] Todea, C. D. M. Laser applications in conservative dentistry. *The Mediaeval Journal*. 2004, 54(4), pp.392-405.
- [63] Bhat, A. M. Lasers in prosthodontics – An overview. Part 1: Fundamentals of dental lasers. *Journal of Indian Prosthodontic Society*. 2010, 10(1), pp.13-26.

- [64] Chanthaboury, R. and Irinakis, T. The use of lasers for periodontal debridement: Marketing tool or proven therapy. *Journal of the Canadian Dental Association*. 2005, 71(9), pp.653-658.
- [65] Deppe, H. and Horch, H. H. Laser applications in oral surgery and implant dentistry. *Lasers in Medical Science*. 2007, 22(4), pp.217-221.
- [66] Kingery, W. D. *Introduction to ceramics*. New York: John Wiley & Sons, Inc., 1960.
- [67] Somiya, S., Aldinger, F., Claussen, N., Spriggs, R. M., Uchino, K., Koumoto, K. and Kaneno, M. *Handbook of advanced ceramics*. London: Elsevier-Academic Press, 2003.
- [68] Dorozhkin, S. V. Bioceramics of calcium orthophosphates. *Biomaterials*. 2010, 31(7), pp.1465-1485.
- [69] Dorozhkin, S. V. Calcium orthophosphates. *Journal of Materials Science*. 2007, 42(4), pp.1061-1095.
- [70] Nelkon, M. and Parker, P. *Advanced level physics*. Seventh edition. London: Heinemann Educational, 1995.
- [71] Lakshmanan, A. (ed). *Sintering of ceramics – new emerging techniques*. Rijeka: InTech, 2012.
- [72] Tolochko, N. K., Khlopkov, Y. V., Mozzharov, S. E., Ignatiev, M. B., Laoui, T. and Titov, V. I. Absorptance of powder materials suitable for laser sintering. *Rapid Prototyping Journal*. 2000, 6(3), pp.155-160.
- [73] Dorozhkin, S. V. Calcium orthophosphates in nature, biology and medicine. *Materials*. 2009, 2(2), pp.399-498.

[74] Dorozhkin, S. V. Calcium orthophosphates: Occurrence, properties, biomineralization, pathological calcification and biomimetic applications. *Biomatter*. 2011, 1(2), pp.121-164.

[75] Markovic, M., Fowler, B. O. and Tung, M. S. Preparation and comprehensive characterization of a calcium hydroxyapatite reference material. *Journal of Research of the National Institute of Standards and Technology*. 2004, 109(6), pp.553-568. In: Dorozhkin, S. V. Calcium orthophosphates. *Journal of Materials Science*. 2007, 42(4), pp.1061-1095.

[76] Cox, S. Synthesis method of hydroxyapatite. *Lucideon (formerly Ceram)*. 2012, [no volume], pp.1-10.

[77] Bilton, M., Milne, S. J. and Brown, A. P. Comparison of hydrothermal and sol – gel synthesis of nano – particulate hydroxyapatite by characterisation at the bulk and particle level. *Open Journal of Inorganic Non-metallic Materials*. 2012, 2(1), pp.1-10.

[78] Eshtiagh-Hosseini, H., Houssaindokht, M. R., Chahkandhi, M. and Youssefi, A. Preparation of anhydrous dicalcium phosphate, DCPA, through sol – gel process, identification and phase transformation evaluation. *Journal of Non-Crystalline Solids*. 2008, 354(32), pp.3854-3857. In: Dorozhkin, S. V. Calcium orthophosphates: Occurrence, properties, biomineralization, pathological calcification and biomimetic applications. *Biomatter*. 2011, 1(2), pp.121-164.

[79] Fathi, M. H. and Hanifi, A. Evaluation and characterization of nanostructure hydroxyapatite powder prepared by simple sol – gel method. *Materials Letters*. 2007, 61(18), pp.3978-3983. In: Bilton, M., Milne, S. J. and Brown, A. P. Comparison of hydrothermal and sol – gel synthesis of nano –

particulate hydroxyapatite by characterisation at the bulk and particle level.

Open Journal of Inorganic Non-metallic Materials. 2012, 2(1), pp.1-10.

[80] Ruys, A. J., Zeigler, K. A., Standard, O. C., Brandwood, A., Milthorpe, B. K. and Sorrell, C. C. Hydroxyapatite sintering phenomena: Densification and dehydration behaviour. In: Bannister, M. J. (ed). *Ceramics, Adding the value, 16-21 August, 1992, Melbourne*. Waverley: The Australian Ceramic Society, pp.605-610. In: Bilton, M., Milne, S. J. and Brown, A. P. Comparison of hydrothermal and sol – gel synthesis of nano – particulate hydroxyapatite by characterisation at the bulk and particle level. *Open Journal of Inorganic Non-metallic Materials*. 2012, 2(1), pp.1-10.

[81] Griot, M. *Introduction to laser technology*. Rochester: CVI Melles Griot. 2010.

[82] Svelto, O. *Principles of lasers*. Fifth edition. New York: Springer, 2010.

[83] Hitz, C. B., Ewing, J. J. and Hecht, J. *Introduction to laser technology*. Fourth edition. Hoboken: John Wiley & Sons Inc., 2012.

[84] Niemz, M. H. *Laser tissue interactions: Fundamentals and applications*. Third edition. Berlin: Springer, 2007.

[85] Parker, S. Laser – tissue interaction. *British Dental Journal*. 2007, 202(2). pp.73-81.

[86] Featherstone, J. and Fried, D. Fundamental interactions of lasers with dental hard tissues. *Medical Laser Application*. 2001, 16(3), pp.181-194.

[87] Welch, A. J., Torres, J. H. and Cheong, W. F. Laser physics and laser – tissue interaction. *Texas Heart Institute Journal*. 1989, 16(3), pp.141-149.

- [88] Ogino, S., Awazu, K. and Tomimasu, T. The effect of free electron laser (FEL) irradiation on dentine. *Journal of Japanese Society for Laser Dentistry*. 1996, 7(1), pp.67-71.
- [89] Awazu, K. Novel aspects of dental laser and tissue interaction. *Elsevier*. 2003, 1248(1), pp.29-36.
- [90] Cox, B. *Introduction to laser – tissue interactions*. MPHY3886 Optics in Medicine. London: University College London, 2013.
- [91] Diaci, J. Laser profilometry for the characterization of craters produced in hard dental tissues by Er:YAG and Er,Cr:YSGG lasers. *Journal of the Laser and Health Academy*. 2008, 2(1), pp.1-10.
- [92] Belikov, A. V., Erofeev, A. V., Shumilin, V. V. and Tkachuk, A. M. Comparative study of the 3 μm laseraction on different hard tissue samples using free running pulsed Er-doped YAG, YSGG, YAP, and YLF lasers. In: Altshuler, G. B. and Hibst, R. (eds). *Dental applications of lasers. August 29 1993, Budapest*. Bellingham: SPIE-The International Society for Optical Engineering, 1993, pp.60-67. In: Stock, K., Hibst, R. and Keller, U. Comparison of Er:YAG and Er:YSGG laser ablation of dental hard tissues. In: Altshuler, B. G., Birngruber, R., Dal Fante, M., Hibst, R., Hoenigsmann, H., Krasner, N. and Laffitte, F. (eds). *Medical Applications of Lasers in Dermatology, Ophthalmology, Dentistry, and Endoscopy. September 04, 1997. San Remo*. Bellingham: SPIE-The International Society for Optical Engineering, 1997, pp.88-95.
- [93] Fried, D., Featherstone, J., Glana, R. E. and Seka, W. The nature of light scattering in dental enamel and dentin at visible and near-IR wavelengths. *Applied Optics*. 1995, 34(7), pp.1278-1285. In: Thomas, S. S.

Spectroscopic investigation of tooth caries and demineralization. Ph.D. thesis, Cochin University of Science and Technology, 2009.

[94] Fried, D., Featherstone, J., Glena, R. E. and Seka, W. The nature of light scattering in dental enamel and dentin at visible and near – infrared wavelengths. *Applied Optics*. 1995, 34(7), pp.1278-1285. In: Kodach, V. M. *Development of functional near – infrared optical coherence tomography*. Ph.D. thesis, The University of Amsterdam, 2012.

[95] Zijp, J. R. *Optical properties of dental hard tissues*. Ph.D. thesis, University of Groningen, 2001.

[96] Vo-Dinh, T. (ed). *Biomedical photonics handbook*. Boca Raton: CRC Press, 2003. In: Sabaeian, M. and Shahzadeh, M. Simulation of temperature and thermally induced stress of human tooth under CO₂ pulsed laser beams using finite element method. *Lasers in Medical Science*. 2015, 30(2). pp.645-651.

[97] Featherstone, J. and Fried, D. Fundamental interactions of lasers with dental hard tissues. *Medical Laser Application*. 2001, 16(3), pp.181-194. In: Zhan, Z., Zhang, X., Guo, W. and Xie. S. Determination of ablation threshold of dental hard tissues irradiated with Er:YAG and Er,Cr:YSGG lasers. *Chinese Optics Letters*. 2013, 11(5), pp.051701:1-5.

[98] Fried, D. Lasers and optics for measuring tooth decay. *The Optical Society*. 2010, 21(4), pp.15-19.

[99] Zuerlein, M. J., Fried, D., Featherstone, J. and Seka, W. Optical properties of dental enamel in the mid – IR determined by pulsed photothermal radiometry. *Journal of Selected Topics in Quantum Electronics*. 1999, 5(4), pp.1083-1089. In: Featherstone, J., Fried, D.

Fundamental interactions of lasers with dental hard tissues. *Medical Laser Application*. 2001, 16(3), pp.181-194.

[100] Perhavec, T., Lukac, M., Diaci, J. and Marincek, M. Heat deposition of erbium lasers in hard dental tissues. *Journal of Oral Laser Applications*. 2009, 9(4), pp.205-212.

[101] Liu, H. C., Lin, C. P. and Lan, W. H. Sealing depth of Nd:YAG laser on human dentinal tubules. *Journal of Endodontics*. 1997, 23(11), pp.691-693.
In: Lan, W. H., Lee, B. S., Liu, H. C. and Lin, C. P. Morphologic study of Nd:YAG laser usage in treatment of dentinal hypersensitivity. *Journal of Endodontics*. 2004, 30(3), pp.131-134.

[102] Eugenioa, S., Sivakumara, M., Vilara, R. and Rego, A. M. Characterisation of dentin surfaces processed with KrF excimer laser radiation. *Biomaterials*. 2005, 26(33), pp.6780-6787.

[103] Zuerlein, M. J. *Interactions of IR lasers with dental hard tissues at clinically relevant wavelengths*. Ph.D. thesis, University of California, 1999.
In: Stanineca, M., Meshkina, N., Manesh, S. K., Ritchieb, R. O. and Fried, D. Weakening of dentin from cracks resulting from laser irradiation. *Dental Materials*. 2009, 25(4), pp.520-525.

[104] Sholom, S., Desrosiers, M., Chumak, V., Luckyanov, N., Simon, S. L. and Bouville, A. UV effects in tooth enamel and their possible application in EPR dosimetry with front teeth. *Health Physics*. 2010, 98(2), pp.360-368.

[105] Zijp, J. R. and Bosch, J. J. Theoretical model for the scattering of light by dentin and comparison with measurements. *Applied Optics*. 1993, 32(4), pp.411-415. In: Thomas, S. S. *Spectroscopic investigation of tooth caries*

and demineralization. Ph.D. thesis, Cochin University of Science and Technology, 2009.

[106] Levy, G. and RizoIU, I. M. New concepts in laser tissue interaction. In: Miserendino, L. J. and Pick, R. M. (eds). *Lasers in dentistry*. Singapore: Quintessence, 1995. pp.299-313. In: Thomas, S. S. *Spectroscopic investigation of tooth caries and demineralization*. Ph.D. thesis, Cochin University of Science and Technology, 2009.

[107] Koort, H. J., and Frentzen, M. YAG lasers in restorative dentistry: A histological investigation. In: Anderson, R. R. (ed). *Laser surgery: Advanced characterization, therapeutics and systems III. January 19 1992, Los Angeles*. Bellingham: SPIE-The International Society for Optical Engineering, 1992, pp.403-411. In: Thomas, S. S. *Spectroscopic investigation of tooth caries and demineralization*. Ph.D. thesis, Cochin University of Science and Technology, 2009.

[108] Tuchin, V. V. and Altshuler, G. B. Dental and oral tissue optics. In: Kishen, A. and Asundi, A. (eds). *Fundamentals and applications of biophotonics in dentistry*. London: Imperial College Press, 2007, pp.245-300. In: Thomas, S. S. *Spectroscopic investigation of tooth caries and demineralization*. Ph.D. thesis, Cochin University of Science and Technology, 2009.

[109] Hale, G. M. and Query, M. R. Optical constants of water in the 200 nm to 200 μm wavelength region. *Applied Optics*. 1973, 12(3), pp.555-563. In: Thomas, S. S. *Spectroscopic investigation of tooth caries and demineralization*. Ph.D. thesis, Cochin University of Science and Technology, 2009.

[110] Nagasawa, A. Research and development of laser in dental and oral surgery. In: Atsumi, K. (ed). *New frontiers in laser medicine and surgery*. Amsterdam: Elsevier Biomedical Press, 1983, pp.233-241. In: Thomas, S. S. *Spectroscopic investigation of tooth caries and demineralization*. Ph.D. thesis, Cochin University of Science and Technology, 2009.

[111] LeGeros, R. Z. *Calcium phosphates in oral biology and medicine*. Basel: Karger, 1991. In: Thomas, S. S. *Spectroscopic investigation of tooth caries and demineralization*. Ph.D. thesis, Cochin University of Science and Technology, 2009.

[112] Fowler, B. and Kuroda, S. Changes in heated and in laser – irradiated human tooth enamel and their probable effects on solubility. *Calcified Tissue International*. 1986, 38(4), pp.197-208. In: Featherstone, J. and Fried, D. Fundamental interactions of lasers with dental hard tissues. *Medical Laser Application*. 2001, 16(3), pp.181-194.

[113] Legeros, R. Z. Calcium phosphates in enamel, dentin and bone. In: Myers, H. M. (ed). *Calcium phosphates in oral biology and medicine*. Basel: Karger, 1991, pp.108-129. In: Featherstone, J. and Fried, D. Fundamental interactions of lasers with dental hard tissues. *Medical Laser Application*. 2001, 16(3), pp.181-194.

[114] Fried, D., Glana, R. E., Featherstone, J. and Seka, W. Permanent and transient changes in the reflectance of CO₂ laser irradiated dental hard tissues at 9.3, 9.6, 10.3 and 10.6 μm and at fluences of 1–20 J/cm². *Lasers in Surgery and Medicine*. 1997, 20(1), pp.22-31. In: Featherstone, J. and Fried, D. Fundamental interactions of lasers with dental hard tissues. *Medical Laser Application*. 2001, 16(3), pp.181-194.

[115] McCormack, S. M., Fried, D., Featherstone, J., Glana, R. E. and Seka, W. Scanning electron microscope observations of CO₂ laser effects on dental enamel. *Journal of Dental Research*. 1995, 74(10), pp.1702-1708. In: Featherstone, J. and Fried, D. Fundamental interactions of lasers with dental hard tissues. *Medical Laser Application*. 2001, 16(3), pp.181-194.

[116] Hibst, R. Lasers for caries removal and cavity preparation: State of the art and future directions. *Journal of Oral Laser Applications*. 2002, 2(4), pp.203-212. In: Diaci, J. Laser profilometry for the characterization of craters produced in hard dental tissues by Er:YAG and Er,Cr:YSGG lasers. *Journal of the Laser and Health Academy*. 2008, 2(1), pp.1-10.

[117] Fahey, M., Onyejekwe, O., Mason, H. L. and Mitra, K. Precise dental ablation using ultra – short – pulsed 1552 nm laser. *International Journal of Heat and Mass Transfer*. 2008, 51(23-24), pp.5732-5739.

[118] Ferreira, J. M., Palamara, J., Phakey, P. P., Rachinger, W. A. and Orams, H. J. Effects of continuous – wave CO₂ laser on the ultrastructure of human dental enamel. *Archives of Oral Biology*. 1989, 34,(7), pp.551-562.

[119] Featherstone, J., Barrett-Vespone, N. A., Fried, D., Kantorowitz, Z., Lofthouse, J. and Seka, W. Rational choice of laser conditions for inhibition of caries progression. In: Harvey W. A., Featherstone, J. and White, J. M. (eds). *Lasers in Dentistry. February 01 1995, San Jose*. Bellingham: SPIE-The International Society for Optical Engineering, 1995, pp.57-67. In: Parker, S. Laser – tissue interaction. *British Dental Journal*. 2007, 202(2), pp.73-81.

[120] Fried, D., Seka, W., Glana, R. E. and Featherstone, J. The thermal response of dental hard tissues to pulsed 9-11 μm CO₂ laser irradiation.

Optical Engineering. 1996, 35(7), pp.1976-1984. In: Parker, S. Laser – tissue interaction. *British Dental Journal*. 2007, 202(2), pp.73-81.

[121] Colluzzi, D. J. *Types of lasers and what your practice needs: Laser dentistry made easy and profitable*. Dentaleconomics [online]. 2007, 97(4). [Accessed 2013]. Available from: <http://www.dentaleconomics.com/>.

[122] Coluzzi, D. J. An overview of laser wavelengths used in dentistry. *Dental Clinics of North America*. 2000, 44(4), pp.753-765. In: Bhat, A. M. Lasers in prosthodontics – An overview Part 1: Fundamentals of dental lasers. *Journal of Indian Prosthodontic Society*. 2010, 10(1), pp.13-26.

[123] Coluzzi, D. J. Fundamentals of dental lasers: Science and instruments. *Dental Clinics of North America*. 2004, 48(4), pp.751-770. In: Bhat, A. M. Lasers in prosthodontics – An overview Part 1: Fundamentals of dental lasers. *Journal of Indian Prosthodontic Society*. 2010, 10(1), pp.13-26.

[124] Schwarz, F., Arweiler, N., Georg, T. and Reich, E. Desensitising effects of an Er: YAG laser on hypersensitive dentine. *Journal of Clinical Periodontology*. 2002, 29(3), pp.211-215.

[125] Kirpa, J. *Fundamentals of laser dentistry*. New Delhi: Jaypee Brothers Medical Publishers, 2011. In: Mao, T. and Toby, J. Lasers as a treatment modality for dentinal hypersensitivity. *Journal of Medical and Dental Sciences*. 2013, 9(2), pp.29-32.

[126] Lopes, A. O. and Aranha, A. C. Comparative evaluation of the effects of Nd:YAG laser and a desensitizer agent on the treatment of dentin hypersensitivity: A clinical study. *Photomedicine and Laser Surgery*. 2013, 31(3), pp.132-138. In: Mao, T. and Toby, J. Lasers as a treatment modality

for dentinal hypersensitivity. *Journal of Medical and Dental Sciences*. 2013, 9(2), pp.29-32.

[127] Han, S. Y., Jung, H. I., Kwon, H. K. and Kim, B. I. Combined effects of Er:YAG laser and nano – carbonate apatite dentifrice on dentinal tubule occlusion: In vitro study. *Photomedicine and Laser Surgery*. 2013, 31(7), pp.342-348. In: Mao, T. and Toby, J. Lasers as a treatment modality for dentinal hypersensitivity. *Journal of Medical and Dental Sciences*. 2013, 9(2), pp.29-32.

[128] Umberto, R., Claudia, R., Gaspare, P., Gianluca, T. and Alessandro, V. Treatment of dentine hypersensitivity by diode laser: A clinical study. *International Journal of Dentistry*. 2012, 2012, pp.1-8.

[129] Umberto, R., Claudia, R., Gaspare, P., Gianluca, T. and Alessandro, V. Treatment of dentine hypersensitivity by diode laser: A clinical study. *International Journal of Dentistry*. 2012, 2012, pp.1-8. In: Mao, T. and Toby, J. Lasers as a treatment modality for dentinal hypersensitivity. *Journal of Medical and Dental Sciences*. 2013, 9(2), pp.29-32.

[130] Aranha, A. and Eduardo, C. Effects of Er:YAG and Er,Cr:YSGG lasers on dentine hypersensitivity: Short – term clinical evaluation. *Lasers in Medical Science*. 2012, 27(4), pp.813-818. In: Asnaashari, M. and Moeini, M. Effectiveness of lasers in the treatment of dentin hypersensitivity. *Journal of Lasers in Medical Sciences*. 2013, 4(1), pp.1-7.

[131] Furuoka, M., Yokoi, T., Fukuda, S., Usuki, M., Matsuo, S., Taniguchi, K. et al. Effects of GaAlAs laser diode in treatment of hypersensitive dentine. *Journal of Fukuoka Dental College*. 1988, 15(1), pp.42-48. In: Mao, T. and

Toby, J. Lasers as a treatment modality for dentinal hypersensitivity. *Journal of Medical and Dental Sciences*. 2013, 9(2), pp.29-32.

[132] Yamaguchi, M., Ito, M., and Miwata, T. Clinical study on the treatment of hypersensitive dentin by GaAlAs laser diode using double blind test. *Aichi Gakuin Journal of Dental Science*. 1990, 28(2), pp.703-707. In: Mao, T. and Toby, J. Lasers as a treatment modality for dentinal hypersensitivity. *Journal of Medical and Dental Sciences*. 2013, 9(2), pp.29-32.

[133] Orchardson, R., Gangarosa, L. P., Holland, G. R., Pashley, D. H., Trowbridge, H. O., Ashley, F. P., Kleinberg, I. and Zappa, U. Dentine hypersensitivity—into the 21st century. *Archives of Oral Biology*. 1994, 39(Suppl. 1), pp.113S-119S. In: Asnaashari, M. and Moeini, M. Effectiveness of lasers in the treatment of dentin hypersensitivity. *Journal of Lasers in Medical Sciences*. 2013, 4(1), pp.1-7.

[134] Lan, W. H. and Liu, H. C. Sealing of human dentinal tubules by Nd:YAG laser. *Journal of Clinical Laser Medicine & Surgery*. 1995, 13(5), pp.329-333. In: Asnaashari, M. and Moeini, M. Effectiveness of lasers in the treatment of dentin hypersensitivity. *Journal of Lasers in Medical Sciences*. 2013, 4(1), pp.1-7.

[135] Lan, W. H. and Lui, H. C. Treatment of dentin hypersensitivity by Nd:YAG Laser. *Journal of Clinical Laser Medicine & Surgery*. 1996, 14(2), pp.89-92. In: Asnaashari, M. and Moeini, M. Effectiveness of lasers in the treatment of dentin hypersensitivity. *Journal of Lasers in Medical Sciences*. 2013, 4(1), pp.1-7.

[136] Hsu, P. J., Chen, J. H., Chuang, F.H. and Roan, R. T. The combined occluding effects of fluoride – containing dentin desensitizer and Nd – Yag

laser irradiation on human dentinal tubules: An in vitro study. *Kaohsiung Journal of Medical Sciences*. 2006, 22(1), pp.24-29. In: Asnaashari, M. and Moeini, M. Effectiveness of lasers in the treatment of dentin hypersensitivity. *Journal of Lasers in Medical Sciences*. 2013, 4(1), pp.1-7.

[137] Schwarz, F., Arweiler, N., Georg, T. and Reich, E. Desensitizing effects of an Er:YAG laser on hypersensitive dentine. *Journal of Clinical Periodontology*. 2002, 29(3), pp.211-215. In: He, S., Wang, Y., Li, X. and Hu, D. Effectiveness of laser therapy and topical desensitising agents in treating dentine hypersensitivity: A systematic review. *Journal of Oral Rehabilitation*. 2011, 38(5), pp.348-358.

[138] Moritz, A., Gutknecht, N., Schoop, U., Wernisch, J., Lampert, F. and Sperr, W. Effects of CO₂ laser irradiation on treatment of hypersensitive dental necks: Results of an in vitro study. *Journal of Clinical Laser Medicine & Surgery*. 1995, 13(6), pp.397-400.

[139] Bakry, A. S., Takahashi, H., Otsuki, M., Sadr, A., Yamashita, K. and Tagami, J. CO₂ laser improves 45S5 bioglass interaction with dentin. *Journal of Dental Research*. 2011, 90(2), pp.246-250. In: Mao, T. and Toby, J. Lasers as a treatment modality for dentinal hypersensitivity. *Journal of medical and dental sciences*. 2013, 9(2), pp.29-32.

[140] Zhang, C., Matsumoto, K., Kimura, Y., Harashima, T., Takeda, F. H. and Zhou, H. Effects of CO₂ laser in treatment of cervical dentinal hypersensitivity. *Journal of Endodontics*. 1998, 24(9), pp.595-597.

[141] Lan, W. H., Liu, H. C. and Lin, C. P. The combined occluding effect of sodium fluoride varnish and Nd:YAG laser irradiation on human dentinal tubules. *Journal of Endodontics*. 1999, 25(6), pp.424-426.

- [142] Goharkhay, K., Wernisch, J., Schoop, U. and Moritz, A. Laser Treatment of hypersensitive dentin: Comparative ESEM investigations. *Journal of Oral Laser Applications*. 2007, 7(4), pp.211-223. In: Asnaashari, M. and Moeini, M. Effectiveness of lasers in the treatment of dentin hypersensitivity. *Journal of Lasers in Medical Sciences*. 2013, 4(1), pp.1-7.
- [143] Raichur, P. S., Setty, S. B. and Thakur, S. L. Comparative evaluation of diode laser, stannous fluoride gel, and potassium nitrate gel in the treatment of dentinal hypersensitivity. *General dentistry*. 2013, 61(3), pp.66-71. In: Mao, T. and Toby, J. Lasers as a treatment modality for dentinal hypersensitivity. *Journal of medical and dental sciences*. 2013, 9(2), pp.29-32.
- [144] Sgolastra, F., Petrucci, A., Gatto, R. and Monaco, A. Effectiveness of laser in dentinal hypersensitivity treatment: A systematic review. *Journal of Endodontics*. 2011, 37(3), pp.297-303. In: Asnaashari, M. and Moeini, M. Effectiveness of lasers in the treatment of dentin hypersensitivity. *Journal of Lasers in Medical Sciences*. 2013, 4(1), pp.1-7.
- [145] Kimura, Y., Wilder-Smith, P., Yonaga, K. and Matsumoto, K. Treatment of dentine hypersensitivity by lasers: A review. *Journal of Clinical Periodontology*. 2000, 27(10), pp.715-721. In: Asnaashari, M. and Moeini, M. Effectiveness of lasers in the treatment of dentin hypersensitivity. *Journal of Lasers in Medical Sciences*. 2013, 4(1), pp.1-7.
- [146] Elliot, J. C. *Structure and chemistry of the apatites and other calcium orthophosphates*. Amsterdam: Elsevier, 1994. In: Dorozhkin, S. V. Calcium orthophosphates. *Journal of Materials Science*. 2007, 42(4), pp.1061-1095.

- [147] Mirtchi, A. A., Lemaitre, J. and Terao, N. Calcium phosphate cements: Study of the beta – tricalcium phosphate – monocalcium phosphate system. *Biomaterials*. 1989, 10(7), pp.475-480. In: Dorozhkin, S. V. Calcium orthophosphates. *Journal of Materials Science*. 2007, 42(4), pp.1061-1095.
- [148] Bermudez, O., Boltong, M. G., Driessens, F. C. M. and Planell, J. A. Development of an octacalcium phosphate cement. *Journal of Materials Science: Materials in Medicine*. 1994, 5(3), p.67. In: Dorozhkin, S. V. Calcium orthophosphates. *Journal of Materials Science*. 2007, 42(4), pp.1061-1095.
- [149] Huan, Z. and Chang, J. Novel bioactive composite bone cements based on the β – tricalcium phosphate – monocalcium phosphate monohydrate composite cement system. *Acta Biomaterialia*. 2009, 5(4), pp.1253-1264. In: Dorozhkin, S. V. Calcium orthophosphates in nature, biology and medicine. *Materials*. 2009, 2(2), pp.399-498.
- [150] Roveri, N., Foresti, E., Lelli, M. and Lesci, I. G. Recent advancements in preventing teeth health hazard: The daily use of hydroxyapatite instead of fluoride. *Recent Patents on Biomedical Engineering*. 2009, 2(3), pp.197-215. In: Dorozhkin, S. V. Calcium orthophosphates in dentistry. *Journal of Materials Science: Materials in Medicine*. 2013, 24(6), pp.1335-1363.
- [151] Budavari, S., O'neil, M. J., Smith, A., Heckelman, P. E., Kinneary, J. F. *The Merck Index: An encyclopedia of chemicals, drugs, and biologicals*. Twelfth edition. London: Chapman & Hall, 1996. In: Dorozhkin, S. V. Calcium orthophosphates. *Journal of Materials Science*. 2007, 42(4), pp.1061-1095.

[152] Stein, H. H., Kadzere, C. T., Kim, S. W. and Miller, P. S. Influence of dietary phosphorus concentration on the digestibility of phosphorus in monocalcium phosphate by growing pigs. *Journal of Animal Science*. 2008, 86(8), pp1861-1867. In: Dorozhkin, S. V. Calcium orthophosphates in nature, biology and medicine. *Materials*. 2009, 2(2), pp.399-498.

[153] Joseph, K. C., Parekh, B. B. and Joshi, M. J. Inhibition of growth of urinary type calcium hydrogen phosphate dihydrate crystals by tartaric acid and tamarind. *Current Science*. 2005, 88(8), p.1232. In: Rajendran, K. and Keefe, C. D. Growth and characterization of calcium hydrogen phosphate dihydrate crystals from single diffusion gel technique. *Crystal Research and Technology*. 2010, 45(9), pp.939-945.

[154] Legeros, R. Z. Biological and synthetic apatites. 1994. In: Brown, P. W. and Constantz, B. *Hydroxyapatite and related materials*. Boca Raton: CRC Press, pp.3-28. In: Dorozhkin, S. V. Calcium orthophosphates. *Journal of Materials Science*. 2007, 42(4), pp.1061-1095.

[155] LeGeros, R. Z. *Calcium phosphates in oral biology and medicine*. Basel: Karger, 1991. In: Dorozhkin, S. V. Calcium orthophosphates in nature, biology and medicine. *Materials*. 2009, 2(2), pp.399-498.

[156] LeGeros, R. Z. *Calcium phosphates in oral biology and medicine*. Basel: Karger, 1991. In: Dorozhkin, S. V. Calcium orthophosphates: Occurrence, properties, biomineralization, pathological calcification and biomimetic applications. *Biomatter*. 2011, 1(2), pp.121-164.

[157] Hesse, A. and Heimbach, D. Causes of phosphate stone formation and the importance of metaphylaxis by urinary acidification: A review. *World*

Journal of Urology. 1999, 17(5), pp.308-315. In: Dorozhkin, S. V. Calcium orthophosphates. *Journal of Materials Science*. 2007, 42(4), pp.1061-1095.

[158] Takagi, S., Chow, L. C. and Ishikawa, K. Formation of hydroxyapatite in new calcium phosphate cements. *Biomaterials*. 1998, 19(17), pp.1593-1599. In: Dorozhkin, S. V. Calcium orthophosphates. *Journal of Materials Science*. 2007, 42(4), pp.1061-1095.

[159] Takagi, S., Chow, L. C. and Ishikawa, K. Formation of hydroxyapatite in new calcium phosphate cements. *Biomaterials*. 1998, 19(17), pp.1593-1599. In: Dorozhkin, S. V. Calcium orthophosphates in nature, biology and medicine. *Materials*. 2009, 2(2), pp.399-498.

[160] Takagi, S., Chow, L. C. and Ishikawa, K. Formation of hydroxyapatite in new calcium phosphate cements. *Biomaterials*. 1998, 19(17), pp.1593-1599. In: Dorozhkin, S. V. Calcium orthophosphates: Occurrence, properties, biomineralization, pathological calcification and biomimetic applications. *Biomatter*. 2011, 1(2), pp.121-164.

[161] Crall, J. J. and Bjerga, J. M. Effects of DCPD / APF application and prolonged exposure to fluoride on caries – like lesion formation in vitro. *Journal of Oral Pathology*. 1987, 16(10), pp.488-491. In: Dorozhkin, S. V. Calcium orthophosphates in nature, biology and medicine. *Materials*. 2009, 2(2), pp.399-498.

[162] Budavari, S., O'neil, M. J., Smith, A., Heckelman, P. E., Kinneary, J. F. *The Merck Index: An encyclopedia of chemicals, drugs, and biologicals*. Twelfth edition. London: Chapman & Hall, 1996. In: Dorozhkin, S. V. Calcium orthophosphates: Occurrence, properties, biomineralization,

pathological calcification and biomimetic applications. *Biomatter*. 2011, 1(2), pp.121-164.

[163] Budavari, S., O'neil, M. J., Smith, A., Heckelman, P. E., Kinneary, J. F. *The Merck Index: An encyclopedia of chemicals, drugs, and biologicals*. Twelfth edition. London: Chapman & Hall, 1996. In: Dorozhkin, S. V. Calcium orthophosphates in nature, biology and medicine. *Materials*. 2009, 2(2), pp.399-498.

[164] Chow, L. C. and Brown, W. E. An approach to remineralisation via saliva. In: *foods, nutrition and dental health, 10-12 October 1979, Chicago*. Chicago: American Dental Association Health Foundation. 1982, pp.217-222. In: Dorozhkin, S. V. Calcium orthophosphates. *Journal of Materials Science*. 2007, 42(4), pp.1061-1095.

[165] Joshi, V. S. and Joshi, M. J. FTIR spectroscopic, thermal and growth morphological studies of calcium hydrogen phosphate dihydrate crystals. *Crystal Research and Technology*. 2003, 38(9), p.817. In: Rajendran, K. and Keefe, C. D. Growth and characterization of calcium hydrogen phosphate dihydrate crystals from single diffusion gel technique. *Crystal Research and Technology*. 2010, 45(9), pp.939-945.

[166] Rajendran, K. and Keefe, C. D. Growth and characterization of calcium hydrogen phosphate dihydrate crystals from single diffusion gel technique. *Crystal Research and Technology*. 2010, 45(9), pp.939-945.

[167] Arsic, J., Kaminski, D., Poodt, P. and Vlieg, E. Liquid ordering at the brushite-{010}-water interface. *Physical Review B*. 2004, 69(24), p.245406. In: Dorozhkin, S. V. Calcium orthophosphates in nature, biology and medicine. *Materials*. 2009, 2(2), pp.399-498.

- [168] Arsic, J., Kaminski, D., Poodt, P. and Vlieg, E. Liquid ordering at the brushite-{010}-water interface. *Physical Review B*. 2004, 69(24), pp.245406-245410. In: Dorozhkin, S. V. Calcium orthophosphates: Occurrence, properties, biomineralization, pathological calcification and biomimetic applications. *Biomatter*. 2011, 1(2), pp.121-164.
- [169] Xu, H. H. K., Weir, M. D. and Sun, L. Nanocomposites with Ca and PO₄ release: Effects of reinforcement, dicalcium phosphate particle size and silanization. *Dental Materials*. 2007, 23(12), pp.1482-1491. In: Dorozhkin, S. V. Calcium orthophosphates in dentistry. *Journal of Materials Science: Materials in Medicine*. 2013, 24(6), pp.1335-1363.
- [170] Brown, W. E., Mathew, M. and Tung, M. S. Crystal chemistry of octacalcium phosphate. *Progress in Crystal Growth and Characterization of Materials*. 1981, 4(1-2), p.59. In: Dorozhkin, S. V. Calcium orthophosphates. *Journal of Materials Science*. 2007, 42(4), pp.1061-1095.
- [171] Schroeder, H. E. Formation and inhibition of dental calculus. *Journal of Periodontol*. 1969, 40(11), pp.643-646. In: Dorozhkin, S. V. Calcium orthophosphates. *Journal of Materials Science*. 2007, 42(4), pp.1061-1095.
- [172] LeGeros, R. Z. Variations in the crystalline components of human dental calculus: I. crystallographic and spectroscopic methods of analysis. *Journal of Dental Research*. 1974, 53(1), pp.45-50. In: Dorozhkin, S. V. Calcium orthophosphates in nature, biology and medicine. *Materials*. 2009, 2(2), pp.399-498.
- [173] Chow, L. C. and Eanes, E. D. *Octacalcium phosphate*. Basel: Karger, 2001, p.167. In: Dorozhkin, S. V. Calcium orthophosphates: Occurrence,

properties, biomineralization, pathological calcification and biomimetic applications. *Biomatter*. 2011, 1(2), pp.121-164.

[174] Brown, W. E. Octacalcium phosphate and hydroxyapatite: Crystal structure of octacalcium phosphate. *Nature*. 1962, 196(4859), pp.1048-1050. In: Dorozhkin, S. V. Calcium orthophosphates. *Journal of Materials Science*. 2007, 42(4), pp.1061-1095.

[175] Brown, W. E. Crystal growth of bone mineral. *Clinical Orthopaedics and Related Research*. 1966, 44, pp.205-220. In: Dorozhkin, S. V. Calcium orthophosphates. *Journal of Materials Science*. 2007, 42(4), pp.1061-1095.

[176] Brown, W. E. Octacalcium phosphate and hydroxyapatite: Crystal structure of octacalcium phosphate. *Nature*. 1962, 196(4859), pp.1048-1050. In: Dorozhkin, S. V. Calcium orthophosphates in nature, biology and medicine. *Materials*. 2009, 2(2), pp.399-498.

[177] Brown, W. E. Crystal growth of bone mineral. *Clinical Orthopaedics and Related Research*. 1966, 44, pp.205-220. In: Dorozhkin, S. V. Calcium orthophosphates in nature, biology and medicine. *Materials*. 2009, 2(2), pp.399-498.

[178] Brown, W. E. Octacalcium phosphate and hydroxyapatite: Crystal structure of octacalcium phosphate. *Nature*. 1962, 196(4859), pp.1048-1050. In: Dorozhkin, S. V. Calcium orthophosphates: Occurrence, properties, biomineralization, pathological calcification and biomimetic applications. *Biomatter*. 2011, 1(2), pp.121-164.

[179] Brown, W. E. Crystal growth of bone mineral. *Clinical Orthopaedics and Related Research*. 1966, 44, pp.205-220. In: Dorozhkin, S. V. Calcium

orthophosphates: Occurrence, properties, biomineralization, pathological calcification and biomimetic applications. *Biomatter*. 2011, 1(2), pp.121-164.

[180] Tomazic, B. B., Brown, W. E and Shoen, F. J. Physicochemical properties of calcific deposits isolated from porcine bioprosthetic heart valves removed from patients following 2-13 years function. *Journal of Biomedical Materials Research*. 1994, 28(1), pp.35-47. In: Dorozhkin, S. V. Calcium orthophosphates. *Journal of Materials Science*. 2007, 42(4), pp.1061-1095.

[181] Tomazic, B. B., Brown, W. E and Shoen, F. J. Physicochemical properties of calcific deposits isolated from porcine bioprosthetic heart valves removed from patients following 2-13 years function. *Journal of Biomedical Materials Research*. 1994, 28(1), pp.35-47. In: Dorozhkin, S. V. Calcium orthophosphates in nature, biology and medicine. *Materials*. 2009, 2(2), pp.399-498.

[182] Tomazic, B. B., Brown, W. E and Shoen, F. J. Physicochemical properties of calcific deposits isolated from porcine bioprosthetic heart valves removed from patients following 2-13 years function. *Journal of Biomedical Materials Research*. 1994, 28(1), pp.35-47. In: Dorozhkin, S. V. Calcium orthophosphates: Occurrence, properties, biomineralization, pathological calcification and biomimetic applications. *Biomatter*. 2011, 1(2), pp.121-164.

[183] Stefanic, M., Krnel, K., Pribosic, I. and Kosmac, T. Rapid biomimetic deposition of octacalcium phosphate coatings on zirconia ceramics (Y-TZP) for dental implant applications. *Applied Surface Science*. 2012, 258(10), pp.4649-4656. In: Dorozhkin, S. V. Calcium orthophosphates in dentistry.

Journal of Materials Science: Materials in Medicine. 2013, 24(6), pp.1335-1363.

[184] Miura, K., Matsui, K., Kawai, T., Kato, Y., Matsui, A., Suzuki, O., Kamakura, S. and Echigo, S. Octacalcium phosphate collagen composites with titanium mesh facilitate alveolar augmentation in canine mandibular bone defects. *International Journal of Oral and Maxillofacial Surgery*. 2012, 41(9), pp.1161-1169. In: Dorozhkin, S. V. Calcium orthophosphates in dentistry. *Journal of Materials Science: Materials in Medicine*. 2013, 24(6), pp.1335-1363.

[185] Kamakura, S., Sasano, Y., Homma, H., Suzuki, O., Kagayama, M. and Motegi, K. Implantation of octacalcium phosphate nucleates isolated bone formation in rat skull defects. *Oral Diseases*. 2001, 7(4), pp.259-265. In: Dorozhkin, S. V. Calcium orthophosphates. *Journal of Materials Science*. 2007, 42(4), pp.1061-1095.

[186] Kamakura, S., Sasano, Y., Homma, H., Suzuki, O., Kagayama, M. and Motegi, K. Implantation of octacalcium phosphate nucleates isolated bone formation in rat skull defects. *Oral Diseases*. 2001, 7(4), pp.259-265. In: Dorozhkin, S. V. Calcium orthophosphates in nature, biology and medicine. *Materials*. 2009, 2(2), pp.399-498.

[187] Kamakura, S., Sasano, Y., Homma, H., Suzuki, O., Kagayama, M. and Motegi, K. Implantation of octacalcium phosphate nucleates isolated bone formation in rat skull defects. *Oral Diseases*. 2001, 7(4), pp.259-265. In: Dorozhkin, S. V. Calcium orthophosphates: Occurrence, properties, biomineralization, pathological calcification and biomimetic applications. *Biomatter*. 2011, 1(2), pp.121-164.

[188] Albee, F. H. Studies in bone growth: Triple calcium phosphate as stimulus to osteogenesis. *Annals of Surgery*. 1920, 71(1), pp.32-39. In: Dorozhkin, S. V. Bioceramics of calcium orthophosphates. *Biomaterials*. 2010, 31(7), pp.1465-1485.

[189] Nery, E. B., Lynch, K. L., Hirthe, W. M. and Mueller, K. H. Bioceramic implants in surgically produced infrabony defects. *Journal of Periodontol*. 1975, 46(6), pp.328-347. In: Dorozhkin, S. V. Bioceramics of calcium orthophosphates. *Biomaterials*. 2010, 31(7), pp.1465-1485.

[190] Daculsi, G., LeGeros, R. Z., Nery, E., Lynch, K. and Kerebel, B. Transformation of biphasic calcium phosphate ceramics in vivo: Ultrastructural and physicochemical characterization. *Journal of Biomedical Materials Research*. 1989, 23(8), p.883. In: Dorozhkin, S. V. Calcium orthophosphates. *Journal of Materials Science*. 2007, 42(4), pp.1061-1095.

[191] Mirtchi, A. A., Lemaitre, J. and Munting, E. Calcium phosphate cements: Study of the β – tricalcium phosphate – dicalcium phosphate – calcite cements. *Biomaterials*. 1990, 11(2), pp.83-88. In: Dorozhkin, S. V. Calcium orthophosphates in nature, biology and medicine. *Materials*. 2009, 2(2), pp.399-498.

[192] Ohura, K., Bohner, M., Hardouin, P., Lemaitre, J., Pasquier, G. and Flautre, B. Resorption of, and bone formation from, new β – tricalcium phosphate – monocalcium phosphate cements: An in vivo study. *Journal of Biomedical Materials Research*. 1996, 30(2), pp.193-200. In: Dorozhkin, S. V. Calcium orthophosphates: Occurrence, properties, biomineralization, pathological calcification and biomimetic applications. *Biomatter*. 2011, 1(2), pp.121-164.

[193] Metsger, D. S., Driskell, T. D. and Paulsrud, J. R. Tricalcium phosphate ceramic--a resorbable bone implant: review and current status. *Journal of the American Dental Association*. 1982, 105(6), p.1035. In: Dorozhkin, S. V. Calcium orthophosphates. *Journal of Materials Science*. 2007, 42(4), pp.1061-1095.

[194] Lecomte, A., Gautier, H., Bouler, J. M., Gouyette, A., Pegon, Y., Daculsi, G. and Merle, C. Biphasic calcium phosphate: A comparative study of interconnected porosity in two ceramics. *Journal of Biomedical Materials Research Part B: Applied Biomaterials*. 2008, 84(1), pp.1-6. In: Dorozhkin, S. V. Calcium orthophosphates in nature, biology and medicine. *Materials*. 2009, 2(2), pp.399-498.

[195] Hou, X. J., Mao, K. Y. and Chen, D. F. Bone formation performance of beta – tricalcium phosphate sintered bone. *Journal of Clinical Rehabilitative Tissue Engineering*. 2008, 12(49), pp.9627-9630. In: Dorozhkin, S. V. Calcium orthophosphates: Occurrence, properties, biomineralization, pathological calcification and biomimetic applications. *Biomatter*. 2011, 1(2), pp.121-164.

[196] Sayer, M., Stratilatov, A. D., Reid, J. W., Calderin, L., Stott, M. J., Yin, X., MacKenzie, M., Smith, T. J. N., Hendry, J. A. and Langstaff, S. D. Structure and composition of silicon – stabilized tricalcium phosphate. *Biomaterials*. 2003, 24(3), pp.369-382. In: Dorozhkin, S. V. Calcium orthophosphates in nature, biology and medicine. *Materials*. 2009, 2(2), pp.399-498.

[197] Sayer, M., Stratilatov, A. D., Reid, J. W., Calderin, L., Stott, M. J., Yin, X., MacKenzie, M., Smith, T. J. N., Hendry, J. A. and Langstaff, S. D.

Structure and composition of silicon – stabilized tricalcium phosphate.

Biomaterials. 2003, 24(3), pp.369-382. In: Dorozhkin, S. V. Calcium orthophosphates: Occurrence, properties, biomineralization, pathological calcification and biomimetic applications. *Biomatter*. 2011, 1(2), pp.121-164.

[198] Nery, E. B., Lynch, K. L. and Rooney, G. E. Alveolar ridge augmentation with tricalcium phosphate ceramic. *Journal of Prosthetic Dentistry*. 1978, 40(6), pp.668-675. In: Dorozhkin, S. V. Calcium orthophosphates in dentistry. *Journal of Materials Science: Materials in Medicine*. 2013, 24(6), pp.1335-1363.

[199] Niwa, K., Ogawa, K., Miyazawa, K., Aoki, T., Kawai, T. and Goto, S. Application of alpha – tricalcium phosphate coatings on titanium subperiosteal orthodontic implants reduces the time for absolute anchorage: A study using rabbit femora. *Dental Materials Journal*. 2009, 28(4), pp.477-486. In: Dorozhkin, S. V. Calcium orthophosphates in dentistry. *Journal of Materials Science: Materials in Medicine*. 2013, 24(6), pp.1335-1363.

[200] Bilginer, S., Esener, T., Soylemezoglu, F. and Tiftik, A. M. The investigation of biocompatibility and apical microleakage of tricalcium phosphate based root canal sealers. *Journal of Endodontics*. 1997, 23(2), pp.105-109. In: Dorozhkin, S. V. Calcium orthophosphates in dentistry. *Journal of Materials Science: Materials in Medicine*. 2013, 24(6), pp.1335-1363.

[201] Elliot, J. C. *Structure and chemistry of the apatites and other calcium orthophosphates*. Amsterdam: Elsevier. 1994. In: Dorozhkin, S. V. Calcium orthophosphates in nature, biology and medicine. *Materials*. 2009, 2(2), pp.399-498.

- [202] Elliot, J. C. *Structure and chemistry of the apatites and other calcium orthophosphates*. Amsterdam: Elsevier. 1994. In: Dorozhkin, S. V. Calcium orthophosphates: Occurrence, properties, biomineralization, pathological calcification and biomimetic applications. *Biomatter*. 2011, 1(2), pp.121-164.
- [203] Dickens-Venz, S. H., Takagi, S., Chow, L. C., Bowen, R. L., Johnston, A. D. and Dickens, B. Physical and chemical properties of resin – reinforced calcium phosphate cements. *Dental Materials*. 1994, 10(2), pp.100-106. In: Dorozhkin, S. V. Calcium orthophosphates in dentistry. *Journal of Materials Science: Materials in Medicine*. 2013, 24(6), pp.1335-1363.
- [204] Driessens, F. C. M., Boltong, M. G., Bermudez, O., Planell, J. A., Ginebra, M. P. and Fernandez, E. Effective formulations for the preparation of calcium phosphate bone cements. *Journal of Materials Science: Materials in Medicine*. 1994, 5(3), p.164. In: Dorozhkin, S. V. Calcium orthophosphates. *Journal of Materials Science*. 2007, 42(4), pp.1061-1095.
- [205] Fernandez, E., Gil, F. J., Ginebra, M. P., Driessens, F. C. M., Planell, J. A. and Best, S. M. Calcium phosphate bone cements for clinical applications. Part I: Solution chemistry. *Journal of Materials Science: Materials in Medicine*. 1999, 10(3), pp169-176. In: Dorozhkin, S. V. Calcium orthophosphates in nature, biology and medicine. *Materials*. 2009, 2(2), pp.399-498.
- [206] Fernandez, E., Gil, F. J., Ginebra, M. P., Driessens, F. C. M., Planell, J. A. and Best, S. M. Calcium phosphate bone cements for clinical applications. Part I: Solution chemistry. *Journal of Materials Science: Materials in Medicine*. 1999, 10(3), pp169-176. In: Dorozhkin, S. V. Calcium

orthophosphates: Occurrence, properties, biomineralization, pathological calcification and biomimetic applications. *Biomatter*. 2011, 1(2), pp.121-164.

[207] Yoshikawa, M., Hayami, S., Tsuji, I. and Toda, T. Histopathological study of a newly developed root canal sealer containing tetracalcium – dicalcium phosphates and 1.0 % chondroitin sulfate. *Journal of Endodontics*. 1997, 23(3), pp.162-166. In: Dorozhkin, S. V. Calcium orthophosphates in dentistry. *Journal of Materials Science: Materials in Medicine*. 2013, 24(6), pp.1335-1363.

[208] Eanes, E. D., Termine, J. D. and Nysten, M. U. An electron microscopic study of the formation of amorphous calcium phosphate and its transformation to crystalline apatite. *Calcified tissue research*. 1973, 12(2), p.143. In: Dorozhkin, S. V. Calcium orthophosphates. *Journal of Materials Science*. 2007, 42(4), pp.1061-1095.

[209] Eanes, E. D., Termine, J. D. and Nysten, M. U. An electron microscopic study of the formation of amorphous calcium phosphate and its transformation to crystalline apatite. *Calcified tissue research*. 1973, 12(2), pp.143.-158. In: Dorozhkin, S. V. Calcium orthophosphates in nature, biology and medicine. *Materials*. 2009, 2(2), pp.399-498.

[210] Eanes, E. D., Termine, J. D. and Nysten, M. U. An electron microscopic study of the formation of amorphous calcium phosphate and its transformation to crystalline apatite. *Calcified tissue research*. 1973, 12(2), pp.143.-158. In: Dorozhkin, S. V. Calcium orthophosphates: Occurrence, properties, biomineralization, pathological calcification and biomimetic applications. *Biomatter*. 2011, 1(2), pp.121-164.

- [211] Keller, L. and Dollase, W. A. X – ray determination of crystalline hydroxyapatite to amorphous calcium – phosphate ratio in plasma sprayed coatings. *Journal of Biomedical Materials Research*. 2000, 49(2), pp.244-249. In: Dorozhkin, S. V. Calcium orthophosphates: Occurrence, properties, biomineralization, pathological calcification and biomimetic applications. *Biomatter*. 2011, 1(2), pp.121-164.
- [212] Onuma, K. and Ito, A. Cluster growth model for hydroxyapatite. *Chemistry of Materials*. 1998, 10(11), p.3346. In: Dorozhkin, S. V. Calcium orthophosphates. *Journal of Materials Science*. 2007, 42(4), pp.1061-1095.
- [213] Onuma, K. and Ito, A. Cluster growth model for hydroxyapatite. *Chemistry of Materials*. 1998, 10(11), pp.3346-3351. In: Dorozhkin, S. V. Calcium orthophosphates in nature, biology and medicine. *Materials*. 2009, 2(2), pp.399-498.
- [214] Onuma, K. and Ito, A. Cluster growth model for hydroxyapatite. *Chemistry of Materials*. 1998, 10(11), pp.3346-3351. In: Dorozhkin, S. V. Calcium orthophosphates: Occurrence, properties, biomineralization, pathological calcification and biomimetic applications. *Biomatter*. 2011, 1(2), pp.121-164.
- [215] Tadic, D., Beckmann, F., Schwarz, K. and Epple, M. A novel method to produce hydroxylapatite objects with interconnecting porosity that avoids sintering. *Biomaterials*. 2004, 25(16), pp.3335-3340. In: Dorozhkin, S. V. Bioceramics of calcium orthophosphates. *Biomaterials*. 2010, 31(7), pp.1465-1485.
- [216] Cushnie, E. K., Khan, Y. M. and Laurencin, C. T. Amorphous hydroxyapatite – sintered polymeric scaffolds for bone tissue regeneration:

Physical characterization studies. *Journal of Biomedical Materials Research A*. 2008, 84(1), pp.54-62. In: Dorozhkin, S. V. Bioceramics of calcium orthophosphates. *Biomaterials*. 2010, 31(7), pp.1465-1485.

[217] Dorozhkin, S. V. Amorphous calcium (ortho)phosphates. *Acta Biomaterialia*. 2010, 6(12), pp.4457-4475. In: Dorozhkin, S. V. Calcium orthophosphates: Occurrence, properties, biomineralization, pathological calcification and biomimetic applications. *Biomatter*. 2011, 1(2), pp.121-164.

[218] Skrtic, D., Hailer, A. W., Takagi, S., Antonucci, J. M. and Eanes, E. D. Quantitative assessment of the efficacy of amorphous calcium phosphate / methacrylate composites in remineralizing caries – like lesions artificially produced in bovine enamel. *Journal of Dental Research*. 1996, 75(9), p.1679. In: Dorozhkin, S. V. Calcium orthophosphates. *Journal of Materials Science*. 2007, 42(4), pp.1061-1095.

[219] Skrtic, D., Hailer, A. W., Takagi, S., Antonucci, J. M. and Eanes, E. D. Quantitative assessment of the efficacy of amorphous calcium phosphate / methacrylate composites in remineralizing caries – like lesions artificially produced in bovine enamel. *Journal of Dental Research*. 1996, 75(9), p.1679. In: Dorozhkin, S. V. Calcium orthophosphates in nature, biology and medicine. *Materials*. 2009, 2(2), pp.399-498.

[220] Skrtic, D., Hailer, A. W., Takagi, S., Antonucci, J. M. and Eanes, E. D. Quantitative assessment of the efficacy of amorphous calcium phosphate / methacrylate composites in remineralizing caries – like lesions artificially produced in bovine enamel. *Journal of Dental Research*. 1996, 75(9), p.1679. In: Dorozhkin, S. V. Calcium orthophosphates: Occurrence,

properties, biomineralization, pathological calcification and biomimetic applications. *Biomatter*. 2011, 1(2), pp.121-164.

[221] Mathew, M. and Takagi, S. Structures of biological minerals in dental research. *Journal of Research of the National Institute of Standards and Technology*. 2001, 106(6), pp.1035-1044.

[222] Bigi, A., Boanini, E., Capuccini, C. and Gazzano, M. Strontium – substituted hydroxyapatite nanocrystals. *Inorganica Chimica Acta*. 2007, 360(3), pp.1009-1016.

[223] Elliott, J. C. *Structure and chemistry of the apatites and other calcium orthophosphates*. Amsterdam: Elsevier, 1994. In: Bigi, A., Boanini, E., Capuccini, C. and Gazzano, M. Strontium – substituted hydroxyapatite nanocrystals. *Inorganica Chimica Acta*. 2007, 360(3), pp.1009-1016.

[224] Stephenson, P. K., Freeman, M. A., Revell, P. A., Germain, J., Tuke, M. and Pirie, C. J. The effect of hydroxyapatite coating on ingrowth of bone into cavities in an implant. *Journal of Arthroplasty*. 1991, 6(1), pp.51-58.

[225] Elliott, J. C., Mackie, P. E. and Young, R. A. Monoclinic hydroxyapatite. *Science*. 1973, 180(4090), pp.1055-1057. In: Dorozhkin, S. V. Calcium orthophosphates in nature, biology and medicine. *Materials*. 2009, 2(2), pp.399-498.

[226] Elliott, J. C., Mackie, P. E. and Young, R. A. Monoclinic hydroxyapatite. *Science*. 1973, 180(4090), pp.1055-1057. In: Dorozhkin, S. V. Calcium orthophosphates: Occurrence, properties, biomineralization, pathological calcification and biomimetic applications. *Biomatter*. 2011, 1(2), pp.121-164.

[227] Kay, M. I., Young, R. A. and Posner, A. S. Crystal structure of hydroxyapatite. *Nature*. 1964, 204, p.1050. In: Dorozhkin, S. V. Calcium orthophosphates. *Journal of Materials Science*. 2007, 42(4), pp.1061-1095.

[228] Kay, M. I., Young, R. A. and Posner, A. S. Crystal structure of hydroxyapatite. *Nature*. 1964, 204, pp.1050-1052. In: Dorozhkin, S. V. Calcium orthophosphates in nature, biology and medicine. *Materials*. 2009, 2(2), pp.399-498.

[229] Kay, M. I., Young, R. A. and Posner, A. S. Crystal structure of hydroxyapatite. *Nature*. 1964, 204, pp.1050-1052. In: Dorozhkin, S. V. Calcium orthophosphates: Occurrence, properties, biomineralization, pathological calcification and biomimetic applications. *Biomatter*. 2011, 1(2), pp.121-164.

[230] Klawitter, J. J. and Hulbert, S. F. Application of porous ceramics for the attachment of load bearing internal orthopedic applications. *Journal of Biomedical Materials Research*. 1971, 5(6), pp.161-229. In: He, L. H., Standard, O. C., Huang, T. T., Latella, B. A. and Swain, M. V. Mechanical behaviour of porous hydroxyapatite. *Acta Biomaterialia*. 2008, 4(3), pp.577-586.

[231] He, L. H., Standard, O. C., Huang, T. T., Latella, B. A. and Swain, M. V. Mechanical behaviour of porous hydroxyapatite. *Acta Biomaterialia*. 2008, 4(3), pp.577-586.

[232] Linhart, W., Briem, D., Amling, M., Rueger, J. M. and Windolf, J. Mechanical failure of porous hydroxyapatite ceramics 7.5 years after implantation in the proximal tibial. *The trauma surgeon*. 2004, 107(2),

pp.154-157. In: Dorozhkin, S. V. Calcium orthophosphates in nature, biology and medicine. *Materials*. 2009, 2(2), pp.399-498.

[233] Willmann, G. Coating of implants with hydroxyapatite – material connections between bone and metal. *Advanced Engineering Materials*. 1999, 1(2), p.95. In: Dorozhkin, S. V. Calcium orthophosphates. *Journal of Materials Science*. 2007, 42(4), pp.1061-1095.

[234] Willmann, G. Coating of implants with hydroxyapatite – material connections between bone and metal. *Advanced Engineering Materials*. 1999, 1(2), pp.95-105. In: Dorozhkin, S. V. Calcium orthophosphates in nature, biology and medicine. *Materials*. 2009, 2(2), pp.399-498.

[235] Willmann, G. Coating of implants with hydroxyapatite – material connections between bone and metal. *Advanced Engineering Materials*. 1999, 1(2), pp.95-105. In: Dorozhkin, S. V. Calcium orthophosphates: Occurrence, properties, biomineralization, pathological calcification and biomimetic applications. *Biomatter*. 2011, 1(2), pp.121-164.

[236] Nicholson, J. W., Hawkins, S. J. and Smith, J. E. The incorporation of hydroxyapatite into glass – polyalkenoate (“glass-ionomer”) cements: A preliminary study. *Journal of Materials Science: Materials in Medicine*. 1993, 4(4), pp.418-421. In: Dorozhkin, S. V. Calcium orthophosphates in dentistry. *Journal of Materials Science: Materials in Medicine*. 2013, 24(6), pp.1335-1363.

[237] Domingo, C., Arcis, R. W., Macipe, A. L., Osorio, R., Clemente, R. R., Murtra, J., Fanovich, M. A. and Toledano, M. Dental composites reinforced with hydroxyapatite: Mechanical behavior and absorption/elution characteristics. *Journal of Biomedical Materials Research*. 2001, 56(2),

pp.297-305. In: Dorozhkin, S. V. Calcium orthophosphates in dentistry. *Journal of Materials Science: Materials in Medicine*. 2013, 24(6), pp.1335-1363.

[238] Friedman, C. D., Constantino, P. D., Jones, K., Chow, L. C., Pelzer, H. and Sisson, G. Hydroxyapatite cement. II. Obliteration and reconstruction of the cat frontal sinus. *Archives of Otolaryngology Head & Neck Surgery*. 1991, 117(4), pp.385-389. In: Dorozhkin, S. V. Calcium orthophosphates in dentistry. *Journal of Materials Science: Materials in Medicine*. 2013, 24(6), pp.1335-1363.

[239] Heling, L., Heindel, R. and Merin, B. Calcium – fluorapatite. A new material for bone implants. *Journal of Oral Implantology*. 1981, 9(4), p.548. In: Dorozhkin, S. V. Calcium orthophosphates. *Journal of Materials Science*. 2007, 42(4), pp.1061-1095.

[240] Heling, L., Heindel, R. and Merin, B. Calcium – fluorapatite. A new material for bone implants. *Journal of Oral Implantology*. 1981, 9(4), pp.548-555. In: Dorozhkin, S. V. Calcium orthophosphates in nature, biology and medicine. *Materials*. 2009, 2(2), pp.399-498.

[241] Heling, L., Heindel, R. and Merin, B. Calcium – fluorapatite. A new material for bone implants. *Journal of Oral Implantology*. 1981, 9(4), pp.548-555. In: Dorozhkin, S. V. Calcium orthophosphates: Occurrence, properties, biomineralization, pathological calcification and biomimetic applications. *Biomatter*. 2011, 1(2), pp.121-164.

[242] BenAbdeslam, H. B., Ginebra, M. P., Vert, M. and Boudeville, P. Wet or dry mechanochemical synthesis of calcium phosphates? Influence of the water content on DCPD – CaO reaction kinetics. *Acta Biomaterialia*. 2008,

4(2), pp.378-386. In: Dorozhkin, S. V. Calcium orthophosphates in nature, biology and medicine. *Materials*. 2009, 2(2), pp.399-498.

[243] BenAbdeslam, H. B., Ginebra, M. P., Vert, M. and Boudeville, P. Wet or dry mechanochemical synthesis of calcium phosphates? Influence of the water content on DCPD – CaO reaction kinetics. *Acta Biomaterialia*. 2008, 4(2), pp.378-386. In: Dorozhkin, S. V. Calcium orthophosphates: Occurrence, properties, biomineralization, pathological calcification and biomimetic applications. *Biomatter*. 2011, 1(2), pp.121-164.

[244] Yeong, B., Junmin, X. and Wang, J. Mechanochemical synthesis of hydroxyapatite from calcium oxide and brushite. *Journal of the American Ceramic Society*. 2001, 84(2), p.465. In: Dorozhkin, S. V. Calcium orthophosphates. *Journal of Materials Science*. 2007, 42(4), pp.1061-1095.

[245] Yeong, B., Junmin, X. and Wang, J. Mechanochemical synthesis of hydroxyapatite from calcium oxide and brushite. *Journal of the American Ceramic Society*. 2001, 84(2), pp.465-467. In: Dorozhkin, S. V. Calcium orthophosphates in nature, biology and medicine. *Materials*. 2009, 2(2), pp.399-498.

[246] Yeong, B., Junmin, X. and Wang, J. Mechanochemical synthesis of hydroxyapatite from calcium oxide and brushite. *Journal of the American Ceramic Society*. 2001, 84(2), pp.465-467. In: Dorozhkin, S. V. Calcium orthophosphates: Occurrence, properties, biomineralization, pathological calcification and biomimetic applications. *Biomatter*. 2011, 1(2), pp.121-164.

[247] Montero, M. L., Saenz, A., Rodriguez, J. G., Arenas, J. and Castano, V. M. Electrochemical synthesis of nanosized hydroxyapatite. *Journal of*

Materials Sciences. 2006, 41(7), p.2141. In: Dorozhkin, S. V. Calcium orthophosphates. *Journal of Materials Science*. 2007, 42(4), pp.1061-1095.

[248] Angelescu, N., Ungureanu, D. N. and Anghelina, F. V. Synthesis and characterization of hydroxyapatite obtained in different experimental conditions. *The Scientific Bulletin of Valahia University – Materials and Mechanics*. 2011, 6(9), pp.15-18.

[249] Monmaturapoj, N. Nano – size hydroxyapatite powders preparation by wet – chemical precipitation route. *Journal of the Minerals Metals & Materials Society*. 2008, 18(1), pp.15-20.

[250] Garcia, C., Paucar, C., Gaviria, J. and Duran, A. Effect of some physical – chemical variables in the synthesis of hydroxyapatite by the precipitation route. *Key Engineering Materials*. 2005, 17(284-286), pp.47-50.

[251] Vazquez, C. G., Barba, C. P. and Munguia, N. Stoichiometric hydroxyapatite obtained by precipitation and sol gel processes. *Revista Mexicana De Fisica*. 2005, 51(3) pp.284-293.

[252] Ashok, M., Kalkura, S. N., Sundaram, N. M. and Arivuoli, D. Growth and characterization of hydroxyapatite crystals by hydrothermal method. *Journal of Materials Science: Materials in Medicine*. 2007, 18(5), pp.895-898.

[253] Liu, J., Ye, X., Wang, H., Zhu, M., Wang, B. and Yan, H. The influence of pH and temperature on the morphology of hydroxyapatite synthesized by hydrothermal method. *Ceramics International*. 2003, 29(6), pp.629-633.

[254] Agrawal, K., Singh, G., Puri, D. and Prakash, S. Synthesis and characterization of hydroxyapatite powder by sol – gel method for biomedical

application. *Journal of Minerals and Materials Characterization and Engineering*. 2011, 10(8), pp.727-734.

[255] Palanivelu, R. and Rubankumar, A. Synthesis and spectroscopic characterization of hydroxyapatite by sol – gel method. *International Journal of ChemTech Research*. 2013, 5(6), pp.2965-2969.

[256] Brown, P. W. and Martin, R. I. An analysis of hydroxyapatite surface layer formation. *Journal of Physical Chemistry B*. 1999, 103(10), p.1671. In: Dorozhkin, S. V. Calcium orthophosphates. *Journal of Materials Science*. 2007, 42(4), pp.1061-1095.

[257] Brown, P. W. and Martin, R. I. An analysis of hydroxyapatite surface layer formation. *Journal of Physical Chemistry B*. 1999, 103(10), pp.1671-1675. In: Dorozhkin, S. V. Calcium orthophosphates in nature, biology and medicine. *Materials*. 2009, 2(2), pp.399-498.

[258] Brown, P. W. and Martin, R. I. An analysis of hydroxyapatite surface layer formation. *Journal of Physical Chemistry B*. 1999, 103(10), pp.1671-1675. In: Dorozhkin, S. V. Calcium orthophosphates: Occurrence, properties, biomineralization, pathological calcification and biomimetic applications. *Biomatter*. 2011, 1(2), pp.121-164.

[259] Rey, C., Combes, C., Drouet, C. and Sfihi, H. Chemical diversity of apatites. *Advances in Science and Technology*. 2006, 49, pp.27-36. In: Dorozhkin, S. V. Calcium orthophosphates in nature, biology and medicine. *Materials*. 2009, 2(2), pp.399-498.

[260] Rey, C., Combes, C., Drouet, C. and Sfihi, H. Chemical diversity of apatites. *Advances in Science and Technology*. 2006, 49, pp.27-36. In: Dorozhkin, S. V. Calcium orthophosphates: Occurrence, properties,

biomineralization, pathological calcification and biomimetic applications. *Biomatter*. 2011, 1(2), pp.121-164.

[261] Lorenzo, L. R. Studies on calcium deficient apatites structure by means of MAS – NMR spectroscopy. *Journal of Materials Science: Materials in Medicine*. 2005, 16(5), p.393. In: Dorozhkin, S. V. Calcium orthophosphates. *Journal of Materials Science*. 2007, 42(4), pp.1061-1095.

[262] Lorenzo, L. R. Studies on calcium deficient apatites structure by means of MAS – NMR spectroscopy. *Journal of Materials Science: Materials in Medicine*. 2005, 16(5), pp.393-398. In: Dorozhkin, S. V. Calcium orthophosphates in nature, biology and medicine. *Materials*. 2009, 2(2), pp.399-498.

[263] Lorenzo, L. R. Studies on calcium deficient apatites structure by means of MAS – NMR spectroscopy. *Journal of Materials Science: Materials in Medicine*. 2005, 16(5), pp.393-398. In: Dorozhkin, S. V. Calcium orthophosphates: Occurrence, properties, biomineralization, pathological calcification and biomimetic applications. *Biomatter*. 2011, 1(2), pp.121-164.

[264] Tancret, F., Bouler, J. M., Chamousset, J. and Minois, L. M. Modelling the mechanical properties of microporous and macroporous biphasic calcium phosphate bioceramics. *Journal of the European Ceramic Society*. 2006, 26(16), pp.3647-3656. In: Dorozhkin, S. V. Calcium orthophosphates in nature, biology and medicine. *Materials*. 2009, 2(2), pp.399-498.

[265] Lecomte, A., Gautier, H., Bouler, J. M., Gouyette, A., Pegon, Y., Daculsi, G. and Merle, C. Biphasic calcium phosphate: A comparative study of interconnected porosity in two ceramics. *Journal of Biomedical Materials Research Part B: Applied Biomaterials*. 2008, 84(1), pp.1-6. In: Dorozhkin,

S. V. Calcium orthophosphates in nature, biology and medicine. *Materials*. 2009, 2(2), pp.399-498.

[266] Lecomte, A., Gautier, H., Bouler, J. M., Gouyette, A., Pegon, Y., Daculsi, G. and Merle, C. Biphasic calcium phosphate: A comparative study of interconnected porosity in two ceramics. *Journal of Biomedical Materials Research Part B: Applied Biomaterials*. 2008, 84(1), pp.1-6. In: Dorozhkin, S. V. Calcium orthophosphates: Occurrence, properties, biomineralization, pathological calcification and biomimetic applications. *Biomatter*. 2011, 1(2), pp.121-164.

[267] Suchanek, W. L. and Yoshimura, M. Processing and properties of hydroxyapatite based biomaterials for use as hard tissue replacement implants. *Journal of Materials Research*. 1998, 13(1), pp.94-117. In: Dorozhkin, S. V. Bioceramics of calcium orthophosphates. *Biomaterials*. 2010, 31(7), pp.1465-1485.

[268] Haynes, W. H. (ed). *Handbook of chemistry and physics*. Ninety third edition. Boca Raton: CRC Press, 2012.

[269] Mann, S. *Biomineralization: Principles and concepts in bioinorganic materials chemistry*. New York: Oxford University Press, 2001.

[270] Moseke, C. and Gbureck, U. Tetracalcium phosphate: Synthesis, properties and biomedical applications. *Acta Biomaterialia*. 2010, 6(10), pp.3815-3823.

[271] Fernandez, E., Gil, F. J., Ginebra, M. P., Driessens, F. C., Planell, J. A. and Best, S. M. Calcium phosphate bone cements for clinical applications. Part I: Solution chemistry. *Journal of Materials Science: Materials in*

Medicine. 1999, 10(3), p.169. In: Dorozhkin, S. V. Calcium orthophosphates.

Journal of Materials Science. 2007, 42(4), pp.1061-1095.

[272] Fernandez, E., Gil, F. J., Ginebra, M. P., Driessens, F. C., Planell, J. A. and Best, S. M. Calcium phosphate bone cements for clinical applications. Part I: Solution chemistry. *Journal of Materials Science: Materials in Medicine*. 1999, 10(3), pp.169-176. In: Dorozhkin, S. V. Calcium orthophosphates: Occurrence, properties, biomineralization, pathological calcification and biomimetic applications. *Biomatter*. 2011. 1(2), pp.121-164.

[273] Fernandez, E., Gil, F. J., Ginebra, M. P., Driessens, F. C., Planell, J. A. and Best, S. M. Calcium phosphate bone cements for clinical applications. Part I: Solution chemistry. *Journal of Materials Science: Materials in Medicine*. 1999, 10(3), pp.169-176. In: Dorozhkin, S. V. Calcium orthophosphates in nature, biology and medicine. *Materials*. 2009, 2(2), pp.399-498.

[274] McDowell, H., Gregory, T. M. and Brown, W. E. Solubility of $\text{Ca}_5(\text{PO}_4)_3\text{OH}$ in the system $\text{Ca}(\text{OH})_2 - \text{H}_3\text{PO}_4 - \text{H}_2\text{O}$ at 5, 15, 25, and 37 °C. *Journal of Research of the National Bureau of Standards, Section A: Physics and Chemistry*. 1977, 81A(2-3), pp.273-281. In: Dorozhkin, S. V. Calcium orthophosphates in nature, biology and medicine. *Materials*. 2009, 2(2), pp.399-498.

[275] Dorozhkin, S. V. Calcium orthophosphates in nature, biology and medicine. *Materials*. 2009, 2(2), pp.399-498. In: Dorozhkin, S. V. Calcium orthophosphates: Occurrence, properties, biomineralization, pathological calcification and biomimetic applications. *Biomatter*. 2011, 1(2), pp.121-164.

[276] Ohura, K., Bohner, M., Hardouin, P., Lemaitre, J., Pasquier, G. and Flautre, B. Resorption of, and bone formation from, new β – tricalcium phosphate – monocalcium phosphate cements: An in vivo study. *Journal of Biomedical Materials Research*. 1996, 30(2), pp.193-200. In: Dorozhkin, S. V. Calcium orthophosphates: Occurrence, properties, biomineralization, pathological calcification and biomimetic applications. *Biomatter*. 2011, 1(2), pp.121-164.

[277] Lide, D. R. (ed). *The CRC handbook of chemistry and physics*. Eighty sixth edition. Boca Raton: CRC Press, 2005. In: Dorozhkin, S. V. Calcium orthophosphates. *Journal of Materials Science*. 2007, 42(4), pp.1061-1095.

[278] Notholt, A. J. G., Sheldon, R. P. and Davidson, D. F. (eds). *Phosphate deposits of the world*. Second edition. Cambridge: Cambridge University Press, 1989. In: Dorozhkin, S. V. Calcium orthophosphates. *Journal of Materials Science*. 2007, 42(4), pp.1061-1095.

[279] White, T.J. and ZhiLi, D. Structural derivation and crystal chemistry of apatites. *Acta Crystallographica Section B: Structural Science*. 2003, 59(Pt1), pp.1-16. In: Dorozhkin, S. V. Calcium orthophosphates in nature, biology and medicine. *Materials*. 2009, 2(2), pp.399-498.

[280] Mathew, M. and Takagi, S. Structures of biological minerals in dental research. *Journal of Research of the National Institute of Standards and Technology*. 2001, 106(6), pp.1035-1044. In: Dorozhkin, S. V. Calcium orthophosphates in nature, biology and medicine. *Materials*. 2009, 2(2), pp.399-498.

[281] Hughes, J. M. and Rakovan, J. The crystal structure of apatite, $\text{Ca}_5(\text{PO}_4)_3(\text{F},\text{OH},\text{Cl})$. In: Hughes, J. M., Kohn, M. and Rakovan, J. (eds).

Phosphates: Geochemical, geobiological and materials importance. Fourty eighth volume. Washington, D.C.: Mineralogical Society of America. 2002, pp.1-12. In: Dorozhkin, S. V. Calcium orthophosphates in nature, biology and medicine. *Materials*. 2009, 2(2), pp.399-498.

[282] White, T.J. and ZhiLi, D. Structural derivation and crystal chemistry of apatites. *Acta Crystallographica Section B: Structural Science*. 2003, 59(Pt1), pp.1-16. In: Dorozhkin, S. V. Calcium orthophosphates: Occurrence, properties, biomineralization, pathological calcification and biomimetic applications. *Biomatter*. 2011, 1(2), pp.121-164.

[283] Mathew, M. and Takagi, S. Structures of biological minerals in dental research. *Journal of Research of the National Institute of Standards and Technology*. 2001, 106(6), pp.1035-1044. In: Dorozhkin, S. V. Calcium orthophosphates: Occurrence, properties, biomineralization, pathological calcification and biomimetic applications. *Biomatter*. 2011, 1(2), pp.121-164.

[284] Palmer, L. C., Newcomb, C. J., Kaltz, S. R., Spoerke, E. D. and Stupp, S. I. Biomimetic systems for hydroxyapatite mineralization inspired by bone and enamel. *Chemical Reviews*. 2008, 108(11), pp.4754-4783.

[285] Pasteris, J. D., Wopenka, B. and Jones, E. V. Bone and tooth mineralization: Why apatite?. *Elements*. 2008, 4(2), pp.97-104. In: Dorozhkin, S. V. Calcium orthophosphates in nature, biology and medicine. *Materials*. 2009, 2(2), pp.399-498.

[286] Pasteris, J. D., Wopenka, B. and Jones, E. V. Bone and tooth mineralization: Why apatite?. *Elements*. 2008, 4(2), pp.97-104. In: Dorozhkin, S. V. Calcium orthophosphates: Occurrence, properties,

biomineralization, pathological calcification and biomimetic applications.

Biomatter. 2011, 1(2), pp.121-164.

[287] Lowenstam, H. A. and Weiner, S. *On biomineralization*. New York: Oxford University Press, 1989. In: Dorozhkin, S. V. Calcium orthophosphates. *Journal of Materials Science*. 2007, 42(4), pp.1061-1095.

[288] Lowenstam, H. A. and Weiner, S. *On biomineralization*. New York: Oxford University Press, 1989. In: Dorozhkin, S. V. Calcium orthophosphates in nature, biology and medicine. *Materials*. 2009, 2(2), pp.399-498.

[289] LeGeros, R. Properties of osteoconductive biomaterials: Calcium phosphates. *Clinical Orthopaedics and Related Research*. 2002, 395, pp.81-98. In: Milev, A., Kannangara, G. S. K. and Ben-Nissan, B. Morphological stability of hydroxyapatite precursor. *Materials Letters*. 2003, 57(13-14), pp.1960-1965.

[290] Roseberry, H. H., Hastings, A. B. and Morse, J. K. X – ray analysis of bone and teeth. *Journal of Biological Chemistry*. 1931, 90(2), pp.395-407.

[291] Driessens, F. C. M. Physiology of hard tissues in comparison with the solubility of synthetic calcium phosphates. *Annals of the New York Academy of Sciences*. 1988, 523, pp.131-136. In: Dorozhkin, S. V. Calcium orthophosphates. *Journal of Materials Science*. 2007, 42(4), pp.1061-1095.

[292] Palmer, L. C., Newcomb, C. J., Kaltz, S. R., Spoerke, E. D. and Stupp, S. I. Biomimetic systems for hydroxyapatite mineralization inspired by bone and enamel. *Chemical Reviews*. 2008, 108(11), pp.4754-4783. In: Dorozhkin, S. V. Calcium orthophosphates in nature, biology and medicine. *Materials*. 2009, 2(2), pp.399-498.

[293] Palmer, L. C., Newcomb, C. J., Kaltz, S. R., Spoerke, E. D. and Stupp, S. I. Biomimetic systems for hydroxyapatite mineralization inspired by bone and enamel. *Chemical Reviews*. 2008, 108(11), pp.4754-4783. In: Dorozhkin, S. V. Calcium orthophosphates: Occurrence, properties, biomineralization, pathological calcification and biomimetic applications. *Biomatter*. 2011, 1(2), pp.121-164.

[294] Vallet-Regi, M. and Arcos, D. Biomimetic nanoceramics in clinical use: From materials to applications. Cambridge: Royal Society of Chemistry. 2008. In: Dorozhkin, S. V. Calcium orthophosphates. *Journal of Materials Science*. 2007, 42(4), pp.1061-1095.

[295] Vallet-Regi, M. and Arcos, D. *Biomimetic nanoceramics in clinical use: From materials to applications*. Cambridge: Royal Society of Chemistry. 2008. In: Dorozhkin, S. V. Calcium orthophosphates in nature, biology and medicine. *Materials*. 2009, 2(2), pp.399-498.

[296] Vallet-Regi, M. and Arcos, D. *Biomimetic nanoceramics in clinical use: From materials to applications*. Cambridge: Royal Society of Chemistry. 2008. In: Dorozhkin, S. V. Calcium orthophosphates: Occurrence, properties, biomineralization, pathological calcification and biomimetic applications. *Biomatter*. 2011, 1(2), pp.121-164.

[297] Apella, M. C., Venegas, S. C., Rodenas, L. A. G., Blesa, M. A. and Morando, P. J. Synthetic hydroxyapatite as a surface model for dental enamel and dentine. *Journal of the Argentine Chemical Society*. 2009, 97(1), pp.109-118.

- [298] Liao, S., Watari, F., Xu, G., Ngiam, M., Ramakrishna, S. and C. K. Chan. Morphological effects of variant carbonates in biomimetic hydroxyapatite. *Materials Letters*. 2007, 61(17), pp.3624-3628.
- [299] LeGeros, R. Z. *Calcium phosphates in oral biology and medicine*. Basel: Karger, 1991. In: Liao, S., Watari, F., Xu, G., Ngiam, M., Ramakrishna, S. and C. K. Chan. Morphological effects of variant carbonates in biomimetic hydroxyapatite. *Materials Letters*. 2007, 61(17), pp.3624-3628.
- [300] Fleet, M. E. and Liu, X. Coupled substitution of type A and B carbonate in sodium – bearing apatite. *Biomaterials*. 2007, 28(6), pp.916-926.
- [301] Elliot, J. C. Holcomb, D. W. and Young, R. A. Infrared determination of the degree of substitution of hydroxyl by carbonate ions in human dental enamel. *Calcified Tissue International*. 1985, 37(4), pp.372-375. In: Mathew, M. and Takagi, S. Structures of biological minerals in dental research. *Journal of Research of the National Institute of Standards and Technology*. 2001, 106(6), pp.1035-1044.
- [302] Rey, C., Collins, B., Goehl, T., Dickson, I. R. and Glimcher, M. The carbonate environment in bone mineral: A resolution – enhanced Fourier transform infrared spectroscopy study. *Calcified Tissue International*. 1989, 45(3), pp.157-164. In: Ibrahim, D. M., Mostafa, A. A. and Korowash, S. I. Chemical characterization of some substituted hydroxyapatites. *Chemistry Central Journal*. 2011, 5(1), pp.1-11.
- [303] Hanlie, H., Liyun, T. and Tao, J. The crystal characteristics of enamel and dentine by XRD method. *Journal Of Wuhan University Of Technology- Materials Science Edition*. 2006, 21(1), pp.9-12.

[304] Ibrahim, D. M., Mostafa, A. A. and Korowash, S. I. Chemical characterization of some substituted hydroxyapatites. *Chemistry Central Journal*. 2011, 5(1), pp.1-11.

[305] Legeros, R. Z. *Calcium phosphates in oral biology and medicine*. Basel: Karger, 1991. In: Dorozhkin, S. V. Calcium orthophosphates. *Journal of Materials Science*. 2007, 42(4), pp.1061-1095.

[306] Daculsi, G., Bouler, J. M. and Legeros, R. Z. Adaptive crystal formation in normal and pathological calcifications in synthetic calcium phosphate and related biomaterials. *International Review of Cytology*. 1997, 172, p.129. In: Dorozhkin, S. V. Calcium orthophosphates. *Journal of Materials Science*. 2007, 42(4), pp.1061-1095.

[307] Daculsi, G., Bouler, J. M. and Legeros, R. Z. Adaptive crystal formation in normal and pathological calcifications in synthetic calcium phosphate and related biomaterials. *International Review of Cytology*. 1997, 172, pp.129-191. In: Dorozhkin, S. V. Calcium orthophosphates in nature, biology and medicine. *Materials*. 2009, 2(2), pp.399-498.

[308] Clark, N. A. The system $P_2O_5 - CaO - H_2O$ and the recrystallization of monocalcium phosphate. *Journal of Physical Chemistry*. 1931, 35(5), pp.1232-1238. In: Dorozhkin, S. V. Calcium orthophosphates: Occurrence, properties, biomineralization, pathological calcification and biomimetic applications. *Biomatter*. 2011, 1(2), pp.121-164.

[309] Wopenka, B. and Pasteris, J. D. A mineralogical perspective on the apatite in bone. *Materials Science and Engineering C*. 2005, 25(2), pp.131-143.

[310] Penel, G., Leroy, G., Rey, C. and Bres, E. MicroRaman spectral study of the PO₄ and CO₃ vibrational modes in synthetic and biological apatites. *Calcified Tissue International*. 1998, 63(6), p.475. In: Wopenka, B. and Pasteris, J. D. A mineralogical perspective on the apatite in bone. *Materials Science and Engineering C*. 2005, 25(2), pp.131-143.

[311] Schramm, D. U., Terra, J., Rossi, A. M. and Ellis, D. E. Configuration of CO₂ radicals in γ – irradiated A – type carbonated apatites: Theory and experimental EPR and ENDOR studies. *Physical Reviews B*. 2000, 63(2), p.63. In: Wopenka, B. and Pasteris, J. D. A mineralogical perspective on the apatite in bone. *Materials Science and Engineering C*. 2005, 25(2), pp.131-143.

[312] Suetsugu, Y., Takahashi, Y., Okamura, F. P. and Tanaka, J. Structure analysis of A – type carbonate apatite by a single – crystal X – ray diffraction method. *Journal of Solid State Chemistry*. 2000, 155(2), p.292. In: Wopenka, B. and Pasteris, J. D. A mineralogical perspective on the apatite in bone. *Materials Science and Engineering C*. 2005, 25(2), pp.131-143.

[313] Balamurugan, A., Kannan, S. and Rajeswari, S. Bioactive sol – gel hydroxyapatite surface for biomedical applications – in vitro study. *Trends in Biomaterials and Artificial Organs*. 2002, 16(1), pp.18-20.

[314] Yamaguchi, K., Hirano, T., Yoshida, G. and Iwasaki, K. Degradation – resistant character of synthetic hydroxyapatite blocks filled in bone defects. *Biomaterials*. 1995, 16(13), pp.983-985.

[315] Netz, D. J., Sepulveda, P., Pandolfelli, V. C., Spadaro, A. C., Alencastre, J. B., Bentley, M. V. and Marchetti, J. M. Potential use of

gelcasting hydroxyapatite porous ceramic as an implantable drug delivery system. *International Journal of Pharmaceutics*. 2001, 213(1-2), pp.117-125.

[316] Salinas, A. J. and Regi, M. V. Evolution of ceramics with medical applications. *Journal of Inorganic Chemistry*. 2007, 633(11-12), pp.1762-1773. In: Dorozhkin, S. V. Bioceramics of calcium orthophosphates. *Biomaterials*. 2010, 31(7), pp.1465-1485.

[317] Liu, T. Y., Chen, S. Y., Liu, D. M. and Liou, S. C. On the study of BSA – loaded calcium – deficient hydroxyapatite nano – carriers for controlled drug delivery. *Journal of Controlled Release*. 2005, 107(1), p.112. In: Dorozhkin, S. V. Calcium orthophosphates. *Journal of Materials Science*. 2007, 42(4), pp.1061-1095.

[318] Liu, T. Y., Chen, S. Y., Liu, D. M. and Liou, S. C. On the study of BSA – loaded calcium – deficient hydroxyapatite nano – carriers for controlled drug delivery. *Journal of Controlled Release*. 2005, 107(1), pp.112-121. In: Dorozhkin, S. V. Calcium orthophosphates in nature, biology and medicine. *Materials*. 2009, 2(2), pp.399-498.

[319] Salinas, A. J. and Regi, M. V. Evolution of ceramics with medical applications. *Journal of Inorganic Chemistry*. 2007, 633(11-12), pp.1762-1773. In: Dorozhkin, S. V. Calcium orthophosphates in nature, biology and medicine. *Materials*. 2009, 2(2), pp.399-498.

[320] Palazzo, B., Sidoti, M. C., Roveri, N., Tampieri, A., Sandri, M., Bertolazzi, L., Galbuserac, F., Dubinic, G., Venac, P. and Controc, R. Controlled drug delivery from porous hydroxyapatite grafts: An experimental and theoretical approach. *Materials Science and Engineering C*. 2005, 25(2), pp.207-213. In: Dorozhkin, S. V. Calcium orthophosphates: Occurrence,

properties, biomineralization, pathological calcification and biomimetic applications. *Biomatter*. 2011, 1(2), pp.121-164.

[321] Uchida, A., Shinto, Y., Araki, N. and Ono, K. Slow release of anticancer drugs from porous calcium hydroxyapatite ceramic. *Journal of Orthopaedic Research*. 1992, 10(3), pp.440-445. In: Dorozhkin, S. V. Bioceramics of calcium orthophosphates. *Biomaterials*. 2010, 31(7), pp.1465-1485.

[322] Shinto, Y., Uchida, A., Korkusuz, F., Araki, N. and K. Ono. Calcium hydroxyapatite ceramic used as a delivery system for antibiotics. *Journal of bone and joint surgery (British volume)*. 1992, 74(4), pp.600-604. In: Dorozhkin, S. V. Bioceramics of calcium orthophosphates. *Biomaterials*. 2010, 31(7), pp.1465-1485.

[323] Ben-Nissan, B. Natural bioceramics: From coral to bone and beyond. *Current Opinion in Solid State and Materials Science*. 2003, 7(4-5), p.283. In: Dorozhkin, S. V. Calcium orthophosphates. *Journal of Materials Science*. 2007, 42(4), pp.1061-1095.

[324] Salinas, A. J. and Regi, M. V. Evolution of ceramics with medical applications. *Journal of Inorganic Chemistry*. 2007, 633(11-12), pp.1762-1773. In: Dorozhkin, S. V. Calcium orthophosphates: Occurrence, properties, biomineralization, pathological calcification and biomimetic applications. *Biomatter*. 2011, 1(2), pp.121-164.

[325] Boskey, A. L. Assessment of bone mineral and matrix using backscatter electron imaging and FTIR imaging. *Current Osteoporosis Reports*. 2006, 4(2), pp.71-75. In: Dorozhkin, S. V. Calcium orthophosphates in nature, biology and medicine. *Materials*. 2009, 2(2), pp.399-498.

[326] Vallet-Regi, M. and Gonzalez-Calbet, J. M. Calcium phosphates as substitution of bone tissues. *Progress in Solid State Chemistry*. 2004, 32(1-2), pp.1-31. In: Dorozhkin, S. V. Calcium orthophosphates: Occurrence, properties, biomineralization, pathological calcification and biomimetic applications. *Biomatter*. 2011, 1(2), pp.121-164.

[327] Byrappa, K. and Yoshimura, M. *Handbook of hydrothermal technology – A Technology for Crystal Growth and Materials Processing*. New Jersey: Noyse, 2001.

[328] Suchanek, W. L. and Riman, R. E. Hydrothermal synthesis of advanced ceramic powders. In: Vincenzini, P. (ed). *11th International Ceramics Congress, 4-9 June 2006, Sicily*. Zuerich: Trans Tech Publications, 2006, pp.184-193.

[329] West, A. R. *Solid state chemistry and its applications*. Second edition. Chichester: John Wiley & Sons, Inc., 2014.

[330] Bianco, A., Cacciotti, I., Lombardi, M. and Montanaro, L. Thermal stability and sintering behavior of hydroxyapatite nanopowders. *Journal of Thermal Analysis & Calorimetry*. 2007, 88(1), pp.237-243. In: Salma, K., Cimdina, L. B. and Borodajenko, N. Calcium phosphate bioceramics prepared from wet chemically precipitated powders. *Processing and Application of Ceramics*. 2010, 4(1), pp.45-51.

[331] Salma, K., Cimdina, L. B. and Borodajenko, N. Calcium phosphate bioceramics prepared from wet chemically precipitated powders. *Processing and Application of Ceramics*. 2010, 4(1), pp.45-51.

- [332] Yoruc, A. B. H. and Koca, Y. Double step stirring: A novel method for precipitation of nano – sized hydroxyapatite powder. *Digest Journal of Nanomaterials and Biostructures*. 2009, 4(1), pp.73-81.
- [333] Hamilton, J. *Synthesis and characterization of nano particles hydroxyapatite by precipitation method for tissue engineering*. Ph.D. thesis, University of Leeds, 2003.
- [334] Pang, Y. X. and Bao, X. Influence of temperature, ripening time and calcination on the morphology and crystallinity of hydroxyapatite nanoparticles. *Journal of the European Ceramic Society*. 2003, 23(10), pp.1697-1704.
- [335] Jarcho, M., Bolen, C. H., Thomas, M. B., Bobick, J., Kay, J. F. and Doremus, R. H. Hydroxyapatite synthesis and characterization in dense polycrystalline form. *Journal of Materials Science*. 1976, 11(11), pp.2027-2035. In: Monmaturapoj, N. Nano – size hydroxyapatite powders preparation by wet – chemical precipitation route. *Journal of the Minerals Metals & Materials Society*. 2008, 18(1), pp.15-20.
- [336] Morales, J. G., Burgues, J. T., Boix, T., Fraile, J. and Clemente, R. R. Precipitation of stoichiometric hydroxyapatite by a continuous method. *Crystal Research and Technology*. 2001, 36(1), pp.15-26.
- [337] Cao, L., Zhang, C. and Huang, J. Synthesis of hydroxyapatite nanoparticles in ultrasonic precipitation. *Ceramics International*. 2005, 31(8), pp.1041-1044. In: Monmaturapoj, N. Nano – size hydroxyapatite powders preparation by wet – chemical precipitation route. *Journal of the Minerals Metals & Materials Society*. 2008, 18(1), pp.15-20.

[338] Kong, L. B., Ma, J. and Boey, F. Nanosized hydroxyapatite powders derived from coprecipitation process. *Journal of Materials Science*. 2002, 37(6), pp.1131-1134. In: Monmaturapoj, N. Nano – size hydroxyapatite powders preparation by wet – chemical precipitation route. *Journal of the Minerals Metals & Materials Society*. 2008, 18(1), pp.15-20.

[339] Suchanek, W. and Yoshimura, M. Processing and properties of hydroxyapatite – based biomaterials for use as hard tissue replacement implants. *Journal of Materials Science*. 1998, 13(1), p.94. In: Vallet-Regi, M. and Arcos, D. *Biomimetic nanoceramics in clinical use: From materials to applications*. Cambridge: Royal Society of Chemistry, 2008.

[340] Narasaraju, T. S. and Phebe, D. E. Some physico – chemical aspects of hydroxyapatite. *Journal of Materials Science*. 1996, 31(1), p.1. In: Vallet-Regi, M. and Arcos, D. *Biomimetic nanoceramics in clinical use: From materials to applications*. Cambridge: Royal Society of Chemistry, 2008.

[341] Ferraz, M. P., Monteiro, F. J. and Manuel, C. M. Hydroxyapatite nanoparticles: A review of preparation methodologies. *Journal of Applied Biomaterials and Biomechanics*. 2004, 2(2), pp.74-80.

[342] Nayak, A. K. Hydroxyapatite synthesis methodologies: An overview. *International Journal of ChemTech Research*. 2010, 2(2), pp.903-907.

[343] Manuel, C. M., Ferraz, M. P. and Monteiro, F. J. Synthesis of hydroxyapatite and tricalcium phosphate nanoparticles – preliminary studies. *Key Engineering Materials*. 2003, 240-242, pp.555-558.

[344] Manuel, C. M., Ferraz, M. P. and Monteiro, F. J. Synthesis of hydroxyapatite and tricalcium phosphate nanoparticles – preliminary studies. *Key Engineering Materials*. 2003, 240-242, pp.555-558. In: Nayak, A. K.

Hydroxyapatite synthesis methodologies: An overview. *International Journal of ChemTech Research*. 2010, 2(2), pp.903-907.

[345] Santos, M. H., Oliveira, M., Souza, P. F., Mansur, H. S. and Vasconcelos, W. L. Synthesis control and characterization of hydroxyapatite prepared by wet precipitation process. *Materials Research*. 2004, 7(4), pp.625-630. In: Nayak, A. K. Hydroxyapatite synthesis methodologies: An overview. *International Journal of ChemTech Research*. 2010, 2(2), pp.903-907.

[346] Webster, T. J., Ergun, C., Doremus, R. H., Siegel, R. W., and Bizios, R. Enhanced functions of osteoblasts on nanophase ceramics. *Biomaterials*. 2000, 21(17), pp.1803-1810.

[347] Webster, T. J., Ergun, C., Doremus, R. H., Siegel, R. W., and Bizios, R. Enhanced functions of osteoblasts on nanophase ceramics. *Biomaterials*. 2000, 21(17), pp.1803-1810. In: Nayak, A. K. Hydroxyapatite synthesis methodologies: An overview. *International Journal of ChemTech Research*. 2010, 2(2), pp.903-907.

[348] Ferraz, M. P., Monteiro, F. J. and Manuel, C. M. Hydroxyapatite nanoparticles: A review of preparation methodologies. *Journal of Applied Biomaterials and Biomechanics*. 2004, 2(2), pp.74-80. In: Nayak, A. K. Hydroxyapatite synthesis methodologies: An overview. *International Journal of ChemTech Research*. 2010, 2(2), pp.903-907.

[349] Tas, A. C. Synthesis of biomimetic Ca-hydroxyapatite powders at 37 degrees C in synthetic body fluids. *Biomaterials*. 2000, 21(14), pp.1429-1438.

- [350] Thamaraiselvi, T. V., Prabakaran, K. and Rajeswari, S. Synthesis of hydroxyapatite that mimic bone mineralogy. *Trends in Biomaterials and Artificial Organs*. 2006, 19(2), pp.81-83.
- [351] Janackovic, D., Prelevic, I. P., Gvozdenovic, L. K., Petrovic, R., Jokanovic, V. and Uskokovic, D. Influence of synthesis parameters on the particle sizes of nanostructured calcium – hydroxyapatite. *Key Engineering Materials*. 2001, 192(5), pp.203-206.
- [352] Janackovic, D., Prelevic, I. P., Gvozdenovic, L. K., Petrovic, R., Jokanovic, V. and Uskokovic, D. Influence of synthesis parameters on the particle sizes of nanostructured calcium – hydroxyapatite. *Key Engineering Materials*. 2001, 192(5), pp.203-206. In: Nayak, A. K. Hydroxyapatite synthesis methodologies: An overview. *International Journal of ChemTech Research*. 2010, 2(2), pp.903-907.
- [353] Brinker, C. J. and Scherer, G. W. *Sol – gel Science: The physics and chemistry of sol – gel processing*. Boston: Academic Press, 1990. pp.787. In: Agrawal, K., Singh, G., Puri, D. and Prakash, S. Synthesis and characterization of hydroxyapatite powder by sol – gel method for biomedical application. *Journal of Minerals and Materials Characterization and Engineering*. 2011, 10(8), pp.727-734.
- [354] Kumar, R., Prakash, K. H., Cheang, P. and Khor, K .A. Temperature driven morphological changes of chemically precipitated hydroxyapatite nanoparticles. *Langmuir*. 2004, 20(13), pp.5196-5200. In: Palanivelu, R. and Rubankumar, A. Synthesis and spectroscopic characterization of hydroxyapatite by sol – gel method. *International Journal of ChemTech Research*. 2013, 5(6), pp.2965-2969.

[355] Weng, W. and Baptista, J. L. Alkoxide route for preparing hydroxyapatite and its coatings. *Biomaterials*. 1998, 19(1-3), pp.125-131. In: Agrawal, K., Singh, G., Puri, D. and Prakash, S. Synthesis and characterization of hydroxyapatite powder by sol – gel method for biomedical application. *Journal of Minerals and Materials Characterization and Engineering*. 2011, 10(8), pp.727-734.

[356] Rigo, E. C. S., Boschi, A. O., Yoshimoto, M., Allegrini Jr, S., Konig Jr, B. and Carbonari, M. J. Evaluation in vitro and in vivo of biomimetic hydroxyapatite coated on titanium dental implants. *Materials Science and Engineering C*. 2004, 24(5), pp.647-651. In: Palanivelu, R. and Rubankumar, A. Synthesis and spectroscopic characterization of hydroxyapatite by sol – gel method. *International Journal of ChemTech Research*. 2013, 5(6), pp.2965-2969.

[357] Li, P. and Groot, K. Better bioactive ceramics through sol – gel process. *Journal of Sol-Gel Science and Technology*. 1994, 2(1), pp.797-801. In: Nayak, A. K. Hydroxyapatite synthesis methodologies: An overview. *International Journal of ChemTech Research*. 2010, 2(2), pp.903-907.

[358] Liu, D. M., Troczynski, T. and Tseng, W. J. Water – based sol – gel synthesis of hydroxyapatite process development. *Biomaterials*. 2001, 22(13), pp.1721-1730.

[359] Brendel, T., Engel, A. and Russel, C. Hydroxyapatite coating by a polymeric route. *Journal of Materials Science: Materials in Medicine*. 1992, 3(3), pp.175-179.

[360] Brendel, T., Engel, A. and Russel, C. Hydroxyapatite coating by a polymeric route. *Journal of Materials Science: Materials in Medicine*. 1992,

3(3), pp.175-179. In: Ferraz, M. P., Monteiro, F. J. and Manuel, C. M. Hydroxyapatite nanoparticles: A review of preparation methodologies. *Journal of Applied Biomaterials and Biomechanics*. 2004, 2(2), pp.74-80.

[361] Takahashi, H., Yashima, M., Kakihana, M. and Yoshimura, M. Synthesis of stoichiometric hydroxyapatite by a gel route from the aqueous solution of citric and phosphonoacetic acids. *European Journal of Solid State and Inorganic Chemistry*. 1995, 32, pp.829-835.

[362] Takahashi, H., Yashima, M., Kakihana, M. and Yoshimura, M. Synthesis of stoichiometric hydroxyapatite by a gel route from the aqueous solution of citric and phosphonoacetic acids. *European Journal of Solid State and Inorganic Chemistry*. 1995, 32, pp.829-835. In: Nayak, A. K. Hydroxyapatite synthesis methodologies: An overview. *International Journal of ChemTech Research*. 2010, 2(2), pp.903-907.

[363] Gross, K. A., Chai, C. S., Kannangara, G. S. K., Nissan, B. B. and Hanley, L. Thin hydroxyapatite coatings via sol – gel synthesis. *Journal of Materials Science: Materials in Medicine*. 1998, 9(12), pp.839-843.

[364] Masuda, Y., Matubara, K. and Sakka, S. Synthesis of hydroxyapatite from metal alkoxides through sol – gel technique. *Journal of the Ceramic Society of Japan*. 1990, 98(1143), pp.1255-1266.

[365] Chai, C. S., Gross, K. A. and Nissan, B. B. Critical ageing of hydroxyapatite sol – gel solution. *Biomaterials*. 1998, 19(24), pp.2291-2296.

[366] Haddow, D. B., James, P. F. and Van Noort, R. Characterization of sol – gel surfaces for biomedical applications. *Journal of Materials Science: Materials in Medicine*. 1996, 7(5), pp.255-260.

[367] Haddow, D. B., James, P. F. and Van Noort, R. Characterization of sol – gel surfaces for biomedical applications. *Journal of Materials Science: Materials in Medicine*. 1996, 7(5), pp.255-260. In: Nayak, A. K. Hydroxyapatite synthesis methodologies: An overview. *International Journal of ChemTech Research*. 2010, 2(2), pp.903-907.

[368] Jillavenkatesa, A. and Condrate, R. A. Sol – gel processing of hydroxyapatite. *Journal of Materials Science*. 1998, 33(16), pp.4111-4119.

[369] Fernandes, G. F. and Laranjeira, M. C. M. Calcium phosphate biomaterials from marine algae. Hydrothermal synthesis and characterisation. *Quimica Nova*. 2000, 23(4), pp.441-446.

[370] Suchanek, W. L. and Riman, R. E. Hydrothermal synthesis of advanced ceramic powders. In: Vincenzini, P. (ed). *11th International Ceramics Congress, 4-9 June 2006, Sicily*. Zuerich: Trans Tech Publications, 2006, pp.184-193. In: Nayak, A. K. Hydroxyapatite synthesis methodologies: An overview. *International Journal of ChemTech Research*. 2010, 2(2), pp.903-907.

[371] Morey, G. W. and Niggli, P. The hydrothermal formation of silicates: A review. *Journal of the American Chemical Society*. 1913, 35(9), pp.1086-1130. In: Byrappa, K. and Yoshimura, M. *Handbook of hydrothermal technology – A Technology for Crystal Growth and Materials Processing*. New Jersey: Noyse, 2001.

[372] Rabenau, A. The role of hydrothermal synthesis in preparative chemistry. *Angewandte Chemie*. 1985, 24(12), pp.1026-1040. In: Byrappa, K. and Yoshimura, M. *Handbook of hydrothermal technology – A*

Technology for Crystal Growth and Materials Processing. New Jersey: Noyse, 2001.

[373] Roy, R. Accelerating the kinetics of low – temperature inorganic syntheses. *Journal of Solid State Chemistry*. 1994, 111(1), p.11. In: Suchanek, W. L. and Riman, R. E. Hydrothermal synthesis of advanced ceramic powders. In: Vincenzini, P. (ed). *11th International Ceramics Congress, 4-9 June 2006, Sicily*. Zuerich: Trans Tech Publications, 2006, pp.184-193.

[374] Laudise, R. A. *The growth of single crystals*. New Jersey: Prentice Hall, 1970. pp.278-281. In: Byrappa, K. and Yoshimura, M. *Handbook of hydrothermal technology – A Technology for Crystal Growth and Materials Processing*. New Jersey: Noyse, 2001.

[375] Yoshimura, M., Sujaridworakun, P., Koh, F., Fujiwara, T., Pongkao, D. and Ahniyaz, A. Hydrothermal conversion of calcite crystals to hydroxyapatite. *Materials Science and Engineering C*. 2004, 24(4), p.521. In: Ashok, M., Kalkura, S. N., Sundaram, N. M. and Arivuoli, D. Growth and characterization of hydroxyapatite crystals by hydrothermal method. *Journal of Materials Science: Materials in Medicine*. 2007, 18(5), pp.895-898.

[376] Shojai, M. S. Preparation of hydroxyapatite nanoparticles: comparison between hydrothermal and treatment processes and colloidal stability of produced nanoparticles in a dilute experimental dental adhesives. *Journal of the Iranian Chemical Society*. 2009, 6(2), pp.386-392. In: Nayak, A. K. Hydroxyapatite synthesis methodologies: An overview. *International Journal of ChemTech Research*. 2010, 2(2), pp.903-907.

- [377] Earl, J. S., Wood, D. J. and Milne, S. J. Hydroxyapatite nanoparticle synthesis and in – vitro study of dentinal tubule occlusion. In: *Nanotech*, 7-11 May, 2006, Boston. Boca Raton: Nano Science and Technology Institute, 2006, pp.407-410.
- [378] Orlovskii, V. P., Komlev, V. S. and Barinov, S. M. Hydroxyapatite and hydroxyapatite – based ceramics. *Inorganic Materials*. 2002, 38(10), pp.973-984.
- [379] Yubao, L., De Groot, K., De Wijn, J., Klein, C. P. A. T. and Meer, S. V. D. Morphology and composition of nanograde calcium phosphate needle – like crystals formed by simple hydrothermal treatment. *Journal of Materials Science: Materials in Medicine*. 1994, 5(6), pp.326-331.
- [380] Manafi, S. A. and Joughehdoust, S. Synthesis of hydroxyapatite nanostructure by hydrothermal condition for biomedical application. *Iranian Journal of Pharmaceutical Sciences*. 2009, 5(2), pp.89-94. In: Nayak, A. K. Hydroxyapatite synthesis methodologies: An overview. *International Journal of ChemTech Research*. 2010, 2(2), pp.903-907.
- [381] Yubao, L., De Groot, K., De Wijn, J., Klein, C. P. A. T. and Meer, S. V. D. Morphology and composition of nanograde calcium phosphate needle – like crystals formed by simple hydrothermal treatment. *Journal of Materials Science: Materials in Medicine*. 1994, 5(6), pp.326-331. In: Orlovskii, V. P., Komlev, V. S. and Barinov, S. M. Hydroxyapatite and hydroxyapatite – based ceramics. *Inorganic Materials*. 2002, 38(10), pp.973-984.
- [382] Yubao, L., Klein, C. P., De Wijn, J., Meer, S. V. D. and De Groot, K. Shape change and phase transition of needle – like non – stoichiometric apatite crystals. *Journal of Materials Science: Materials in Medicine*. 1991,

2(1), pp.51-55. In: Orlovskii, V. P., Komlev, V. S. and Barinov, S. M. Hydroxyapatite and hydroxyapatite – based ceramics. *Inorganic Materials*. 2002, 38(10), pp.973-984.

[383] HAN, Y., XU, K. and LU, J. Morphology and composition of hydroxyapatite coatings prepared by hydrothermal treatment on electrodeposited brushite coatings. *Journal of Materials Science: Materials in Medicine*. 1999, 10(4), p.243. In: Ashok, M., Kalkura, S. N., Sundaram, N. M. and Arivuoli, D. Growth and characterization of hydroxyapatite crystals by hydrothermal method. *Journal of Materials Science: Materials in Medicine*. 2007, 18(5), pp.895-898.

[384] Adzila, S., Murad, M. and Sopyan, I. Doping metal into calcium phosphate phase for better performance of bone implant materials. *Recent Patents on Materials Science*. 2012, 5(1), pp.18-47.

[385] Medri, V., Mazzocchi, M. and Bellosi, A. Doped calcium – aluminium – phosphate cements for biomedical applications. *Journal of Materials Science: Materials in Medicine*. 2011, 22(2), pp.229-236.

[386] Iconaru, S. L., Heino, M. M. and Predoi, D. Study on europium doped hydroxyapatite nanoparticles by Fourier transform infrared spectroscopy and their antimicrobial properties. *Journal of Spectroscopy*. 2013, 2013(4675), pp.1-10.

[387] Barrett, S. D. and Dhesi, S. S. *The structure of rare – earth metal surfaces*. London: Imperial College Press, 2001.

[388] Netzert, F. P. and Matthew, J. A. D. Surfaces of rare earth metals. *Reports on Progress in Physics*. 1986, 49(6), pp.621-681.

[389] Petersen, L. *High – resolution spectroscopy of praseodymium ions in a solid matrix: Towards single – ion detection sensitivity*. Sc.D. thesis, Ludwig Maximilian University of Munich, 2006.

[390] Knyazev, Y. V. and Nosko, M. M. The optical properties of rare earth metals. *physica status solidi B*. 1977, 80(1), pp.11-29.

[391] Denning, R. G. New optics – new materials. *Journal of Materials Chemistry*. 2001, 11(1), p.19. In: Ballato, J., Lewis, J. S. and Holloway, P. Display applications of rare – earth-doped materials. *MRS Bulletin*. 1999, 24(9), p.51. In: Bartl, M. H., Scott, B. J., Huang, H. C., Wirnsberger, G., Popitsch, A., Chmelkac, B. F. and Stucky, G. D. Synthesis and luminescence properties of mesostructured thin films activated by in – situ formed trivalent rare earth ion complexes. *Chemical Communications*. 2002, 21, pp.2474-2475.

[392] Butler, K. H. *Fluorescent Lamp Phosphors*. Michigan: The Pennsylvania State University Press, 1980. In: Rakovan, J. and Reeder, R. J. Intracrystalline rare earth element distributions in apatite: Surface structural influences on incorporation during growth. *Geochimica et Cosmochimica Acta*. 1996, 60(22), pp.4435-4445.

[393] Bartl, M. H., Scott, B. J., Huang, H. C., Wirnsberger, G., Popitsch, A., Chmelkac, B. F. and Stucky, G. D. Synthesis and luminescence properties of mesostructured thin films activated by in – situ formed trivalent rare earth ion complexes. *Chemical Communications*. 2002, 21, pp.2474-2475.

[394] Crosby, G. A., Whan, R. E. and Alire, R. M. Intramolecular energy transfer in rare earth chelates. Role of the triplet state. *Journal of Chemical Physics*. 1961, 34(3), p.743. In: Dawson, W. R., Kropp, J. L. and Windsor,

M. W. Internal – energy – transfer efficiencies in Eu³⁺ and Tb³⁺ chelates using excitation to selected ion levels. *Journal of Chemical Physics*. 1966, 45(7), p.2410. In: Sato, S. and Wada, M. Relations between Intramolecular energy transfer efficiencies and triplet state energies in rare earth β – diketone chelates. *Bulletin of the Chemical Society of Japan*. 1970, 43(7), p.1955. In: Bartl, M. H., Scott, B. J., Huang, H. C., Wirnsberger, G., Popitsch, A., Chmelkac, B. F. and Stucky, G. D. Synthesis and luminescence properties of mesostructured thin films activated by in – situ formed trivalent rare earth ion complexes. *Chemical Communications*. 2002, 21, pp.2474-2475.

[395] Righini, G. C. and Ferrari, M. Photoluminescence of rare – earth – doped glasses. *Rivista Del Nuovo Cimento*. 2005, 28(12), pp.1-53.

[396] Yliniemi, S. *Studies on passive and active ion – exchanged glass waveguides and devices*. Sc.D. thesis, Helsinki University of Technology, 2007.

[397] Becker, P. C., Olsson, N. A. and Simpson, J. R. *Erbium – doped fiber amplifiers: Fundamentals and technology*. San Diego: Academic Press, 1999. In: Yliniemi, S. *Studies on passive and active ion – exchanged glass waveguides and devices*. Sc.D. thesis, Helsinki University of Technology, 2007.

[398] Adams, J. W. The visible region absorption spectra of rare – earth minerals. *American Mineralogist*. 1965, 50, pp.356-366.

[399] Fleet, M. E., Liu, X. and Pan, Y. Site preference of rare earth elements in hydroxyapatite. *Journal of Solid State Chemistry*. 2000, 149(2), pp.391-398.

[400] Fleet, M. E. and Pan, Y. Site preference of rare earth elements in fluorapatite. *American Mineralogist*. 1995, 80(3-4), pp.329-335.

[401] Rakovan, J. and Reeder, R. J. Intracrystalline rare earth element distributions in apatite: Surface structural influences on incorporation during growth. *Geochimica et Cosmochimica Acta*. 1996, 60(22), pp.4435-4445.

[402] Mackie, P. E. and Young, R. A. Location of Nd dopant in fluorapatite, Ca₅(PO₄)₃F:Nd. *Journal of Applied Crystallography*. 1973, 6(1), pp.26-31. In: Fleet, M. E. and Pan, Y. Site preference of rare earth elements in fluorapatite. *American Mineralogist*. 1995, 80(3-4), pp.329-335.

[403] Wang, W., Shi, D., Lian, J., Guo, Y., Liu, G., Wang, L. and Ewing, R. C. Luminescent hydroxylapatite nanoparticles by surface functionalization. *Applied Physics Letters*. 2006, 89(18), pp.183106:1-3.

[404] Ohta, M., Yasuda, M., Sugiyama, Y., Suzuki, Y. and Okamura, H. The behaviors of rare earth ion in hydroxyapatite crystal. *Electrochemical Society Transactions*. 2009, 16(31), pp.141-144.

[405] Yasukawa, A., Gotoh, K., Tanaka, H. and Kandorid, K. Preparation and structure of calcium hydroxyapatite substituted with light rare earth ions. *Colloids and Surfaces A: Physicochemical and Engineering Aspects*. 2012, 393(5), pp.53-59.

[406] Rakovan, J. and Reeder, R. J. Intracrystalline rare earth element distributions in apatite: Surface structural influences on incorporation during growth. *Geochimica et Cosmochimica Acta*. 1996, 60(22), pp.4435-4445. In: Yasukawa, A., Gotoh, K., Tanaka, H. and Kandorid, K. Preparation and structure of calcium hydroxyapatite substituted with light rare earth ions.

Colloids and Surfaces A: Physicochemical and Engineering Aspects. 2012, 393(5), pp.53-59.

[407] Hirai, H., Masui, T., Imanaka, N. and Adachi, G. Characterization and thermal behavior of amorphous rare earth phosphates. *Journal of Alloys and Compounds*. 2004, 374(1-2), p.84. In: Yasukawa, A., Gotoh, K., Tanaka, H. and Kandorid, K. Preparation and structure of calcium hydroxyapatite substituted with light rare earth ions. *Colloids and Surfaces A: Physicochemical and Engineering Aspects*. 2012, 393(5), pp.53-59.

[408] Perera, T. S. H., Han, Y., Lu, X., Wang, X., Dai, H. and Li, S. Rare earth doped apatite nanomaterials for biological application. *Journal of Nanomaterials*. 2015, 2015, pp.1-6.

[409] Ouenzerfi, R. El, Ariguib, N. K., Ayedi, M. T. and B. Piriou. Spectroscopic study of Eu³⁺ in strontium hydroxyapatite Sr₁₀(PO₄)₆(OH)₂. *Journal of Luminescence*. 1999, 85(1-3), pp.71-77. In: Perera, T. S. H., Han, Y., Lu, X., Wang, X., Dai, H. and Li, S. Rare earth doped apatite nanomaterials for biological application. *Journal of Nanomaterials*. 2015, 2015, pp.1-6.

[410] Han, Y., Wang, X., Dai, H. and Li, S. Synthesis and luminescence of Eu³⁺ doped hydroxyapatite nanocrystallines: Effects of calcinations and Eu³⁺ content. *Journal of Luminescence*. 2013, 135, pp.281-287. In: Perera, T. S. H., Han, Y., Lu, X., Wang, X., Dai, H. and Li, S. Rare earth doped apatite nanomaterials for biological application. *Journal of Nanomaterials*. 2015, 2015, pp.1-6.

[411] Fleet, M. E., Liu, X. and Pan, Y. Rare – earth elements in chlorapatite [Ca₁₀(PO₄)₆Cl₂]: Uptake, site preference, and degradation of monoclinic structure. *American Mineralogist*. 2000, 85(10), pp.1437-1446.

[412] Fleet, M. E. and Pan, Y. Rare earth elements in apatite: Uptake from H₂O-bearing phosphate-fluoride melts and the role of volatile components. *Geochimica et Cosmochimica Acta*. 1997, 61(22), p.4745. In: Fleet, M. E., Liu, X. and Pan, Y. Site preference of rare earth elements in hydroxyapatite. *Journal of Solid State Chemistry*. 2000, 149(2), pp.391-398.

[413] Fleet, M. E. and Pan, Y. Rare earth elements in apatite: Uptake from H₂O – bearing phosphate – fluoride melts and the role of volatile components. *Geochimica et Cosmochimica Acta*. 1997, 61(22), p.4745. In: Fleet, M. E., Liu, X. and Pan, Y. Rare – earth elements in chlorapatite [Ca₁₀(PO₄)₆Cl₂]: Uptake, site preference, and degradation of monoclinic structure. *American Mineralogist*. 2000, 85(10), pp.1437-1446.

[414] Ronsbo, J. G. Coupled substitutions involving REEs and Na and Si in apatites in alkaline rocks from the Ilimaussaq intrusion, South Greenland, and the petrologic implications. *American Mineralogist*. 1989, 74(7), pp.896-901. In: Rakovan, J. and Reeder, R. J. Intracrystalline rare earth element distributions in apatite: Surface structural influences on incorporation during growth. *Geochimica et Cosmochimica Acta*. 1996, 60(22), pp.4435-4445.

[415] Fleet, M. E. and Pan, Y. Site preference of Nd in fluorapatite [Ca₁₀(PO₄)₆F₂]. *Journal of Solid State Chemistry*. 1994, 112(1), pp.78-81. In: Fleet, M. E. and Pan, Y. Site preference of rare earth elements in fluorapatite. *American Mineralogist*. 1995, 80(3-4), pp.329-335.

[416] Yasukawa, A., Kandori, K., Tanaka, H. and Gotoh, K. Preparation and structure of carbonated calcium hydroxyapatite substituted with heavy rare earth ions. *Materials Research Bulletin*. 2012, 47(5), pp.1257-1263.

[417] Sampaio, J. A., Baesso, M. L., Gama, S., Coelho, A. A., Eiras, J. A. and Santos, I. A. Rare earth doping effect on the elastic moduli of low silica calcium aluminosilicate glasses. *Journal of Non-Crystalline Solids*. 2002, 304(1-3), pp.293-298.

[418] Hamadouche, M. and Sedel, L. Ceramics in orthopaedics. *Journal of Bone and Joint Surgery (British volume)*. 2000, 82(8), p.1095. In: Wang, W., Shi, D., Lian, J., Guo, Y., Liu, G., Wang, L. and Ewing, R. C. Luminescent hydroxylapatite nanoparticles by surface functionalization. *Applied Physics Letters*. 2006, 89(18), pp.183106:1-3.

[419] Lide, D. R. (ed). *CRC Handbook of Chemistry and Physics*. Eighty third edition. Boca Raton: CRC Press, 2002.

[420] Andrievskaya, E. R., Lopato, L. M. and Smirnov, V. P. The system HFO₂ – Y₂O₃ – Er₂O₃. *Journal of the American Ceramic Society*. 1996, 79(3), pp.714-720. In: Neuman, A., Platero, M., Romero, R., McClellan, K. J. and Petrovic, J. J. Fabrication and properties of erbium oxide. In: Singh, J. P. (ed), *Conference on Composites, Advanced Ceramics, Materials, and Structures, 12-16 January 1997, Cocoa Beach*. Westerville: The American Ceramic Society, 1997, [no pagination].

[421] Neuman, A., Platero, M., Romero, R., McClellan, K. J. and Petrovic, J. J. Fabrication and properties of erbium oxide. In: Singh, J. P. (ed), *Conference on Composites, Advanced Ceramics, Materials, and Structures*,

12-16 January 1997, Cocoa Beach. Westerville: The American Ceramic Society, 1997, [no pagination].

[422] Que, W., Zhou, Y., Kam, C. H., Lam, Y. L., Chan, Y. C., Gan, L. H. and Deen, G. R. Fluorescence characteristics from microemulsion technique derived erbium (III) oxide nanocrystals. *Materials Research Bulletin*. 2001, 36(5-6), pp.889-895.

[423] Desurvire, E. Lightwave communications: The fifth generation. *Scientific American*. 1992, 266(1), p.96. In: Que, W., Zhou, Y., Kam, C. H., Lam, Y. L., Chan, Y. C., Gan, L. H. and Deen, G. R. Fluorescence characteristics from microemulsion technique derived erbium (III) oxide nanocrystals. *Materials Research Bulletin*. 2001, 36(5-6), pp.889-895.

[424] Staley, J. T. and Haupin, W. Aluminium and aluminium alloys. 1992. In: Kroschwitz, J. I. and Grant, M. H. (eds). *Kirk – Othmer encyclopedia of chemical technology*. New York: John Wiley & Sons, Inc., 1991-1998, pp.248-249. In: U.S. Department of Health and Human Services. *Toxicological profile for aluminium*. Atlanta: Agency for Toxic Substances and Disease Registry, 2008.

[425] Krewski, D., Yokel, R. A., Nieboer, E., Borchelt, D., Cohen, J., Harry, J., Kacew, S., Lindsay, J., Mahfouz, A. M. and Rondeau, V. Human Health risk Assessment for aluminium, aluminium oxide and aluminium hydroxide. *Journal of Toxicology and Environmental Health, Part B: Critical Reviews*. 2007, 10(1), pp.1-269.

[426] U.S. Department of Health and Human Services. *Toxicological profile for Aluminium*. Atlanta: Agency for Toxic Substances and Disease Registry, 2008.

[427] Wilson, A. D., Groffman, D. M., Powis, D. R. and Scott, R. P. An evaluation of the significance of the impinging jet method or measuring the acid erosion of dental cements. *Biomaterials*. 1986, 7(1), pp.55-60.

[428] Eng, P. J., Trainor, T. P., Brown, G. E., Waychunas, G. A., Newville, M. and Sutton, S. R. Structure of the hydrated α -Al₂O₃ (0001) surface. *Science*. 2000, 288(5468), pp.1029-1033. In: Krewski, D., Yokel, R. A., Nieboer, E., Borchelt, D., Cohen, J., Harry, J., Kacew, S., Lindsay, J., Mahfouz, A. M. and Rondeau, V. Human Health risk Assessment for aluminium, aluminium oxide and aluminium hydroxide. *Journal of Toxicology and Environmental Health, Part B: Critical Reviews*. 2007, 10(1), pp.1-269.

[429] Chung, D. D. L. Acid aluminium phosphate for the binding and coating of materials. *Journal of Materials Science*. 2003, 38(13), pp.2785-2791.

[430] Borsa, C. E. and Brook, R. J. Fabrication of Al₂O₃/SiC nanocomposites using a polymeric precursor for SiC. In: Hausner, H., Messing, G. L. and Hirano, S. I. (eds). *Ceramic Processing Science and Technology*, 1-3 May 1995, Ohio. Westerville: The American Ceramic Society, 1995, p.653. In: Jiansirisomboon, S. and MacKenzie, K. J. D. Sol – gel processing and phase characterization of Al₂O₃ and Al₂O₃/SiC nanocomposite powders. *Materials Research Bulletin*. 2006, 41(4), pp.791-803.

[431] Hareesh, U. S., Damodaran, A. D. and Warriar, K. G. K. Sol – gel precursors for alumina – silicon carbide nanocomposites through controlled flocculation and humidity drying. *British ceramic transactions*. 1997, 96(3), p.99. In: Jiansirisomboon, S. and MacKenzie, K. J. D. Sol – gel processing

and phase characterization of Al₂O₃ and Al₂O₃/SiC nanocomposite powders. *Materials Research Bulletin*. 2006, 41(4), pp.791-803.

[432] Ananthakumar, S., Hareesh, U. S., Damodaran, A. D. and Warriar, K. G. K. Microwave processing of boehmite coated SiC composite precursors for alumina – silicon carbide nanocomposites. *Journal of Materials Science Letters*. 1998, 17(2), p.145. In: Jiansirisomboon, S. and MacKenzie, K. J. D. Sol – gel processing and phase characterization of Al₂O₃ and Al₂O₃/SiC nanocomposite powders. *Materials Research Bulletin*. 2006, 41(4), pp.791-803.

[433] Winn, A. J., Wang, Z. C., Todd, R. I. and Sale, F. R. Alumina – SiC nanocomposites by mixed powder and chemical processing routes: A preliminary examination of microstructure and response to abrasion. *Silicon Industrial*. 1998, 63(11-12), p.147. In: Jiansirisomboon, S. and MacKenzie, K. J. D. Sol – gel processing and phase characterization of Al₂O₃ and Al₂O₃/SiC nanocomposite powders. *Materials Research Bulletin*. 2006, 41(4), pp.791-803.

[434] Sato, T. Preparation of gelatinous aluminium hydroxide. *Journal of Inorganic Chemistry*. 1972, 391(1), p.69. In: Sato, T. and Sato, K. Thermal decomposition of precipitates from aqueous aluminium phosphate solution by reaction with alkali. *Thermochimica Acta*. 1989, 148(4), pp.295-300.

[435] O'Neil, M. J., Smith, A., Heckelman, P. E. and Budavari, S. Aluminium and aluminium compounds. In: *The Merck index: An encyclopedia of chemicals, drugs, and biological*. New Jersey: Merck & Co. Inc., 2001. pp.59-65. In: U.S. Department of Health and Human Services. *Toxicological*

profile for aluminium. Atlanta: Agency for Toxic Substances and Disease Registry, 2008.

[436] Billotte, W. G. Ceramic Biomaterials. In: Bronzino, J. D. (ed). *The biomedical engineering handbook*. Second edition. Boca Raton: CRC Press, 2000.

[437] Cotton, F. A. and Wilkinson, G. *Advanced inorganic chemistry*. Fourth edition. New York: John Wiley & Sons, Inc., 1980. In: Krewski, D., Yokel, R. A., Nieboer, E., Borchelt, D., Cohen, J., Harry, J., Kacew, S., Lindsay, J., Mahfouz, A. M. and Rondeau, V. Human Health risk Assessment for aluminium, aluminium oxide and aluminium hydroxide. *Journal of Toxicology and Environmental Health, Part B: Critical Reviews*. 2007, 10(1), pp.1-269.

[438] Jiansirisomboon, S. and MacKenzie, K. J. D. Sol – gel processing and phase characterization of Al₂O₃ and Al₂O₃/SiC nanocomposite powders. *Materials Research Bulletin*. 2006, 41(4), pp.791-803.

[439] Sato, T. and Sato, K. Thermal decomposition of precipitates from aqueous aluminium phosphate solution by reaction with alkali. *Thermochimica Acta*. 1989, 148(4), pp.295-300.

[440] Hazardous Substances Data Bank. *Aluminium compounds* [Online]. Bethesda: U.S. National Library of Medicine, 2007. [Accessed 2013]. Available from: <http://toxnet.nlm.nih.gov/>. In: U.S. Department of Health and Human Services. *Toxicological profile for aluminium*. Atlanta: Agency for Toxic Substances and Disease Registry, 2008.

[441] Lewis, R. J. *Hawley's condensed chemical dictionary*. New York: John Wiley & Sons, Inc., 2001, pp.39-46. In: U.S. Department of Health and

Human Services. *Toxicological profile for aluminium*. Atlanta: Agency for Toxic Substances and Disease Registry, 2008.

[442] Hench, L. L. Bioceramics: From concept to clinic. *Journal of the American Ceramic Society*. 1991, 74(7), pp.1487-1510. In: Billotte, W. G. Ceramic Biomaterials. In: Bronzino, J. D. (ed). *The biomedical engineering handbook*. Second edition. Boca Raton: CRC Press, 2000.

[443] Greger, H. H. *Preparation of aluminum phosphates*. US 2460344 A,1949. In: Maier, C. R. and Jones, L. E. The influence of aluminium phosphates on graphite oxidation. *Carbon*. 2005, 43(11), pp.2272-2276.

[444] ZhenYu, L., Haoran, G., MingXi, Z. and XianQin, H. Preparation of aluminium borate whisker reinforced aluminium phosphate wave – transparent materials. *Chinese Science Bulletin*. 2008, 53(19), pp.3073-3076.

[445] Chiou, J. M. and Chung, D. D. L. Improvement of the temperature resistance of aluminium – matrix composites using an acid phosphate binder. *Journal of Materials Science*. 1993, 28(6), p.1435. In: Chung, D. D. L. Acid aluminium phosphate for the binding and coating of materials. *Journal of Materials Science*. 2003, 38(13), pp.2785-2791.

[446] Stanley, J. M. Hydrothermal synthesis of large aluminum phosphate crystals. *Industrial & Engineering Chemistry*. 1954, 46(8), pp.1684-1989, In: Byrappa, K., Venkatachalapathy, V. and Puttaraj, B. Crystallization of aluminium orthophosphate. *Journal of Materials Science*. 1984, 19(9), 2855-2862.

[447] Deng, S., Wang, C., Zhou, Y., Huang, F. and Du, L. Preparation and properties of aluminum phosphate/organosilicon resin organic – inorganic

hybrid materials and fiber reinforced composites. *Materials Science and Engineering A*. 2008, 477(1-2), pp.96-99.

[448] Maier, C. R. and Jones, L. E. The influence of aluminium phosphates on graphite oxidation. *Carbon*. 2005, 43(11), pp.2272-2276.

[449] Byrappa, K., Venkatachalapathy, V. and Puttaraj, B. Crystallization of aluminium orthophosphate. *Journal of Materials Science*. 1984, 19(9), 2855-2862.

[450] Chung, D. D. L. Acid aluminium phosphate for the binding and coating of materials. *Journal of Materials Science*. 2003, 38(13), pp.2785-2791. In: Deng, S., Wang, C., Zhou, Y., Huang, F. and Du, L. Preparation and properties of aluminum phosphate/organosilicon resin organic – inorganic hybrid materials and fiber reinforced composites. *Materials Science and Engineering A*. 2008, 477(1-2), pp.96-99.

[451] Hoshii, S., Kojima, A., Tamaki, T. and Otani, S. Carbon fiber/ceramic composite using aluminium phosphate with different P/Al molar ratios. *Journal of Materials Science Letters*. 2000, 19(7), pp.557-560. In: Deng, S., Wang, C., Zhou, Y., Huang, F. and Du, L. Preparation and properties of aluminum phosphate/organosilicon resin organic – inorganic hybrid materials and fiber reinforced composites. *Materials Science and Engineering A*. 2008, 477(1-2), pp.96-99.

[452] Han, H. J. and Kim, D. P. Studies on curing chemistry of aluminum – chromium – phosphates as low temperature curable binders. *Journal of Sol-Gel Science and Technology*. 2003, 26(1), pp.223-228. In: Deng, S., Wang, C., Zhou, Y., Huang, F. and Du, L. Preparation and properties of aluminum phosphate/organosilicon resin organic – inorganic hybrid materials and fiber

reinforced composites. *Materials Science and Engineering A*. 2008, 477(1-2), pp.96-99.

[453] He, L., Chen, D. and Shang, S. Fabrication and wear properties of Al₂O₃SiC ceramic coatings using aluminum phosphate as binder. *Journal of Materials Science*. 2004, 39(15), pp.4887-4892. In: Deng, S., Wang, C., Zhou, Y., Huang, F. and Du, L. Preparation and properties of aluminum phosphate/organosilicon resin organic – inorganic hybrid materials and fiber reinforced composites. *Materials Science and Engineering A*. 2008, 477(1-2), pp.96-99.

[454] LU, W. and Chung, D. D. L. Oxidation Protection of Carbon Materials by Acid Phosphate Impregnation. *Carbon*. 2002, 40(8), p.1249. In: Chung, D. D. L. Acid aluminium phosphate for the binding and coating of materials. *Journal of Materials Science*. 2003, 38(13), pp.2785-2791.

[455] Holloway, J. A. and Denry, I. Effect of aluminum phosphate additions on the crystallization and bioactivity of fluorrichterite glass – ceramics for biomedical applications. *Journal of the American Ceramic Society*. 2007, 90(9), pp.2941-2946.

[456] Denry, I. and Holloway, J. Effect of additives on the microstructure and thermal properties of a mica – based glass – ceramic. *Journal of Biomedical Materials Research*. 2002, 63(2), pp.146-151. In: Holloway, J. A. and Denry, I. Effect of aluminum phosphate additions on the crystallization and bioactivity of fluorrichterite glass – ceramics for biomedical applications. *Journal of the American Ceramic Society*. 2007, 90(9), pp.2941-2946.

[457] Hench, L. L. Bioceramics: From concept to clinic. *American Ceramic Society Bulletin*. 1993, 72(4), pp.93-98. In: Holloway, J. A. and Denry, I.

Effect of aluminum phosphate additions on the crystallization and bioactivity of fluorrichterite glass – ceramics for biomedical applications. *Journal of the American Ceramic Society*. 2007, 90(9), pp.2941-2946.

[458] Hench, L. L. Bioceramics. *Journal of the American Ceramic Society*. 1998, 81(7), pp.1705-1728. In: Holloway, J. A. and Denry, I. Effect of aluminum phosphate additions on the crystallization and bioactivity of fluorrichterite glass – ceramics for biomedical applications. *Journal of the American Ceramic Society*. 2007, 90(9), pp.2941-2946.

[459] Hench, L. L. and Andersson, O. Bioactive glass coatings. In: Hench, L. L. and Wilson, J. (eds). *An introduction to bioceramics*. New Jersey: World Scientific, 1993. pp.41-62. In: Holloway, J. A. and Denry, I. Effect of aluminum phosphate additions on the crystallization and bioactivity of fluorrichterite glass – ceramics for biomedical applications. *Journal of the American Ceramic Society*. 2007, 90(9), pp.2941-2946.

[460] Hench, L. L. and Andersson, O. Bioactive glass coatings. In: Hench, L. L. and Wilson, J. (eds). *An introduction to bioceramics*. New Jersey: World Scientific, 1993, pp.239-259. In: Holloway, J. A. and Denry, I. Effect of aluminum phosphate additions on the crystallization and bioactivity of fluorrichterite glass – ceramics for biomedical applications. *Journal of the American Ceramic Society*. 2007, 90(9), pp.2941-2946.

[461] Chen, D., He, L. and Shang, S. Study on aluminium phosphate binder and related Al₂O₃ – SiC ceramic coating. *Materials Science and Engineering A*. 2003, 348(1-2), p.29. In: Chung, D. D. L. Acid aluminium phosphate for the binding and coating of materials. *Journal of Materials Science*. 2003, 38(13), pp.2785-2791.

- [462] Cassidy, J. E. Phosphate Bonding then and Now. *American Ceramic Society Bulletin*. 1977, 56(7), p.640. In: Chung, D. D. L. Acid aluminium phosphate for the binding and coating of materials. *Journal of Materials Science*. 2003, 38(13), pp.2785-2791.
- [463] Kingery, W. D. Fundamental Study of Phosphate Bonding in Refractories: I, Literature Review. *Journal of the American Ceramic Society*. 1950, 33(8), p.239. In: Chung, D. D. L. Acid aluminium phosphate for the binding and coating of materials. *Journal of Materials Science*. 2003, 38(13), pp.2785-2791.
- [464] Kingery, W. D. Cold setting properties. *Journal of the American Ceramic Society*. 1950, 33(8), p.242. In: Chung, D. D. L. Acid aluminium phosphate for the binding and coating of materials. *Journal of Materials Science*. 2003, 38(13), pp.2785-2791.
- [465] Rothon, R. N. Solution – deposited metal phosphate coatings. *Thin Solid Films*. 1981, 77(1-3), p.149. In: Chung, D. D. L. Acid aluminium phosphate for the binding and coating of materials. *Journal of Materials Science*. 2003, 38(13), pp.2785-2791.
- [466] Hong, L. Y., Han, H. J., Ha, H., Lee, J. Y. and Kim, D. P. Development of Cr – free aluminium phosphate binders and their composite applications. *Composites Science and Technology*. 2007, 67(6), pp.1195-1201.
- [467] Morris, J. H., Perkins, P. G., Rose, A. E. A. and Smith, W. E. The chemistry and binding properties of aluminium phosphates. *Chemical Society Reviews*. 1977, 6(2), pp.173-194. In: Hong, L. Y., Han, H. J., Ha, H., Lee, J. Y. and Kim, D. P. Development of Cr – free aluminium phosphate

binders and their composite applications. *Composites Science and Technology*. 2007, 67(6), pp.1195-1201.

[468] Mellor, E. g. J. W. *Comprehensive treatise of inorganic chemistry*. London: Longmans, 1935. In: *Gmelin Handbook of Inorganic Chemistry*. Weinheim: *Verlag Chemie GmbH*, 1965. In: Van Wazer, J. R. *Phosphorus and its compounds*. New York: Interscience, 1966. In: Bailar, J. C. and Trotman-Dickenson, A. F. *Comprehensive Inorganic Chemistry*. Oxford: Pergamon Press, 1973. In: Sato, T. and Sato, K. Thermal decomposition of precipitates from aqueous aluminium phosphate solution by reaction with alkali. *Thermochimica Acta*. 1989, 148(4), pp.295-300.

[469] Sekar, C., Kanchana, P., Nithyaselvi, R. and Girija, E. K. Effect of fluorides (KF and NaF) on the growth of dicalcium phosphate dihydrate (DCPD) crystal. *Materials Chemistry and Physics*. 2009, 115(1), pp.21-27.

[470] Pandurangappa, C. and Lakshminarasappa, B. N. Optical absorption and Photoluminescence studies in Gamma – irradiated nanocrystalline CaF₂. *Journal of Nanomedicine & Nanotechnology*. 2011, 2(2), pp.1-4.

[471] Public Health England. *Water fluoridation: Health monitoring report for England 2014*. London: PHE publications, 2014.

[472] Faculty of Dentistry. *Water fluoridation: Questions and answers*. Toronto: University of Toronto, 2012.

[473] Evis, Z. and Sun, Z. P. Structural and mechanical investigations of magnesium and fluoride doped nanosize calcium phosphates. *Journal of Ceramic Processing Research*. 2010, 11(6), pp.701-715.

- [474] Fawell, J., Bailey, K., Chilton, J., Dahi, E., Fewtrell, L. and Magara, Y. *Fluoride in drinking – water*. London: IWA Publishing, 2006. In: Sekar, C., Kanchana, P., Nithyaselvi, R. and Girija, E. K. Effect of fluorides (KF and NaF) on the growth of dicalcium phosphate dihydrate (DCPD) crystal. *Materials Chemistry and Physics*. 2009, 115(1), pp.21-27.
- [475] Franz, E. D. and Telle, R. Reaction hot pressing of fluorapatite for dental implants. In: Vincenzini, P. (ed). *High Technology Ceramics*. Amsterdam: Elsevier Science, 1987, pp.31-41. In: Kim, H. W., Noh, Y. J., Koh, Y. H., Kim, H. E. and Kim, H. M. Effect of CaF₂ on densification and properties of hydroxyapatite – zirconia composites for biomedical applications. *Biomaterials*. 2002, 23(20), pp.4113-4121.
- [476] Krajewski, A., Ravaglioli, A., Roveri, N., Bigi, A. and Foresi, E. Effect of fluoride, chloride and carbonate ions introduced by cyclic pH fluctuation on the physico – chemical properties of apatite – based ceramics. *Journal of Materials Science*. 1990, 25(7), pp.3203-3207. In: Kim, H. W., Noh, Y. J., Koh, Y. H., Kim, H. E. and Kim, H. M. Effect of CaF₂ on densification and properties of hydroxyapatite – zirconia composites for biomedical applications. *Biomaterials*. 2002, 23(20), pp.4113-4121.
- [477] Kim, H. W., Kong, Y. M., Koh, Y. H., Kim, H. E., Kim, H. M. and Ko, J. S. Pressureless sintering and mechanical and biological properties of fluor – hydroxyapatite composites with zirconia. *Journal of the American Ceramic Society*. 2003, 86(12), pp.2019-2026. In: Evis, Z. and Sun, Z. P. Structural and mechanical investigations of magnesium and fluoride doped nanosize calcium phosphates. *Journal of Ceramic Processing Research*. 2010, 11(6), pp.701-715.

[478] Nakade, O., Koyama, H., Arai, J., Arijji, H., Takad, J. and Kaku, T. Stimulation by low concentrations of fluoride of the proliferation and alkaline phosphatase activity of human dental pulp cells in vitro. *Archives of Oral Biology*. 1999, 44(1), pp.89-92. In: Evis, Z. and Sun, Z. P. Structural and mechanical investigations of magnesium and fluoride doped nanosize calcium phosphates. *Journal of Ceramic Processing Research*. 2010, 11(6), pp.701-715.

[479] Moreno, E. C., Kresak, M. and Zahradnik, R. T. Fluoridated hydroxyapatite solubility and caries formation. *Nature*. 1974, 247(5435), pp.64-65. In: Kim, H. W., Noh, Y. J., Koh, Y. H., Kim, H. E. and Kim, H. M. Effect of CaF₂ on densification and properties of hydroxyapatite – zirconia composites for biomedical applications. *Biomaterials*. 2002, 23(20), pp.4113-4121.

[480] Legeros, R. Z., Silverstone, L. M., Daculsi, G. and Kerebel, L. M. In vitro caries – like lesion formation in F – containing tooth enamel. *Journal of Dental Research*. 1985, 62(2), pp.138-144. In: Kim, H. W., Noh, Y. J., Koh, Y. H., Kim, H. E. and Kim, H. M. Effect of CaF₂ on densification and properties of hydroxyapatite – zirconia composites for biomedical applications. *Biomaterials*. 2002, 23(20), pp.4113-4121.

[481] Ingram, G. S. and Nash, P. F. Mechanism for the anticaries action of fluoride. *Caries Research*, 1980, 14(5), pp.298–303, In: Kim, H. W., Noh, Y. J., Koh, Y. H., Kim, H. E. and Kim, H. M. Effect of CaF₂ on densification and properties of hydroxyapatite – zirconia composites for biomedical applications. *Biomaterials*. 2002, 23(20), pp.4113-4121.

- [482] Kim, H. W., Noh, Y. J., Koh, Y. H. and Kim, H. E. Enhanced performance of fluorine substituted hydroxyapatite composites for hard tissue engineering. *Journal of Materials Science: Materials in Medicine*. 2003, 14(10), pp.899-904.
- [483] Elliot, J. C. *Structure and chemistry of the apatites and other calcium orthophosphates*. Amsterdam: Elsevier, 1994. In: Evis, Z. and Sun, Z. P. Structural and mechanical investigations of magnesium and fluoride doped nanosize calcium phosphates. *Journal of Ceramic Processing Research*. 2010, 11(6), pp.701-715.
- [484] Okazaki, M. Magnesium – containing fluoridated apatites. *Journal of Fluorine Chemistry*. 1988, 41(1), pp.45-52. In: Evis, Z. and Sun, Z. P. Structural and mechanical investigations of magnesium and fluoride doped nanosize calcium phosphates. *Journal of Ceramic Processing Research*. 2010, 11(6), pp.701-715.
- [485] Kim, H. W., Noh, Y. J., Koh, Y. H., Kim, H. E. and Kim, H. M. Effect of CaF₂ on densification and properties of hydroxyapatite – zirconia composites for biomedical applications. *Biomaterials*. 2002, 23(20), pp.4113-4121.
- [486] Webster, T. J., Schlueter, E. A. M., Smith, J. L. and Slamovich, E. B. Osteoblast response to hydroxyapatite doped with divalent and trivalent cations. *Biomaterials*. 2004, 25(11), pp.2111-2121. In: Evis, Z. and Sun, Z. P. Structural and mechanical investigations of magnesium and fluoride doped nanosize calcium phosphates. *Journal of Ceramic Processing Research*. 2010, 11(6), pp.701-715.

[487] Julien, M., Khairoun, I., Delplace, S., Pilet, P., LeGeros, R. Z., Weiss, P., Bouler, J. M. and Guicheux, J. Physico – chemical and in vitro biological properties of novel doped amorphous calcium phosphate – based cements. *Biomaterials*. 2007, 28(6), pp.956-965.

[488] Sivakumar, M. and Manjubala, I. Preparation of hydroxyapatite/fluoroapatite – zirconia composites using Indian corals for biomedical applications. *Materials Letters*. 2001, 50(4), pp.199-205. In: Evis, Z. and Sun, Z. P. Structural and mechanical investigations of magnesium and fluoride doped nanosize calcium phosphates. *Journal of Ceramic Processing Research*. 2010, 11(6), pp.701-715.

[489] Farley, J. R., Wergedal, J. E. and Baylink, D. J. Fluoride directly stimulates proliferation and alkaline phosphatase activity of bone – forming cells. *Science*. 1983, 222(4621), pp.330-332. In: Evis, Z. and Sun, Z. P. Structural and mechanical investigations of magnesium and fluoride doped nanosize calcium phosphates. *Journal of Ceramic Processing Research*. 2010, 11(6), pp.701-715.

[490] McCann, H. G. Reactions of fluoride ion with hydroxyapatite. *Journal of Biological Chemistry*. 1952, 201(1), pp.247-259.

[491] Giesecke, F. and Rathje, W. Hydroxyl – Fluorapatit, das Mineral des Rohphosphates. *Journal of the American Chemical Society*. 1941, 74B, p.349. In: McCann, H. G. Reactions of fluoride ion with hydroxyapatite. *Journal of Biological Chemistry*. 1952, 201(1), pp.247-259.

[492] Mehta, S. and Simpson, D. R. Fluoride in apatite: Substitution of monofluorophosphate for orthophosphate. *American Mineralogist*, 1975, 60, pp.134-138.

[493] Ericsson, Y. The mechanism of the monofluorophosphate action on hydroxyl apatite and dental enamel. *Acta Odontologica Scandinavica*. 1953, 21(5), pp.341-358. In: Mehta, S. and Simpson, D. R. Fluoride in apatite: Substitution of monofluorophosphate for orthophosphate. *American Mineralogist*, 1975, 60, pp.134-138.

[494] Simpson, D. R. Substitutions in apatite. II. Low temperature fluoride – hydroxyl apatite. *American Mineralogist*. 1968, 53, pp.1953-1964. In: Mehta, S. and Simpson, D. R. Fluoride in apatite: Substitution of monofluorophosphate for orthophosphate. *American Mineralogist*, 1975, 60, pp.134-138.

[495] Rintoul, L., Wentrup-Byrne, E., Suzuki, S. and Grondahl, L. FT – IR spectroscopy of fluoro – substituted hydroxyapatite: Strengths and limitations. *Journal of Materials Science: Materials in Medicine*. 2007, 18(9), pp.1701-1709.

[496] Tan, C. Y., Singh, R., The, Y. C., Tan, Y. M. and Yap, B. K. The Effects of calcium – to – phosphorus ratio on the densification and mechanical properties of hydroxyapatite ceramic. *International Journal of Applied Ceramic Technology*. 2014, 12(1), pp.1-5.

[497] Fanovich, M. A. and Porto Lopez, J. M. Influence of temperatures and additives on the microstructure and sintering behaviour of hydroxyapatite with different Ca/P ratios. *Journal of Materials Science: Materials in Medicine*. 1998, 9(1), pp.53-60. In: Ramesh, S., Tan, C. Y., Hamdi, M., Sopyan, I. and Teng, W. D. The influence of Ca/P ratio on the properties of hydroxyapatite bioceramics. In: Du, S., Leng, J. and Asundi, A. K. (eds). *International conference on smart materials and nanotechnology in*

engineering, 1-4 July 2007, Harbin. Bellingham: SPIE-The International Society for Optical Engineering, 2007, pp.64233A:1-6.

[498] Slosarczyk, A. and Piekarczyk, J. Ceramic materials on the basis of hydroxyapatite and tricalcium phosphate. *Ceramics International*. 1999, 25(6), pp.561-565. In: Ramesh, S., Tan, C. Y., Hamdi, M., Sopyan, I. and Teng, W. D. The influence of Ca/P ratio on the properties of hydroxyapatite bioceramics. In: Du, S., Leng, J. and Asundi, A. K. (eds). *International conference on smart materials and nanotechnology in engineering, 1-4 July 2007, Harbin*. Bellingham: SPIE-The International Society for Optical Engineering, 2007, pp.64233A:1-6.

[499] Ramesh, S., Tan, C. Y., Hamdi, M., Sopyan, I. and Teng, W. D. The influence of Ca/P ratio on the properties of hydroxyapatite bioceramics. In: Du, S., Leng, J. and Asundi, A. K. (eds). *International conference on smart materials and nanotechnology in engineering, 1-4 July 2007, Harbin*. Bellingham: SPIE-The International Society for Optical Engineering, 2007, pp.64233A:1-6.

[500] Annala, T. *Hydroxyapatite/tricalciumphosphate composites: Tissue engineerin applications*. Tampere: Scaffdex, 2008.

[501] Bobyn, J. D., Stackpool, G. J., Hacking, S. A., Tanzer, M. and Krygier, J. J. Characteristics of bone ingrowth and interface mechanics of a new porous tantalum biomaterial. *Journal of bone and joint surgery (British volume)*. 1999, 81(5), pp.907-914.

[502] Tancret, F., Bouler, J. M., Chamousset, J. and Minois, L. M. Modelling the mechanical properties of microporous and macroporous biphasic calcium phosphate bioceramics. *Journal of the European Ceramic Society*.

2006, 26(16), pp.3647-3656. In: Dorozhkin, S. V. Bioceramics of calcium orthophosphates. *Biomaterials*. 2010, 31(7), pp.1465-1485.

[503] Bouler, J. M., Trecant, M., Delecrin, J., Royer, J., Passuti, N. and Daculsi, G. Macroporous biphasic calcium phosphate ceramics: Influence of five synthesis parameters on compressive strength. *Journal of Biomedical Materials Research*. 1996, 32(4), pp.603-609. In: Dorozhkin, S. V. Bioceramics of calcium orthophosphates. *Biomaterials*. 2010, 31(7), pp.1465-1485.

[504] Suchanek, W., Yashima, M., Kakihana, M. and Yoshimura, M. Hydroxyapatite ceramics with selected sintering additives. *Biomaterials*, 1997, 18(13), pp.923-933, In: Earl, J. S. *In vitro Study of dentine tubule infiltration by hydroxyapatite and silica nanoparticles*. Ph.D. thesis, University of Leeds, 2007.

[505] Lide, D. R. (ed). *The CRC handbook of chemistry and physics*. Eighty sixth edition. Boca Raton: CRC Press, 2005.

[506] Boanini, E., Gazzano, M. and Bigi, A. Ionic substitutions in calcium phosphates synthesized at low temperature. *Acta Biomaterialia*. 2010, 6(6), pp.1882-1894.

[507] Ranjitkar, S., Kaidonis, J. A. and Smales, R. J. Gastroesophageal reflux disease and tooth erosion. *International Journal of Dentistry*. 2012, 2012, pp.1-10.

[508] Sadeghian, Z. *Laser sintering of hydroxyapatite by layer – wise slurry deposition (LSD)*. Ph.D. thesis, Clausthal University of Technology, 2005.

- [509] Shuai, C., Feng, P., Cao, C. and Peng, S. Processing and characterization of laser sintered hydroxyapatite scaffold for tissue engineering. *Biotechnology and Bioprocess Engineering*. 2013, 18(3), pp.520-527.
- [510] Shin, S. I., Lee, E. K., Kim, J. H., Lee, J. H., Kim, S. H., Kwon, Y. H., Herr, Y. and Chung, J. H. The effect of Er:YAG laser irradiation on hydroxyapatite-coated implants and fluoride – modified TiO₂ – blasted implant surfaces: A microstructural analysis. *Lasers in Medical Science*. 2013, 28(3), pp.823-831.
- [511] Wong, J., Otsuka, M., Higuchi, W. I., Powell, G. L. and Fox, J. L. Effect of laser irradiation on the dissolution kinetics of hydroxyapatite preparations. *Journal of Pharmaceutical Sciences*. 1990, 79(6), pp.510-515.
- [512] Kim, S. W., Kwon, Y. H., Chung, J. H., Shin, S. II. and Herr, Y. The effect of Er:YAG laser irradiation on the surface microstructure and roughness of hydroxyapatite – coated implant. *Journal of Periodontal & Implant Science*. 2010, 40(6), pp.276-282.
- [513] Meurman, J. H., Hemmerle, J., Voegel, J. C., Makinen, R. R. and Luomanen, M. Transformation of hydroxyapatite to fluorapatite by irradiation with high – energy CO₂ laser. *Caries Research*. 1997, 31(5), pp.397-400.
- [514] Rabelo, J. S., Ana, P. A., Valerio, M. E. G., Mazzocchi, V. L., Baldochi, S. L. and Zezell, D. M. Nanostructured synthetic hydroxyapatite and dental enamel heated irradiated by ER,CR:YSGG. Characterised by FTIR and XRD. *Brazilian Synchrotron Light Laboratory*. 2008, 3, pp.1-2.
- [515] ZHANG, S. *CO₂ laser induced structural changes of dental enamel*. Ph.D. thesis, University of Hamburg, 2008.

[516] Rabelo, J. S. *Nanostructured synthetic hydroxyapatite and dental enamel heated and irradiated by ER,CR:YSGG. Characterized by FTIR and XRD*. M.Sc. thesis, University of Sao Paulo, 2009.

[517] Nagasawa, A., Koizumi, H., Nakayama, D., Kazama, H., Matsumura, H. and Nishikawa, K. Fusing of inorganic materials to enamel and porcelain surfaces with Nd:YAG laser. *International Chinese Journal of Dentistry*. 2009, 9(1), pp.19-22.

[518] Hirosuke, G., Masatoshi, T., Nobukazu, W., Hideo, K., Takashi, T., Shigeto, A., Yutaka, D. and Yasuo, T. Calcium phosphates as fissure sealant materials fused to enamel by CO₂ laser. I. Monocalcium phosphate monohydrate and dicalcium phosphate dihydrate as fissure sealant materials. *Journal of Gifu Dental Society*. 2008, 35(2), pp.48-54.

[519] Stewart, L., Powell, G. L. and Wright, S. Hydroxyapatite attached by laser: A potential sealant for pits and fissures. *Operative Dentistry*. 1985, 10(1), pp.2-5. In: Hirosuke, G., Masatoshi, T., Nobukazu, W., Hideo, K., Takashi, T., Shigeto, A., Yutaka, D. and Yasuo, T. Calcium phosphates as fissure sealant materials fused to enamel by CO₂ laser. I. Monocalcium phosphate monohydrate and dicalcium phosphate dihydrate as fissure sealant materials. *Journal of Gifu Dental Society*. 2008, 35(2), pp.48-54.

[520] Shimizu, Y. Study of histostructure of fused human enamel by laser irradiation. *journal of the Japan Prosthodontic Society*. 1989, 33(5), pp.1212-1225. In: Hirosuke, G., Masatoshi, T., Nobukazu, W., Hideo, K., Takashi, T., Shigeto, A., Yutaka, D. and Yasuo, T. Calcium phosphates as fissure sealant materials fused to enamel by CO₂ laser. I. Monocalcium phosphate

monohydrate and dicalcium phosphate dihydrate as fissure sealant materials. *Journal of Gifu Dental Society*. 2008, 35(2), pp.48-54.

[521] Lin, C. P., Lin, F. H., Tseng, Y. C., Kok, S. H., Lan, W. H. and Liao, J. D. Treatment of tooth fracture by medium energy of CO₂ laser and DP – bioactive glass paste: Compositional, structural and phase change of DP – bioglass paste after irradiation by CO₂ laser. *Biomaterials*. 2000, 21(6), pp.637-643. In: Hirosuke, G., Masatoshi, T., Nobukazu, W., Hideo, K., Takashi, T., Shigeto, A., Yutaka, D. and Yasuo, T. Calcium phosphates as fissure sealant materials fused to enamel by CO₂ laser. I. Monocalcium phosphate monohydrate and dicalcium phosphate dihydrate as fissure sealant materials. *Journal of Gifu Dental Society*. 2008, 35(2), pp.48-54.

[522] Lin, C. P., Tseng, Y. C., Lin, F. H., Liao, J. D. and Lan, W. H. Treatment of tooth fracture by medium energy of CO₂ laser and DP – bioactive glass paste: The interaction of enamel and DP – bioactive glass paste during irradiation by CO₂ laser. *Biomaterials*. 2001, 22(5), pp.489-496. In: Hirosuke, G., Masatoshi, T., Nobukazu, W., Hideo, K., Takashi, T., Shigeto, A., Yutaka, D. and Yasuo, T. Calcium phosphates as fissure sealant materials fused to enamel by CO₂ laser. I. Monocalcium phosphate monohydrate and dicalcium phosphate dihydrate as fissure sealant materials. *Journal of Gifu Dental Society*. 2008, 35(2), pp.48-54.

[523] Nihei, T., Kurata, S., Umemoto, K. and Teranaka, T. Ceramic coating on enamel surface by a CO₂ laser. *Japanese Journal of Conservative Dentistry*. 2002, 45, pp.649-656. In: Hirosuke, G., Masatoshi, T., Nobukazu, W., Hideo, K., Takashi, T., Shigeto, A., Yutaka, D. and Yasuo, T. Calcium phosphates as fissure sealant materials fused to enamel by CO₂ laser. I.

Monocalcium phosphate monohydrate and dicalcium phosphate dihydrate as fissure sealant materials. *Journal of Gifu Dental Society*. 2008, 35(2), pp.48-54.

[524] Hirosuke, G., Masatoshi, T., Nobukazu, W., Hideo, K., Takashi, T., Shigeto, A., Yutaka, D. and Yasuo, T. Calcium phosphates as fissure sealant materials fused to enamel by CO₂ laser. I. Monocalcium phosphate monohydrate and dicalcium phosphate dihydrate as fissure sealant materials. *Journal of Gifu Dental Society*. 2008, 35(2), pp.55-60.

[525] Fowler, B. O. and Kuroda, S. Changes in heated and in laser – irradiated tooth enamel and their probable effects on solubility. *Calcified Tissue International*. 1986, 38(4), pp.197-208. In: Hirosuke, G., Masatoshi, T., Nobukazu, W., Hideo, K., Takashi, T., Shigeto, A., Yutaka, D. and Yasuo, T. Calcium phosphates as fissure sealant materials fused to enamel by CO₂ laser. I. Monocalcium phosphate monohydrate and dicalcium phosphate dihydrate as fissure sealant materials. *Journal of Gifu Dental Society*. 2008, 35(2), pp.55-60.

[526] Fernandez, T. T. Femtosecond laser written optical waveguide amplifier in phosphotellurite glass. *Optics express*. 2010, 18(19), pp.20289-20297.

[527] A. Jha, B. Richards, G. Jose, M. Irannejad, T. T. Fernandez, P. Joshi, X. Jiang. Rare earth ion doped TeO₂ and GeO₂ glasses as laser materials. *Progress in Materials Science*. 2012, 57(8), pp.1426-1491.

[528]. Parker, S. P. *Dictionary of scientific and technical terms*. Third edition., New York: McGraw Hill Book Company, 1984. In: Webb, P. A. *Interpretation*

of particle size reported by different analytical techniques. Norcross: Micromeritics Instrument Corporation, 2002.

[529] Allen, T. *Particle size measurement*. Third edition. London: Chapman & Hall, 1981. In: Earl, J. S. *In vitro Study of dentine tubule infiltration by hydroxyapatite and silica nanoparticles*. Ph.D. thesis, University of Leeds, 2007.

[530] Malvern Instruments Ltd. *A basic guide to particle characterization*. Malvern Instruments, 2012.

[531] Webb, P. A. *Interpretation of particle size reported by different analytical techniques*. Norcross: Micromeritics Instrument Corporation, 2002.

[532] CPS Instruments. *Comparison of particle sizing methods*. Oosterhout: CPS Instruments Europe, 2001-2013.

[533] Kelsall, R. W., Hamley, I. W. and Geoghegan, M. (eds). *Front Matter, in Nanoscale Science and Technology*. Chichester: John Wiley & Sons, Inc., 2005.

[534] Chatterjee, N. *Electron Microprobe Analysis*. Course 12.141. Massachusetts Institute of Technology, January, 2012.

[535] Goldstein, J. I., Newbury, D. E., Echlin, P., Joy, D. C., Lyman, C. E., Lifshin, E., Sawyer, L. C. and Michael, J. R. *Scanning electron microscopy and X – ray microanalysis*. Third edition. New York: Springer, 2003.

[536] Barker, W. and Fournelle, J. *X – ray compositional microanalysis: EDS and WDS*. 660 Electron Microscopy: Theory and Practice. University of Wisconsin-Madison, 12 October 1996.

- [537] Hammond, C. *Introduction to crystallography*. New York: Oxford University Press, 1990.
- [538] Hollas, J. M. *Modern spectroscopy*, Fourth edition. Chichester: John Wiley & Sons, Inc., 2004.
- [539] Derrick, M. R., Stulik, D. and Landry, J. M. *Infrared spectroscopy in conservation science*. Los Angeles: J. Paul Getty Trust, 1999.
- [540] Coates, J. Interpretation of infrared spectra: A practical approach. In: Meyers, R. A. (ed). *Encyclopedia of analytical chemistry*. Chichester: John Wiley & Sons, Inc., 2000. pp.10815-10837.
- [541] Brown, M. E. *Introduction to thermal analysis*. Second edition. New York: Kluwer Academic Publishers, 2001.
- [542] Ashby, M. F. and Jones, D. R. H. *Engineering Materials: An introduction to their properties and applications*. Oxford: Pergamon Press, 1980.
- [543] PerkinElmer, Inc. *The 30 – minute guide to ICP-MS*. PerkinElmer, 2004-2011.
- [544] Soleimani, N. *Light trapping in fluorescent solar collectors*. Ph.D. thesis, University of Southampton, 2012.
- [545] Stor-Pellinen, J. and Luukkala, M. Paper roughness measurement using airborne ultrasound. *Sensors and Actuators A Physical*. 1995, 49(1), pp.37-40. In: Alam, A., Manuilskiy, A., Thim, J., O’Nils, M., Lindgren, J. and Liden, J. Online surface roughness characterization of paper and paperboard using a line of light triangulation technique. *Nordic Pulp and Paper Research Journal*. 2012, 27(3), pp.662-670.

- [546] Alam, A., Manuilskiy, A., Thim, J., O’Nils, M., Lindgren, J. and Liden, J. Online surface roughness characterization of paper and paperboard using a line of light triangulation technique. *Nordic Pulp and Paper Research Journal*. 2012, 27(3), pp.662-670.
- [547] Shojai, M. S., Atai, M. and Nodehi, A. Design of Experiments (DOE) for the Optimization of Hydrothermal Synthesis of Hydroxyapatite Nanoparticles. *Journal of the Brazilian Chemical Society*. 2011, 22(3), pp.571-582.
- [548] Neira, I. S., Kolenko, Y. V., Lebedev, O. I., Tendeloo, G. V., Gupta, H. S., Guitian, F. and Yoshimura, M. An Effective Morphology Control of Hydroxyapatite Crystals via Hydrothermal Synthesis. *Crystal Growth & Design*. 2009, 9(1), pp.466-474.
- [549] Martins, M. A., Santos, C., Almeida, M. M. and Costa, M. E. V. Hydroxyapatite micro – and nanoparticles: Nucleation and growth mechanisms in the presence of citrate species. *Journal of Colloid and Interface Science*. 2008, 318(2), pp.210-216.
- [550] Jinlong, N., Zhenxi, Z. and Dazong, J. Investigation of phase evolution during the thermochemical synthesis of tricalcium phosphate. *Journal of Materials Synthesis and Processing*. 2001, 9(5), pp.235-240.
- [551] Alshaaer, M., Cuypers, H., Rahier, H. and Wastiels, J. Production of monetite – based inorganic phosphate cement (M-IPC) using hydrothermal post curing (HTPC). *Cement and Concrete Research*. 2011, 41(1), pp.30-37.
- [552] Cimdina, L. B. and Borodajenko, N. Research of calcium phosphates using Fourier transform infrared spectroscopy. In: Theophanides, T. (ed). *Infrared Spectroscopy – Materials Science, Engineering and Technology*. Rijeka: InTech, 2012, pp.123-149.

[553] Xu, J., Butler, I. S. and Gilson, D. F. R. FT – Raman and high – pressure infrared spectroscopic studies of dicalcium phosphate dihydrate ($\text{CaHPO}_4 \cdot 2\text{H}_2\text{O}$) and anhydrous dicalcium phosphate (CaHPO_4). *Spectrochimica Acta A: Molecular and Biomolecular Spectroscopy*. 1999, 55(14), pp.2801-2809.

[554] Nilen, R. W. N. and Richter P. W. The thermal stability of hydroxyapatite in biphasic calcium phosphate ceramics. *Journal of Materials Science: Materials in Medicine*. 2008, 19(4), pp.1693-1702. In: Cimdina, L. B. and Borodajenko, N. Research of calcium phosphates using Fourier transform infrared spectroscopy. In: Theophanides, T. (ed). *Infrared Spectroscopy – Materials Science, Engineering and Technology*. Rijeka: InTech, 2012, pp.123-149.

[555] Krishna, S. R. D., Siddharthan, A., Seshadri, S. K. and kumar, S. T. S. A novel route for synthesis of nanocrystalline hydroxyapatite from eggshell waste. *Journal of Materials Science: Materials in Medicine*. 2007, 18(9), pp.1735-1743. In: Cimdina, L. B. and Borodajenko, N. Research of calcium phosphates using Fourier transform infrared spectroscopy. In: Theophanides, T. (ed). *Infrared Spectroscopy – Materials Science, Engineering and Technology*. Rijeka: InTech, 2012, pp.123-149.

[556] Kothapalli, C., Wei, M., Vasiliev, A. and Shaw, M. T. Influence of temperature and concentration on the sintering behavior and mechanical properties of hydroxyapatite. *Acta Materialia*, 2004, 52(19), pp.5655-5663. In: Cimdina, L. B. and Borodajenko, N. Research of calcium phosphates using Fourier transform infrared spectroscopy. In: Theophanides, T. (ed).

Infrared Spectroscopy – Materials Science, Engineering and Technology.

Rijeka: InTech, 2012, pp.123-149.

[557] Landi, E., Tampieri, A., Celotti, G. and Sprio, S. Densification behaviour and mechanisms of synthetic hydroxyapatites. *Journal of the European Ceramic Society*, 2000, 20(14-15), pp.2377-2387. In: Cimdina, L. B. and Borodajenko, N. Research of calcium phosphates using Fourier transform infrared spectroscopy. In: Theophanides, T. (ed). *Infrared Spectroscopy – Materials Science, Engineering and Technology.* Rijeka: InTech, 2012, pp.123-149.

[558] Lioua, S. C., Chen, S. Y., Lee, H. Y. and Bow, J. S. Structural characterization of nano – sized calcium deficient apatite powders. *Biomaterials*, 2004, 25(2), pp.189-196. In: Cimdina, L. B. and Borodajenko, N. Research of calcium phosphates using Fourier transform infrared spectroscopy. In: Theophanides, T. (ed). *Infrared Spectroscopy – Materials Science, Engineering and Technology.* Rijeka: InTech, 2012, pp.123-149.

[559] Barinov, S. M., Rau, J. V., Cesaro, S. N., Durisin, J., Fadeeva, I. V., Ferro, D., Medvecky, L. and Trionfetti, G. Carbonate release from carbonated hydroxyapatite in the wide temperature range. *Journal of Materials Science: Materials in Medicine.* 2006, 17(7), pp.597-604. In: Cimdina, L. B. and Borodajenko, N. Research of calcium phosphates using Fourier transform infrared spectroscopy. In: Theophanides, T. (ed). *Infrared Spectroscopy – Materials Science, Engineering and Technology.* Rijeka: InTech, 2012, pp.123-149.

[560] Gasga, J. R., Garcia, R. G., Jimenez, M. J. A., Pastenes, E. S., Orozco, G. E. T., Chavarria, I. M. G. and Gasga, G. G. Structural and

thermal behaviour of human tooth and three synthetic hydroxyapatites from 20 to 600°C. *Journal of Physics D: Applied Physics*. 2008, 41(22), pp.1-11.

[561] Shannon, R. D. Revised effective ionic radii and systematic studies of interatomic distances in halides and chalcogenides. *Acta Crystallographica A*. 1976, A32(5), pp.751-767.

[562] Webster, T. J., Schlueter, E. A. M., Smith, J. L. and Slamovich, E. B. Osteoblast response to hydroxyapatite doped with divalent and trivalent cations. *Biomaterials*. 2004, 25(11), pp.2111-2121.

[563] Wei, M., Evans, J. H., Bostrom, T. and Grondahl, L. Synthesis and characterization hydroxyapatite, fluoride – substituted hydroxyapatite and fluorapatite. *Journal of Materials Science: Materials in Medicine*. 2003, 14(4), pp.311-320.

[564] Azad, F. and Maqsood, A. Fabrication, structural characterization, dielectric and electrical parameters of the synthesized nano – crystalline erbium oxide. *Electronic Materials Letters*. 2014, 10(3), pp.557-563.

[565] Devamani, R. H. P. and Alagar, M. Synthesis and characterization of aluminium phosphate nanoparticles. *International Journal of Applied Science and Engineering Research*. 2012, 1(6), pp.769-775.

[566] Mekky, W. and Nicholson, P. S. Nano – aluminum – phosphate via a polymerized organic – inorganic complex route. *Journal of Materials Processing Technology*. 2007, 190(1-3), pp.393-396.

[567] Byrappa, K., Srikantaswamy, S., Gopalakrishna, G. S. and Venkatachalapathy, V. Infrared spectra of aluminium orthophosphate crystals. *Journal of Materials Science Letters*. 1986, 5(2), pp.203-205.

[568] Tahvildari, K., pour, E. M., Ghammamy, Sh. and Nabipour, H. CaF₂ nanoparticles: Synthesis and characterization. *International Journal of Nano Dimension*. 2012, 2(4), pp.269-273.

[569] Wua, C. C., Huang, S. T., Tseng, T. W., Rao, Q. L. and Lin, H. C. FT-IR and XRD investigations on sintered fluoridated hydroxyapatite composites. *Journal of Molecular Structure*. 2010, 979(1-3), pp.72-76.

[570] Suguna, K. and Sekar, C. Role of strontium on the crystallization of calcium Hydrogen phosphate dihydrate (CHPD). *Journal of Minerals and Materials Characterization and Engineering*. 2011, 10(7), pp.625-636.

[571] Ramesh, S., Aw, K. L., Tolouei, R., Amiriyan, M., Tan, C. Y., Hamdi, M., Purbolaksono, J., Hassan, M. A. and Teng, W. D. Sintering properties of hydroxyapatite powders prepared using different methods. *Ceramics International*. 2013, 39(1), pp.111-119.

[572] Friedlander, S. K. Synthesis of nanoparticles and their agglomerates: aerosol reactors. In: Johnson P. M. H. (ed). *Nanoparticles, Nanostructured Materials, and Nanodevices, May 8-9 1997, Arlington*. Lanchaster: World Technology Evaluation Center, 1998, pp.83-88.

[573] Parhami, F., McMeeking, R. M., Cocks, A. C. F. and Suo, Z. A model for the sintering and coarsening of rows of spherical particles. *Mechanics of Materials*. 1999, 31(1), pp.43-61.

[574] Das, S. Physical aspects of process control in direct selective laser sintering of metals. *Advanced Engineering Materials*. 2003, 5(10), pp.701-711.

[575] Demirskyia, D., Agrawala, D. and Ragulya, A. Neck formation between copper spherical particles under single – mode and multimode microwave sintering. *Materials Science and Engineering A*. 2010, 527(7-8), pp.2142-2145.

[576] Barron, R. P., Carmichael, R. P., Marcon, M. A. and Sandor, G. K. Dental erosion in gastroesophageal reflux disease. *Journal of the Canadian Dental Association*. 2003, 69(2), pp.84-89. In: Dawes, C. What is the critical pH and why does a tooth dissolve in acid?. *Journal of the Canadian Dental Association*. 2003, 69(11), pp.722-724.

[577] Dawes, C. What is the critical pH and why does a tooth dissolve in acid?. *Journal of the Canadian Dental Association*. 2003, 69(11), pp.722-724.

[578] Higuchi, W., Mir, N., Patel, P., Becker, J. and Hefferren, J. Quantitation of enamel demineralization mechanisms: III. A critical examination of the hydroxyapatite model. *Journal of Dental Research*. 1969, 48(3), pp.396-409.

[579] Featherstone, J. and Lussi, A. Understanding the chemistry of dental erosion. In: Lussi, A. (ed). *Dental erosion: From diagnosis to therapy*. Basel: Karger, 2006. pp.66-76.

[580] Bin Zainuddin, M. F. *A syudy on mold material and coating effect in sand casting process*. B.Eng. thesis, University Malaysia Pahang, 2009.

[581] Lowe, H. F. and Spindloe, C. White light interferometric profilometry of surface structured glass for high power laser microtargets. In: *Laser Science and Development*. Didcot: Central Laser Facility, 2006-2007.